AFRL-RQ-WP-TM-2013-0200

MICHIGAN/AIR FORCE RESEARCH LABORATORY (AFRL) COLLABORATIVE CENTER IN AERONAUTICAL SCIENCES (MACCAS)

Kenneth G. Powell and Wei Shyy

Regents of the University of Michigan

SEPTEMBER 2012
Final Report

STINFO COPY

AIR FORCE RESEARCH LABORATORY
AEROSPACE SYSTEMS DIRECTORATE
WRIGHT-PATTERSON AIR FORCE BASE, OH 45433-7542
AIR FORCE MATERIEL COMMAND
UNITED STATES AIR FORCE

NOTICE AND SIGNATURE PAGE

*//Signature//
SAMUEL C. MILLER, 1st Lt, USAF
Project Manager
Design and Analysis Branch
Aerospace Vehicles Division

//Signature//
THOMAS C. CO, Maj, USAF, PhD
Chief, Design and Analysis Branch
Aerospace Vehicles Division

//Signature//
 FRANK C. WITZEMAN, Chief
Aerospace Vehicles Division
Aerospace Systems Directorate

REPORT DOCUMENTATION PAGE

1. REPORT DATE *(DD-MM-YY)*	2. REPORT TYPE	3. DATES COVERED *(From - To)*
September 2013	Final	10 April 2006 – 30 September 2013

4. TITLE AND SUBTITLE	5a. CONTRACT NUMBER
MICHIGAN/AIR FORCE RESEARCH LABORATORY (AFRL) COLLABORATIVE CENTER IN AERONAUTICAL SCIENCES (MACCAS)	FA8650-06-2-3625
	5b. GRANT NUMBER
	5c. PROGRAM ELEMENT NUMBER 62201F

6. AUTHOR(S)	5d. PROJECT NUMBER
Kenneth G. Powell and Wei Shyy	2404
	5e. TASK NUMBER N/A
	5f. WORK UNIT NUMBER Q078

7. PERFORMING ORGANIZATION NAME(S) AND ADDRESS(ES)	8. PERFORMING ORGANIZATION REPORT NUMBER
Regents of the University of Michigan Division of Research Development and Administration Department of Aerospace Engineering, University of Michigan 3003 S. State Street, Room 1058 Ann Arbor, MI 48109-1274	

9. SPONSORING/MONITORING AGENCY NAME(S) AND ADDRESS(ES)	10. SPONSORING/MONITORING AGENCY ACRONYM(S)
Air Force Research Laboratory Aerospace Systems Directorate Wright-Patterson Air Force Base, OH 45433-7542 Air Force Materiel Command United States Air Force	AFRL/RQVC
	11. SPONSORING/MONITORING AGENCY REPORT NUMBER(S) AFRL-RQ-WP-TM-2013-0200

12. DISTRIBUTION/AVAILABILITY STATEMENT
Approved for public release; distribution unlimited.

13. SUPPLEMENTARY NOTES
PA Case Number: 88ABW-2013-5059; Clearance Date: 02 Dec 2013. This report contains color and published articles/papers. Research described in journal articles and proceedings reproduced in the appendix was funded by the Government, and though Government personnel may not assert copyright, the stated copyrights apply for the respective publishers and listed contractor authors and should be observed by all recipients of information in the reproduced material. The U.S. Government is joint author of some of the works in the appendix and has the right to use, modify, reproduce, release, perform, display, or disclose the work. For work that was funded in whole or in part by Department of the Air Force contract FA8650-06-2-3625, the U.S. Government has for itself and others acting on its behalf an unlimited, paid-up, nonexclusive, irrevocable worldwide license to use, modify, reproduce, release, perform, display, or disclose the work by or on behalf of the U.S. Government. Some of the published articles have not been cleared for public release by the Air Force, but are already available to the public, and so are de facto cleared.

14. ABSTRACT
The Michigan/AFRL Collaborative Center in Aeronautical Sciences (MACCAS) was awarded as a partnership with the Computational Sciences Center of AFRL. MACCAS consisted of a number of highly accomplished faculty members along with research staff and graduate students from the University of Michigan (UM).

The initial focus of the MACCAS was on developing and integrating all of the computational tools required to perform reliable, high-fidelity, multidisciplinary analysis of air-breathing, hypersonic vehicle concepts. High-performance software was the critical medium of research and an important product of the collaboration. In addition to high-speed aerophysics that is related to hypersonic flight, AFRL's current and projected interest in the following areas was also fully incorporated into our plan: fine-scale unsteady fluid dynamics, and enabling computational technologies and software engineering research.

The following titles (on reverse side) published in professional journals and conference proceedings are provided in the appendix: *See reverse for conclusion of Abstract→*

15. SUBJECT TERMS

16. SECURITY CLASSIFICATION OF:			17. LIMITATION OF ABSTRACT:	18. NUMBER OF PAGES	19a. NAME OF RESPONSIBLE PERSON (Monitor)
a. REPORT Unclassified	**b. ABSTRACT** Unclassified	**c. THIS PAGE** Unclassified	SAR	350	Samuel C. Miller
					19b. TELEPHONE NUMBER *(Include Area Code)* N/A

14. ABSTRACT (concluded)

- "Numerical Study of Energy Deposition Requirements for Aerodynamic Control of Hypersonic Vehicles"
- "Numerical Study of Plasma-Assisted Aerodynamic Control for Hypersonic Vehicles"
- "Numerical Study of Electromagnetic Aerodynamic Control of Hypersonic Vehicles"
- "Numerical Study of Magnetoaerodynamic Flow around a Hemisphere" (published in the Proceedings of the 48th AIAA Aerospace Sciences Meeting)
- "Numerical Study of a MHD-Heat Shield"
- "Numerical Study of Plasma-Assisted Aerodynamic Control for Hypersonic Vehicles"
- "Numerical Study of Magnetoaerodynamic Flow Around a Hemisphere" (published in the *Journal of Spacecraft and Rockets*)
- "State Resolved Vibrational Relaxation Modeling for Strongly Nonequilibrium Flows"
- "Evaluation of a Hybrid Boltzmann-Continuum Method for High Speed Nonequilibrium Flows"
- "A Novel Cartesian Implementation of the Direct Simulation Monte Carlo Method" (published in the Proceedings of the 49th AIAA Aerospace Sciences Meeting)
- "Novel Cartesian Implementation of the Direct Simulation Monte Carlo Method" (published in the *Journal of Thermophysics and Heat Transfer*)
- "Evaluation of a Hybrid Boltzmann-Continuum Method for High-Speed Nonequilibrium Flows"
- "X-HALE: A Very Flexible UAV for Nonlinear Aeroelastic Tests"
- "Flapping-Wing Structural Dynamics Formulation Based on a Corotational Shell Finite Element"
- "Experimental Investigation of Corner Flows in Rectangular Supersonic Inlets with 3D Shock-Boundary Layer Effects"
- "3-D Inlet Shock-Boundary Layer Interactions - PIV Database for the Second SBLI Workshop"
- "Design of a Glass Supersonic Wind Tunnel Experiment for Mixed Compression Inlet Investigations"
- "Implicit LES Simulations of a Flexible Flapping Wing"

Table of Contents

List of Figures

List of Tables

1.0 Executive Summary

In May 2006, the Michigan/AFRL Collaborative Center in Aeronautical Sciences (MACCAS) was established, setting up an ongoing partnership between researchers at the University of Michigan (U-M), Michigan State University (MSU), and the Computational Sciences Center of AFRL.

Based on AFRL needs and the capabilities of faculty researchers, three primary areas of concentration were chosen for MACCAS:

- High-speed aerophysics
- Low-speed and unsteady flows
- Enabling CFD technologies.

Projects were chosen with AFRL input, and many were carried out though close collaboration of researchers at U-M and AFRL. An annual review process was put in place, to ensure that the work of the center was responsive to Air Force needs.

This report summarizes results of several of the projects in each area of concentration. The accompanying digital repository (which can be found at https://umich.box.com/CCASFinal) comprises conference and journal articles that give more full descriptions of the work carried out in MACCAS; it is the definitive final report for the Center.

2.0 High-Speed Aero-Physics

2.1 Numerical Study of Plasma-Assisted Aerodynamic Control for Hypersonic Vehicles
- Iain D. Boyd, Nicholas Bisek, Jon Poggie (AFRL)

Plasma actuators and various forms of volumetric energy deposition have received a good deal of research attention recently as a means of hypersonic flight control. Ground-based and flight experiments are extremely expensive and potentially dangerous, thus creating a need for computational tools capable of quickly and accurately modeling these devices and their effects on the flow-field. This Task addressed these limitations by developing and incorporating several new features into an existing parallelized three-dimensional flow solver to accurately account for electromagnetic effects. A phenomenological heating model was developed and coupled to the fluid solver to investigate whether a practical level of pitch moment control could be achieved from volumetric energy deposition for a representative hypersonic vehicle. The results implied that the shape of the deposition volume does not have a significant effect on the flow structure, whereas the amount of energy deposited greatly influences the flow- field. The results suggest that these systems could be potential replacements for traditional mechanical flaps. While the phenomenological heating model sufficiently characterizes the downstream flow properties, it is a highly simplified physical model. To improve the physical fidelity and accuracy in the near-field, a three-dimensional magnetohydrodynamics (MHD) solver was developed and coupled to the fluid solver. This solver accurately computes the current density and electric field, and accounts for their effects on the flow-field. A particularly important parameter in the MHD solver is the electrical conductivity. Although several semi-empirical models exist in the literature, none provides generality across different flight regimes and gas compositions. Boltzmann's equation provides the necessary generality, but directly coupling a Boltzmann solver to a fluid solver is computationally prohibitive, even for a modern, multi-processor computing facility. A surrogate model of solutions to Boltzmann's equation was developed and coupled to the fluid solver to provide the accuracy and generality of the Boltzmann solver without the computational expense. With this accurate electrical conductivity module, the coupled MHD-fluid solver was used to investigate the effectiveness of a MHD-heat shield, a device that uses a magnet positioned near the bow of the vehicle to reduce the amount of heat transferred to the vehicle.

2.2 High-Fidelity Conjugate Thermal Load Analysis for Hypersonic Vehicles
- Iain D. Boyd, Jonathan Wiebenga, Ryan Gosse (AFRL)

Hypersonic vehicles generate very strong shock waves that heat the air surrounding the vehicle leading to significant heat transfer issues. Ablative thermal protection systems (TPS) are often employed on hypersonic vehicles of interest to the USAF. The analysis of such vehicles requires an approach that couples together the effects of the heated air flow on the ablating TPS, and vice versa. In order to provide high-fidelity analysis of the coupling that exists between the air flow and the TPS, a three-dimensional heat conduction code was developed and coupled with an existing parallelized three-dimensional flow solver. This procedure is used to compute the in-depth heating of a material as well as the mass loss and surface recession of a TPS that occurs due to ablation. This information is then used to update the flow field solution to reflect the new surface location of the vehicle and the additional chemical species introduced into the flow due to ablation. Results from applying this methodology to the ablative nose tip of a reentry vehicle indicate that using a multi-dimensional heat conduction code can lead to significantly different vehicle heating predictions as compared with a one-dimensional heating approximation, especially in regions of high curvature. The different heating predictions can also lead to very different surface recession rates due to changes in the amount of ablative mass loss. These results suggest that for some vehicle geometries such as nose tips or wing leading edges a multi-dimensional heat conduction solution must be computed to accurately predict TPS ablation.

When dealing with coupled flow and structural phenomena, it is often difficult to experimentally validate a numerical code. It is still possible, however, to verify that the implementation and solution of the governing equations is correct. In order to verify the heat conduction code and the coupling procedure between it and the flow code, the Method of Manufactured Solutions was implemented in both codes. Results from this verification

2

technique indicate that the expected order of accuracy for the heat conduction code is observed, which suggests that the governing equations and solution techniques are correctly implemented.

Flow-induced heating can have several effects on a vehicle that are separate from ablation. These include, among other things, thermal degradation of structural materials and flutter or buckling of the vehicle's structure. To aid in the prediction of these types of phenomena, a structural mechanics solver is being added to the heat conduction code. This solver will use the temperatures calculated by the heat conduction code as well as the pressure and viscous stresses from the flow code to compute the stress, strain, and deformation of a structure. The predicted deformations will be passed to the flow code to allow for updated flow predictions based on the updated vehicle geometry. This, along with the heating analysis, allows for high-fidelity coupled predictions of flow induced thermal effects on a hypersonic vehicle.

2.3 Aerothermoelastic and Aeroelastic Studies of Hypersonic Vehicles using CFD

- P. Friedmann

In the final portion of the research on this topic, which was partially funded by MACCAS, the emphasis was on determining the effects of turbulence modeling and real gas equations of state on the aeroelastic and aerothermoelastic stability boundary of a hypersonic vehicle. A framework for aerothermoelastic stability boundary calculation for hypersonic vehicles using CFD combined with radial basis functions for mesh deformation was developed and used to study different turbulence conditions, laminar or turbulent, and different models of the air mixture, in particular real gas model which accounts for dissociation of molecules at high temperature. The effect of transition on the flutter boundary of the heated structure was also considered using an uncertainty propagation framework. The aerothermoelastic stability boundary of a three-dimensional low aspect ratio wing, representative of a control surface of a hypersonic vehicle was examined for various flight conditions. The system is found to be sensitive to turbulence modeling as well as the location of the transition from laminar to turbulent flow. It was found that real gas effects play a minor role on vehicle aerothermoelastic behavior for the flight conditions considered.

The study also demonstrated the importance of accounting for uncertainty at an early stage of the analysis and highlighted the important relation between transition from laminar to turbulent, thermal stresses and stability margins of hypersonic vehicles.

3.0 Low-Speed and Unsteady Flows

3.1 X-HALE: An Experimental Platform to Study Nonlinear/Nonlinear Fluid-Structure Interaction on Very Flexible Aircraft

- C.E.S. Cesnik

Persistent intelligence, surveillance, and reconnaissance (ISR) represent a game-changing capability that is essential for supporting air and space superiority, and by extension, national security of the U.S. [1]. However, successful development of such systems is currently obstructed by a litany of challenges, many of which stem from: 1) large lifting surface deformations that lead to geometric nonlinear motions, 2) tight nonlinear coupling between the aerodynamic, structural, and control subsystems, 3) extremely high aerodynamic efficiency required for long loiter times while flying under Reynolds conditions that is susceptible to flow transition, driving complex fluid-structure interactions, and 4) need to sustain gust loads that may cause evolving vehicle dynamic properties and stability characteristics changes inside the flight envelope. Research is critically needed in order to successfully overcome these issues and enable the development of persistent ISR systems.

While we have been developing numerical tools to address these issues (e.g., [2], [3]), ours and all other numerical efforts must eventually be validated against experimental data so they can be applied to new HALE aircraft concepts. The various components of most of the existing codes have been partially validated with limited experimental data coming from bench and/or small-scale wind tunnel tests. Some of the discipline components have also been compared against well-established numerical solutions (e.g., nonlinear composite beam analyses, rigid flight dynamics, and computational fluid dynamics). There has been, however, no validation of the integrated solution that brings the coupling effects between nonlinear aeroelasticity and flight dynamics, as no data is available for such exercise.

Using the University of Michigan's Nonlinear Aeroelastic Simulation Toolbox (UM/NAST) [3], [4], an experiment (X-HALE) in the form of a remotely piloted aircraft was designed so to be:

- Aeroelastically representative of VFA aircraft, with coupling between rigid body and flexible states;
- Linearly stable under trimmed flight with enough control authority to excite various nonlinear vehicle responses; and
- Capable of static wing deformations greater than 25-percent tip deflection.

The purpose of X-HALE is to provide a platform for conducting fundamental aeroelastic studies and collecting nonlinear aeroelastic-coupled rigid body flight dynamics data in support of validating nonlinear aeroelastic codes. The design presents an unstable (but controllable) Dutch-roll coupled first wing-bending mode when subjected to large disturbances. This lateral behavior would have been very difficult to test in a wind tunnel environment. The choice of construction, materials, and geometry were such that they allow accurate characterization of the stiffness and inertia properties of the aircraft. Detailed description of the initial design is presented in Refs. [4]-[6].

The X-HALE aircraft is a flexible, high aspect ratio wing-boom-tail configuration (see Figure 1) 6-m or 8-m span aircraft, with a 0.2-m chord, five 0.83-m booms with horizontal tails attached, and five motor pods with propellers, batteries, and processor boards. The X-HALE weighs 11 kg (6 m) and 12 kg (8 m) with a flight speed in the range of 12 to 18 m/s. Pitch is controlled by the horizontal elevons and yaw is controlled using differential thrust from the motors. There are ailerons on the dihedral wing segments whose main purpose is to provide known disturbances to the plane (simulating gust excitation).

Approved for public release; distribution unlimited.
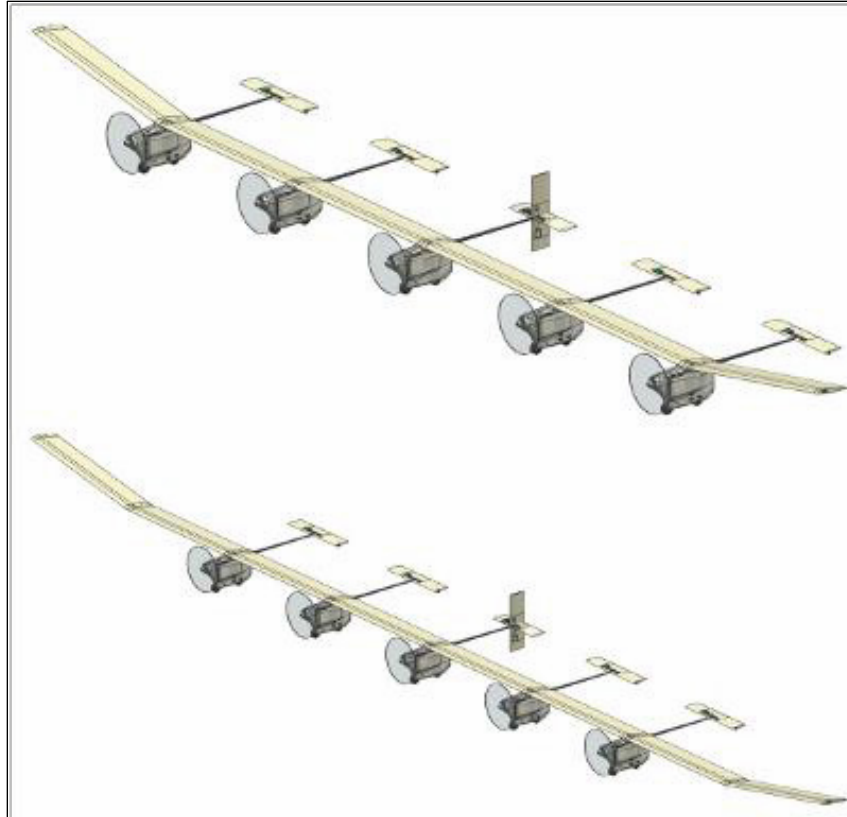
Figure 1: Isoview of the 6-m (top) and 8-m (bottom) X-HALE Configurations

As a risk reduction path for developing a fully instrumented X-HALE, multiple vehicles were conceived with various levels of instrumentation. The primary purpose of the X-HALE Risk Reduction Vehicle (RRV), shown in Figure 2, was to verify the aeroelastic properties of the airframe design and its overall behavior in flight before a fully instrumented X-HALE Aeroelastic Test Vehicle (ATV) could be manufactured. The results of the RRV flight tests showed that the aircraft does exhibit the expected aeroelastic behavior, including a large, sustained wingtip displacement during flight, and an unstable lateral dynamic mode that can be excited using the aircraft's ailerons. Moreover, the aircraft was controllable although presented poor handling qualities. These results successfully confirmed the design goals and opened the way for the assembly of a new fully- instrumented airframe for aeroelastic flight tests. Simulations of the aircraft response due to two segments of one flight associated with two different aileron disturbances were conducted using UM/NAST and comparison with the experimental data were made [7]. In general, due to the poor quality of the data obtained from these initial flights, no conclusions can be made regarding the quality of the correlation. With the fully instrumented ATV airframe, quality data will be obtained and a more realistic correlation study can be conducted. It is our intention to continue on with this program, for which financial support is needed.

Figure 2: X-HALE Risk Reduction Vehicle on the ground (left) and in flight (right)

Approved for public release; distribution unlimited.

3.2 Development of an Approximate Aeroelastic Model for Flapping Wing MAV's, it's Validation and Application to Optimization of Rigid and Flexible Flapping Wings in Hover for Enhanced Performance

- P. Friedmann

An approximate aeroelastic model for simulating flapping-wing micro air vehicles (MAV) has been developed. The aerodynamic model was based on an unsteady vortex model that was initially developed at Cranfield University in UK for flapping rigid wings in hover. We have extended the model to account for wing flexibility and forward flight. An approximate correction for viscosity was also introduced. The approximate unsteady aerodynamic model was validated by comparison with CFD computations and experimental data obtained in the water tunnel at the University of Michigan. Reasonably good correlation between the calculation and the experimental data was obtained as shown in Figures 3 and 4. Table 1 presents the average values of thrust and lateral force during a cycle. Figures 3 and 4 illustrate thrust (C_T) and lateral force (C_L) coefficients time histories are plotted over one cycle. The blue line is the experimental data, the red line is the unsteady approximate vortex model (UAVM) and the black line is the CFD result obtained from solving the Navier Stokes (NS) equations.

Table 1: Time averaged values of CT and CL over one flap pitch cycle

HM1	Experiment	CFD	UAVM
C_L	2.64	2.29	2.17
C_T	2.98	2.50	2.39
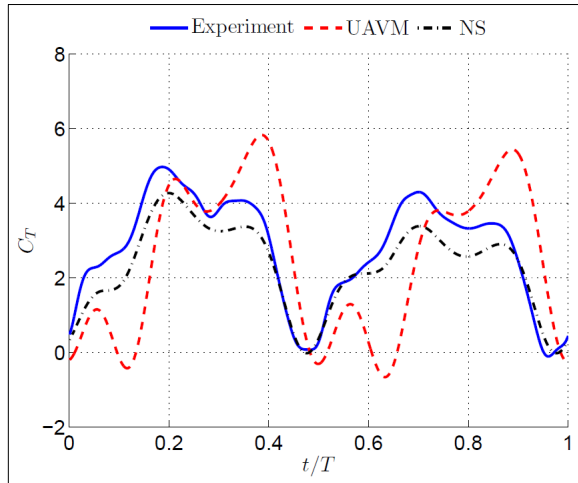
Figure 3: Thrust coefficient
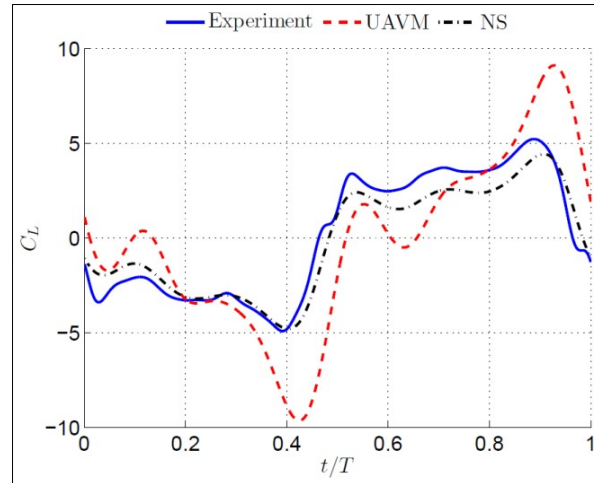
Figure 4: Lateral force coefficient

The approximate aeroelastic model was obtained by combining the approximate unsteady aerodynamic model with a nonlinear structural dynamic model, where the nonlinearity is due to moderate or large elastic deflections of the flexible flapping wing. The structural dynamic model was also suitable for representing complex composite wing structures. The approximate aeroelastic model was used to determine the effect of wing flexibility on the thrust produced by the flapping wing for kinematics representative of hawk moths' wings.

In the final portion of this research the approximate aeroelastic model was combined with an optimizer and the kinematics of both rigid and flexible wings were optimized for enhanced performance. For computational efficiency a surrogate-based approximation of the aerodynamic loads was used. The surrogate was generated

7

using kriging interpolation of time-averaged thrust produced and the power consumed by the flapping wings. For the case of flexible wings in addition to kinematics the composite structure of the wing was also optimized. Thrust and power were found to be competing design objectives. The phase angle between flap and pitch motion was found to be one of the important parameters governing wing performance, for fixed stroke amplitudes and frequency. In some regions of the design space rigid wings performed better than flexible wings indicating that the choice between rigid and flexible wings is not straightforward. Note that the optimization study represented the culmination of this research activity, because without the approximate aeroelastic model the computer resources required for the optimization study would have been prohibitive.

4.0 Enabling CFD Technologies

4.1 The Entropy-Adjoint Approach for Error Estimation and Mesh Refinement

- K. Fidkowski

Output-based error estimation and adaptation relies on the solution of an auxiliary, linear, adjoint problem for the output of interest. This adjoint problem adds computational expense and, often more importantly, implementation overhead for existing computational fluid dynamics codes. In 2009, Fidkowski and Roe proposed an alternative adaptive indicator that shares many features of output-based indicators but does not rely on auxiliary adjoint solutions. Instead, in this entropy-adjoint approach, entropy variables serve as the adjoint solutions and the output is an entropy balance statement. Adapting on this indicator produced meshes and output values that were often comparable to refinement using standard engineering output adjoints. In more recent work under CCAS, we have extended this approach to unsteady problems and to error estimation. The unsteady extension was relatively straightforward and relied on an unsteady adjoint interpretation of the entropy variables. Obtaining useful error estimates was more subtle because the output addressed by the entropy adjoint is an entropy balance statement that is not typically of engineering interest. However, using a relationship between entropy generation and drag, we were able to establish drag error estimates by measuring spurious entropy generation. This led to a capability of estimating the drag error and adapting on it without having to solve an auxiliary adjoint problem. The capability is quite general and includes inviscid, viscous, and Reynolds-averaged turbulent flows in two dimensions. In three dimensions the drag error estimate in its current form deteriorates because it is polluted by spurious entropy from numerically-dissipating trailing vortices – the adaptive indicator, however, is a great vortex indicator. Extending to three dimensions is thus left for future work.
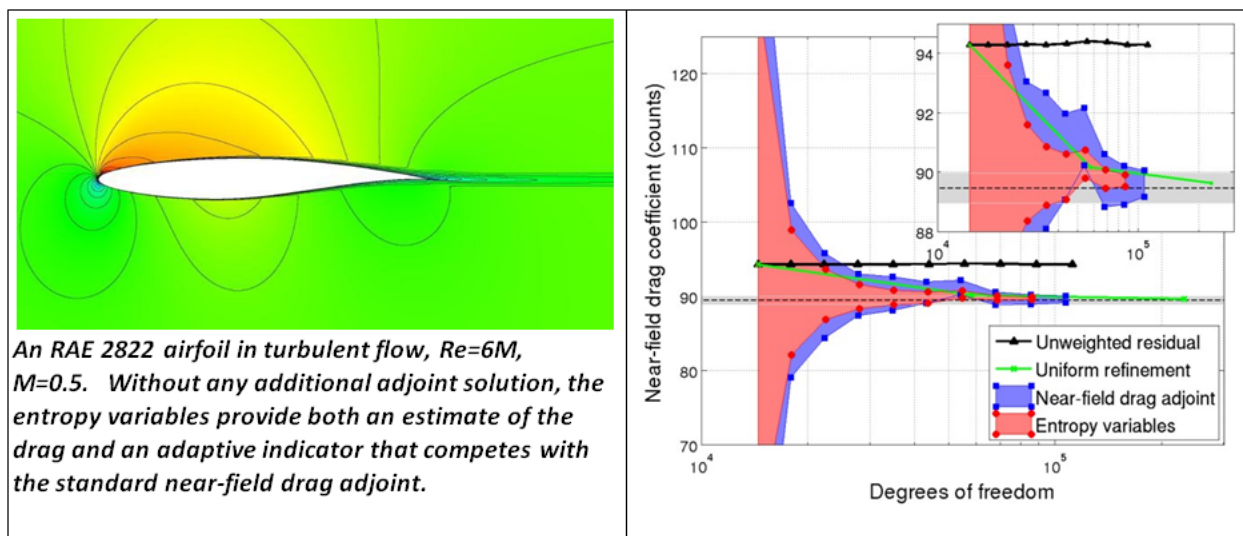
Figure 5: Example of error estimation and mesh refinement for drag prediction

(An RAE 2822 airfoil in turbulent flow, Re=6M, M=0.5. Without any additional adjoint solution, the entropy variables provide both an estimate of the drag and an adaptive indicator that competes with the standard near-field drag adjoint.)

4.2 Output-Based hp-Adaptive Algorithms for High-Order Discretizations

- K. Fidkowski

We have developed robust output-based adaptive algorithms for high-order discretizations of practical three-dimensional flows. These algorithms are based on discrete adjoint solutions, which yield output errors and adaptive indicators for refinement. Using solutions of local sub-problems, we equip the error estimates with the capability to determine anisotropy of refinement for most efficiently reducing the targeted error. Including order refinement as a candidate refinement option gives rise to an hp-adaptive algorithm that does not need an ad-hoc smoothness indicator. Application of these techniques to practical problems brings several solver challenges: for example, on coarse grids used early in adaptation, a zero-residual solution may not be possible due to under-resolution. In addition, solutions of the Reynolds-averaged Navier-Stokes equations on complex three-dimensional domains without good initial guesses require sophisticated continuation strategies. To address these problems, we have developed a pseudo-transient continuation algorithm that constrains the iterative solution path to respect physical requirements such as positive density and pressure. This algorithm is used together with a residual-based robustness refinement technique that is active in cases of unrecoverable solver errors due to severe mesh under-resolution.

Note in Figure 6, on the left, output-based drag convergence for the CRM used in the fifth AIAA drag prediction workshop, showing error bars available from the adjoint-based error assessment. On the right, adaptive results for an unsteady staggered airfoil simulation, showing substantial benefits of adapting on error estimates obtained from unsteady adjoints
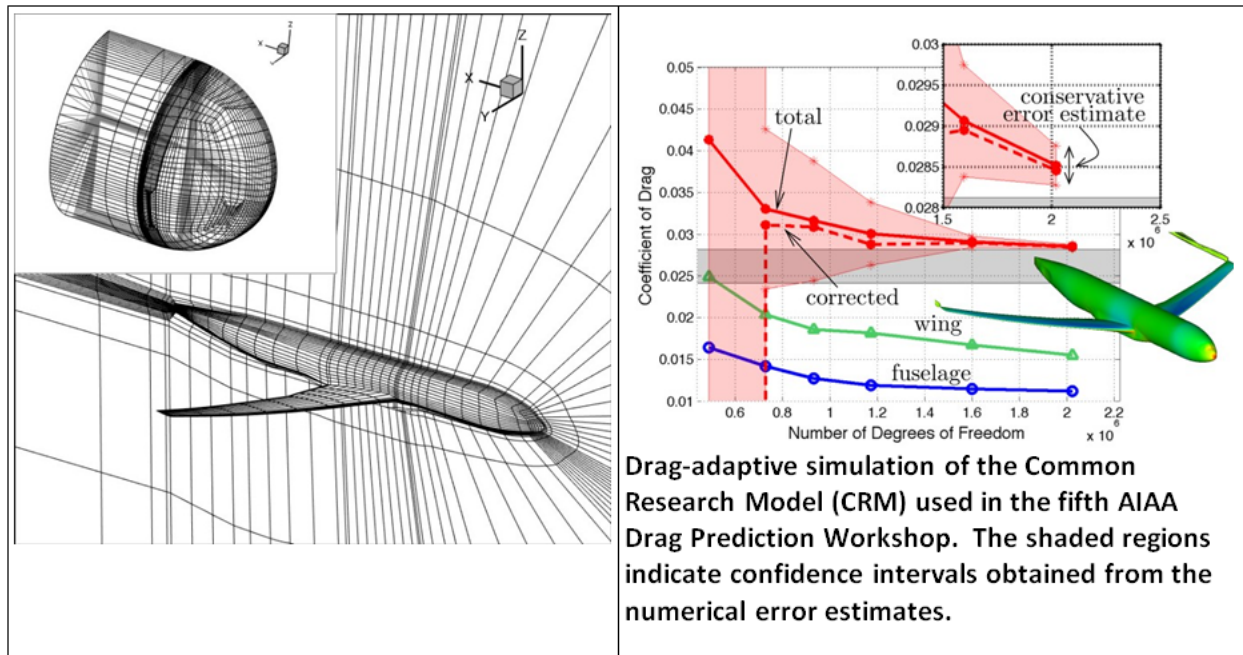
Figure 6: Drag-adaptive Simulation of the Common Research Model

4.3 Aerodynamic Shape Optimization for a Blended Wing-Body (BWB) Aircraft

- J. Martins

The objective of this project was to explore the design space for the BWB aerodynamic shape optimization while considering trim and stability constraints. In the process, we identified weaknesses in the aerodynamic model originally used, and developed the capability to perform design optimization with the Reynolds-averaged Navier-Stokes equations.

To achieve the objectives of this project, we used a framework previously developed that incorporated a CFD solver, a geometry engine, a mesh warping algorithm, and gradient-based numerical optimization software. The key component in this framework is the capability of computing gradients of objectives and constraints with respect to thousands of design variables efficiently using an adjoint method.

We started by performing a series of aerodynamic shape optimization runs using Euler CFD and found various interesting tradeoffs between the trim and stability requirements (see attached figure and reference 10). However, we identified a weakness in this model, because it allowed large non-physical pressure recovery regions. Hence, we decided to develop the adjoint method for the full Reynolds- averaged Navier-Stokes (RANS) equations. This effort was successful, and lead to the publication of a new technique to develop the adjoint equations and to the comparison of Euler and RANS optimization results [8]. We also ran a RANS version of the BWB optimization cases, and found that the RANS optimization behaved a lot better, and lead to different conclusions when it comes to BWB design. More details can be found in Reference 9.
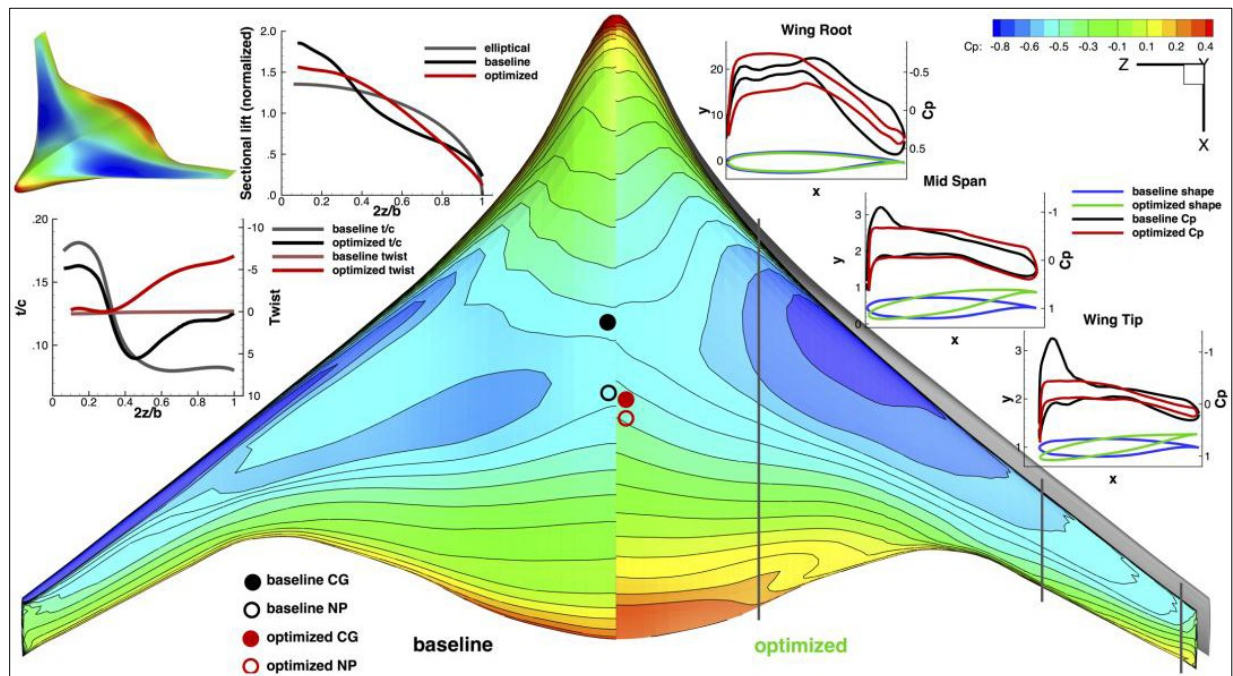
Figure 7: Baseline (left) and Optimized (right) blended wing-body aircraft

4.4 Solid-boundary condition for moment systems

- Bram van Leer and Loc Khieu

This project focused on developing physically plausible and unambiguous boundary conditions for Grad-type hyperbolic-relaxation moment systems, which we propose as an alternative to the prevalent Navier-Stokes-Fourier (NSF) system. For non-equilibrium physics, the NSF system is severely limited due to its intrinsic assumption that the flow is in local equilibrium.

Moment systems, such as Grad's 13-moment (13M) system, are derived by taking a number of velocity moments of the Boltzmann-BGK (BGK) equation. Such systems potentially encompass more flow phenomena (than the NSF system) owing to a larger set of independent flow variables. Compared to the BGK equation, however, they contain less information about the fluid's evolution; thus, it makes sense to use solutions of the BGK equation to benchmark solutions of moment systems.

To achieve physical plausibility and unambiguity, the boundary conditions must be derived from a microscopic view of the fluid-wall interaction; the conditions for the moment systems are conceptually the same as for the BGK equation. We have formulated two boundary-condition models: the 1-C condition based on non-penetration only, and the 2-C condition satisfying an additional normalization constraint.

The chief effort in this project is the validation of the 13M system by the BGK equation by numerically simulating low-speed Couette and Poiseuille flows, utilizing both boundary conditions. The BGK and 13M codes both existed with a Finite-Volume and a Discontinuous Galerkin option. In order to ensure that all our flow codes produce the correct physics, we spent great efforts in running grid- convergence studies for each one of them. This helped us make the most efficient grid selection for each Knudsen number.

Our experiments show that all wall quantities (u_x, P_{xy}, q_x, q_y) compare reasonably well with the values produced by the BGK equation, up to and including Kn=1. In contrast, the NSF system with a velocity-slip condition yields only a reasonable value for P_{xy}. On the other hand, the profiles of u_x, q_x, q_y away from the wall as computed by 13M do not match the smoothness of the BGK solutions, particularly for Kn≤1. We therefore recommend the use of the 13M system in applications where it is especially important to have accurate wall values, and the solutions away from the wall are less important. The description is suited for subsonic and transonic flows, at low to moderate Knudsen numbers.
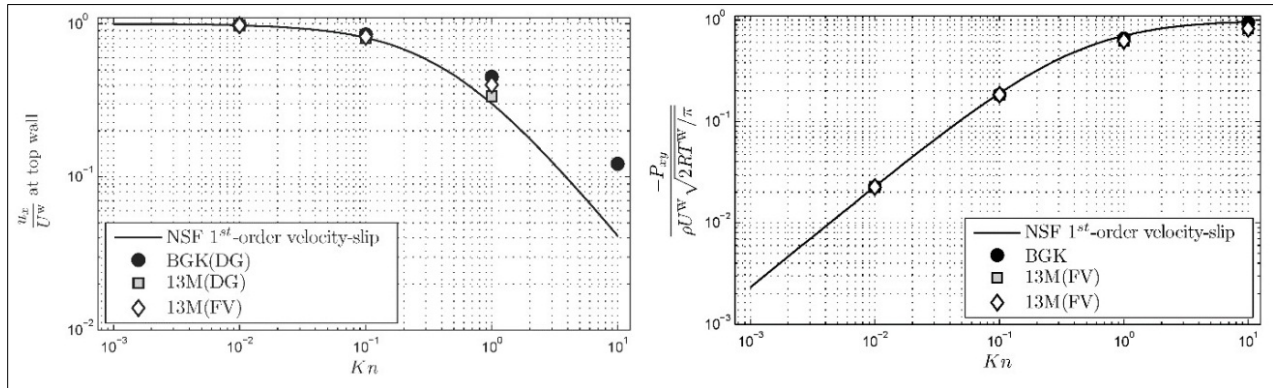
Figure 8: Horizontal velocity u_x and shear stress P_{xy} at the solid boundary for Couette flow, obtained by 1-C boundary condition

(The 13M system matches the BGK equation reasonably well for all Kn≤1, while the Navier-Stokes-Fourier (NSF) system with a velocity-slip boundary condition yields only a reasonable value for P_{xy}. The value of ux for �=10 is omitted due to the appearance of divergent and spurious oscillations in its solution profile; a plausible explanation is that the 13M system lacks inherent dissipation.)

<u>Optimal Accuracy of Discontinuous Galerkin for Diffusion</u>

- Bram van Leer, Marcus Lo and Loc Khieu

This research project aimed at achieving the highest accuracy for diffusion operators possible with a Discontinuous Galerkin (DG) method, and establishing the superiority of Recovery-based DG (RDG), developed by us earlier.

DG was originally developed for advection-type operators, for which it is pre- eminently suited, but soon got applied to diffusion operators because of the need to model advection-diffusion processes with one numerical strategy. DG, however, is not naturally suited for diffusion operators, precisely because of the discontinuous solution representation, and requires a special step to overcome this handicap. Most of the newer methods require rewriting the second-order differential operator as a system of first-order operators, in order to arrive at a stable and accurate approximation. In RDG a smooth solution basis, weakly identical to the discontinuous basis, is introduced for computing diffusive fluxes. We posed the following question: for a given order p of its polynomial basis, what is the maximum order of accuracy DG can reach for diffusion-shear, if we allow only the direct neighbors of an element to participate in the discretization? The answer was only known in part. On a Cartesian grid, which brings out the best in all DG methods, RDG was previously demonstrated to achieve the order 3p+2 or 3p+1 for p even or odd, respectively; this is the highest order found so far among DG schemes for diffusion. During the period of the CCAS contract, this result has been proven to be robust: it holds in any number of dimensions, for nonlinear equations and equations with mixed derivatives, provided that

- A tensor-product basis is used for the solution (sufficient for linear diffusion);
- Solution enhancement, a technique of weak interpolation from element boundary to interior, is used to improve the volume integral in the DG equation for nonlinear diffusion;
- An extra recovery step is used to improve the element-boundary integral in the presence of shear.

When the tensor-product basis is abandoned for a lean basis of order p, the resulting order of RDG for diffusion on a Cartesian grid, with solution enhancement but without the extra recovery step, reduces to 2p+2, which is still attractive. On simplex elements one cannot maintain a tensor basis anyway, so we expect that on unstructured triangular or tetrahedral grids the order barrier is at best 2p+2. Most DG methods for diffusion, including basic RDG-1x, reduce to the order of accuracy p+1 even on a structured grid of orthogonal triangles; only Hybrid DG (developed by J. Peraire) has been shown to yield p+2, owing to the use of independent face data.

Shortly before the closing of this research project we have been able to show for a linear diffusion operator on triangles that the optimal order of accuracy indeed is 2p+2, but only for even p; for odd p the same method reduces to order 2p. Whether this last result can be improved upon remains to be seen. On the other hand, our experience in the Cartesian case gives us confidence that the orders achieved for linear diffusion will extend to Navier-Stokes discretizations.

5.0 References

[1] Tilmann, C.P., Flick P.M., Martin C.A., and Love M.H. High-Altitude Long Endurance Technologies for SensorCraft. RTO AVT Symposium on Novel and Emerging Vehicle and Vehicle Technology Concepts. Brussels, Belgium, April 2003. RTO Paper MP-104-P-26, 2003

[2] Hallissy, B.P. and Cesnik, C.E.S., "High-fidelity Aeroelastic Analysis of Very Flexible Aircraft," 52nd AIAA/ASME/ASCE/AHS/ASC Structures, Structural Dynamics, and Materials Conference, Denver, Colorado, April 4-7, 2011.

[3] Su, W. and Cesnik, C.E.S., "Dynamic Response of Highly Flexible Flying Wings," AIAA Journal, Vol. 49, No. 2, February 2011, pp. 324-339.

[4] Cesnik, C.E.S., Senatore, P.J., Su, W., Atkins, E.M., and Shearer, C.M, "X-HALE: A Very Flexible Unmanned Aerial Vehicle for Nonlinear Aeroelastic Tests," AIAA Journal, Vol. 50, No. 12, 2012, pp. 2820-2833.

[5] Cesnik, C.E.S., Senatore, P.J., Su, W., Atkins, E.M., Shearer, C.M., and Pitcher, N.A., "X-HALE: A Very Flexible UAV for Nonlinear Aeroelastic Tests," 51st AIAA/ASME/ASCE/AHS/ASC Structures, Structural Dynamics, and Materials Conference, Orlando, Florida, April 12-15, 2010.

[6] Cesnik, C.E.S. and Su, W., "Nonlinear Aeroelastic Simulation of X-HALE: a Very Flexible UAV," 49th AIAA Aerospace Sciences Meeting, 4 - 7 January 2011, Orlando, Florida.

[7] Jones, J.R. and Cesnik, C.E.S., "Preliminary Flight Test Correlations of the X- HALE Aeroelastic Experiment," International Forum on Aeroelasticity and Structural Dynamics, Bristol, UK, June 2013.

[8] Z. Lyu, G. K. Kenway, C. Paige, and J. R. R. A. Martins. Automatic differentiation adjoint of the Reynolds-averaged Navier–Stokes equations with a turbulence model. In 21st AIAA Computational Fluid Dynamics Conference, San Diego, CA, Jul 2013. DOI: 10.2514/6.2013-2581

[9]. Z. Lyu and J. R. R. A. Martins. RANS-based aerodynamic shape optimization of a blended-wing-body aircraft. In 21st AIAA Computational Fluid Dynamics Conference, San Diego, CA, Jul 2013. DOI: 10.2514/6.2013-2586

[10] Z. Lyu and J. R. R. A. Martins. Aerodynamic shape optimization of a blended-wing-body aircraft. In Proceedings of the 51st AIAA Aerospace Sciences Meeting, Grapevine, TX, Jan. 2013. AIAA 2013-0283.

Approved for public release; distribution unlimited.

6.0 List of Acronyms, Abbreviations, and Symbols

Acronym	Description
AFRL	Air Force Research Laboratory
AIAA	American Institute for Aeronautics and Astronautics
ATV	Aeroelastic Test Vehicle
BGK	Boltzmann-BGK equation
BWB	Blended Wing Body
CCAS	Collaborative Center in Aeronautical Sciences
CFD	Computational Fluid Dynamics
C_L	Coefficient of lateral force
CRM	Common Research Model
C_T	Coefficient of thrust
DG	Discontinuous Galerkin
ISR	Intelligence, surveillance, and reconnaissance
MACCAS	Michigan/AFRL Collaborative Center in Aeronautical Sciences
MAV	Micro Air Vehicle
MHD	Magnetohydrodynamics
MSU	Michigan State University
NS	Navier Stokes
NSF	Navier-Stokes-Fourier
RANS	Reynolds-Averaged Navier-Stokes
RDG	Recovery-based Discontinuous Galerkin
RRV	Risk Reduction Vehicle
TPS	Thermal protection systems
UAVM	unsteady approximate vortex model
UM	University of Michigan
UM/NAST	University of Michigan's Nonlinear Aeroelastic Simulation Toolbox
VFA	Very Flexible Aircraft

Numerical Study of Energy Deposition Requirements
for Aerodynamic Control of Hypersonic Vehicles

Nicholas J. Bisek[*] and Iain D. Boyd[†]

Department of Aerospace Engineering, University of Michigan, Ann Arbor, MI, 48109, USA

and

Jonathan Poggie[‡]

Air Force Research Laboratory, Wright-Patterson AFB, OH, 45433-7512, USA

Plasma actuators and various forms of volumetric energy deposition have received a good deal of research attention recently as a means of hypersonic flight control. An open question remains as to whether the required power expenditures for such devices can be achieved for practical systems. To address this issue, a numerical study is carried out for Mach 12 flow over a blunt nose elliptic cone to determine the amount of energy deposition necessary for flight control. Energy deposition is simulated by means of a phenomenological dissipative heating model. Validation studies of the flow simulation code in the absence of energy deposition are presented for a Mach 8 elliptic cone flow and a Mach 14 blunt elliptic cone. A parametric study of the effects of energy deposition is carried out for two blunt-nosed elliptic cone configurations: a 3 m long cone at Mach 12.6 and 40 km altitude, and a 0.2 m long cone at Mach 14.2 and roughly 42 km effective altitude. Three different volumetric energy deposition patterns are considered: a spherical pattern, a 'pancake' pattern (oblate spheroid), and a 'bean' pattern (prolate spheroid). The effects of energy deposition are seen to be relatively independent of these patterns. For the Mach 12.6 cone case, the pitching moment generated by energy deposition is 10-30% of that generated by a 0.05 m^2 mechanical flap at $2°$ deflection. For the Mach 14.2 case, the corresponding figure of merit is on the order of 1000%. The effectiveness of volumetric energy deposition for flight control appears to scale strongly on the nondimensional parameter $Q/(\rho_\infty u_\infty^3 L^2)$, and additional computations are warranted to explore this effect.

Nomenclature

ρ	= mass density
μ	= coefficient of viscosity
$\mathbf{u}$	= velocity vector (u, v, w)
x, y, z	= streamwise, spanwise, and transverse coordinates
i, j, k	= computational grid indices along the axial, radial, and circumferential directions
a, b, c	= the equatorial radii and the polar radius of an ellipsoid
ϕ	= angle between the x-axis of the ellipsoid and the x-axis of the flow
θ	= ramp angle
A	= surface area of grid cell
$\mathbf{n}$	= normal vector
p	= pressure
τ	= viscous stress
E	= total energy per volume
$\mathbf{q}$	= heat flux (translational, rotational, and vibrational)

[*]Graduate Student, Student Member AIAA

[†]Professor, Associate Fellow AIAA

[‡]Senior Aerospace Engineer, AFRL/VAAC. Bldg. 146 Rm. 225, 2210 Eighth St. Associate Fellow AIAA

American Institute of Aeronautics and Astronautics Paper 2008-1109

16

S = source term
Q = total power input by actuator
$\tilde{Q}$ = nondimensional total power input by actuator, $Q/(\rho_\infty u_\infty^3 L^2)$
T = temperature (translational and rotational)
Tv = temperature (vibrational)
h = enthalpy
χ = mole fraction
L = axial surface length
C_p = pressure coefficient, $[2(p_w - p_\infty)]/[\rho_\infty u_\infty^2]$
St = Stanton number, $q_w/[\rho_\infty u_\infty (h_0 - h_w)]$
Re_x = running Reynolds number, $\rho_\infty u_\infty x/\mu_\infty$

Subscript
∞ = free stream
w = wall

I.   Introduction

Aerodynamic control and drag reduction are major challenges for hypersonic vehicle designers. A good deal of research attention has recently focused on hypersonic plasma interactions and plasma flow control to explore ways of confronting these challenges.[3,4]

Minimizing drag in vehicle design leads to long thin bodies with sharp leading edges. This constrains the materials available for the vehicle's Thermal Protection System (TPS) because there is a required minimum thickness which may not be achieved for a given vehicle configuration. In addition, small defects in the production of the sharp edges can result in serious or even catastrophic problems for the TPS.[5] Blunting the leading edge reduces these drawbacks but results in a much larger wave drag.[6] Recent experimental and computational research by Shang *et al.*[7] has investigated ways of reducing drag on blunt nose bodies by means of plasma injection, while research by Kremeyer *et al.*[8] and Yan[9] focused on drag reduction and flow control using laser deposition (filamentation) ahead of conic and spherical geometries.

In addition to the design constraints, extreme heat, and pressure, traditional control surfaces (flaps) need to be positioned away from the center of gravity to extend the maneuverability of the vehicle. The location of such flaps is limited because the bow shock surrounding the vehicle will impinge on surfaces that extend beyond the shock envelope. This results in extreme pressure and heat transfer rates at the impingement point. As such, vehicle configurations tend to be streamlined with minimal protrusions from the fuselage. Mechanically driven flaps require clearance below the surface of the flap to provide space for the flap control arm and a strong attachment point to push from. In addition, there is a small gap in the TPS as the flap extends out to deflect the flow. This gap is difficult to protect and can cause heat related damage to the vehicle.

Plasma actuators are advantageous over mechanical controllers because they do not have moving parts, can be located either in or beneath the TPS, and use an electric power source. This extends the range of possible locations for the actuator and allows for multiple actuators to be powered by a central energy source. They can potentially be turned on and off very rapidly, and should have a minimal aerothermal penalty when turned off. Plasma actuators can serve multiple roles. They can be used to provide steering moments,[10] changes in vehicle lift,[11] control of flow separation,[12,13] and local heat load mitigation.[14]

The primary objective of this research effort is to determine whether a useful degree of flight control can be achieved with practical levels of energy deposition by investigating the effects of energy deposition on a realistic hypersonic vehicle and its surrounding flow-field. In the following, we first present code validation studies using experimental data in the literature. Having successfully validated LeMANS, the code is applied to investigate plasma-based aerodynamic control.

II.   Method

Flow-field results are obtained using Computational Fluid Dynamics (CFD) to solve the Navier-Stokes equations. The CFD computations are executed using the Michigan Aerothermodynamic Navier-Stokes

(LeMANS) code which was developed at the University of Michigan.[15, 16]

LeMANS is a general 2D/axisymmetric/3D, parallel, unstructured finite-volume CFD code. The numerical fluxes between cells are discretized using a modified Steger-Warming Flux Vector Splitting (FVS) scheme, except near shock waves. In these regions the original Steger-Warming FVS scheme is used. LeMANS employs a two-temperature model to account for thermal-nonequilibrium and a standard finite rate chemistry model for non-equilibrium chemistry. The two temperature model assumes that a single temperature T accounts for the translational and rotational energy modes of all species while the vibrational energy mode is accounted for by a separate temperature Tv.

The usual conservation equations are solved:

$$\frac{\partial \rho}{\partial t} + \nabla \cdot (\rho \mathbf{u}) = 0 \tag{1}$$

$$\frac{\partial \rho \mathbf{u}}{\partial t} + \nabla \cdot (\rho \mathbf{u}^2 + p\delta_{ij} - \tau) = 0 \tag{2}$$

$$\frac{\partial E}{\partial t} + \nabla \cdot ((E + p)\mathbf{u} - \tau \cdot \mathbf{u} - \mathbf{q}) = S \tag{3}$$

LeMANS assumes the fluid is continuous and Newtonian. It also assumes Stokes' hypothesis when determining the viscous stresses.

$$\tau_{ij} = \mu \left(\frac{\partial u_j}{\partial x_i} + \frac{\partial u_i}{\partial x_j} \right) - \frac{2}{3}\mu \nabla \cdot \mathbf{u}\delta_{ij} \tag{4}$$

A thermal actuator is considered as the plasma control device in this study. It is represented by a phenomenological model of dissipative heating. This model is accounted for in the Navier-Stokes equations by the addition of a source term S to the right side of energy equation (3). The shape, strength, and location of the actuator are modeled using exponential decay of an ellipsoidal region.[17]

$$S = \frac{Q}{\pi^{3/2}\, a \cdot b \cdot c} e^{\left(-\left(\frac{\hat{x}}{a}\right)^2 - \left(\frac{\hat{y}}{b}\right)^2 - \left(\frac{\hat{z}}{c}\right)^2\right)} \tag{5}$$

$$\begin{aligned} \hat{x} &= (x - x_0)\cos\phi - (z - z_0)\sin\phi \\ \hat{y} &= (y - y_0) \\ \hat{z} &= (x - x_0)\sin\phi + (z - z_0)\cos\phi \end{aligned} \tag{6}$$

Variables a and b are the equatorial radii (along the x and y axes) and c is the polar radius (along the z-axis). The angle ϕ is the angle between the x-axis of the ellipsoid and the x-axis of the flow. Coordinates (x_0, y_0, z_0) represent the centroid of the ellipsoid. Note that Q represents the total power deposited in the flow and $\iiint_{-\infty}^{\infty} S\, dx\, dy\, dz = Q$

The simulations are performed using second-order accurate discretization and carry double precision arithmetic throughout. Thermal equilibrium and a five species air chemistry model (N_2, O_2, NO, N, and O) are used in the simulations presented.

III.   Results

III.A.   3D Sharp Elliptic Cone

Three dimensional calculations are carried out for a Mach 8 sharp elliptic cone originally studied experimentally by Kimmel $et\ al.$.[1, 18] The cone was mounted parallel to the freestream and consisted of a 2:1 aspect ratio, a half angle along the major axis of 14°, and a length $L = 1.016$ m. It was machined from stainless steel with a 40 μm nose radius and surface roughness less than 0.81 μm. The flow conditions are listed in Table 1.

A structured grid is generated because it is known to produce better results in regions near the surface of the body and through a shock.[19] One quarter of the geometry is used in the simulation because planes of symmetry exist along the major and minor axes. The 40 μm nose radius is accounted for along the tip's minor axis, resulting in a 80 μm radius along the major axis because of the elliptic geometry.

18

Approved for public release; distribution unlimited.

Parameter	Value	
M	7.93	
u_∞	1175.0	$^m/_s$
T_∞	54.6	K
T_w	303.0	K
T_0	728.0	K
p_∞	165.0	Pa
ρ_∞	0.010533	kg/m^3
μ_∞	3.77×10^{-6}	$kg/_{m \cdot s}$
Re_L	3.33×10^6	

Table 1. Flow conditions for the experiment of Kimmel et al.[1,18]

The model is aligned with the x-axis in the axial direction, the y-axis in the horizontal direction, and the z-axis in the vertical direction. A cylindrical coordinate system is also employed with $\theta = 0°$ at the top centerline of the model (z-axis) and $\theta = 90°$ at the leading edge (y-axis) as seen in Figure 1.

A gradual increase in grid spacing is used along the conic body with the smallest spacing near the tip. Radial points are algebraically spaced to increase the number of points close to the body. Grid points are equally spaced along the circumference. As a result, cell clustering occurs near the surface and the tip of the body. A grid independence study is conducted with $i \times j \times k$ grid dimensions changing from $330 \times 40 \times 30$ (coarse), to $440 \times 50 \times 40$ (medium), to $550 \times 60 \times 50$ (fine). Figure 2 shows very little change in Cp or St between the medium and fine grids, therefore the medium grid ($440 \times 50 \times 40$) is considered grid independent and used in the rest of the analysis.

Cross-sectional slices of the computed surface conditions are extracted to match the locations of the experimental measurements. Figure 3(a) shows the non-dimensional pressure along the circumference of the body at x/L = 0.625. The pressure is relatively constant from the top centerline ($\theta = 0°$) to the shoulder ($\theta = 45°$), followed by a noticeable rise between the shoulder and the leading edge ($\theta = 90°$). This behavior was also observed by Burke for a Mach 10 flow.[20] Kimmel et al. also provided computational results from a parabolized Navier-Stokes (PNS) solver[1,18] which are included in the figures as an additional reference.

Although the cone is sharp, the formation of the boundary layer at its tip results in a sharp rise in pressure and temperature near the stagnation point. This rise in pressure can be seen in Figure 3(b) for two different rays. The pressure quickly relaxes as the flow proceeds along the rest of the cone due to the viscous interaction.

The high length Reynolds number (Re_L) and overall length of the model cause the flow to transition to turbulence as it proceeds along the body. LeMANS does not currently have a turbulence model implemented, so numerical results in the transition and turbulent regions should be disregarded. Plots of the Stanton number as a function of Reynolds number are presented in Figures 4(a), 4(b) and 4(c) for $\theta = 0°$, $45°$, $88°$. In all three plots, the flow starts laminar and then transitions to turbulent as it proceeds along the body. The measured data were for $Re_L = 1.7 \times 10^6$ and 6.6×10^6, whereas the case run by LeMANS has $Re_L = 3.3 \times 10^6$. As observed in the figures, the length Reynolds number does not affect the Stanton number in the laminar region for these cases.

III.B.   3D Blunt Elliptic Cone

A second three dimensional validation study is performed on a Mach 14 blunt elliptic cone originally studied experimentally by Nowlan et al..[2] The model was mounted parallel to the freestream and had a 2:1 aspect ratio, a half angle along the major axis of $10°$, and a length L = 0.21 m. Details of cone geometry are provided in Fig. 5. The flow conditions are listed in Table 2.

A structured grid is generated following the same procedures and coordinate system as the sharp elliptic cone. A grid independence study is conducted with $i \times j \times k$ grid dimensions changing from $150 \times 30 \times 30$ (coarse), to $300 \times 60 \times 60$ (medium), to $380 \times 80 \times 80$ (fine). Figure 6 shows very little change in Cp or St between the medium and fine grids, therefore the medium grid ($300 \times 60 \times 60$) is considered grid independent and used in the rest of the analysis.

19

Parameter	Value	
Mach	14.15	
u_∞	2184.8	$^m/_s$
T_∞	59.3	K
T_w	294.4	K
T_0	2105.0	K
p_∞	51.0	Pa
ρ_∞	0.002995	$^{kg}/_{m^3}$
μ_∞	4.3×10^{-6}	$^{kg}/_{m \cdot s}$
Re_L	3.17×10^5	

Table 2. Flow conditions for Run 15 of the Nowlan *et al.* experiment.[2]

Figure 7 shows the non-dimensional pressure along the circumference of the body at two axial locations and along two rays. Following a similar trend as the sharp cone observations, the pressure is relatively constant from the top centerline to the shoulder, followed by a gradual rise between the shoulder and the leading edge. The variation in pressure distribution along the rays is much more dramatic compared to the sharp cone because the blunt tip results in a strong detached bow shock and, consequently, a large stagnation region.

Stanton number distributions in Fig. 8 show that LeMANS follows the same trends as those observed in the measurements. Overall, LeMANS effectively demonstrates its capability of accurately computing three dimensional hypersonic flows.

III.C. Realistic Hypersonic Geometry

The blunt elliptic cone geometry is selected to represent a realistic hypersonic vehicle, with $L = 3$ m set as the representative vehicle length. Assuming the vehicle has constant material density, its center of gravity (CG) is located 1.95 m from the tip along the x-axis (x/L = 0.65). The model is simulated in air at 40 km altitude, with a freestream velocity of 4000 $^m/_s$. The complete flow conditions are provided in Table 3.

Parameter	Value	
Mach	12.6	
u_∞	4000.0	$^m/_s$
T_∞	250.4	K
T_w	300.0	K
T_0	8300.0	K
p_∞	289.2	Pa
ρ_∞	0.003995	$^{kg}/_{m^3}$
μ_∞	1.6×10^{-5}	$^{kg}/_{m \cdot s}$
Re_L	3.0×10^6	

Table 3. Flow conditions for Mach 12.6 air flow at an altitude of 40 km.

A grid independence study is conducted with $i \times j \times k$ grid dimensions changing from $150 \times 30 \times 30$ (coarse), to $300 \times 60 \times 60$ (medium), to $380 \times 80 \times 80$ (fine), to $400 \times 80 \times 120$ (very fine). Figure 9 shows very little change in Cp or St between the fine and very fine grids. Grid independence is achieved with the $380 \times 80 \times 80$ (fine) grid and is used in the following simulations that include energy deposition.

III.C.1. Nominal Force Requirement

An estimate of the pitching moment produced by a mechanical flap attached to this nominal vehicle is found by assuming a 2° flap with a cross-sectional area of 0.05 m² (0.5 m × 0.1 m) is attached along the vehicle's

American Institute of Aeronautics and Astronautics Paper 2008-1109

Approved for public release; distribution unlimited.

top centerline as illustrated in Fig. 10. Figure 11 plots a cross-sectional slice of Mach number contours where the beginning of the flap protrudes from the body. Setting $M_\infty = 1.5$ and $\theta = 2°$, oblique shock theory is used to find $p_{flap} \approx 1000$ Pa. This results in a pitching moment of about 50 N-m.

III.C.2. Parametric Study Conditions

To limit the scope of the problem, three volumetric deposition shapes are selected. Namely a sphere, pancake (oblate spheroid), and bean (prolate spheroid) are employed such that the volume of the ellipsoid ($V = 4/3\pi abc$) remains constant. The values used are listed in Table 4.

	a	b	c
Sphere	0.007 m	0.007 m	0.007 m
Pancake	0.01852 m	0.01852 m	0.001 m
Bean	0.001852 m	0.1 m	0.001852 m

Table 4. Deposition geometry parameters.

The centroid of the deposition is positioned along the top centerline ($y_0 = 0$) and must be at least three characteristic length scales (σ) away from the surface of the body to ensure the entire deposition is deposited into the flow-field ($\iiint_{-3\sigma}^{3\sigma} S\, dx\, dy\, dz = 0.9999 * Q$). This distance is the minimal length from the centroid of a spherical energy deposition to the surface of the body and is denoted, f, in Figure 12. With f $= 3\sigma = 3$ a $= 0.021$ m, the values of z_0 and ϕ can be determined for a given x_0 by enforcing equation (7). This determines the location of $[x_1, z_1]$ and its outward normal unit vector $\vec{n}$. Equation (9) is used to determine ϕ so the cross-section of the deposition is parallel to the body as illustrated in Figure 13 for a pancake deposition.

$$x_0 = x_1 + \text{f} \cdot ||n_{x_1}|| \tag{7}$$

$$z_0 = z_1 + \text{f} \cdot ||n_{z_1}|| \tag{8}$$

$$\phi = tan^{-1}\left(\left|\left|\frac{n_{x_1}}{n_{z_1}}\right|\right|\right) \tag{9}$$

Using the Mach 5 flat plate experiment originally studied by Kimmel et al.[4, 11, 13, 21–26] and recent power generation experiments,[27] realistic power input is assumed to lie in the range of 1000 W to 15,000 W. The deposition is positioned near the vehicle tip to maximize the distance from the center of gravity (CG). Variation in the input power, Q, and the distance along the body, x/L, leads to the test matrix shown in Table 5.

	Q [W]	x/L		Q [W]	x/L		Q [W]	x/L
Sphere	1000	5%	Pancake	1000	5%	Bean	1000	5%
Sphere	4000	5%	Pancake	4000	5%	Bean	4000	5%
Sphere	15000	5%	Pancake	15000	5%	Bean	15000	5%
Sphere	1000	10%	Pancake	1000	10%	Bean	1000	10%
Sphere	4000	10%	Pancake	4000	10%	Bean	4000	10%
Sphere	15000	10%	Pancake	15000	10%	Bean	15000	10%

Table 5. Parametric study for three different deposition shapes.

III.C.3. Parametric Study Results

The total amount of energy deposited into the flow is characterized by the nondimensional total energy deposition value $\tilde{Q}$. For the cases in the study $\tilde{Q} = 4.3 \times 10^{-7}$, 1.7×10^{-6}, and 6.5×10^{-6} for Q $= 1000$ W, 4000 W, 15000 W respectively. This parameter provides some information on vehicle and application scaling.

American Institute of Aeronautics and Astronautics Paper 2008-1109

Approved for public release; distribution unlimited.

$$\tilde{Q} = \frac{Q}{\rho_\infty u_\infty^3 L^2} \tag{10}$$

The axial location of the energy deposition is apparent after investigating the pressure coefficient and Stanton number along the top centerline ($\theta = 0°$) for the three shapes in Figure 14. Although there is a slight increase in the Stanton number, it is accompanied by a noticeable rise in the pressure coefficient, particularly in the sphere and pancake depositions. The total forces acting on the body in the Cartesian coordinate system are found by multiplying the combined stress tensor and pressure matrices by the corresponding area vector.

$$\left\{ \begin{array}{c} F_x \\ F_y \\ F_z \end{array} \right\}_{ij} = \left\{ \left[\begin{array}{ccc} \tau_{xx} & \tau_{xy} & \tau_{xz} \\ \tau_{yx} & \tau_{yy} & \tau_{yz} \\ \tau_{zx} & \tau_{zy} & \tau_{zz} \end{array} \right] - \left[\begin{array}{ccc} p & 0 & 0 \\ 0 & p & 0 \\ 0 & 0 & p \end{array} \right] \right\} \left[\begin{array}{c} n_x \\ n_y \\ n_z \end{array} \right] A \tag{11}$$

With the local force known, the pitching moment is determined by multiplying the downward force ($F_{z_{ij}}$) by the moment arm ($\Delta x = x_{ij} - x_{CG}$). For each scenario, the pitching moment is compared to the baseline and then normalized by the effective pitching moment due to the mechanical flap found previously ($M_{p_{flap}} = 50$ Nm). Figure 15 plots the normalized change in total pitching moment for each of the shapes. The points are fitted with a parametric spline because of their assumed non-linearity. The plots show the energy deposition is unable to provide the same level of control authority as the mechanical flap. In addition, while the shape of the deposition appears to have noticeable effects on the local pressure coefficient and Stanton number, it does not appear to have a large impact on the overall change in the pitching moment.

III.D.   Small Blunt Elliptic Cone With Energy Deposition

The effects of energy deposition are also simulated for a few cases using the $L = 0.2$ m blunt elliptic cone with freestream conditions found in Table 2. Using the smaller geometry and the higher altitude freestream conditions increases the non-dimensional total energy deposition value $\tilde{Q}$ by several orders of magnitude. For the cases run, $\tilde{Q} = 4.0 \times 10^{-4}$, 8.0×10^{-4}, and 1.6×10^{-3} for Q = 500 W, 1000 W, and 2000 W respectively.

The deposition is modeled as an oblate spheroid (Pancake), though its geometry is not identical to the one run in the $L = 3$ m parametric study. Table 6 lists the values used to represent the energy deposition volume and location. The energy deposition is positioned near the bow shock (x/L =0.15 m).

x_0	y_0	z_0	a	b	c	θ
3 cm	0.0 cm	1.7 cm	0.3 cm	0.4 cm	0.1 cm	0°

Table 6. The location of energy deposition for Mach 14 blunt elliptic cone.

Unlike the larger geometry cases, the energy deposition on the smaller blunt cone results in a large temperature rise at and downstream of the deposition as illustrated in Figure 16 for $Q = 1000$ W deposition. This results in a strong heat transfer penalty, but gives rise to a dramatic increase in the local peak pressure coefficient distribution as seen in Figure 17. The pitching moment due to the flap is found following the layout covered in subsection III.C.1 with the flap geometry scaled to match the previous flap dimensions ($M_{p_{flap}} = 4 \times 10^{-3}$ Nm). The effective pitching moment, shown in Figure 18, indicates that energy deposition is an viable replacement for the mechanical flap under these conditions. These results are combined with those obtained for the large blunt elliptic cone using the using the non-dimensional total energy deposition parameter $\tilde{Q}$. Figure 19 shows a strong correlation between $\tilde{Q}$ and the effective pitching moment and suggests that energy deposition is a viable replacement for a mechanical flap when $\tilde{Q} > 1 \times 10^{-4}$.

IV.   Conclusions

The Michigan Aerothermodynamic Navier-Stokes (LeMANS) code was successfully validated for three-dimensional blunt and sharp elliptic cones. In addition, a phenomenological heating model was implemented to investigate whether a practical level of control could be achieved for a realistic hypersonic vehicle. A parametric study was completed investigating the shape, location, and total amount of energy volumetrically deposited into the flow-field for two blunt-nosed elliptic cone configurations. The effectiveness of

Approved for public release; distribution unlimited.

volumetric energy deposition for flight control appeared to scale strongly on the nondimensional parameter $Q/(\rho_\infty u_\infty^3 L^2)$, warranting additional computations to explore this effect.

V.   Future Work

In future studies, we will consider the potential additional benefits of electromagnetic fields. The addition of the magnetohydrodynamics (MHD) equations to LeMANS by means of a current continuity equation module will provide additional design tools to model design configurations that incorporate the use of a magnetic field to help with flow control. The Mach 5 flat plate experiment mentioned previously had some experiments measuring the effects of a magnetic field on the flow, with and without energy deposition from the plasma actuator.[13, 22] Their work showed an additional increase in resulting forces, when the plasma actuator was on. This experiment will be used to verify the addition of the MHD module.

Acknowledgments

References

[1]Kimmel, R. L., Poggie J., and Schwoerke S. N., "Laminar-Turbulent Transition in a Mach 8 Elliptic Cone Flow," *AIAA Journal*, Vol. 37, No. 9, September 1999, pp. 1080-1087.

[2]Nowlan, D., Burke, A., and Bird, K., "Pressure and Heat Transfer Distribution on ASD Elliptic Cone (W3) and ASD Sortie (W4) in the CAL 48-Inch Hypersonic Shock Tunnel," CAL Report AM-1800-Y-2, December 1963. ASC 94 2649

[3]Fomin, V. M., Tretyakov, P. K., and Taran J.-P., "Flow Control using Various Plasma and Aerodynamic Approaches," *Aerospace Science and Technology*, Vol. 8, No. 5, July 2004, pp. 411-421.

[4]Shang, J. S., Surzhikov, S. T., Kimmel, R., Gaitonde, D., Menart, J., and Hayes, J., "Mechanisms of Plasma Actuators for Hypersonic Flow Control," *Progress in Aerospace Sciences*, Vol. 41, No. 8, November 2005, pp. 642-668.

[5]Mason, W. H., and Lee, J., "Aerodynamically Blunt and Sharp Bodies," AIAA paper 1992-2727, American Institute of Aeronautics and Astronautics, Palo Alto CA, June 1992.

[6]Santos, W. F. N., and Lewis, M. J., "Aerothermodynamic Performance Analysis of Hypersonic Flow on Power Law Leading Edges," *Journal of Spacecraft and Rockets,* Vol. 42, No. 4, July-August 2005, pp. 588-597.

[7]Shang, J. S., Hayes, J., and Menart, J., "Hypersonic Flow over a Blunt Body with Plasma Injection," *Journal of Spacecraft and Rockets,* Vol. 39, No. 3, May-June 2002, pp. 367-375.

[8]Kremeyer, K., Sebastian, K., and Shu, C.-W., "Computational Study of Shock Mitigation and Drag Reduction by Pulsed Energy Lines," *AIAA Journal,* Vol. 44, No. 8, August 2006.

[9]Yan, H., and Gaitonde, D., "Control of Edney IV Interaction by Energy Pulse," AIAA Paper 2006-562, American Institute of Aeronautics and Astronautics, Reno NV, January 2006.

[10]Girgis, I. G., Shneider, M. N., Macheret, S. O., Brown, G. L., and Miles, R. B., "Creation of Steering Moments in Supersonic Flow by Off-Axis Plasma Heat Addition," AIAA paper 2002-0129, American Institute of Aeronautics and Astronautics, Reno NV, January 2002.

[11]Menart, J., Stanfield, S., Shang, J., Kimmel, R., and Hayes, J., "Study of Plasma Electrode Arrangements for Optimum Lift in a Mach 5 Flow," AIAA paper 2006-1172, American Institute of Aeronautics and Astronautics, Reno NV, January 2006.

[12]Updike, G. A., Shang, J. S., and Gaitonde, D. V., "Hypersonic Separated Flow Control Using Magneto-Aerodynamic Interaction," AIAA paper 2005-164, American Institute of Aeronautics and Astronautics, Reno NV, January 2005.

[13]Kimmel, R. L., Hayes, J. R., Crafton., J. W., Fonov, S. D., Menart, J., and Shang, J., "Surface Discharge for High-Speed Boundary Layer Control," AIAA paper 2006-710, American Institute of Aeronautics and Astronautics, Reno NV, January 2006.

[14]Miles, R. B., Macheret, S. O., Shneider, M. N., Steeves, C., Murray, R. C., Smith, T., and Zaidi, S. H., "Plasma-Enhanced Hypersonic Performance Enabled by MHD Power Extraction," AIAA paper 2005-561, American Institute of Aeronautics and Astronautics, Reno NV, January 2005.

[15]Scalabrin, L. C., and Boyd, I. D., "Development of an Unstructured Navier-Stokes Solver For Hypersonic Nonequilibrium Aerothermodynamics," AIAA Paper 2005-5203, American Institute of Aeronautics and Astronautics, Toronto Canada, June 2005.

[16]Scalabrin, L. C., and Boyd, I. D., "Numerical Simulation of Weakly Ionized Hypersonic Flow for Reentry Configurations," AIAA Paper 2006-3773, American Institute of Aeronautics and Astronautics, San Francisco CA, June 2006.

[17]Poggie J., "Plasma-Based Hypersonic Flow Control," AIAA Paper 2006-3567, American Institute of Aeronautics and Astronautics, San Francisco CA, June 2006.

[18]Kimmel, R., Klein, M., Schwoerke, S., "Three-Dimensional Hypersonic Laminar Boundary-Layer Computations for Transition Experiment Design," *AIAA Journal*, Vol. 34 No. 4, July-August 1997, pp. 409-415.

[19]Candler, G., "Unstructured Grid Approaches for Accurate Aeroheating Simulations," AIAA Paper 2007-3959, American Institute of Aeronautics and Astronautics, Miami FL, June 2007.

[20]Burke, G., "Heat Transfer and Pressure Distributions about Sharp and Blunt Elliptic Cones at Angles of Attack and high Mach Numbers," U.S. Air Force Flight Dynamics Lab., TR AFFDL-TR-64-172, Wright-Patterson AFB, OH, May 1965.

[21]Shang, J., Kimmel, R., Hayes, J., and Tyler, C., "Performance of a Low-Density Hypersonic Magneto-Aerodynamic Facility," AIAA Paper 2003-329, American Institute of Aeronautics and Astronautics, Reno NV, January 2003.

[22]Menart, J., Shang, J., Kimmel, R., and Hayes, J., "Effects of Magnetic Fields on Plasmas Generated in a Mach 5 Wind Tunnel," AIAA Paper 2003-4165, American Institute of Aeronautics and Astronautics, Reno NV, January 2003.

[23]Kimmel, R. L., Hayes, J. R., Menart, J. A., and Shang, J., "Effect of Surface Plasma Discharges on Boundary Layers at Mach 5," AIAA Paper 2004-509, American Institute of Aeronautics and Astronautics, Reno NV, January 2004.

[24]Kimmel, R., Hayes, J., Menart, J., and Shang, J., "Effects on Magnetic Fields on Surface Plasma Discharges at Mach 5," AIAA Paper 2004-2661, American Institute of Aeronautics and Astronautics, Reno NV, January 2004.

[25]Menart, J., Henderson, S., Shang, J., Kimmel, R., Hayes, J.,"DC Plasma Discharge Effects on a Mach 5 Flow Between Small Plate Electrodes," AIAA Paper 2004-2264, American Institute of Aeronautics and Astronautics, Reno NV, January 2004.

[26]Kimmel, R., Hayes, J., Menart, J., and Shang, J, "Supersonic Plasma Flow Control Experiments," U.S. Air Force Research Lab., TR ARFL-VA-WP-TR-2006-3006, Wright-Patterson Air Force Base, OH, December 2005.

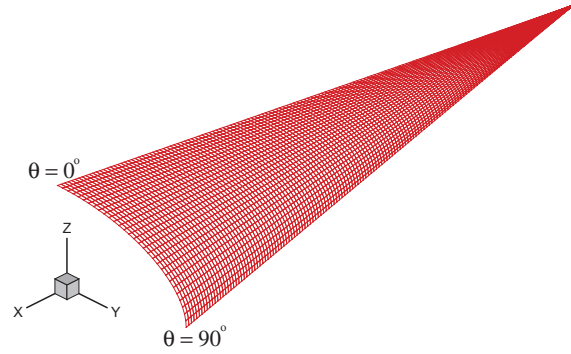[27]Velocci, A. L. Jr., "A General Atomics-led Team," Aviation Week & Space Technology, March 19/26, 2007, pp. 36.

American Institute of Aeronautics and Astronautics Paper 2008-1109
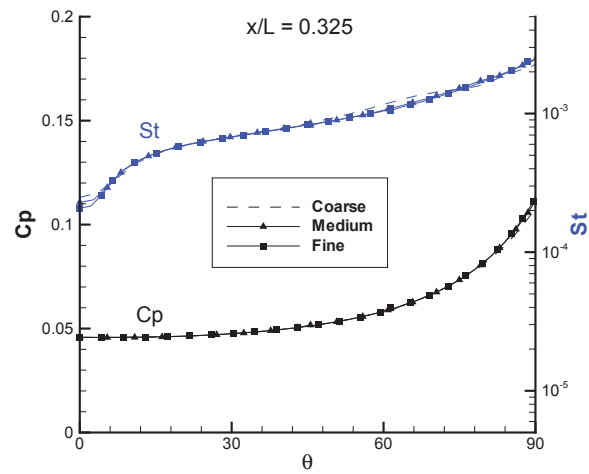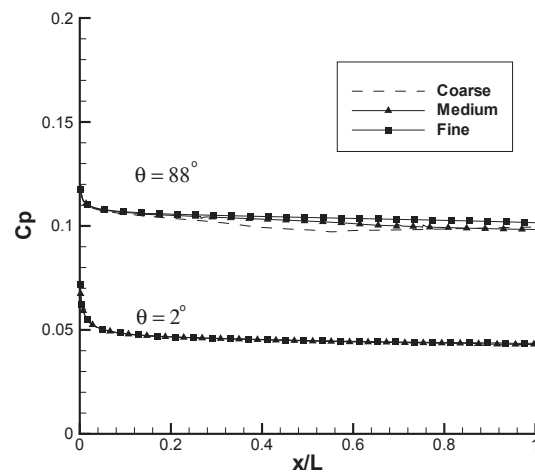
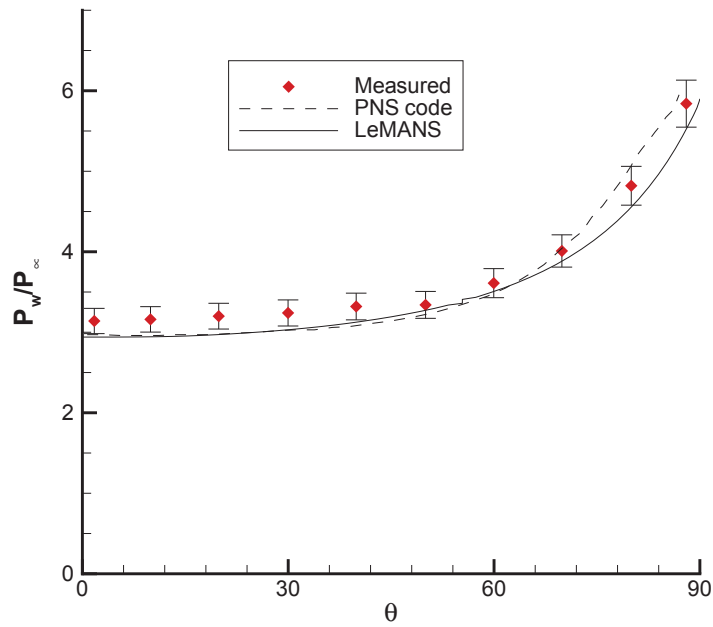**Figure 1. Surface of the sharp elliptic cone grid with both Cartesian and cylindrical coordinate systems.**
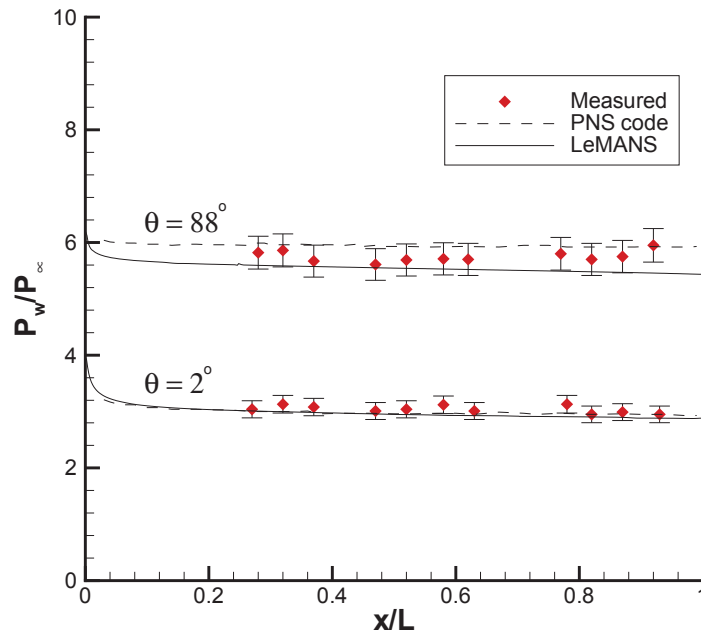

(a) Around the circumference

(b) Along rays

Figure 2. Grid independence study for Mach 8 sharp elliptic cone.

American Institute of Aeronautics and Astronautics Paper 2008-1109

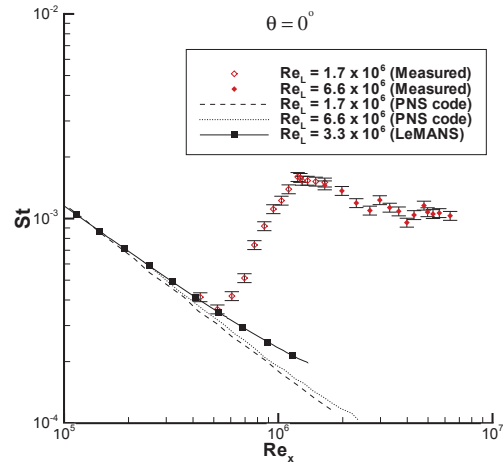Approved for public release; distribution unlimited.

(a) Pressure around the circumference

(b) Pressure along rays

Figure 3. Normalized surface pressure distributions for the Mach 8 sharp elliptic cone (±5 percent uncertainty).[1]

American Institute of Aeronautics and Astronautics Paper 2008-1109

(a) Top centerline, $\theta = 0°$

(b) Shoulder, $\theta = 45°$
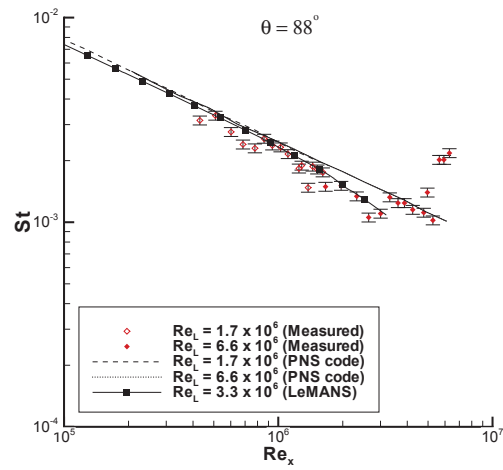
(c) Leading edge, $\theta = 88°$

Figure 4. Stanton number distributions for the Mach 8 sharp elliptic cone (±10 percent uncertainty).[1]
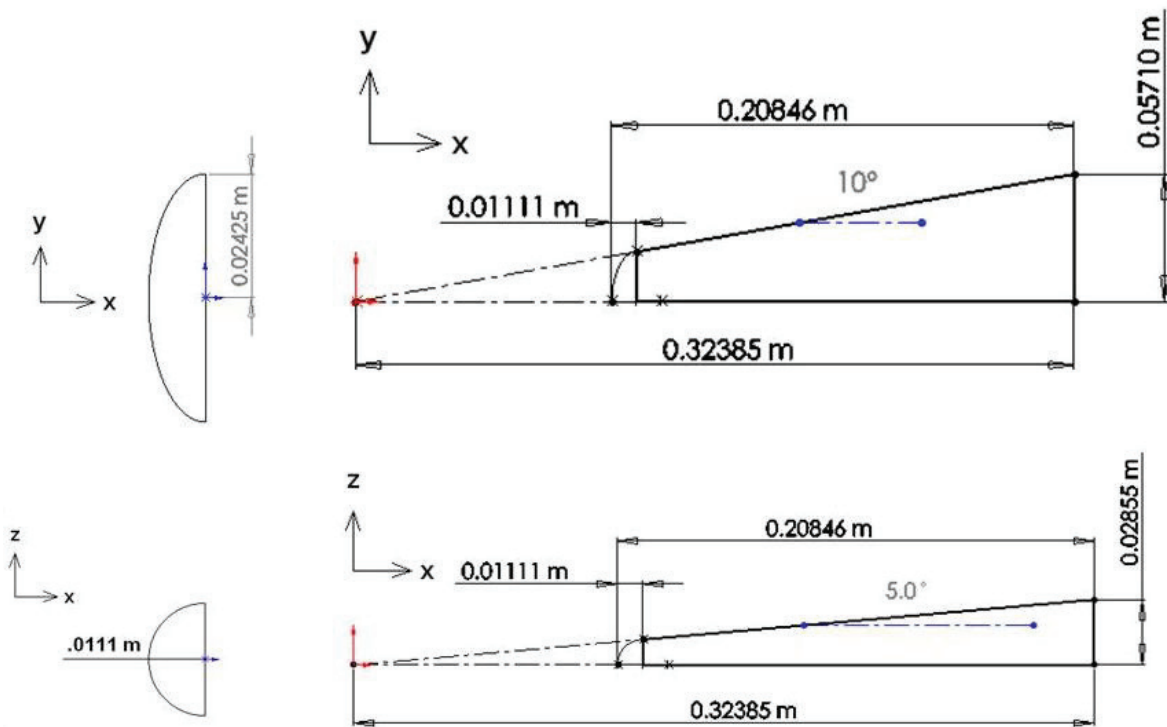
Figure 5. Blunt elliptic cone geometry. Dimensions are in meters.[2]

American Institute of Aeronautics and Astronautics Paper 2008-1109

Approved for public release; distribution unlimited.
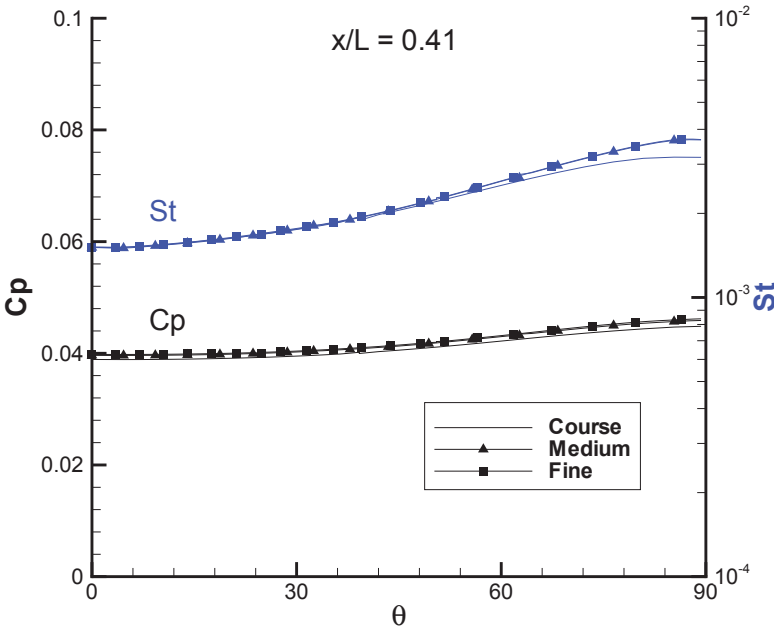
(a) Around the circumference
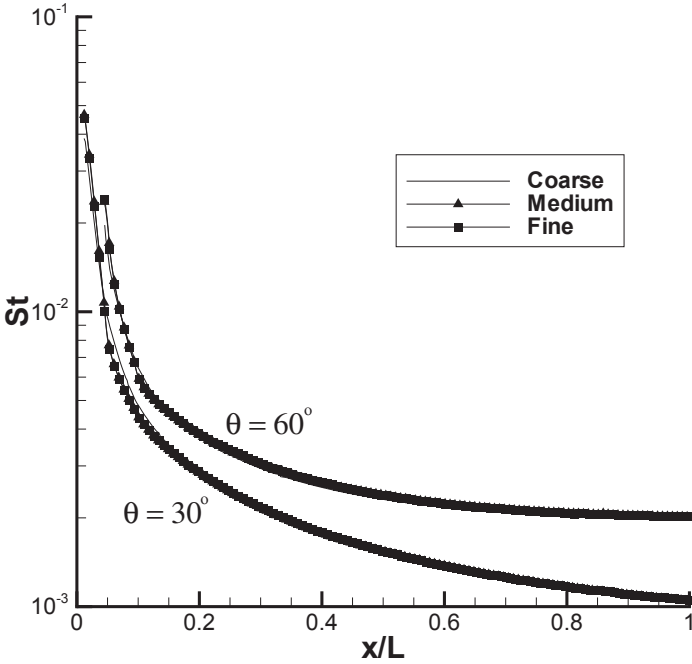
(b) Along rays

Figure 6. Grid independence study for Mach 14 blunt elliptic cone ($L = 0.2$ m).

American Institute of Aeronautics and Astronautics Paper 2008-1109

29

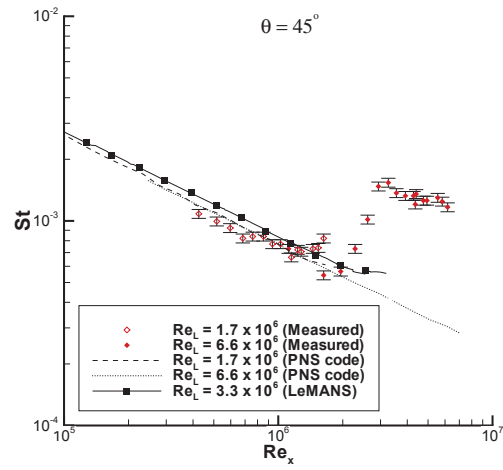Approved for public release; distribution unlimited.

(a) Pressure around the circumference
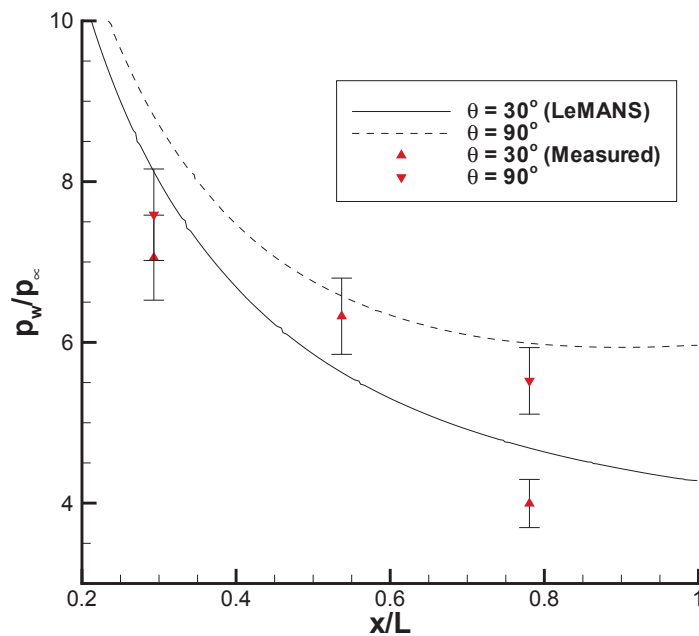
(b) Pressure along rays

Figure 7. Normalized surface pressure distributions for Mach 14 blunt elliptic cone ($\pm$7 percent uncertainty).[2]

American Institute of Aeronautics and Astronautics Paper 2008-1109

Approved for public release; distribution unlimited.
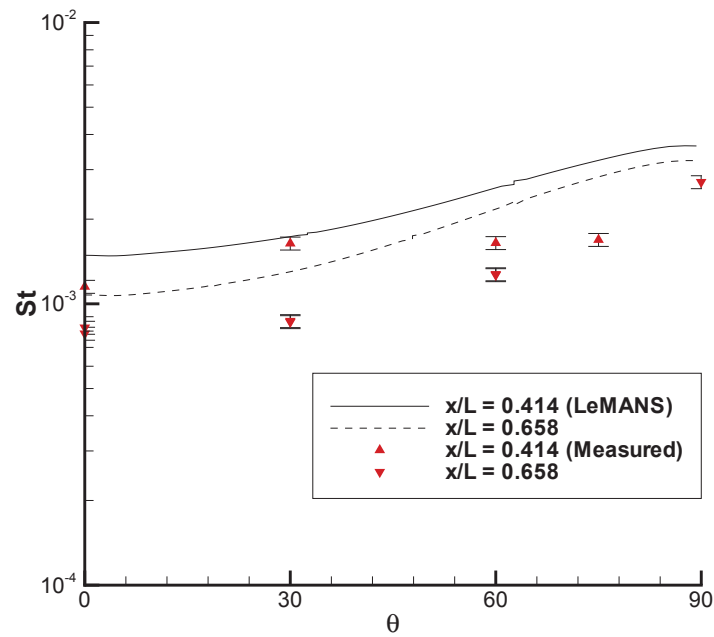
(a) Stanton number around the circumference
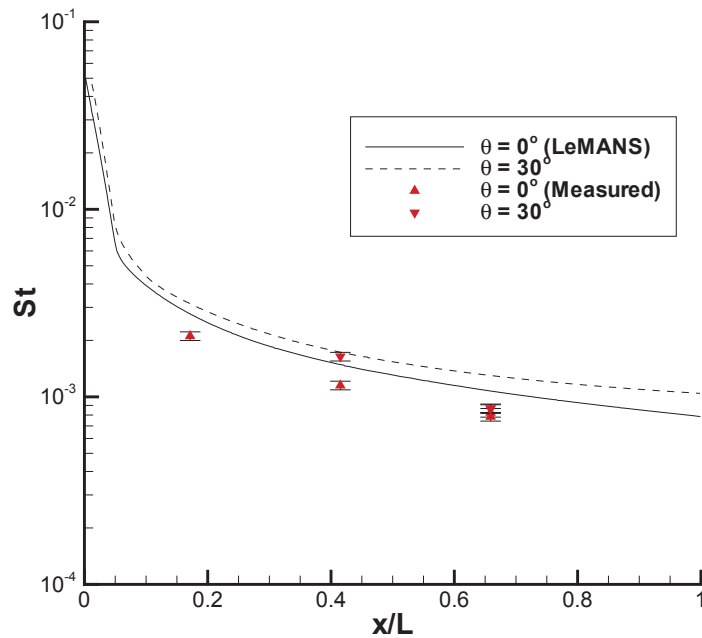
(b) Stanton number along rays

Figure 8. Stanton number distributions for Mach 14 blunt elliptic cone (±4.5 percent uncertainty).[2]

American Institute of Aeronautics and Astronautics Paper 2008-1109

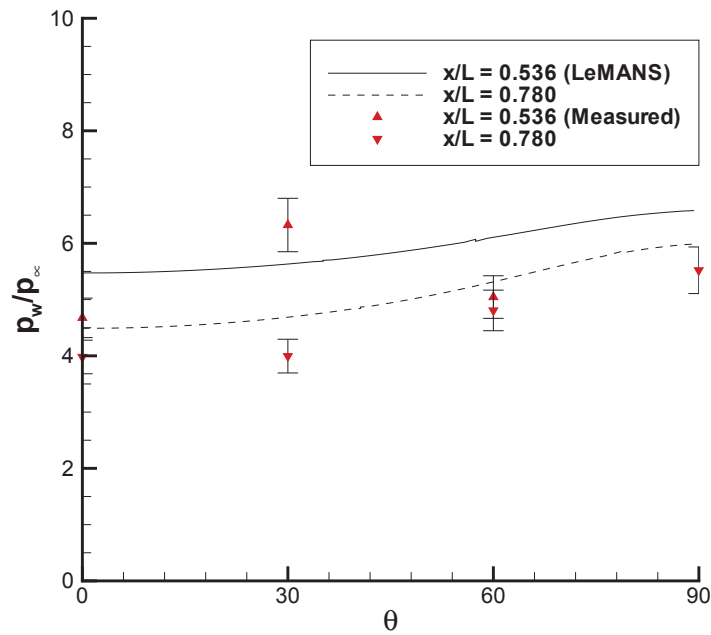Approved for public release; distribution unlimited.
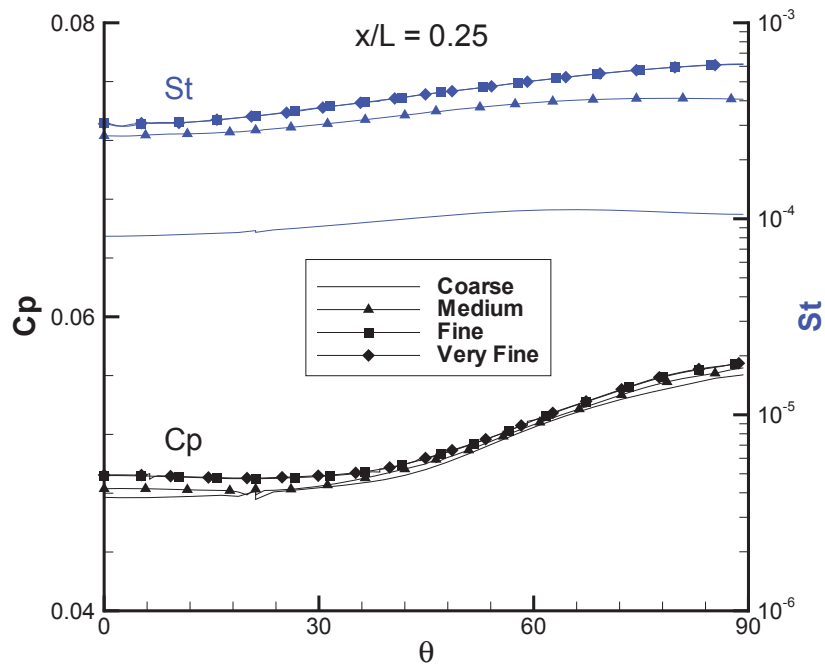
(a) Around the circumference
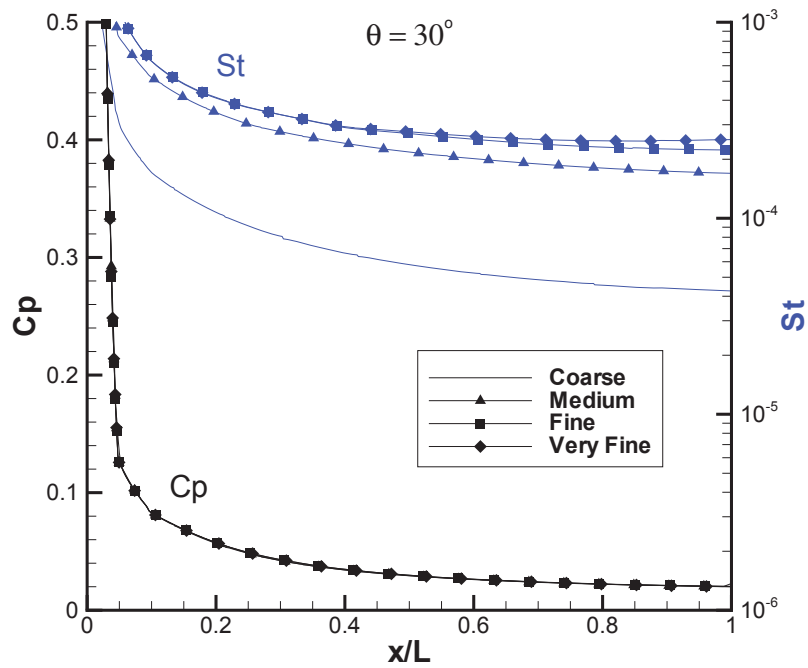
(b) Along rays

Figure 9. Grid independence study for Mach 12 blunt elliptic cone ($L = 3$ m).

American Institute of Aeronautics and Astronautics Paper 2008-1109

Approved for public release; distribution unlimited.
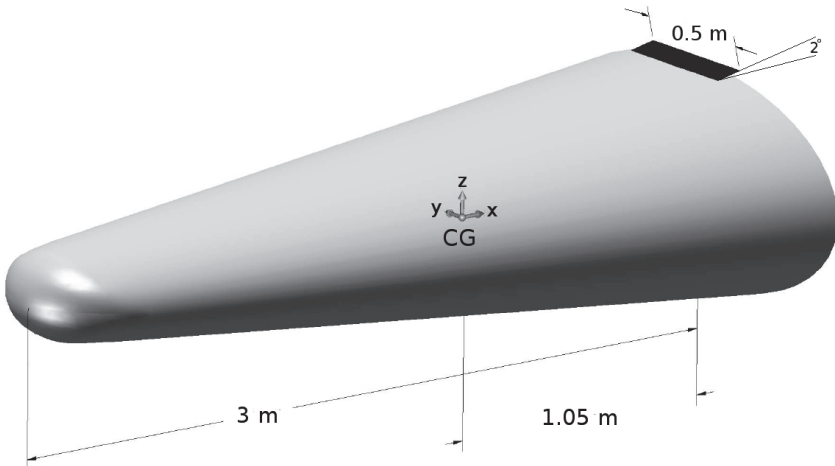
Figure 10. Model of a 2° mechanical flap attached to a blunt elliptic body.
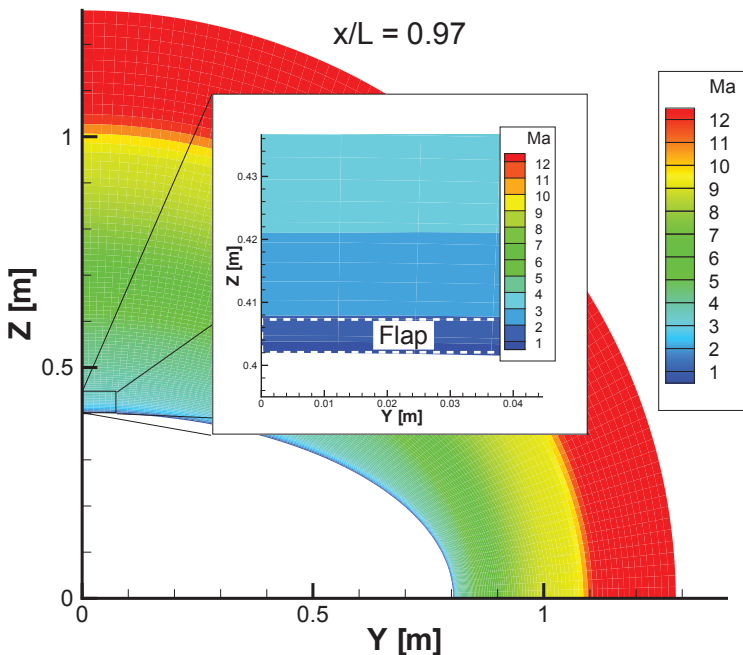
Figure 11. Mach profile at x/L=0.97 for Mach 12 blunt elliptic cone ($L = 3$ m).

American Institute of Aeronautics and Astronautics Paper 2008-1109

33

Approved for public release; distribution unlimited.
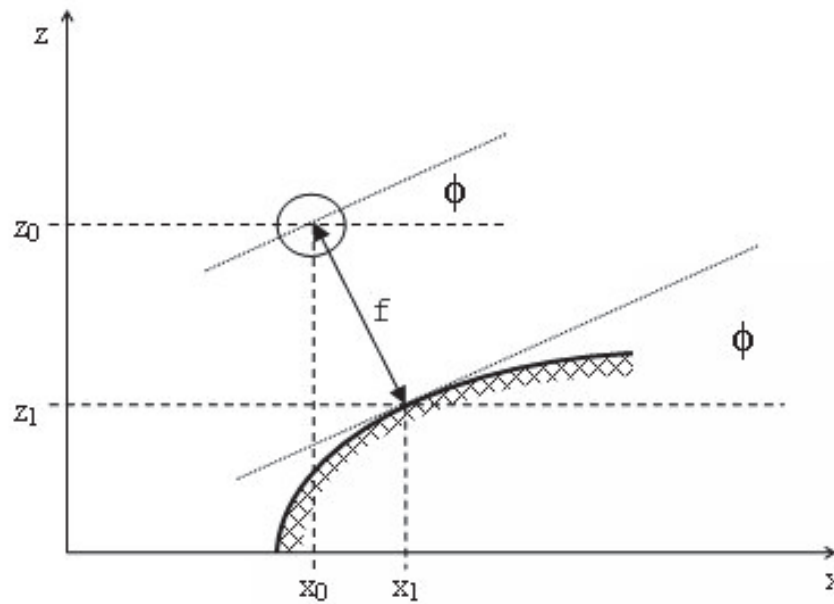
Figure 12. Illustration of the constant height parameter used to determine z_0 and ϕ for parametric study.

Pancake
Q = 1000 W
x/L = 0.05

T [K]
5500
4500
3500
2500
2000
1500
500
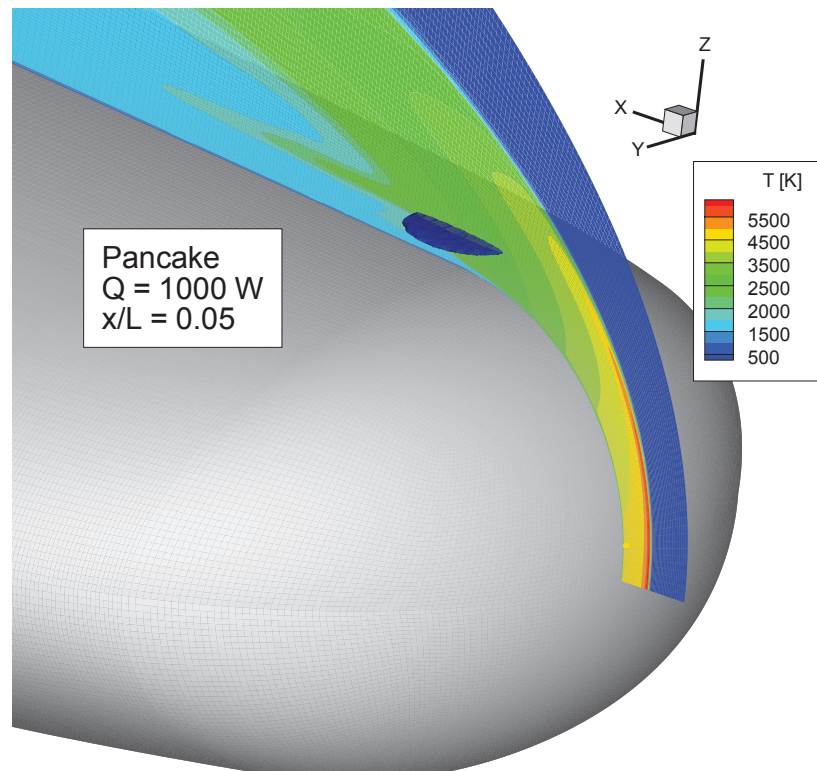
Figure 13. Slice of the temperature contour along the top centerline for a pancake deposition.

American Institute of Aeronautics and Astronautics Paper 2008-1109

34

Approved for public release; distribution unlimited.
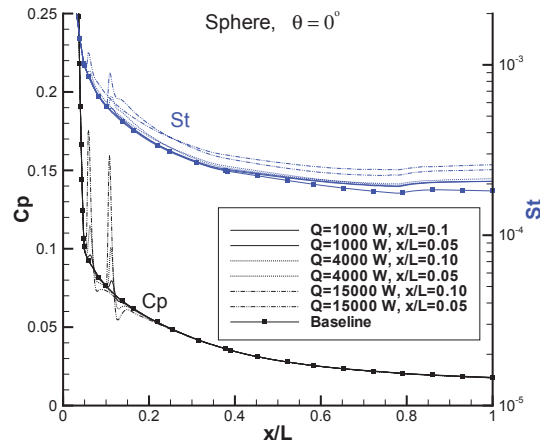
(a) Sphere deposition
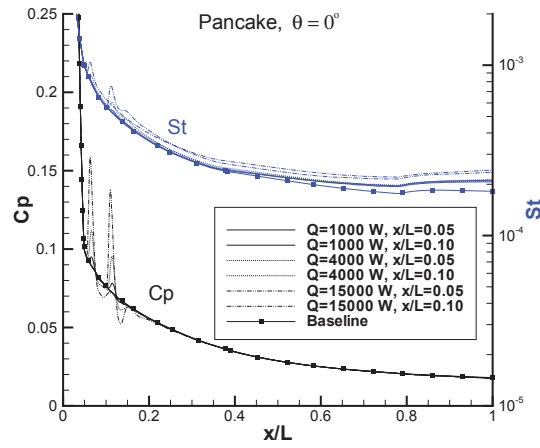
(b) Pancake deposition
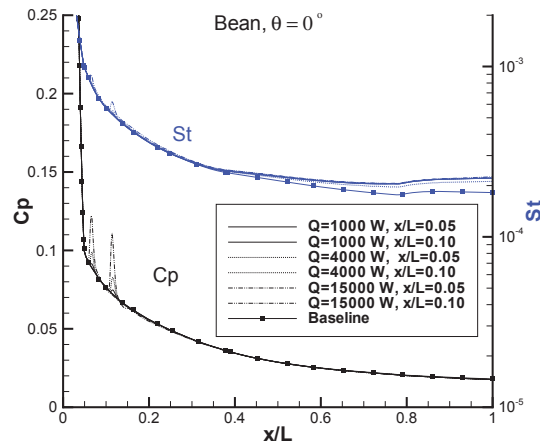
(c) Bean deposition

Figure 14. Pressure coefficient and Stanton number distributions for the Mach 12 blunt elliptic cone ($L = 3$ m) for various energy deposition patterns.

American Institute of Aeronautics and Astronautics Paper 2008-1109

Approved for public release; distribution unlimited.
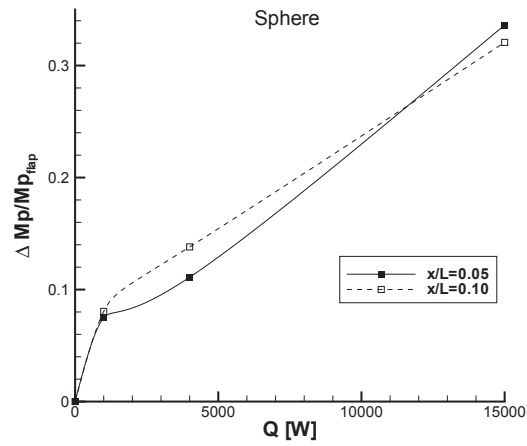
(a) Sphere deposition
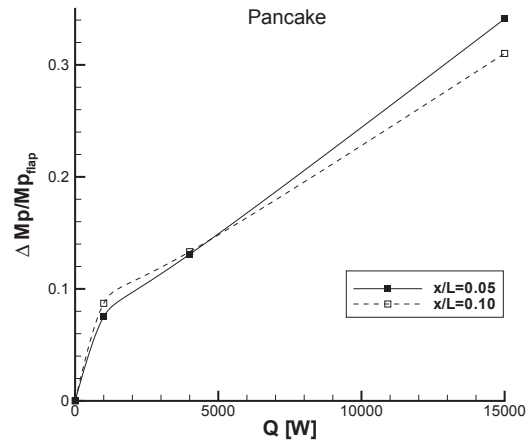
(b) Pancake deposition
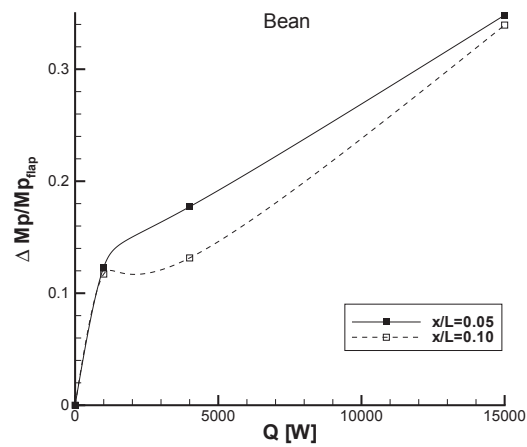
(c) Bean deposition

Figure 15. Normalized change in pitching moment for a Mach 12 blunt elliptic cone ($L = 3$ m) for various energy deposition patterns.

American Institute of Aeronautics and Astronautics Paper 2008-1109

Approved for public release; distribution unlimited.
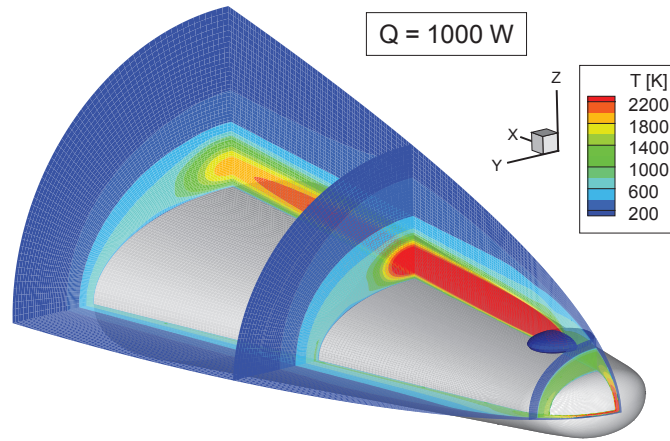
Figure 16. Temperature contours for blunt elliptic cone ($L = 0.2$ m) with $Q = 1000$ W.
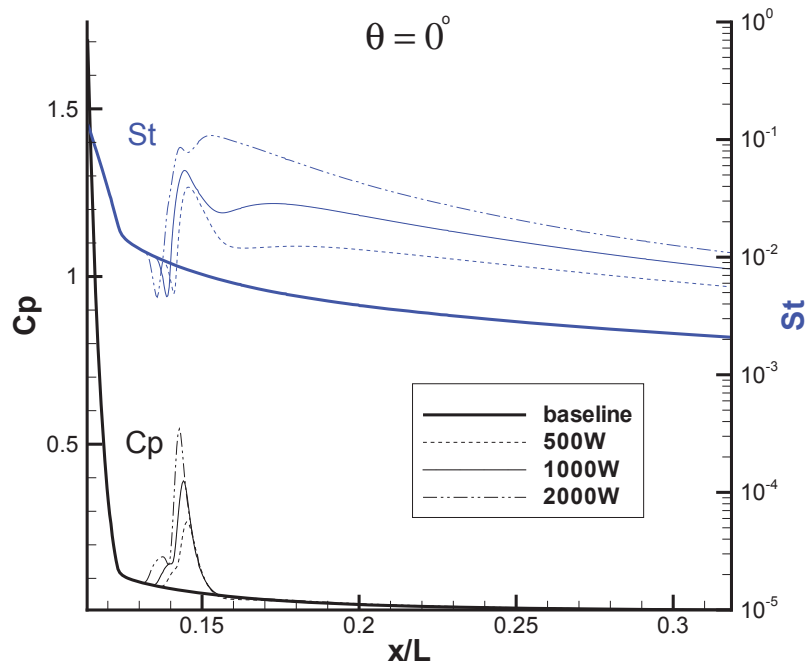
Figure 17. Pressure coefficient and Stanton number distributions along the top center line of a Mach 14 blunt elliptic cone ($L = 0.2$ m) with various amounts of energy deposition

American Institute of Aeronautics and Astronautics Paper 2008-1109

Approved for public release; distribution unlimited.

Figure 18. Normalized change in pitching moment for a Mach 14 blunt elliptic cone ($L = 0.2$ m) for a pancake energy deposition.
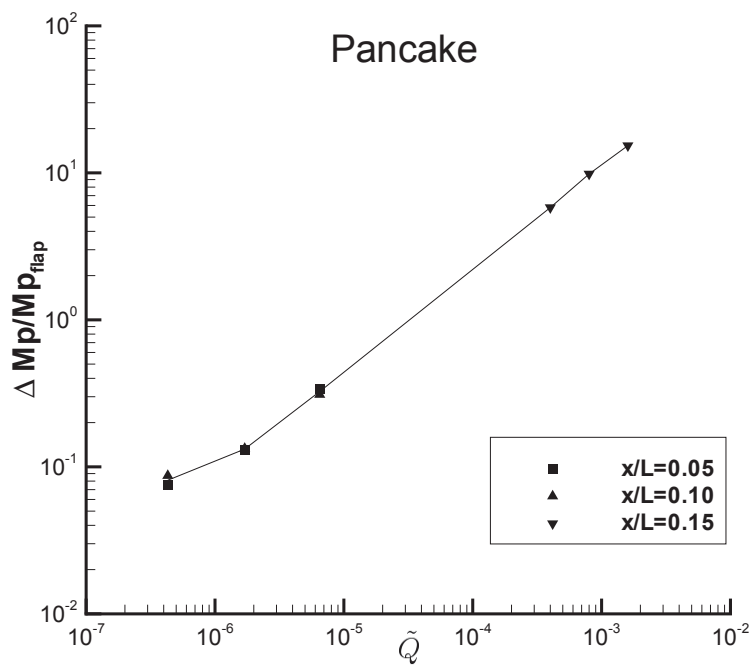
Figure 19. Normalized change in pitching moment versus the non-dimensional total energy deposition $\tilde{Q}$ for a pancake energy deposition.

Approved for public release; distribution unlimited.

Numerical Study of Plasma-Assisted Aerodynamic Control for Hypersonic Vehicles

Nicholas J. Bisek[*] and Iain D. Boyd[†]

University of Michigan, Ann Arbor, MI, 48109, USA

and

Jonathan Poggie[‡]

Air Force Research Laboratory, Wright-Patterson AFB, OH, 45433-7512, USA

Plasma actuators and various forms of volumetric energy deposition have received a good deal of research attention recently as a means of hypersonic flight control. An open question remains as to whether the required power expenditures for such devices can be achieved for practical systems. To address this issue, a numerical study is carried out for hypersonic flow over a blunt nose elliptic cone to determine the amount of energy deposition necessary for flight control. Energy deposition is simulated by means of a phenomenological dissipative heating model. Validation studies of the flow simulation code in the absence of energy deposition are presented for a Mach 8 elliptic cone flow and a Mach 14 blunt elliptic cone flow. A parametric study of the effects of energy deposition is carried out for three blunt elliptic cone configurations: a 3 m long cone at Mach 12.6 and 40 km effective altitude, a 0.6 m long cone at Mach 12.6 and 40 km altitude, and a 0.2 m long cone at Mach 14.2 and 42 km altitude. Three different volumetric energy deposition patterns are considered: a spherical pattern, a 'pancake' pattern (oblate spheroid), and a 'bean' pattern (prolate spheroid). The effects of energy deposition are seen to be relatively independent of these patterns. For the 3 m cone case, the pitching moment generated by 0.5-15 kW of energy deposition is 25-75% of that generated by a 0.1 m^2 mechanical flap at 2° deflection. For the 0.6 m cone, plasma actuators provided control authority several times greater than an equivalently scaled flap, whereas the smallest cone (0.2 m) experienced an order of magnitude increase in control 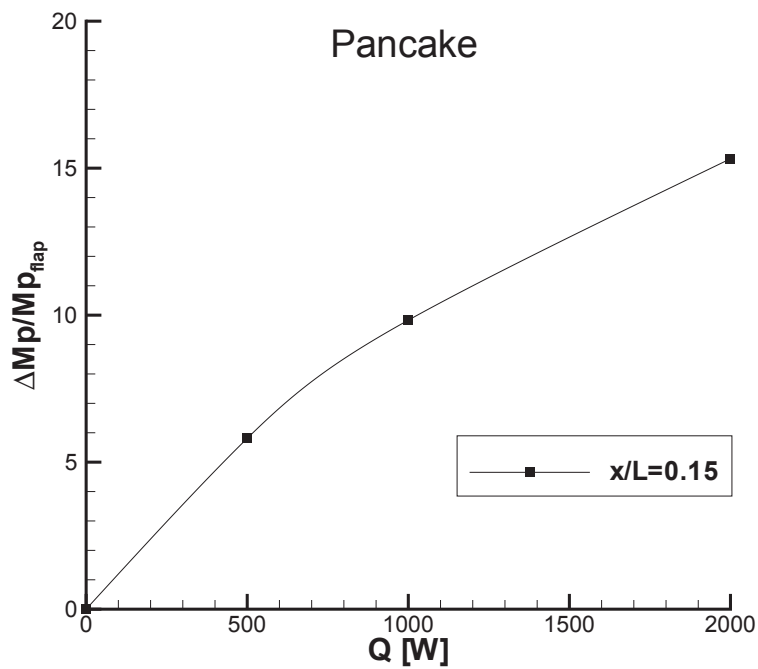authority versus its equivalently scaled flap. The effectiveness of volumetric energy deposition for flight control appears to scale strongly with a nondimensional parameter based on the freestream flow kinetic energy flux.

Nomenclature

a, b, c = the equatorial radii and the polar radius of an ellipsoid
A = surface area of grid cell
C_m = moment coefficient, $[2M_p]/[\rho_\infty u_\infty{}^2 L^2 d]$
C_p = pressure coefficient, $[2(p_w - p_\infty)]/[\rho_\infty u_\infty{}^2]$
d = maximum spanwise length
E = total energy per volume
h = enthalpy
i, j, k = computational grid indices along the axial, radial, and circumferential directions
$\mathbf{J}$ = mass diffusion flux (x, y, z directions)
L = axial surface length
M_p = moment about center of gravity
$\mathbf{n}$ = normal vector
p = pressure

[*]Graduate Student, Department of Aerospace Engineering, 1320 Beal Avenue, Student Member AIAA
[†]Professor, Department of Aerospace Engineering, 1320 Beal Avenue, Associate Fellow AIAA
[‡]Senior Aerospace Engineer, AFRL/RBAC. Bldg. 146 Rm. 225, 2210 Eighth St. Associate Fellow AIAA
Approved for public release, distribution unlimited, WPAFB 08-0720

Approved for public release; distribution unlimited.

$\mathbf{q}$	= heat flux (translational-rotational, and vibrational-electronic)
Q	= total power input by actuator
$\tilde{Q}$	= nondimensional total power input by actuator, $Q/(\rho_\infty u_\infty^3 L^2)$
Re_x	= running Reynolds number, $\rho_\infty u_\infty x/\mu_\infty$
S	= source term
St	= Stanton number, $q_w/[\rho_\infty u_\infty (h_0 - h_w)]$
T	= temperature (translational and rotational)
T_v	= temperature (vibrational and electronic)
$\mathbf{u}$	= velocity vector (u, v, w)
x, y, z	= streamwise, spanwise, and transverse coordinates
ϵ	= emissivity
θ	= angle along circumference of the body (cylindrical coordinate system)
λ	= characteristic length
μ	= coefficient of viscosity
ρ	= mass density
σ	= Stefan-Boltzmann constant, $5.67 \times 10^{-8} W/[m^2 K^4]$
$\boldsymbol{\tau}$	= viscous stress
ϕ	= inclination of the deposition to the freestream flow

Subscript

s	= species
w	= wall
0	= stagnation
∞	= freestream

Species

N_2	= molecular nitrogen
O_2	= molecular oxygen
NO	= nitric oxide
N	= atomic nitrogen
O	= atomic oxygen
N_2^+	= molecular nitrogen ion
O_2^+	= molecular oxygen ion
NO^+	= nitric oxide ion
N^+	= atomic nitrogen ion
O^+	= atomic oxygen ion
e^-	= free electron

I.   Introduction

Aerodynamic control and drag reduction are major challenges for hypersonic vehicle designers. A good deal of research attention has recently focused on hypersonic plasma interactions and plasma flow control to explore ways of confronting these challenges.[1,2]

Minimizing drag in vehicle design leads to long thin bodies with sharp leading edges. This constrains the materials available for the vehicle's Thermal Protection System (TPS) because there is a required minimum thickness which may not be achieved for a given vehicle configuration. In addition, small defects in the production of the sharp edges can result in serious or even catastrophic problems for the TPS.[3] Blunting the leading edge reduces these drawbacks but results in a much larger wave drag.[4] Recent experimental and computational research by Shang *et al.*[5] has investigated ways of reducing drag on blunt nose bodies by means of plasma injection, while research by Kremeyer *et al.*[6] and Yan[7] focused on drag reduction and flow control using laser deposition (filamentation) ahead of conic and spherical geometries.

In addition to these design constraints, traditional control surfaces (flaps) need to be positioned away from the center of gravity to extend the maneuverability of the vehicle. The location of such flaps is limited because the bow shock surrounding the vehicle will impinge on surfaces that extend beyond the shock envelope. This results in extreme pressure and heat transfer rates at the impingement point. As such,

vehicle configurations tend to be streamlined with minimal protrusions from the fuselage. Mechanically driven flaps require clearance below the surface of the flap to provide space for the flap control arm and a strong attachment point to push from. In addition, there is a small gap in the TPS as the flap extends out to deflect the flow. This gap is difficult to protect and can cause heat related damage to the vehicle. In addition, sustained cruise and other long duration hypersonic missions also suffer from nonuniform ablation of the flap causing nonuniform control authority on the vehicle.

Plasma actuators are advantageous over mechanical controllers because they do not have moving parts, can be located either in or beneath the TPS, and are uninhibited by the bow shock. This extends the range of possible locations for the actuator and allows for multiple actuators to be powered by a central energy source. They can potentially be turned on and off very rapidly, and should have a minimal aerothermal penalty when turned off. Plasma actuators can serve multiple roles. They can be used to provide steering moments,[8,9] changes in vehicle lift,[10] control of flow separation,[11,12] and local heat load mitigation.[13]

The primary objective of this research effort is to determine whether a useful degree of flight control can be achieved with practical levels of energy deposition by investigating the effects of energy deposition on a realistic hypersonic vehicle and its surrounding flow-field. In the following, we first present validation studies of the flow code, LeMANS, using relevant experimental data available in the literature. Having successfully validated LeMANS, the code is applied to investigate plasma-based aerodynamic control. We investigate how the shape, location, and input power of deposition affect vehicle control. In addition, hot wall effects, thermodynamic models, and additional vehicle configurations are explored to help draw conclusions over different flight regimes.

II.   Method

Flow-field results are obtained using Computational Fluid Dynamics (CFD) to solve the Navier-Stokes equations. The CFD computations are executed using the Michigan Aerothermodynamic Navier-Stokes (LeMANS) code which was developed at the University of Michigan.[14–17]

LeMANS is a general 2D/axisymmetric/3D, parallel, unstructured finite-volume CFD code. The numerical fluxes between cells are discretized using a modified Steger-Warming Flux Vector Splitting (FVS) scheme, except near shock waves. In these regions the original Steger-Warming FVS scheme is used.

LeMANS may be employed with any of three thermodynamic models: perfect gas, equilibrium thermochemistry, and non-equilibrium. LeMANS employs a two-temperature model to account for thermal nonequilibrium and a standard finite rate chemistry model for nonequilibrium chemistry. The two temperature model assumes that a single temperature T accounts for the translational and rotational energy modes of all species while the vibrational and electronic energy modes are accounted for by a separate temperature T_v.

The simulations are performed using second-order accurate spatial discretization and carry double precision arithmetic throughout. Thermal equilibrium and a five species finite rate air chemistry model (N_2, O_2, NO, N, and O) are used in the simulations presented unless otherwise stated.

For a single temperature (equilibrium) model with finite rate chemistry:

$$\frac{\partial \rho_s}{\partial t} + \nabla \cdot (\rho_s \mathbf{u} + \mathbf{J}_s) = \dot{\omega}_s \tag{1}$$

$$\frac{\partial \rho \mathbf{u}}{\partial t} + \nabla \cdot (\rho \mathbf{u}^2 + p\boldsymbol{\delta} - \boldsymbol{\tau}) = 0 \tag{2}$$

$$\frac{\partial E}{\partial t} + \nabla \cdot ((E + p)\mathbf{u} - \boldsymbol{\tau} \cdot \mathbf{u} - \mathbf{q} + \Sigma \mathbf{J}_s h_s) = S \tag{3}$$

For the two temperature (nonequilibrium) cases, the following vibrational energy equation is also employed.

$$\frac{\partial E_v}{\partial t} + \nabla \cdot ((E_v)\mathbf{u} - q_v + \Sigma \mathbf{J}_s e_{v,s}) = \dot{\omega}_v \tag{4}$$

LeMANS assumes the fluid is continuous and Newtonian. It assumes Stokes' hypothesis when determining the viscous stresses. The species mass diffusion flux is determined using Fick's law modified to enforce that

Approved for public release; distribution unlimited.

the sum of the diffusion fluxes is zero and plasma charge neutrality. A harmonic oscillator is used to model the species vibrational energy per unit mass ($e_{v,s}$).

For the nonequilibrium cases, we assume that 100% of the deposition energy goes initially into the translational energy equation. As the solution converges, some of the energy transfers to into the vibrational energy equation by means of the source term ($\dot{\omega}_v$). Production of vibrational energy is due to reactions in the finite rate chemistry model and energy exchange between the translational-rotational and the vibrational-electronic energy modes. Deposition of all the energy into the translational mode is a strong assumption, but is adequate for the purpose of illustrating the effects of thermal nonequilibrium.

A thermal actuator is considered as the plasma control device in this study. It is represented by a phenomenological model of dissipative heating. This model is accounted for in the Navier-Stokes equations by the addition of a source term S to the right side of energy equation (3). The shape and location of the actuator are modeled with contours of constant S having an ellipsoidal shape.[18] The strength or total power deposited into the flow uses exponential decay from the centroid of the energy deposition pattern.

$$S = \frac{Q}{\pi^{3/2}\, a \cdot b \cdot c} e^{\left(-\left(\frac{\hat{x}}{a}\right)^2 - \left(\frac{\hat{y}}{b}\right)^2 - \left(\frac{\hat{z}}{c}\right)^2\right)} \tag{5}$$

$$\begin{aligned}
\hat{x} &= (x - x_0)\cos\phi - (z - z_0)\sin\phi \\
\hat{y} &= (y - y_0) \\
\hat{z} &= (x - x_0)\sin\phi + (z - z_0)\cos\phi
\end{aligned} \tag{6}$$

Variables a and b are the equatorial radii (along the x and y axes) and c is the polar radius (along the z-axis for an ellipsoid with $0°$ inclination to the freestream). The angle ϕ is the angle between the major axis of the ellipsoid and the freestream flow. Coordinates (x_0, y_0, z_0) represent the centroid of the ellipsoid. Note that Q represents the total power deposited in the flow and $\iiint_{-\infty}^{\infty} S\, dx\, dy\, dz = Q$

III. Validation

A.   3D Sharp Elliptic Cone

Three dimensional calculations are carried out for a Mach 8 sharp elliptic cone originally studied experimentally by Kimmel et al.[19, 20] The cone was mounted parallel to the freestream and consisted of a 2:1 aspect ratio, a half angle along the major axis of $14°$, and a length $L = 1.016$ m. It was machined from stainless steel with a 40 μm nose radius and surface roughness less than 0.81 μm. The flow conditions are listed in Table 1.

Table 1. Flow conditions for the experiment of Kimmel et al.[19, 20]

Parameter	Value	
M	7.93	
u_∞	1180.0	m/s
T_∞	54.6	K
T_w	303.0	K
T_0	728.0	K
p_∞	165.0	Pa
ρ_∞	0.011	kg/m³
μ_∞	3.77×10^{-6}	kg/m·s
Re_L	3.33×10^6	

A structured grid is generated because it is known to produce better results than unstructured meshes in regions near the surface of the body and through a shock.[21] One quarter of the geometry is used in the simulation because planes of symmetry exist along the major and minor axes. The 40 μm nose radius is accounted for along the tip's minor axis, resulting in an 80 μm radius along the major axis because of the elliptic geometry.

4 of 24

The model is aligned with the x-axis in the axial direction, the y-axis in the horizontal direction, and the z-axis in the vertical direction. A cylindrical coordinate system is also employed with $\theta = 0°$ at the top centerline of the model (z-axis) and $\theta = 90°$ at the leading edge (y-axis) as seen in Figure 1.

A gradual increase in grid spacing is used along the conic body with the smallest spacing near the tip. Radial points are algebraically spaced to increase the number of points close to the body. Grid points are equally spaced along the circumference. As a result, cell clustering occurs near the surface and the tip of the body. A grid independence study is conducted with $i \times j \times k$ grid dimensions changing from $330 \times 40 \times 30$, to $440 \times 50 \times 40$, to $550 \times 60 \times 50$. Based on comparisons of the solutions obtained on these meshes the $440 \times 50 \times 40$ grid is considered sufficiently refined and is used in the rest of the analysis. See Ref. 22 for more details.

Cross-sectional slices of the computed surface conditions are extracted to match the locations of the experimental measurements. Figure 2(a) shows the nondimensional pressure along the circumference of the body at x/L = 0.625. The pressure is relatively constant from the top centerline ($\theta = 0°$) to the shoulder ($\theta = 45°$), followed by a noticeable rise between the shoulder and the leading edge ($\theta = 90°$). Kimmel *et al.* also provided computational results from a parabolized Navier-Stokes (PNS) solver[19, 20] which are included in the figures as an additional reference.

Although the cone is sharp, the formation of the boundary layer at its tip results in a noticeable rise in pressure and temperature near the stagnation point. This rise in pressure can be seen in Figure 2(b) for two different rays. The pressure quickly relaxes as the flow proceeds along the rest of the cone due to the viscous interaction. It is worth noting that the PNS solution does not capture the behavior of the flow field in the stagnation region of the cone because of the physical simplifications inherent in that method.

The high length Reynolds number (Re_L) and overall length of the model cause the flow to transition to turbulence as it proceeds along the body. LeMANS does not currently have a turbulence model implemented, so numerical results in the transitional and turbulent regions should be disregarded. Plots of the Stanton number as a function of Reynolds number are presented in Figures 3(a), 3(b) and 3(c) for $\theta = 0°$, $45°$, $88°$. In all three plots, the flow starts out laminar and then transitions to turbulent as it proceeds along the body. The measured data were for $Re_L = 1.7 \times 10^6$ and 6.6×10^6, whereas the case run by LeMANS has $Re_L = 3.3 \times 10^6$. Because of flow similarity, the length Reynolds number does not affect the Stanton number in the laminar region and LeMANS accurately predicts its distribution for these cases.

B. 3D Blunt Elliptic Cone

A second three dimensional validation study is performed on a Mach 14 blunt elliptic cone originally studied experimentally by Nowlan *et al.*[23] The model was mounted parallel to the freestream and had a 2:1 aspect ratio, a half angle along the major axis of $10°$, and a length $L = 0.21$ m. Details of cone geometry are provided in Fig. 4. The flow conditions are listed in Table 2.

Table 2. Flow conditions for Run 15 of the Nowlan *et al.* experiment.[23]

Parameter	Value	
Mach	14.2	
u_∞	2190.	$^m/_s$
T_∞	59.3	K
T_w	294.0	K
T_0	211.0	K
p_∞	51.0	Pa
ρ_∞	0.003	$^{kg}/_{m^3}$
μ_∞	4.3×10^{-6}	$^{kg}/_{m \cdot s}$
Re_L	3.17×10^5	

A structured grid is generated following the same procedures and coordinate system as the sharp elliptic cone. A grid independence study is conducted with $i \times j \times k$ grid dimensions changing from $150 \times 30 \times 30$, to $300 \times 60 \times 60$, to $380 \times 80 \times 80$. The $300 \times 60 \times 60$ grid is considered sufficiently refined and is used in

Approved for public release; distribution unlimited.

the rest of the analysis. Additional details on grid convergence are available in Ref. 22.

Figure 5 shows the nondimensional pressure along the circumference of the body at two axial locations and along two rays. Following a similar trend as the sharp cone observations, the pressure is relatively constant from the top centerline to the shoulder, followed by a gradual rise between the shoulder and the leading edge. The variation in pressure distribution along the rays is more dramatic compared to the sharp cone because the blunt tip results in a strong detached bow shock and, consequently, a large stagnation region. Stanton number distributions in Fig. 6 show the profiles obtained with LeMANS follow the same general trends as those observed in the measurements.

Overpredictions observed in the nondimensional pressure and Stanton number distributions may be due to several influences not accounted for in the simulations. Nowlan *et al.* noted an uncertainty of ± 7 percent in the freestream flow conditions and the very cold freestream flow conditions ($T_\infty = 59.3$ K) could have lead to condensation on the nozzle. In addition, the CAL 48-inch shock tunnel could have developed 'frozen' freestream conditions ($T_v \gg T_\infty$) as the flow accelerated through the nozzle. Nompelis *et al.* computationally demonstrated that accounting for vibrational nonequilibrium freestream conditions greatly improved agreement between computational and experiment heat transfer measurements collected in a CAL shock tunnel for their hypersonic double-cone experiment.[24] Despite the discrepancies, overall, LeMANS effectively demonstrates its capability of accurately computing three dimensional hypersonic flows.

IV. Energy Deposition

The blunt elliptic cone geometry is selected to represent a fairly realistic hypersonic vehicle, with $L = 3$ m set as the representative vehicle length. Assuming the vehicle has constant material density, its center of gravity (CG) is located 1.95 m from the tip along the x-axis ($x/L = 0.65$). The model is simulated in air at 40 km altitude, a freestream velocity of 4000 $^\mathrm{m}/_\mathrm{s}$, and 0° angle of attack. The complete flow conditions are provided in Table 3.

Table 3. Flow conditions for Mach 12.6 air flow at an altitude of 40 km.

Parameter	Value	
Mach	12.6	
u_∞	4000.0	$^\mathrm{m}/_\mathrm{s}$
T_∞	250.0	K
T_w	300.0	K
T_0	8300.0	K
p_∞	289.0	Pa
ρ_∞	0.004	$^\mathrm{kg}/_\mathrm{m^3}$
μ_∞	1.6×10^{-5}	$^\mathrm{kg}/_\mathrm{m \cdot s}$
Re_L	3.0×10^6	

A grid independence study is conducted with $i \times j \times k$ grid dimensions changing from $300 \times 60 \times 60$, to $380 \times 80 \times 80$, to $400 \times 80 \times 120$. Grid independence is achieved with the $380 \times 80 \times 80$ grid that is used in the following simulations that include energy deposition. Details on the grid convergence study are available in Ref. 22.

A. Reference Pitching Moment

A nominal reference pitching moment is found by assuming a 2° flap with a cross-sectional area of 0.2 m × 0.5 m is attached along the vehicle's top centerline as illustrated in Fig. 7. The size and location of the flap are based on illustrations of the hypersonic test vehicle shown in Ref. 25. The control authority provided by the mechanical flap is estimated computationally by incorporating the flap with the blunt elliptic cone geometry.

The flap is accounted for in the blunt elliptic cone geometry by flaring the last 0.2 m of the cone. The flair extends around the circumference of the cone and has a 2° inclination. Extending the flair around the

Approved for public release; distribution unlimited.

circumference of the body simplifies the geometry and eliminates unnecessary complexities (ie. modeling the edge of the extended flap). Since the spanwise width of the actual flap extends 0.25 m ($\theta = 18°$) from the top centerline ($\theta = 0°$), the estimated control authority provided by the flap is computed by multiplying the increased body force within that region by its moment arm (1.05 m). This results in a pitching moment ($M_{p\,\text{flap}}$) of 22.8 N-m.

B. Parametric Study

To limit the scope of the problem, three volumetric deposition shapes are selected. Namely a sphere, pancake (oblate spheroid), and bean (prolate spheroid) are employed such that a representative volume of the ellipsoidal region ($V = 4/3\pi abc$) remains constant. The values used are listed in Table 4.

Table 4. Deposition geometry parameters for Mach 12 blunt elliptic cone ($L = 3$ m).

	a	b	c
Sphere	0.007 m	0.007 m	0.007 m
Pancake	0.01852 m	0.01852 m	0.001 m
Bean	0.001852 m	0.1 m	0.001852 m

The centroid of the deposition is positioned along the top centerline ($y_0 = 0$ m) and is at least three characteristic length scales (λ) away from the surface of the body to ensure the entire deposition is deposited into the flow-field ($\iiint_{-3\lambda}^{3\lambda} S\, dx\, dy\, dz = 0.9999Q$). This distance is the minimum length from the centroid of a spherical deposition to the surface of the body as illustrated in Figure 8.

$$x_0 = x_1 + 3\lambda \cdot ||n_{x_1}|| \tag{7}$$

$$z_0 = z_1 + 3\lambda \cdot ||n_{z_1}|| \tag{8}$$

$$\phi = \tan^{-1}\left|\left|\frac{n_{x_1}}{n_{z_1}}\right|\right| \tag{9}$$

With $3\lambda = 3a$, the values of z_0 and ϕ are determined for a given x_0 by enforcing equations (7) and (8). This determines the location of $[x_1, z_1]$ and its outward unit normal vector $\mathbf{n}$. Equation (9) is used to determine ϕ so the polar radii of the ellipsoidal deposition aligns with $\mathbf{n}$. The oblate spheroid is positioned so its major axis is parallel to the freestream flow, whereas the major axis of the prolate spheroid is perpendicular to the freestream flow.

Using the Mach 5 flat plate experiment originally studied by Kimmel *et al.*[26, 27] and recent MHD power generation experiments[28] for reference, realistic power input is assumed to lie in the range of 1 kW to 15 kW. The deposition is positioned near the nose of the vehicle tip to maximize the distance from the center of gravity (CG). This is done not only to increase the moment arm of the body force due to the deposition, but also because larger force changes are observed when the actuator is placed near the leading edge bow shock.[10] The three deposition shapes are studied with variation of two additional parameters: the deposition input power (Q) and the distance along the body (x/L).

The total amount of power deposited into the flow is characterized by the nondimensional total power deposition value $\tilde{Q}$.

$$\tilde{Q} = \frac{Q}{\rho_\infty u_\infty^3 L^2} \tag{10}$$

For the cases in the study $\tilde{Q} = 4.3 \times 10^{-7}$, 1.7×10^{-6}, and 6.5×10^{-6} for Q = 1 kW, 4 kW, and 15 kW respectively. This parameter provides some information on vehicle and application scaling.

The axial location of the energy deposition is apparent after investigating the pressure coefficient and Stanton number along the top centerline ($\theta = 0°$) for the three shapes in Figure 9. Although there is a slight increase in the Stanton number, it is accompanied by a noticeable rise in the pressure coefficient, particularly in the sphere and pancake depositions. This may be due to the fact that a sphere has the minimum surface

Approved for public release; distribution unlimited.

area of a spheroid, and consequently, has the highest power deposited per projected surface area onto the body. The total force acting on the body in the Cartesian coordinate system is found by taking the scalar product of the combined stress tensor and pressure matrices with the corresponding area vector.

With the local force known, the pitching moment is determined in the conventional manner. Because of the deposition on the top half of the vehicle, the pitching moment for each scenario is its deviation from the baseline ($M_p = M_{p\,\text{deposition}} - M_{p\,\text{baseline}}$). It is normalized by the moment due to the mechanical flap ($M_{p\,\text{flap}} = 22.8$ N-m). Figure 10 plots the normalized change in pitching moment for each of the shapes. The points are fitted with a parametric spline because of their assumed non-linearity.

All simulations are computed assuming thermal equilibrium and use a 5 species finite rate chemistry model (N_2, O_2, NO, N, and O) except for the largest deposition scenario (Q = 50 kW, x/L = 0.10, 'pancake'). This scenario is repeated for two additional conditions: thermal equilibrium, 11 species chemistry model; and thermal nonequilibrium, 11 species chemistry model. The 11 species chemistry model (N_2, O_2, NO, N, O, N_2^+, O_2^+, NO^+, N^+, O^+, e) accounts for weakly ionized plasmas. These additional cases are compared against their respective baseline cases to determine the effectiveness of the deposition.

For thermal equilibrium air, the inclusion of a larger chemistry model has a relatively small impact on the total pitching moment as seen in the Q=50 kW case (equilibrium, 5 sp vs. equilibrium, 11 sp). Thermal nonequilibrium noticeably reduces the effectiveness of the energy deposition because only the energy going into the translational temperature can affect the local pressure and thus the net force. Comparing the results for the thermal equilibrium, 5 species simulations to the thermal nonequilibrium, 11 species simulations for the Q=30, 50 kW cases, it is clear that thermal nonequilibrium and weakly ionized plasma effects become increasing significant as the total power deposited increases and the flow deviates from a perfect gas.

Figure 10 shows energy deposition is able to provide the same order of magnitude of control authority as the mechanical flap. In addition, while the shape of the deposition appears to have noticeable effects on the local pressure coefficient and Stanton number, it does not appear to have a large impact on the overall change in the pitching moment (control authority).

C.   Hot Wall Effect

The previous simulations used a constant wall temperature of 300 K as seen Table 3. This is cooler than the expected wall temperature of a real hypersonic vehicle. Assuming blackbody emissivity ($\epsilon = 1$), the Stefan-Boltzmann Law is used along with the computed heat flux on the body to estimate the expected wall temperature.

$$T_w = \left(\frac{q_w}{\epsilon\sigma}\right)^{1/4} \tag{11}$$

This estimated wall temperature varies from 600 - 1900 K along the cone, with an average temperature of 1000 K in the region where the deposition would be located. A new set of simulations is carried out with $T_w = 1000$ K, and all other conditions equal to those listed in Table 3. The simulations are performed using the 'pancake' deposition parameters listed in Table 4 and the centroid of the deposition located at x/L = 0.1. The moment coefficient is calculated for each simulation using equation (12).

$$C_m = \frac{M_p}{\frac{1}{2}\rho_\infty u_\infty^2 L^2 d} \tag{12}$$

The reference area is taken to be the maximum spanwise width ($d = 1.644$ m) multiplied by the body length ($L = 3$ m). Figure 11 plots the moment coefficient versus power deposited for two constant wall temperatures. The higher wall temperature reduces the moment coefficient (control authority) of the vehicle because a smaller portion of the energy deposited goes into the translational temperature.

V.   Additional Vehicle Configurations

The freestream conditions used in the simulations of the 3 m configuration (Table 3) are also applied to two additional, scaled geometries. The 'medium' scaled vehicle has a length $L = 0.62$ m. The nondimensional total power deposition value $\tilde{Q}$ for the cases run is, $\tilde{Q} = 4.0 \times 10^{-5}$, 1.0×10^{-4}, and 1.5×10^{-4} for Q = 4 kW, 10 kW, and 15 kW respectively.

The deposition is modeled as an oblate spheroid (pancake), scaled to match the one used in the $L = 3$ m parametric study. Table 5 lists the values used to represent the energy deposition volume with the deposition positioned near the bow shock (x/L = 0.10).

Table 5. The location of energy deposition for Mach 12.6 blunt elliptic cone ($L = 0.6$ m).

a	b	c
0.00386 m	0.00386 m	0.00021 m

The moment coefficient for the simulations is found using Eq. (12) with $d = 0.343$ m. The pitching moment due to the mechanical flap is found following the approach covered in section IV.A with the large geometry flap dimensions proportionately scaled (10.5 cm $\times$ 4.2 cm). This results in a pitching moment ($M_{p\,\text{flap}}$) of 0.148 N-m. The smaller geometry produces a weaker bow shock and consequently a lower post shock temperature. Similar to section IV.C, the cooler temperature improves the control authority provided by energy deposition. However, a large spike in the Stanton number distribution is observed in Figure 12. This coincides with location of the deposition and partially recovers to the baseline distribution as the flow progresses along the body. The distribution can not fully recover because of the additional energy added to the flow.

The effects of energy deposition are also simulated for several cases using a 'small' $L = 0.21$ m blunt elliptic cone with freestream conditions found in Table 2. These conditions represent an altitude of 42 km in air, based on the unit Reynolds number. The decrease in freestream velocity along with the significantly smaller geometry increases the nondimensional total power deposition value $\tilde{Q}$ by several orders of magnitude. For the cases run, $\tilde{Q} = 4.0 \times 10^{-4}$, 8.0×10^{-4}, and 1.6×10^{-3} for Q = 500 W, 1 kW, and 2 kW respectively.

The deposition is modeled as an oblate spheroid (pancake), similar to the one used in the $L = 3$ m parametric study. Table 6 lists the values used to represent the energy deposition volume and centroid. Unlike the medium cone, the deposition shape is larger than a pro

Table 6. The location of energy deposition for Mach 14 blunt elliptic cone ($L = 0.2$ m).

x_0	y_0	z_0	a	b	c	θ
0.0292 m	0 m	0.017 m	0.003 m	0.004 m	0.001 m	$0°$

Compared to the previous configurations, the small geometry produces an even weaker bow shock, which further reduces the post shock temperature. In addition, the freestream temperature and total enthalpy are much lower in these simulations (refer to Table 2). This allows for a larger portion of the deposition to increase the translational temperature (net force increase). In addition, the shorter body length (L) means the flow passes over the vehicle quicker so the large temperature rise observed within the region of the deposition extends farther along the vehicle. This is apparent in the significant downstream temperatures observed in Figure 13.

Coinciding with the high temperature, a strong heat transfer penalty is detected, along with a dramatically increase in the pressure coefficient distribution (Fig. 14). Although the Stanton number remains significantly elevated downstream of the deposition, the pressure coefficient quickly returns to the baseline (equilibrium) state which is consistent to the observations seen in the large and medium cone simulations.

The moment coefficient is found using equation (12) with $d = 0.114$ m. Consistent with previous simulations, the pitching moment due to the mechanical flap is computed following the method presented in section IV.A with the large geometry flap dimensions scaled down proportionately (3.5 cm $\times$ 1.4 cm). This results in a pitching moment ($M_{p\,\text{flap}}$) of 10^{-3} N-m.

These results, along with those obtained for the medium and large blunt elliptic cone simulations, are plotted together in Figure 15 using the nondimensional total power deposition parameter $\tilde{Q}$. Figure 15(a) shows a strong correlation between $\tilde{Q}$ and the moment coefficient for the various simulations. As previously noted, the scale deposition shape of the small cone does not exactly match the medium or large cones, but these results further demonstrate the minimal contribution deposition shape has on the net control authority. The results appear to follow a near linear curve when plotted on a log-log scale ($C_m \approx \tilde{Q}^{1.1}$). The different

deposition locations, along with different vehicle lengths and freestream conditions, and real gas effects cause the results to deviate slightly from the linear curve.

Using the reference pitching moment found for each of the configurations, the normalized pitching moment for each configurations is plotted in Fig. 15(b). Again, the results follow a near linear curve on a log-log scale ($M_p/M_{p\,\text{flap}} \approx \tilde{Q}^{1.3}$) with deviations from the curve due to the aforementioned reasons. The figure shows that energy deposition is a viable replacement for a mechanical flap when $\tilde{Q} \geq 10^{-5}$. Given that $\tilde{Q} = Q/\rho_\infty u_\infty^3 L^2$, this suggests smaller geometries, flying a lower velocities, and/or higher altitudes (lower densities) would make energy deposition a viable replacement for a mechanical flap. For completeness, the pitching moment (M_p) for all simulations is listed in the Appendix Tables 7 - 10.

VI.   Conclusions

The Michigan Aerothermodynamic Navier-Stokes code was successfully validated for hypersonic flow around three-dimensional blunt and sharp elliptic cones. In addition, a phenomenological heating model was implemented to investigate whether a practical level of control could be achieved from volumetric energy deposition for a realistic hypersonic vehicle. A parametric study was completed investigating the shape, location, and total amount of energy volumetrically deposited into the flow-field for two blunt-nosed elliptic cone configurations. The shape of the deposition resulted in relatively small changes in the effectiveness of the deposition, whereas an increased wall temperature noticeably decreased the moment coefficient. Thermal nonequilibrium and weakly ionized plasma effects also decrease the control authority as input power increases. The effectiveness of volumetric energy deposition for flight control appeared to scale strongly with the nondimensional parameter based on the freestream flow kinetic energy flux. It appears to be a viable means of control for configurations at higher altitude, with slower velocities, and smaller vehicle length.

Acknowledgments

References

[1]Fomin, V. M., Tretyakov, P. K., and Taran, J.-P., "Flow Control using Various Plasma and Aerodynamic Approaches," *Aerospace Science and Technology*, Vol. 8, No. 5, 2004, pp. 411–421.

[2]Shang, J. S., Surzhikov, S. T., Kimmel, R., Gaitonde, D., Menart, J., and Hayes, J., "Mechanisms of Plasma Actuators for Hypersonic Flow Control," *Progress in Aerospace Sciences*, Vol. 41, No. 8, 2005, pp. 642–668.

[3]Mason, W. H. and Lee, J., "Aerodynamically Blunt and Sharp Bodies," *10th AIAA Applied Aerodynamics Conference*, AIAA Paper 1992-2727, 1992.

[4]Santos, W. F. N. and Lewis, M. J., "Aerothermodynamic Performance Analysis of Hypersonic Flow on Power Law Leading Edges," *Journal of Spacecraft and Rockets*, Vol. 42, No. 4, 2005, pp. 588–597.

[5]Shang, J. S., Hayes, J., and Menart, J., "Hypersonic Flow over a Blunt Body with Plasma Injection," *Journal of Spacecraft and Rockets*, Vol. 39, No. 3, 2002, pp. 367–375.

[6]Kremeyer, K., Sebastian, K., and Shu, C.-W., "Computational Study of Shock Mitigation and Drag Reduction by Pulsed Energy Lines," *AIAA Journal*, Vol. 44, No. 8, 2006, pp. 1720–1731.

[7]Yan, H. and Gaitonde, D., "Control of Edney IV Interaction by Energy Pulse," *44th AIAA Aerospace Sciences Meeting and Exhibit*, AIAA Paper 2006-562, 2006.

[8]Girgis, I. G., Shneider, M. N., Macheret, S. O., Brown, G. L., and Miles, R. B., "Creation of Steering Moments in Supersonic Flow by Off-Axis Plasma Heat Addition," *40th AIAA Aerospace Sciences Meeting and Exhibit*, 2002, AIAA Paper 2002-129.

[9]Gnemmi, P., Charon, R., Dupéroux, J.-P., and George, A., "Feasibility Study for Steering a Supersonic Projectile by a Plasma Actuator," *AIAA Journal*, Vol. 46, No. 6, 2008, pp. 1308–1317.

[10]Menart, J., Stanfield, S., Shang, J., Kimmel, R., and Hayes, J., "Study of Plasma Electrode Arrangements for Optimum Lift in a Mach 5 Flow," *44th AIAA Aerospace Sciences Meeting and Exhibit*, 2006, AIAA Paper 2006-1172.

[11]Updike, G. A., Shang, J. S., and Gaitonde, D. V., "Hypersonic Separated Flow Control Using Magneto-Aerodynamic Interaction," *43rd AIAA Aerospace Sciences Meeting and Exhibit*, AIAA Paper 2005-164, 2005.

[12]Kimmel, R. L., Hayes, J. R., Crafton., J. W., Fonov, S. D., Menart, J., and Shang, J., "Surface Discharge for High-Speed Boundary Layer Control," *44th AIAA Aerospace Sciences Meeting and Exhibit*, AIAA Paper 2006-710, 2006.

[13]Miles, R. B., Macheret, S. O., Shneider, M. N., Steeves, C., Murray, R. C., Smith, T., and Zaidi, S. H., "Plasma-Enhanced Hypersonic Performance Enabled by MHD Power Extraction," *43th AIAA Aerospace Sciences Meeting and Exhibit*, AIAA Paper 2005-561, 2005.

[14]Scalabrin, L. C. and Boyd, I. D., "Development of an Unstructured Navier-Stokes Solver For Hypersonic Nonequilibrium Aerothermodynamics," *38th AIAA Thermophysics Conference*, AIAA Paper 2005-5203, 2005.

[15]Scalabrin, L. C. and Boyd, I. D., "Numerical Simulation of Weakly Ionized Hypersonic Flow for Reentry Configurations," *9th AIAA/ASME Joint Thermophysics and Heat Transfer Conference*, AIAA Paper 2006-3773, 2006.

[16]Scalabrin, L. C. and Boyd, I. D., "Numerical Simulation of the FIRE-II Convective and Radiative Heating Rates," *39th AIAA Thermophysics Conference*, AIAA Paper 2007-4044, 2007.

[17]Scalabrin, L. C., "Numerical Simulation of Weakly Ionized Hypersonic Flow Over Reentry Capsules," Ph.D. Thesis, Univ. of Michigan, 2007.

[18]Poggie, J., "Plasma-Based Hypersonic Flow Control," *37th AIAA Plasmadynamics and Lasers Conference*, AIAA Paper 2006-3567, 2006.

[19]Kimmel, R. L., Poggie, J., and Schwoerke, S. N., "Laminar-Turbulent Transition in a Mach 8 Elliptic Cone Flow," *AIAA Journal*, Vol. 37, No. 9, 1999, pp. 1080–1087.

[20]Kimmel, R., Klein, M., and Schwoerke, S., "Three-Dimensional Hypersonic Laminar Boundary-Layer Computations for Transition Experiment Design," *AIAA Journal*, Vol. 34, No. 4, 1997, pp. 409–415.

[21]Candler, G., "Unstructured Grid Approaches for Accurate Aeroheating Simulations," *18th AIAA Computational Fluid Dynamics Conference*, AIAA Paper 2007-3959, 2007.

[22]Bisek, N. J., Boyd, I. D., and Poggie, J., "Numerical Study of Energy Deposition Requirements for Aerodynamic Control of Hypersonic Vehicles," *46nd AIAA Aerospace Sciences Meeting and Exhibit*, AIAA Paper 2008-1109, 2008.

[23]Nowlan, D., Burke, A., and Bird, K., "Pressure and Heat Transfer Distribution on ASD Elliptic Cone (W3) and ASD Sortie (W4) in the CAL 48-Inch Hypersonic Shock Tunnel," Tech. Rep. AM-1800-Y-2, Cornell Aeronautical Laboratory, Inc., Buffalo, NY, December 1963, ASC 94 2649.

[24]Nompelis, I., Candler, G., and Holden, M., "Effect of Vibrational Nonequilibrium on Hypersonic Double-Cone Experiments," *AIAA Journal*, Vol. 41, No. 11, 2003, pp. 2162–2169.

[25]Walker, S. H. and Rodgers, F., "Falcon Hypersonic Technology Overview," *13th AIAA/CIRA International Space Planes and Hypersonics Systems and Technologies Conference*, AIAA Paper 2005-3253, 2005.

[26]Kimmel, R. L., Hayes, J. R., Menart, J. A., and Shang, J., "Effect of Surface Plasma Discharges on Boundary Layers at Mach 5," *42nd AIAA Aerospace Sciences Meeting and Exhibit*, AIAA Paper 2004-509, 2004.

[27]Kimmel, R., Hayes, J., Menart, J., and Shang, J., "Supersonic Plasma Flow Control Experiments," Tech. Rep. ARFL-VA-WP-TR-2006-3006, U.S. Air Force Research Laboratory, Wright-Patterson AFB, OH, December 2005, AFRL/WS 06-0097.

[28]Velocci, A. L. J., "A General Atomics-led Team," *Aviation Week and Space Technology*, 2007.

Appendix

Table 7. Pitching moment for large cone simulations with freestream conditions found in Table 3 and deposition parameters listed in Table 4. ($L = 3$ m, $T_w = 300$ K).

Shape	x/L	Q [kW]	M_p [N-m]
thermal equilibrium, 5 sp.			
flap			22.8
sphere	0.05	1	3.73
sphere	0.05	4	5.55
sphere	0.05	15	16.81
sphere	0.10	1	4.03
sphere	0.10	4	6.91
sphere	0.10	15	16.04
bean	0.05	1	6.16
bean	0.05	4	8.86
bean	0.05	15	17.41
bean	0.10	1	5.86
bean	0.10	4	6.57
bean	0.10	15	16.97
pancake	0.05	1	3.75
pancake	0.05	4	6.54
pancake	0.05	15	17.05
pancake	0.10	1	4.35
pancake	0.10	4	6.66
pancake	0.10	15	15.51
pancake	0.10	30	18.36
pancake	0.10	50	27.28
thermal equilibrium, 11 sp.			
pancake	0.10	50	25.76
thermal nonequilibrium, 11 sp.			
pancake	0.10	30	15.9
pancake	0.10	50	21.29

50
Approved for public release; distribution unlimited.

Table 8. Pitching moment for large cone simulations with freestream conditions found in Table 3 and deposition parameters listed in Table 4. ($L = 3$ m, $T_w = 1000$ K).

Shape	x/L	Q [kW]	M_p [N-m]
thermal equilibrium, 5 sp.			
flap			21.6
pancake	0.10	0.5	0.58
pancake	0.10	1	0.75
pancake	0.10	4	3.22
pancake	0.10	15	10.04

Table 9. Pitching moment for medium cone simulations with freestream conditions found in Table 3 and deposition parameters listed in Table 5. ($L = 0.6$ m, $T_w = 300$ K).

Shape	x/L	Q [kW]	M_p [N-m]
thermal equilibrium, 5 sp.			
flap			0.15
pancake	0.10	4	0.36
pancake	0.10	10	0.78
pancake	0.10	15	1.08

Table 10. Pitching moment for small cone simulations with freestream conditions found in Table 2 and deposition parameters listed in Table 6. ($L = 0.2$ m, $T_w = 294$ K).

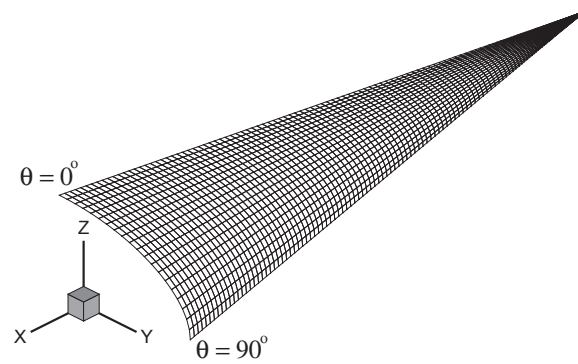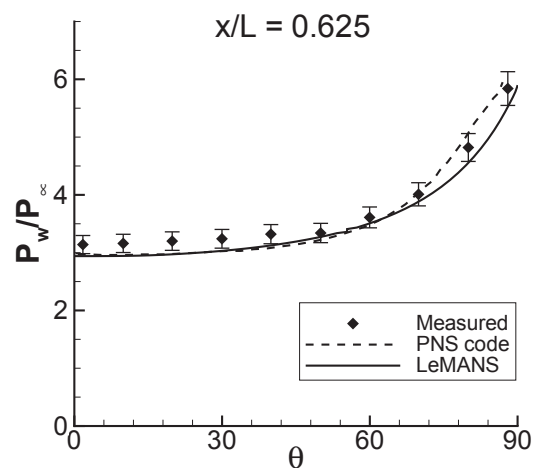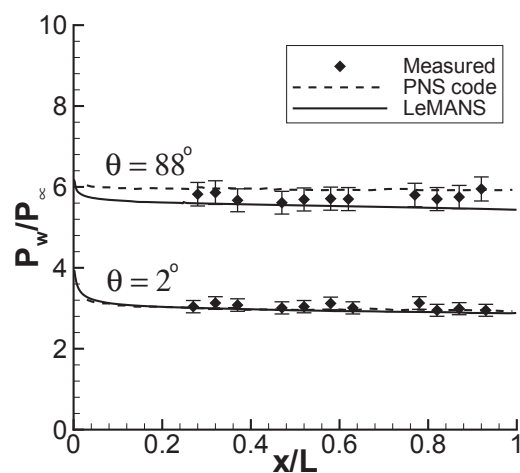| Shape	x/L	Q [kW]	M_p [N-m]
thermal equilibrium, 5 sp.			
flap			0.001
pancake	0.10	0.5	0.023
pancake	0.10	1	0.039
pancake	0.10	2	0.061

Approved for public release; distribution unlimited.

Figure 1. Surface of the sharp elliptic cone grid with both Cartesian and cylindrical coordinate systems.

Approved for public release; distribution unlimited.

(a) Pressure around the circumference

(b) Pressure along rays

Figure 2. Normalized surface pressure distributions for the Mach 8 sharp elliptic cone (±5 percent experimental uncertainty). PNS calculations and experimental data from Ref. 19.
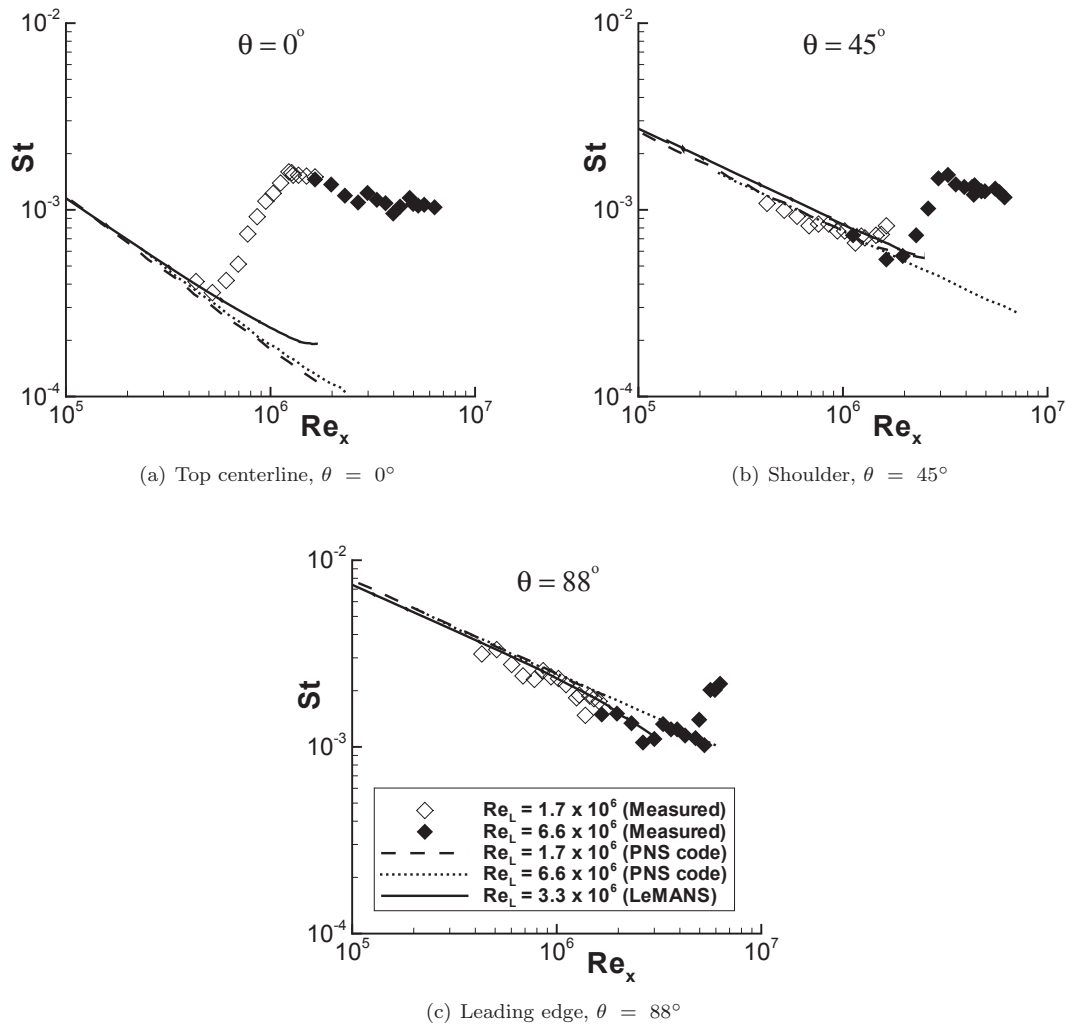
Approved for public release; distribution unlimited.

(a) Top centerline, $\theta = 0°$

(b) Shoulder, $\theta = 45°$

(c) Leading edge, $\theta = 88°$

Figure 3. Stanton number distributions for the Mach 8 sharp elliptic cone (symbol size reflects ±10 percent experimental uncertainty). Experimental data and PNS calculations from Ref. 19.
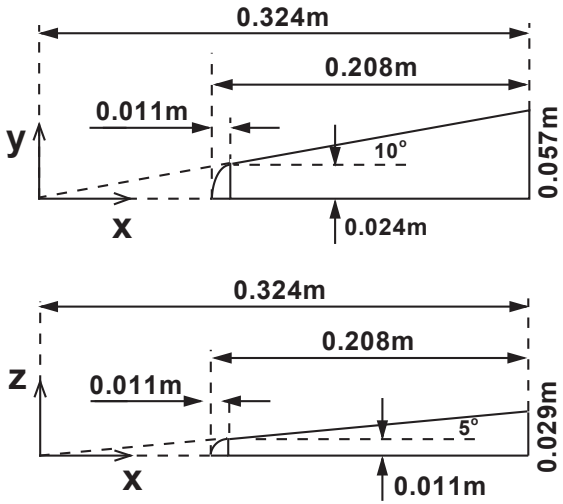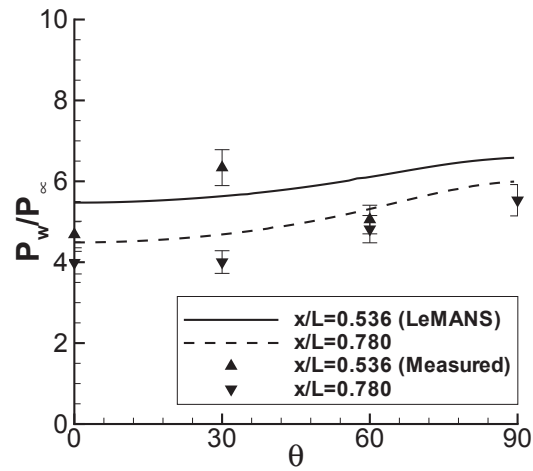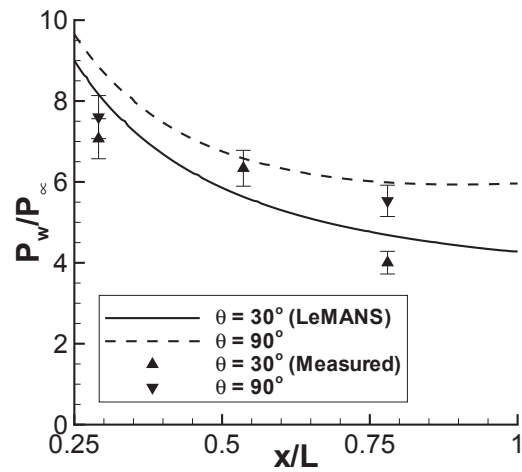
Approved for public release; distribution unlimited.

Figure 4. Blunt elliptic cone geometry. Adapted from Ref. 23.
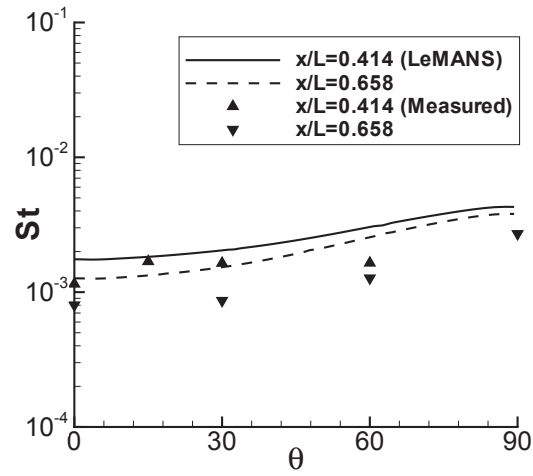
Approved for public release; distribution unlimited.
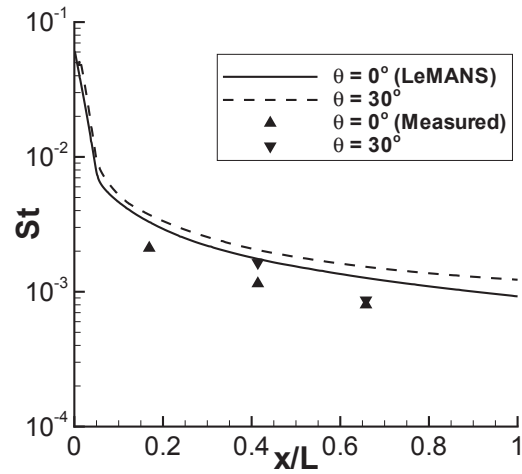
(a) Pressure around the circumference

(b) Pressure along rays

Figure 5. Normalized surface pressure distributions for Mach 14 blunt elliptic cone ($\pm$7 percent experimental uncertainty). Experimental data from Ref. 23.

Approved for public release; distribution unlimited.

(a) Stanton number around the circumference

(b) Stanton number along rays

Figure 6. Stanton number distributions for Mach 14 blunt elliptic cone (symbol size reflects ±4.5 percent experimental uncertainty). Experimental data from Ref. 23.
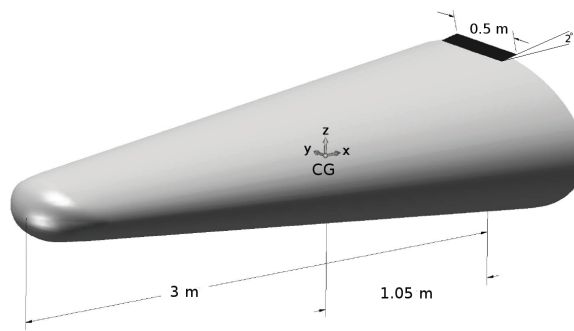

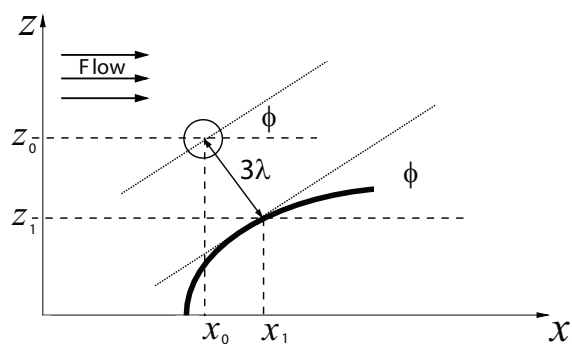**Figure 7. Model of a 2° mechanical flap attached to a blunt elliptic body.**

Approved for public release; distribution unlimited.

Figure 8. The constant height parameter used to determine z_0 and ϕ.

(a) Sphere deposition

(b) 'Pancake' deposition
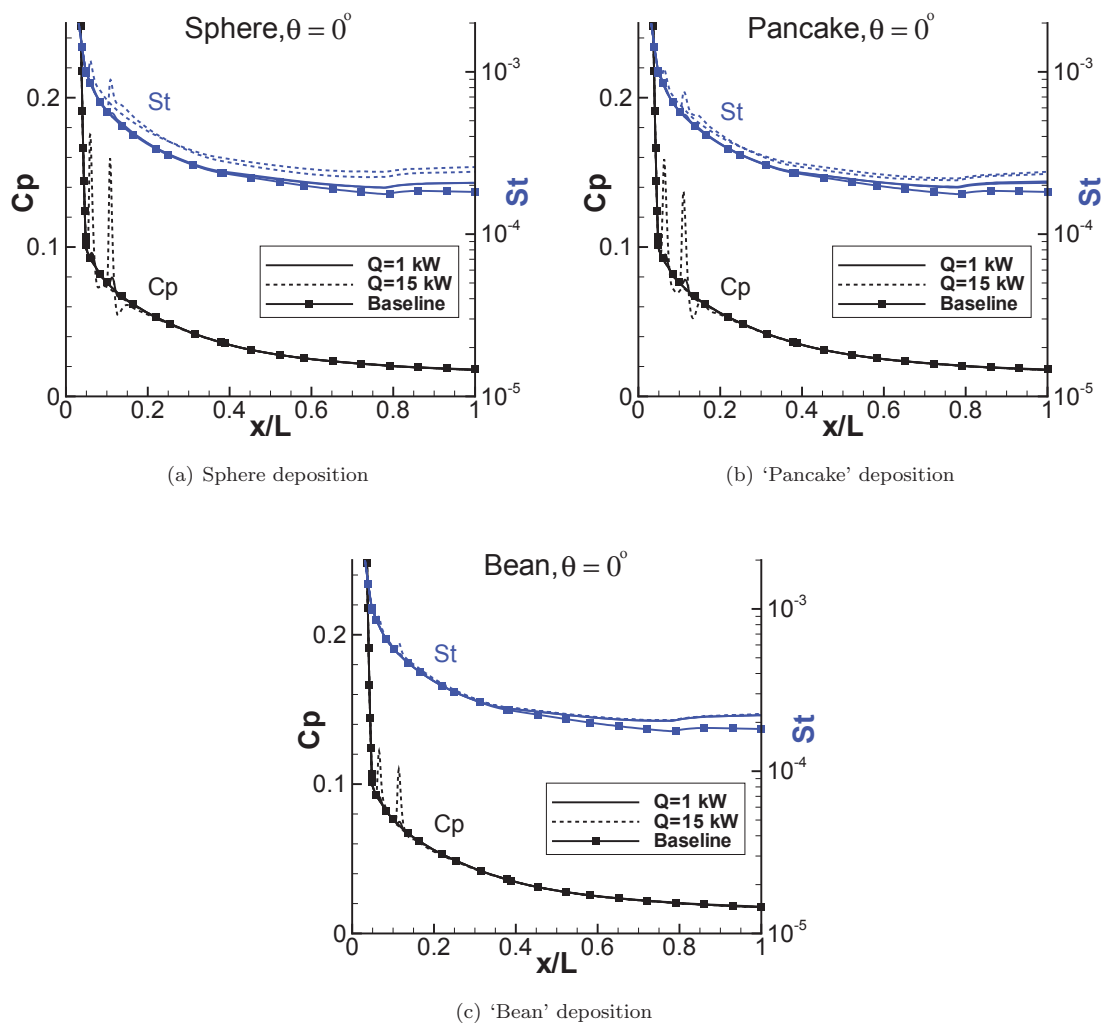

(c) 'Bean' deposition

Figure 9. Pressure coefficient and Stanton number distributions for the Mach 12 blunt elliptic cone ($L = 3$ m) for various energy deposition patterns along the top centerline ($T_w = 300$ K).

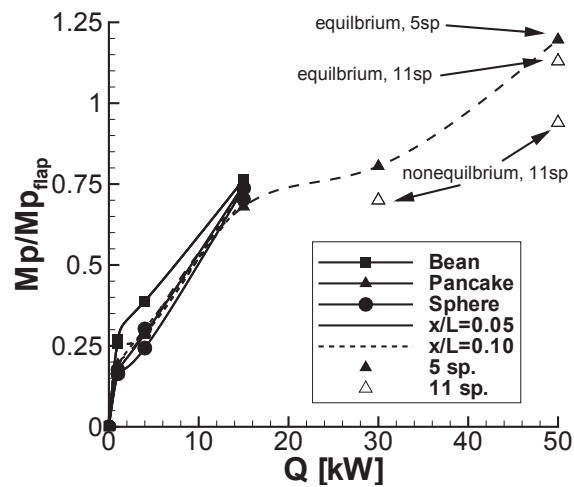Approved for public release; distribution unlimited.

Figure 10. Normalized change in pitching moment for a Mach 12 blunt elliptic cone ($L = 3$ m) for various energy deposition patterns ($T_w = 300$ K).
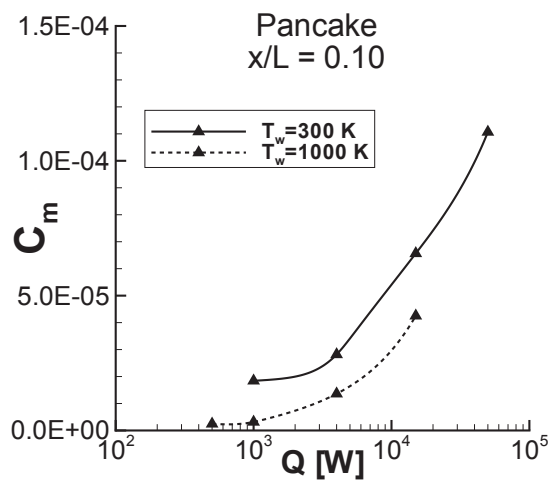
Figure 11. Moment coefficient for a Mach 12 blunt elliptic cone ($L = 3$ m) for two constant wall temperatures.

Approved for public release; distribution unlimited.

Figure 12. Pressure coefficient and Stanton number distributions along the top center line ($\theta = 0°$) of a Mach 12 blunt elliptic cone ($L = 0.6$ m) with different amounts of energy deposition ($T_w = 300$ K).
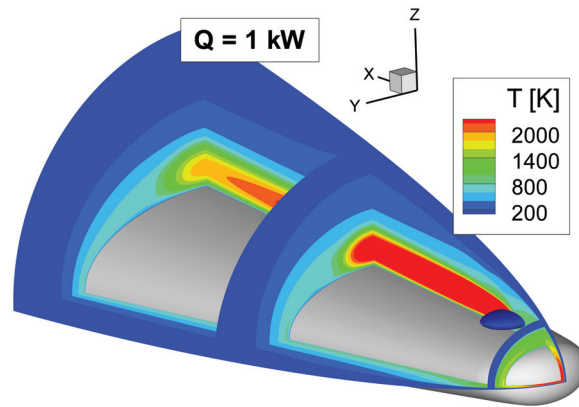
Figure 13. Temperature contours for Mach 14 blunt elliptic cone ($L = 0.2$ m) with $Q = 1$ kW.
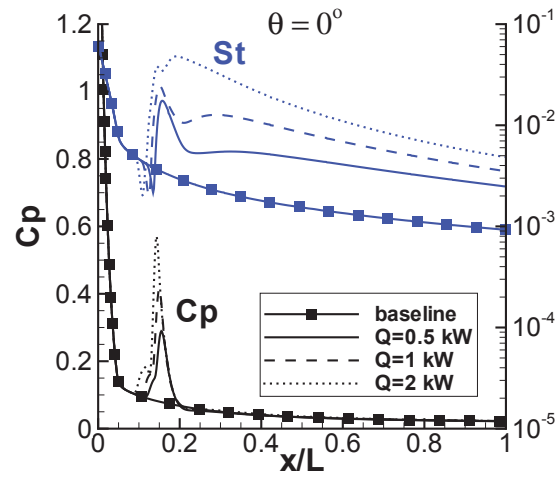
Approved for public release; distribution unlimited.

Figure 14. Pressure coefficient and Stanton number distributions along the top center line ($\theta = 0°$) of a Mach 14 blunt elliptic cone ($L = 0.2$ m) with various levels of energy deposition ($T_w = 294$ K).
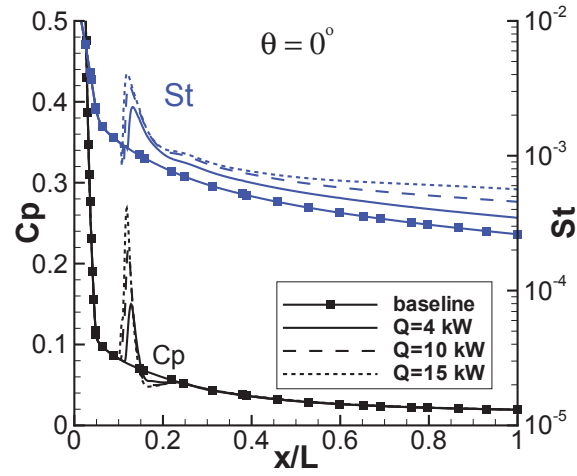
Approved for public release; distribution unlimited.

(a) Moment coefficient

(b) Non-dimensional pitching moment

Figure 15. **Moment coefficient and normalized change in pitching moment versus the nondimensional to-tal power deposition** $\tilde{Q}$ **for various vehicle configurations** ($T_w = 300$ **K, thermal equilibrium, 5 sp., pancake deposition).**

24 of 24

Approved for public release; distribution unlimited.

47th AIAA Aerospace Sciences Meeting Including The New Horizons Forum and Aerospace Exposition
5 - 8 January 2009, Orlando, Florida

AIAA 2009-1000

Numerical Study of Electromagnetic Aerodynamic Control of Hypersonic Vehicles

Nicholas J. Bisek[*] and Iain D. Boyd[†]

Department of Aerospace Engineering, University of Michigan, Ann Arbor, MI, 48109, USA

and

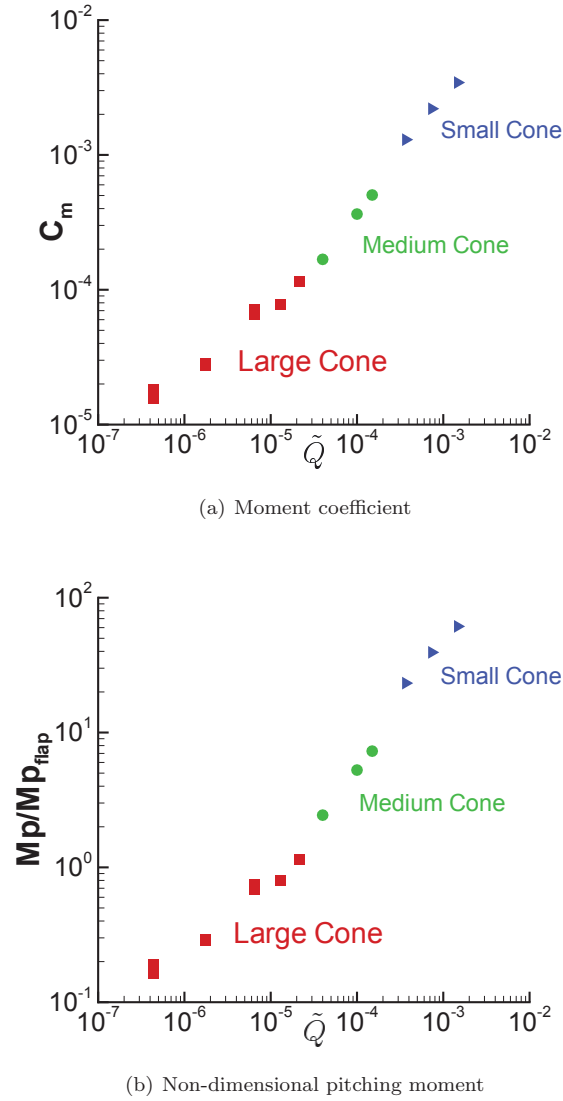Jonathan Poggie[‡]

Air Force Research Laboratory, Wright-Patterson AFB, OH, 45433-7512, USA

A computational study of several analytical test cases is carried out to verify the implementation of the low magnetic Reynolds number approximation into a hypersonic flow solver. An investigation in several electrical conductivity models, including solutions to Boltzmann's equation, is made to determine the appropriate method for approximating the flow's electrical conductivity, since the conductivity is an essential part of the magnetohydrodynamic approximations. These improvements will facilitate future computational studies of the effects of externally applied magnetic fields on plasma-assisted flow control devices and provide more physically accurate modeling of these techniques.

Nomenclature

ρ = mass density
μ = coefficient of viscosity
u = streamwise velocity component
$\mathbf{u}$ = velocity vector (u, v, w)
x, y, z = streamwise, spanwise, and transverse coordinates
i, j, k = computational grid indices along the axial, radial, and circumferential directions
θ = angle along circumference of the body (cylindrical coordinate system)
A = surface area of grid cell
$\mathbf{n}$ = normal vector
N = total number density
p = pressure
τ = viscous stress
E = total energy per volume
$\mathbf{q}$ = heat flux (translational, rotational, and vibrational)
T = temperature (translational and rotational)
T_v = temperature (vibrational)
h = enthalpy
χ = mole fraction
d = distance between electrodes
L = axial surface length
St = Stanton number, $q_w/[\rho_\infty u_\infty (h_0 - h_w)]$
Re_m = magnetic Reynolds number, uL/η_m
η_m = magnetic diffusivity, $\mu_0^{-1}\sigma^{-1}$
σ = electrical conductivity
$\tilde{\sigma}$ = electrical conductivity tensor (including Hall effect and ion-slip)

---

[*]Graduate Student, Student Member AIAA
[†]Professor, Associate Fellow AIAA
[‡]Senior Aerospace Engineer, AFRL/RBAC. Bldg. 146 Rm. 225, 2210 Eighth St. Associate Fellow AIAA
This material is declared a work of the U.S. Government and is not subject to copyright protection in the United States.

American Institute of Aeronautics and Astronautics

ϕ = electric potential
B = magnetic field vector
E = electric field vector
j = current field vector
μ_0 = permeability of free space, $4\pi \times 10^{-7}$ N/A^2
ϵ_0 = permittivity of free space, $8.85 \times 10^{-}12$ F/m
C = scaling vector, $\mathbf{C} = (\tilde{\sigma}^T \cdot \mathbf{n})A$
ω = relaxation parameter for successive over-relaxation method

Subscript
∞ = free stream
w = wall

I.   Introduction

Plasma-assisted hypersonic flow control has experienced a renewed interest over the past decade.[1,2] This resurgence has been credited to many factors including the expanding requirements for sustained hypersonic flight and rapid access to space. These desires have produced several new challenges, particularly in air-breathing propulsion, where conventional means of flow control may be inadequate to meet the precise demands of scramjet and ramjet technologies. Plasma-based control systems are one of the options being explored to fill these needs. In addition to propulsion, these devices are also being applied to many other vehicle systems that could be enhanced by their abilities.

Recent experimental and computational research by Shang *et al.*[3] has investigated ways of reducing drag on blunt nose bodies by means of plasma injection, while research by Kremeyer *et al.*[4] and Yan[5] focused on drag reduction and flow control using laser deposition (filamentation) ahead of conic and spherical geometries. Plasma actuators are being used to provide steering moments,[6,7] changes in vehicle lift,[8] control of flow separation,[9,10] and in local heat load mitigation.[11]

A potential limitation of these devices is the large energy requirement necessary when they are employed to control large scale hypersonic flows by means of Joule heating through energy deposition.[12] One possible way of improving the effectiveness and/or providing finer control is to utilize the ionized portion of the flow. The ionized flow can be subjected to electric and magnetic fields producing additional/improved flow control. In order to simulate these effects, computational fluid codes need to be modified to accurately account for the magnetohydrodynamic (MHD) effects. This is accomplished by solving some form of Maxwell's equations. Although it is possible to solve Maxwell's equations directly,[13,14] most computational work in the area assumes the current continuity equation by means of the low magnetic Reynolds number approximation.

Barmin *et al.* demonstrated the need for 3D calculations when computing the MHD equations in order to prevent the introduction of unstable disturbances into the solution.[15] MHD work by Gaitonde has included detailed high order numerical modeling[16] and investigations into the Hall effect and ion-slip.[17,18] Shang *et al.*[19] investigated plasma actuators embedded at the entrance of a hypersonic inlet cowl, while Wan *et al.* studied MHD power generation.[20] With DARPA's Falcon program entering its 3rd phase[21] and several other hypersonic test programs being conducted in other organizations and countries,[22–25] the demand for continued development of computational tools in hypersonic flows continues to be strong.

The effort of this work is to implement the MHD effects into the 3D fluid solver used in previous work to quantify the required power expenditures for plasma-assisted devices in realistic hypersonic systems.[12,26] In the following, we first provide a review of the flow code, LeMANS. The Lorentz force and Joule heating (MHD effects) are added to the conservation equations for a perfect gas solver. The low magnetic Reynolds number approximation is made to simplify Maxwell's equations in order to compute the electric and current fields. A solution to the MHD model is achieved using a finite volume, finite difference scheme. An examination of several electrical conductivity models is made, including results from a Boltzmann solver. Finally, solutions validating the MHD module are presented for an analytical case and for flow between two parallel electrode plates with a potential difference.

American Institute of Aeronautics and Astronautics

II. Method

A. Governing Equations

Flow-field results are obtained using Computational Fluid Dynamics (CFD) to solve the Navier-Stokes equations. The CFD computations are executed using the Michigan Aerothermodynamic Navier-Stokes (LeMANS) code which was developed at the University of Michigan.[27, 28]

LeMANS is a general 2D/axisymmetric/3D, parallel, unstructured finite-volume CFD code. The numerical fluxes between cells are discretized using a modified Steger-Warming Flux Vector Splitting (FVS) scheme, except near shock waves. In these regions the original Steger-Warming FVS scheme is used. LeMANS is able to employ a two-temperature model to account for thermal-nonequilibrium and a standard finite rate chemistry model for non-equilibrium chemistry. The two temperature model assumes that a single temperature T accounts for the translational and rotational energy modes of all species while the vibrational energy mode is accounted for by a separate temperature T_v.

The usual conservation equations are solved:

$$\frac{\partial \rho}{\partial t} + \nabla \cdot (\rho \mathbf{u}) = 0 \tag{1}$$

$$\frac{\partial \rho \mathbf{u}}{\partial t} + \nabla \cdot (\rho \mathbf{u}^2 + p\delta_{ij} - \tau) = \mathbf{j} \times \mathbf{B} \tag{2}$$

$$\frac{\partial E}{\partial t} + \nabla \cdot ((E + p)\mathbf{u} - \tau \cdot \mathbf{u} - \mathbf{q}) = \mathbf{j} \cdot \mathbf{E} \tag{3}$$

LeMANS assumes the fluid is continuous and Newtonian. It also assumes Stokes' hypothesis when determining the viscous stresses.

$$\tau_{ij} = \mu \left(\frac{\partial u_j}{\partial x_i} + \frac{\partial u_i}{\partial x_j} \right) - \frac{2}{3}\mu \nabla \cdot \mathbf{u}\delta_{ij} \tag{4}$$

Previous work considered a phenomenological model of dissipative heating to account for a thermal actuator.[26] This was represented as an additional source term on the right side of the energy equation (3), but is replaced with Joule heating ($\mathbf{j} \cdot \mathbf{E}$) in the equation's current form. The conservation of momentum equation is modified to include the Lorentz force ($\mathbf{j} \times \mathbf{B}$) on the right hand side of equation (2). These additions constitute the effects the electric and magnetic fields have on the flow. The vibrational energy equation is also modified with the inclusion of a Joule heating term ($\gamma \, \mathbf{j} \cdot \mathbf{j}/\sigma$), where γ is a factor that accounts for partitioning of electromagnetic energy deposition between different nonequilibrium modes. This equation is not included with the abovementioned governing equations because the remainder of the paper only employs a single temperature model and equilibrium chemistry.

The simulations are performed using second-order accurate spatial discretization and carry double precision arithmetic throughout. Thermal equilibrium and an eleven species, non-reacting air chemistry model (N_2, O_2, NO, N, O, N_2^+, O_2^+, NO^+, N^+, O^+, and e) are used in the simulations, where e is the electrons.

B. Low Magnetic Reynolds Number Approximation

The three additional variables appearing in the modified governing equations ($\mathbf{j}, \mathbf{B}, \mathbf{E}$) are determined by first noting that the magnetic Reynolds number, equation (5), is small for the cases of interest. Consequently, it can be shown that the induced magnetic field can be ignored.[29] This means only external magnetic fields are present in the flow (and must be specified).

$$Re_m = \frac{uL}{\eta_m} \tag{5}$$

The current and electric field vectors are determined by starting with a generalized form of Ohm's law (adjusted for a flow moving relative to a magnetic field $\mathbf{B}$) which relates the two vectors as seen in equation (6). Following the outline in Ref. 30, the electrical conductivity tensor $\tilde{\sigma}$ is employed as a compact way of accounting for ion-slip and the Hall effect. The electrical conductivity tensor is further simplified by ignoring ion-slip and the Hall effect, which reduces the tensor to its scalar σ multiplied by the identity matrix ($\tilde{\sigma} = \sigma I$).

American Institute of Aeronautics and Astronautics

Approved for public release; distribution unlimited.

$$\mathbf{j} = \tilde{\sigma} \cdot (\mathbf{E} + \mathbf{u} \times \mathbf{B}) \tag{6}$$

Ampère - Maxwell's law, equation (7), is simplified by neglecting the current displacement term $\frac{\partial \mathbf{E}}{\partial t}$. This assumption is valid when its magnitude is compared to the conduction current ($\mathbf{j} = \sigma\mathbf{E}$) for typical conditions of air, see Ref. 31 for details. The reduced Ampère - Maxwell law is combined with charge conservation, equation (8), to yield the steady state form of the current continuity equation, equation (9).

$$\nabla \times \mathbf{B} = \mu_0 \mathbf{j} + \mu_0 \epsilon_0 \frac{\partial \mathbf{E}}{\partial t} \tag{7}$$

$$\nabla \cdot \mathbf{j} = -\frac{\partial \rho}{\partial t} \tag{8}$$

$$\nabla \cdot \mathbf{j} = 0 \tag{9}$$

Gauss's Law for magnetism ($\nabla \cdot \mathbf{B} = 0$) ensures the magnetic field is divergence free and absent of magnetic monopoles. This law is combined with the magnetic vector potential ($\mu\mathbf{B} = \nabla \times \mathbf{A}$) to prove that $\mathbf{A}$ (the vector potential) must exist.

Assuming the electric field vector is smooth and rapidly decaying, Helmholtz's theorem is used to decompose it into irrotational and divergence-free component vector fields. This is represented as a scalar potential ϕ and a vector potential $\mathbf{A}$. ($\mathbf{E} = -\nabla\phi + \nabla \times \mathbf{A}$) Using the low magnetic Reynolds number assumption, the right side of Faraday's law of induction, equation (10), must be zero for the external magnetic field specified in this work. Since ($\nabla \times \mathbf{E} = 0$), the electric field is irrotational (curl-free), so Helmholtz's decomposition of $\mathbf{E}$ is equation (11).

$$\nabla \times \mathbf{E} = -\frac{\partial \mathbf{B}}{\partial t} \tag{10}$$

$$\mathbf{E} = -\nabla\phi \tag{11}$$

Combining equations (6, 9, and 11) produces the Poisson type equation observed in equation (12).

$$\nabla \cdot \tilde{\sigma} \cdot [-\nabla\phi + \mathbf{u} \times \mathbf{B}] = 0 \tag{12}$$

To find the solution for ϕ, and subsequently $\mathbf{E}$ and $\mathbf{j}$, a finite volume method is employed to be consistent with the flow solver. Rearranging the equation and integrating over an arbitrary volume yields

$$\int_V \nabla \cdot [\tilde{\sigma} \cdot (\nabla\phi)]dV = \int_V \nabla \cdot [\tilde{\sigma} \cdot (\mathbf{u} \times \mathbf{B})]dV \tag{13}$$

Applying the Divergence Theorem, equation (13) can be rearranged and written in a more compact form by introducing scaling vector $\mathbf{C}$ which is the sum of the face area multiplied with the dot product of the transpose of the electrical conductivity tensor and the outward facing normal as described in equation (14). The face area is A and should not be confused with the vector potential. In 3D: $\mathbf{C} = [(\sigma_{1,1}n_x + \sigma_{2,1}n_y + \sigma_{3,1}n_z)A, (\sigma_{1,2}n_x + \sigma_{2,2}n_y + \sigma_{3,2}n_z)A, (\sigma_{1,3}n_x + \sigma_{2,3}n_y + \sigma_{3,3}n_z)A]$. Equating the surface integral to a sum over an arbitrary number of faces in a specific cell produces equation (15).

$$\mathbf{C} = (\tilde{\sigma}^T \cdot \mathbf{n})A \tag{14}$$

$$\sum^{faces} (\nabla \cdot \phi) \cdot \mathbf{C} = \sum^{faces} (\mathbf{u} \times \mathbf{B}) \cdot \mathbf{C} \tag{15}$$

During every iteration of LeMANS, a Poisson solver (MHD subroutine) is called to compute the electric and current field vectors by determining the electric potential ϕ. With the velocity and magnetic field vectors provided by LeMANS, the right side of equation (15) is computed directly by approximating each face vector as a volumetric average of the adjoining cells. A finite difference approach is used to determine the electric potential flux ($\nabla \cdot \phi$) through each face as seen in Figure 1. Following Refs. 32 and 33, a second order, nonuniform difference for the flux is written as

American Institute of Aeronautics and Astronautics

Approved for public release; distribution unlimited.

$$\frac{\partial \phi}{\partial x} = \frac{\phi_{right} + (\alpha^2 - 1)\phi_{face} - \alpha^2 \phi_{left}}{\alpha(\alpha + 1)\Delta x} \tag{16}$$

where Δx is the difference between the left cell center and the face center ($\Delta x = |x_{face} - x_{left}|$) and α is the ratio of the right and left cell center differences ($\alpha = |\frac{x_{face} - x_{right}}{x_{face} - x_{left}}|$). Equations (15 and 16) are applied to all cells using the Successive Over-Relaxation (SOR) iterative technique. The SOR technique is an iterative explicit solver that utilizes the direction of change to the solution to extrapolate an improved solution based on a relaxation constant ω. The method converges more slowly than an implicit scheme,[33] but is easier to implement and parallelize. For all computations presented here, $\omega = 1.70$.

Mixed boundary conditions are generally employed at a solid surface. For electrodes that are good conductors, the potential is specified, either as a fixed value or determined by auxiliary equations representing an external circuit. For an insulated boundary, the normal component of current is set to zero: $\mathbf{j} \cdot \mathbf{n} = \tilde{\sigma} \cdot (\mathbf{E} + \mathbf{u} \times \mathbf{B}) \cdot \mathbf{n} = 0$. This can be a quite complicated boundary condition in the general case of tensor conductivity, but in the case of scalar conductivity and a no-slip wall, it reduces to $\mathbf{E} \cdot \mathbf{n} = 0$.

The outward direction of symmetry plane must have a zero gradient electric field ($\mathbf{E} \cdot \mathbf{n} = 0$). By definition the ghost cell center lies on the outward normal vector, so the symmetry plane boundary condition is $\nabla \phi = 0$. The proper boundary conditions in the far-field are less clear for aerodynamic MHD problems. For high accuracy, it may be necessary to solve the current continuity equation on a larger domain than the fluid conservation laws since the magnetic field can interact with the far-field. However, for external flows, the conductivity should drop to a negligible value far from the body such that it is assumed permissible to set the normal component of the electric field to zero. The normal component of the electric field is assumed to be very small at the inlet and is neglected ($\mathbf{E} \cdot \mathbf{n} = 0$). Finally, the outlet is assumed to be sufficiently downstream of the primary MHD interaction such that it is reasonable to set the normal component of the electric field to zero. The inlet and outlet boundary conditions are further simplified by their corresponding ghost cells ($\nabla \phi = 0$). Table 1 lists all domain boundaries and their respective conditions.

Table 1. Boundary conditions for MHD solver

Location	Type	Condition
Inlet	Neumann	$\mathbf{E} \cdot \mathbf{n} = 0$
Far-field	Neumann	$\mathbf{E} \cdot \mathbf{n} = 0$
Symmetry	Neumann	$\mathbf{E} \cdot \mathbf{n} = 0$
Outlet	Neumann	$\mathbf{E} \cdot \mathbf{n} = 0$
Wall (electrode)	Dirichlet	$\phi = \text{specified}$
Wall (insulating)	Neumann	$\mathbf{j} \cdot \mathbf{n} = 0$

The Dirichlet conditions are directly substituted into the ghost cells joining the wall (electrode) boundary such that the wall face equals the specified value. The Neumann boundary conditions require the electric potential ϕ in the ghost cell to be determined iteratively in conjunction with the rest of the MHD solver. Since each ghost cell only has one face, they are updated to ensure ($\nabla \phi = 0$) for the face between the ghost cell and its adjoining real cell before the domain's interior cells are computed using equation (15).

III. Electrical Conductivity

A. Equilibrium Air

Over the years, equilibrium air properties have been the subject of several researchers.[34–39] Research in this area continues to be further refined because it is necessary to accurately determine the correct thermal characteristics of a flow field, particularly in reacting flows like hypersonics. In addition to having the appropriate heat conduction, some electrical conductivity models are a function of the species mole fraction, another result of the flow field thermal characteristics. A range of input conditions to facilitate comparisons between various electrical conductivity models is generated utilizing computational research conducted by Godin and Trépanier[40] to produce plots of the mole fractions of equilibrium air for a range of temperatures and pressures.

American Institute of Aeronautics and Astronautics

Approved for public release; distribution unlimited.

Simulations are run for a temperature range of $10^2 - 10^5$ K with pressures ranging from $10^{-3} - 1$ atm for dry air (including 0.93 % argon). Figure 2 shows the species mole fractions consistent with the eleven species computed in LeMANS (N_2, O_2, NO, N, O, N_2^+, O_2^+, NO^+, N^+, O^+, and e). As seen in the figures, a pressure increase shifts the distributions to higher temperatures. Another noticeable result is the missing species at higher temperatures (T > 15,000 K). These missing species are primarily multi-ionized atomic nitrogen (N^{++}, N^{3+}, and N^{4+}) as seen in Figure 3 and are usually neglected in hypersonic flow simulations because the post-shock flow field rarely achieves thermal equilibrium at these temperatures before exiting the domain.

B. Conductivity Models

As this research area has matured, several models have been developed to capture the behavior of the electrical conductivity in air which appears to be a function of both pressure and temperature as seen in Figure 4, reproduced from Sutton's *Engineering Magnetohydrodynamics*.[31] Several empirical models only attempt to capture the conductivity once it starts to approach a constant (at high temperatures) because the conductivity is negligibly small at lower temperatures. Figure 5 is a photocopy from Cambel's text, *Plasma Physics and Magnetofluid-Mechanics.* It shows two such approximations for the electrical conductivity of argon at p = 0.01 atm.[41] The Spitzer-Harm model, equation (17), was developed for fully ionized gases, whereas the model developed by Chapman and Cowling, equation (18), was developed for weakly ionized flows.

$$\sigma = \frac{1.56 \times 10^{-4} \times T^{1.5}}{ln(1.23 \times 10^4 \times T^{1.5}/n_e^{0.5})} \ \Omega^{-1}cm^{-1} \tag{17}$$

$$\sigma = 3.34 \times 10^{-12} \frac{\alpha}{Q \, T^{0.5}} \ \Omega^{-1}cm^{-1} \tag{18}$$

where α is the degree of ionization and Q is the collision cross section. Using research by Bush,[42] Poggie and Gaitonde developed an electrical conductivity model that is only a function of temperature as seen in equation (19).[43] This model has been adopted by others, including work by Otsu *et al.*,[44,45] which set $n = 2$ (Poggie and Gaitonde set $n = 4$). σ_0 is a reference conductivity and T_0 is the peak post-shock temperature. One set of reference values employed are $\sigma_0 = 731 \ \Omega^{-1} \cdot cm^{-1}$ at $T_0 = 8000K$ (p = 34 Pa).

$$\sigma = \sigma_0 \left(\frac{T}{T_0} \right)^n \tag{19}$$

Another weakly ionized model that is only a function of temperature was developed by Raizer. His method relates the conductivity to an exponential function as seen in equation (20), where T is specified in Kelvin. This model is considered valid for air, nitrogen, and argon at p = 1 atm.

$$\sigma = 83 \times e^{-36000/T} \ \Omega^{-1}cm^{-1} \tag{20}$$

These semi-empirical models are compared against solutions to Boltzmann's equation using a Boltzmann solver developed by Weng and Kushner.[46] The method of solving Boltzmann's equation is functionally equivalent to that proposed by Rockwood.[47,48] Although the solver requires the translational temperature, pressure, and species mole fractions as input parameters, the solution of Boltzmann's equation only depends on E/N and each species mole fraction (E is the magnitude of the electric field and N is the total number density). This means the input temperature and pressure are not adjusted to match the actual flow field. The solution is achieved using an extensive list of collision cross-section data taken from the compilations discussed in Refs. 49 and 50. The Boltzmann solver outputs the equilibrium transport coefficients for a range of E/N which are used to compute the electrical conductivity.

A disadvantage of computing solutions to Boltzmann's equation is that **E** is coupled to σ. This means the MHD solver depends on σ to determine **E**, see equation (12). Thus, the Boltzmann solver must be coupled to the MHD solver in order to compute σ, **E**, and **j** simultaneously, which increases the computational cost of the simulation.

Once solutions of Boltzmann's equation are computed, σ is determined using the resulting transport coefficients. Using the definition of conductivity for a dc current, equation (21) relates electrical conductivity to the electric charge ($q = 1.6 \times 10^{-19}$ C), the electron number density (n_e), the electron mass (9.11×10^{-31}

American Institute of Aeronautics and Astronautics

Approved for public release; distribution unlimited.

kg), and the electron momentum transfer collision frequency (ν_m). The electrical conductivity definition is combined with the definition of electron mobility, equation (22), to yield equation (23).

$$\sigma = \frac{q^2 \, n_e}{m_e \, \nu_m} \tag{21}$$

$$\mu = \frac{q}{m_e \, \nu_m} \tag{22}$$

$$\sigma = \mu \, q \, n_e \tag{23}$$

The transport coefficients are given for values at standard conditions ($T = 273$ K, p = 1 atm). The electrical conductivity is then computed for a given total number density (N) by utilizing equation (24) which states the product of the electron mobility and total number density is a constant. This is substituted into equation (23) to yield equation (25) which relates the electrical conductivity to the electron mobility (a transport coefficient produced by solutions to Boltzmann's equation), and the degree of ionization.

$$\mu = \mu_0 \left(\frac{N_0}{N} \right) \tag{24}$$

$$\sigma = \mu_0 \, N_0 \, q \left(\frac{n_e}{N} \right) \ \ \Omega^{-1} cm^{-1} \tag{25}$$

C.   Conductivity Results

To facilitate comparisons between the various electrical conductivity models, a list of species mole fractions for a range of pressures and temperatures is made using the plots in Figure 2. The table is listed in the Appendix (Table 2). For the Chapman-Cowling model, the degree of ionization α is the sum of the ionized species divided by the total number density ($\alpha = \Sigma n_I / N$), and for simplicity, the collision cross-section is set equal to the vibrational cross-section for an ideal molecule ($Q = 5 \times 10^{-17} cm^2$).

The list of collision cross-section data available in the Boltzmann solver does not include NO^+ and must be neglected from the Boltzmann solutions. Fortunately, Table 2 and Figure 2 indicate the mole fraction of NO^+ is very low for all configurations being tested, so its absence is assumed inconsequential. For a low degree of ionization, the majority of the collisions are electron-neutral or electron-ion. As the degree of ionization increases, electron - electron collisions must be included, which dramatically increases the computational time of the solver.

Figures 6-8 show the electrical conductivity distributions of all the models versus temperature at p = 0.001, 0.1, and 1 atm. The solid line shown for the Boltzmann solver is the conductivity for $E/N = 10$ Townsend (Td). (1 Td $= 10^{-17}$ V cm^2) None of the semi-empirical models fully capture the behavior of the Boltzmann solver, although the Chapman-Cowling model appears to closely follow its behavior. This is because both the Chapman-Cowling model and Boltzmann solver directly depend on the degree of ionization.

While the semi-empiric models deviate from the electrical conductivity estimated by the Boltzmann solver, their reference parameters could be adjusted to better fit specific ranges of conditions. In addition, they are usually much easier to implement and computationally cheaper than a coupled MHD-Boltzmann approach. These advantages suggest the use of a semi-empirical model is a better choice for estimating the electrical conductivity used in the MHD solver as long as the model is valid for flow field conditions. However, large differences in the electrical conductivity (between the computed and real conductivity) will result in large changes in the current field and, subsequently, produce incorrect Lorentz force and Joule heating effects. Therefore, it is essential that care is taken when selecting reference parameters.

IV.   MHD Results

In previous work, LeMANS was validated for two different hypersonic cases. Simulations for hypersonic laminar air over elliptic blunt and sharp cones were compared to experimental work investigated by Nowlan et al.[51] and Kimmel et al.[52, 53] These experimental validation cases were selected because they are considered representative of a realistic hypersonic air-vehicle geometry and because of the limited amount of experimental data available. Figure 9 shows the experimental and computational Stanton number (St) distributions for the Mach 14 blunt elliptic cone investigated by Nowlan et al.[51] Full details of the validation

exercises and results are available in Refs. 12 and 26. Overall, LeMANS is capable of accurately computing three dimensional hypersonic laminar flows.

A.   MHD Validation Cases

1.   Analytical case with Dirichlet Boundary Conditions

Validation of the MHD module is accomplished by utilizing the analytical test case developed in the computational work by Gaitonde et al.[30] This validation exercise has been utilized previously by Wan et al.,[20] and is selected for this work because it is simple, has magnetic and velocity field vectors, and an analytical solution. The governing equation for the test problem is

$$\nabla^2 \phi = x e^z \tag{26}$$

Dirichlet boundary conditions are assigned to the outer cells for each side of the domain based on the analytical solution ($\phi = x e^z$). To simplify the work, the electrical conductivity tensor is set to unity ($\tilde{\sigma} = 1$), although its exact value does not affect the solution. The magnetic and velocity field vectors are chosen as $\mathbf{B} = [0, \frac{1}{2}e^z, 0]$ and $\mathbf{u} = [u, 0, \frac{-1}{2}x^2]$ respectively.

Several meshes are employed including a uniform rectilinear, a nonuniform rectilinear (with cell clustering near $x = 0$, $y = 0$, $z = 0$), and a rotated nonuniform rectilinear mesh, as seen in Figure 10. Each mesh has sides with length equal to one and the non-rotated meshes lie within the domain $0 \le x \le 1, 0 \le y \le 1, 0 \le z \le 1$. The formal order of accuracy is estimated using the Richardson extrapolation function predefined in Tecplot 360®. This method determines the formal order of accuracy by extrapolating the results from a sequence of meshes refined by a factor of two, i.e. the medium mesh has twice as many grid points on each side compared to the coarse mesh. For the cases examined, coarse = $10 \times 10 \times 10$, medium = $20 \times 20 \times 20$, and fine = $40 \times 40 \times 40$. The uniform mesh has a formal order of accuracy of 1.999, which is expected since a 2nd order accurate finite difference scheme is employed. The nonlinear mesh produces a formal order of accuracy of 1.98 and the rotated mesh yields 1.80 due to the limitations of the finite difference approach employed.

Figure 11 shows the computed and analytical solutions for the rotated nonuniform mesh with part of the mesh removed to reveal the interior cells. The computed solutions are almost identical to the analytical solutions. Figure 12 plots the Least Squares Norm, for each of the meshes versus the number of iterations using the SOR method ($\omega = 1.7$). The uniform mesh requires more iterations to converge because ω is not optimized for its geometry and grid spacing.

2.   Flow Between Two Electrodes

A second validation exercise is performed simulating flow between two parallel electrodes separated by a distance d, where d is measured from the bottom electrode ($z = 0$). Again, this validation exercise follows the computational work by Gaitonde et al.[30] The electrodes have a specified potential in which the top electrode plate is equal to one and the bottom is set to zero ($\phi_{top} = 1, \phi_{bottom} = 0$). Neumann boundary conditions are employed along the remaining sides of the domain so the normal component of the gradient is zero ($\frac{\partial \phi}{\partial n} = 0$). Figure 13 illustrates the domain with a rectilinear nonuniform mesh used in the simulation. For these grids, cell clustering is applied near both electrodes using a bi-exponential decay of cell size along the z axis.

The simulations are computed assuming the velocity vector is zero ($\mathbf{u} = 0$) which significantly simplifies equation (12) to obtain a theoretical solution such that the current is constant ($\mathbf{j} = -\tilde{\sigma} \cdot \nabla \phi = $ constant). Two different electrical conductivity models are simulated. In the first case, σ is constant ($\sigma = 1$), while the second case assumes the electrical conductivity diminishes as d increases ($\sigma = 1/2^d$) as seen in Figure 14.

For constant electrical conductivity ($\sigma = 1$), the theoretical solution reduces such that the gradient of the potential equals zero. The resulting electric potential is $\phi = z = d$ for the given boundary conditions. The theoretical solution for the second case is determined by recalling the Neumann boundary conditions applied to the four side walls, which indicate that the solution ϕ will not vary along the x or y axes. Since ion-slip and Hall effects are being neglected, the current equation reduces to

$$j_z = \sigma \, \nabla_z \phi = 2^{-d} \, \nabla_z \phi = \text{constant} = \text{C} \tag{27}$$

American Institute of Aeronautics and Astronautics

This equation can be further simplified by noting d equals z for the domain ($\frac{\partial \phi}{\partial z} = C\ 2^d = C\ 2^z$). Integrating both sides over the domain and applying the electric potential from both plates yields

$$\int_0^1 \frac{\partial \phi}{\partial z}\ dz = \int_0^1 C\ 2^z dz \tag{28}$$

$$\frac{\partial \phi}{\partial z} = \ln 2\ 2^z \tag{29}$$

This is extended using each plate's electric potential to obtain the theoretical solution, which is written noting d equals z for the domain.

$$\phi = 2^d - 1 \tag{30}$$

Figure 15 plots the computed and analytical solutions for the constant electrical conductivity problem on the nonuniform mesh with part of the mesh cut away to reveal the interior cells. Figure 16 plots the electric potential distributions along the $x = 0.5$, $y = 0.5$ ray for both electrical conductivity problems. The figures demonstrate that the MHD solver accurately computes the electric potential for the validation cases performed.

V.   Conclusions

A low magnetic Reynolds number approximation was made to simplify Maxwell's equations in order to accurately account for electromagnetic effects for weakly ionized flows. A solution to the resulting MHD model was presented using a finite volume, finite difference scheme and coupled to LeMANS, an unstructured Navier-Stokes solver. Validation cases were successfully run for an analytical case and for flow between two parallel electrode plates with a potential difference.

In addition to the MHD solver, an examination of several electrical conductivity models was made. Although the semi-empiric models did not fully capture the behavior of the electrical conductivity distribution produced by the Boltzmann solver, they are valid for specific ranges of conditions and reference parameters. A more general approach would be to couple the Boltzmann solver to the MHD module. While this increases the computational cost of the simulation, the generality of the approach makes it attractive.

VI.   Future Work

In further studies, we will focus on the parallelization of the MHD solver and the MHD effects for thermal nonequilibrium flows. This includes modifications to the mass diffusion terms within the conservation equations (finite chemistry). These improvements will be used to investigate whether additional enhancements to the flow field can be achieved by introducing a magnetic field to the flow over a realistic hypersonic vehicle which is using an arc discharge between a cathode and anode on the vehicle's surface.

Acknowledgments

References

[1]Shang, J. S., Surzhikov, S. T., Kimmel, R., Gaitonde, D., Menart, J., and Hayes, J., "Mechanisms of Plasma Actuators for Hypersonic Flow Control," *Progress in Aerospace Sciences*, Vol. 41, No. 8, November 2005, pp. 642–668.

[2]Fomin, V. M., Tretyakov, P. K., and Taran, J.-P., "Flow Control using Various Plasma and Aerodynamic Approaches," *Aerospace Science and Technology*, Vol. 8, No. 5, July 2004, pp. 411–421.

[3]Shang, J. S., Hayes, J., and Menart, J., "Hypersonic Flow over a Blunt Body with Plasma Injection," *Journal of Spacecraft and Rockets*, Vol. 39, No. 3, May-June 2002, pp. 367–375.

[4]Kremeyer, K., Sebastian, K., and Shu, C.-W., "Computational Study of Shock Mitigation and Drag Reduction by Pulsed Energy Lines," *AIAA Journal*, Vol. 44, No. 8, August 2006, pp. 1720–1731.

[5]Yan, H. and Gaitonde, D., "Control of Edney IV Interaction by Energy Pulse," *44th AIAA Aerospace Sciences Meeting and Exhibit*, AIAA Paper 2006-562, 2006.

Approved for public release; distribution unlimited.

[6]Girgis, I. G., Shneider, M. N., Macheret, S. O., Brown, G. L., and Miles, R. B., "Creation of Steering Moments in Supersonic Flow by Off-Axis Plasma Heat Addition," *40th AIAA Aerospace Sciences Meeting and Exhibit*, 2002, AIAA Paper 2002-129.

[7]Gnemmi, P., Charon, R., Dupéroux, J.-P., and George, A., "Feasibility Study for Steering a Supersonic Projectile by a Plasma Actuator," *AIAA Journal*, Vol. 46, No. 6, June 2008, pp. 1308–1317.

[8]Menart, J., Stanfield, S., Shang, J., Kimmel, R., and Hayes, J., "Study of Plasma Electrode Arrangements for Optimum Lift in a Mach 5 Flow," *44th AIAA Aerospace Sciences Meeting and Exhibit*, 2006, AIAA Paper 2006-1172.

[9]Updike, G. A., Shang, J. S., and Gaitonde, D. V., "Hypersonic Separated Flow Control Using Magneto-Aerodynamic Interaction," *43th AIAA Aerospace Sciences Meeting and Exhibit*, AIAA Paper 2005-164, 2005.

[10]Kimmel, R. L., Hayes, J. R., Crafton., J. W., Fonov, S. D., Menart, J., and Shang, J., "Surface Discharge for High-Speed Boundary Layer Control," *44th AIAA Aerospace Sciences Meeting and Exhibit*, AIAA Paper 2006-710, 2006.

[11]Miles, R. B., Macheret, S. O., Shneider, M. N., Steeves, C., Murray, R. C., Smith, T., and Zaidi, S. H., "Plasma-Enhanced Hypersonic Performance Enabled by MHD Power Extraction," *43th AIAA Aerospace Sciences Meeting and Exhibit*, AIAA Paper 2005-561, 2005.

[12]Bisek, N. J., Boyd, I. D., and Poggie, J., "Numerical Study of Plasma-Assisted Aerodynamic Control for Hypersonic Vehicles," *39th AIAA Plasmadynamics and Lasers Conference*, AIAA Paper 2008-4226, 2008.

[13]MacCormack, R., "Numerical Simulation of Aerodynamic Flow Including Induced Magnetic and Electric Fields," *39th Plasmadynamics and Lasers Conference*, AIAA Paper 2008-4010, 2008.

[14]D'Ambrosio, D. and Giordano, D., "Two-Dimensional Numerical Methods in Electromagnetic Hypersonics Including Fully Coupled Maxwell Equations," *39th Plasmadynamics and Lasers Conference*, AIAA Paper 2008-4013, 2008.

[15]Barmin, A. A., Kulikovskiy, A. G., and Pogorelov, N. V., "Shock-Capturing Approach and Nonevolutionary Solutions in Magnetohydrodynamics," *Journal of Computational Physics*, Vol. 126, No. 1, June 1996, pp. 77–90.

[16]Gaitonde, D. V., "A High-Order Implicit Procedure for the 3-D Electric Field in Complex Magnetogasdynamic Simulations," *Computers and Fluids*, Vol. 33, No. 3, March 2004, pp. 345–374.

[17]Gaitonde, D. V. and Poggie, J., "An implicit Technique for 3-D Turbulent MGD with the Generalized Ohm's Law," *32th AIAA Plasmadynamics and Lasers Conference*, AIAA Paper 2001-2736, 2001.

[18]Gaitonde, D. V., "Effect of Hall Currents on Simulated Three-Dimensional Scramjet with Magnetohydrodynaic Bypass," *Journal of Propulsion and Power*, Vol. 22, No. 3, May-June 2006, pp. 700–703.

[19]Shang, J. S., Huang, H. Y., Surzhikov, S. T., and Gaitonde, D. V., "Hypersonic Flow Control Utilizing Electronmaggetic-Aerodynamic Interaction," *15th AIAA International Space Planes and Hypersonic Systems and Technologies Conference*, AIAA Paper 2008-2606, 2008.

[20]Wan, T., Suzuki, R., Candler, G., Macheret, S., and Schneider, M., "Three Dimensional Simulation of Electric Field and MHD Power Generation During Re-Entry," *36th AIAA Plasmadynamics and Lasers Conference*, AIAA Paper 2005-5045, 2005.

[21]Walker, S., Tang, M. T., Morris, S., and Mamplata, C., "Falcon HTV-3X - A Reusable Hypersonic Test Bed," *15th AIAA International Space Planes and Hypersonic Systems and Technologies Conference*, AIAA Paper 2008-2544, 2008.

[22]Fujii, K. and Ishimoto, S., "Research Activities to Realize Advanded Space Transportation System," *15th AIAA International Space Planes and Hypersonic Systems and Technologies Conference*, AIAA Paper 2005-2575, 2008.

[23]Mutzman, R., Murphy, J., and Hank, J., "X-51A Scramjet Engine Flight Demonstration Program," *15th AIAA International Space Planes and Hypersonic Systems and Technologies Conference*, AIAA Paper 2005-2540, 2008.

[24]Falempin, F. and Serre, L., "French LEA Flight Test Program: Status in 2008," *15th AIAA International Space Planes and Hypersonic Systems and Technologies Conference*, AIAA Paper 2005-2541, 2008.

[25]Weihs, H., Longo, J., and Turner, J., "Sharp Edge Flight Experience SHEFEX II: A Mission Overview and Status," *15th AIAA International Space Planes and Hypersonic Systems and Technologies Conference*, AIAA Paper 2005-2542, 2008.

[26]Bisek, N. J., Boyd, I. D., and Poggie, J., "Numerical Study of Energy Deposition Requirements for Aerodynamic Control of Hypersonic Vehicles," *46nd AIAA Aerospace Sciences Meeting and Exhibit*, AIAA Paper 2008-1109, 2008.

[27]Scalabrin, L. C. and Boyd, I. D., "Development of an Unstructured Navier-Stokes Solver For Hypersonic Nonequilibrium Aerothermodynamics," *38th AIAA Thermophysics Conference*, AIAA Paper 2005-5203, 2005.

[28]Scalabrin, L. C. and Boyd, I. D., "Numerical Simulation of Weakly Ionized Hypersonic Flow for Reentry Configurations," *9th AIAA/ASME Joint Thermophysics and Heat Transfer Conference*, AIAA Paper 2006-3773, 2006.

[29]Shercliff, J., *A Textbook of Magnetohydrodynamics*, Pergamon Press, 1965.

[30]Gaitonde, D. V. and Poggie, J., "Elements of a Numerical Procedure for 3-D MGD Flow Control Analysis," *40th AIAA Aerospace Sciences Metting and Exhibit*, AIAA Paper 2002-198, 2002.

[31]Sutton, G. W. and Sherman, A., *Engineering Magnetohydrodynamics*, McGraw-Hill, 1965.

[32]Hoffman, K. A. and Chiang, S. T., *Computational Fluid Dynamics - Vol. 1, 4th ed.*, Engineering Education System, 2000.

[33]Tannehill, J. C., Anderson, D. A., and Pletcher, R. H., *Computational Fluid Mechanics and Heat Transfer, 2nd ed.*, Hemisphere Publishing Corporation, 1997.

[34]Hansen, C., "Approximations for the Thermodynamic and Transport Properties of High-Temperature Air," Tech. Rep. TR-R-50, NASA, 1959.

[35]Srinivasan, S., Tannehill, J., and Weilmuenster, K., "Simplified Curve Fits for the Thermodynamic Properties of Equilibrium Air," Tech. Rep. RP-1181, NASA, 1987.

[36]Gupta, R. N., Lee, K.-P., Thompson, R. A., and Yos, J. M., "Calculation and Curve Fits of Thermodynamic and Transport Properties for Equilibrium Air to 30,000 K," Tech. Rep. RP-1260, NASA, 1991.

[37]Sokolova, I. A., "Transport Properties of Weakly Ionized Air," *32nd AIAA Plasmadynamics and Lasers Conference and 4th Weakly Ionized Gases Workshop*, AIAA Paper 2001-3083, 2001.

American Institute of Aeronautics and Astronautics

[38]D'Angola, A., Colonna, G., Gorse, C., and Capitelli, M., "Thermodynamic and Transport Properties in Equilibrium Air Plasmas in a Wide Pressure and Temperature Range," *The European Physical Journal D*, Vol. 46, No. 1, January 2008, pp. 129–150.

[39]Henderson, S. J. and Menart, J. A., "Equilibrium Properties of High-Temperature Air for a Number of Pressures," *Journal of Thermophysics and Heat Transfer*, Vol. 22, No. 4, October 2008, pp. 718–726.

[40]Godin, D. and Trépanier, J. Y., "A Robust and Efficient Method for the Computation of Equilbrium Composition in Gaseous Mixtures," *Plasma Chemistry and Plasma Processing*, Vol. 24, No. 3, September 2004, pp. 447–473.

[41]Cambel, A. B., *Plasma Physics and Magnetofluid-Mechanics*, McGraw-Hill, 1963, p. 171.

[42]Bush, W. B., "The Stagnation-Point Boundary Layer in the Presence of an Applied Magnetic Field," *Journal of Aerospace Sciences*, Vol. 28, No. 8, August 1961, pp. 610–611, 630.

[43]Poggie, J. and Gaitonde, D. V., "Computational Studies of Magnetic Control in Hypersonic Flow," *39th Aerospace Sciences Meeting and Exhibit*, AIAA Paper 2001-0196, 2001.

[44]Otsu, H., Abe, T., and Konigorski, D., "Influence of the Hall Effect on the Electrodynamic Heat Shield System for Reentry Vehicles," *36th AIAA Plasmadynamics and Lasers Conference*, AIAA Paper 2005-5049, 2005.

[45]Otsu, H., Matsuda, A., Abe, T., and Konigorski, D., "Numerical Validation of the Magnetic Flow Control for Reentry Vehicles," *37th AIAA Plasmadynamics and Lasers Conference*, AIAA Paper 2006-3236, 2006.

[46]Weng, Y. and Kushner, M. J., "Method for Including Electron-Electron Collisions in Monte Carlo Simulations of Electron Swarms in Partially Ionized Gases," *Physical Review A*, Vol. 42, No. 10, November 1990, pp. 6192–6200.

[47]Rockwood, S. D., "Elastic and Inelastic Cross Sections for Electron-Hg Scattering from Hg Transport Data," *Physical Review A*, Vol. 8, No. 5, November 1973, pp. 2348–2358.

[48]Rockwood, S. D., "Effect of Electron-Electron and Electron-Ion Collisions in Hg, CO_2/N_2/He, and CO/N_2 discharges," *Journal of Applied Physics*, Vol. 45, No. 12, December 1974, pp. 5229–5234.

[49]Dorai, R. and Kushner, M. J., "A Model for Plasma Modification of Polypropylene using Atmospheric Pressure Discharges," *Journal of Physics D: Applied Physics*, Vol. 36, No. 6, March 2003, pp. 666–685.

[50]Stafford, D. S. and Kushner, M. J., "$O_2(^1\Delta)$ Production in He/O_2 mixtures in Flowing Low Pressure Plasmas," *Journal of Applied Physics*, Vol. 96, No. 5, September 2004, pp. 2451–2465.

[51]Nowlan, D., Burke, A., and Bird, K., "Pressure and Heat Transfer Distribution on ASD Elliptic Cone (W3) and ASD Sortie (W4) in the CAL 48-Inch Hypersonic Shock Tunnel," Tech. Rep. AM-1800-Y-2, Cornell Aeronautical Laboratory, Inc., Buffalo, NY, December 1963, ASC 94 2649.

[52]Kimmel, R. L., Poggie, J., and Schwoerke, S. N., "Laminar-Turbulent Transition in a Mach 8 Elliptic Cone Flow," *AIAA Journal*, Vol. 37, No. 9, September 1999, pp. 1080–1087.

[53]Kimmel, R., Klein, M., and Schwoerke, S., "Three-Dimensional Hypersonic Laminar Boundary-Layer Computations for Transition Experiment Design," *AIAA Journal*, Vol. 34, No. 4, July-August 1997, pp. 409–415.

Appendix

Table 2. Temperature, pressure, and mole fractions for air computed using the computational code cited in Ref. 40. ($\chi = N_2/O_2/NO/N/O/N_2^+/O_2^+/NO^+/N^+/O^+/e$)

Pressure	Temperature	Mole Fractions [χ]
0.001 atm	2000 K	0.80/0.18/0.01/0.00/0.01/0.00/0.00/0.00/0.00/0.00/0.00
0.001 atm	4000 K	0.64/0.00/0.00/0.04/0.31/0.00/0.00/0.00/0.00/0.00/0.00
0.001 atm	6000 K	0.01/0.00/0.00/0.79/0.19/0.00/0.00/0.00/0.00/0.00/0.00
0.001 atm	8000 K	0.00/0.00/0.00/0.70/0.17/0.00/0.00/0.00/0.06/0.01/0.07
0.001 atm	10000 K	0.00/0.00/0.00/0.19/0.06/0.00/0.00/0.00/0.32/0.06/0.38
0.001 atm	12000 K	0.00/0.00/0.00/0.01/0.01/0.00/0.00/0.00/0.40/0.09/0.49
0.100 atm	2000 K	0.81/0.19/0.01/0.00/0.00/0.00/0.00/0.00/0.00/0.00/0.00
0.100 atm	4000 K	0.68/0.00/0.02/0.00/0.30/0.00/0.00/0.00/0.00/0.00/0.00
0.100 atm	6000 K	0.32/0.00/0.00/0.42/0.25/0.00/0.00/0.00/0.00/0.00/0.00
0.100 atm	8000 K	0.01/0.00/0.00/0.79/0.19/0.00/0.00/0.00/0.01/0.00/0.01
0.100 atm	10000 K	0.00/0.00/0.00/0.69/0.17/0.00/0.00/0.00/0.06/0.01/0.07
0.100 atm	12000 K	0.00/0.00/0.00/0.36/0.10/0.00/0.00/0.00/0.23/0.03/0.27
1.000 atm	2000 K	0.81/0.19/0.01/0.00/0.00/0.00/0.00/0.00/0.00/0.00/0.00
1.000 atm	4000 K	0.69/0.03/0.04/0.00/0.24/0.00/0.00/0.00/0.00/0.00/0.00
1.000 atm	6000 K	0.53/0.00/0.01/0.17/0.29/0.00/0.00/0.00/0.00/0.00/0.00
1.000 atm	8000 K	0.06/0.00/0.00/0.73/0.20/0.00/0.00/0.00/0.00/0.00/0.00
1.000 atm	10000 K	0.00/0.00/0.00/0.76/0.18/0.00/0.00/0.00/0.02/0.00/0.02
1.000 atm	12000 K	0.00/0.00/0.00/0.62/0.16/0.00/0.00/0.00/0.10/0.01/0.11

American Institute of Aeronautics and Astronautics

Approved for public release; distribution unlimited.
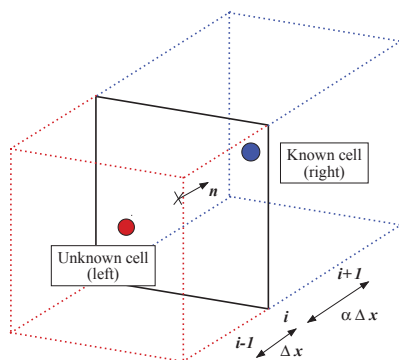
Figure 1. An illustration of the nonuniform finite difference methodology used to find the flux through face i from $i-1$ to $i+1$. (ϕ is known at $i+1$ [blue] and unknown at $i-1$ [red])

(a) p = 0.001 atm

(b) p = 1.0 atm
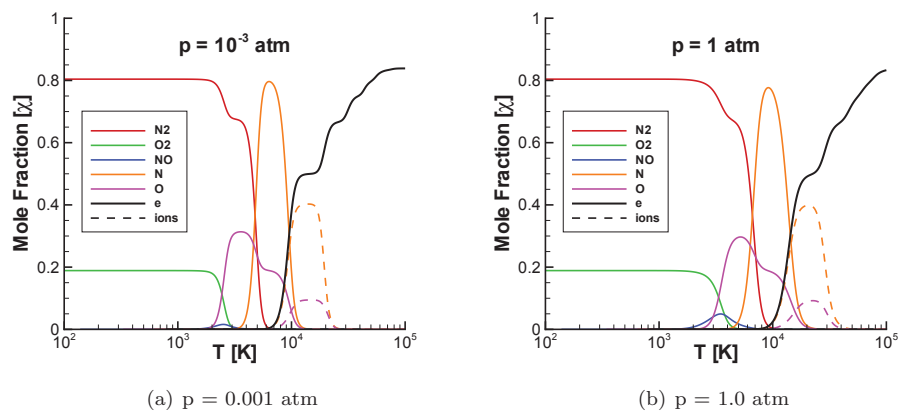
Figure 2. Mole fractions of equilibrium air versus temperature for various pressures. (11 species)
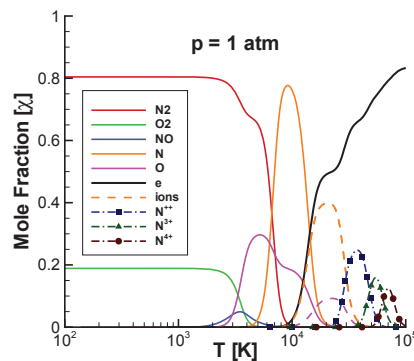
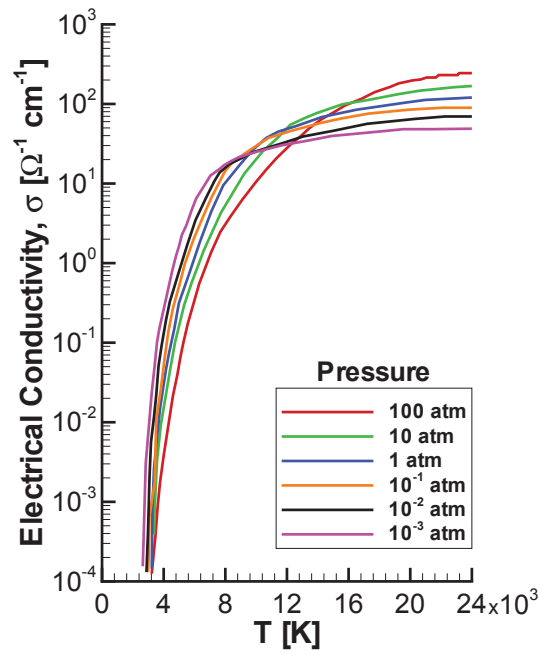**Figure 3. Mole fractions of equilibrium air versus temperature for p = 1 atm. (14 species)**

Approved for public release; distribution unlimited.

Figure 4. Electrical conductivity of equilibrium air for various temperatures and pressures reproduced from Ref. 31.
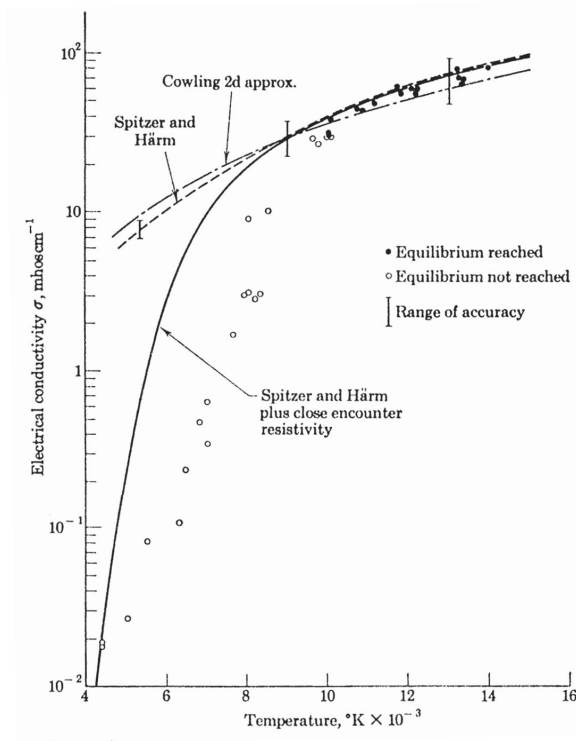
Figure 5. Electrical conductivity of equilibrium argon at p = 0.013 atm from Ref. 41.

Approved for public release; distribution unlimited.
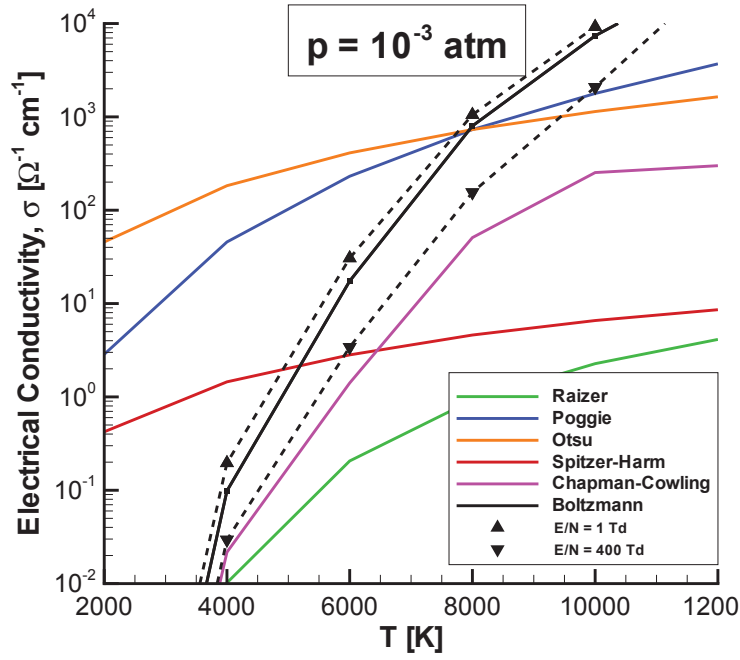
Figure 6. Electrical conductivity distribution versus temperature for various electrical conductivity models. (p = 0.001 atm)
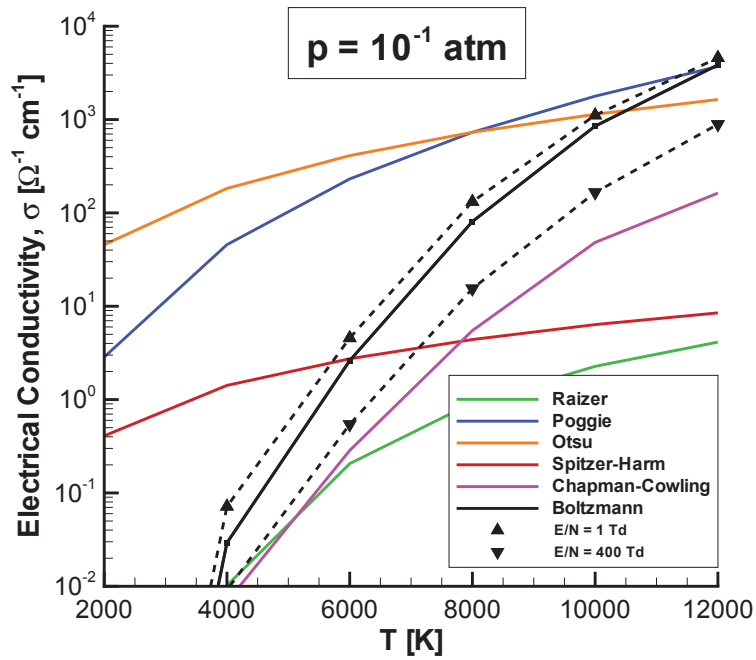
Figure 7. Electrical conductivity distribution versus temperature for various electrical conductivity models. (p = 0.1 atm)
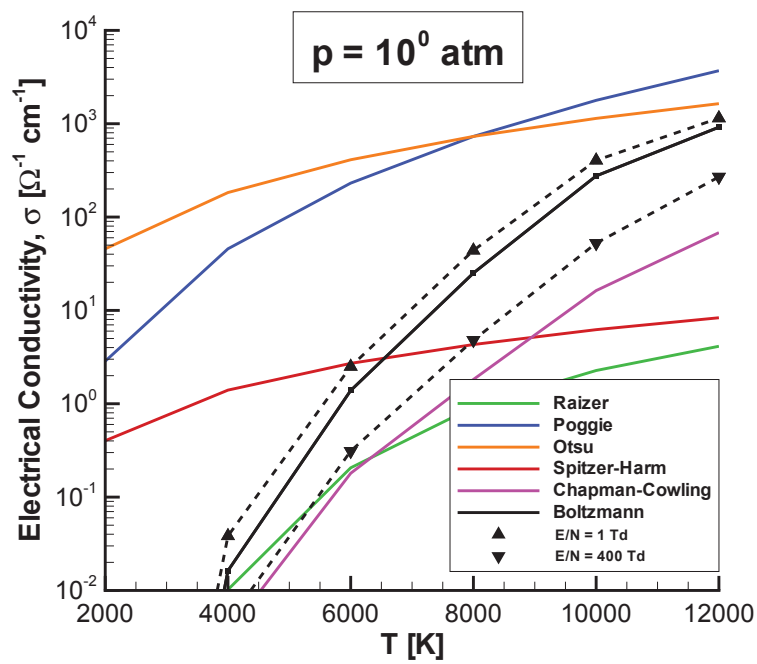
Figure 8. Electrical conductivity distribution versus temperature for various electrical conductivity models. (p = 1 atm)

Approved for public release; distribution unlimited.
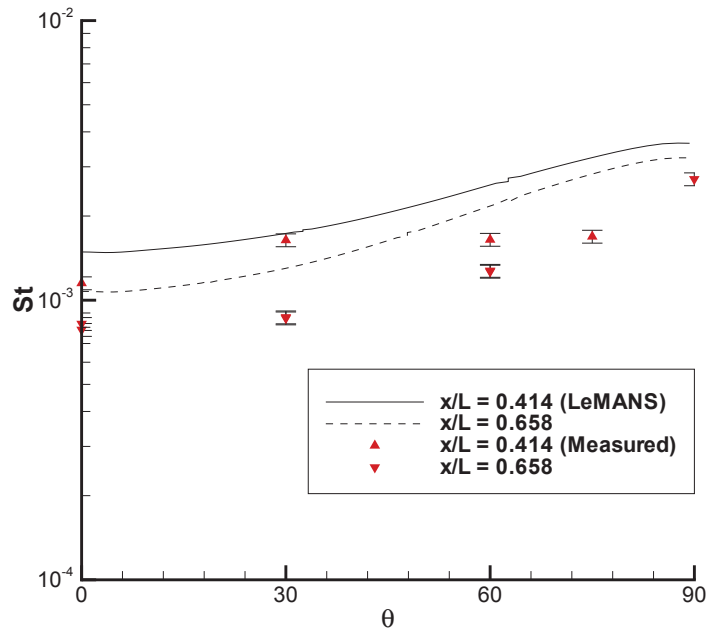
(a) Stanton number around the circumference
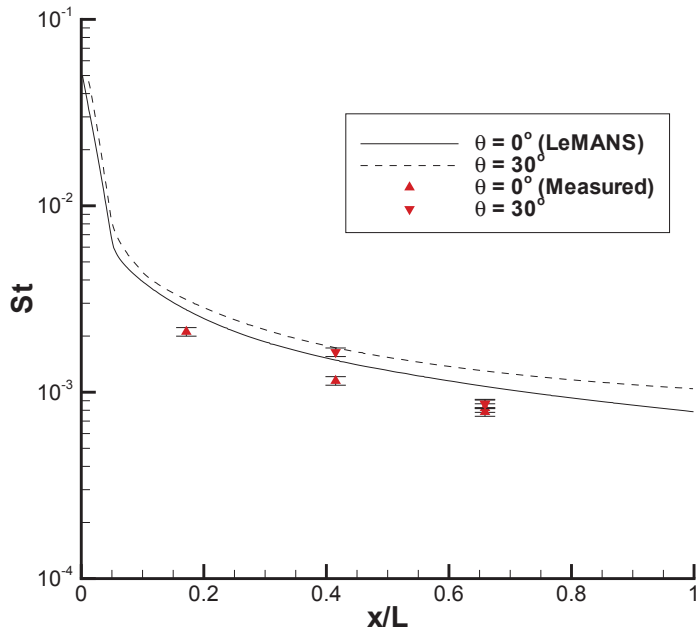
(b) Stanton number along rays

Figure 9. Stanton number distributions for Mach 14 blunt elliptic cone ($\pm$4.5 percent experimental uncertainty).[51]

American Institute of Aeronautics and Astronautics

Approved for public release; distribution unlimited.

(a) Uniform

(b) Nonuniform

(c) Nonuniform (rotated 30° along each axis)
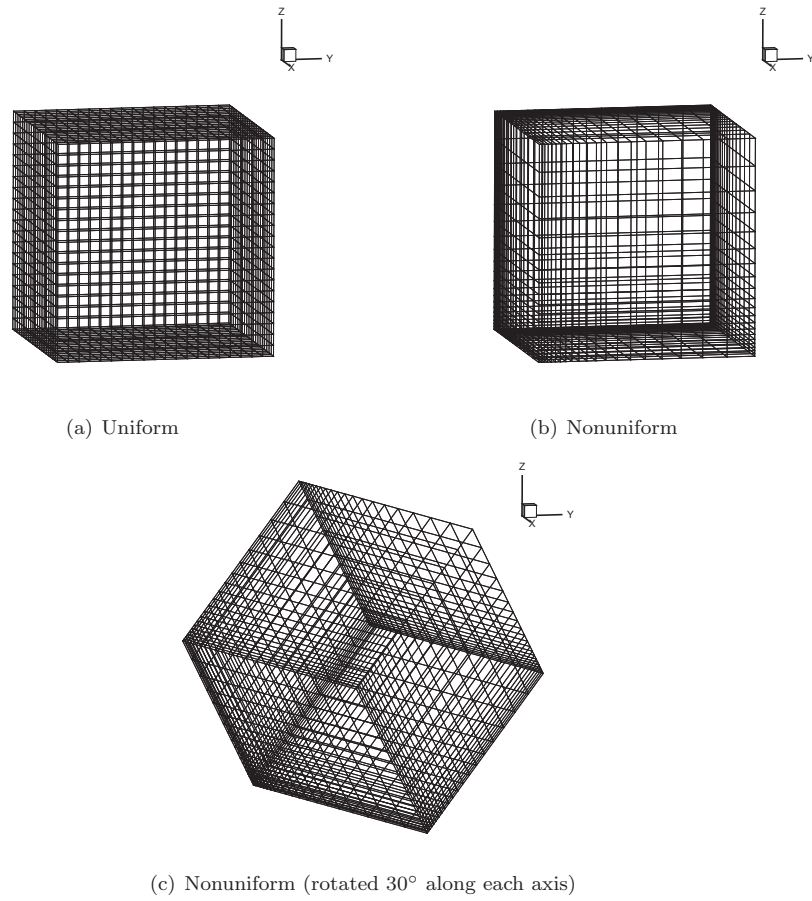
Figure 10. Sample rectilinear meshes used in the analytical MHD validation case. $(20 \times 20 \times 20)$
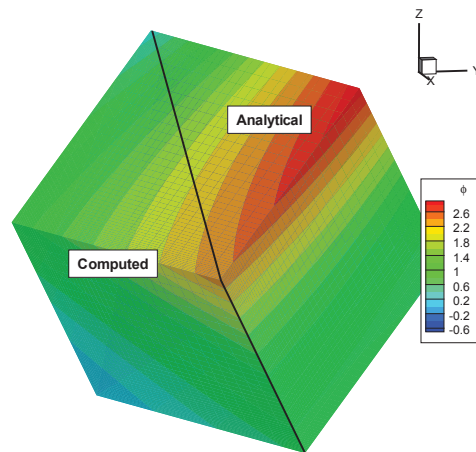
Figure 11. Contours of the electric potential ϕ for the analytical MHD validation case. The left side of the domain is composed of computed values while the right side is theoretical. $(20 \times 20 \times 20)$

American Institute of Aeronautics and Astronautics

Approved for public release; distribution unlimited.
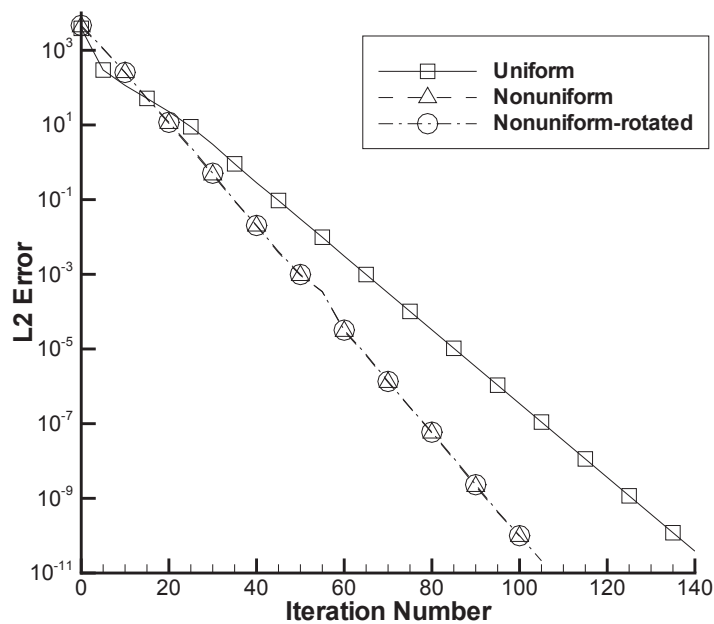
Figure 12. Least Square Normal versus iteration number for the various meshes used in the analytical validation case. Computations where made using the SOR method with $\omega = 1.70$. $(20 \times 20 \times 20)$
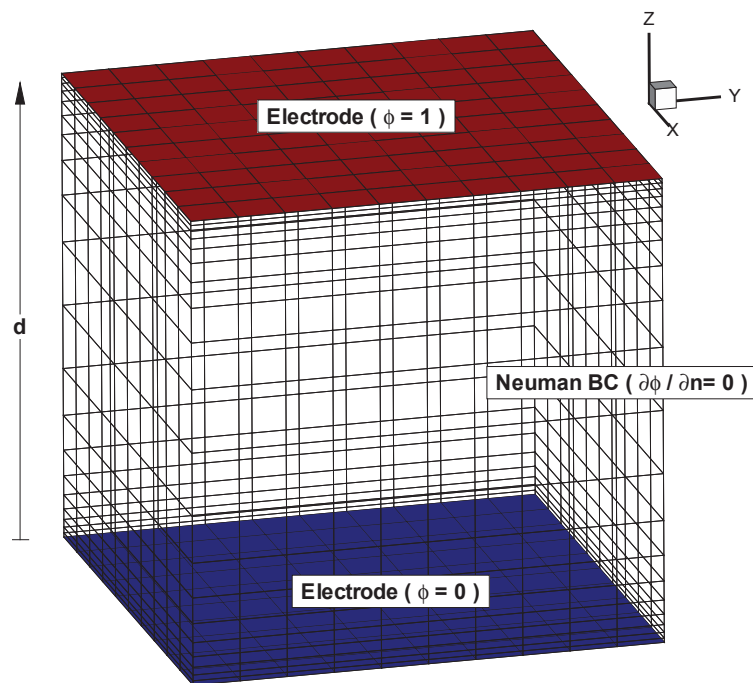
Figure 13. Nonuniform mesh for current flow between parallel electrode plates. $(10 \times 10 \times 20)$
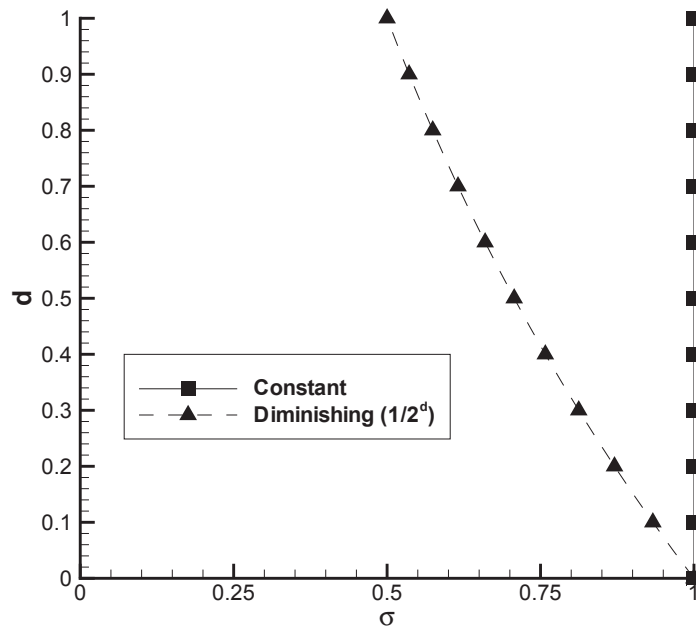
American Institute of Aeronautics and Astronautics

Approved for public release; distribution unlimited.

Figure 14. Various conductivity models used in flow between parallel electrode plates.
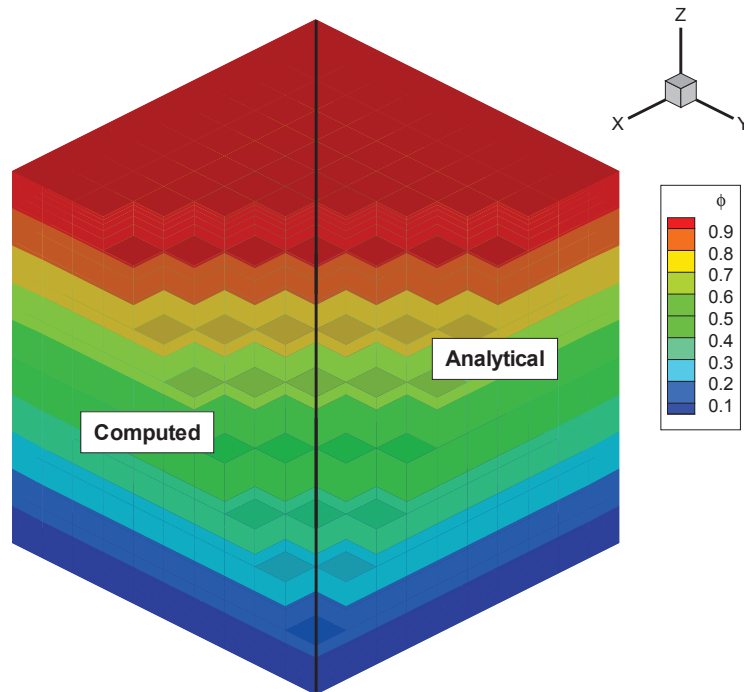
Figure 15. Contours of the electric potential ϕ for parallel electrodes with no flow (σ = Constant). The left side of the domain is composed of computed values while the right side is theoretical. ($10 \times 10 \times 20$)
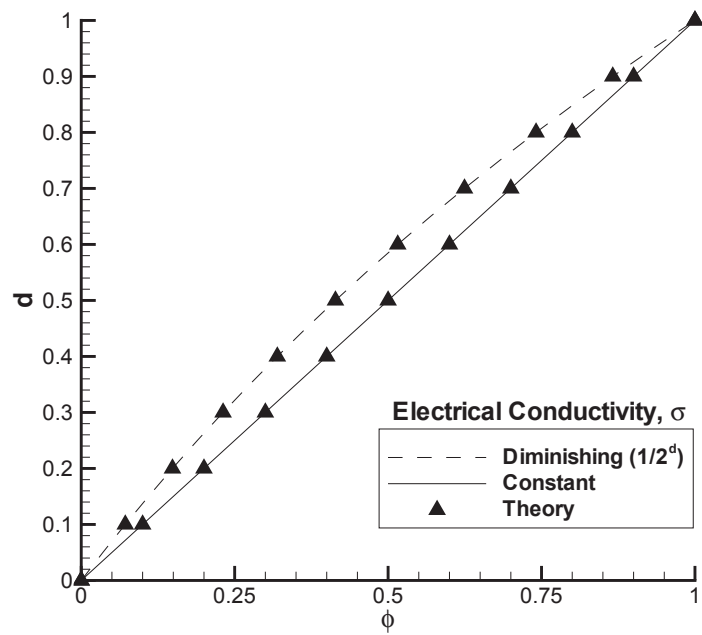
Approved for public release; distribution unlimited.

Figure 16. Electric potential distributions between parallel electrode plates with no flow. Two electrical conductivity models are shown ($\sigma = 1$ and $\sigma = 1/2^d$). The distribution is extracted along $x = 0.5$, $y = 0.5$.

American Institute of Aeronautics and Astronautics

Approved for public release; distribution unlimited.

48th AIAA Aerospace Sciences Meeting Including the New Horizons Forum and Aerospace Exposition
4 - 7 January 2010, Orlando, Florida

AIAA 2010-227s.

Numerical Study of Magnetoaerodynamic Flow around a Hemisphere

Nicholas J. Bisek[*] and Iain D. Boyd[†]

Department of Aerospace Engineering, University of Michigan, Ann Arbor, MI, 48109, USA

and

Jonathan Poggie[‡]

Air Force Research Laboratory, Wright-Patterson AFB, OH, 45433-7512, USA

Newly developed computational tools are used to compute hypersonic flow around a hemisphere capped geometry which utilizes a magnet located within the body as a means of heat flux mitigation. These tools include an improved electrical conductivity model and a parallelized 3D magnetohydrodynamic module that is loosely coupled to a 3D fluid code. Results show the shock standoff distance increases when the magnetic field is applied. The change in shock standoff distance is consistent with experimental measurements. The increase in shock standoff distance reduces the gradients in the shock layer thereby reducing the peak heat flux to the body. However, the total heat flux increases due to increased heating on the aft section of the geometry.

Nomenclature

ρ = mass density
μ = coefficient of viscosity
u = streamwise velocity component
$\mathbf{u}$ = velocity vector (u, v, w)
x, y, z = streamwise, spanwise, and transverse coordinates
N = total number density, m^{-3}
p = pressure
$\mathbf{I}$ = identity matrix
τ = viscous stress
δ_{ij} = delta operator, $\delta_{ij} = \begin{cases} 1, i=j \\ 0, i \neq j \end{cases}$
E = total energy per volume
$\mathbf{q}$ = heat flux (translational, rotational, and vibrational)
T = temperature
L = geometry length
Re_m = magnetic Reynolds number, uL/η_m
η_m = magnetic diffusivity, $\mu_0^{-1}\sigma^{-1}$
μ_0 = permeability of free space, $4\pi \times 10^{-7}$ N/A²
ν_m = electron-neutral particle collision frequency
m_e = electron mass, 9.11×10^{-31}kg
e = electron charge, 1.6×10^{-19}C
σ = electrical conductivity, Ω^{-1}m^{-1}
$\tilde{\sigma}$ = electrical conductivity tensor (including Hall effect)
α = degree of ionization

---

[*]Graduate Student, Student Member AIAA.
[†]Professor, Associate Fellow AIAA.
[‡]Senior Aerospace Engineer, AFRL/RBAC. Associate Fellow AIAA.

American Institute of Aeronautics and Astronautics

Q	= collision cross-section, cm^2
ϕ	= electric potential, V
B	= magnetic field vector
B	= magnetic field magnitude, T
E	= electric field vector
E	= electric field magnitude, V/m
j	= current density vector
r	= radius
β	= Hall parameter, $\sigma B/[en_e]$
n	= species number density, m^{-3}
χ	= species mole fraction
C$_p$	= pressure coefficient, $[2(p_w - p_\infty)]/[\rho_\infty u_\infty^2]$
C$_h$	= nondimensional heat flux, $2q_w/[\rho_\infty u_\infty^3]$

Subscript

∞	= free stream
w	= wall
n	= nose

Species

Ar	= argon
Ar$^+$	= argon ion
e	= electron

I.   Introduction

The idea of using an applied magnetic field to reduce the heat transfer to a hypersonic vehicle has been a topic of scientific research since the late 1950's when Kantrowitz[1] and Resler and Sears[2,3] conducted the first calculations demonstrating the potential benefits an applied magnetic field has on an incoming weakly ionized flow, a condition typically observed during re-entry. The magnetic field, if properly aligned, creates a magnetic force which opposes the incoming flow, effectively increasing the shock standoff distance. The thickening of the shock layer reduces the gradients near the stagnation point, and thus lowers the peak heat transfer rate.

In the midst of the space race, this novel idea attracted a lot of attention as many groups looked to further explore and refine the semi-analytical calculations by making various approximations to the conservation equations. Of these efforts, the work by Bush[4,5] is considered to be one of the most complete approximate analytic solutions.[6] Bush's approach used a local solution at the stagnation point of the hypersonic flow over an axisymmetric blunt body, and predicted significant flow deceleration with the presence of a magnetic field. The first modern computational fluid dynamic (CFD) simulations of the magnetohydrodynamic (MHD) blunt body problem were completed about a decade later by Coakley and Porter.[7] Because of the lack of computational resources at the time, the simulations still required significant simplifications, including that the gas was ideal, non-reacting, and inviscid.

The first experimental work to complement the computational activity was completed by Ziemer[8] and focused on measuring the shock standoff distance. Bush's approximate results were in reasonable agreement with these first experiments. The first heat transfer measurements for this concept were collected in the experimental work by Wilkinson[9] for Mach 3 ionized argon at the stagnation point of a blunt cone.

Another experimental effort was conducted by Kranc *et al.*[10] in the late 1960's. This work provided additional experimental validation sets for the continuing computational efforts, as it explored shock standoff distance and drag measurements for hypersonic flow over two different axisymmetric geometries. These experiments were run in a flow regime where both the viscosity and Hall effect are important, and confirmed the increase in the shock standoff distance and total drag on the geometry in the presence of a dipole magnetic field. The experiments also exhibited an increase in total heating, which has been attributed to the Hall effect.[11,12] This was unexpected because the thickening of the shock layer reduces gradients within the stagnation region, which should reduce the heat flux to the body. Previous semi-analytic work had predicted that the Hall effect would only reduce the effectiveness of the magnetic force on increasing the shock standoff

American Institute of Aeronautics and Astronautics

Approved for public release; distribution unlimited.

distance and total drag.[13] Regardless of this unexpected outcome, it was determined that the large magnetic field strength needed to make the technology practical required a magnet that was too heavy to be placed on re-entry vehicles and the research area faded.[14]

While hypersonic research continued to experience strong support through the rest of the twentieth century due, in part, to various programs like Apollo and Shuttle,[15]a it was not until the mid-1990's that interest in plasma-assisted hypersonic flow control started to reappear.[16–18] This resurgence has been credited to many factors including the increasing demand for sustained hypersonic flight, rapid access to space, and numerous mechanical and material advances in the area of flight-weight MHD technologies. One of the first to reevaluate the technology using modern CFD was Palmer,[19] who performed first-order spatially accurate simulations of the time-dependent Maxwell's equations coupled to the Navier-Stokes equations to analyze a Mars return vehicle.

The rising costs for hypersonic experiments and the need for results within a greater range of flow-field conditions for increasing geometric complexity has continued to motivate the development of computational tools that are capable of accurately computing these plasma-based hypersonic flow control devices. This need has spurred numerous computational studies in the recent years exploring all aspects of plasma-based flow enhancements including flow control,[20–25] local heat load mitigation,[26–28] communications blackout,[29,30] and MHD power extraction.[31–33]

Despite the large financial costs, limited facilities, and technical challenges, some recent experimental studies have been performed by Lineberry et al.,[34] Takizawa et al.,[35] Kimmel et al.,[36] Matsuda et al.,[37] and Gülhan et al.[38] to explore electromagnetic effects on hypersonic flows. While these efforts have provided new insight into electromagnetic phenomena in hypersonic flows, more precise measurements, and additional validation exercises for testing the accuracy of fluid-MHD codes, the rising costs (increased maintenance for aging facilities and additional safety protocol), associated with conducting hypersonic experiments greatly limits the number of experiments being conducted.

At the same time, supercomputing systems continue to experience exponential performance increases with substantial decreases in cost. This has led to a continued increase in computational research. In fact, Padilla estimates that if current trends continue, over 70% of hypersonic research will involve computational analysis by 2020.[15]

This work focuses on the previously mentioned experiment conducted by Kranc et al.[10] and Bush's semi-analytical effort.[4,5] Bush's computational work was previously explored computationally by Poggie and Gaitonde[39–41] and Damevin and Hoffmann.[42] In the work by Poggie and Gaitonde, several of Bush's simplifications were removed and the Hall effect was added and investigated, while Damevin and Hoffmann explored chemistry effects for a single temperature model. In both efforts, a simplified model was used to estimate the flow's electrical conductivity. The present work extends these efforts by investigating several electrical conductivity models, including a surrogate model of solutions to Boltzmann's equation. The results show the percent change in shock standoff distance, due to the presence of the magnetic field, corresponds very well with the experimental measurements, especially when employing the surrogate electrical conductivity model. In addition, the solutions show an increase in total heating to the geometry, which is consistent with the observations made by Nowak et al.[11,12] The increase in total heating is due to a slight increase in heating on the cylinder (aft) section of the geometry.

II.   Method

A.   Governing Equations

Flow-field results are obtained using Computational Fluid Dynamics (CFD) to solve the Navier-Stokes equations. The CFD computations are executed using the Michigan Aerothermodynamic Navier-Stokes (LeMANS) code which was developed at the University of Michigan.[43,44]

LeMANS is a general 2D/axisymmetric/3D, parallel, unstructured finite-volume CFD code. The numerical fluxes between cells are discretized using a modified Steger-Warming Flux Vector Splitting (FVS) scheme, except near shock waves. In these regions the original Steger-Warming FVS scheme is used because it provides sufficient dissipation to accommodate the discontinuity.[45] LeMANS is able to employ a two-temperature or three-temperature model to account for thermal-nonequilibrium and a standard finite rate chemistry model for non-equilibrium chemistry. The two-temperature model assumes a single temperature, T, accounts for the translational and rotational energy modes of all species, while the vibrational energy mode is accounted for by a separate temperature, T_{ve}. In the three-temperature model, the rotational energy

American Institute of Aeronautics and Astronautics

Approved for public release; distribution unlimited.

mode is independent of the translational energy mode.[46]

For a single temperature (local thermal equilibrium) model with MHD, but without finite chemistry, the conservation equations are:

$$\frac{\partial \rho}{\partial t} + \nabla \cdot (\rho \mathbf{u}) = 0 \tag{1}$$

$$\frac{\partial \rho \mathbf{u}}{\partial t} + \nabla \cdot (\rho \mathbf{u}\mathbf{u} + p\mathbf{I} - \tau) = \mathbf{j} \times \mathbf{B} \tag{2}$$

$$\frac{\partial E}{\partial t} + \nabla \cdot ((E + p)\mathbf{u} - \tau \cdot \mathbf{u} - \mathbf{q}) = \mathbf{j} \cdot \mathbf{E} \tag{3}$$

where $\mathbf{u}\mathbf{u}$ in the conservation of momentum equation (2), is the 3×3 tensor containing all the products of the components of the velocity vector as seen in equation (4).

$$\mathbf{u}\mathbf{u} = \begin{bmatrix} u^2 & uv & uw \\ vu & v^2 & vw \\ wu & wy & w^2 \end{bmatrix} \tag{4}$$

LeMANS assumes the fluid is continuous and Newtonian. It also assumes Stokes' hypothesis when determining the viscous stresses:

$$\tau_{ij} = \mu \left(\frac{\partial u_j}{\partial x_i} + \frac{\partial u_i}{\partial x_j} \right) - \frac{2}{3}\mu \nabla \cdot \mathbf{u}\delta_{ij}$$

The total energy deposition term, $\mathbf{j} \cdot \mathbf{E}$, appears on the right side of the total energy equation (3). The conservation of momentum equation is modified to include a magnetic force, $\mathbf{j} \times \mathbf{B}$, on the right hand side of equation (2). These additions constitute the effects the current density, $\mathbf{j}$, electric field, $\mathbf{E}$, and magnetic field, $\mathbf{B}$, have on the flow.

B.   Low Magnetic Reynolds Number Approximation

The three additional variables appearing in the modified governing equations ($\mathbf{j}, \mathbf{B}$, and $\mathbf{E}$), are determined by first noting that the magnetic Reynolds number, equation (5), is small for the cases of interest.

$$Re_m = \frac{uL}{\eta_m} \tag{5}$$

Consequently, it can be shown that the induced magnetic field can be neglected.[47] This means only external magnetic fields are present in the flow (and must be specified). The current and electric fields are determined by solving the current continuity equation, which has the form of a Poisson equation as seen in equation (6).

$$\nabla \cdot \tilde{\sigma} \cdot [-\nabla \phi + \mathbf{u} \times \mathbf{B}] = 0 \tag{6}$$

where $\tilde{\sigma}$ is the electrical conductivity tensor, a compact way of accounting for the Hall effect[48] and is described in the next section. The electric potential, ϕ, is computed using a finite-volume method and appropriate boundary conditions as outlined in previous work.[49] The electric field is computed directly from the electric potential ($\mathbf{E} = -\nabla \phi$), which allows the electric current, $\mathbf{j}$, to be computed using a generalized form of Ohm's law ($\mathbf{j} = \tilde{\sigma} \cdot [\mathbf{E} + \mathbf{u} \times \mathbf{B}]$). Full details and validation of the magnetohydrodynamic solver are available in Ref. 49, while Ref. 50 provides details on its parallelization.

C.   Hall Effect

As seen in equation (6), the MHD module incorporates the tensor nature of the electrical conductivity by following the computational work of Gaitonde and Poggie.[40,48] This approach provides a compact way of accounting for ion-slip and the Hall effect. While ion-slip is still assumed negligible for the scope of this paper, the Hall effect is not. Equation (7) shows the electrical conductivity tensor with the Hall effect for Cartesian coordinates:

American Institute of Aeronautics and Astronautics

Approved for public release; distribution unlimited.

$$\tilde{\sigma} = \frac{\sigma}{B^2 \left(1 + \beta^2\right)} \begin{bmatrix} B^2 + \beta^2 \, B_x^2 & \beta \left(\beta \, B_x \, B_y - B \, B_z\right) & \beta \left(\beta \, B_x \, B_z + B \, B_y\right) \\ \beta \left(\beta \, B_y \, B_x + B \, B_z\right) & B^2 + \beta^2 \, B_y^2 & \beta \left(\beta \, B_y \, B_z - B \, B_x\right) \\ \beta \left(\beta \, B_z \, B_x - B \, B_y\right) & \beta \left(\beta \, B_z \, B_y + B \, B_x\right) & B^2 + \beta^2 \, B_z^2 \end{bmatrix} \tag{7}$$

where σ is the electrical conductivity of the fluid. B_x, B_y, and B_z are the components of the magnetic field vector and B is its magnitude. The Hall parameter, β, is defined in equation (8):

$$\beta = \frac{e \, B}{m_e \, \nu_m} \tag{8}$$

where an elemental charge $e = 1.6022 \times 10^{-19}$ C, the mass of an electron $m_e = 9.11 \times 10^{-31}$ kg, and ν_m is the electron-neutral particle momentum transfer collision frequency which is related to the electrical conductivity in equation (9):

$$\nu_m = \frac{e^2 \, n_e}{m_e \, \sigma} \tag{9}$$

where n_e is the electron number density. Equation (9) is combined with equation (8) to yield equation (10), which is directly computed from the fluid properties:

$$\beta = \frac{\sigma \, B}{e \, n_e} \tag{10}$$

Validation of the Hall effect is carried out by utilizing a computational study performed by Oliver and Mitchner.[51] In the experiment, finite segmented electrodes are infinitely repeated along the two walls of a channel as seen in Fig. 1. An externally applied magnetic field is positioned perpendicular to the channel velocity, **u**.
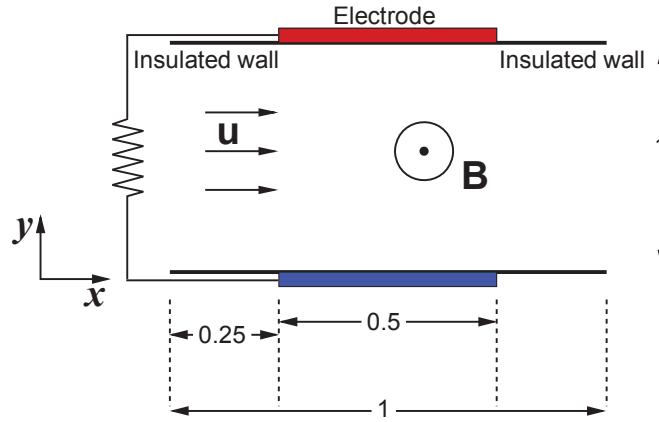
Figure 1. Schematic of the channel flow with finitely segmented electrodes. Units are in meters.

This exercise is inherently two-dimensional, but it is transformed into three dimensions by allowing the channel walls to be infinitely tall. Although this makes the problem computationally more expensive, the MHD routine is only suited for three-dimensional simulations. By using symmetric boundary conditions along the top and bottom planes of the domain, the actual height of the channel domain is set to a finite value of 0.1 m for the simulation, as seen in Fig. 2.

Because the channel is infinitely long, periodic boundary conditions are developed and employed at the domain inlet and outlet. The five point overlapping stencil, shown in Fig. 3, transfers information between the periodic inlet and outlet planes. The scheme is selected because it is well suited for structured grids and is straight-forward to implement when the entire domain is situated on a single processor (serial). In this approach, a row of cells starts at the inlet and ends at the outlet. Along this row, the periodic boundary conditions state that the values in the first two cells nearest the inlet (the ghost cell and adjoining real cell),
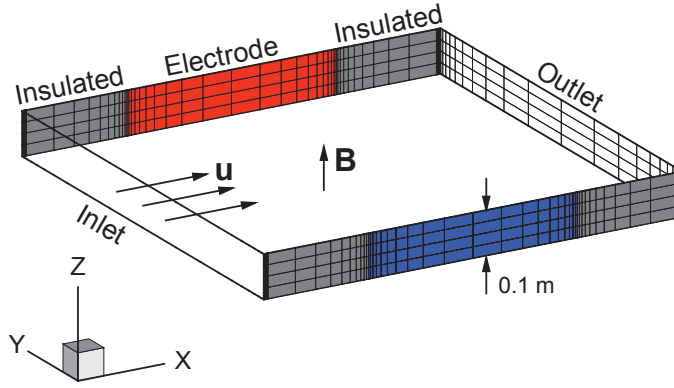
American Institute of Aeronautics and Astronautics

Approved for public release; distribution unlimited.

Figure 2. **Geometry and boundary conditions for the 3D channel flow with finitely segmented electrodes.** ($50 \times 20 \times 4$)

are set equal to the fifth and fourth cells from the outlet. These cells (the fifth and fourth cells from the outlet), along with the rest of the domain's interior cells, are determined by solving equation (6) numerically. Likewise, the last two cells in the row (the last real cell and its adjoining ghost cell), are set equal to the values in the fourth and fifth cells from the inlet.
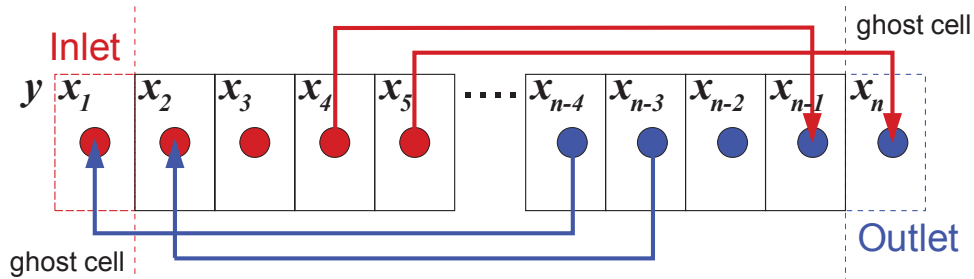
Figure 3. **Cartoon of a five point stencil used for period boundary conditions.**

Oliver and Mitchner carefully formulated this exercise so that the fluid velocity field did not affect the solution as long as $\nabla \times (\mathbf{u} \times \mathbf{B}) = 0$. For one iteration of the flow solver, the MHD routine is executed assuming the velocity profile is only a function of the distance between the plates $\mathbf{u} = f(y)$ which satisfies $\nabla \times (\mathbf{u} \times \mathbf{B}) = 0$ as long as $\mathbf{B} = f(z)$. The velocity profile is assumed to be fully developed Poiseuille flow between parallel plates,[52] as seen in equation (11):

$$\mathbf{u} = f(y) = u_{\max}(1 - \frac{(y - y_h)^2}{h^2}) \tag{11}$$

where $u_{\max}$ is the maximum velocity and is set to unity for this scenario ($u_{\max} = 1$ m/s). The y location is measured from the center of the channel width ($y_h = 0.5$ m) and $h = 0.5$ m is the channel half-width.

A grid independence study is performed using non-reacting argon with a constant electrical conductivity of $\sigma = 1$ $\Omega^{-1}m^{-1}$. The channel walls are 1 m apart and the segmented electrodes are 0.5 m wide, with 0.5 m of insulated wall between them, so that the domain simulated has a length of 1 m in both the x and y-directions. The channel walls are set to a height of 0.1 m in the z-direction with symmetric boundaries applied at the $z = 0, 0.1$ m planes, effectively making the walls infinitely tall. Periodic boundaries are applied at the inlet and outlet, $x = 0, 1$ m, respectively.

The grid utilizes exponential spacing along the wall surface such that cell clustering occurs near the junction between the insulated wall and the electrode. Additionally, five uniform points are located near both the inlet and outlet (along the wall surfaces) to maintain smooth periodic boundary conditions. Exponential

American Institute of Aeronautics and Astronautics

Approved for public release; distribution unlimited.

spacing is also employed between the two walls such that cell clustering occurs near each surface. Uniform spacing is employed along the height of the wall (z-direction), as seen in Fig. 2. The 'coarse' grid employs 50 points along the wall ($x-$direction), 20 points between the walls ($y-$direction), and 4 points in the $z-$direction. Two additional, doubly refined grids are also developed: $100 \times 40 \times 8$ (medium), $200 \times 80 \times 16$ (fine).

Grid independence is assessed by comparing solutions of the electric potential, ϕ, for the scenario without a magnetic field ($\mathbf{B} = 0$). Since the wall is infinitely tall, the solution in the z-direction is constant and is only plotted along the $z = 0$ m plane. Extracting solutions of ϕ at two slices of the domain ($x = 0.25$, 0.5 m), Figs. 4(a) and 4(b) show the potential does not vary significantly between the 'medium' and 'fine' grids, so the 'medium' solution is considered grid-independent and is employed in the rest of the section.

(a) $x = 0$ m
(b) $x = 0.25$ m
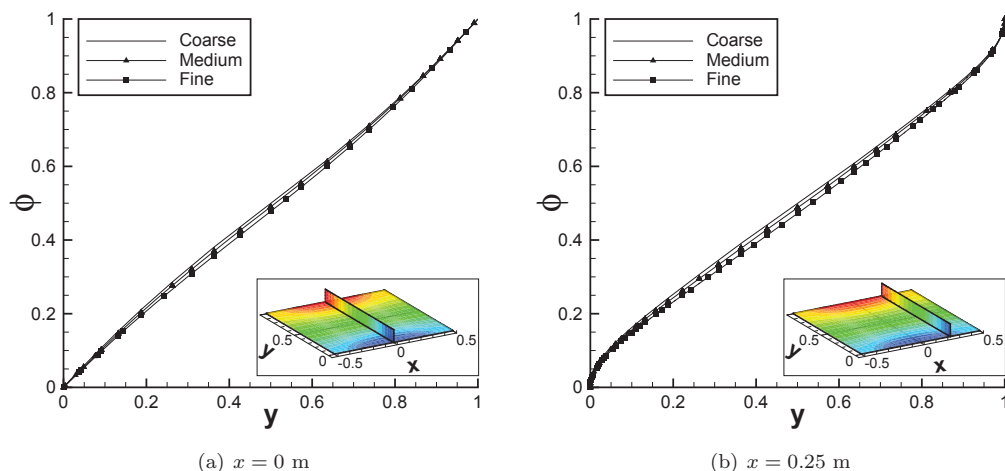
Figure 4. Electric potential (ϕ), between two segmented electrodes at two different locations ($x = 0$ m and 0.25 m), for various grids. ($z = 0$ m)

Without the presence of the magnetic field, the Hall effect has no significance so the electrical conductivity tensor reverts to a scalar. The resultant electric potential solution is symmetric about the center of the electrode as seen in Fig. 5, where Fig. 5(a) is obtained by Gaitonde[40] and Fig. 5(b) is obtained using the 'medium' grid. Close examination of Figs. 5(a) and 5(b) shows that the results obtained are consistent, further validating the MHD solver.

(a) From Gaitonde.[40]
(b) Medium grid ($100 \times 40 \times 8$) at $z = 0$.
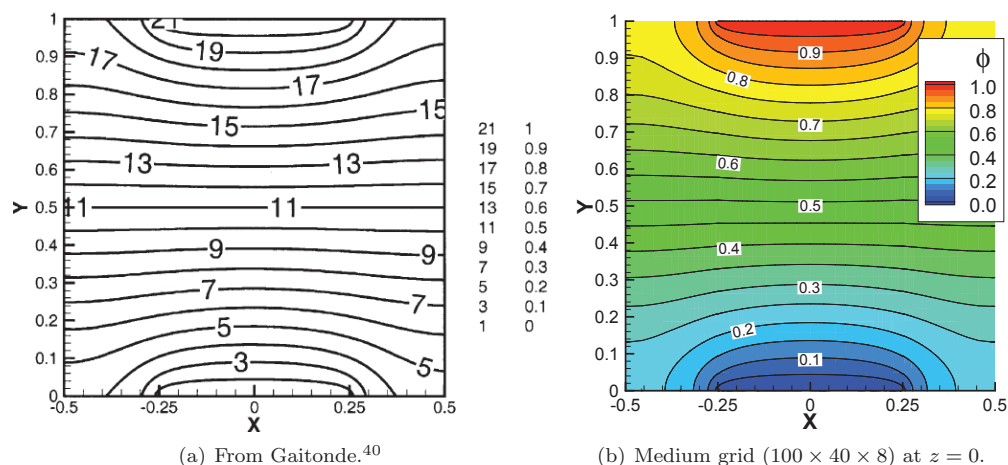
Figure 5. Electric potential contours for the segmented electrode channel without a magnetic field and constant electrical conductivity. ($\mathbf{B} = 0$, $\sigma = 1\,\Omega^{-1}\mathbf{m}^{-1}$)

American Institute of Aeronautics and Astronautics

90

Approved for public release; distribution unlimited.

To test the Hall effect, a second scenario is simulated. In this case, a nonzero magnetic field is externally applied. Consistent with the original analysis, the magnetic field is aligned with the z axis, whereas the velocity is aligned with the x axis. Without the Hall effect, a substantial current would only be created in the y direction. With the Hall effect, magnetic effects also appear in the off-diagonal components of the electrical conductivity tensor seen in equation (7). This results in the 'stretching' of the streamwise component of the current density vector, j_x, which becomes apparent by comparing the current density lines of Figs. 6(a) and 6(b). The results are also compared to the computational work by Gaitonde[40] in Fig. 6(c).

| (a) Without the Hall effect | (b) With the Hall effect | (c) From Gaitonde.[40] |
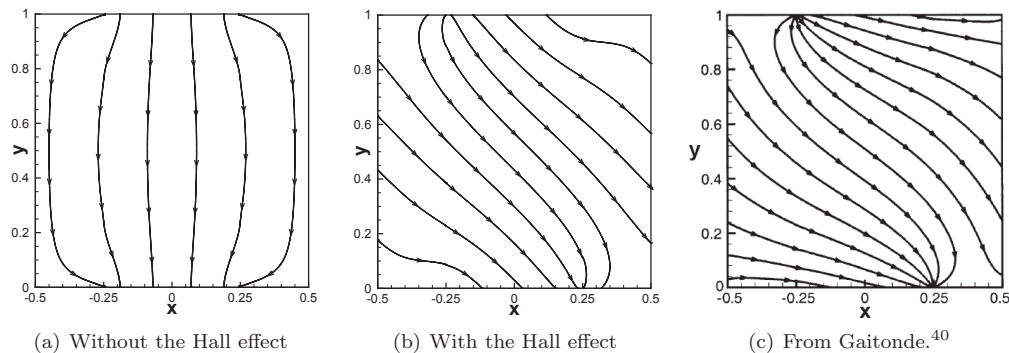
Figure 6. Current density streamlines j between two segmented electrodes with a magnetic field ($B_z = 1$ T), constant electrical conductivity ($\sigma = 1 \, \Omega^{-1}\mathrm{m}^{-1}$), and a streamwise velocity ($u = f(y)$). ($100 \times 40 \times 8$)

The results obtained by Gaitonde in Fig. 6(c) do not exactly match the results shown in Fig. 6(b) because Gaitonde employed a nondimensional MHD formulation, which results in additional coefficients in his electrical conductivity vector. Nonetheless, both figures portray similar characteristics, and indicate that the Hall effect is successfully implemented.

D. Electrical Conductivity

The experiment performed by Kranc *et al.* used pre-ionized argon (Ar, Ar$^+$, and e). The electrical conductivity profile for weakly-ionized argon is shown in Fig. 7. As seen in the figure, the electrical conductivity exhibits two distinct regions, namely, weakly ionized (T $\lesssim$ 10,000 K) and fully ionized (T > 10,000 K). Both regions display exponential growth versus temperature, which means a highly accurate conductivity model is important in order to accurately capture its behavior across the entire temperature range.

Three different electrical conductivity models are explored for this work. Raizer developed an electrical conductivity model that is an exponential function of temperature, assuming that electron-neutral collisions affect the conductivity more than the electron-ion collisions and that the ionization is in thermal equilibrium,[54] as seen in Eqn. 12:

$$\sigma = 83 \times e^{-36000/\mathrm{T}} \quad \Omega^{-1}\mathrm{cm}^{-1} \tag{12}$$

where the temperature T is specified in Kelvin. This model is considered valid for air, nitrogen, and argon at p = 1 atm for a temperature range of 8000 to 14000 K. However, the model's coefficients (83 and -36000), can be adjusted depending on the temperature range, pressure, or gas composition of interest, but are used as specified for this study.

Chapman and Cowling[55] developed a model for a weakly-ionized gas by assuming there is a coupling between the charge and mass diffusion terms and that the resultant electron energy distribution function from solutions to Boltzmann's equation is only a function of this coupled, binary diffusion coefficient. This assumption results in a semi-analytic model for the electrical conductivity, as seen in Eqn. 13:

$$\sigma = 3.34 \times 10^{-12} \frac{\alpha}{Q \sqrt{\mathrm{T}}} \quad \Omega^{-1}\mathrm{cm}^{-1} \tag{13}$$

where Q [cm^2] is the collision cross-section of the gas, and the degree of ionization $\alpha = {}^{\Sigma \, n_{\mathrm{ions}}}/_{N}$. One limitation of using the Chapman and Cowling model is that Q must be determined by an outside source (i.e., experimental data, reference tables, an ideal molecule approximation, etc.). For this work, the collision
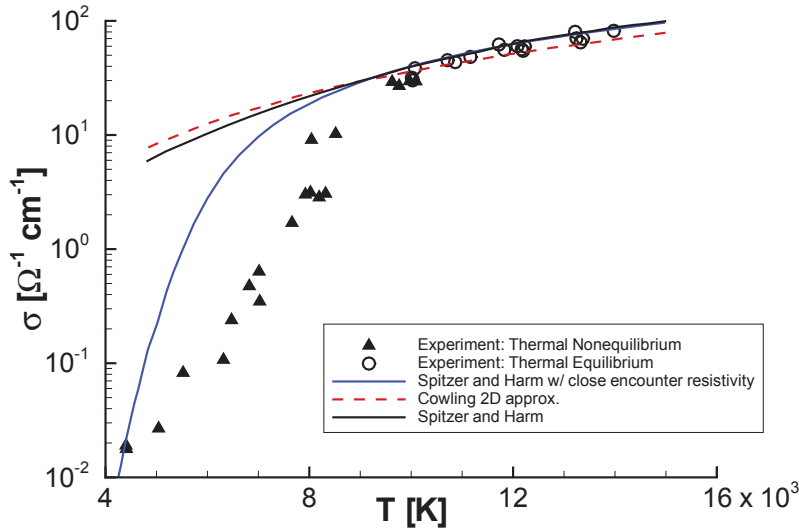
American Institute of Aeronautics and Astronautics

Approved for public release; distribution unlimited.

Figure 7. Electrical conductivity of argon ($p = 0.013$ atm), reproduced from Lin *et al.*[53]

cross-section is taken to be the total collision cross-section for argon-argon collisions using hard sphere model,[56] with a diameter of 4.04×10^{-10} m,[57] to yield: $Q \simeq 5 \times 10^{-17}$ cm^2. This assumption is made because it is unclear what the best choice for Q should be, and because this assumption produces results that are consistent with the other models in previous work.[49,50]

A surrogate model of solutions to Boltzmann's equation is the third electrical conductivity model studied. A 2nd order polynomial response surface is employed to capture the behavior of the solutions to Boltzmann's equations by developing a three-dimensional Design of Experiment (DOE). The solutions to Boltzmann's equation are determined using a Boltzmann solver developed by Kushner *et al.*,[58] which is functionally equivalent to that proposed by Rockwood.[59,60] The Boltzmann solver's input parameters, namely, E/N, χ_{Ar}, and χ_{Ar^+}, define the three-dimensions of the DOE (χ_e is unnecessary because of the assumed local charge neutrality). Details of this approach were discussed in previous work,[50] but have been modified to improve the accuracy of the model as described below.

With the DOE determined, solutions to the model's 'learning' and 'testing' points are obtained from individual Boltzmann solutions, while accounting for electron-electron collisions. Figure 8 plots the resulting electrical conductivity contours, which show a region of high conductivity for low χ_{Ar} (high degree of ionization), and a weak normalized electric field, E/N.

Decreasing electrical conductivity for an increasing electric field strength was also observed in previous work for the electrical conductivity of air.[49] As such, the electrical conductivity appears to be a function of E/N, which is anticipated by factoring the electron number density out of the definition of electrical conductivity for a DC current ($\sigma = e^2\,n_e/m_e\,\nu_m$), to yield: $\sigma/n_e \sim \nu_m^{-1}$. Since the electron collision frequency, ν_m, usually increases with increasing E/N, as seen in Fig. 9, the electrical conductivity should decrease with increasing electric field strength.

Since the model's dependent variable, σ, has a large range of values, the Polynomial Response Surface (PRS) surrogate model may have trouble capturing the behavior, especially in regions with a large gradient. An open-source MATLAB® library, *SURROGATES Toolbox*,[61] is used to create the PRS model. In order to improve the accuracy of the model, it is useful to transform the function that the PRS model is trying to mimic, by reducing the range of the dependent variable. Dividing the electrical conductivity by the degree of ionization does not require any additional information (parameters), since $\alpha = \Sigma\,\chi_{ions} = \chi_{Ar^+}$, but helps to normalize the solution. However, this leads to a division by zero error when $\alpha = 0$, so the dependent variable is inverted: α/σ. This transformation is similar to the Chapman-Cowling model, which also utilizes the degree of ionization in the numerator. Unfortunately, this formulation has a small solution range for this scenario ($10^{-8}\,\Omega \cdot m \leq \alpha/\sigma \leq 10^{-6}\,\Omega \cdot m$), so the natural logarithm is also applied to renormalize the solution range. Equation (14) lists the model formulation provided to *SURROGATES Toolbox*:
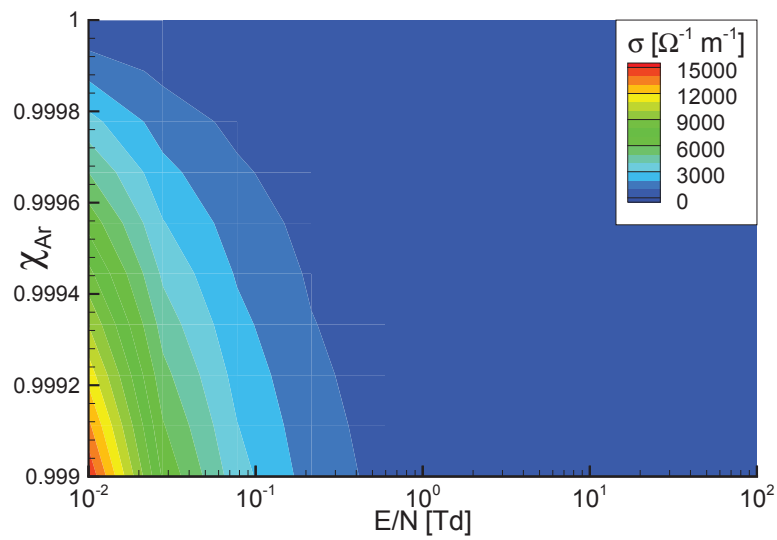
American Institute of Aeronautics and Astronautics

Approved for public release; distribution unlimited.

Figure 8. Electrical conductivity contours for weakly-ionized argon.
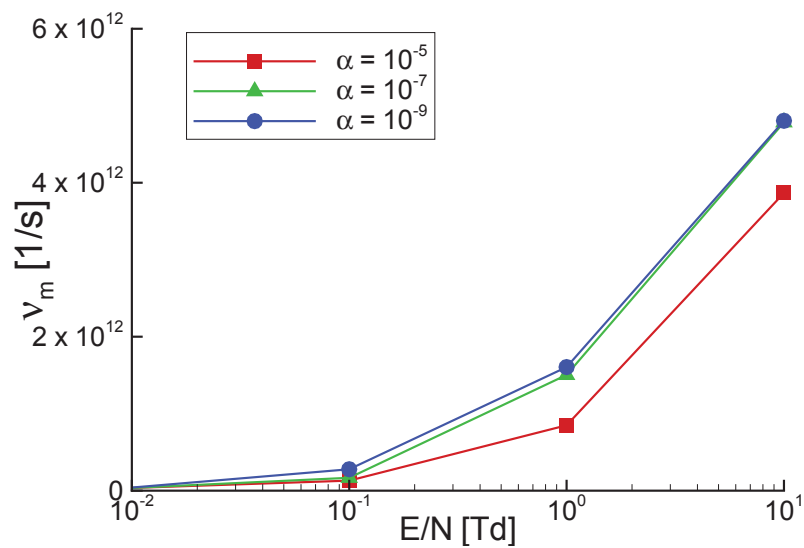
Figure 9. Electron collision frequency for weakly-ionized argon at $p = 1$ atm.

American Institute of Aeronautics and Astronautics

93

Approved for public release; distribution unlimited.

$$\ln\left(\frac{\alpha}{\sigma}\right) = f\left(E/N, \chi_{\text{Ar}}, \chi_{\text{Ar+}}\right) \tag{14}$$

Applying the natural logarithm function provides a second advantage when the model is employed. Since the formulated model is a function of the natural logarithm and the degree of ionization, the electrical conductivity must be extracted from the model solution by dividing the degree of ionization by the exponential function of the model's prediction: $\sigma = \alpha/\exp\left(\textbf{PRS}\left(E/N, \chi_{\text{Ar}}, \chi_{\text{Ar+}}\right)\right)$. Since the exponential of any real number (the result of using the PRS model), is positive, the resulting electrical conductivity predicted will always be greater than or equal to zero. This characteristic (the model will always provide a positive value), is critical for the implementation of the model in the MHD module, since the electrical conductivity of a real gas is always greater than or equal to zero.

Although this formulation of the model incurs additional computational expense (i.e., evaluation of the exponential function), higher accuracy is achieved for lower order PRS models because the DOE's surface gradients are reduced. The model accuracy is determined by computing the Mean Absolute Error (MAE) and the Mean Absolute Percent Error (MAPE):

$$\text{Mean Absolute Error (MAE)} = \frac{1}{n}\sum_{i=1}^{n}|\hat{\sigma} - \sigma|_i \tag{15}$$

$$\text{Mean Absolute Percent Error (MAPE)} = \frac{1}{n}\sum_{i=1}^{n}\left|\frac{\hat{\sigma} - \sigma}{(\hat{\sigma} + \sigma)/2}\right|_i \tag{16}$$

where $\hat{\sigma}$ is the solution computed by the Boltzmann solver and σ is the solution computed by the model. The percent error is the normalized percent error to remove the bias when evaluating an over-prediction.[62] A summary of the surrogate response surface model performance metrics is tabulated in Table 1.

Table 1. Summary of surrogate model performance metrics.

Surrogate	MAPE	MAE	coefficients	conservativeness
PRS - 2$^{\text{nd}}$ order	16.35 %	90.72 $\Omega^{-1}\text{m}^{-1}$	10	100%

The 2nd order PRS model with its coefficients is listed in equation (17).

$$\begin{aligned}\sigma = &-842.64 + 128.02(E/N) + 2558.28(\chi_{\text{Ar}}) - 4112.52(\chi_{\text{Ar+}})\\ &-4.82(E/N)^2 - 118.25(E/N)(\chi_{\text{Ar}}) - 121.33(E/N)(\chi_{\text{Ar+}})\\ &-1732.34(\chi_{\text{Ar}})^2 + 3229.51(\chi_{\text{Ar}})(\chi_{\text{Ar+}}) - 7342.51(\chi_{\text{Ar+}})^2\end{aligned} \tag{17}$$

where E/N is normalized from 0 to 1 for a range of 0.01 to 100 Td. (1 Td = 10^{-17} V·cm^2)

E.   Viscosity Model

Chemically non-reacting, thermodynamic equilibrium simulations are computed using the variable hard sphere (VHS) viscosity model. The VHS model is used because the viscosity is assumed to only be a function of temperature, since the species present (argon, argon ion, and electrons), have a single energy mode and are chemically non-reacting:

$$\mu = \mu_{ref}\left(\frac{T}{T_{ref}}\right)^{\omega} \tag{18}$$

where μ is the viscosity, the reference viscosity coefficient, $\mu_{ref} = 2.117 \times 10^{-5}$ N s/m^2, for a reference temperature, $T_{ref} = 273$ K, and a viscosity index, $\omega = 0.81$. This method, as outlined by Schwartzentruber et al.,[63] requires several reference coefficients which are listed in Ref. 56.

American Institute of Aeronautics and Astronautics

III. Results

Three-dimensional calculations are carried out for Mach 4.75 argon flow over a hemisphere-shaped fore-body attached to a cylinder, which was originally studied experimentally by Kranc et al.[10] The forebody hemisphere has a radius of 1.5 inch (r_n = 0.0381 m), and the geometry is mounted parallel to the freestream, as seen in Fig. 10. The freestream flow is composed of strongly ionized argon (the degree of ionizion was estimated by Kranc et al. as $\alpha = 0.025$), which is produced by a plasma torch (direct-current arc-heater). The heater is located before the converging-diverging nozzle, which accelerates the gas into the test chamber. Kranc et al. state that the electrons are 'frozen' in the nozzle, and that the flow is not chemically reacting after it is initially ionized by the heater. The flow conditions reported by Kranc et al. are listed in Table 2.
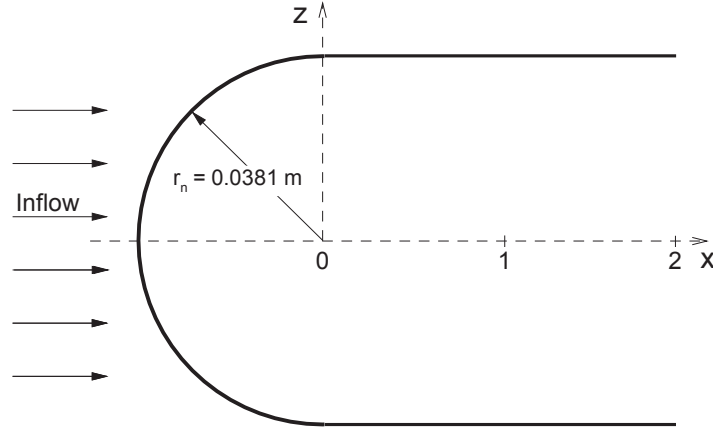
Figure 10. Hemisphere capped geometry. Adapted from.[10]

Table 2. Flow conditions for the MHD-Heat Shield experiment as reported by Kranc et al.[10]

Parameter	Value	
M	4.75	
u_∞	3000.0	m/s
T_∞	1100.0	K
T_w	300.0	K
p_∞	27.8	Pa
ρ_∞	1.035×10^{-4}	kg/m³
n_e	4×10^{19}	m^{-3}
α	0.025	
r_n	0.0381	m
μ_∞	8×10^{-5}	kg/m·s
Re_L	3880	m^{-1}
Re	148	

A structured grid is generated, but is decomposed into two grid domains because of the hemispherical forebody. The first domain includes the forebody, while the second accommodates the rest of the geometry. While the baseline flow solution (the flow without the magnetic field), is axisymmetric, the rest of the simulations are computed using a three-dimensional grid because the MHD routine developed is currently only implemented for three-dimensional domains.

The grid is generated with equal spacing along the hemisphere portion of the geometry (first domain),

American Institute of Aeronautics and Astronautics

95

Approved for public release; distribution unlimited.

and gradually increases in spacing along the remaining surface (second domain). Grid points are equally spaced around the circumference of the geometry and the radial points are algebraically spaced to increase the number of points close to the body. As a result, cell clustering occurs primarily in the hemispherical forebody and near the body surface. The baseline grid uses 50 points along the body (30 in the hemispherical region), 30 points along one quarter of the circumference, and 30 radial points. Two refined grids are also developed and used in the grid-independence study, giving the following set of computational meshes: $50 \times 30 \times 30$ (coarse), to $100 \times 60 \times 60$ (medium), to $200 \times 120 \times 120$ (fine).

Figure 11 plots the pressure coefficient and nondimensional heat flux for the baseline flow along the surface of the geometry, as defined in equations (19) and (20), respectively:

$$C_p = \frac{p_w - p_\infty}{1/2 \rho_\infty u_\infty^2} \tag{19}$$

$$C_h = \frac{q_w}{1/2 \rho_\infty u_\infty^3} \tag{20}$$

where (q_w) is the total heat flux to the wall. The grid-independence study shows little difference between the 'medium' and 'fine' grids, therefore the 'medium' grid is considered sufficiently refined and is used in the rest of the analysis. However, the MHD module might require its own grid resolution study.
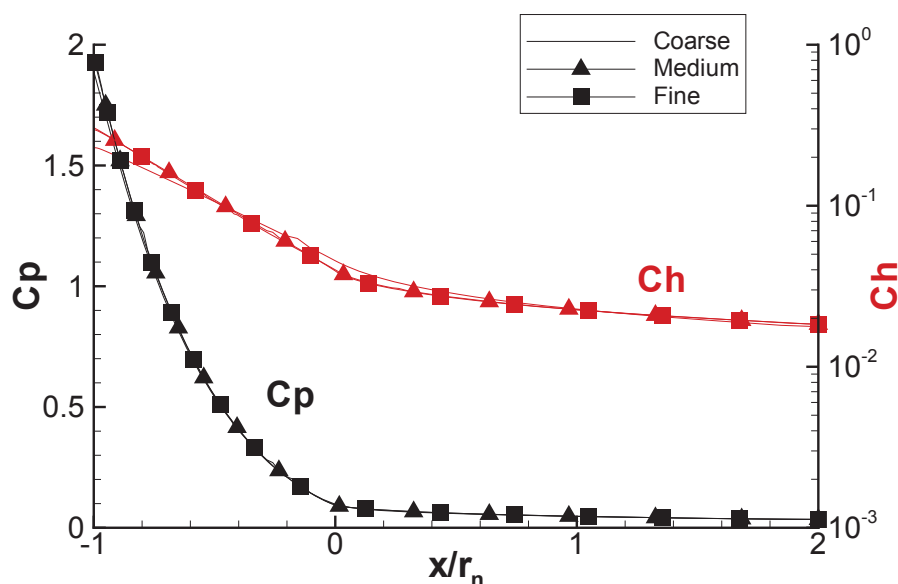
Figure 11. Nondimensional pressure and heat flux along the surface of Mach 4.75 argon flow around a hemisphere capped geometry for various grids.

A closer examination of the freestream conditions, specifically, the degree of ionization, reveals α was estimated by Kranc *et al.* using tables from Arave and Huseley,[64] along with the stagnation temperature and pressure. While this approach may be approximately correct, the degree of ionization is better estimated by using the Saha equation for a singly ionized atomic gas:[65]

$$\frac{\alpha^2}{1 - \alpha^2} p = 3.16 \times 10^{-7} \, T^{5/2} \, \exp\left(-\frac{\varepsilon_i}{kT}\right) \tag{21}$$

where p is the pressure in atmospheres, T is the temperature in Kelvin, Boltzmann's constant is 1.3807×10^{-23} J/K, and ε_i is the ionization energy required to remove the electron from the atom in the gas considered. The ionization potential for argon, $\varepsilon_i = 2.53 \times 10^{-18}$ J, and the stagnation pressure and temperature are 0.49 atm and 9700 K, respectively. Using the Saha equation yields a degree of ionization $\alpha = 0.00623$.

This new estimate for the degree of ionization only changes two values listed in Table 2, namely, $\alpha = 6.23 \times 10^{-3}$ and $n_e = 1 \times 10^{19}$ m^{-3}, which results in a slight modification to the freestream conditions, as seen in Table 3.

Approved for public release; distribution unlimited.

Table 3. Modifications to the freestream conditions for the MHD-Heat Shield experiment of Kranc _et al._[10]

Parameter	Value	
	Reported	Adjusted
u_∞ [m/s]	3000	3000
T_∞ [K]	1100	1100
T_w [K]	300	300
α	0.025	0.00623
ρ_{Ar} [kg/m³]	1.01×10^{-4}	1.09×10^{-4}
ρ_{Ar^+} [kg/m³]	2.65×10^{-6}	6.85×10^{-7}
ρ_e [kg/m³]	3.64×10^{-11}	9.41×10^{-12}

Since the changes to the individual species densities are minimal, and the flow is assumed chemically non-reacting, these slight adjustments to the freestream conditions are assumed not to noticeably alter the resulting flow-field. Therefore, the 'medium' grid discussed previously is assumed to provide sufficient grid-independence and is used in the rest of the analysis. The remaining simulations reported in this section use the freestream conditions corresponding to $\alpha = 0.00623$.

Figure 12 plots the temperature contours for the flow without the magnetic field. As seen in the figure, the peak temperature is 9000 K, which is 150 K hotter than the solution computed using the freestream conditions corresponding to $\alpha = 0.025$. The temperature increase is the result of the slight increase in total density. Using the baseline flow-field solutions from both simulations (i.e. $\alpha = 0.025$ and 0.00623), the expected range of electrical conductivity, estimated from the models presented in the previous section, is displayed in Table 4. The results indicate slight discrepancies in estimated electrical conductivities, with the 2nd order PRS predictions residing between the semi-empirical models.
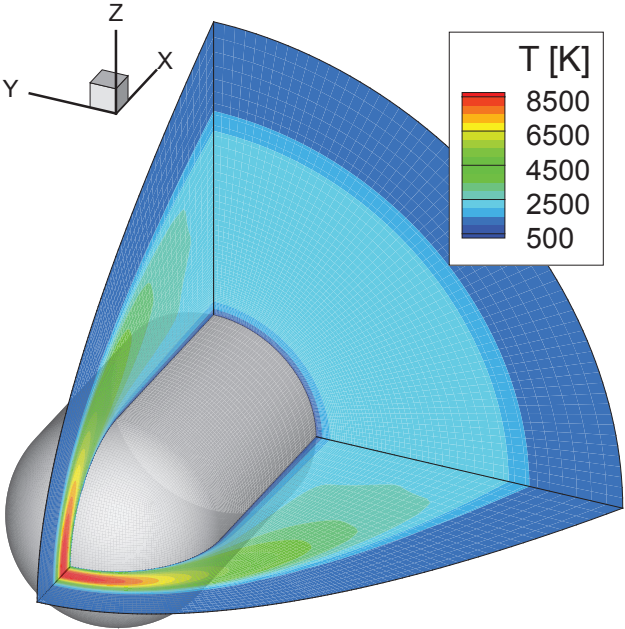
Figure 12. Temperature contours for Mach 4.75 argon flow around a hemisphere capped geometry. ($\alpha = 0.00623$)

In the experiment of Kranc _et al._, the applied magnetic field is produced by an electromagnet located inside the hemisphere-shaped forebody, that can be approximated by a dipole. The magnetic field decays as r^{-3} from its centroid, which is assumed to be located along the x-axis, where the forebody merges with the

American Institute of Aeronautics and Astronautics

Table 4. Electrical conductivity estimates for the MHD-Heat Shield experiment without an applied magnetic field. ($E/N = 0$)

σ [$\Omega^{-1}\mathbf{cm}^{-1}$]	$\alpha = 0.025$	$\alpha = 0.00623$
Raizer	0 - 1.4	0 - 1.5
Chapman and Cowling	17.7 - 50.4	4.4 - 24.2
2nd order PRS	0.1 - 0.2	7.1 - 8.1

rest of geometry ($x/r_n = 0$), as seen in Fig. 13. The magnetic field contours are nondimensionalized by the peak magnetic field strength, B_{max}, which occurs at the stagnation point ($x/r_n = -1$ for the configuration shown in Fig. 13). Note that the peak magnetic field strength is used to designate each simulation for the rest of this analysis.
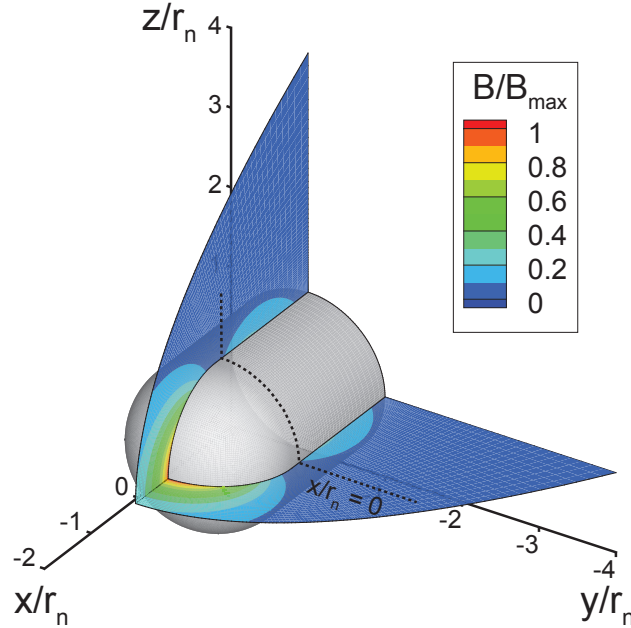
Figure 13. Nondimensional dipole magnetic field contours from a magnet located in the hemisphere capped geometry.

In Cartesian coordinates, the dipole magnetic field is:

$$\mathbf{B} = B_{max} \frac{\cos \theta}{2} \frac{r_n^3}{r^5} \begin{bmatrix} r^2 - x^2 \\ -3xy \\ -3xz \end{bmatrix}$$

where the angle $\theta = \arcsin(\sqrt{y^2 + z^2}/r)$.

The flow-field around the geometry (without the applied magnetic field), is axisymmetric and steady, as evident in the temperature contours seen in Fig. 12. This means the electric current must only travel in the azimuthal direction (perpendicular to the incoming flow, around the axis of symmetry), and the electric field must be zero.[4] This reduces the magnetic force in the momentum equation to $\tilde{\sigma} \cdot (\mathbf{u} \times \mathbf{B}) \times \mathbf{B}$, and sets the energy deposition term in the total energy equation to zero, $\mathbf{j} \cdot \mathbf{E} = 0$. Note that Joule heating is still present under these assumptions, $\gamma(\mathbf{E} + \mathbf{u} \times \mathbf{B}) \cdot \mathbf{j} \neq 0$. Since the electric field is assumed zero and the magnetic field is applied, only the current density field ($\mathbf{j} = \tilde{\sigma} \cdot [\mathbf{u} \times \mathbf{B}]$), needs to be updated in the MHD module.

Simulations are carried out for several magnetic field strengths and electrical conductivity models. The simulations start from the steady-state 'baseline' solution (without an applied magnetic field), and iterate

American Institute of Aeronautics and Astronautics

Approved for public release; distribution unlimited.

until the flow-field has achieved a new steady-state (converged). Steady-state is assumed once the L2 residual error from the conservation equations decays to the minimum allowed by machine precision zero, as seen in Fig. 14 for a typical simulation. In this scenario, at least 10 characteristic flow times worth of time steps are required to achieve a steady-state flow-field solution. A characteristic flow time is defined as the time it takes for the flow to traverse the length of the geometry (i.e. flow time = L/u_∞).
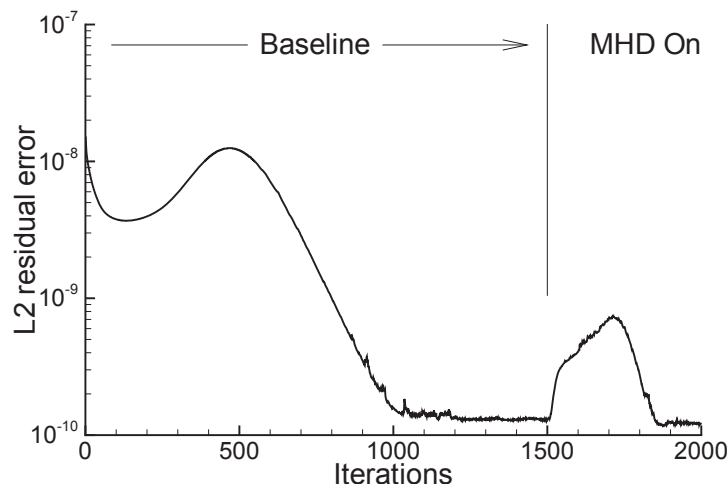
Figure 14. L2 residual error from a simulation of Mach 4.75 argon flow around a hemisphere capped geometry with a 0.13 T magnet. (Chapman and Cowling conductivity model)

The assumption that the electric field is negligible ($\mathbf{E} = 0$), is verified by simulating the flow with and without computing the electric field. The Chapman and Cowling electrical conductivity model is employed for both simulations with $B_{max} = 0.28$ T. The MHD module is used to update the electric field every 5 fluid iterations. Figure 15 plots the temperature contours and current lines for both scenarios. As seen in the figures, computing $\mathbf{E}$ from the MHD module does not alter the flow structure or current lines.

(a) Assuming $\mathbf{E} = 0$.

(b) Computing $\mathbf{E}$.
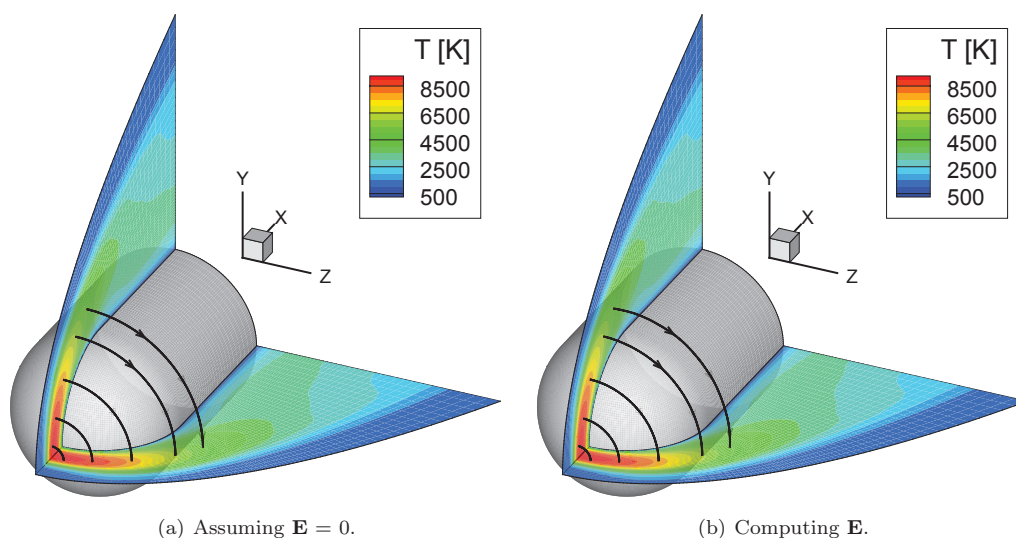
Figure 15. Temperature contours and current lines for Mach 4.75 argon flow around a hemisphere capped geometry with a 0.28 T magnetic field. Chapman and Cowling conductivity model)

Kranc *et al.* reported an increase in shock standoff distance due to the applied magnetic field.[10] The increase was measured by comparing photographs of the flow with and without the applied magnetic field. In their analysis, they assume the upstream edge of the shock can be inferred from the boundary of the flow's

American Institute of Aeronautics and Astronautics

99

Approved for public release; distribution unlimited.

luminosity. This photographic technique for measuring the shock standoff distance was previously used by Ziemer[8] and Bailey and Sims[66] in similar experiments.

Although the computational solutions provide many ways of estimating the shock location, the change in shock standoff distance is computed by comparing the location, along the stagnation line, where the density ratio exceeds the ideal gas, infinite Mach number threshold for a normal shock wave:

$$\lim_{M_1 \to \infty} \frac{\rho_2}{\rho_1} = \lim_{M_1 \to \infty} \frac{(\gamma+1)M_1^2}{(\gamma-1)M_1^2 + 2} = \frac{\gamma+1}{\gamma-1} \tag{22}$$

where M_1 is the upstream Mach number, γ is the ratio of specific heats, ρ_1 is the upstream density, and ρ_2 is the downstream density. Using this equation, the density ratio limit for argon is 4 ($\gamma = 5/3$). This approach provides a consistent method for defining the shock location, so it should provide adequate estimates of the change in shock standoff distance due to an applied magnetic field. Figure 16 plots the density ratio contours for the electrical conductivity models with a peak magnetic field of 0.13 T (1 telsa $= 10^4$ gauss [G]).

(a) Raizer   (b) Chapman and Cowling   (c) 2nd order PRS
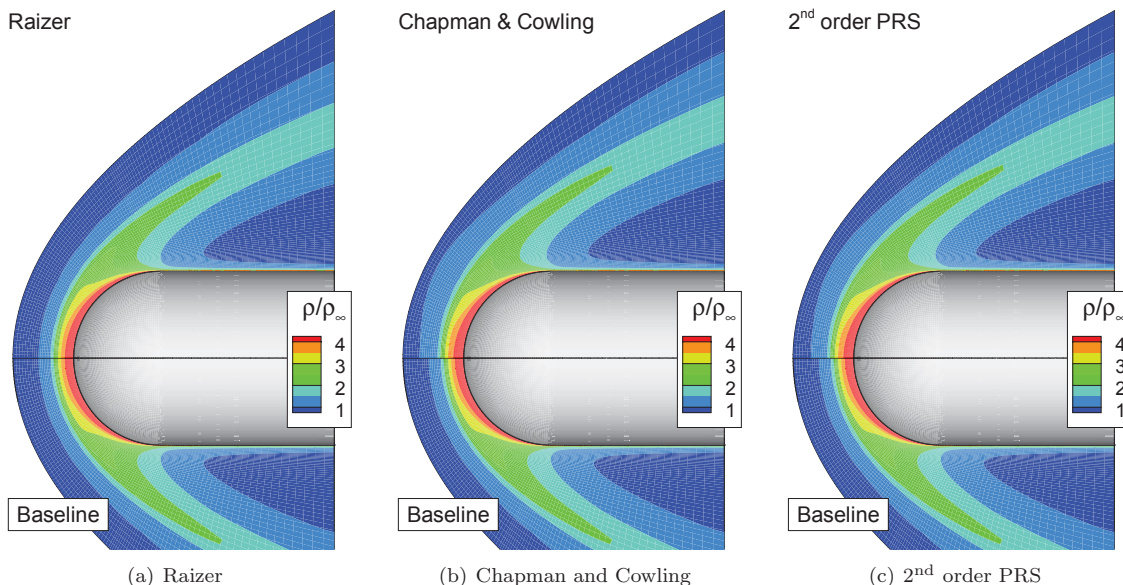
Figure 16. Density ratio contours for Mach 4.75 argon flow around a hemisphere capped geometry for various electrical conductivity models. ($B_{max} = 0.13$ T)

The change in shock standoff distance is computed for the various models, and plotted in Fig. 17 with experimental measurements collected using the photographic technique described previously.

The experimental uncertainty was ±10% (error in determining shock location for one run), but the repeatability (difference in shock location between nominally identical runs) was ±30% as seen for $B_{max}^2 \simeq 13 \times 10^6$ G^2. Both the 2nd order PRS model and Chapman and Cowling models match the experimental data well, with the 2nd order PRS model fitting much better, particularly at larger magnetic field strengths. Solutions obtained by using Raizer's model observed almost no change in shock standoff distance because the model predicts a lower range of electrical condicitivities (as seen in Table 4). In addition, Raizer's model is only temperature dependant, so its peak conductivity is just downstream of the bow shock (where the temperature is the highest), yet the magnetic field strength has already significantly decayed due to its r^{-3} dependency.

The heat transfer to the surface for the various electrical conductivity models is shown in Fig. 18. Integrating the heat flux over the surface produces the total heating to the geometry. The change in peak heating is computing by comparing the heat flux at the stagnation point ($\Delta q_w = \frac{q_{w,MHD} - q_{w,baseline}}{q_{w,baseline}}$). Table 5 lists the percent change in peak heat flux and total heating for various magnetic field strengths and electrical conductivity models.

Except for the results from Raizer's model, the total heating to the surface actually slightly increases because of increased heating to the cylindrical portion of the geometry (i.e. aft of the stagnation region),
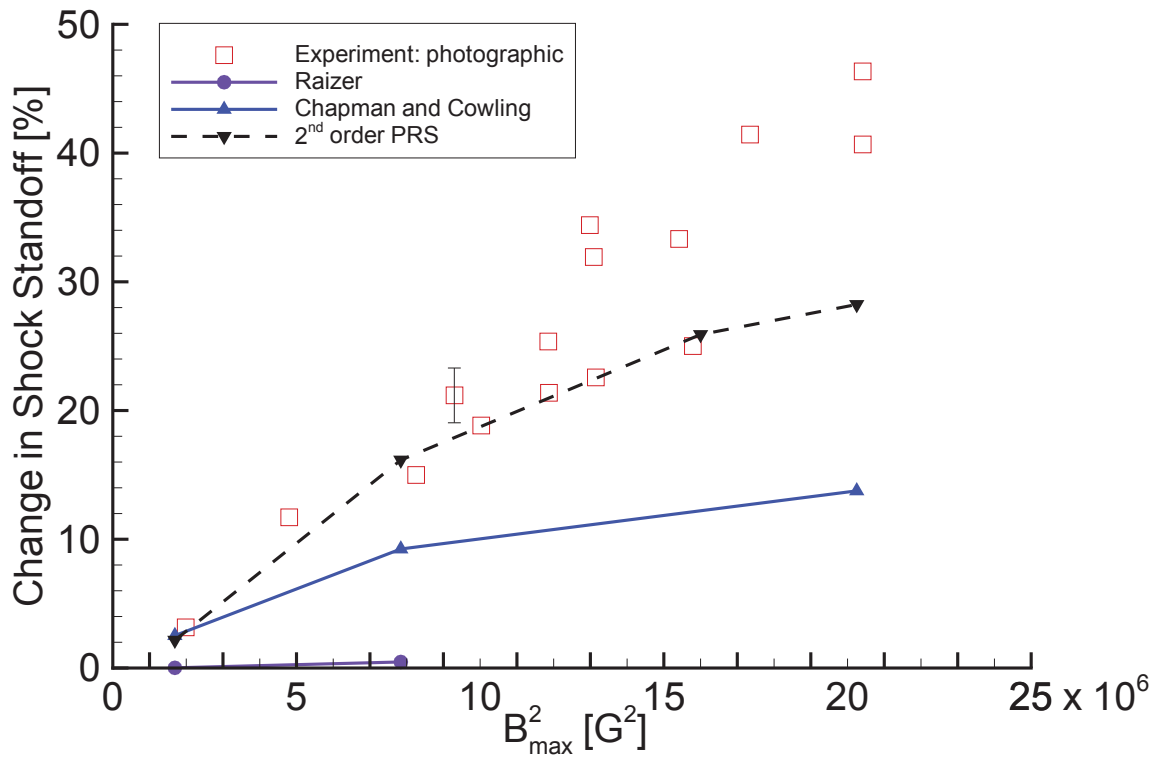
Figure 17. Percent change in shock standoff distance versus magnetic field strength for Mach 4.75 argon flow around a hemisphere capped geometry with various electrical conductivity models. Measurements from.[10] (experimental uncertainty ±10%)
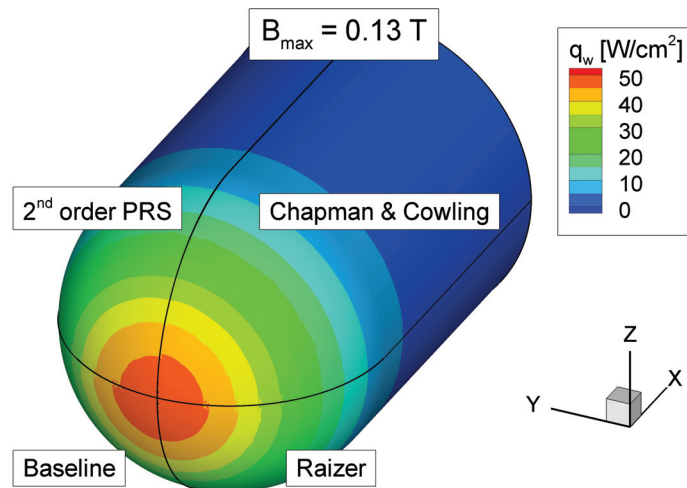

Figure 18. Heat flux contours for Mach 4.75 argon flow around a hemisphere capped geometry with a 0.13 T magnetic field and various electrical conductivity models.

American Institute of Aeronautics and Astronautics

101

Approved for public release; distribution unlimited.

Table 5. Percent change in heat flux to the surface for Mach 4.75 argon flow around a hemisphere capped geometry with an MHD-Heat Shield.

Model	Δ Total Heating		Δ Peak Heating	
	B = 0.13 T	B = 0.28 T	B = 0.13 T	B = 0.28 T
Raizer	-0.1 %	-0.3 %	-0.3 %	-1.2 %
Chapman and Cowling	0.6 %	1.5 %	-1.6 %	-6.3 %
2nd order PRS	0.4 %	1.1 %	-2.5 %	-5.6 %

due to the direction of the magnetic field lines in the region where the hemisphere capped forebody merges with the cylindrical aft section. Raizer's model fails to capture this behavior because its predicted electrical conductivity is too low throughout the domain, but particularly in the aft region where the freestream temperature is much cooler than in the bow shock. In general, an applied magnetic field moderately increases the total heating to the geometry, but significantly decreases the peak heat flux at the stagnation point. Both the 2nd order PRS model and the Chapman and Cowling model yield similar results, but since the 2nd order PRS model provides better estimates in the percent change in shock standoff distance, its results for the heat flux to the geometry may be more accurate.

IV.   Conclusions

Newly developed computational tools were used to compute hypersonic flow around a hemisphere capped geometry which utilizes a magnet located within the body as a means of heat flux mitigation. These tools include an improved electrical conductivity model and a parallelized 3D MHD module that is loosely coupled to a 3D fluid code. In addition, the Hall effect was implemented and verified by investigating flow between finite electrodes.

A Mach 4.75 argon flow over a hemisphere-shaped forebody attached to a cylinder was then explored, corresponding to the experiment of Kranc *et al.*. The magnetic field worked to oppose and slow the flow near the stagnation region, and increased the shock standoff distance. The increase in shock standoff distance decreased the peak heating to the body (at the stagnation point), but also increased the total heating to the geometry because of increased heating to the cylindrical portion of the body. This result has important implications for design of MHD-Heat Shield devices: they can reduce peak heat loads, but with a potential penalty in total heating. Since both peak and total heat load are important aspects to consider when designing a thermal protection system, this technology provides additional scenarios for vehicle designers to evaluate.

Acknowledgments

References

[1]Kantrowitz, A. R., "A Survey of Physical Phenomena Occurring in Flight at Extreme Speeds," *Proceedings of the Conference on High-Speed Aeronautics*, edited by A. Ferri, N. J. Hoff, and P. A. Libby (Polytechnic Institute of Brooklyn, New York, 1955), pp. $335 - 339$.

[2]Resler, E. L. and Sears, W. R., "The Prospects for Magneto-Aerodynamics," *Journal of Aeronatuical Sciences*, Vol. 25, April 1958, pp. 235–245, 258.

[3]Resler, E. L. and Sears, W. R., "The Prospects for Magneto-Aerodynamics Correction and Addition," *Journal of Aero/Space Sciences*, Vol. 26, No. 5, May 1959, pp. 319.

[4]Bush, W. B., "Magnetohydrodynamic-Hypersonic Flow Past a Blunt Body," *Journal of Aerospace Sciences*, Vol. 25, 1958, pp. 685.

[5]Bush, W. B., "The Stagnation-Point Boundary Layer in the Presence of an Applied Magnetic Field," *Journal of Aerospace Sciences*, Vol. 28, No. 8, August 1961, pp. 610–611, 630.

[6]Poggie, J. and Gaitonde, D. V., "Magnetic Control of Flow Past a Blunt Body: Numerical Validation and Exploration," *Physics of Fluids*, Vol. 14, No. 5, May 2002, pp. 1720–1731.

[7]Coakley, J. F. and Porter, R. W., "Time-Dependent Numerical Analysis of MHD Blunt Body Problem," *AIAA Journal*, Vol. 9, No. 8, August 1971, pp. 1624–1626.

[8]Ziemer, R. W., "Experimental Investigations in Magnetoaerodynamics," *Journal of American Rocket Society*, Vol. 29, No. 9, 1959, pp. 642.

[9]Wilkinson, B., "Magnetohydrodynamic Effects on Stagnation-Point Heat Transfer from Partially Ionized Nonequilibrium Gases in Supersonic Flow," *Engineering Aspects of Magnetohydrodynamics: Proceedings, 3rd Symposium*, edited by N. W. Mather and G. W. Sutton (Gordon and Breach, New York, 1964), pp. $413 - 438$.

[10]Kranc, S., Yuen, M. C., and Cambel, A. B., "Experimental Investigation of Magnetoaerodynamic Flow around Blunt Bodies," Tech. rep., National Aeronautics and Space Administration, Washington, D.C., August 1969, NASA CR-1392.

[11]Nowak, R. J., Kran, S., Porter, R. W., Yuen, M. C., and Cambel, A. B., "Magnetogasdynamic Re-Entry Phenomena," *Journal of Spacecraft*, Vol. 4, No. 11, November 1967, pp. 1538–1542.

[12]Nowak, R. J. and Yuen, M. C., "Heat Transfer to a Hemispherical Body in Supersonic Argon Plasma," *AIAA Journal*, Vol. 11, No. 11, November 1973, pp. 1463–1464.

[13]Porter, R. W. and Cambel, A. B., "Hall Effect if Flight Magnetogasdynamics," *AIAA Journal*, Vol. 5, No. 12, December 1967, pp. 2208–2213.

[14]Romig, M. F., "The Influence of Electric and Magnetic Fields on Heat Transfer to Electrically Conducting Fluids," *Advances in Heat Transfer*, edited by T. F. Irvine and J. P. Hartnett (Academic, New York, 1964), Vol. 1, pp. $267 - 354$.

[15]Padilla, J. F., *Assessement of Gas-Surface Interaction Models for Computation of Rarefied Hypersonic Flows*, 2008, PhD thesis, Department of Aerospace Engineering, University of Michigan.

[16]Fomin, V. M., Tretyakov, P. K., and Taran, J.-P., "Flow Control using Various Plasma and Aerodynamic Approaches," *Aerospace Science and Technology*, Vol. 8, No. 5, July 2004, pp. 411–421.

[17]Shang, J. S., Surzhikov, S. T., Kimmel, R., Gaitonde, D., Menart, J., and Hayes, J., "Mechanisms of Plasma Actuators for Hypersonic Flow Control," *Progress in Aerospace Sciences*, Vol. 41, No. 8, November 2005, pp. 642–668.

[18]Bityurin, V., Bocharov, A., and Lineberry, J., "MHD Flow Control in Hypersonic Flight," *13th International Space Planes and Hypersonic Systems Technologies Conference*, AIAA Paper 2005-3225, 2005.

[19]Palmer, G., "Magnetic Field Effects on the Computed Flow over a Mars Return Aerobrake," *Journal of Thermophysics and Heat Transfer*, Vol. 7, No. 2, April-June 1993, pp. 294–301.

[20]Bisek, N. J., Boyd, I. D., and Poggie, J., "Numerical Study of Plasma-Assisted Aerodynamic Control for Hypersonic Vehicles," *Journal of Spacecraft and Rockets*, Vol. 46, No. 3, May-June 2009.

[21]Kremeyer, K., Sebastian, K., and Shu, C.-W., "Computational Study of Shock Mitigation and Drag Reduction by Pulsed Energy Lines," *AIAA Journal*, Vol. 44, No. 8, August 2006, pp. 1720–1731.

[22]Yan, H. and Gaitonde, D., "Control of Edney IV Interaction by Energy Pulse," *44th AIAA Aerospace Sciences Meeting and Exhibit*, AIAA Paper 2006-562, 2006.

[23]Menart, J., Stanfield, S., Shang, J., Kimmel, R., and Hayes, J., "Study of Plasma Electrode Arrangements for Optimum Lift in a Mach 5 Flow," *44th AIAA Aerospace Sciences Meeting and Exhibit*, 2006, AIAA Paper 2006-1172.

[24]Girgis, I. G., Shneider, M. N., Macheret, S. O., Brown, G. L., and Miles, R. B., "Creation of Steering Moments in Supersonic Flow by Off-Axis Plasma Heat Addition," *40th AIAA Aerospace Sciences Meeting and Exhibit*, 2002, AIAA Paper 2002-129.

[25]Gnemmi, P., Charon, R., Dupéroux, J.-P., and George, A., "Feasibility Study for Steering a Supersonic Projectile by a Plasma Actuator," *AIAA Journal*, Vol. 46, No. 6, June 2008, pp. 1308–1317.

[26]Bityurin, V. A., Vatazhin, A. B., and Gus'kov, O. V., "Hypersonic Flow Past the Spherical Nose of a Body in the Presence of a Magnetic Field," *Fluid Dynamics*, Vol. 39, No. 4, July 2004, pp. 657–666.

[27]Miles, R. B., Macheret, S. O., Shneider, M. N., Steeves, C., Murray, R. C., Smith, T., and Zaidi, S. H., "Plasma-Enhanced Hypersonic Performance Enabled by MHD Power Extraction," *43rd AIAA Aerospace Sciences Meeting and Exhibit*, AIAA Paper 2005-561, 2005.

[28]Katsurayama, H., Kawamura, M., Matsuda, A., and T., A., "Kinetic and Continuum Simulations of Electromagnetic Control of a Simulated Reentry Flow," *Journal of Spacecraft and Rockets*, Vol. 45, No. 2, March-April 2008, pp. 248–254.

[29]Hodara, H., "The Use of Magnetic Fields in the Elimination of the Re-Entry Radio Blackout," *Proceedings of the IRE*, Vol. 4, No. 12, December 1961, pp. 1825–1830.

[30]Kim, M., Keidar, M., and Boyd, I. D., "Analysis of an Electromagnetic Mitigation Scheme for Reentry Telemetry Through Plasma," *Journal of Spacecraft and Rockets*, Vol. 45, No. 6, November-December 2008, pp. 1223–1229.

[31]Macheret, S. O., Shneider, M. N., and Candler, G. V., "Modeling of MHD Power Generation on Board Reentry Vehicles," *42nd AIAA Aerospace Sciences Meeting*, AIAA Paper 2004-1024, 2004.

[32]Wan, T., Suzuki, R., Candler, G., Macheret, S., and Schneider, M., "Three Dimensional Simulation of Electric Field and MHD Power Generation During Re-Entry," *36th AIAA Plasmadynamics and Lasers Conference*, AIAA Paper 2005-5045, 2005.

[33]Fujino, T., Yoshino, T., and Ishikawa, M., "Prediction of Generator Performance and Aerodynamic Heating of Reentry Vehicle Equipped with On-board Surface Hall Type MHD Generator," *39th Plasmadynamics and Lasers Conference*, AIAA Paper 2008-4225, 2008.

[34]Linberry, J. T., Bityurin, V. A., and Vatazhin, A. B., "Cylinder with Current in Hypersonic Flow," *Proc. 3rd Workshop on Magneto-Plasma Aerodynamics in Aerospace Applications*, Institute of High Temperatures of RAS (IVTAN) (2001), pp. 15.

[35]Takizawa, Y., Sato, S., Abe, T., and Konigorski, D., "Electro-Magnetic Effect on Shock Layer Structure in Reentry-Related High-Enthalpy Flow," *35th AIAA Plasmadynamics and Lasers Conference*, AIAA Paper 2004-2162, 2004.

[36]Kimmel, R., Hayes, J., Menart, J., and Shang, J., "Supersonic Plasma Flow Control Experiments," Tech. rep., U.S. Air Force Research Laboratory, Wright-Patterson AFB, OH, December 2005, ARFL-VA-WP-TR-2006-3006.

American Institute of Aeronautics and Astronautics

[37]Matsuda, A., Kawamura, M., Takizawa, Y., Otsu, H., Konigorski, D., Sato, S., and Abe, T., "Experimental Investigation of the Hall Effect for the Interaction between the Weakly-Ionized Plasma Flow and Magnetic Body," *45th Aerospace Sciences Meeting*, AIAA Paper 2007-1437, 2007.

[38]Gülhan, A., Esser, B., Koch, U., Siebe, F., Riehmer, J., Giordano, D., and Konigorski, D., "Experimental Verification of Heat-Flux Mitigation by Electromagnetic Fields in Partially-Ionized-Argon Flows," *Journal of Spacecraft and Rockets*, Vol. 46, No. 2, March-April 2009, pp. 274–283.

[39]Gaitonde, D. V. and Poggie, J., "An Implicit Technique for 3-D Turbulent MGD with the Generalized Ohm's Law," *32th AIAA Plasmadynamics and Lasers Conference*, AIAA Paper 2001-2736, 2001.

[40]Gaitonde, D. V., "A High-Order Implicit Procedure for the 3-D Electric Field in Complex Magnetogasdynamic Simulations," *Computers and Fluids*, Vol. 33, No. 3, March 2004, pp. 345–374.

[41]Gaitonde, D. V. and Poggie, J., "An Implicit Technique for Three-Dimensional Turbulent Magnetoaerodynamics," *AIAA Journal*, Vol. 41, No. 11, November 2003, pp. 2179–2191.

[42]Damevin, H.-M. and Hoffmann, K. A., "Numerical Simulations of Magnetic Flow Control in Hypersonic Chemically Reacting Flows," *Journal of Thermophysics and Heat Transfer*, Vol. 16, No. 4, October-December 2002, pp. 498–507.

[43]Scalabrin, L. C. and Boyd, I. D., "Development of an Unstructured Navier-Stokes Solver For Hypersonic Nonequilibrium Aerothermodynamics," *38th AIAA Thermophysics Conference*, AIAA Paper 2005-5203, 2005.

[44]Scalabrin, L. C. and Boyd, I. D., "Numerical Simulation of Weakly Ionized Hypersonic Flow for Reentry Configurations," *9th AIAA/ASME Joint Thermophysics and Heat Transfer Conference*, AIAA Paper 2006-3773, 2006.

[45]MacCormack, R. W. and Candler, G. V., "The solution of the Navier-Stokes Equations Using Gauss-Seidel Line Relaxation." *Computers and Fluids*, Vol. 17, No. 1, January 1989, pp. 135–150.

[46]Holman, T. D. and Boyd, I. D., "Numerical Investigation of the Effects of Continuum Breakdown on Hypersonic Vehicle Surface Properties," *40th AIAA Thermophysics Conference*, AIAA Paper 2008-3928, 2008.

[47]Shercliff, J., *A Textbook of Magnetohydrodynamics*, Pergamon Press, 1965.

[48]Gaitonde, D. V. and Poggie, J., "Elements of a Numerical Procedure for 3-D MGD Flow Control Analysis," *40th AIAA Aerospace Sciences Metting and Exhibit*, AIAA Paper 2002-198, 2002.

[49]Bisek, N. J., Boyd, I. D., and Poggie, J., "Numerical Study of Electromagnetic Aerodynamic Control of Hypersonic Vehicles," *47th AIAA Aerospace Sciences Meeting and Exhibit*, AIAA Paper 2009-1000, 2009.

[50]Bisek, N. J., Boyd, I. D., and Poggie, J., "Three Dimensional Simulations of Hypersonic MHD Flow Control," *40th AIAA Plasmadynamics and Lasers Conference*, AIAA Paper 2009-3731, 2009.

[51]Oliver, D. A. and Mitchner, M., "Nonuniform Electrical Conduction in MHD Channel," *AIAA Journal*, Vol. 5, No. 8, August 1967, pp. 1424–1432.

[52]White, F. M., *Viscous Fluid Flow, 3rd ed.*, 2006, McGraw-Hill.

[53]Lin, S.-C., Resler, E. L., and Kantrowitz, A., "Electrical Conductivity of Highly Ionized Argon Produced by Shock Waves," *Journal of Applied Physics*, Vol. 26, No. 1, January 1955, pp. 95–109.

[54]Raizer, Y. P., *Gas Discharge Physics*, Springer-Verlag, 1991.

[55]Cambel, A. B., *Plasma Physics and Magnetofluid-Mechanics*, McGraw-Hill, 1963, p. 171.

[56]Bird, G. A., *Molecular Gas Dynamics and the Direct Simulation of Gas Flows*, 1994, Oxford Science Publications.

[57]Bird, G. A., "Monte-Carlo Simulation in an Engineering Context," *Rarefied Gas Dynamics*, edited by S. S. Fisher, Vol. 74 of *Progress of Astronautics and Aeronautics*, AIAA, New York, 1981, pp. 239–255.

[58]Weng, Y. and Kushner, M. J., "Method for Including Electron-Electron Collisions in Monte Carlo Simulations of Electron Swarms in Partially Ionized Gases," *Physical Review A*, Vol. 42, No. 10, November 1990, pp. 6192–6200.

[59]Rockwood, S. D., "Elastic and Inelastic Cross Sections for Electron-Hg Scattering from Hg Transport Data," *Physical Review A*, Vol. 8, No. 5, November 1973, pp. 2348–2358.

[60]Rockwood, S. D., "Effect of Electron-Electron and Electron-Ion Collisions in Hg, $CO_2/N_2/He$, and CO/N_2 discharges," *Journal of Applied Physics*, Vol. 45, No. 12, December 1974, pp. 5229–5234.

[61]Viana, F. A. C. and Goel, T., *SURROGATES Toolbox User's Guide*, 2008.

[62]Makridakis, S., "Accuracy Measures: Theoretical and Practical Concerns," *International Journal of Forecasting*, Vol. 9, No. 4, December 1993, pp. 527–529.

[63]Schwartzentruber, T. E., Scalabrin, L. C., and Boyd, I. D., "Hybrid Particle-Coontinuum Simulations of Non-Equilibrium Hypersonic Blunt Body Flow Fields," *9th AIAA/ASME Joint Thermophysics and Heat Transfer Conference*, AIAA Paper 2006-3602, 2006.

[64]Arave, R. J. and Huseley, O. A., "Aerothermodynamic Properties of High Temperature Argon," Tech. rep., Boeing, Seattle, WA, February 1962, D2-11238.

[65]Messerle, H. K., *Magnetohydrodynamic Electrical Power Generation*, 1995, John Wiley & Sons, Inc.

[66]Bailey, A. B. and Sims, W. H., "Shock Detachment Distance for Blunt Bodies in Argon at Low Reynolds Number," *AIAA Journal*, Vol. 1, No. 12, December 1963, pp. 2867–2868.

American Institute of Aeronautics and Astronautics

Numerical Study of a MHD-Heat Shield

Nicholas J. Bisek[*] and Jonathan Poggie[†]

Air Force Research Laboratory, Wright-Patterson AFB, OH, 45433-7512, USA

and

Iain D. Boyd[‡]

Department of Aerospace Engineering, University of Michigan, Ann Arbor, MI, 48109, USA

Newly developed computational tools are used to compute hypersonic flow around a hemisphere-cylinder which utilizes a magnet located within the body. The magnetic force generated opposes the incoming flow thereby increasing the shock standoff distance and providing heat mitigation to the stagnation region. Several surface temperature scenarios are explored, though none result in significant change to the shock standoff distance. The Hall effect and ion slip phenomena are added to the plasma model through the electrical conductivity tensor and are validated by simulating channel flow between infinitely repeating electrodes with an applied magnetic field. The Hall effect stretches the current in the streamwise direction while ion slip reduces the stretching for the channel flow scenario. In the hemisphere-cylinder scenario, the strong Hall effect significantly lessens the effectiveness of the magnet at increasing the shock standoff distance while Joule heating reduces the effectiveness of heat mitigation observed in the stagnation region.

Nomenclature

B	=	magnetic field magnitude, T
B	=	magnetic field vector
b	=	magnetic field unit vector
C_h	=	nondimensional heat flux, $2q_w/[\rho_\infty u_\infty^3]$
C_p	=	pressure coefficient, $2(p_w - p_\infty)/[\rho_\infty u_\infty^2]$
E	=	electric field magnitude, V/m
E	=	electric field vector
E	=	total energy per volume
e	=	electron charge, 1.6×10^{-19}C
j	=	current density vector
L	=	geometry length, m
N	=	total number density, m^{-3}
n	=	species number density, m^{-3}
p	=	pressure, Pa
q	=	heat flux (translational, rotational, and vibrational)
r	=	radius, m
Re_m	=	magnetic Reynolds number, $\mu_0\, \sigma\, u\, L$
s	=	ion slip coefficient, $(\rho_{\text{neutrals}}/\rho)^2\, \beta_e\, \beta_i$
S_{local}	=	local magnetic-interaction number, $\sigma\, B^2\, r_n/[\rho\, u]$
T	=	temperature, K
u	=	velocity vector (u, v, w), m/s

[*]Senior Researcher, Ohio Aerospace Institute, Member AIAA.
[†]Senior Aerospace Engineer, AFRL/RBAC. Associate Fellow AIAA.
[‡]Professor, Associate Fellow AIAA.

American Institute of Aeronautics and Astronautics Paper 2010-4487

u $\quad$ = velocity magnitude, $\mathrm{m/s}$
α $\quad$ = degree of ionization
β_e $\quad$ = Hall parameter (electrons), $\mu_\mathrm{e}\,\mathrm{B}$
β_i $\quad$ = Hall parameter (ions)
γ $\quad$ = ratio of specific heats
μ_e $\quad$ = electron mobility, $\sigma/e\,n_\mathrm{e}$
μ_0 $\quad$ = permeability of free space, $4\,\pi \times 10^{-7}\ \mathrm{N/A^2}$
ρ $\quad$ = mass density, $\mathrm{kg/m^3}$
σ $\quad$ = electrical conductivity, $\Omega^{-1}\,\mathrm{m}^{-1}$
$\tilde{\sigma}$ $\quad$ = electrical conductivity tensor (including Hall effect and ion slip)
τ $\quad$ = viscous stress
ϕ $\quad$ = electric potential, V
χ $\quad$ = species mole fraction

Subscript

n $\quad$ = nose
w $\quad$ = wall
s $\quad$ = species
∞ $\quad$ = free stream

Species

Ar $\quad$ = argon
Ar^+ $\quad$ = argon ion
e $\quad$ = electron

I. Introduction

In the late 1950's Kantrowitz[1] and Resler and Sears[2,3] demonstrated the benefits an applied magnetic field has on an incoming weakly ionized flow, a condition typically observed during re-entry. The concept used the magnetic field to produce a magnetic force which opposed the momentum of the freestream flow. Since the majority of the magnetic force is located within the shock layer, the shock standoff distance from the body increased, which reduced the gradients in the layer (including the heat transfer rate).

The potential benefits of this concept generated a lot of research activity as groups refined semi-analytical calculations by making various approximations to the conservation equations. One of the most complete approximate analytic solutions was obtained by Bush, who used a local solution at the stagnation point of the hypersonic flow over an axisymmetric blunt body to predict significant flow declaration in the presence of a magnetic field.[4,5] A decade later, Coakley and Porter computed the first modern Computational Fluid Dynamic (CFD), simulations of the Magnetohydrodynamic (MHD), blunt body problem,[6] but the simulations still required significant simplifications to the governing equations due to limited computing resources available during that period.

To verify Bush's computational predictions, Ziemer carried out experimental measurements of the shock standoff distance for a similar geometry and found reasonable agreement.[7] The first heat transfer measurements for this concept were collected in the experimental work by Wilkinson[8] for Mach 3 ionized argon at the stagnation point of a blunt cone.

While the effects of the magnetic force can be visually observed to increase in the shock standoff distance, the force also increases drag on the vehicle, which can be measured in tunnel experiments with a load cell. In the late 1960's, experimental effort conducted by Kranc *et al.* provided additional experimental validation sets for the continuing computational efforts.[9] In addition to measuring the shock standoff distance, the work measured the increase in drag for two different axisymmetric geometries. These experiments were conducted in a flow regime where both the viscosity and Hall effect are important, and confirmed the increase in the shock standoff distance and total drag on the geometry in the presence of a dipole magnetic field.

Kranc's experiment also exhibited an increase in total heating, which has been attributed to the Hall effect.[10,11] This was unexpected because the thickening of the shock layer reduces gradients within the stagnation region, which should reduce the heat flux to the body. Previous semi-analytic work had predicted that the Hall effect would only reduce the effectiveness of the magnetic force on increasing the shock standoff

American Institute of Aeronautics and Astronautics Paper 2010-4487

distance and total drag.[12] Regardless of this unexpected outcome, it was determined that the large magnetic field strength required to make the technology practical was too heavy to be placed on re-entry vehicles, and, as such, interest and funding of the research area faded.[13]

During the mid to late 1990's a renewed interest in plasma-assisted hypersonics started to generate new research activity.[14–16] This revival of hypersonic-MHD has been credited to many influences including increasing demand for rapid access to space and the numerous advancements in materials necessary for flight-weight MHD technologies. One of the first to reevaluate the technology using modern CFD was Palmer, who performed first-order spatially accurate simulations of the time-dependent Maxwell's equations coupled to the Navier-Stokes equations to analyze a Mars return vehicle.[17] In addition to increasing the shock standoff distance, MHD technology is being applied and investigated to many subsystems required by a hypersonic vehicle, including flow control,[18–23] local heat load mitigation,[24–26] communications blackout,[27] and MHD power extraction.[28–30]

Despite the technical challenges, limited facilities, and financial costs, some recent experimental studies have been performed to explore electromagnetic effects on hypersonic flows.[31–35] While these efforts have provided new insight into electromagnetic phenomena in hypersonic flows and provided additional validation exercises for testing the accuracy of fluid-MHD codes, the rising costs associated with conducting the experiments (i.e., aging facilities and additional safety protocol), greatly limits the number of experiments being conducted. These limitations generate additional demand for high fidelity computational codes that are capable of predicting the complex flows generated by MHD technology.

This paper is a continuation of a computational study of the experimental research conducted by Kranc *et al.*[9] While the previous results showed an electrical conductivity model based on solutions to Boltzmann's equation provided results consistent with experimental measurements, several additional influences were left unexplored.[36] An axisymmetric version of the MHD code is developed and verified against three-dimensional computations. Several wall boundary conditions, including a fully radiative wall are implemented, but found to have minimal effect on the change in shock standoff distance. A compact tensor notation for accounting for the Hall effect and ion slip through the electrical conductivity tensor is introduced and validated by simulating channel flow between segmented finite electrodes. The Hall effect and ion slip are accounted for in the hemisphere-cylinder simulations which reduce the effectiveness of the magnet and produce Joule heating around the forebody. The local temperature increase reduces the effectiveness of the magnet for heat mitigation.

II. Method

A. Governing Equations

Flow-field results are obtained using CFD to solve the Navier-Stokes equations. The CFD computations are executed using The Michigan Aerothermodynamic Navier-Stokes code (LeMANS), which was developed at the University of Michigan.[37,38]

LeMANS is a general 2D/axisymmetric/3D, parallel, unstructured finite-volume CFD code. LeMANS is able to employ a two-temperature or three-temperature model to account for thermal-nonequilibrium and a standard finite rate chemistry model for non-equilibrium chemistry. For a single temperature model (local thermal equilibrium), with MHD but without finite chemistry, the conservation equations are:

$$\frac{\partial \rho_s}{\partial t} + \nabla \cdot (\rho_s \mathbf{u}) = 0 \tag{1}$$

$$\frac{\partial \rho \mathbf{u}}{\partial t} + \nabla \cdot (\rho \mathbf{u}\mathbf{u} + p\mathbf{I} - \tau) = \mathbf{j} \times \mathbf{B} \tag{2}$$

$$\frac{\partial E}{\partial t} + \nabla \cdot ((E + p)\mathbf{u} - \tau \cdot \mathbf{u} + \mathbf{q}) = \mathbf{j} \cdot \mathbf{E} \tag{3}$$

where ρ_s is the density of species s, and $\mathbf{u}$ is the mass averaged bulk velocity vector. LeMANS assumes the fluid is continuous, Newtonian, and uses Stokes' hypothesis when determining the viscous stress τ. The conservation of momentum, Eqn. (2), contains the total density, ρ, the pressure, p, the identity matrix, $\mathbf{I}$, and a 3×3 tensor containing all the products of the components of the velocity vector, as seen in Eqn. (4):

American Institute of Aeronautics and Astronautics Paper 2010-4487

$$\mathbf{uu} = \begin{bmatrix} u^2 & uv & uw \\ vu & v^2 & vw \\ wu & wy & w^2 \end{bmatrix} \tag{4}$$

B.   Magnetohydrodynamics

Magnetohydrodynamic effects ($\mathbf{j}$, $\mathbf{B}$, and $\mathbf{E}$), are determined using a loosely coupled MHD module which is described in detail in Ref. 36. The module operates by solving a generalized form of Ohm's law to determine the electric potential, ϕ, as seen in Eqn. (5):

$$\nabla \cdot \tilde{\sigma} \cdot [-\nabla \phi + \mathbf{u} \times \mathbf{B}] = 0 \tag{5}$$

Noting the magnetic Reynolds number ($Re_m = \mu_0\, \sigma\, u\, L << 1$) is small for the cases of interest in this work, the induced magnetic field can be assumed negligible.[39] This means only the external applied magnetic field is present in the flow and must be specified. Hall effect and ion slip are included in the simulations by utilizing the electrical conductivity tensor, $\tilde{\sigma}$, as seen in Eqn. (6):

$$\tilde{\sigma} = \frac{\sigma}{(1+s)^2 + \beta_e^2} \left\{ (1+s)\delta_{ij} + [s(1+s) + \beta_e^2] \frac{B_i\, B_j}{B^2} - \varepsilon_{ijk}\beta_e \frac{B_k}{B} \right\} \tag{6}$$

where σ is the electrical conductivity of the fluid, B_i represents the components of the magnetic field vector, and B is its magnitude. A derivation of Eqn. (6) is provided in the Appendix. The Hall parameter, β_e, and ion slip coefficient, s, are defined in Eqns. (7) and (8), respectively:

$$\beta_e = \mu_e\, B \tag{7}$$

$$s = \left(\frac{\rho_{\text{neutral}}}{\rho} \right)^2 \beta_e\, \beta_i \tag{8}$$

where μ_e is the mobility of the electrons, ρ_{neutral} is the sum of the neutral species, and $\beta_i = \mu_i\, B$. The electron mobility is determined directly from the electrical conductivity ($\mu_e = \sigma/e\, n_e$). The ion mobility is determined by setting the ratio of mobilities to a constant. Using values reported in literature,[40, 41] the ratio of mobilities is set to 400 ($\mu_e/\mu_i = 400$), unless otherwise specified.

Investigation of the electrical conductivity tensor reveals the ion slip coefficient is only appreciable when its magnitude is on the order of one or larger. Since the ratio of mobilities is constant ($\mu_e/\mu_i = 400$), the Hall parameter must be on the order of 10 or greater before the ion slip coefficient becomes substantial.
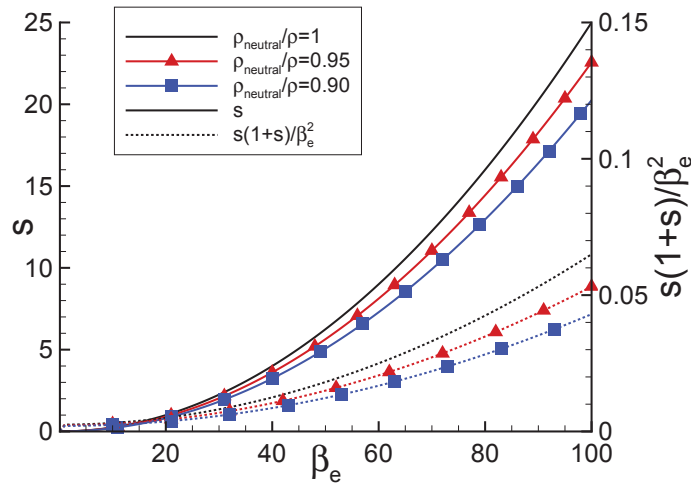
Figure 1. Hall parameter versus ion slip coefficient for various ionization fractions.

American Institute of Aeronautics and Astronautics Paper 2010-4487

Approved for public release; distribution unlimited.

Figure 1 plots the ratio of $s(1+s)$ over β_e^2. This curve indicates when the ion slip coefficient may become important since the terms in the ratio appear in the second term of Eqn. (6). As seen in the figure, $s(1+s)/\beta_e^2$ remains relatively small even though the ion slip coefficient is on the order of ten. Thus, the influence ion slip has on the electrical conductivity tensor remains minor while $\beta_e \leq 100$.

C. The Hall Effect and Ion Slip

Validation of the Hall effect and ion slip was performed by utilizing a computational study developed by Hurwitz et al.,[42] and rigorously explored by Oliver and Mitchner.[43] In the numerical experiment, finite segmented electrodes were infinitely repeated along the two walls of a channel, as seen in Fig. 2. An externally applied magnetic field was employed perpendicular to the channel velocity, $\mathbf{u}$.
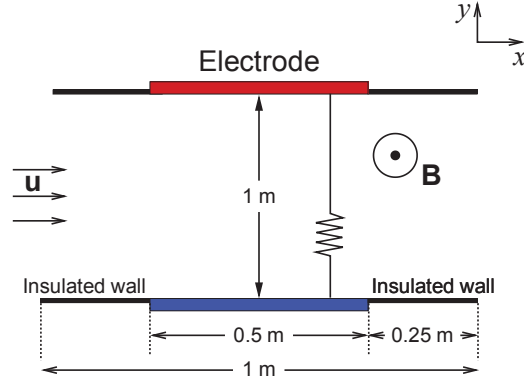
Figure 2. Schematic of the channel flow with finitely segmented electrodes.

Because the channel was infinitely long, periodic boundary conditions were developed and employed at the domain inlet and outlet. Oliver and Mitchner demonstrated that two of the four 'global' conditions (i.e., streamwise and spanwise current or voltage), were required to determine a unique solution.[43] In this validation exercise, the applied voltage between the electrode pairs and neighbors were specified (streamwise and spanwise voltages).

A two-point overlapping stencil, shown in Fig. 3, transfers information between the periodic inlet and outlet, while either adding or subtracting the specified streamwise voltage, $\Delta\phi_x$. Since solutions for the interior cells are computed using a non-uniform, second order stencil, the two point stencil provides sufficient information to accurately update the adjacent interior points. Using this approach, a row of cells starts at the inlet and ends at the outlet (constant y). The inlet ghost cell is set equal to the last interior cell next to the outlet (minus the applied streamwise voltage). Likewise, the outlet's ghost cell is set equal to the interior cell adjacent to the inlet (plus the applied streamwise voltage).
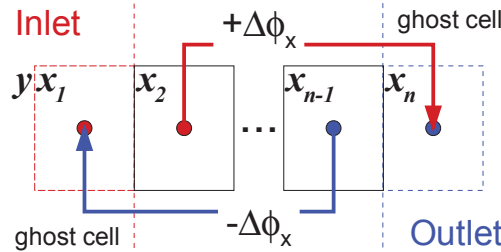
Figure 3. Cartoon of a two point stencil used for period boundary conditions.

Oliver and Mitchner formulated this problem so that the fluid velocity field did not affect the solution as long as $\nabla \times (\mathbf{u} \times \mathbf{B}) = 0$. During one iteration of the flow solver, the MHD routine is executed assuming the velocity profile is only a function of the distance between the plates $\mathbf{u} = f(y)$, which satisfies $\nabla \times (\mathbf{u} \times \mathbf{B}) = 0$

American Institute of Aeronautics and Astronautics Paper 2010-4487

109

Approved for public release; distribution unlimited.

as long as $\mathbf{B} = f(z)$. The velocity profile was assumed to be fully developed Poiseuille flow between parallel plates,[44] as seen in Eqn. (9):

$$\mathbf{u} = f(y) = u_{\max}(1 - \frac{(y - y_h)^2}{h^2}) \tag{9}$$

where $u_{\max}$ is the maximum velocity and was set to unity for this scenario ($u_{\max} = 1$ m/s). The y location was measured from the center of the channel width ($y_h = 0.5$ m), so $h = 0.5$ m was the channel half-width.

A grid was developed based on the grid convergence study preformed previously for similar three-dimensional simulations.[36] The grid utilized exponential spacing along the wall surface such that cell clustering occurs near the junction between the insulated wall and the electrode. Exponential spacing was employed between the two walls such that cell clustering occurs near each surface. The grid employed 100 points along the wall ($x-$direction) and 60 points between the walls.

For the scenario with Hall effect, a one tesla uniform magnetic field was externally applied perpendicular to both the streamwise flow and the spanwise voltage. The applied spanwise voltage between an electrode pair was set to one volt, but the spanwise electrode pair was offset by 0.28 m for the Hall parameter of one ($\beta_e = 1$), as seen in Fig. 4. Hurwitz et al. also specified the applied streamwise voltage ($\Delta\phi_x = 0.4305$ V).[42]
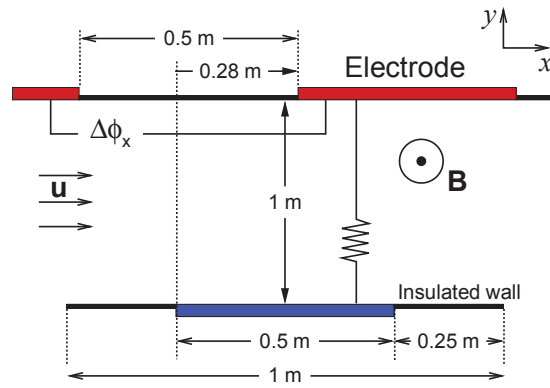
Figure 4. Schematic of channel flow with finitely segmented electrodes used by Hurwitz et al. with Hall effect ($\beta_e = 1$).

The inclusion of the Hall effect allows the magnetic effects into the antisymmetric components of the electrical conductivity tensor, as seen in Eqn. (6). These components 'stretch' the streamwise component of the current density vector, j_x. Hurwitz et al. computed the potential and electric field, as seen in Fig. 5. Current flows along a diagonal of the squares shown in Fig. 5(a) (i.e., the current lines cross the orthogonal squares in the figures).[40]

(a) Reproduced from Hurwitz et al.[42]

(b) Medium grid (100×60) at $z = 0$.
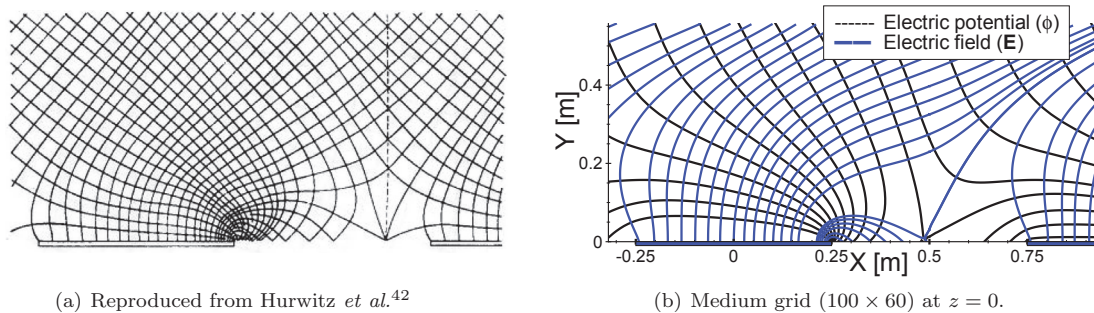
Figure 5. Potential contours and electric field streamlines between segmented electrodes with the Hall effect. ($\mathbf{B}_z = 1$ T, $\sigma = 1$ Ω^{-1}m^{-1}, $\beta_e = 1$, and $\Delta\phi_x = 0.4305$ V)

While the computed solution closely resembles Hurwtiz's semi-analytic solution, it is not identical. Hurwitz assumed a negligible streamwise current ($j_x = 0$), when the solution was sufficiently away from the wall

American Institute of Aeronautics and Astronautics Paper 2010-4487

Approved for public release; distribution unlimited.

(i.e., $y = 0.5$ m). While this approximation allowed an analytical solution to be determined, it is not completely accurate, and is not enforced in the computations performed here. Nonetheless, the figures portray similar characteristics, and indicate that the Hall effect was successfully implemented.

The ion slip parameter acts to reduce the stretching of the streamwise current. Figure 6 plots the current lines for Hurwtiz's scenario with and without ion slip. The ion slip coefficient was set to one ($s = 1$) for the simulation. While this scenario is unphysical unless the flow's ion mobility is greater than its electron mobility (i.e., $\rho_{neutral}/\rho \leq 1$ therefore $\beta_i > 1$ since $\beta_e = 1$), it does illustrate the influence of the ion slip coefficient.

(a) Only the Hall effect. ($\beta_e = 1$, $s = 0$)

(b) Hall effect and ion slip. ($\beta_e = 1$, $s = 1$)
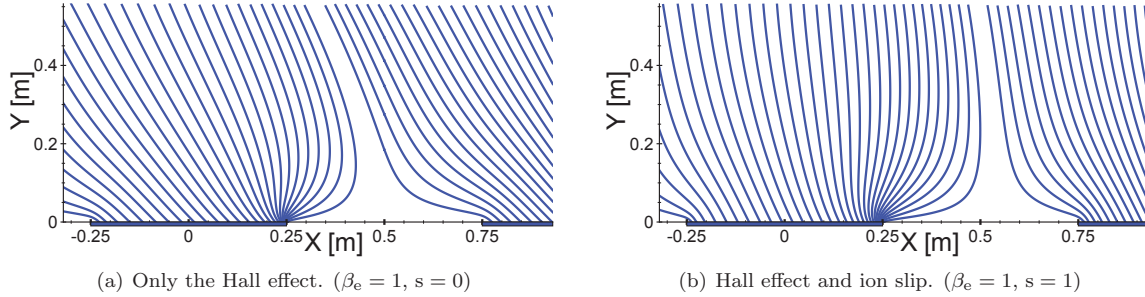
Figure 6. Current streamlines between segmented electrodes with the Hall effect and ion slip. ($B_z = 1$ T, $\sigma = 1\ \Omega^{-1}m^{-1}$, and $\Delta\phi_x = 0.4305$ V)

Since ion slip allows the ions to carry more of the current, the current lines appear more vertical in the center of the channel ($y = 0.5$ m), which is qualitatively consistent with results obtained by Gaitonde for a similar scenario.[45] Likewise, the angle at which the current enters electrodes is also reduced, which should reduce the spanwise impedance between the electrode pair.

D. Electrical Conductivity

The experiment performed by Kranc *et al.* used pre-ionized argon (Ar, Ar$^+$, and e). The electrical conductivity profile for weakly-ionized argon is shown in Fig. 7. As seen in the figure, the electrical conductivity exhibits two distinct regions, namely, weakly ionized (T $\lesssim$ 10,000 K) and fully ionized (T > 10,000 K). Both regions display exponential growth versus temperature, which means a highly accurate model is critical to accurately predict the electrical conductivity across the entire temperature range.
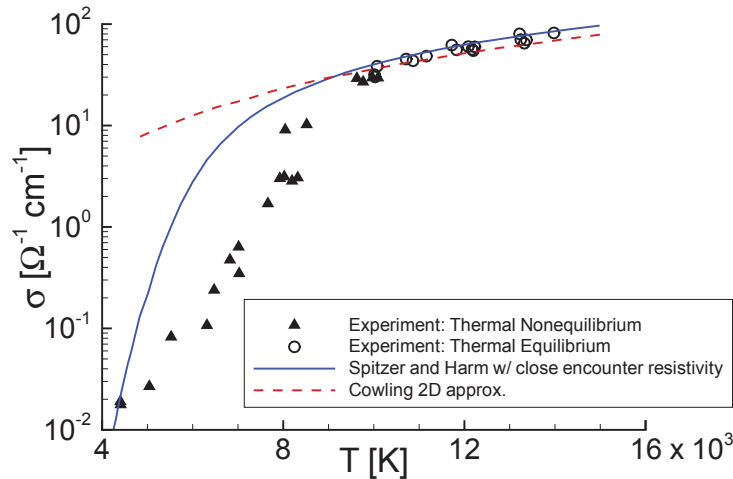
Figure 7. Electrical conductivity of argon ($p = 0.013$ atm), reproduced from Lin *et al.*[46]

Previous work explored different electrical conductivity models for the MHD-Heat Shield study and found

Approved for public release; distribution unlimited.

the conductivity model based on a polynomial response surface (PRS) to solutions of Boltzmann's equation provided solutions to the change in shock standoff distance that agreed reasonably well with experimental measurements.[36] The 2$^\text{nd}$ PRS model is shown in Eqn. (10):

$$\sigma = \frac{\chi_\text{e}}{\exp{(\mathbf{PRS})}}$$

$$
\begin{aligned}
\mathbf{PRS} = & -842.64 + 128.02(\text{E}/N) + 2558.28(\chi_{\text{Ar}}) - 4112.52(\chi_{\text{Ar}^+}) \\
& -4.82(\text{E}/N)^2 - 118.25(\text{E}/N)(\chi_{\text{Ar}}) - 121.33(\text{E}/N)(\chi_{\text{Ar}^+}) \\
& -1732.34(\chi_{\text{Ar}})^2 + 3229.51(\chi_{\text{Ar}})(\chi_{\text{Ar}^+}) - 7342.51(\chi_{\text{Ar}^+})^2
\end{aligned}
\tag{10}
$$

where E/N is the normalized electric field, and χ_s is the species mole fractions. This definition of the model requires the normalized electric field to be re-normalized from 0 to 1 for a range of 0.01 to 100 Td. (1 townsend [Td] = 10^{-17} V·cm^2) The species mole fractions (χ_s), are used directly in the equation. This model was developed for an ionized mole fraction less than one percent (i.e., $\chi_{\text{Ar}^+} < 0.01$). However, the model could be expanded to accommodate a larger range of mole fractions if necessary.

E.   Viscosity Model

Chemically non-reacting, thermodynamic equilibrium simulations were computed using the variable hard sphere (VHS) viscosity model. The VHS model was used because the viscosity is assumed to only be a function of temperature, since the species present (argon, argon ion, and electrons), have a single energy mode and were chemically non-reacting:

$$\mu = \mu_\text{ref}\left(\frac{T}{T_\text{ref}}\right)^\omega \tag{11}$$

where μ is the viscosity, the reference viscosity coefficient, $\mu_\text{ref} = 2.117 \times 10^{-5}$ N s/m², for a reference temperature, $T_\text{ref} = 273$ K, and a viscosity index, $\omega = 0.81$. This method, as outlined by Schwartzentruber et al.,[47] requires several reference coefficients which are listed in Ref. 48.

III.   Hemisphere-Cylinder Results

Three-dimensional calculations were carried out for Mach 4.75 argon flow over a hemisphere-cylinder, which was originally studied experimentally by Kranc et al.[9] The forebody hemisphere has a radius of 0.75 inch ($r_\text{n} = 0.01905$ m), and the geometry was mounted parallel to the freestream, as seen in Fig. 8.
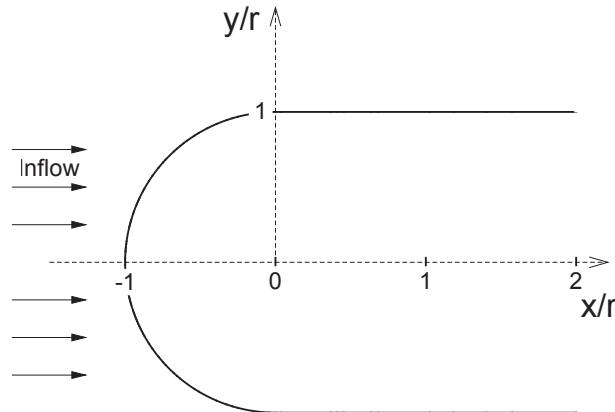
Figure 8.   Hemisphere capped geometry. Adapted from Ref. 9.

American Institute of Aeronautics and Astronautics Paper 2010-4487

Approved for public release; distribution unlimited.

The freestream flow was composed of strongly ionized argon (the degree of ionization was estimated by Kranc *et al.* as $\alpha = 0.025$), which was produced by a plasma torch (direct-current arc-heater). The heater was located before the converging-diverging nozzle, which accelerates the gas into the test chamber. Kranc *et al.* state that the electrons were 'frozen' in the nozzle, and that the flow was not chemically reacting after it was partially ionized by the heater. Previous work showed Kranc *et al.* may have overestimated the freestream ionization fraction,[36] which was updated using the Saha equation for a singly ionized atomic gas.[49] The 'adjusted' flow conditions used in this analysis and are listed in Table 1.

Table 1. Flow conditions for the MHD-Heat Shield experiment in argon.

Parameter	Value	
M	4.75	
u_∞	3000.0	m/s
T_∞	1100.0	K
T_w	300.0	K
p_∞	27.8	Pa
ρ_∞	1.1×10^{-4}	kg/m³
n_e	1.03×10^{19}	m⁻³
α	0.00623	
r_n	0.01905	m
μ_∞	8×10^{-5}	kg/m·s

A.   Magnetic Field

In the experiment of Kranc *et al.*, the applied magnetic field was produced by an electromagnet located inside the hemisphere-shaped forebody. The electromagnetic was approximately 1 inch (0.0254 m), long by 1.25 inch (0.03175 m), in diameter with a 0.375 inch (0.0095 m) core. The core was composed of vanadium permandur and the windings were made of #19 Anaconda HML (Polyimide Enamel) coated wire with a magnetic resistance of 0.5 Ω.[9] Measurements made by Kranc *et al.* found the magnet behaved like an ideal dipole near the stagnation region of the flow, and was modeled as such for this analysis.

The magnetic field decays as r^{-3} from its centroid, which was assumed to be located along the x-axis, where the forebody merges with the rest of geometry ($x/r_n = 0$), as seen in Fig. 9. The magnetic moment was aligned along the x-axis and was positioned to oppose the incoming flow along the stagnation line. The magnetic field contours in the figure are nondimensionalized by the peak magnetic field strength, B_{max}, which occurs at the stagnation point ($x/r_n = -1$). Note that the peak magnetic field strength is used to designate each simulation for the rest of this analysis.

In Cartesian coordinates, the ideal dipole magnetic field is:

$$\mathbf{B} = \frac{-B_{max}}{2\left(x^2 + y^2 + z^2\right)^{5/2}} \begin{bmatrix} 2x^2 - (y^2 + z^2) \\ 3xy \\ 3xz \end{bmatrix} \tag{12}$$

The negative sign in front of the peak field strength, B_{max}, is due to the direction of the field flux. The centroid of the dipole is located at the origin of the coordinate system, though the computational domain does not contain the magnetic field centroid.

B.   Grid Convergence

A structured grid was generated using two grid domains. The first domain includes the hemispherical forebody, while the second accommodates the rest of the geometry. A grid convergence study was conducted for the baseline flow in previous work.[36] While this is sufficient for simulations without MHD effects, a more complete convergence study also verifies the grid is sufficiently resolved in the presence of the magnetic field. The magnetic field in the presence of a pre-ionized gas presents an additional challenge because it is initially

American Institute of Aeronautics and Astronautics Paper 2010-4487

Approved for public release; distribution unlimited.
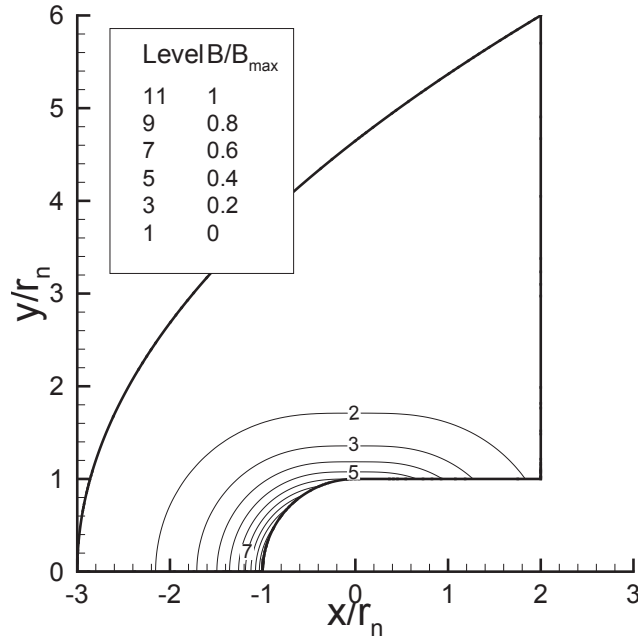
Figure 9. Nondimensional dipole magnetic field contours from a magnet located in the hemisphere capped geometry.

unclear how much the flow field will change because of the magnetic field (i.e., how large does the domain need to be to capture the magnetic effects on the flow).

The grid was generated with equal spacing along the hemisphere portion of the geometry (first domain), and gradually increases in spacing along the remaining surface (second domain). Grid points were equally spaced around the circumference of the geometry and the radial points were algebraically spaced to increase the number of points close to the body. As a result, cell clustering occurred primarily in the hemispherical forebody and near the body surface. The 'coarse' grid uses 50 points along the body (30 points in the hemispherical region), 30 points along one quarter of the circumference, and 30 radial points. Two doubly refined grids were also developed and used in the grid convergence study, giving the following set of computational meshes: $50 \times 30 \times 30$ (coarse), to $100 \times 60 \times 60$ (medium), to $200 \times 120 \times 120$ (fine).

Since the flow experiences an increase in shock standoff distance due to the presence of a magnetic field, it is also important to ensure grid independence when the magnetic fields are present. To this end, simulations were also computed in the presence of a large magnetic field ($B_{max} = 0.45$ T). These simulations neglected the Hall effect. However, the Hall effect should diminish the effectiveness of the magnetic field at influencing the shock location. Therefore, the grid study solutions neglecting Hall effect provide sufficient resolution even when the Hall effect and ion slip are present.

Figure 10 plots the pressure coefficient and nondimensional heat flux for both the baseline flow and the flow with the magnetic field along the surface of the geometry, as defined in Eqns. (13) and (14), respectively:

$$C_p = \frac{p_w - p_\infty}{1/2\,\rho_\infty u_\infty^2} \tag{13}$$

$$C_h = \frac{q_w}{1/2\,\rho_\infty u_\infty^3} \tag{14}$$

where q_w is the total heat flux to the wall.

The grid convergence study showed little difference between the 'medium' and 'fine grids for both the baseline scenario and the scenario with an applied magnetic field $B_{max} = 0.45$ T. Therefore, the 'medium' grid spacing was considered sufficiently refined.

The magnetic-interaction number is the ratio of the magnetic body force to the inertia force. This global nondimensional number helps predict when flows will be influenced by the presence of a magnetic field, but

American Institute of Aeronautics and Astronautics Paper 2010-4487
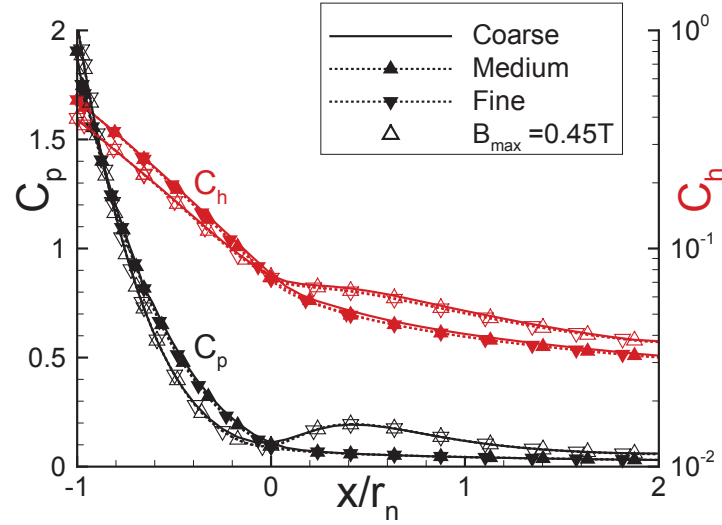
Figure 10. Nondimensional pressure and heat flux along the surface of Mach 4.75 argon flow around a hemisphere-cylinder for various grids.

is traditionally applied to flows that are not pre-ionized.[40]

Because the freestream flow was sufficiently pre-ionized, the freestream electrical conductivity allowed the applied magnetic field to influence the flow-field upstream of the shock. In order to estimate the proper domain size required to account for the expected changes in the flow-field due to the presence of an applied magnetic field, a local magnetic-interaction number was developed, as seen in Eqn. (15).

$$S_{local} = \frac{\sigma \, B^2 \, r_n}{\rho \, u} \tag{15}$$

where u is the magnitude of the local velocity.

The baseline flow-field solution is used to estimate the electrical conductivity and a large magnetic field ($B_{max} = 0.45$ T), was applied to the domain. With these values, the local magnetic-interaction was estimated, as seen in Fig. 11.

As seen in the figure, the magnetic interaction number decreases as the magnetic field strength decays. Using these contours as a guide, two additional grids were created. The first extends radially along the x-axis to $x/r_n = -3$, while the second only extends to $x/r_n = -2.5$. These sizes correspond to $S_{local} \geq 0.01$ and $S_{local} \geq 0.05$, respectively. Figure 12 plots the temperature contours with an applied magnetic field of $B_{max} = 0.45$ T for these grids.

As seen in Fig. 12, the computed flow-field is unable to fully extend from the body as the domain size is reduced. From the figures it appears that a reasonable solution is obtained if the domain is large enough to ensure $S_{local} \geq 0.01$ along the stagnation line (x-axis). To verify this, the baseline solution was used to estimate the local magnetic-interaction for a magnetic field of $B_{max} = 0.6$ T, as seen in Fig. 13.

Maintaining $S_{local} \geq 0.01$ along the stagnation line, a grid was developed to extend to $x/r_n = -3.5$. Figure 14 shows the flow-field is not significantly influenced by the domain reduction. Since the maximum magnetic field strength employed in the analysis is $B_{max} = 0.45$ T, the grid extending to $x/r_n = -3$ was employed for the rest of the analysis.

This paper estimates the leading edge of the shock to correspond to the location where the density ratio exceeds the ideal gas infinite Mach number threshold for a normal shock wave along the stagnation line:

$$\lim_{M_1 \to \infty} \frac{\rho_2}{\rho_1} = \frac{\gamma + 1}{\gamma - 1} \tag{16}$$

where γ is the ratio of specific heats, ρ_1 is the freestream density, and ρ_2 is the downstream density. Using this equation, the density ratio limit for argon is four ($\gamma = 5/3$).

American Institute of Aeronautics and Astronautics Paper 2010-4487

Approved for public release; distribution unlimited.
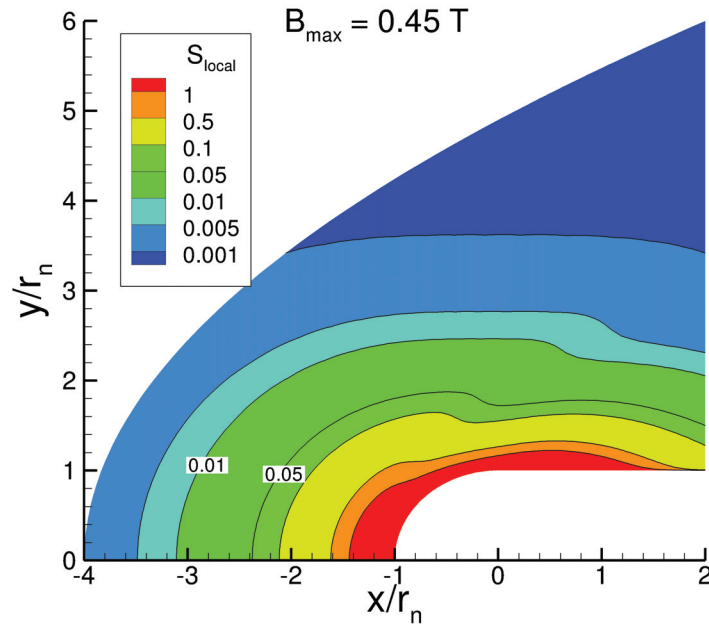
Figure 11. Contours of the local magnetic-interaction number for Mach 4.75 argon flow around a hemisphere-cylinder using the baseline flow-field solution. (B_{max} = 0.45 T)

(a) Grid extent based on $S_{local} \geq 0.01$ contour.

(b) Grid extent based on $S_{local} \geq 0.05$ contour.

Figure 12. Temperature contours for Mach 4.75 argon flow around a hemisphere-cylinder with various domain sizes. (B_{max} = 0.45 T) Bottom: extended grid.

American Institute of Aeronautics and Astronautics Paper 2010-4487

116
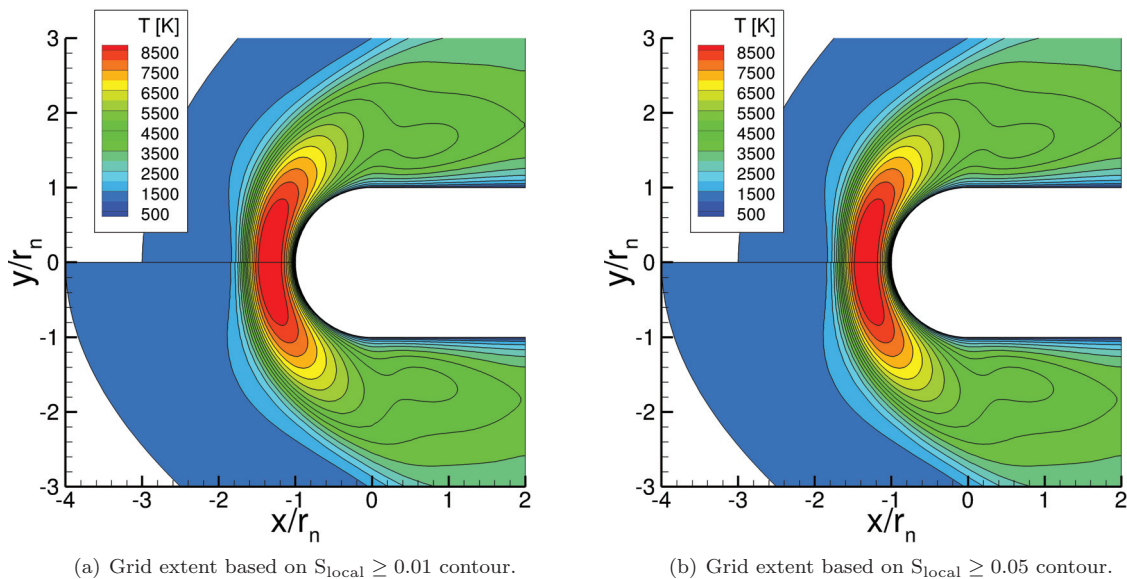
Approved for public release; distribution unlimited.
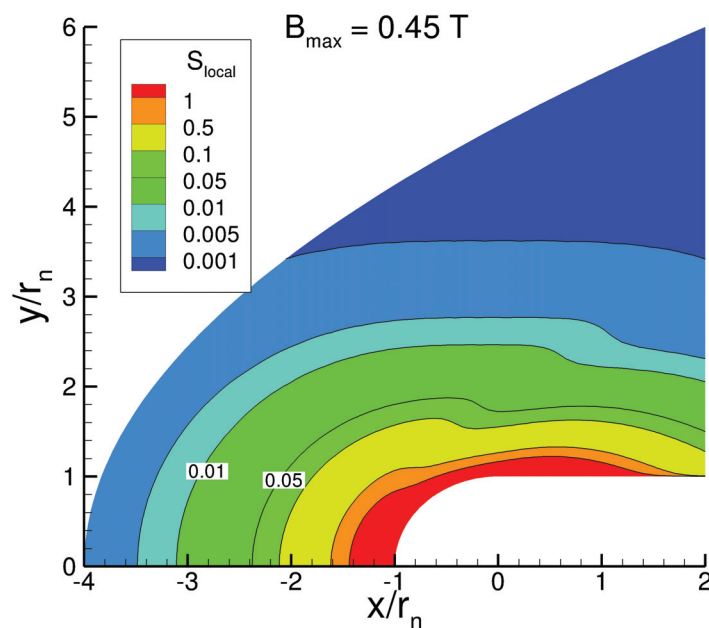
Figure 13. Local magnetic-interaction number contours for Mach 4.75 argon flow around a hemisphere-cylinder using the baseline flow-field solution. ($\mathbf{B_{max}} = 0.60$ T)
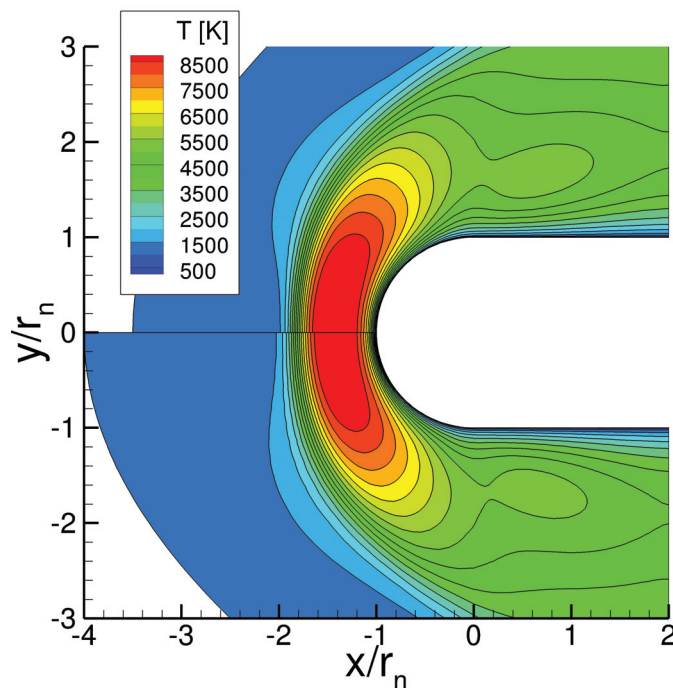
Figure 14. Temperature contours for Mach 4.75 argon flow around a hemisphere-cylinder with various domain sizes. ($\mathbf{B_{max}} = 0.60$ T) Bottom: extended grid.

American Institute of Aeronautics and Astronautics Paper 2010-4487

117

Approved for public release; distribution unlimited.

C. Hot Wall Effects

Previous work assumed the hemisphere-cylinder held a constant wall temperature of 300 K. This assumption was made because the actual surface temperature was unknown, the magnet was being actively cooled by a water bath, and because the experiment's short run times would have limited the surface heating. To verify this assumption, a set of simulations was computed assuming the surface has a constant wall temperature of 1000 K. In addition, another set of simulations was computed assuming the wall temperature was in radiative equilibrium using the Stefan-Boltzmann Law ($T_w^4 = q_w / \epsilon \, \sigma^*$).

Three peak magnetic field strengths were explored for the different wall conditions. Figure 15 plots the density ratio on the stagnation line for a peak magnetic field strength of 0.45 T. The fully radiative wall temperature varied from 950 K along the cylinder portion of the geometry to 1800 K at the stagnation point.
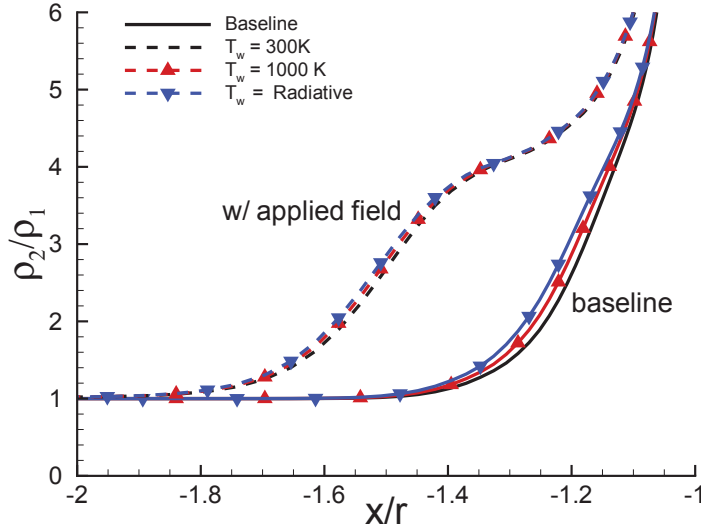
Figure 15. Density ratio on the stagnation line for Mach 4.75 argon flow around a hemisphere-cylinder with a dipole magnetic field for various wall temperature boundary conditions. ($B_{max} = 0.45$ T, $\beta_e = 0$)

While the various wall conditions do influence the actual location of the shock, the change in shock standoff distance was not significantly influenced, as seen in Table 2. Therefore a constant wall temperature of 300 K was assumed sufficient and used in the rest of the analysis.

Table 2. Percent change in shock standoff distance for various magnetic field strengths and wall conditions. ($\beta_e = 0$)

B_{max}	$T_w = 300$ K	$T_w = 1000$ K	T_w = Radiative Equilibrium
0.13	2.5%	1.2%	2.3%
0.28	10.6%	9.2%	9.7%
0.45	23.5%	22.5%	21.6%

D. Hall Effect and Ion Slip

The flow-field around the geometry (without the applied magnetic field), is axisymmetric and steady, as evident in the temperature contours seen in Fig. 16. Without the Hall effect the electric field can be shown to be zero[4] and, thus, the electric current must only travel in the azimuthal direction (perpendicular to the incoming flow, around the axis of symmetry). This reduces the magnetic force in the momentum equation to $\tilde{\sigma} \cdot (\mathbf{u} \times \mathbf{B}) \times \mathbf{B}$, and sets the energy deposition term in the total energy equation to zero, $\mathbf{j} \cdot \mathbf{E} = 0$. Note that Joule heating is still present under these assumptions, $(\mathbf{E} + \mathbf{u} \times \mathbf{B}) \cdot \mathbf{j} \neq 0$.
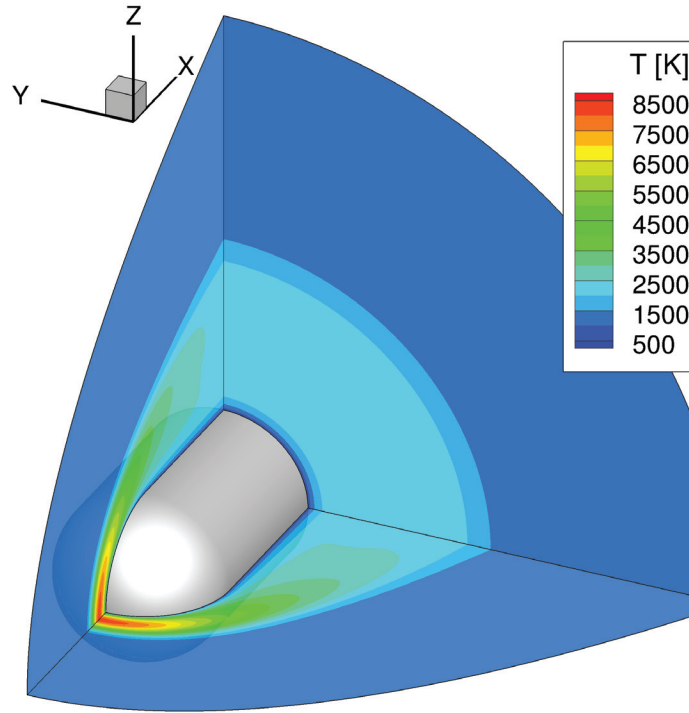
Figure 16. Temperature contours for Mach 4.75 argon flow around a hemisphere-cylinder.

Although the baseline flow-field is axisymmetric, the Hall effect and ion slip create antisymmetric terms in the conductivity tensor. This means it is no longer justifiable to assume the electric field is zero. In addition, the current is now primarily located in the meridian planes (i.e., planes that contain the x-axis), with a weakened current still present in the azimuthal direction. These effects result in a torque on the magnet, or since computations are computed in a relative frame (i.e., the geometry and magnet are fixed and the fluid is moving), the current lines corkscrew toward the geometry, as seen in Fig. 17.

The current lines twist to the right (i.e., clockwise), while they are located over the hemisphere portion of the geometry due to the direction of the magnetic moment. However, the current lines switch rotation direction (i.e, counter-clockwise), along the cylinder portion of the geometry because the change in direction of the magnetic field lines changes the direction of the force acting on the electrons.

Figure 18 shows the Hall parameter contours for the flow with an applied magnetic field of 0.13 T. Because the flow is pre-ionized, the Hall parameter is quite large for the flow, especially near the stagnation region. The strong Hall effect almost completely diminishes the increase in shock standoff distance observed in previous work without the Hall effect,[36] a result that is consistent with findings by Porter *et al.*,[12] though the study is still ongoing.

In addition to weakening the effectiveness of the magnetic force at increasing shock standoff distance, the presence of the electric field results in an increase in total heating to the fluid domain ($\mathbf{j} \cdot \mathbf{E} \neq 0$). The increase in total temperature slightly increases the heat flux to the geometry surface (versus the same scenario without accounting for the Hall effect).

IV. Conclusions

Recently developed computational tools were used to compute hypersonic flow around a hemisphere capped geometry which utilizes a magnet located within the body as a means of heat flux mitigation. These tools include a procedure to accurately account for the Hall effect and ion slip. These phenomena produce antisymmetric components of the electrical conductivity tensor which lead to a stretching of the current streamlines in the direction of the flow.

Mach 4.75 argon flow over a hemisphere-cylinder corresponding to the experiment conducted by Kranc

American Institute of Aeronautics and Astronautics Paper 2010-4487

119

Approved for public release; distribution unlimited.
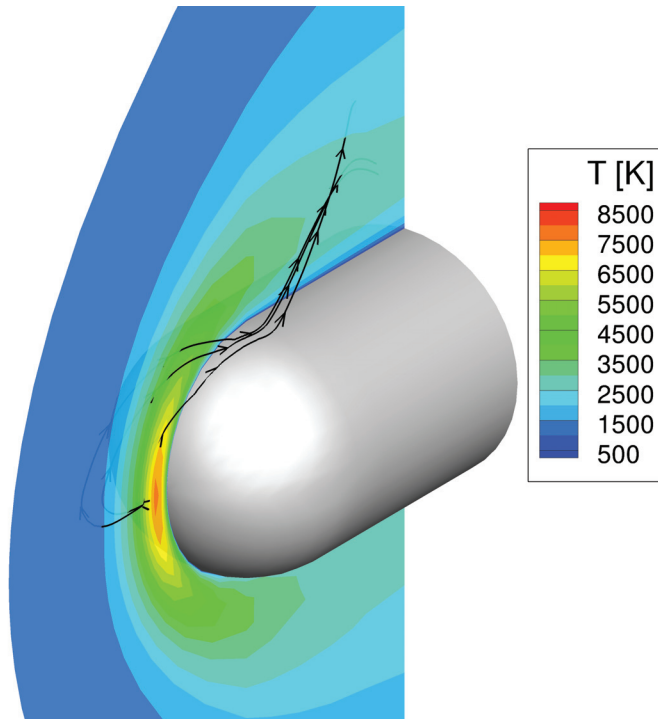
Figure 17. Temperature contours and current lines for Mach 4.75 argon flow around a hemisphere-cylinder with a 0.13 T magnetic field (including Hall effect and ion slip).
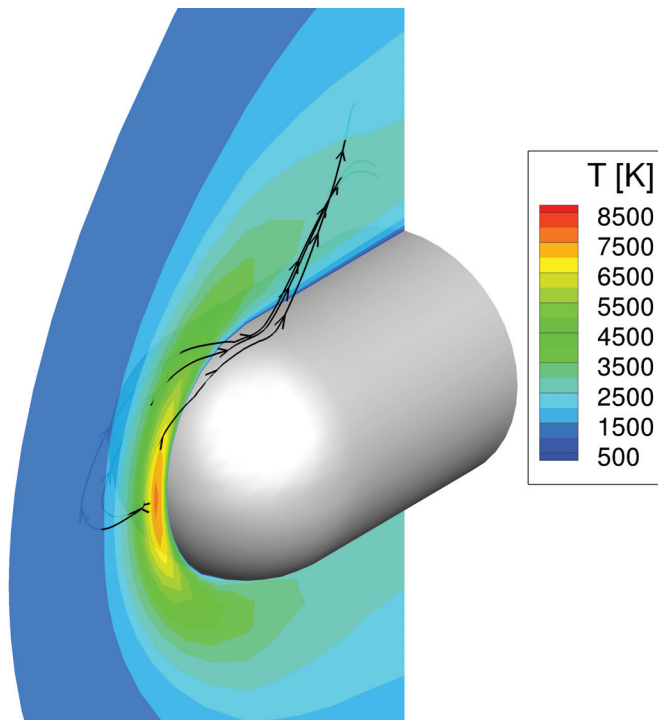
Figure 18. Hall coefficient contours for Mach 4.75 argon flow around a hemisphere-cylinder with a 0.13 T magnetic field.

120

Approved for public release; distribution unlimited.

et al. was investigated computationally using modern CFD techniques. Because the geometry surface temperature was unknown in the experiment, several approaches were computationally explored, but the change in shock standoff distance did not greatly depend on the surface temperature. Simulations were also computed with the Hall effect and ion slip. Compared to simulations without these phenomena, the Hall effect and ion slip reduced the effectiveness of the magnetic force at increasing the shock standoff distance while producing additional heating in the flow through Joule heating. Since the Hall parameter is directly related to the magnitude of the magnetic field, use of weaker magnetic fields should reduce the negative implications of these phenomena. However, weaker fields are less effective at increasing the shock standoff distance and thereby providing sufficient heat mitigation.

These results have important implications for design of MHD-Heat Shield devices: they can reduce peak heat loads, but with a potential penalty in total heating. Since both peak and total heat load are important aspects to consider when designing a thermal protection system, this technology provides additional scenarios for vehicle designers to evaluate.

References

[1]Kantrowitz, A. R., "A Survey of Physical Phenomena Occurring in Flight at Extreme Speeds," *Proceedings of the Conference on High-Speed Aeronautics*, edited by A. Ferri, N. J. Hoff, and P. A. Libby (Polytechnic Institute of Brooklyn, New York, 1955), pp. $335 - 339$.

[2]Resler, E. L. and Sears, W. R., "The Prospects for Magneto-Aerodynamics," *Journal of Aeronatuical Sciences*, Vol. 25, April 1958, pp. 235–245, 258.

[3]Resler, E. L. and Sears, W. R., "The Prospects for Magneto-Aerodynamics Correction and Addition," *Journal of Aero/Space Sciences*, Vol. 26, No. 5, May 1959, pp. 318.

[4]Bush, W. B., "Magnetohydrodynamic-Hypersonic Flow Past a Blunt Body," *Journal of Aerospace Sciences*, Vol. 25, 1958, pp. 685.

[5]Bush, W. B., "The Stagnation-Point Boundary Layer in the Presence of an Applied Magnetic Field," *Journal of Aerospace Sciences*, Vol. 28, No. 8, August 1961, pp. 610–611, 630.

[6]Coakley, J. F. and Porter, R. W., "Time-Dependent Numerical Analysis of MHD Blunt Body Problem," *AIAA Journal*, Vol. 9, No. 8, August 1971, pp. 1624–1626.

[7]Ziemer, R. W., "Experimental Investigations in Magnetoaerodynamics," *Journal of American Rocket Society*, Vol. 29, No. 9, 1959, pp. 642.

[8]Wilkinson, B., "Magnetohydrodynamic Effects on Stagnation-Point Heat Transfer from Partially Ionized Nonequilibrium Gases in Supersonic Flow," *Engineering Aspects of Magnetohydrodynamics: Proceedings, 3rd Symposium*, edited by N. W. Mather and G. W. Sutton (Gordon and Breach, New York, 1964), pp. $413 - 438$.

[9]Kranc, S., Yuen, M. C., and Cambel, A. B., "Experimental Investigation of Magnetoaerodynamic Flow around Blunt Bodies," Tech. rep., National Aeronautics and Space Administration, Washington, D.C., August 1969, NASA CR-1392.

[10]Nowak, R. J., Kran, S., Porter, R. W., Yuen, M. C., and Cambel, A. B., "Magnetogasdynamic Re-Entry Phenomena," *Journal of Spacecraft*, Vol. 4, No. 11, November 1967, pp. 1538–1542.

[11]Nowak, R. J. and Yuen, M. C., "Heat Transfer to a Hemispherical Body in Supersonic Argon Plasma," *AIAA Journal*, Vol. 11, No. 11, November 1973, pp. 1463–1464.

[12]Porter, R. W. and Cambel, A. B., "Hall Effect if Flight Magnetogasdynamics," *AIAA Journal*, Vol. 5, No. 12, December 1967, pp. 2208–2213.

[13]Romig, M. F., "The Influence of Electric and Magnetic Fields on Heat Transfer to Electrically Conducting Fluids," *Advances in Heat Transfer*, edited by T. F. Irvine and J. P. Hartnett (Academic, New York, 1964), Vol. 1, pp. $267 - 354$.

[14]Fomin, V. M., Tretyakov, P. K., and Taran, J.-P., "Flow Control using Various Plasma and Aerodynamic Approaches," *Aerospace Science and Technology*, Vol. 8, No. 5, July 2004, pp. 411–421.

[15]Shang, J. S., Surzhikov, S. T., Kimmel, R., Gaitonde, D., Menart, J., and Hayes, J., "Mechanisms of Plasma Actuators for Hypersonic Flow Control," *Progress in Aerospace Sciences*, Vol. 41, No. 8, November 2005, pp. 642–668.

[16]Bityurin, V., Bocharov, A., and Lineberry, J., "MHD Flow Control in Hypersonic Flight," *13th International Space Planes and Hypersonic Systems Technologies Conference*, AIAA Paper 2005-3225.

[17]Palmer, G., "Magnetic Field Effects on the Computed Flow over a Mars Return Aerobrake," *Journal of Thermophysics and Heat Transfer*, Vol. 7, No. 2, April-June 1993, pp. 294–301.

[18]Girgis, I. G., Shneider, M. N., Macheret, S. O., Brown, G. L., and Miles, R. B., "Creation of Steering Moments in Supersonic Flow by Off-Axis Plasma Heat Addition," *40th AIAA Aerospace Sciences Meeting and Exhibit*, AIAA Paper 2002-129.

[19]Kremeyer, K., Sebastian, K., and Shu, C.-W., "Computational Study of Shock Mitigation and Drag Reduction by Pulsed Energy Lines," *AIAA Journal*, Vol. 44, No. 8, August 2006, pp. 1720–1731.

[20]Menart, J., Stanfield, S., Shang, J., Kimmel, R., and Hayes, J., "Study of Plasma Electrode Arrangements for Optimum Lift in a Mach 5 Flow," *44th AIAA Aerospace Sciences Meeting and Exhibit*, AIAA Paper 2006-1172.

[21]Yan, H. and Gaitonde, D., "Control of Edney IV Interaction by Energy Pulse," *44th AIAA Aerospace Sciences Meeting and Exhibit*, AIAA Paper 2006-562.

[22]Gnemmi, P., Charon, R., Dupéroux, J.-P., and George, A., "Feasibility Study for Steering a Supersonic Projectile by a Plasma Actuator," *AIAA Journal*, Vol. 46, No. 6, June 2008, pp. 1308–1317.

American Institute of Aeronautics and Astronautics Paper 2010-4487

Approved for public release; distribution unlimited.

[23]Bisek, N. J., Boyd, I. D., and Poggie, J., "Numerical Study of Plasma-Assisted Aerodynamic Control for Hypersonic Vehicles," *Journal of Spacecraft and Rockets*, Vol. 46, No. 3, May-June 2009, pp. 568–576.

[24]Bityurin, V. A., Vatazhin, A. B., and Gus'kov, O. V., "Hypersonic Flow Past the Spherical Nose of a Body in the Presence of a Magnetic Field," *Fluid Dynamics*, Vol. 39, No. 4, July 2004, pp. 657–666.

[25]Miles, R. B., Macheret, S. O., Shneider, M. N., Steeves, C., Murray, R. C., Smith, T., and Zaidi, S. H., "Plasma-Enhanced Hypersonic Performance Enabled by MHD Power Extraction," *43th AIAA Aerospace Sciences Meeting and Exhibit*, AIAA Paper 2005-561.

[26]Katsurayama, H., Kawamura, M., Matsuda, A., and T., A., "Kinetic and Continuum Simulations of Electromagnetic Control of a Simulated Reentry Flow," *Journal of Spacecraft and Rockets*, Vol. 45, No. 2, March-April 2008, pp. 248–254.

[27]Kim, M., Keidar, M., and Boyd, I. D., "Analysis of an Electromagnetic Mitigation Scheme for Reentry Telemetry Through Plasma," *Journal of Spacecraft and Rockets*, Vol. 45, No. 6, November-December 2008, pp. 1223–1229.

[28]Macheret, S. O., Shneider, M. N., and Candler, G. V., "Modeling of MHD Power Generation on Board Reentry Vehicles," *42nd AIAA Aerospace Sciences Meeting*, AIAA Paper 2004-1024.

[29]Wan, T., Suzuki, R., Candler, G., Macheret, S., and Schneider, M., "Three Dimensional Simulation of Electric Field and MHD Power Generation During Re-Entry," *36th AIAA Plasmadynamics and Lasers Conference*, AIAA Paper 2005-5045.

[30]Fujino, T., Yoshino, T., and Ishikawa, M., "Prediction of Generator Performance and Aerodynamic Heating of Reentry Vehicle Equipped with On-board Surface Hall Type MHD Generator," *39th Plasmadynamics and Lasers Conference*, AIAA Paper 2008-4225.

[31]Bityurin, V., Bocharov, A., and Lineberry, J., "Results of Experiments on MHD Hypersonic Flow Control," *35th AIAA Plasmadynamics and Lasers Conference*, AIAA Paper 2004-2263.

[32]Takizawa, Y., Sato, S., Abe, T., and Konigorski, D., "Electro-Magnetic Effect on Shock Layer Structure in Reentry-Related High-Enthalpy Flow," *35th AIAA Plasmadynamics and Lasers Conference*, AIAA Paper2004-2162.

[33]Kimmel, R., Hayes, J., Menart, J., and Shang, J., "Supersonic Plasma Flow Control Experiments," Tech. rep., U.S. Air Force Research Laboratory, Wright-Patterson AFB, OH, December 2005, ARFL-VA-WP-TR-2006-3006.

[34]Matsuda, A., Kawamura, M., Takizawa, Y., Otsu, H., Konigorski, D., Sato, S., and Abe, T., "Experimental Investigation of the Hall Effect for the Interaction between the Weakly-Ionized Plasma Flow and Magnetic Body," *45th AIAA Aerospace Sciences Meeting*, AIAA Paper 2007-1437.

[35]Gülhan, A., Esser, B., Koch, U., Siebe, F., Riehmer, J., Giordano, D., and Konigorski, D., "Experimental Verification of Heat-Flux Mitigation by Electromagnetic Fields in Partially-Ionized-Argon Flows," *Journal of Spacecraft and Rockets*, Vol. 46, No. 2, March-April 2009, pp. 274–283.

[36]Bisek, N. J., Boyd, I. D., and Poggie, J., "Numerical Study of Magnetoaerodynamic Flow around a Hemisphere," *Journal of Spacecraft and Rockets*, (accepted for publication).

[37]Scalabrin, L. C. and Boyd, I. D., "Development of an Unstructured Navier-Stokes Solver For Hypersonic Nonequilibrium Aerothermodynamics," *38th AIAA Thermophysics Conference*, AIAA Paper 2005-5203.

[38]Scalabrin, L. C. and Boyd, I. D., "Numerical Simulation of Weakly Ionized Hypersonic Flow for Reentry Configurations," *9th AIAA/ASME Joint Thermophysics and Heat Transfer Conference*, AIAA Paper 2006-3773.

[39]Shercliff, J., "A Textbook of Magnetohydrodynamics," Pergamon Press, 1965.

[40]Sutton, G. W. and Sherman, A., "Engineering Magnetohydrodynamics," McGraw-Hill, 1965.

[41]Raizer, Y. P., "Gas Discharge Physics," Springer-Verlag, 1991.

[42]Hurwitz Jr., H., Kilb, R. W., and Sutton, G. W., "Influence of Tensor Conductivity on Current Distribution in MHD Generator," *Journal of Applied Physics*, Vol. 32, No. 2, February 1961, pp. 205–216.

[43]Oliver, D. A. and Mitchner, M., "Nonuniform Electrical Conduction in MHD Channel," *AIAA Journal*, Vol. 5, No. 8, August 1967, pp. 1424–1432.

[44]White, F. M., "Viscous Fluid Flow, 3rd ed." McGraw-Hill, 2006.

[45]Gaitonde, D. V., "A High-Order Implicit Procedure for the 3-D Electric Field in Complex Magnetogasdynamic Simulations," *Computers and Fluids*, Vol. 33, No. 3, March 2004, pp. 345–374.

[46]Lin, S.-C., Resler, E. L., and Kantrowitz, A., "Electrical Conductivity of Highly Ionized Argon Produced by Shock Waves," *Journal of Applied Physics*, Vol. 26, No. 1, January 1955, pp. 95–109.

[47]Schwartzentruber, T. E., Scalabrin, L. C., and Boyd, I. D., "Hybrid Particle-Coontinuum Simulations of Non-Equilibrium Hypersonic Blunt Body Flow Fields," *9th AIAA/ASME Joint Thermophysics and Heat Transfer Conference*, AIAA Paper 2006-3602.

[48]Bird, G. A., "Molecular Gas Dynamics and the Direct Simulation of Gas Flows," Oxford University Press, 1994.

[49]Messerle, H. K., "Magnetohydrodynamic Electrical Power Generation," John Wiley & Sons, Inc., 1995.

[50]Mitchner, M. and Kruger Jr., C. H., "Partially Ionized Gases," John Wiley and Sons, Inc., 1973.

Appendix

Equation 6 is formulated by starting from the definition of the generalized form of Ohm's Law, including Hall effect and ion slip, but neglecting the electron pressure gradient:[50]

$$\mathbf{j} = \sigma\left[\mathbf{E} + \mathbf{u} \times \mathbf{B}\right] - \beta_{\mathrm{e}} \cdot \mathbf{j} \times \mathbf{b} - \mathrm{s} \cdot \mathbf{b} \times (\mathbf{j} \times \mathbf{b}) \tag{17}$$

where β_{e} and s are the Hall parameter and ion slip coefficient, which are defined in Eqns. (7) and (8), respectively. It is important to note that $\mathbf{B}$ is the magnetic field vector, while $\mathbf{b} = \mathbf{B}/\mathrm{B}$ is the magnetic field unit vector.

American Institute of Aeronautics and Astronautics Paper 2010-4487

Setting $\mathbf{E}' = \mathbf{E} + \mathbf{u} \times \mathbf{B}$, and combining terms, Eqn. (17) is written as:

$$\sigma\mathbf{E}' = \begin{pmatrix} 1 + \frac{s}{B^2}\left(B_y^2 + B_z^2\right) & \frac{\beta_e}{B}B_z - \frac{s}{B^2}B_xB_y & -\frac{\beta_e}{B}B_y - \frac{s}{B^2}B_xB_z \\ -\frac{\beta_e}{B}B_z - \frac{s}{B^2}B_xB_y & 1 + \frac{s}{B^2}\left(B_x^2 + B_z^2\right) & \frac{\beta_e}{B}B_x - \frac{s}{B^2}B_yB_z \\ \frac{\beta_e}{B}B_y - \frac{s}{B^2}B_xB_z & -\frac{\beta_e}{B}B_x - \frac{s}{B^2}B_yB_z & 1 + \frac{s}{B^2}\left(B_x^2 + B_y^2\right) \end{pmatrix}\mathbf{j} \tag{18}$$

Setting the matrix in Eqn. (18) to be equal to $\mathbf{M} = (M_0, M_1, M_2)$, where M_i is a column vector, allows Ohm's law to be reformulated for the current density by determining the inverse of $\mathbf{M}$ (i.e., $\mathbf{j} = \sigma M^{-1} \cdot \mathbf{E}'$):

$$\mathbf{M}^{-1} = \frac{1}{det(\mathbf{M})}\begin{pmatrix} (M_1 \times M_2)^T \\ (M_2 \times M_0)^T \\ (M_0 \times M_1)^T \end{pmatrix} = \frac{1}{det(\mathbf{M})}\begin{pmatrix} c_{11} & c_{12} & c_{13} \\ c_{21} & c_{22} & c_{23} \\ c_{31} & c_{32} & c_{33} \end{pmatrix} \tag{19}$$

$$
\begin{aligned}
det(\mathbf{M}) &= (1+s)^2 + \beta_e^2 \\[4pt]
c_{11} &= 1 + s + \left[s\left(1+s\right) + \beta_e^2\right]\frac{B_x^2}{B^2} \\[4pt]
c_{12} &= \left[s\left(1+s\right) + \beta_e^2\right]\frac{B_xB_y}{B^2} - \beta_e\frac{B_z}{B} \\[4pt]
c_{13} &= \left[s\left(1+s\right) + \beta_e^2\right]\frac{B_xB_z}{B^2} + \beta_e\frac{B_y}{B} \\[4pt]
c_{21} &= \left[s\left(1+s\right) + \beta_e^2\right]\frac{B_yB_x}{B^2} + \beta_e\frac{B_z}{B} \\[4pt]
c_{22} &= 1 + s + \left[s\left(1+s\right) + \beta_e^2\right]\frac{B_y^2}{B^2} \\[4pt]
c_{23} &= \left[s\left(1+s\right) + \beta_e^2\right]\frac{B_yB_z}{B^2} - \beta_e\frac{B_x}{B} \\[4pt]
c_{31} &= \left[s\left(1+s\right) + \beta_e^2\right]\frac{B_zB_x}{B^2} - \beta_e\frac{B_y}{B} \\[4pt]
c_{23} &= \left[s\left(1+s\right) + \beta_e^2\right]\frac{B_zB_y}{B^2} + \beta_e\frac{B_x}{B} \\[4pt]
c_{33} &= 1 + s + \left[s\left(1+s\right) + \beta_e^2\right]\frac{B_z^2}{B^2}
\end{aligned}
\tag{20}
$$

Noting the repeated terms, the matrix can be written compactly in tensor notation using the Kronecker delta (δ_{ij}), and the Levi-Civita symbol (ε_{ijk}):

$$c_{ij} = (1+s)\delta_{ij} + \left[s(1+s) + \beta_e^2\right]\frac{B_i\,B_j}{B^2} - \varepsilon_{ijk}\beta_e\frac{B_k}{B} \tag{21}$$

Equation (21) is combined with previous solutions to yield a compact form for the electrical conductivity tensor, which is the same as Eqn. (6):

$$\tilde{\sigma} = \frac{\sigma}{(1+s)^2 + \beta_e^2}\left\{(1+s)\delta_{ij} + \left[s(1+s) + \beta_e^2\right]\frac{B_i\,B_j}{B^2} - \varepsilon_{ijk}\beta_e\frac{B_k}{B}\right\} \tag{22}$$

Note that the dimensional formulation described in Eqn. (6) can be recovered from Gaitonde's non-dimensional formulation[45] by replacing $R_H\,\beta$ with $\beta_e/[\sigma\,B]$ and $I_s\,\alpha$ with $s/[\sigma\,B^2]$.

Approved for public release; distribution unlimited.

Numerical Study of Plasma-Assisted Aerodynamic Control for Hypersonic Vehicles

Nicholas J. Bisek* and Iain D. Boyd[†]
University of Michigan, Ann Arbor, Michigan 48109
and
Jonathan Poggie[‡]
U.S. Air Force Research Laboratory, Wright–Patterson Air Force Base, Ohio, 45433-7512

Plasma actuators and various forms of volumetric energy deposition have received a good deal of research attention recently as a means of hypersonic flight control. An open question remains as to whether the required power expenditures for such devices can be achieved for practical systems. To address this issue, a numerical study is carried out for hypersonic flow over a blunt-nose elliptic cone to determine the amount of energy deposition necessary for flight control. Energy deposition is simulated by means of a phenomenological dissipative heating model. A parametric study of the effects of energy deposition is carried out for several blunt elliptic cone configurations. Three different volumetric energy deposition patterns are considered: a spherical pattern, a "pancake" pattern (oblate spheroid), and a "bean" pattern (prolate spheroid). The effectiveness of volumetric energy deposition for flight control appears to scale strongly with a nondimensional parameter based on the freestream flow kinetic energy flux.

Nomenclature

A	=	surface area of grid cell
a, b, c	=	the equatorial radii and the polar radius of an ellipsoid
C_m	=	moment coefficient, $[2M_p]/[\rho_\infty u_\infty^2 L^2 d]$
C_p	=	pressure coefficient, $[2(p_w - p_\infty)]/[\rho_\infty u_\infty^2]$
d	=	maximum spanwise length
E	=	total energy per volume
h	=	enthalpy
i, j, k	=	computational grid indices along the axial, radial, and circumferential directions
J	=	mass diffusion flux, x, y, z directions
L	=	axial surface length
M_p	=	moment about center of gravity
n	=	normal vector
p	=	pressure
Q	=	total power input by actuator
q	=	heat flux, translational–rotational and vibrational–electronic
$\tilde{Q}$	=	nondimensional total power input by actuator, $Q/(\rho_\infty u_\infty^3 L^2)$
Re_x	=	running Reynolds number, $\rho_\infty u_\infty x/\mu_\infty$
S	=	source term
St	=	Stanton number, $q_w/[\rho_\infty u_\infty (h_0 - h_w)]$
T	=	temperature, translational and rotational
T_v	=	temperature, vibrational and electronic
u	=	velocity vector (u, v, w)
x, y, z	=	streamwise, spanwise, and transverse coordinates
ϵ	=	emissivity
θ	=	angle along circumference of the body, cylindrical coordinate system
λ	=	characteristic length
μ	=	coefficient of viscosity
ρ	=	mass density
σ	=	Stefan–Boltzmann constant, 5.67×10^{-8} W/[m² K⁴]
τ	=	viscous stress
ϕ	=	inclination of the deposition to the freestream flow

Subscripts

s	=	species
w	=	wall
0	=	stagnation
∞	=	freestream

I. Introduction

AERODYNAMIC control and drag reduction are major challenges for hypersonic vehicle designers. A good deal of research attention has recently focused on hypersonic plasma interactions and plasma flow control to explore ways of confronting these challenges [1,2].

Minimizing drag in vehicle design leads to long, thin bodies with sharp leading edges. This constrains the materials available for the vehicle's thermal protection system (TPS) because there is a required minimum thickness that may not be achieved for a given vehicle configuration. In addition, small defects in the production of the sharp edges can result in serious or even catastrophic problems for the TPS [3]. Blunting the leading edge reduces these drawbacks but results in a much larger wave drag [4]. Recent experimental and computational research by Shang et al. [5] has investigated ways of reducing drag on blunt-nose bodies by means of plasma injection, and research by Kremeyer et al. [6] and Yan and Gaitonde [7] focused on drag reduction and flow control using laser deposition (filamentation) ahead of conic and spherical geometries. Riggins and Nelson [8] used volumetric heating in front of the bow shock to reduce drag for 2-D hypersonic blunt bodies. Virtual cowls for off-design scram engines have also been studied using electron beam ionization by Macheret et al. [9] and dc discharges by Shang et al. [10].

In addition to these design constraints, traditional control surfaces (flaps) need to be positioned away from the center of gravity to extend the maneuverability of the vehicle. The location of such flaps

*Graduate Student, Department of Aerospace Engineering, 1320 Beal Avenue. Student Member AIAA.
†Professor, Department of Aerospace Engineering, 1320 Beal Avenue. Associate Fellow AIAA.
‡Senior Aerospace Engineer, AFRL/RBAC, 2210 Eighth Street, Building 146, Room 225. Associate Fellow AIAA.

is limited because the bow shock surrounding the vehicle will impinge on surfaces that extend beyond the shock envelope. This results in extreme pressure and heat transfer rates at the impingement point. As such, vehicle configurations tend to be streamlined with minimal protrusions from the fuselage. Mechanically driven flaps require clearance below the surface of the flap to provide space for the flap control arm and a strong attachment point to push from. In addition, there is a small gap in the TPS as the flap extends out to deflect the flow. This gap is difficult to protect and can cause heat-related damage to the vehicle. In addition, sustained cruise and other long-duration hypersonic missions also suffer from nonuniform ablation of the flap causing nonuniform control authority on the vehicle.

Plasma actuators are advantageous over mechanical controllers because they do not have moving parts, can be located either in or beneath the TPS, and are uninhibited by the bow shock. This extends the range of possible locations for the actuator and allows for multiple actuators to be powered by a central energy source. They can potentially be turned on and off very rapidly and should have a minimal aerothermal penalty when turned off. Plasma actuators can serve multiple roles. They can be used to provide steering moments [11,12], changes in vehicle lift [13], control of flow separation [14,15], and local heat load mitigation [16].

The primary objective of this research effort is to determine whether a useful degree of flight control can be achieved with practical levels of energy deposition by investigating the effects of energy deposition on a realistic hypersonic vehicle and its surrounding flowfield. In the following, we first present validation studies of the flow code LeMANS (Michigan aerothermodynamic Navier–Stokes) using relevant experimental data available in the literature. Having successfully validated LeMANS, the code is applied to investigate plasma-based aerodynamic control. We investigate how the shape, location, and input power of deposition affect vehicle control. In addition, hot wall effects, thermodynamic models, and additional vehicle configurations are explored to help draw conclusions over different flight regimes.

II.   Method

Flowfield results are obtained using computational fluid dynamics (CFD) to solve the Navier–Stokes equations. The CFD computations are executed using the LeMANS code, which was developed at the University of Michigan [17–20].

LeMANS is a general 2-D/axisymmetric/3-D, parallel, unstructured, finite-volume CFD code. The numerical fluxes between cells are discretized using a modified Steger–Warming flux vector splitting (FVS) scheme, except near shock waves. In these regions the original Steger–Warming FVS scheme is used.

LeMANS may be employed with any of three thermodynamic models: perfect gas, equilibrium thermochemistry, and nonequilibrium. LeMANS employs a two-temperature model to account for thermal nonequilibrium and a standard finite-rate chemistry model for nonequilibrium chemistry. The two-temperature model assumes that a single temperature T accounts for the translational and rotational energy modes of all species whereas the vibrational and electronic energy modes are accounted for by a separate temperature T_v.

The simulations are performed using second-order accurate spatial discretization and carry double-precision arithmetic throughout. Thermal equilibrium and a 5-species finite-rate air chemistry model (N_2, O_2, NO, N, and O) are used in the simulations presented unless otherwise stated.

For a single temperature (equilibrium) model with finite-rate chemistry

$$\frac{\partial \rho_s}{\partial t} + \nabla \cdot (\rho_s \mathbf{u} + \mathbf{J}_s) = \dot{\omega}_s \qquad (1)$$

$$\frac{\partial \rho \mathbf{u}}{\partial t} + \nabla \cdot (\rho \mathbf{u}^2 + p\delta - \tau) = 0 \qquad (2)$$

$$\frac{\partial E}{\partial t} + \nabla \cdot ((E + p)\mathbf{u} - \tau \cdot \mathbf{u} - \mathbf{q} + \Sigma \mathbf{J}_s h_s) = S \qquad (3)$$

For the two-temperature (nonequilibrium) cases, the following vibrational energy equation is also employed:

$$\frac{\partial E_v}{\partial t} + \nabla \cdot ((E_v)\mathbf{u} - q_v + \Sigma \mathbf{J}_s e_{v,s}) = \dot{\omega}_v \qquad (4)$$

LeMANS assumes the fluid is continuous and Newtonian. It assumes Stokes' hypothesis when determining the viscous stresses. The species mass diffusion flux ($\mathbf{J}_s$) is determined using Fick's law modified to enforce that the sum of the diffusion fluxes is zero and plasma charge neutrality. A harmonic oscillator is used to model the species vibrational energy per unit mass ($e_{v,s}$).

For the nonequilibrium cases, we assume that 100% of the deposition energy goes initially into the translational energy equation. As the solution converges, some of the energy transfers into the vibrational energy equation by means of the source term ($\dot{\omega}_v$). Production of vibrational energy ($\dot{\omega}_v$) is due to reactions in the finite-rate chemistry model and energy exchange between the translational–rotational and the vibrational–electronic energy modes. Deposition of all the energy into the translational mode is a strong assumption but is adequate for the purpose of illustrating the effects of thermal nonequilibrium.

A thermal actuator is considered as the plasma control device in this study. It is represented by a phenomenological model of dissipative heating. This model is accounted for in the Navier–Stokes equations by the addition of a source term S to the right side of energy Eq. (3). The shape and location of the actuator are modeled with contours of constant S having an ellipsoidal shape [21]. The strength or total power deposited into the flow uses exponential decay from the centroid of the energy deposition pattern

$$S = \frac{Q}{\pi^{32} a \cdot b \cdot c} e^{(-(\frac{\hat{x}}{a})^2 - (\frac{\hat{y}}{b})^2 - (\frac{\hat{z}}{c})^2)} \qquad (5)$$

$$\begin{aligned}\hat{x} &= (x - x_0)\cos\phi - (z - z_0)\sin\phi \qquad \hat{y} = (y - y_0)\\ \hat{z} &= (x - x_0)\sin\phi + (z - z_0)\cos\phi\end{aligned} \qquad (6)$$

Variables a and b are the equatorial radii (along the x and y axes) and c is the polar radius (along the z-axis for an ellipsoid with 0 deg inclination to the freestream). The angle ϕ is the angle between the major axis of the ellipsoid and the freestream flow. Coordinates (x_0, y_0, z_0) represent the centroid of the ellipsoid. Note that Q represents the total power deposited in the flow and $\iiint_{-\infty}^{\infty} S \mathrm{d}x \mathrm{d}y \mathrm{d}z = Q$.

III.   Validation

LeMANS is validated for two different hypersonic cases. Simulations for hypersonic laminar airflow over blunt and sharp cones are compared to experimental work. These experimental validation cases are selected because they are considered representative of the two main types of realistic hypersonic air-vehicle geometries and because of the limited amount of experimental data available.

A.   3-D Sharp Elliptic Cone

3-D calculations are carried out for a Mach 8 sharp elliptic cone originally studied experimentally by Kimmel et al. [22,23]. The cone was mounted parallel to the freestream and consisted of a 2:1 aspect ratio, a half-angle along the major axis of 14 deg, and a length $L = 1.016$ m. It was machined from stainless steel with a 40 μm nose radius and surface roughness less than 0.81 μm. The flow conditions are listed in Table 1.

A structured grid is generated because it is known to produce better results than unstructured meshes in regions near the surface of the body and through a shock [24]. One quarter of the geometry is

Table 1 Flow conditions for the experiment of Kimmel et al. [22,23]

Parameter	Value
M	7.93
u_∞	1180.0 m/s
T_∞	54.6 K
T_w	303.0 K
T_0	728.0 K
p_∞	165.0 Pa
ρ_∞	0.011 kg/m^3
μ_∞	3.77×10^{-6} kg/m $\cdot$ s
Re_L	3.33×10^6

used in the simulation because planes of symmetry exist along the major and minor axes. The 40 μm nose radius is accounted for along the tip's minor axis, resulting in an 80 μm radius along the major axis because of the elliptic geometry.

The model is aligned with the x axis in the axial direction, the y axis in the horizontal direction, and the z axis in the vertical direction. A cylindrical coordinate system is also employed with $\theta = 0$ deg at the top centerline of the model (z axis) and $\theta = 90$ deg at the leading edge (y axis), as seen in Fig. 1.

A gradual increase in grid spacing is used along the conic body with the smallest spacing near the tip. Radial points are algebraically spaced to increase the number of points close to the body. Grid points are equally spaced along the circumference. As a result, cell clustering occurs near the surface and the tip of the body. A grid independence study is conducted with $i \times j \times k$ grid dimensions changing from $330 \times 40 \times 30$ to $440 \times 50 \times 40$ to $550 \times 60 \times 50$. Based on comparisons of the solutions obtained on these meshes the $440 \times 50 \times 40$ grid is considered sufficiently refined and is used in the rest of the analysis. See [25] for more details.

Cross-sectional slices of the computed surface conditions are extracted to match the locations of the experimental measurements. Figure 2a shows the nondimensional pressure along the circumference of the body at $x/L = 0.625$. The pressure is relatively constant from the top centerline ($\theta = 0$ deg) to the shoulder ($\theta = 45$ deg), followed by a noticeable rise between the shoulder and the leading edge ($\theta = 90$ deg). Kimmel et al. [22,23] also provided computational results from a parabolized Navier–Stokes (PNS) solver, which are included in the figures as an additional reference.

Although the cone is sharp, the formation of the boundary layer at its tip results in a noticeable rise in pressure and temperature near the stagnation point. This rise in pressure can be seen in Fig. 2b for two different rays. The pressure quickly relaxes as the flow proceeds along the rest of the cone due to the viscous interaction. It is worth noting that the PNS solution does not capture the behavior of the flowfield in the stagnation region of the cone because of the physical simplifications inherent in that method.

The high-length Reynolds number (Re_L) and overall length of the model cause the flow to transition to turbulence as it proceeds along the body. LeMANS does not currently have a turbulence model implemented, and so numerical results in the transitional and turbulent regions should be disregarded. Plots of the Stanton number as a function of Reynolds number are presented in Figs. 3a–3c for

$\theta = 0$, 45, and 88 deg. In all three plots, the flow starts out laminar and then transitions to turbulent as it proceeds along the body. The measured data were for $Re_L = 1.7 \times 10^6$ and 6.6×10^6, whereas the case run by LeMANS has $Re_L = 3.3 \times 10^6$. Because of flow similarity, the length Reynolds number does not affect the Stanton number in the laminar region and LeMANS accurately predicts its distribution for these cases.

B. 3-D Blunt Elliptic Cone

A second 3-D validation study is performed on a Mach 14 blunt elliptic cone originally studied experimentally by Nowlan et al. [26] The model was mounted parallel to the freestream and had a 2:1 aspect ratio, a half-angle along the major axis of 10 deg, and a length $L = 0.21$ m. Details of cone geometry are provided in Fig. 4. The flow conditions are listed in Table 2.

A structured grid is generated following the same procedures and coordinate system as the sharp elliptic cone. A grid independence study is conducted with $i \times j \times k$ grid dimensions changing from $150 \times 30 \times 30$ to $300 \times 60 \times 60$ to $380 \times 80 \times 80$. The $300 \times 60 \times 60$ grid is considered sufficiently refined and is used in the rest of the analysis. Additional details on grid convergence are available in [25].

Figure 5 shows the nondimensional pressure along the circumference of the body at two axial locations and along two rays. Following a similar trend as the sharp cone observations, the pressure is relatively constant from the top centerline to the shoulder, followed by a gradual rise between the shoulder and the leading edge. The variation in pressure distribution along the rays is more dramatic compared with the sharp cone because the blunt-tip results in a strong detached bow shock and, consequently, a large stagnation region. Stanton number distributions in Fig. 6 show the profiles obtained with LeMANS follow the same general trends as those observed in the measurements.

Overpredictions observed in the nondimensional pressure and Stanton number distributions may be due to several influences not
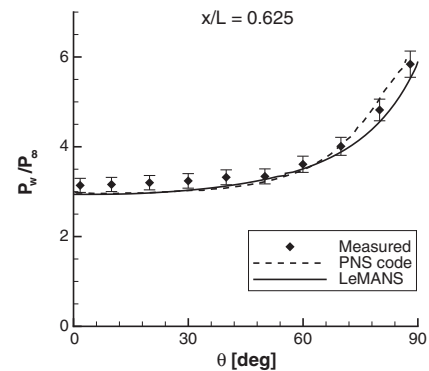
a) **Pressure around the circumference**
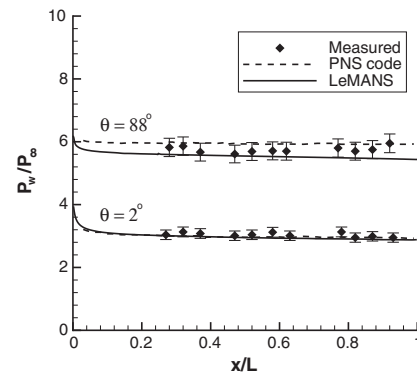
b) **Pressure along rays**

Fig. 2 **Normalized surface pressure distributions for the Mach 8 sharp elliptic cone ($\pm 5\%$ experimental uncertainty), with PNS calculations and experimental data from [22].**

Fig. 1 **Surface of the sharp elliptic cone grid with both Cartesian and cylindrical coordinate systems.**

a) Top centerline, $\theta = 0^\circ$

b) Shoulder, $\theta = 45^\circ$

c) Leading edge, $\theta = 88^\circ$
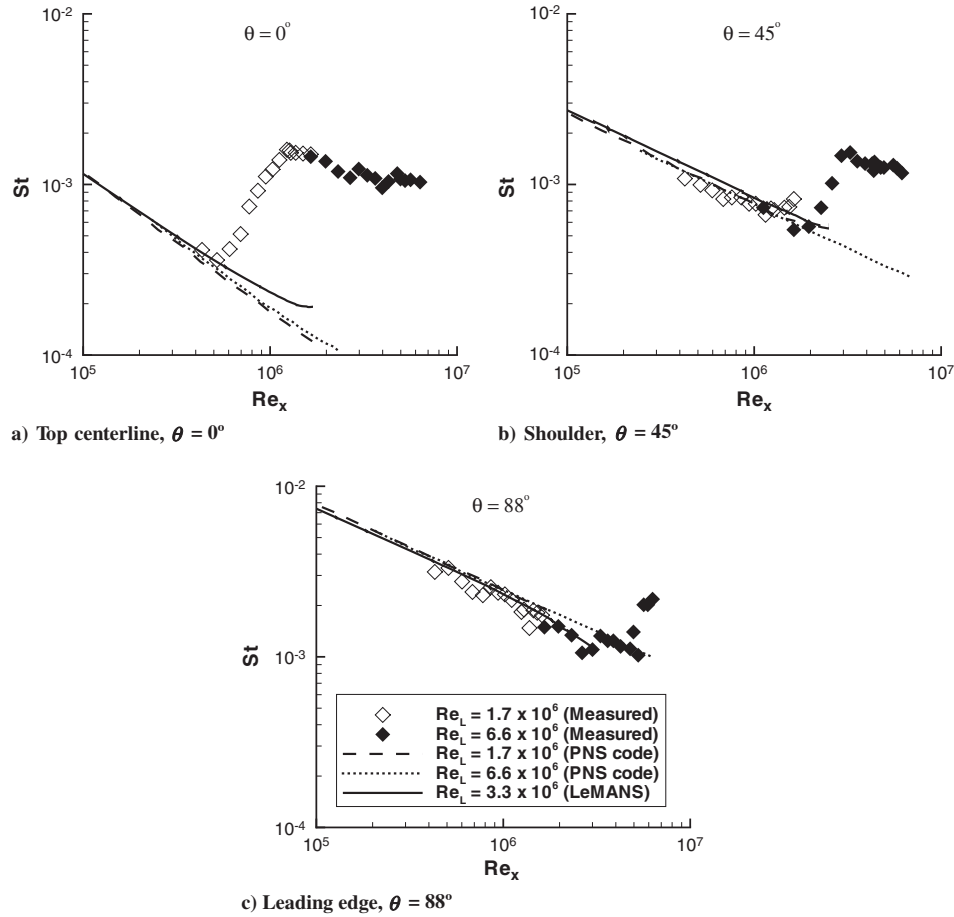
Fig. 3 Stanton number distributions for the Mach 8 sharp elliptic cone (symbol size reflects $\pm 10\%$ experimental uncertainty), with experimental data and PNS calculations from [22].
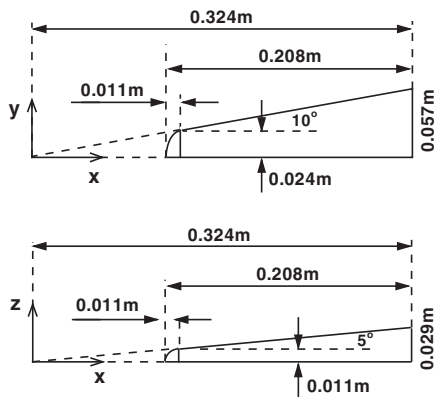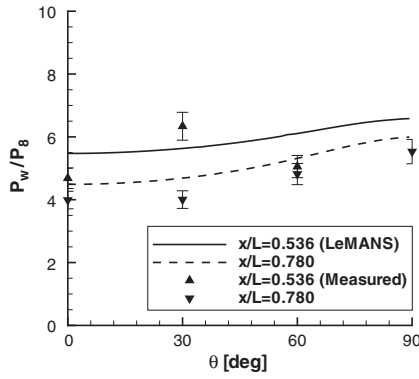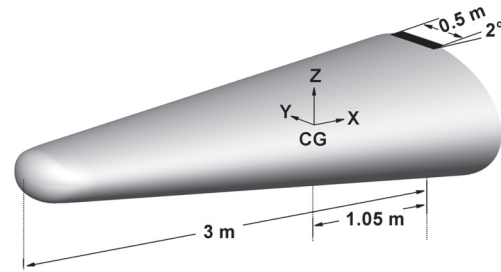

Fig. 4 Blunt elliptic cone geometry, from [26].

IV. Energy Deposition

The blunt elliptic cone geometry is selected to represent a fairly realistic hypersonic vehicle, with $L = 3$ m set as the representative vehicle length. Assuming the vehicle has constant material density, its center of gravity (CG) is located 1.95 m from the tip along the x axis ($x/L = 0.65$). The model is simulated in air at a 40 km altitude, a freestream velocity of 4000 m/s, and a 0 deg angle of attack. The complete flow conditions are provided in Table 3.

A grid independence study is conducted with $i \times j \times k$ grid dimensions changing from $300 \times 60 \times 60$ to $380 \times 80 \times 80$ to $400 \times 80 \times 120$. Grid independence is achieved with the $380 \times 80 \times 80$ grid that is used in the following simulations that include energy deposition. Details on the grid convergence study are available in [25].

accounted for in the simulations. Nowlan et al. [26] noted an uncertainty of ± 7 percent in the freestream flow conditions and the very cold freestream flow conditions ($T_\infty = 59.3$ K) could have lead to condensation on the nozzle. In addition, the CAL 48 in. shock tunnel could have developed "frozen" freestream conditions ($T_v \gg T_\infty$) as the flow accelerated through the nozzle. Nompelis et al. [27] computationally demonstrated that accounting for vibrational nonequilibrium freestream conditions greatly improved agreement between computational and experiment heat transfer measurements collected in a CAL shock tunnel for their hypersonic double-cone experiment. Despite the discrepancies, overall, LeMANS effectively demonstrates its capability of accurately computing 3-D hypersonic flows.

Table 2 Flow conditions for run 15 of the Nowlan et al. experiment [26]

Parameter	Value
Mach	14.2
u_∞	2190. m/s
T_∞	59.3 K
T_w	294.0 K
T_0	211.0 K
p_∞	51.0 Pa
ρ_∞	0.003 kg/m^3
μ_∞	4.3×10^{-6} kg/m $\cdot$ s
Re_L	3.17×10^5

a) Pressure around the circumference
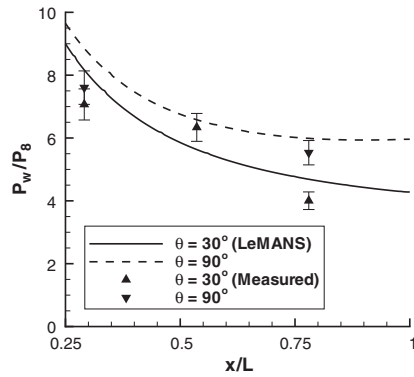
b) Pressure along rays

Fig. 5 Normalized surface pressure distributions for Mach 14 blunt elliptic cone ($\pm7\%$ experimental uncertainty), with experimental data from [26].

a) Stanton number around the circumference

b) Stanton number along rays

Fig. 6 Stanton number distributions for Mach 14 blunt elliptic cone (symbol size reflects $\pm4.5\%$ experimental uncertainty), with experimental data from [26].

A. Reference Pitching Moment

A nominal reference pitching moment is found by assuming a 2 deg flap with a cross-sectional area of 0.2×0.5 m is attached along the vehicle's top centerline as illustrated in Fig. 7. The size and location of the flap are based on illustrations of the hypersonic test vehicle shown in [28]. The control authority provided by the mechanical flap is estimated computationally by incorporating the flap with the blunt elliptic cone geometry.

The flap is accounted for in the blunt elliptic cone geometry by flaring the last 0.2 m of the cone. The flair extends around the circumference of the cone and has a 2 deg inclination. Extending the flair around the circumference of the body simplifies the geometry and eliminates unnecessary complexities (i.e., modeling the edge of the extended flap). Because the spanwise width of the actual flap extends 0.25 m ($\theta = 18$ deg) from the top centerline ($\theta = 0$ deg), the estimated control authority provided by the flap is computed by multiplying the increased body force within that region by its moment arm (1.05 m). This results in a pitching moment ($M_{p_{\text{flap}}}$) of 22.8 N $\cdot$ m.

Table 3 Flow conditions for Mach 12.6 airflow at an altitude of 40 km

Parameter	Value
Mach	12.6
u_∞	4000.0 m/s
T_∞	250.0 K
T_w	300.0 K
T_0	8300.0 K
p_∞	289.0 Pa
ρ_∞	0.004 kg/m^3
μ_∞	1.6×10^{-5} kg $\cdot$ m $\cdot$ s
Re_L	3.0×10^6

Fig. 7 Model of a 2 deg mechanical flap attached to a blunt elliptic body.

B. Parametric Study

To limit the scope of the problem, three volumetric deposition shapes are selected. Namely a sphere, pancake (oblate spheroid), and bean (prolate spheroid) are employed such that a representative volume of the ellipsoidal region ($V = 4/3\pi abc$) remains constant. The values used are listed in Table 4.

The centroid of the deposition is positioned along the top centerline ($y_0 = 0$ m) and is at least three characteristic length scales (λ) away from the surface of the body to ensure the entire deposition is deposited into the flowfield ($\iiint_{3\lambda}^{3\lambda} S \mathrm{d}x \mathrm{d}y \mathrm{d}z = 0.9999Q$). This distance is the minimum length from the centroid of a spherical deposition to the surface of the body as illustrated in Fig. 8:

$$x_0 = x_1 + 3\lambda \cdot \|n_{x_1}\| \tag{7}$$

$$z_0 = z_1 + 3\lambda \cdot \|n_{z_1}\| \tag{8}$$

Table 4 Deposition geometry parameters for a Mach 12 blunt elliptic cone ($L = 3$ m)

	a	b	c
Sphere	0.007 m	0.007 m	0.007 m
Pancake	0.01852 m	0.01852 m	0.001 m
Bean	0.001852 m	0.1 m	0.001852 m

$$\phi = \tan^{-1}\left\|\frac{n_{x_1}}{n_{z_1}}\right\| \tag{9}$$

With $3\lambda = 3a$, the values of z_0 and ϕ are determined for a given x_0 by enforcing Eqs. (7) and (8). This determines the location of $[x_1, z_1]$ and its outward unit normal vector **n**. Equation (9) is used to determine ϕ so that the polar radii of the ellipsoidal deposition aligns with **n**. The oblate spheroid is positioned so that its major axis is parallel to the freestream flow, whereas the major axis of the prolate spheroid is perpendicular to the freestream flow.

Using the Mach 5 flat plate experiment originally studied by Kimmel et al. [29,30] and recent magnetohydrodynamic power-

Fig. 8 The constant height parameter used to determine z_0 and ϕ.

generation experiments [31] for reference, realistic power input is assumed to lie in the range of 1 to 15 kW. The deposition is positioned near the nose of the vehicle tip to maximize the distance from the CG. This is done not only to increase the moment arm of the body force due to the deposition, but also because larger force changes are observed when the actuator is placed near the leading-edge bow shock [13]. The three deposition shapes are studied with variation of two additional parameters: the deposition input power (Q) and the distance along the body (x/L).

The total amount of power deposited into the flow is characterized by the nondimensional total power deposition value $\tilde{Q}$:

$$\tilde{Q} = \frac{Q}{\rho_\infty u_\infty^3 L^2} \tag{10}$$

For the cases in the study $\tilde{Q} = 4.3 \times 10^{-7}$, 1.7×10^{-6}, and 6.5×10^{-6} for $Q = 1$, 4, and 15 kW, respectively. This parameter provides some information on vehicle and application scaling.

The axial location of the energy deposition is apparent after investigating the pressure coefficient and Stanton number along the top centerline ($\theta = 0$ deg) for the three shapes in Fig. 9. Although there is a slight increase in the Stanton number, it is accompanied by a noticeable rise in the pressure coefficient, particularly in the sphere and pancake depositions. This may be due to the fact that a sphere has the minimum surface area of a spheroid and, consequently, has the highest power deposited per projected surface area onto the body. The total force acting on the body is determined by numerical integration of the pressure and viscous force components over the body surface, using a method consistent with the finite-volume formulation of LeMANS.

With the local force known, the pitching moment is determined in the conventional manner. Because of the deposition on the top half of the vehicle, the pitching moment for each scenario is its deviation from the baseline ($M_p = M_{p_{\text{deposition}}} - M_{p_{\text{baseline}}}$). It is normalized by the moment due to the mechanical flap ($M_{p_{\text{flap}}} = 22.8$ N · m). Figure 10 plots the normalized change in pitching moment for each

a) Sphere deposition

b) "Pancake" deposition

c) "Bean" deposition
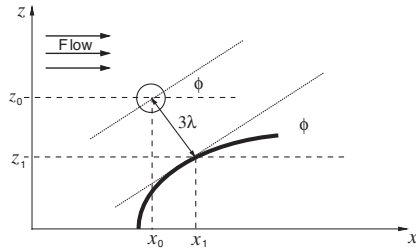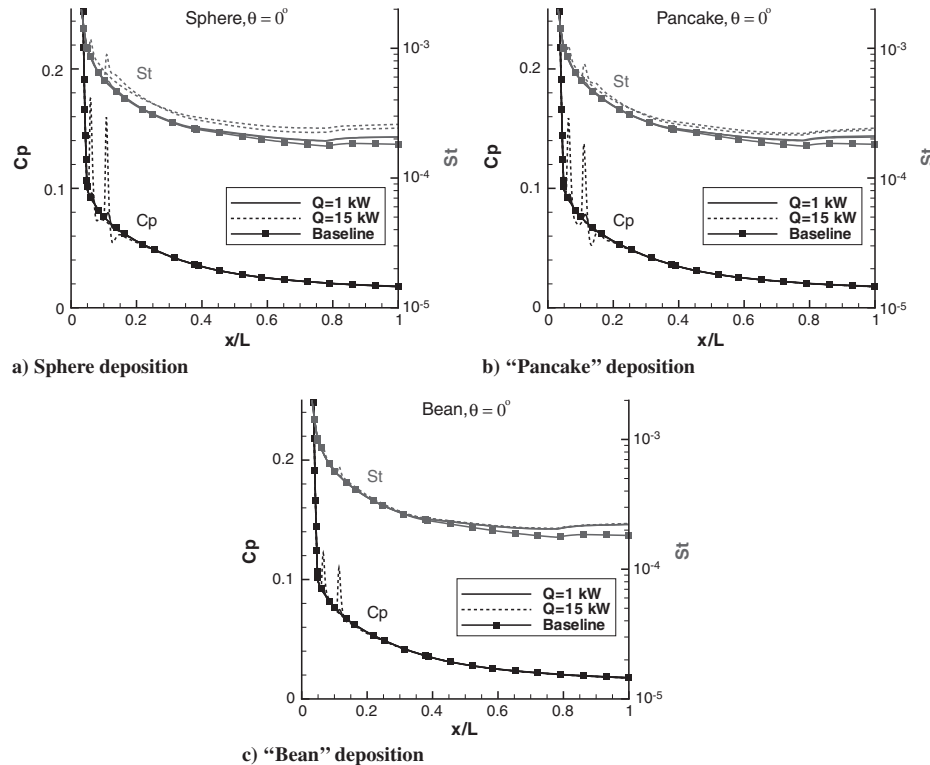
Fig. 9 Pressure coefficient and Stanton number distributions for the Mach 12 blunt elliptic cone ($L = 3$ m) for various energy deposition patterns along the top centerline ($T_w = 300$ K).

of the shapes. The points are fitted with a parametric spline because of their assumed nonlinearity.

All simulations are computed assuming thermal equilibrium and use a 5-species finite-rate chemistry model (N_2, O_2, NO, N, and O) except for the largest deposition scenario ($Q = 50$ kW, $x/L = 0.10$, pancake). This scenario is repeated for two additional conditions: thermal equilibrium, 11-species chemistry model; and thermal non-equilibrium, 11-species chemistry model. The 11-species chemistry model (N_2, O_2, NO, N, O, N_2^+, O_2^+, NO^+, N^+, O^+, e) accounts for weakly ionized plasmas. These additional cases are compared against their respective baseline cases to determine the effectiveness of the deposition.

For thermal equilibrium air, the inclusion of a larger chemistry model has a relatively small impact on the total pitching moment as seen in the $Q = 50$ kW case [equilibrium, 5 sp (species) vs equilibrium, 11 sp]. Thermal nonequilibrium noticeably reduces the effectiveness of the energy deposition because only the energy going into the translational temperature can affect the local pressure and, thus, the net force. Comparing the results for the thermal equilibrium, 5-species simulations to the thermal nonequilibrium, 11-species simulations for the $Q = 30$, 50 kW cases, it is clear that thermal nonequilibrium and weakly ionized plasma effects become increasing significant as the total power deposited increases and the flow deviates from a perfect gas.

Figure 10 shows energy deposition is able to provide the same order of magnitude of control authority as the mechanical flap. In addition, although the shape of the deposition appears to have noticeable effects on the local pressure coefficient and Stanton number, it does not appear to have a large impact on the overall change in the pitching moment (control authority).

C. Hot Wall Effect

The previous simulations used a constant wall temperature of 300 K as seen Table 3. This is cooler than the expected wall temperature of a real hypersonic vehicle. Assuming blackbody emissivity ($\epsilon = 1$), the Stefan–Boltzmann Law is used along with the computed heat flux on the body to estimate the expected wall temperature:

$$T_w = \left(\frac{q_w}{\epsilon \sigma} \right)^{1/4} \qquad (11)$$

This estimated wall temperature varies from 600–1900 K along the cone, with an average temperature of 1000 K in the region where the deposition would be located. A new set of simulations is carried out with $T_w = 1000$ K and all other conditions equal to those listed in Table 3. The simulations are performed using the pancake deposition parameters listed in Table 4 and the centroid of the deposition located at $x/L = 0.1$. The moment coefficient is calculated for each simulation using Eq. (12):

$$C_m = \frac{M_p}{\frac{1}{2} \rho_\infty u_\infty^2 L^2 d} \qquad (12)$$

The reference area is taken to be the maximum spanwise width ($d = 1.644$ m) multiplied by the body length ($L = 3$ m). Figure 11 plots the moment coefficient vs power deposited for two constant wall temperatures. The higher wall temperature reduces the moment coefficient (control authority) of the vehicle because a larger portion of the energy deposited goes into the higher energy modes (i.e., rotation, vibration, and dissociation) instead of the translational energy mode.

V. Additional Vehicle Configurations

The freestream conditions used in the simulations of the 3 m configuration (Table 3) are also applied to two additional, scaled geometries. The "medium" scaled vehicle has a length $L = 0.62$ m. The nondimensional total power deposition value $\tilde{Q}$ for the cases run is $\tilde{Q} = 4.0 \times 10^{-5}$, 1.0×10^{-4}, and 1.5×10^{-4} for $Q = 4$, 10, and 15 kW, respectively.

The deposition is modeled as an oblate spheroid (pancake), scaled to match the one used in the $L = 3$ m parametric study. The energy deposition volume is positioned near the bow shock ($x/L = 0.10$) with its equatorial radii and polar radius set as $a = b = 0.00386$ m and $c = 0.00021$ m.

The moment coefficient for the simulations is found using Eq. (12) with $d = 0.343$ m. The pitching moment due to the mechanical flap is found following the approach covered in Sec. IV.A with the large geometry flap dimensions proportionately scaled (10.5×4.2 cm). This results in a pitching moment ($M_{p_{\text{flap}}}$) of 0.148 N · m. The smaller geometry produces a weaker bow shock and consequently a lower post-shock temperature. Similar to Sec. IV.C, the cooler temperature improves the control authority provided by energy deposition. However, a large spike in the Stanton number distribution is observed in Fig. 12. This coincides with the location of the deposition and partially recovers to the baseline distribution as the flow progresses along the body. The distribution can not fully recover because of the additional energy added to the flow.

The effects of energy deposition are also simulated for several cases using a "small" $L = 0.21$ m blunt elliptic cone with freestream conditions found in Table 2. These conditions represent an altitude of 42 km in air, based on the unit Reynolds number. The decrease in freestream velocity along with the significantly smaller geometry increases the nondimensional total power deposition value $\tilde{Q}$ by several orders of magnitude. For the cases' run, $\tilde{Q} = 4.0 \times 10^{-4}$, 8.0×10^{-4}, and 1.6×10^{-3} for $Q = 500$ W, 1 kW, and 2 kW, respectively.

The deposition is modeled as an oblate spheroid (pancake), similar to the one used in the $L = 3$ m parametric study. The energy deposition volume is positioned near the bow shock with its centroid at $x_0 = 0.0292$ m, $y_0 = 0$ m, and $z_0 = 0.017$ m, and its equatorial radii and polar radius are $a = 0.003$ m, $b = 0.004$ m, and $c = 0.001$ m, with $\theta = 0$ deg. Unlike the medium cone, the deposition shape is larger than a proportionally scaled large cone deposition, and the deposition's polar radius is not quite aligned to the surface's normal vector (**n**). The parametric study presented in Sec. IV.B

Fig. 10 Normalized change in pitching moment for a Mach 12 blunt elliptic cone ($L = 3$ m) for various energy deposition patterns ($T_w = 300$ K).
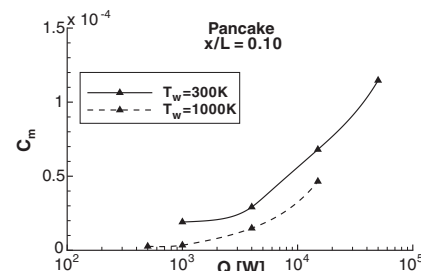
Fig. 11 Moment coefficient for a Mach 12 blunt elliptic cone ($L = 3$ m) for two constant wall temperatures.
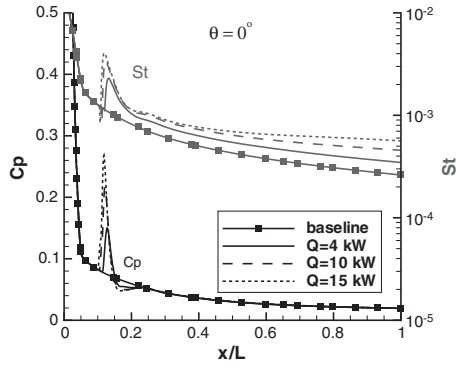
130

Fig. 12 Pressure coefficient and Stanton number distributions along the top center line ($\theta = 0$ deg) of a Mach 12 blunt elliptic cone ($L = 0.6$ m) with different amounts of energy deposition ($T_w = 300$ K).
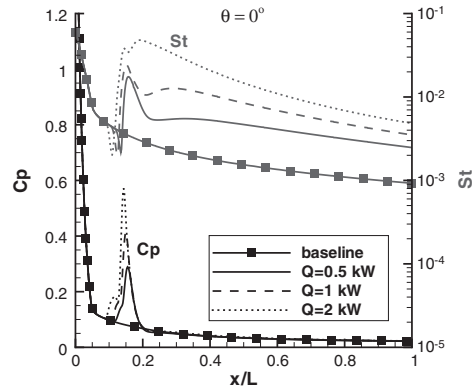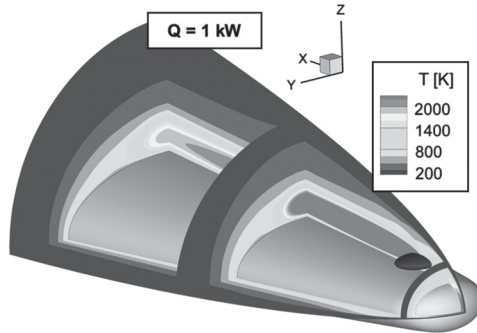

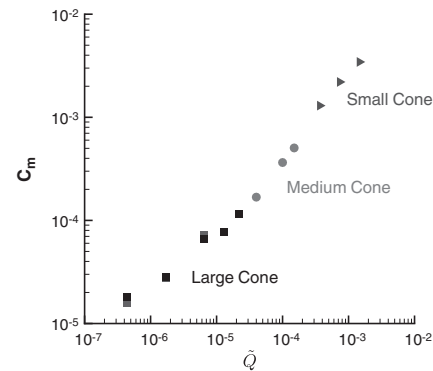**Fig. 13   Temperature contours for Mach 14 blunt elliptic cone ($L=$ 0.2 m) with $Q = 1$ kW.**

Fig. 14 Pressure coefficient and Stanton number distributions along the top center line ($\theta = 0$ deg) of a Mach 14 blunt elliptic cone ($L = 0.2$ m) with various levels of energy deposition ($T_w = 294$ K).

a) Moment coeffcient

b) Nondimensional pitching moment

Fig. 15   Moment coefficient and normalized change in pitching moment vs the nondimensional total power deposition $\tilde{Q}$ for various vehicle configurations ($T_w = 300$ K, thermal equilibrium, 5 sp, pancake deposition).

suggests the deposition shape has a minimal effect on the resulting pitching moment. This indicates these simulations are relevant and particularly useful when drawing conclusions across different configurations. The energy deposition is also positioned slightly farther from the nose than the previous case ($x/L = 0.14$).

Compared with the previous configurations, the small geometry produces an even weaker bow shock, which further reduces the post-shock temperature. In addition, the freestream temperature and total enthalpy are much lower in these simulations (refer to Table 2). This allows for a larger portion of the deposition to increase the translational temperature (net force increase). In addition, the shorter body length (L) means the flow passes over the vehicle quicker, and so the large temperature rise observed within the region of the deposition extends farther along the vehicle. This is apparent in the significant downstream temperatures observed in Fig. 13, where the deposition is illustrated as the oblate spheroid centered above the top centerline near the leading bow shock.

Coinciding with the high temperature, a strong heat transfer penalty is detected, along with a dramatic increase in the pressure coefficient distribution (Fig. 14). Although the Stanton number remains significantly elevated downstream of the deposition, the pressure coefficient quickly returns to the baseline (equilibrium) state, which is consistent to the observations seen in the large and medium cone simulations.

The moment coefficient is found using Eq. (12) with $d=$ 0.114 m. Consistent with previous simulations, the pitching moment due to the mechanical flap is computed following the method presented in Sec. IV.A with the large geometry flap dimensions scaled down proportionately (3.5×1.4 cm). This results in a pitching moment ($M_{p\text{flap}}$) of 10^{-3} N · m.

These results, along with those obtained for the medium and large blunt elliptic cone simulations, are plotted together in Fig. 15 using the nondimensional total power deposition parameter $\tilde{Q}$. Figure 15a shows a strong correlation between $\tilde{Q}$ and the moment coefficient for the various simulations. As previously noted, the scale deposition shape of the small cone does not exactly match the medium or large

cones, but these results further demonstrate the minimal contribution deposition shape has on the net control authority. The results appear to follow a near linear curve when plotted on a log–log scale ($C_m \approx \tilde{Q}^{1.1}$). The different deposition locations, along with different vehicle lengths and freestream conditions, and real gas effects cause the results to deviate slightly from the linear curve.

Using the reference pitching moment found for each of the configurations, the normalized pitching moment for each configuration is plotted in Fig. 15b. Again, the results follow a near-linear curve on a log–log scale ($M_p/M_{p\text{flap}} \approx \tilde{Q}^{1.3}$) with deviations from the curve due to the aforementioned reasons. The figure shows that energy deposition is a viable replacement for a mechanical flap when $\tilde{Q} \geq 10^{-5}$. Given that $\tilde{Q} = Q/\rho_\infty u_\infty^3 L^2$, this suggests smaller geometries, flying at lower velocities and/or higher altitudes (lower

densities) would make energy deposition a viable replacement for a mechanical flap. A full table of the pitching moment (M_p) for all simulations is available in [32].

VI. Conclusions

A numerical study was performed to investigate whether a practical level of control could be achieved from volumetric energy deposition for a realistic hypersonic vehicle. Using a phenomenological heating model, a parametric study was completed investigating the shape, location, and total amount of energy volumetrically deposited into the flowfield for a blunt-nosed elliptic cone configuration. The shape of the deposition resulted in relatively small changes in the effectiveness of the deposition, whereas an increased wall temperature noticeably decreased the moment coefficient. Thermal nonequilibrium and weakly ionized plasma effects also decrease the control authority as input power increases. The effectiveness of volumetric energy deposition for flight control appeared to scale strongly with the nondimensional parameter based on the freestream flow kinetic energy flux. It appears to be a viable means of control for configurations at higher altitude, with slower velocities and smaller vehicle length.

There is an ongoing effort to replace the phenomenological energy deposition model with a magnetohydrodynamic model in low magnetic Reynolds number approximation. This should provide useful insight by providing a more physical representation of the energy deposition physics.

Acknowledgments

References

[1] Fomin, V. M., Tretyakov, P. K., and Taran, J.-P., "Flow Control Using Various Plasma and Aerodynamic Approaches," *Aerospace Science and Technology*, Vol. 8, No. 5, 2004, pp. 411–421.
doi:10.1016/j.ast.2004.01.005

[2] Shang, J. S., Surzhikov, S. T., Kimmel, R., Gaitonde, D., Menart, J., and Hayes, J., "Mechanisms of Plasma Actuators for Hypersonic Flow Control," *Progress in Aerospace Sciences*, Vol. 41, No. 8, 2005, pp. 642–668.
doi:10.1016/j.paerosci.2005.11.001

[3] Mason, W. H., and Lee, J., "Aerodynamically Blunt and Sharp Bodies," *Journal of Spacecraft and Rockets*, Vol. 31, No. 3, 1994, pp. 378–382.
doi:10.2514/3.26449

[4] Santos, W. F. N., and Lewis, M. J., "Aerothermodynamic Performance Analysis of Hypersonic Flow on Power Law Leading Edges," *Journal of Spacecraft and Rockets*, Vol. 42, No. 4, 2005, pp. 588–597.
doi:10.2514/1.9550

[5] Shang, J. S., Hayes, J., and Menart, J., "Hypersonic Flow over a Blunt Body with Plasma Injection," *Journal of Spacecraft and Rockets*, Vol. 39, No. 3, 2002, pp. 367–375.
doi:10.2514/2.3835

[6] Kremeyer, K., Sebastian, K., and Shu, C.-W., "Computational Study of Shock Mitigation and Drag Reduction by Pulsed Energy Lines," *AIAA Journal*, Vol. 44, No. 8, 2006, pp. 1720–1731.
doi:10.2514/1.17854

[7] Yan, H., and Gaitonde, D., "Control of Edney IV Interaction by Energy Pulse," AIAA Paper 06-562, Jan. 2006.

[8] Riggins, D. W., and Nelson, H. F., "Hypersonic Flow Control Using Upstream Focused Energy Deposition," *AIAA Journal*, Vol. 38, No. 4, 2000, pp. 723–725.
doi:10.2514/2.1020

[9] Macheret, S. O., Shneider, M. N., and Miles, R. B., "Magnetohydrodynamic Control of Hypersonic Flows and Scramjet Inlets Using Electron Beam Ionization," *AIAA Journal*, Vol. 40, No. 1, 2002,

pp. 74–81.
doi:10.2514/2.1616

[10] Shang, J. S., Kimmel, R. L., Menart, J., and Surzhikov, S. T., "Hypersonic Flow Control Using Surface Plasma Actuator," *Journal of Propulsion and Power*, Vol. 24, No. 5, 2008, pp. 923–934.
doi:10.2514/1.24413

[11] Girgis, I. G., Shneider, M. N., Macheret, S. O., Brown, G. L., and Miles, R. B., "Creation of Steering Moments in Supersonic Flow by Off-Axis Plasma Heat Addition," AIAA Paper 02-129, Jan. 2002.

[12] Gnemmi, P., Charon, R., Dupéroux, J.-P., and George, A., "Feasibility Study for Steering a Supersonic Projectile by a Plasma Actuator," *AIAA Journal*, Vol. 46, No. 6, 2008, pp. 1308–1317.
doi:10.2514/1.24696

[13] Menart, J., Stanfield, S., Shang, J., Kimmel, R., and Hayes, J., "Study of Plasma Electrode Arrangements for Optimum Lift in a Mach 5 Flow," AIAA Paper 06-1172, Jan. 2006.

[14] Updike, G. A., Shang, J. S., and Gaitonde, D. V., "Hypersonic Separated Flow Control Using Magneto-Aerodynamic Interaction," AIAA Paper 05-164, Jan. 2005.

[15] Kimmel, R. L., Hayes, J. R., Crafton., J. W., Fonov, S. D., Menart, J., and Shang, J., "Surface Discharge for High-Speed Boundary Layer Control," AIAA Paper 06-710, Jan. 2006.

[16] Miles, R. B., Macheret, S. O., Shneider, M. N., Steeves, C., Murray, R. C., Smith, T., and Zaidi, S. H., "Plasma-Enhanced Hypersonic Performance Enabled by MHD Power Extraction," AIAA Paper 05-561, Jan. 2005.

[17] Scalabrin, L. C., and Boyd, I. D., "Development of an Unstructured Navier–Stokes Solver For Hypersonic Nonequilibrium Aerothermodynamics," AIAA Paper 05-5203, June 2005.

[18] Scalabrin, L. C., and Boyd, I. D., "Numerical Simulation of Weakly Ionized Hypersonic Flow for Reentry Configurations," AIAA Paper 06-3773, June 2006.

[19] Scalabrin, L. C., and Boyd, I. D., "Numerical Simulation of the FIRE-II Convective and Radiative Heating Rates," AIAA Paper 07-4044, June 2007.

[20] Scalabrin, L. C., "Numerical Simulation of Weakly Ionized Hypersonic Flow Over Reentry Capsules," Ph.D. Dissertation, Univ. of Michigan, 2007.

[21] Poggie, J., "Plasma-Based Hypersonic Flow Control," AIAA Paper 06-3567, June 2006.

[22] Kimmel, R. L., Poggie, J., and Schwoerke, S. N., "Laminar-Turbulent Transition in a Mach 8 Elliptic Cone Flow," *AIAA Journal*, Vol. 37, No. 9, 1999, pp. 1080–1087.
doi:10.2514/2.836

[23] Kimmel, R., Klein, M., and Schwoerke, S., "Three-Dimensional Hypersonic Laminar Boundary-Layer Computations for Transition Experiment Design," *AIAA Journal*, Vol. 34, No. 4, 1997, pp. 409–415.

[24] Candler, G., "Unstructured Grid Approaches for Accurate Aeroheating Simulations," AIAA Paper 07-3959, June 2007.

[25] Bisek, N. J., Boyd, I. D., and Poggie, J., "Numerical Study of Energy Deposition Requirements for Aerodynamic Control of Hypersonic Vehicles," AIAA Paper 08-1109, Jan. 2008.

[26] Nowlan, D., Burke, A., and Bird, K., "Pressure and Heat Transfer Distribution on ASD Elliptic Cone (W3) and ASD Sortie (W4) in the CAL 48-Inch Hypersonic Shock Tunnel," Cornell Aeronautical Laboratory, Inc., Rept. AM-1800-Y-2, Buffalo, NY, Dec. 1963, ASC 94 2649.

[27] Nompelis, I., Candler, G., and Holden, M., "Effect of Vibrational Nonequilibrium on Hypersonic Double-Cone Experiments," *AIAA Journal*, Vol. 41, No. 11, 2003, pp. 2162–2169.
doi:10.2514/2.6834

[28] Walker, S. H., and Rodgers, F., "Falcon Hypersonic Technology Overview," AIAA Paper 05-3253, May 2005.

[29] Kimmel, R. L., Hayes, J. R., Menart, J. A., and Shang, J., "Effect of Surface Plasma Discharges on Boundary Layers at Mach 5," AIAA Paper 04-509, Jan. 2004.

[30] Kimmel, R., Hayes, J., Menart, J., and Shang, J., "Supersonic Plasma Flow Control Experiments," U.S. Air Force Research Laboratory, Rept ARFL-VA-WP-TR-2006-3006, Wright–Patterson AFB, OH, Dec. 2005, AFRL/WS 06-0097.

[31] Velocci, A. L. J., "A General Atomics-Led Team," *Aviation Week and Space Technology*, March 2007, p. 36.

[32] Bisek, N. J., Boyd, I. D., and Poggie, J., "Numerical Study of Plasma-Assisted Aerodynamic Control for Hypersonic Vehicles," AIAA Paper 08-4226, June 2008.

A. Ketsdever
Associate Editor

Numerical Study of Magnetoaerodynamic Flow Around a Hemisphere

Nicholas J. Bisek* and Iain D. Boyd†
University of Michigan, Ann Arbor, Michigan 48109
and
Jonathan Poggie‡
U.S. Air Force Research Laboratory, Wright-Patterson Air Force Base, Ohio 45433-7512

Newly developed computational tools are used to compute hypersonic flow around a hemisphere cylinder that uses a magnet located within the body as a means of heat flux mitigation. These tools include an improved electrical conductivity model and a parallelized three-dimensional magnetohydrodynamic module that is loosely coupled to a three-dimensional fluid code. Several electrical conductivity models are explored for a range of magnetic field strengths. Results show the shock standoff distance increases when the magnetic field is applied, but the distance is highly dependent on the conductivity model selected. The increase in shock standoff distance reduces the gradients in the shock layer, thereby reducing the peak heat flux to the body. However, the total heat flux slightly increases due to additional heating to the aft section of the geometry.

Nomenclature

B	=	magnetic field magnitude, T
$\mathbf{B}$	=	magnetic field vector
C_h	=	nondimensional heat flux, $2q_w/[\rho_\infty u_\infty^3]$
C_p	=	pressure coefficient, $[2(p_w - p_\infty)]/[\rho_\infty u_\infty^2]$
E	=	electric field magnitude, V/m
E	=	total energy per volume
$\mathbf{E}$	=	electric field vector
e	=	electron charge, 1.6×10^{-19} C
$\mathbf{j}$	=	current density vector
L	=	geometry length
m_e	=	electron mass, 9.11×10^{-31} kg
N	=	total number density, m^{-3}
n	=	species number density, m^{-3}
p	=	pressure
Q	=	collision cross section, cm^2
$\mathbf{q}$	=	heat flux
r	=	radius
Re_m	=	magnetic Reynolds number, $\mu_0 \sigma u L$
T	=	temperature
$\mathbf{u}$	=	velocity vector (u, v, w)
x, y, z	=	streamwise, spanwise, and transverse coordinates
α	=	degree of ionization
β	=	Hall parameter, $\sigma B/[en_e]$
μ	=	coefficient of viscosity
μ_0	=	permeability of free space, $4\pi \times 10^{-7}$ N/A^2
ν_m	=	electron-neutral particle collision frequency
ρ	=	mass density
σ	=	electrical conductivity, Ω^{-1} m^{-1}
$\tilde{\sigma}$	=	electrical conductivity tensor (including Hall effect)
τ	=	viscous stress
ϕ	=	electric potential, V
χ	=	species mole fraction

Subscripts

n	=	nose
s	=	species
w	=	wall
∞	=	freestream

I. Introduction

THE idea of using an applied magnetic field to reduce the heat transfer to a hypersonic vehicle has been a topic of scientific research since the late 1950s, when Kantrowitz [1] and Resler and Sears [2,3] conducted the first calculations demonstrating the potential benefits an applied magnetic field has on a weakly ionized flow, a condition typically observed during reentry. The magnetic field, if properly aligned, creates a magnetic force that opposes the incoming flow, effectively increasing the shock standoff distance. The thickening of the shock layer reduces the gradients near the stagnation point and thus lowers the peak heat transfer rate. In the midst of the space race, this novel idea attracted a lot of attention as many groups looked to further explore and refine the semianalytical calculations by making various approximations to the conservation equations. Of these efforts, the work by Bush [4,5] is considered to be one of the most complete approximate analytic solutions [6]. Bush's approach used a local solution at the stagnation point of the hypersonic flow over an axisymmetric blunt body and predicted significant flow deceleration with the presence of an opposing magnetic field. The first modern computational fluid dynamics (CFD) simulations of the magnetohydrodynamic (MHD) blunt body problem were completed about a decade later by Coakley and Porter [7]. Because of the lack of computational resources at the time, the simulations still required significant simplifications, including the assumptions that the gas was ideal, nonreacting, and inviscid.

The first experimental work to complement the analytical/ computational activity was completed by Ziemer [8] and focused on measuring the shock standoff distance. Bush's approximate results were in reasonable agreement with this experiment. The first heat transfer measurements for this concept were collected in the

experimental work by Wilkinson [9] for Mach 3 ionized argon at the stagnation point of a blunt cone.

Another experimental effort was conducted by Kranc et al. [10] in the late 1960s. This work provided additional experimental validation sets for the continuing computational efforts, as it explored shock standoff distance and drag measurements for hypersonic flow over two different axisymmetric geometries. These experiments were run in a flow regime where both the viscosity and Hall effect are important, and they confirmed the increase in the shock standoff distance and total drag on the geometry in the presence of an opposing magnetic field. Analysis of the experiment by Nowak et al. [11] and Nowak and Yuen [12] showed the geometries also exhibited an increase in total heating that was attributed to the Hall effect. This was an unanticipated result, because the thickening of the shock layer reduces gradients within the stagnation region, which should reduce the heat flux to the body. In addition, previous semianalytic work had predicted that the Hall effect would only reduce the effectiveness of the magnetic force on increasing the shock standoff distance and total drag on the geometry [13]. Regardless, it was determined that the large magnetic field strength needed to make the technology practical required a magnet that was too heavy to be placed on reentry vehicles, and the research area faded [14].

While hypersonic research continued to experience strong support through the rest of the 20th century due, in part, to various programs like Apollo and shuttle [15], it was not until the mid-1990s that interest in plasma-assisted hypersonic flow control started to reappear [16–18]. This resurgence has been credited to many factors, including the increasing demand for sustained hypersonic flight, rapid access to space, and numerous mechanical and material advances in the area of flight-weight MHD technologies. One of the first to reevaluate the technology using modern CFD techniques was Palmer [19], who performed first-order spatially accurate simulations of the time-dependent Maxwell's equations coupled to the Navier–Stokes equations to analyze a Mars return vehicle. The rising costs for hypersonic experiments and the need for results within a greater range of flowfield conditions for increasing geometric complexity has continued to motivate the development of computational tools that are capable of accurately computing these plasma-based hypersonic flow control devices. This need has spurred numerous computational studies in the recent years, exploring all aspects of plasma-based flow enhancements, including flow control [20–25], local heat load mitigation [26–30], communications blackout [31,32], and MHD power extraction [33–35].

Despite the large financial costs, limited facilities, and technical challenges, some recent experimental studies have been performed by Bityurin et al. [36], Takizawa et al. [37], Kimmel et al. [38], Matsuda et al. [39], and Gülhan et al. [40] to explore electromagnetic effects on hypersonic flows. While these efforts have provided new insight into electromagnetic phenomena in hypersonic flows, more precise measurements, and additional validation exercises for testing the accuracy of fluid-MHD codes, the rising costs (increased maintenance for aging facilities and additional safety protocol) associated with conducting hypersonic experiments greatly limits the number of experiments being conducted. At the same time, supercomputing systems continue to experience exponential performance increases with substantial decreases in cost. This has led to a continued increase in computational research. In fact, Padilla estimates that, if current trends continue, over 70% of hypersonic research will involve computational analysis by 2020 [15].

This work focuses on the previously mentioned experiment conducted by Kranc et al. [10], which was similar to the semi-analytical research conducted by Bush [4,5]. Bush's computational work was previously explored computationally by Gaitonde and Poggie [41,43] and Gaitonde [42]. In the work by Poggie and Gaitonde, several of Bush's [4,5] simplifications were removed, and the Hall effect was added and investigated, while Damevin and Hoffmann [44] explored chemistry effects for a single-temperature model. In both efforts, a simplified model was used to estimate the flow's electrical conductivity. The present work extends these efforts by investigating several electrical conductivity models, including a surrogate model of solutions to Boltzmann's equation. The results

show the change in shock standoff distance due to the presence of the magnetic field corresponds very well with the experimental measurements, especially when employing the newly developed surrogate electrical conductivity model. In addition, the solutions show an increase in total heating to the geometry, which is consistent with the observations made by Nowak et al. [11] and Nowak and Yuen [12]. The increase in total heating is due to a slight increase in heating on the cylinder section (aft) of the geometry.

II. Method

A. Governing Equations

Flowfield results are obtained using CFD to solve the Navier–Stokes equations. The computations are executed using the Michigan aerothermodynamic Navier–Stokes (LEMANS) code, which was developed at the University of Michigan [45,46].

LEMANS is a general two-dimensional (2-D)/axisymmetric/three-dimensional (3-D), parallel, unstructured finite-volume CFD code. The numerical fluxes between cells are discretized using a modified Steger–Warming flux vector splitting (FVS) scheme, except near shock waves. In these regions, the original Steger–Warming FVS scheme is used, because it provides sufficient dissipation to accommodate the discontinuity [47]. LEMANS is able to employ a two-temperature or three-temperature model to account for thermal nonequilibrium and a standard finite-rate chemistry model for nonequilibrium chemistry. The two-temperature model assumes a single temperature T and accounts for the translational and rotational energy modes of all species, while the vibrational energy mode is accounted for by a separate temperature T_{ve}. In the three-temperature model, the rotational energy mode is independent of the translational energy mode [48].

For a single temperature (local thermodynamic equilibrium) model with MHD, but without finite-rate chemistry, the conservation equations are

$$\frac{\partial \rho_s}{\partial t} + \nabla \cdot (\rho_s \mathbf{u}) = 0 \tag{1}$$

$$\frac{\partial \rho \mathbf{u}}{\partial t} + \nabla \cdot (\rho \mathbf{u} \mathbf{u} + p\mathbf{I} - \tau) = \mathbf{j} \times \mathbf{B} \tag{2}$$

$$\frac{\partial E}{\partial t} + \nabla \cdot [(E + p)\mathbf{u} - \tau \cdot \mathbf{u} + \mathbf{q}] = \mathbf{j} \cdot \mathbf{E} \tag{3}$$

where $\mathbf{u}\mathbf{u}$ in the conservation of momentum equation is the 3×3 tensor containing all the products of the components of the velocity vector:

$$\mathbf{u}\mathbf{u} = \begin{bmatrix} u^2 & uv & uw \\ vu & v^2 & vw \\ wu & wy & w^2 \end{bmatrix} \tag{4}$$

LEMANS assumes the fluid is continuous and Newtonian. It also assumes Stokes' hypothesis when determining the viscous stresses:

$$\tau_{ij} = \mu\left(\frac{\partial u_j}{\partial x_i} + \frac{\partial u_i}{\partial x_j}\right) - \frac{2}{3}\mu\nabla \cdot \mathbf{u}\delta_{ij}$$

The total energy deposition term $\mathbf{j} \cdot \mathbf{E}$ appears on the right side of Eq. (3). The conservation of momentum equation is modified to include a magnetic force $\mathbf{j} \times \mathbf{B}$ on the right-hand side of Eq. (2). These additions constitute the effects the current density $\mathbf{j}$, the electric field $\mathbf{E}$, and the magnetic field $\mathbf{B}$ have on the flow.

B. Low-Magnetic Reynolds Number Approximation

The three additional variables appearing in the governing equations ($\mathbf{j}$, $\mathbf{B}$, and $\mathbf{E}$) are determined by first noting that the magnetic Reynolds number [Eq. (5)] is small for the cases of interest:

$$Re_m = \mu_0 \sigma u L \tag{5}$$

134

where the permeability of free space $\mu_0 = 4\pi \times 10^{-7}$ N/A^2, σ is the electrical conductivity, u is the streamwise velocity, and L is the reference length. Consequently, it can be shown that the induced magnetic field can be neglected [49]. This means only external magnetic fields are present in the flow (and must be specified). The current density and electric fields are determined by solving the current continuity equation, which has the form of a Poisson equation, as seen in Eq. (6):

$$\nabla \cdot \tilde{\sigma} \cdot [-\nabla\phi + \mathbf{u} \times \mathbf{B}] = 0 \qquad (6)$$

where $\tilde{\sigma}$ is the electrical conductivity tensor, a compact way of accounting for the Hall effect [50] that is described in the next section. The electric potential ϕ is computed using a finite-volume method and appropriate boundary conditions, as outlined in previous work [51]. The electric field is computed directly from the electric potential ($\mathbf{E} = -\nabla\phi$), which allows the electric current $\mathbf{j}$ to be computed using a generalized form of Ohm's law ($\mathbf{j} = \tilde{\sigma} \cdot [\mathbf{E} + \mathbf{u} \times \mathbf{B}]$). Full details and validation of the MHD solver are available in [51], while [52] provides details on its parallelization and implementation into the fluid code.

C. Hall Effect

As seen in Eq. (6), the MHD module incorporates the tensor nature of the electrical conductivity by following the computational work of Gaitonde [42] and Gaitonde and Poggie [50]. This approach provides a compact way of accounting for ion slip and the Hall effect, phenomena that can change the components of the magnetic force and joule heating of the fluid if the parameters are sufficiently large. Equation (7) shows the electrical conductivity tensor with the Hall effect in Cartesian coordinates:

electrodes are infinitely repeated along the two walls of a channel, as seen in Fig. 1. An externally applied magnetic field is positioned perpendicular to the channel velocity $\mathbf{u}$.

This exercise is inherently 2-D, but it is transformed into three dimensions by allowing the channel walls to be infinitely tall. This modification was necessary, since the MHD module is currently only suited for 3-D simulations. Symmetric boundary conditions are applied to the top and bottom planes of the domain, so the actual height of the channel domain is set to a finite value of 0.1 m for the simulation.

Because the channel is infinitely long, periodic boundary conditions are developed and employed at the domain inlet and outlet. Oliver and Mitchner demonstrated that two of the four global conditions (i.e., streamwise and spanwise current or voltage) are required to determine a unique solution [54]. For this analysis, the applied voltage between the electrode pairs and neighbors is specified (streamwise and spanwise voltages). The voltage between an electrode pair (i.e., the spanwise voltage) is set to unity, while the voltage between electrode neighbors (along the same wall) is set, based on specified scenario. The potential along the insulated wall is determined by setting the current into the insulator to zero ($\mathbf{j} \cdot \mathbf{n} = 0$).

A two-point overlapping stencil, shown in Fig. 2, transfers information between the periodic inlet and outlet planes, while either adding or subtracting the specified streamwise voltage ($\Delta\phi_x$). Since the interior cells are computed using a second-order method, the two-point stencil provides sufficient information to allow the last interior points to be accurately updated. A row of cells starts at the inlet and ends at the outlet (constant y and z). The inlet ghost cell is set equal to the last interior cell next to the outlet (minus the applied streamwise voltage). Likewise, the outlet's ghost cell is set equal to the first interior cell next to the inlet (plus the applied streamwise voltage).

$$\tilde{\sigma} = \frac{\sigma}{B^2(1+\beta^2)} \begin{bmatrix} B^2 + \beta^2 B_x^2 & \beta(\beta B_x B_y - BB_z) & \beta(\beta B_x B_z + BB_y) \\ \beta(\beta B_y B_x + BB_z) & B^2 + \beta^2 B_y^2 & \beta(\beta B_y B_z - BB_x) \\ \beta(\beta B_z B_x - BB_y) & \beta(\beta B_z B_y + BB_x) & B^2 + \beta^2 B_z^2 \end{bmatrix} \qquad (7)$$

where σ is the electrical conductivity of the fluid. B_x, B_y, and B_z are the components of the magnetic field vector, and B is its magnitude. The Hall parameter β is defined in Eq. (8):

$$\beta = \frac{\sigma B}{e n_e} \qquad (8)$$

where σ is the electrical conductivity, an elemental charge $e = 1.6022 \times 10^{-19}$ C, and n_e is the electron number density.

Validation of the Hall effect is performed by using a computational study developed by Hurwitz et al. [53] and rigorously explored by Oliver and Mitchner [54]. In the experiment, finite segmented

Oliver and Mitchner [54] formulated this problem so that the fluid velocity field did not affect the solution as long as $\nabla \times (\mathbf{u} \times \mathbf{B}) = 0$. During one iteration of the flow solver, the MHD routine is executed, assuming the velocity profile is only a function of the distance between the channel walls, $\mathbf{u} = f(y)$. This assumption satisfies $\nabla \times (\mathbf{u} \times \mathbf{B}) = 0$ as long as $\mathbf{B} = f(z)$. The velocity profile is assumed to be a fully developed Poiseuille flow between parallel plates [55], as seen in Eq. (9):

$$\mathbf{u} = f(y) = u_{\max}\left(1 - \frac{(y - y_h)^2}{h^2}\right) \qquad (9)$$

where $u_{\max}$ is the maximum velocity and is set to unity for this scenario ($u_{\max} = 1$ m/s). The y location is measured from the center of the channel width ($y_h = 0.5$ m), so $h = 0.5$ m is the channel half-width.

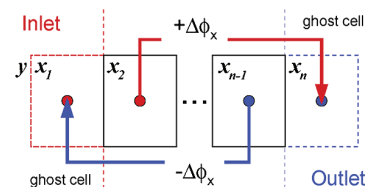**Fig. 1 Schematic of the channel flow with finitely segmented electrodes. Units are in meters.**

Fig. 2 Cartoon of a two-point stencil used for period boundary conditions.

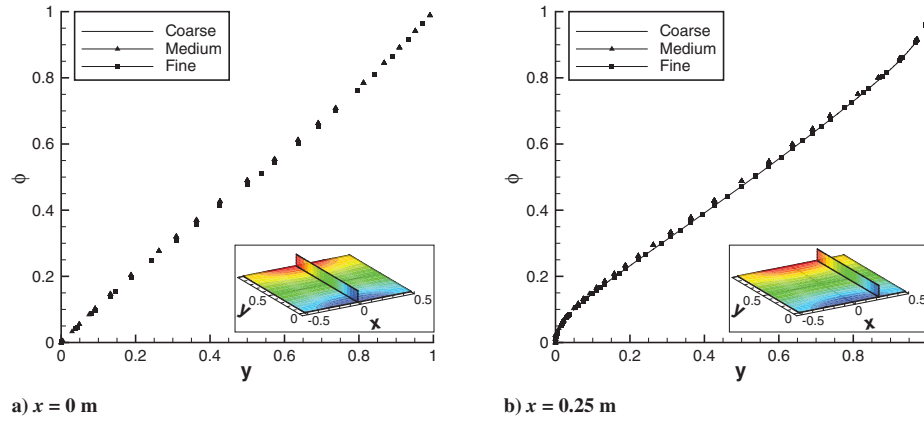**a)** $x = 0$ m   **b)** $x = 0.25$ m

Fig. 3   Electric potential ϕ between two segmented electrodes at two different locations ($x = 0$ and 0.25 m) for various grids ($z = 0$ m).

A grid convergence study was performed using nonreacting argon gas as the fluid, with a constant electrical conductivity $\sigma = 1\ \Omega^{-1}\ \text{m}^{-1}$. The channel walls are 1 m apart, and the segmented electrodes are 0.5 m wide, with 0.5 m of insulated wall between electrode neighbors so that the simulated domain has a length of 1 m in both the x and y directions. The channel walls are set to a height of 0.1 m in the z direction, with symmetric boundaries applied at the $z = 0, 0.1$ m planes. Periodic boundaries are applied at the inlet and outlet ($x = -0.5$ and 0.5 m, respectively), with a streamwise potential equal to zero ($\Delta\phi_x = 0$). The spanwise potential is set to 1 V by setting the bottom electrode ($y = 0$ m) to zero and the potential at the top electrode ($y = 1$ m) to 1 V.

The grid uses exponential spacing along the wall surface, such that cell clustering occurs near the junction between the insulated wall and the electrode. Exponential spacing is employed between the two walls, such that cell clustering occurs near each surface. Uniform spacing is employed along the height of the wall (z direction). The coarse grid employs 50 points along the wall (x direction), 20 points between the walls (y direction), and 4 points in the z direction. Two additional, doubly refined grids are also developed: $100 \times 40 \times 8$ (medium) and $200 \times 80 \times 16$ (fine).

Grid independence is assessed by comparing solutions of the electric potential ϕ for the scenario without a magnetic field ($\mathbf{B} = 0$). Since the wall is infinitely tall, the solution in the z direction is constant and is only plotted along the $z = 0$ m plane. Extracting solutions of ϕ at two slices of the domain ($x = 0$ and 0.25 m) in Figs. 3a and 3b show the potential does not vary significantly between the medium and fine grids, so the medium solution is

considered grid-independent and is employed in the rest of the section.

Without the magnetic field, the Hall effect is nullified, and the electrical conductivity tensor reverts to a scalar. With the streamwise voltage set to zero, the resultant electric potential solution is symmetric about the center of the electrode, as seen in Fig. 4, where Fig. 4a is obtained by Gaitonde [42] and Fig. 4b is obtained using the medium grid. The current lines are also symmetric about the center of the electrode and are primarily created in the y direction, as seen in Fig. 5.

To test the Hall effect, a scenario used by Hurwitz et al. [53] is simulated. In this case, a 1 T uniform magnetic field is externally applied. The magnetic field is aligned with the z axis, whereas the velocity is aligned with the x axis. The spanwise voltage between an electrode pair is kept at 1 V, but the electrode pair is offset by 0.28 m for the Hall parameter of one ($\beta = 1$), as seen in Fig. 6. The streamwise voltage is also specified ($\Delta\phi_x = 0.4305$ V).

Hurwitz et al. [53] computed the potential and electric field, as seen in Fig. 7a. Current flows along a diagonal of the squares, seen in Figs. 7a and 7b (i.e., the current lines cross the orthogonal squares in the figures) [56]. The Hall effect creates values in the offdiagonal components of the electrical conductivity tensor, seen in Eq. (7). The antisymmetric components of the conductivity tensor result in a stretching of the streamwise component of the current density vector, j_x.

While the computed solution (Fig. 7b) closely resembles Hurwitz's [53] semianalytic solution, it is not identical. Hurwitz assumes the streamwise current j_x is zero when it is far from the wall

a) From Gaitonde [42]   **b) Medium grid ($100 \times 40 \times 8$) at $z = 0$**
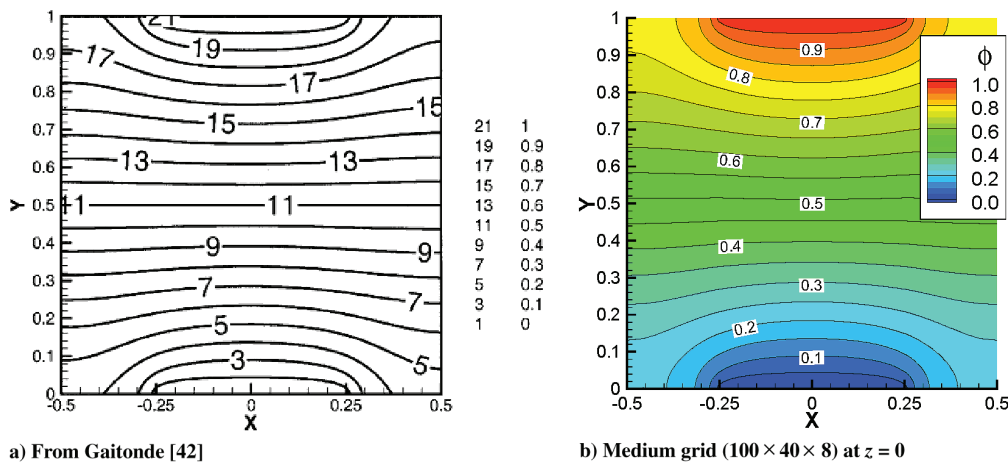
Fig. 4   Electric potential contours for the segmented electrode channel without a magnetic field and constant electrical conductivity ($\mathbf{B} = 0$, $\sigma = 1\ \Omega^{-1}\ \text{m}^{-1}$, and $\Delta\phi_x = 0$).
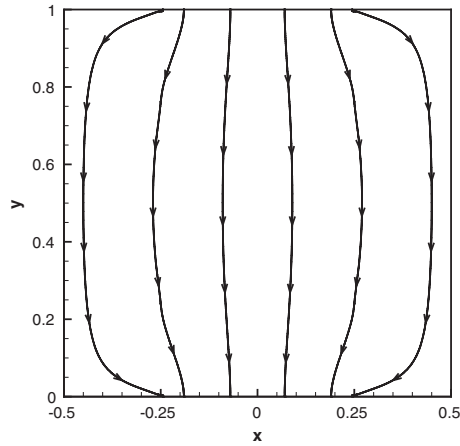
Fig. 5 Current density streamlines between two segmented electrodes without the Hall effect ($B = 0$, $\sigma = 1\ \Omega^{-1}\,m^{-1}$, and $\Delta\phi_x = 0$).
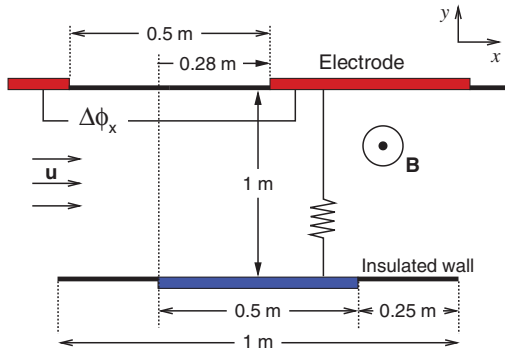
Fig. 6 Schematic of channel flow with finitely segmented electrodes used by Hurwitz et al. [53] with Hall effect ($B_z = 1$ T, $\sigma = 1\ \Omega^{-1}\,m^{-1}$, $\beta = 1$, and $\Delta\phi_x = 0.4305$ V).

(i.e., $y = 0.5$ m). While this is a reasonable approximation, it is not completely accurate and is not enforced in the computational results seen in Fig. 7b. Nonetheless, the figures portray similar characteristics and indicate that the Hall effect is successfully implemented.

D. Electrical Conductivity

The experiment performed by Kranc et al. [10] used preionized argon (Ar, Ar$^+$, and e). The electrical conductivity profile for weakly ionized argon is shown in Fig. 8, as adapted from Lin et al. [57]. As seen in the figure, the electrical conductivity exhibits two distinct regions: namely, weakly ionized ($T \lesssim 10,000$ K) and fully ionized ($T > 10,000$ K). Both regions display exponential growth with temperature, which means a highly accurate conductivity model is important in order to accurately capture its behavior across the entire temperature range.
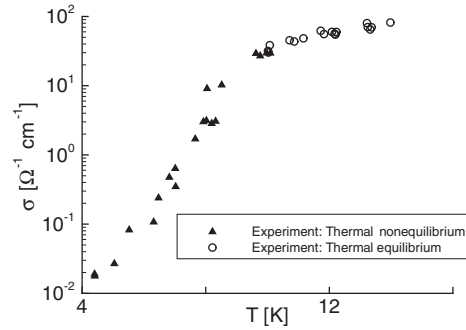
Fig. 8 Electrical conductivity of argon ($p = 0.013$ atm), reproduced from Lin et al. [57].

Three different electrical conductivity models were explored for this work. Raizer developed an electrical conductivity model that is an exponential function of temperature, assuming that electron-neutral collisions affect the conductivity more than the electron–ion collisions and that the ionization is in thermal equilibrium [58], as seen in Eq. (10):

$$\sigma = 83 \times e^{-36,000/T}\ \Omega^{-1}\,cm^{-1} \tag{10}$$

where the temperature T is specified in Kelvins. This model is considered valid for air, nitrogen, and argon at $p = 1$ standard atmosphere (atm) for a temperature range of 8000 to 14,000 K. The model's coefficients (83 and $-36,000$) can be adjusted, depending on the temperature range, pressure, or gas composition of interest, but they are used as specified for this study.

Chapman and Cowling developed a model (as described by Cambel [59]) for a weakly ionized gas by assuming a coupling between the charge and mass diffusion terms and assuming that the resultant electron energy distribution function from solutions to Boltzmann's equation is only a function of this coupled, binary diffusion coefficient. This assumption results in a semianalytic model for the electrical conductivity, as seen in Eq. (11):

$$\sigma = 3.34 \times 10^{-10} \frac{\alpha}{Q\sqrt{T}}\ \Omega^{-1}\,cm^{-1} \tag{11}$$

where Q cm^2 is the collision cross section of the gas, and the degree of ionization $\alpha = \Sigma n_{ions}/N$. One limitation of using the Chapman and Cowling model is that Q must be determined by an outside source (i.e., reference tables, theoretical model, etc.). For this work, the collision cross section is taken to be the total collision cross section for argon–argon collisions using the hard sphere model [60]. The diameter of argon is 4.04×10^{-10} m [61], so $Q = \pi d^2 = \simeq 5 \times 10^{-15}$ cm^2. This assumption is made, because it is unclear what the best choice for Q should be and because it produces results that are consistent with other models studied in previous work [51,52]. Since the model depends on the degree of ionization and temperature, it contains an indirect correlation to pressure and is valid for the cases of interest in this work.

A surrogate model of solutions to Boltzmann's equation is the third electrical conductivity model studied. A second-order

a) Reproduced from Hurwitz et al. [53]
b) Medium grid ($100 \times 40 \times 8$) at $z = 0$
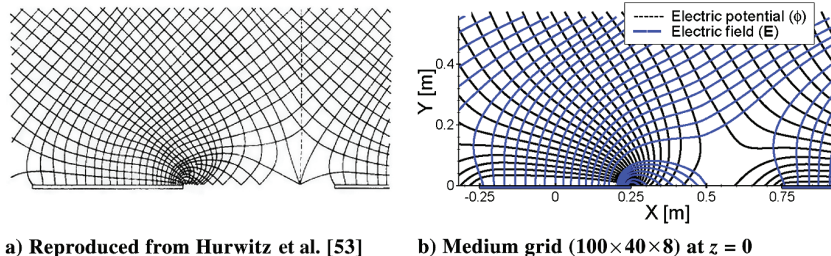
Fig. 7 Potential contours and electric field streamlines between segmented electrodes with the Hall effect ($B_z = 1$ T, $\sigma = 1\ \Omega^{-1}\,m^{-1}$, $\beta = 1$, and $\Delta\phi_x = 0.4305$ V).

polynomial response surface (PRS) is employed to capture the behavior of the solutions to Boltzmann's equations by developing a 3-D design of experiment (DOE). Solutions to Boltzmann's equation are determined using a Boltzmann solver developed by Weng and Kushner [62]. The Boltzmann solver's input parameters, namely, E/N, χ_{Ar}, and χ_{Ar^+}, define the three dimensions of the DOE (χ_e is unnecessary because of the assumed local charge neutrality). Since the solutions from the Boltzmann solver rely on the mole fractions, the model automatically incorporates a pressure dependence and is valid as long as the species fractions are within the DOE. General details of this approach were discussed in previous work [52], but specific modifications have been introduced here to improve the accuracy of the model.

Solutions to the learning and testing points required by the DOE are obtained from individual Boltzmann solutions that account for electron–electron collisions. Figure 9 plots the resulting electrical conductivity contours, which show a region of high conductivity for low χ_{Ar} (high degree of ionization) and a weak normalized electric field E/N.

The correlation between the electrical conductivity and E/N is anticipated by factoring the electron number density out of the definition of electrical conductivity for a dc current ($\sigma = e^2 n_e / m_e \nu_m$) to yield $\sigma/n_e \sim \nu_m^{-1}$. Since the electron collision frequency ν_m usually increases with increasing E/N, as seen in Fig. 10, the electrical conductivity should decrease with increasing electric field strength.

An open-source MATLAB® library, SURROGATES Toolbox [63], was used to create the PRS surrogate model. To improve the accuracy of the model, it is useful to transform the function that the PRS is trying to mimic by reducing the range of the dependent variable. Dividing the electrical conductivity by the degree of ionization does not require any additional variables, since $\alpha = \Sigma \chi_{ions} = \chi_{Ar^+}$, but it does normalize the dependent variable. However, this can lead to a division by zero error when $\alpha = 0$, so the formulation of the dependent variable is inverted. This formulation is similar to the Chapman–Cowling model, which also uses the degree of ionization in the numerator. Since this results in a small solution range for the cases of interest ($10^{-8}\ \Omega \cdot m \le \alpha/\sigma \le 10^{-6}\ \Omega \cdot m$), the natural logarithm is applied to the dependent variable. Equation (12) lists the model formulation provided to the SURROGATES Toolbox:
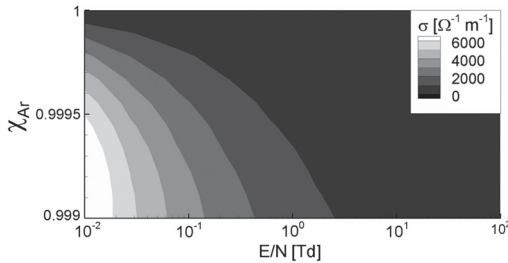
Fig. 9   Electrical conductivity contours for weakly ionized argon.
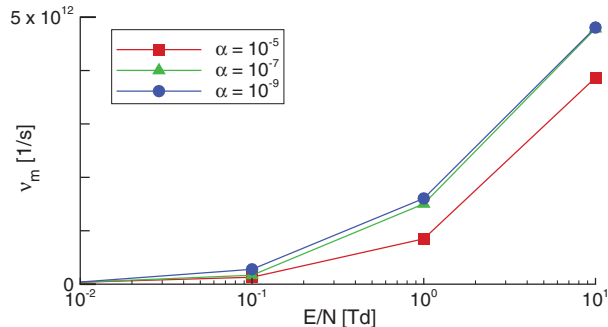
Fig. 10   Electron collision frequency for weakly ionized argon at $p = 1$ atm.

$$\ln\left(\tfrac{\alpha}{\sigma}\right) = f(E/N, \chi_{Ar}, \chi_{Ar^+}) \tag{12}$$

Since the model is a function of the natural logarithm and the degree of ionization, the electrical conductivity must be extracted from the model's solution by dividing the degree of ionization by the exponential function of the model's prediction. The resulting electrical conductivity predicted will always be positive ($\sigma \ge 0$).

Although this formulation of the PRS model incurs additional computational expense (i.e., evaluation of the exponential function and computing α), higher accuracy is achieved with lower-order PRS models, because the DOE's surface gradients are reduced. This improvement may lead to a reduction in total computing expense for a given scenario, because a lower-order PRS model may be sufficient for the simulations of interest. The model accuracy is determined by computing the mean absolute error (MAE) and the mean absolute percent error (MAPE) from the additional testing points computed using the Boltzmann solver:

$$MAE = \frac{1}{n}\sum_{i=1}^{n} |\hat{\sigma} - \sigma|_i \tag{13}$$

$$MAPE = \frac{1}{n}\sum_{i=1}^{n} \left| \frac{\hat{\sigma} - \sigma}{(\hat{\sigma} + \sigma)/2} \right|_i \tag{14}$$

where $\hat{\sigma}$ is the solution computed by the Boltzmann solver, and σ is the solution computed by the model. The percent error is the normalized percent error to remove the bias when evaluating an overprediction [64]. A second-order PRS model is assumed to have sufficient accuracy and acceptable computational cost of the scope of this paper. A summary of the second-order PRS performance metrics yields a MAPE of 16.37% and a MAE of 90.72 $\Omega^{-1}\ m^{-1}$. The second-order PRS model is listed in Eq. (15):

$$\sigma = \frac{\chi_e}{\exp(\mathbf{PRS})}$$

$$\begin{aligned}
\mathbf{PRS} = &-842.64 + 128.02(E/N) + 2558.28(\chi_{Ar}) \\
&- 4112.52(\chi_{Ar^+}) - 4.82(E/N)^2 - 118.25(E/N)(\chi_{Ar}) \\
&- 121.33(E/N)(\chi_{Ar^+}) - 1732.34(\chi_{Ar})^2 \\
&+ 3229.51(\chi_{Ar})(\chi_{Ar^+}) - 7342.51(\chi_{Ar^+})^2 \tag{15}
\end{aligned}$$

where E/N is normalized from 0 to 1 for a range of 0.01 to 100 townsend (Td) (1 Td $= 10^{-17}$ V · cm^2). The species mole fractions χ_s are used directly in the equation, which was developed for an ionized mole fraction of less than 1% (i.e., $\chi_{Ar^+} < 0.01$). However, the model could be expanded to accommodate a large range of mole fractions if necessary. While MAPE may seem relatively high, the result can be misleading, since a large portion of the DOE consists of lower electrical conductivity values, as seen in Fig. 9 (i.e., the MAPE can be quite large when the local solution produced by the Boltzmann solver is small).

E.   Viscosity Model

Chemically nonreacting, thermodynamic equilibrium simulations are computed using the variable hard sphere (VHS) viscosity model. The VHS model is used because the viscosity is assumed to only be a function of temperature, since the species present (argon, argon ion, and electrons) have a single energy mode and are chemically nonreacting:

$$\mu = \mu_{ref}\left(\frac{T}{T_{ref}}\right)^{\omega} \tag{16}$$

where μ is the viscosity, the reference viscosity coefficient $\mu_{ref} = 2.117 \times 10^{-5}$ N s/m^2 for a reference temperature $T_{ref} = 273$ K and a viscosity index $\omega = 0.81$. This method, as outlined by Schwartzentruber et al. [65], requires several reference coefficients, which are listed in [60].

III. Results

Three-dimensional calculations were carried out for Mach 4.75 argon flow over a hemisphere cylinder, which was originally studied experimentally by Kranc et al. [10]. The forebody hemisphere has a radius of 0.75 in. ($r_n = 0.01905$ m), and the geometry is mounted parallel to the freestream, as seen in Fig. 11.

In the experiments, the freestream flow was composed of strongly ionized argon (Kranc et al. [10] estimates the degree of ionization $\alpha = 0.025$), which was produced by a plasma torch (dc arc heater). The heater was located before the converging–diverging nozzle, which accelerated the gas into the test chamber. Kranc et al. [10] state that the electrons were frozen in the nozzle, and that the flow was not chemically reacting after it was initially ionized by the heater. The flow conditions reported by Kranc et al. are listed in Table 1.

A structured grid was generated using two grid domains. The first domain includes the hemispherical forebody, while the second accommodates the rest of the geometry. While the baseline flow solution (the flow without the magnetic field) is axisymmetric, the rest of the simulations were computed using a 3-D grid, because the MHD routine is currently only implemented for 3-D domains.

The grid was generated with equal spacing along the hemisphere portion of the geometry (first domain) and gradually increases in spacing along the remaining surface (second domain). Grid points were equally spaced around the circumference of the geometry, and the radial points were algebraically spaced to increase the number of points close to the body. As a result, cell clustering occurred primarily in the hemispherical forebody and near the body surface. The baseline grid used 50 points along the body (30 in the hemispherical region), 30 points along one quarter of the circumference, and 30 radial points. Two doubly refined grids were also used in the grid convergence study, giving the following set of computational meshes: $50 \times 30 \times 30$ (coarse), to $100 \times 60 \times 60$ (medium), to $200 \times 120 \times 120$ (fine).

Figure 12 plots the pressure coefficient and nondimensional heat flux for the baseline flow along the surface of the geometry, as defined in Eqs. (17) and (18), respectively:

$$C_p = \frac{p_w - p_\infty}{1/2 \rho_\infty u_\infty^2} \qquad (17)$$

$$C_h = \frac{q_w}{1/2 \rho_\infty u_\infty^3} \qquad (18)$$

where q_w is the total heat flux to the wall. The grid convergence study showed little difference between the medium and fine grids; therefore, the medium grid was considered sufficiently refined and was used for the rest of the analysis.

A closer examination of the freestream conditions (specifically, the degree of ionization), reveals Kranc et al. [10] estimated α using tables from Arave and Huseley [66]. While this approach may be approximately correct, the degree of ionization is better estimated by using the Saha equation for a singly ionized atomic gas [67]:

$$\frac{\alpha^2}{1 - \alpha^2} p = 3.16 \times 10^{-7} \, T^{5/2} \exp\left(-\frac{\varepsilon_i}{kT}\right) \qquad (19)$$

where p is the pressure in atmospheres, T is the temperature in Kelvin, Boltzmann's constant $k = 1.3807 \times 10^{-23}$ J/K, and ε_i is the

Table 1 Flow conditions for the MHD-heat-shield experiment as reported by Kranc et al. [10]

Parameter	Value
M	4.75
u_∞	3000.0 m/s
T_∞	1100.0 K
T_w	300.0 K
p_∞	27.8 Pa
ρ_∞	1.035×10^{-4} kg/m^3
n_e	4×10^{19} m^{-3}
α	0.025
r_n	0.01905 m
μ_∞	8×10^{-5} kg/m·s
Re_L	3880 m^{-1}
Re	74

ionization energy required to remove the electron from the atom in the gas considered. The ionization potential for argon, $\varepsilon_i = 2.53 \times 10^{-18}$ J, and the stagnation pressure and temperature are 0.49 atm and 9700 K, respectively. Using the Saha equation yields a degree of ionization of $\alpha = 0.00623$.

This new estimate for the degree of ionization only changes two values listed in Table 1, namely, $\alpha = 0.00623$ and $n_e = 1.03 \times 10^{19}$ m^{-3}, which results in a slight modification to the freestream conditions, as seen in Table 2.

Since the changes to the individual species densities are minimal, and the flow is assumed chemically nonreacting, these slight adjustments to the freestream conditions are assumed not to noticeably alter the resulting flowfield. Therefore, the medium grid, discussed previously, was assumed to provide sufficient resolution and was used in the rest of the analysis. The remaining simulations used the adjusted freestream conditions corresponding to $\alpha = 0.00623$.

Figure 13 plots the temperature contours for the flow without the magnetic field. As seen in the figure, the peak temperature is 9000 K, which is 150 K hotter than the solution computed using the freestream conditions corresponding to $\alpha = 0.025$, a result of the slight increase in total density over the conditions reported by Kranc et al. [10]. Using the baseline flowfield solutions, the expected range of electrical conductivity for the various models is displayed in Table 3. The results indicate slight discrepancies in estimated electrical conductivities, with the second-order PRS predictions residing between the semiempirical models.

In the experiment of Kranc et al. [10], the applied magnetic field was produced by an electromagnet located inside the hemisphere-shaped forebody. The electromagnet was approximately 1 in. (0.0254 m) long by 1.25 in. (0.03175 m) in diameter, with a 0.375 in. (0.0095 m) core. The core was composed of vanadium permandur,
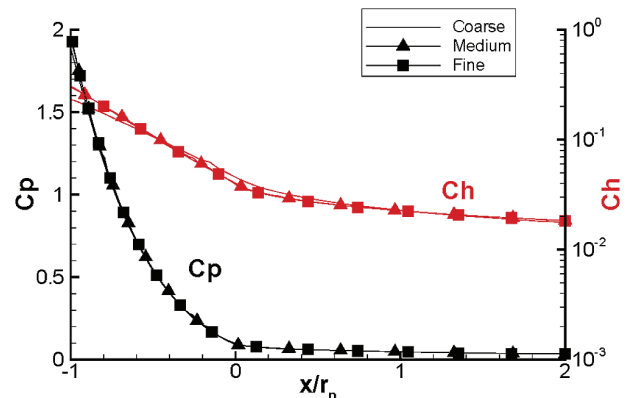

Fig. 11 Hemisphere-capped geometry (adapted from [10]).

Fig. 12 Nondimensional pressure and heat flux along the surface of Mach 4.75 argon flow around a hemisphere-capped geometry for various grids.

Table 2   Corrections to the reported free-stream conditions for the MHD-heat-shield experiment of Kranc et al. [10]

Parameter	Value	
	Reported	Adjusted
u_∞, m/s	3000	3000
T_∞, K	1100	1100
T_w, K	300	300
α	0.025	0.00623
ρ_{Ar}, kg/m^3	1.01×10^{-4}	1.09×10^{-4}
ρ_{Ar^+}, kg/m^3	2.65×10^{-6}	6.85×10^{-7}
ρ_e, kg/m^3	3.64×10^{-11}	9.41×10^{-12}

Table 3   Electrical conductivity estimates for the MHD-heat-shield experiment without an applied magnetic field[a]

	σ [Ω^{-1} cm^{-1}]
Raizer	0–1.5
Chapman and Cowling	4.4–24.2
Second-order PRS	7.1–8.1

[a]$\alpha = 0.00623$ and $E/N = 0$.

and the windings were made of No. 19 Anaconda polyimide enamel (HML)-coated wire with a magnetic resistance of 0.5Ω [10]. Measurements made by Kranc et al. found the magnet behaved like an ideal dipole, and it is modeled as such. The magnetic field decays as r^{-3} from its centroid, which is assumed to be located along the x axis, where the forebody merges with the rest of geometry ($x/r_n = 0$), as seen in Fig. 14. The magnetic moment is aligned along the x axis and is positioned to oppose the incoming flow along the stagnation line. The magnetic field contours are nondimensionalized by the peak magnetic field strength B_{max}, which occurs at the stagnation point ($x/r_n = -1$ for the configuration shown in Fig. 14). Note that the peak magnetic field strength is used to designate each simulation for the rest of this analysis.

In Cartesian coordinates, the ideal dipole magnetic field is

$$\mathbf{B} = \frac{-B_{max}}{2(x^2 + y^2 + z^2)^{5/2}} \begin{bmatrix} 2x^2 - (y^2 + z^2) \\ 3xy \\ 3xz \end{bmatrix}$$

The negative sign in front of the peak field strength B_{max} is due to the direction of the field flux. The centroid of the dipole is located at the origin.

The flowfield around the geometry is axisymmetric and steady, as evident in the temperature contours seen in Fig. 13. This means the electric current must only travel in the azimuthal direction (perpendicular to the incoming flow, around the axis of symmetry), and the electric field must be zero [4]. This reduces the magnetic force in the momentum equation to $\tilde{\sigma} \cdot (\mathbf{u} \times \mathbf{B}) \times \mathbf{B}$ and sets the energy deposition term in the total energy equation to zero, $\mathbf{j} \cdot \mathbf{E} = 0$. Note that joule heating is still present under these assumptions, $(\mathbf{E} + \mathbf{u} \times \mathbf{B}) \cdot \mathbf{j} \neq 0$. Since the electric field is assumed zero and the magnetic field is specified, only the current density field $\mathbf{j}$ needs to be updated in the MHD module.

Simulations were carried out at several magnetic field strengths for the different electrical conductivity models. The simulations were started from the steady-state baseline solution (without an applied magnetic field), and iteration was carried until the flowfield achieved a new, converged steady state. Convergence was assumed once the root mean square residual error from the conservation equations decayed to the minimum allowed by machine precision, as seen in Fig. 15 for a typical simulation. In this scenario, at least 10 characteristic flow times worth of time steps are required to achieve a steady-state flowfield solution. A characteristic flow time is defined as the time it takes for the flow to traverse the length of the geometry.

The assumption that the electric field is negligible ($\mathbf{E} = 0$) is verified by simulating the flow with and without a computation of the electric field. The Chapman and Cowling electrical conductivity model was employed for both simulations with $B_{max} = 0.28$ T. The MHD module was used to update the electric field every five fluid iterations. Figure 16 plots the temperature contours and current lines
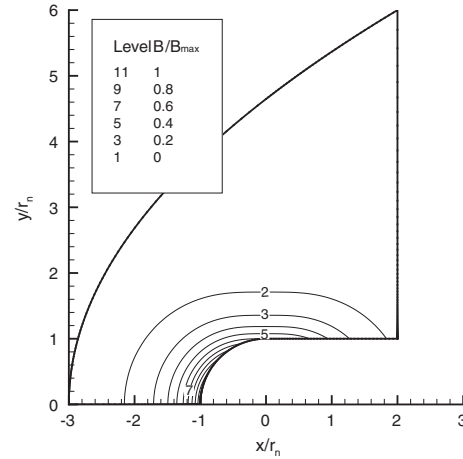
Fig. 14   Nondimensional dipole magnetic field contours from a magnet located in the hemisphere-capped geometry.

Fig. 13   Temperature contours for Mach 4.75 argon flow around a hemisphere-capped geometry ($\alpha = 0.00623$).

Fig. 15   Root mean square residual error from a simulation of Mach 4.75 argon flow around a hemisphere-capped geometry with a 0.13 T magnet (Chapman and Cowling conductivity model).

140

a) Assuming E = 0   b) Computing E

Fig. 16   Temperature contours and current lines for Mach 4.75 argon flow around a hemisphere-capped geometry with a 0.28 T magnetic field (Chapman and Cowling conductivity model).

a) Raizer [58]   b) Chapman and Cowling   c) 2nd order PRS
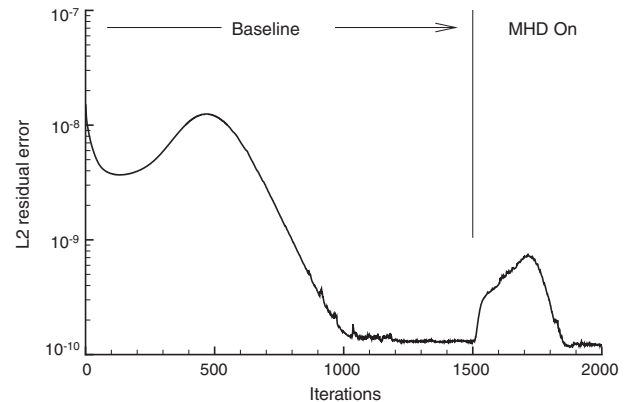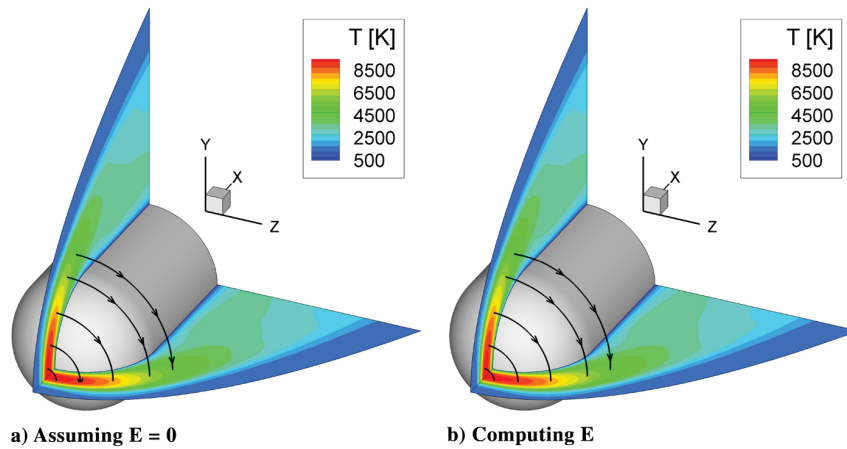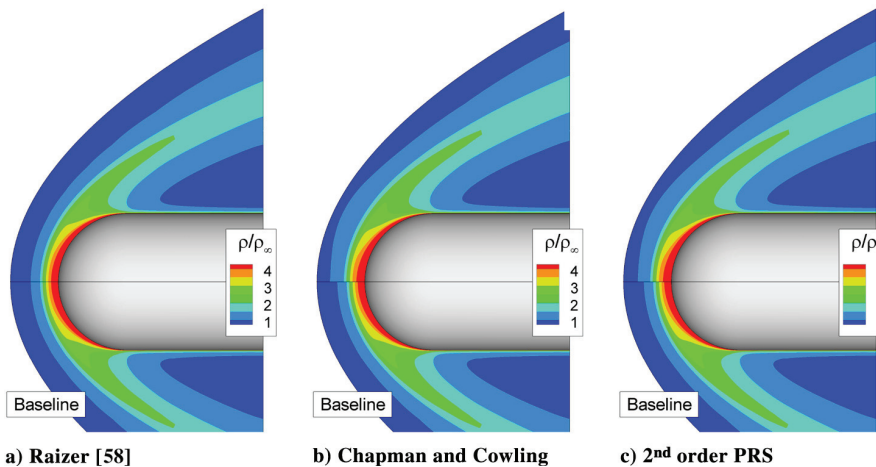
Fig. 17   Density ratio contours for Mach 4.75 argon flow around a hemisphere-capped geometry for various electrical conductivity models ($B_{max} = 0.13$ T).

for both scenarios. As seen in the figures, computing $\mathbf{E}$ from the MHD module does not alter the flow structure or current lines.

Kranc et al. reported an increase in shock standoff distance due to the applied magnetic field [10]. The increase was measured by comparing photographs of the flow with and without the applied magnetic field. In their analysis, they assumed that the upstream edge of the shock can be inferred from the boundary of the flow's luminosity. This photographic technique for measuring the shock standoff distance was previously used by Ziemer [8] and Bailey and Sims [68] in similar experiments.

Although many techniques exist for estimating the shock location, this paper estimates its location to occur where the density ratio exceeds the ideal gas infinite Mach number threshold for a normal shock wave along the stagnation line:
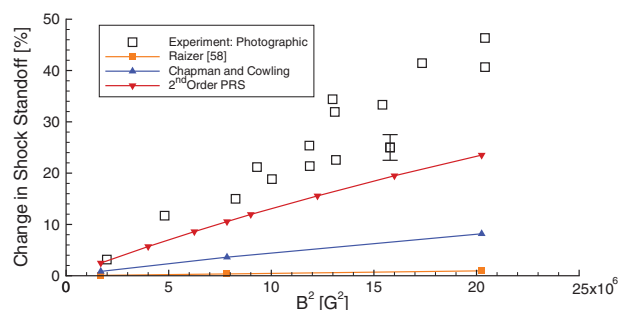
Fig. 18   Percent change in shock standoff distance versus magnetic field strength for Mach 4.75 argon flow around a hemisphere-capped geometry with various electrical conductivity models (measurements from Kranc et al. [10]). (Experimental uncertainty $\pm 10\%$.)
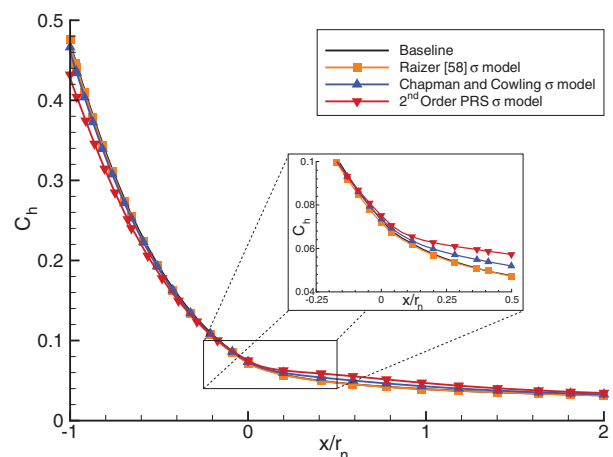
Fig. 19   Nondimensional heat flux along the surface of the geometry for Mach 4.75 argon flow around a hemisphere-capped geometry with a 0.28 T magnetic field and various electrical conductivity models.

141

Approved for public release; distribution unlimited.

Table 4 Percent change in heat flux to the surface for Mach 4.75 argon flow around a hemisphere-capped geometry with an MHD heat shield

Model	Δ total heating, %		Δ peak heating, %	
	$B = 0.13$ T	$B = 0.28$ T	$B = 0.13$ T	$B = 0.28$ T
Raizer	−0.1	−0.6	−0.1	−0.6
Chapman and Cowling	0.3	2.2	−0.7	−2.5
Second-order PRS	1.0	3.4	−2.7	−9.7

$$\lim_{M_1 \to \infty} \frac{\rho_2}{\rho_1} = \frac{\gamma + 1}{\gamma - 1} \qquad (20)$$

where M_1 is the upstream Mach number, γ is the ratio of specific heats, ρ_1 is the freestream density, and ρ_2 is the downstream density. Using this equation, the density ratio limit for argon is four ($\gamma = 5/3$). Figure 17 plots the density ratio contours for the electrical conductivity models with a peak magnetic field of 0.13 T ($1\ \text{T} = 10^4\ \text{G}$).

Figure 18 plots the change in shock standoff distance for the simulations and experimental measurements. The experimental measurements were collected using the photographic technique described previously.

The experimental uncertainty (error in determining shock location for one run) is only ±10%, but the repeatability (difference in shock location between nominally identical runs) is ±20%, as seen for $B_{\max}^2 \simeq 13 \times 10^6\ \text{G}^2$. Both the second-order PRS model and the Chapman and Cowling model match the experimental data well at lower magnetic field strengths, but the second-order PRS model better correlates to the experimental measurements at higher magnetic field strengths.

Solutions obtained by using Raizer's [58] electrical conductivity model show almost no change in shock standoff distance, because the model is only dependent on temperature and could not account for the preionized frozen state of the freestream gas. Since the peak temperature occurs just downstream of the bow shock, the model's peak conductivity is also there. However, the magnetic field strength near the shock front is significantly decayed due to its r^{-3} dependency, which results in only minor changes to the flowfield.

The heat transfer to the surface for the various electrical conductivity models is shown in Fig. 19. The total heating to the geometry is determined by integrating the heat flux over the surface. The change in peak heating is computed by comparing the heat flux at the stagnation point $(\Delta q_w = (q_{w,\text{MHD}} - q_{w,\text{baseline}})/q_{w,\text{baseline}})$. Table 4 lists the percent change in peak heat flux and total heating for various magnetic field strengths and electrical conductivity models.

The total heating to the surface slightly increases because of increased heating to the cylindrical portion of the geometry (i.e., aft of the stagnation region). This is due to the direction of the magnetic field lines in the region where the forebody merges with the cylinder. Results obtained using Raizer's [58] conductivity model fail to capture this behavior (i.e., increased total heating), because its conductivity is not high enough in the aft region, where the direction of the field lines would increase the temperature. In general, an applied magnetic field moderately increases the total heating to the geometry, but it significantly decreases the peak heat flux at the stagnation point. Both the second-order PRS model and the Chapman and Cowling model observe this behavior but, since the second-order PRS model solutions have better agreement with the experimental results, its results for the heat flux to the geometry may be more accurate.

IV. Conclusions

Newly developed computational tools were used to compute hypersonic flow around a hemisphere-cylinder geometry that uses a magnet located within the body as a means of heat flux mitigation. These tools include an improved electrical conductivity model and a parallelized 3-D MHD module that are loosely coupled to a fluid code. In addition, the Hall effect was implemented and verified by investigating flow between finite electrodes.

Mach 4.75 argon flow over a hemisphere cylinder corresponding to the experiment conducted by Kranc et al. [10] was investigated computationally, using modern CFD techniques. The magnetic field generated from inside the forebody of the geometry worked to oppose and slow the flow near the stagnation region, thus increasing the shock standoff distance. The increase in shock standoff distance decreased the peak heating to the body (at the stagnation point), but it also increased the total heating to the geometry because of increased heating to the aft portion of the body. The changes in shock standoff distance and, consequently, surface heating are dependent on the electrical conductivity model implemented. For this work, a new developed conductivity model based on a PRS to solutions to Boltzmann's equation provided results that gave the closest agreement to experimental measurements. While this work demonstrates the importance the electrical conductivity model has on computing MHD effects for preionized hypersonic flow around a hemisphere cylinder, several other factors, including uncertainty in the reported freestream conditions, surface conditions, the physical size and divergence of the magnet, the Hall effect, and ion slip should also be evaluated to determine if these influence the solution.

These results have important implications for the design of MHD-heat-shield devices: they can reduce peak heat loads but with a potential penalty in total heating. Since both peak and total heat loads are important aspects to consider when designing a thermal protection system, this technology provides additional scenarios for vehicle designers to evaluate.

References

[1] Kantrowitz, A. R., "A Survey of Physical Phenomena Occurring in Flight at Extreme Speeds," *Proceedings of the Conference on High-Speed Aeronautics*, edited by A. Ferri, N. J. Hoff, and P. A. Libby, Polytechnic Inst. of Brooklyn, New York, 1955, pp. 335–339.

[2] Resler, E. L., and Sears, W. R., "The Prospects for Magneto-Aerodynamics," *Journal of the Aerospace Sciences*, Vol. 25, No. 4, April 1958, pp. 235–245, 258.

[3] Resler, E. L., and Sears, W. R., "The Prospects for Magneto-Aerodynamics: Correction and Addition," *Journal of the Aerospace Sciences*, Vol. 26, No. 5, May 1959, p. 318.

[4] Bush, W. B., "Magnetohydrodynamic-Hypersonic Flow Past a Blunt Body," *Journal of the Aerospace Sciences*, Vol. 25, No. 11, Nov. 1958, pp. 685–690.

[5] Bush, W. B., "The Stagnation-Point Boundary Layer in the Presence of an Applied Magnetic Field," *Journal of the Aerospace Sciences*, Vol. 28, No. 8, Aug. 1961, pp. 610–611.

[6] Poggie, J., and Gaitonde, D. V., "Magnetic Control of Flow Past a Blunt Body: Numerical Validation and Exploration," *Physics of Fluids*, Vol. 14, No. 5, May 2002, pp. 1720–1731.
doi:10.1063/1.1465424

[7] Coakley, J. F., and Porter, R. W., "Time-Dependent Numerical Analysis of MHD Blunt Body Problem," *AIAA Journal*, Vol. 9, No. 8, Aug. 1971, pp. 1624–1626.
doi:10.2514/3.49966

[8] Ziemer, R. W., "Experimental Investigations in Magnetoaerodynamics," *ARS Journal*, Vol. 29, No. 9, Sept. 1959, p. 642.

[9] Wilkinson, J. B., "Magnetohydrodynamic Effects on Stagnation-Point Heat Transfer from Partially Ionized Nonequilibrium Gases in Supersonic Flow," *Proceedings of the 3rd Symposium of Engineering Aspects of Magnetohydrodynamics*, edited by N. W. Mather, and G. W. Sutton, Gordon and Breach, New York, 1964, pp. 413–438.

[10] Kranc, S., Yuen, M. C., and Cambel, A. B., "Experimental Investigation of Magnetoaerodynamic Flow Around Blunt Bodies," NASA, CR 1393, Aug. 1969.

[11] Nowak, R. J., Kran, S., Porter, R. W., Yuen, M. C., and Cambel, A. B., "Magnetogasdynamic Re-Entry Phenomena," *Journal of Spacecraft*

and Rockets, Vol. 4, No. 11, Nov. 1967, pp. 1538–1542.
doi:10.2514/3.29125

[12] Nowak, R. J., and Yuen, M. C., "Heat Transfer to a Hemispherical Body in Supersonic Argon Plasma," *AIAA Journal*, Vol. 11, No. 11, Nov. 1973, pp. 1463–1464.
doi:10.2514/3.50611

[13] Porter, R. W., and Cambel, A. B., "Hall Effect in Flight Magnetogasdynamics," *AIAA Journal*, Vol. 5, No. 12, Dec. 1967, pp. 2208–2213.
doi:10.2514/3.4410

[14] Romig, M. F., "The Influence of Electric and Magnetic Fields on Heat Transfer to Electrically Conducting Fluids," *Advances in Heat Transfer*, edited by T. F. Irvine, and J. P. Hartnett, Vol. 1, Academic, New York, 1964, pp. 267–354.

[15] Padilla, J. F., "Assessment of Gas-Surface Interaction Models for Computation of Rareed Hypersonic Flows," Ph.D. Thesis, Department of Aerospace Engineering, Univ. of Michigan, Ann Arbor, MI, 2008.

[16] Fomin, V. M., Tretyakov, P. K., and Taran, J.-P., "Flow Control using Various Plasma and Aerodynamic Approaches," *Aerospace Science and Technology*, Vol. 8, No. 5, July 2004, pp. 411–421.
doi:10.1016/j.ast.2004.01.005

[17] Shang, J. S., Surzhikov, S. T., Kimmel, R., Gaitonde, D., Menart, J., and Hayes, J., "Mechanisms of Plasma Actuators for Hypersonic Flow Control," *Progress in Aerospace Sciences*, Vol. 41, No. 8, Nov. 2005, pp. 642–668.
doi:10.1016/j.paerosci.2005.11.001

[18] Bityurin, V., Bocharov, A., and Lineberry, J., "MHD Flow Control in Hypersonic Flight," AIAA Paper 2005-3225, May 2005.

[19] Palmer, G., "Magnetic Field Effects on the Computed Flow over a Mars Return Aerobrake," *Journal of Thermophysics and Heat Transfer*, Vol. 7, No. 2, April–June 1993, pp. 294–301.
doi:10.2514/3.419

[20] Bisek, N. J., Boyd, I. D., and Poggie, J., "Numerical Study of Plasma-Assisted Aerodynamic Control for Hypersonic Vehicles," *Journal of Spacecraft and Rockets*, Vol. 46, No. 3, May–June 2009.
doi:10.2514/1.39032

[21] Kremeyer, K., Sebastian, K., and Shu, C.-W., "Computational Study of Shock Mitigation and Drag Reduction by Pulsed Energy Lines," *AIAA Journal*, Vol. 44, No. 8, Aug. 2006, pp. 1720–1731.
doi:10.2514/1.17854

[22] Yan, H., and Gaitonde, D., "Control of Edney IV Interaction by Energy Pulse," AIAA Paper 2006-562, Jan. 2006.

[23] Menart, J., Staneld, S., Shang, J., Kimmel, R., and Hayes, J., "Study of Plasma Electrode Arrangements for Optimum Lift in a Mach 5 Flow," AIAA Paper 2006-1172, Jan. 2006.

[24] Girgis, I. G., Shneider, M. N., Macheret, S. O., Brown, G. L., and Miles, R. B., "Creation of Steering Moments in Supersonic Flow by Off-Axis Plasma Heat Addition," AIAA Paper 2002-129, Jan. 2002.

[25] Gnemmi, P., Charon, R., Duperoux, J.-P., and George, A., "Feasibility Study for Steering a Supersonic Projectile by a Plasma Actuator," *AIAA Journal*, Vol. 46, No. 6, June 2008, pp. 1308–1317.
doi:10.2514/1.24696

[26] Bityurin, V. A., Vatazhin, A. B., and Gus'kov, O. V., "Hypersonic Flow Past the Spherical Nose of a Body in the Presence of a Magnetic Field," *Fluid Dynamics*, Vol. 39, No. 4, July 2004, pp. 657–666.
doi:10.1023/B:FLUI.0000045682.98147.db

[27] Miles, R. B., Macheret, S. O., Shneider, M. N., Steeves, C., Murray, R. C., Smith, T., and Zaidi, S. H., "Plasma-Enhanced Hypersonic Performance Enabled by MHD Power Extraction," AIAA Paper 2005-561, Jan. 2005.

[28] Fujino, T., Matsumoto, Y., Kasahara, J., and Ishikawa, M., "Numerical Studies of Magnetohydro-dynamic Flow Control Considering Real Wall Electrical Conductivity," *Journal of Spacecraft and Rockets*, Vol. 44, No. 3, May–June 2007, pp. 625–632.
doi:10.2514/1.25824

[29] Katsurayama, H., Kawamura, M., Matsuda, A., and Abe, T., "Kinetic and Continuum Simulations of Electromagnetic Control of a Simulated Reentry Flow," *Journal of Spacecraft and Rockets*, Vol. 45, No. 2, March–April 2008, pp. 248–254.
doi:10.2514/1.31702

[30] Yoshino, T., Fujino, T., and Ishikawa, M., "Possibility of Thermal Protection in Earth Re-Entry Flight by MHD Flow Control with Air-Core Circular Magnet," *IEEJ Transactions on Electrical and Electronic Engineering*, Vol. 4, No. 4, July 2009, pp. 510–517.
doi:10.1002/tee.20437

[31] Hodara, H., "The Use of Magnetic Fields in the Elimination of the Re-Entry Radio Blackout," *Proceedings of the IRE*, Vol. 49, No. 12, Dec. 1961, pp. 1825–1830.

doi:10.1109/JRPROC.1961.287709

[32] Kim, M., Keidar, M., and Boyd, I. D., "Analysis of an Electromagnetic Mitigation Scheme for Reentry Telemetry Through Plasma," *Journal of Spacecraft and Rockets*, Vol. 45, No. 6, Nov.–Dec. 2008, pp. 1223–1229.
doi:10.2514/1.37395

[33] Macheret, S. O., Shneider, M. N., and Candler, G. V., "Modeling of MHD Power Generation on Board Reentry Vehicles," AIAA Paper 2004-1024, Jan. 2004.

[34] Wan, T., Suzuki, R., Candler, G., Macheret, S., and Schneider, M., "Three Dimensional Simulation of Electric Field and MHD Power Generation During Re-Entry," AIAA Paper 2005-5045, June 2005.

[35] Fujino, T., Yoshino, T., and Ishikawa, M., "Prediction of Generator Performance and Aerodynamic Heating of Reentry Vehicle Equipped with On-Board Surface Hall Type MHD Generator," AIAA Paper 2008-4225, June 2008.

[36] Bityurin, V. A., Bocharov, A. N., and Lineberry, J. T., "Results of Experiments on MHD Hypersonic Flow Control," AIAA Paper 2004-2263, June 2004.

[37] Takizawa, Y., Sato, S., Abe, T., and Konigorski, D., "Electro-Magnetic Effect on Shock Layer Structure in Reentry-Related High-Enthalpy Flow," AIAA Paper 2004-2162, June 2004.

[38] Kimmel, R., Hayes, J., Menart, J., and Shang, J., "Supersonic Plasma Flow Control Experiments," U.S. Air Force Research Laboratory, TR ARFL-VA-WP-TR-2006-3006, Wright-Patterson AFB, OH, Dec. 2005.

[39] Matsuda, A., Kawamura, M., Takizawa, Y., Otsu, H., Konigorski, D., Sato, S., and Abe, T., "Experimental Investigation of the Hall Effect for the Interaction between the Weakly-Ionized Plasma Flow and Magnetic Body," AIAA Paper 2007-1437, Jan. 2007.

[40] Gülhan, A., Esser, B., Koch, U., Siebe, F., Riehmer, J., Giordano, D., and Konigorski, D., "Experimental Verication of Heat-Flux Mitigation by Electromagnetic Fields in Partially-Ionized-Argon Flows," *Journal of Spacecraft and Rockets*, Vol. 46, No. 2, March–April 2009, pp. 274–283.
doi:10.2514/1.39256

[41] Gaitonde, D. V., and Poggie, J., "An Implicit Technique for 3-D Turbulent MGD with the Generalized Ohm's Law," AIAA Paper 2001-2736, June 2001.

[42] Gaitonde, D. V., "A High-Order Implicit Procedure for the 3-D Electric Field in Complex Magnetogasdynamic Simulations," *Computers and Fluids*, Vol. 33, No. 3, March 2004, pp. 345–374.
doi:10.1016/j.compfluid.2003.06.001

[43] Gaitonde, D. V., and Poggie, J., "An Implicit Technique for Three-Dimensional Turbulent Magnetoaerodynamics," *AIAA Journal*, Vol. 41, No. 11, Nov. 2003, pp. 2179–2191.
doi:10.2514/2.6810

[44] Damevin, H.-M., and Hoffmann, K. A., "Numerical Simulations of Magnetic Flow Control in Hypersonic Chemically Reacting Flows," *Journal of Thermophysics and Heat Transfer*, Vol. 16, No. 4, Oct.–Dec. 2002, pp. 498–507.
doi:10.2514/2.6724

[45] Scalabrin, L. C., and Boyd, I. D., "Development of an Unstructured Navier–Stokes Solver For Hypersonic Nonequilibrium Aerothermodynamics," AIAA Paper 2005-5203, June 2005.

[46] Scalabrin, L. C., and Boyd, I. D., "Numerical Simulation of Weakly Ionized Hypersonic Flow for Reentry Configurations," AIAA Paper 2006-3773, June 2006.

[47] MacCormack, R. W., and Candler, G. V., "The solution of the Navier–Stokes Equations Using Gauss–Seidel Line Relaxation," *Computers and Fluids*, Vol. 17, No. 1, Jan. 1989, pp. 135–150.
doi:10.1016/0045-7930(89)90012-1

[48] Holman, T. D., and Boyd, I. D., "Numerical Investigation of the Effects of Continuum Breakdown on Hypersonic Vehicle Surface Properties," AIAA Paper 2008-3928, June 2008.

[49] Shercli, J., *A Textbook of Magnetohydrodynamics*, Pergamon, New York, 1965.

[50] Gaitonde, D. V., and Poggie, J., "Elements of a Numerical Procedure for 3-D MGD Flow Control Analysis," AIAA Paper 2002-198, Jan. 2002.

[51] Bisek, N. J., Boyd, I. D., and Poggie, J., "Numerical Study of Electromagnetic Aerodynamic Control of Hypersonic Vehicles," AIAA Paper 2009-1000, Jan. 2009.

[52] Bisek, N. J., Boyd, I. D., and Poggie, J., "Three Dimensional Simulations of Hypersonic MHD Flow Control," AIAA Paper 2009-3731, Jan. 2009.

[53] Hurwitz, H., Jr., Kilb, R. W., and Sutton, G. W., "Influence of Tensor Conductivity on Current Distribution in MHD Generator," *Journal of Applied Physics*, Vol. 32, No. 2, Feb. 1961, pp. 205–216.
doi:10.1063/1.1735979

143

[54] Oliver, D. A., and Mitchner, M., "Nonuniform Electrical Conduction in MHD Channel," *AIAA Journal*, Vol. 5, No. 8, Aug. 1967, pp. 1424–1432.
doi:10.2514/3.4215

[55] White, F. M., *Viscous Fluid Flow*, 3rd ed., McGraw–Hill, New York, 2006.

[56] Sutton, G. W., and Sherman, A., *Engineering Magnetohydrodynamics*, McGraw–Hill, New York, 1965.

[57] Lin, S.-C., Resler, E. L., and Kantrowitz, A., "Electrical Conductivity of Highly Ionized Argon Produced by Shock Waves," *Journal of Applied Physics*, Vol. 26, No. 1, Jan. 1955, pp. 95–109.
doi:10.1063/1.1721870

[58] Raizer, Y. P., *Gas Discharge Physics*, Springer–Verlag, New York1991.

[59] Cambel, A. B., *Plasma Physics and Magnetouid-Mechanics*, McGraw–Hill, New York, 1963.

[60] Bird, G. A., *Molecular Gas Dynamics and the Direct Simulation of Gas Flows*, Oxford Univ. Press, Oxford, England, U.K., 1994.

[61] Bird, G. A., "Monte-Carlo Simulation in an Engineering Context," *Progress of Astronautics and Aeronautics: Rarefied Gas Dynamics*, edited by S. S. Fisher, Vol. 74, AIAA, New York, 1981, pp. 239–255.

[62] Weng, Y., and Kushner, M. J., "Method for Including Electron-Electron Collisions in Monte Carlo Simulations of Electron Swarms in Partially Ionized Gases," *Physical Review A*, Vol. 42, No. 10, Nov. 1990, pp. 6192–6200.
doi:10.1103/PhysRevA.42.6192

[63] Viana, F. A. C., and Goel, T., "SURROGATES Toolbox User's Guide," Univ. of Florida, Gainesville, FL, 2008.

[64] Makridakis, S., "Accuracy Measures: Theoretical and Practical Concerns," *International Journal of Forecasting*, Vol. 9, No. 4, Dec. 1993, pp. 527–529.
doi:10.1016/0169-2070(93)90079-3

[65] Schwartzentruber, T. E., Scalabrin, L. C., and Boyd, I. D., "Hybrid Particle-Coontinuum Simulations of Non-Equilibrium Hypersonic Blunt Body Flow Fields," AIAA Paper 2006-3602, June 2006.

[66] Arave, R. J., and Huseley, O. A., "Aerothermodynamic Properties of High Temperature Argon," Boeing, TR D2-11238, Seattle, WA, Feb. 1962.

[67] Messerle, H. K., *Magnetohydrodynamic Electrical Power Generation*, Wiley, New York, 1995.

[68] Bailey, A. B., and Sims, W. H., "Shock Detachment Distance for Blunt Bodies in Argon at Low Reynolds Number," *AIAA Journal*, Vol. 1, No. 12, Dec. 1963, pp. 2867–2868.
doi:10.2514/3.2195

A. Ketsdever
Associate Editor

49th AIAA Aerospace Sciences Meeting including the New Horizons Forum and Aerospace Exposition
4 - 7 January 2011, Orlando, Florida

AIAA 2011-448

State Resolved Vibrational Relaxation Modeling
for Strongly Nonequilibrium Flows

Iain D. Boyd[*]
Department of Aerospace Engineering, University of Michigan, Ann Arbor, MI, 48109

Eswar Josyula[†]
U.S. Air Force Research Laboratory, Wright-Patterson Air Force Base, OH, 45433

Vibrational relaxation is an important physical process in hypersonic flows. Activation of the vibrational mode affects the fundamental thermodynamic properties and finite rate relaxation can reduce the degree of dissociation of a gas. Low fidelity models of vibrational activation employ a relaxation time to capture the process at a macroscopic level. High fidelity, state-resolved models have been developed for use in continuum gas dynamics simulations based on Computational Fluid Dynamics (CFD). By comparison, such models are not as common for use with the direct simulation Monte Carlo (DSMC) method. In this study, a high fidelity, state-resolved vibrational relaxation model is developed for the DSMC technique. Results obtained for integrated rate coefficients from the DSMC model are consistent with the corresponding CFD model. Comparison of relaxation results obtained with the high-fidelity DSMC model show significantly less excitation of upper vibrational levels in comparison to the standard, lower fidelity DSMC vibrational relaxation model. Application of the new DSMC model to a Mach 7 normal shock wave in carbon monoxide provides better agreement with experimental measurements than the standard DSMC relaxation model.

I. Introduction

Vibrational relaxation is an important physical process in hypersonic flows due to the high temperatures that are generated. For air molecules, when temperatures exceed about 1,000 K, the vibrational mode becomes significantly activated leading to important changes in fundamental thermodynamic properties such as the ratio of specific heats. At low pressure flow conditions, the rate of vibrational activation is finite, and the gas lies in a state of thermal nonequilibrium with different temperatures associated with the translational and vibrational modes. Under such conditions, it is also possible for the distribution of molecules across the quantized vibrational energy states to not follow the equilibrium Boltzmann form. In addition, finite rate activation of the upper vibrational levels has an important coupling to the rate of molecular dissociation.

Computation of hypersonic flows in the continuum flow regime is performed using traditional Computational Fluid Dynamics (CFD). Under non-continuum conditions, the direct simulation Monte Carlo (DSMC) method is most commonly employed. Due to the importance of vibrational relaxation, a number of models have been developed for use in both CFD and DSMC flow simulations. A primary purpose of the present investigation is to assess the current status of the DSMC vibrational relaxation models.

This paper first describes low- and high-fidelity vibrational relaxation models used in CFD formulations. Next, the standard (low-fidelity) approach for DSMC is described. Subsequently, a high-fidelity model for DSMC, that is consistent with the high-fidelity CFD approach, is introduced. Equilibrium heat bath DSMC simulation results are presented to assess the consistency of the new model against the CFD version. Nonequilibrium heat bath studies are presented in heating and cooling environments to compare the new and standard DSMC vibrational relaxation models. Comparison of the models is further undertaken for one-dimensional, normal shock waves that include a case for which experimental data exist. The paper closes with a summary and final conclusions.

---

[*] Professor, Associate Fellow AIAA.
[†] Senior Research Aerospace Engineer, Associate Fellow AIAA.

American Institute of Aeronautics and Astronautics

II. Vibrational Relaxation Models

A. Low-Fidelity CFD Approach

For conditions close to equilibrium, a common description of the vibrational relaxation process is provided by the Landau-Teller equation [1]:

$$\frac{dT_v}{dt} = \frac{T - T_v}{\tau_v}$$

(1)

where T_v is the vibrational temperature, T is the translational temperature, and τ_v is the vibrational relaxation time. In state-of-the-art CFD codes, finite rate vibrational relaxation is almost always modeled in terms of vibrational energy:

$$\frac{d\varepsilon_v}{dt} = \frac{\varepsilon_v^* - \varepsilon_v}{\tau_v}$$

(2)

where ε_v is the vibrational energy, ε_v^* is the vibrational energy at the translational temperature, and τ_v is again the vibrational relaxation time that is usually evaluated as:

$$\tau_v = \tau_{MW} + \tau_P$$

(3)

with the first term due to Millikan and White [2] and the second term, a high temperature correction, due to Park [3], has the following form:

$$\tau_p = \frac{1}{n\sigma_v C}$$

(4a)

where n is the total number density, C is the average thermal speed. Several forms for the vibrational cross section have been proposed from Park's original form

$$\sigma_v = 3 \times 10^{-21}\left(\frac{50,000}{T}\right)^2$$

(4b)

to a form derived from DSMC studies [4]:

$$\sigma_v = 5.81 \times 10^{-21}$$

(4c)

This low fidelity approach will be referred to as CFD-LT and it attempts to describe the detailed processes of actual vibrational relaxation that involves both vibration-translation (VT) and vibration-vibration (VV) energy transfer processes among quantized vibrational energy states using a single relaxation equation.

B. High-Fidelity CFD Approach

Adamovich et al. describe the development of vibrational transition rate coefficients based on the Forced Harmonic Oscillator (FHO) approach [5,6]. The rate coefficients are obtained through analytical, thermal averaging of collision-based transition probabilities. These probabilities are described in more detail in Section D and form the basis of a new, high fidelity DSMC model. Rate coefficient expressions are developed separately for vibration-translation (VT) and vibration-vibration (VV) transitions. The studies of Adamovich et al. [5,6] show that these models provide rate coefficients for nitrogen that are in good agreement with values obtained by Billing and Fisher using a quantum classical model [7]. The VT and VV rate coefficients may then be used in a Master Equation formulation to simulate the state-resolved vibrational relaxation process [8] that has been included in hypersonic flow field modeling [9].

C. Low-Fidelity DSMC Approach

Finite rate vibrational relaxation is usually modeled in the DSMC framework using a probability of vibrational energy exchange for each collision that is consistent at the macroscopic level with the CFD-LT approach [10]. For collisions that are selected for vibrational relaxation, a quantized form [11] of the Larsen-Borgnakke energy exchange model [12] is employed. Usually, the vibrational energy levels are described using a harmonic oscillator model. This low fidelity approach will be referred to as DSMC-LB and it acts to equilibrate the translational and vibrational energy modes of the molecules in the collisions selected for vibrational relaxation.

D. New, High-Fidelity DSMC Approach

The basis for the new, high-fidelty DSMC model is the basic transition probability of the FHO model described by Adamovich et al. [6]. Specifically, in a molecule-molecule collision, the probability of transition from initial vibrational levels (i_1, i_2) to final vibrational levels (f_1, f_2) is given by:

$$P_{VVT}(i_1, i_2 \to f_1, f_2, \varepsilon, \rho) = \left| \sum_{r=0}^{n} C_{r+1,i_2+1}^{i_1+i_2} C_{r+1,f_2+1}^{f_1+f_2} \exp\left[-i(f_1 + f_2 - r)\rho\right] P_{VT}^{1/2}(i_1 + i_2 - r \to f_1 + f_2 - r, 2\varepsilon) \right|^2 \quad (5a)$$

where

$$P_{VT}(i \to f, \varepsilon) = i! f! \varepsilon^{i+f} \exp(-\varepsilon) \left| \frac{(-1)^r}{r!(i-r)!(f-r)!} \frac{1}{\varepsilon^r} \right|^2 \quad (5b)$$

and

$$\varepsilon = S_{VT} \frac{4\pi^3 \omega \left(\tilde{m}^2 / \mu \right) \gamma^2}{\alpha^2 h} \sinh^{-2}\left(\frac{\pi \omega}{\alpha \bar{v}} \right) \quad (5c)$$

$$\rho = \left(S_{VV} \frac{\alpha^2 \bar{v}^2}{\omega_1 \omega_2} \right)^{1/2} \quad (5d)$$

In these equations: $C_{a,b}^{c}$ are transformation matrices defined in Ref. 6, S_{VT} and S_{VV} are steric factors, ω is the oscillator frequency, $\tilde{m}$ is the collision reduced mass, μ is the oscillator reduced mass, γ is oscillator mass ratio, α characterizes the intermolecular potential, h is Planck's constant, and $\bar{v}$ is the symmetrized relative velocity. Further definitions and numerical values of the key parameters are provided in Ref. 6. It should be noted that a number of prior DSMC studies have also considered state-resolved vibrational relaxation [13-16]. For example, in Ref. 16, the purely vibration-translation probability, Eq. (5b), was used to analyze vibrational relaxation processes. The present study represents a significant increase in fidelity by allowing full VVT transitions, and is referred to as the DSMC-FHO model. The vibrational levels are described by an anharmonic oscillator model in the DSMC-FHO model.

Due to the complicated mathematical form of Eqs. (5), the evaluation of transition probabilities for each collision in a DSMC computation is expensive numerically. Therefore, a table of probabilities is pre-computed for a fixed number of relative velocity bins. In the present work, the relative velocity bin size employed is 100 m/s, and transitions of up to ±5 quantum levels are considered. To further aid numerical performance, two different tables are generated. The first table provides the total probability of all transitions from the current vibrational levels of the two molecules in the collision. If it is determined that a transition does occur, a second table is then employed to decide, using an acceptance-rejection scheme, which of the transitions actually occurs. The tabulated approach is found to offer excellent agreement with more expensive DSMC computations in which the transitions are evaluated using the full formulae at a small fraction of the numerical cost.

III. Results

The primary purpose of this study is to develop and assess a high fidelity, state-resolved, vibrational relaxation model for the DSMC technique. This goal is achieved by performing a sequence of investigations that mainly consider molecular nitrogen including: an evaluation of the low-fidelity Larsen-Borgnakke DSMC model; FHO rate coefficient studies; nonequilibrium relaxation studies; shock wave studies, and studies involving carbon monoxide.

A. Evaluation of the Low-Fidelity DSMC Model

A heat bath is a zero dimensional configuration in which the energy modes of the gas are initialized to Boltzmann distributions specified by a mode temperature. For an equilibrium heat bath, used for rate coefficient evaluation, all mode temperatures are equal. For relaxation studies, the translational and rotational temperatures are equal, while the vibrational temperature is set either lower (vibrational heating) or higher (vibrational cooling). A vibrational heating relaxation study is first performed to compare the low-fidelity Larsen-Borgnakke model for DSMC (DSMC-LB) with the low-fidelity Landau-Teller (CFD-LT) and high-fidelity Forced Harmonic Oscillator (CFD-FHO) CFD models. Figures 1a shows the time evolution of the translational and vibrational temperatures obtained with the CFD-LT and DSMC-LB models for a nitrogen heat bath with initial conditions: p=101,325 Pa,

Ttr=10,000 K, Tv=1,000 K. Clearly, the two approaches offer almost identical relaxation profiles. However, when the vibrational energy distribution functions (VEDFs) from these simulations are compared, see Fig. 1b, it is clear that while the CFD-LT approach assumes Boltzmann distributions at the vibrational temperature, the DSMC-LB model predicts strongly nonequilibrium distributions. The DSMC-LB model essentially predicts that the molecules consist of two distinct populations given by the initial cold temperature and the final equilibrium temperature. This is not surprising as the basic concept of the DSMC-LB model is to instantly equilibrate the internal modes of a very small fraction of all collisions. Similar bi-modal vibrational energy distributions have been seen in previous DSMC studies [14,16,17], and one of the primary goals of the present study is to try and determine whether this behavior is physically accurate. Figure 1c re-plots the DSMC-LB data using vibrational energy as the variable and the straight lines are Boltzmann distributions based on the vibrational temperatures computed in the simulation. The nonequilibrium behavior of the DSMC-LB model in Fig. 1c can be compared with the profiles shown in Fig. 1d that are obtained using the CFD-FHO model including both VT and VV transitions up to five quantum steps. Clearly, the CFD-FHO model predicts a significantly smaller degree of nonequilibrium for the vibrational relaxation process.
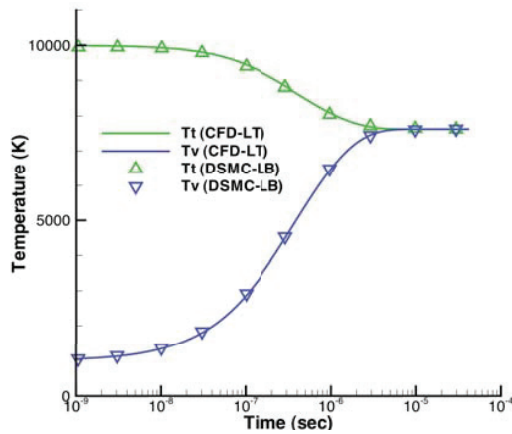
Figure 1a. Relaxation of N$_2$ in a heat bath for a vibrational heating environment.
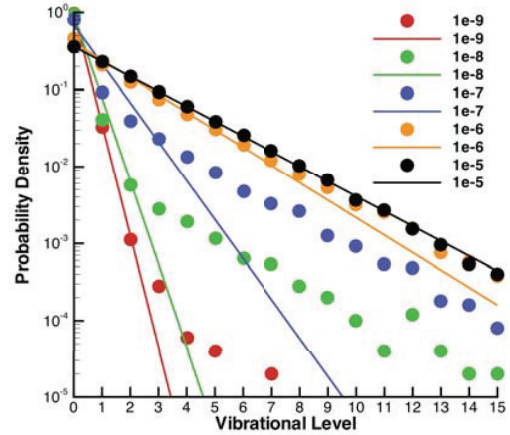
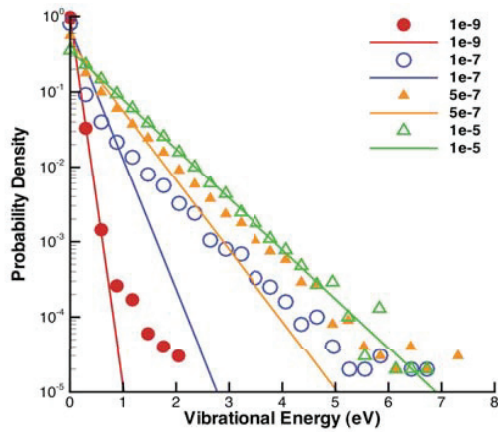**Figure 1b. Time evolution of the VEDF: lines=CFD-LT; symbols=DSMC-LB.**
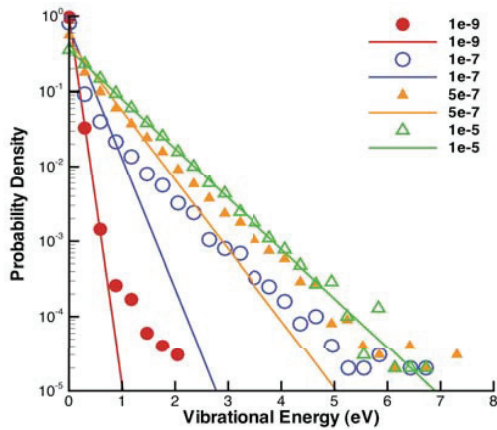
Figure 1c. Time evolution of the VEDF: lines=Boltzmann; symbols=DSMC-LB.
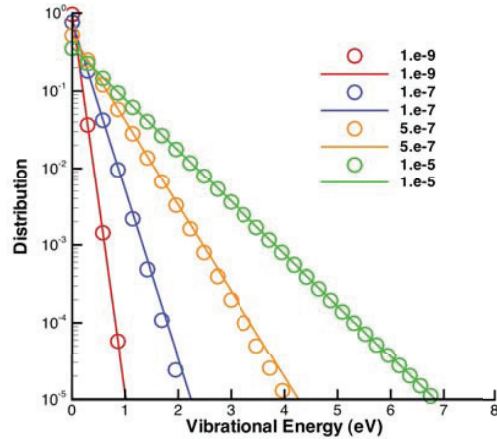
Figure 1d. Time evolution of the VEDF: lines=Boltzmann; symbols=CFD-FHO.

Since a heath bath is a zero dimensional case without flow, it is useful to consider the performance of the DSMC-LB model in a one-dimensional shock wave to determine whether the highly nonequilibrium vibrational energy distribution is again predicted. Using nitrogen as the test gas again, a computation is performed at Mach 10 matching the highest Mach number flow condition of the experiments performed by Alsmeyer [18]. Alsmeyer used an electron beam fluorescence technique to measure the density profiles through a series of normal shock waves. It

is stated in his study that vibrational relaxation effects are not important even at Mach 10, and we use this opportunity to assess that statement. Figure 2a shows profiles of density (ρ), and the temperatures associated with the translational (Tt), rotational (Tr), and vibrational (Tv) modes. The profiles are normalized using the same approach as Alsmeyer. The solid line profiles represent results in which vibrational relaxation is included in the analysis whereas the dotted lines with circles are obtained from a simulation that omits vibrational relaxation. The excellent agreement between the two sets of profiles confirms Alsmeyer's statement that his experimental measurements of the shock structure are not greatly affected by the vibrational relaxation process, even at Mach 10. Of course, the profiles far downstream of the shock front are significantly influenced by the vibrational activation process. Figure 2b shows the evolution of the vibrational energy distribution function through the shock wave. These distributions are very similar to those predicted by the DSMC-LB approach shown in Fig. 1b for the heat bath environment. It is therefore concluded that the prediction by the DSMC-LB model of strongly nonequilibrium vibrational energy distributions is a general result that needs to be checked against a high fidelity DSMC model.
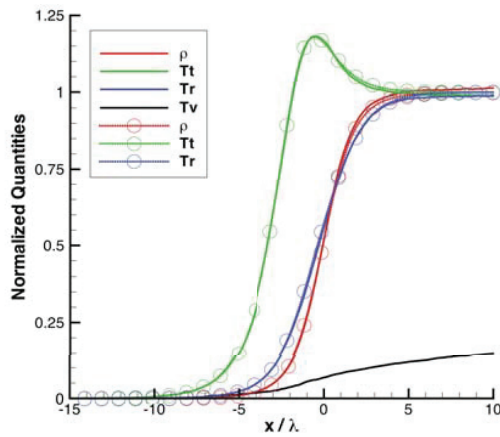
Figure 2a. Profiles at the front of a Mach 10 normal shock wave in nitrogen: symbols=vibration omitted
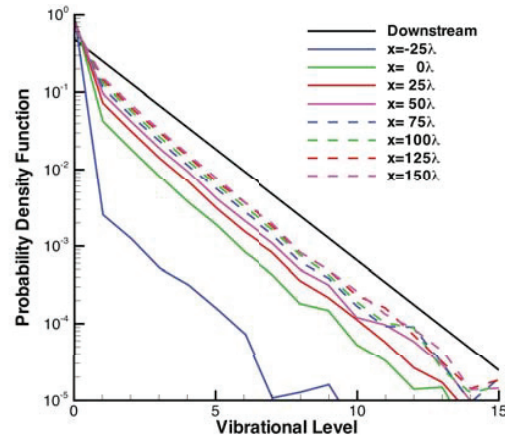
Figure 2b. Spatial evolution of the vibrational energy distribution function in the Mach 10 shock.

B. Assessment of the High-Fidelity DSMC Model

The prior results indicate that the low-fidelity DSMC-LB model predicts a degree of thermal nonequilibrium in both heat bath and shock wave studies that is much stronger than that predicted by the high-fidelity CFD-based FHO model. This finding motivates the development of the high-fidelity DSMC-FHO model described earlier. In the present section, equilibrium heat bath studies are first performed using DSMC-FHO in which the transition probabilities are integrated over all collisions to determine the transition rates. All values of the FHO parameters employed in Ref. 6 for N_2-N_2 transitions are employed in the DSMC-FHO model except for the steric factors that are set to: $S_{VT} = 1/9$ and $S_{VV} = 1/40$ (compared to $S_{VT} = 1/2$ and $S_{VV} = 1/25$ used in Ref. 6). The rates obtained from DSMC-FHO are compared in Figs. 3 with published data for the CFD-FHO model [6] as well as to results obtained using a quantum classical method by Billing and Fisher [7]. In general, the rates evaluated using the DSMC model are in good agreement with the CFD-FHO model of Adamovich et al. [6] which provides some validation of the approximations employed in the development of the CFD-FHO approach. The fact that different steric factors are required to achieve good agreement between these two FHO models suggests that the CFD-FHO approximations mainly result in an inaccuracy that can be accounted for through a multiplicative constant. The comparisons of the DSMC-FHO model with the detailed computations of Billing and Fisher [7] are also satisfactory including the VV transition rates (Fig. 3d).
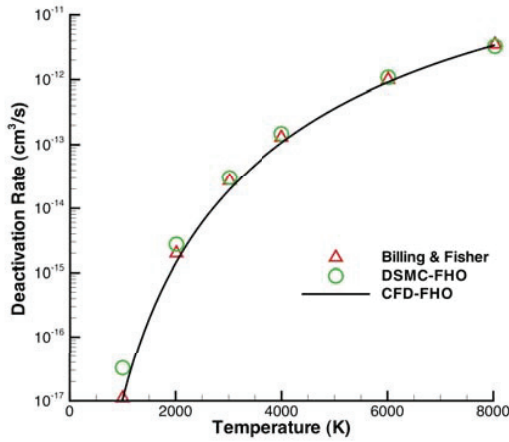
Figure 3a. VT de-excitation rate (1,0) to (0,0) as a function of temperature.
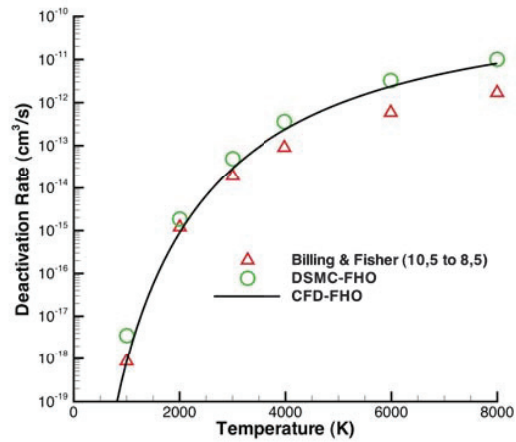
Figure 3b. VT de-excitation rate (10,0) to (8,0) as a function of temperature.
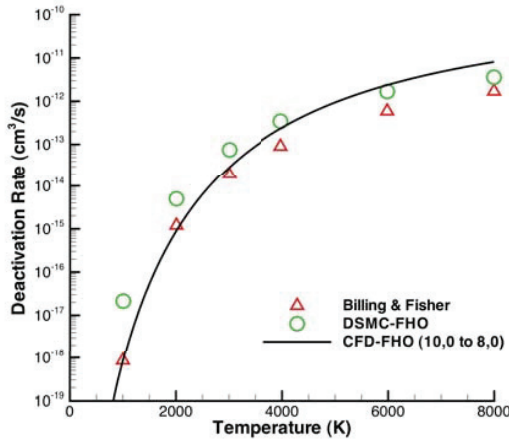
Figure 3c. VT de-excitation rate (10,5) to (8,5) as a function of temperature.
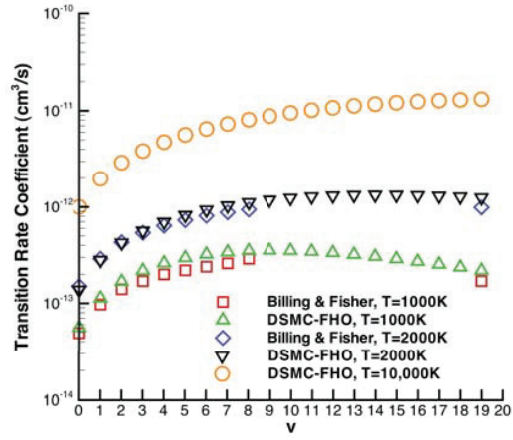
Figure 3d. VV transition rate (v,1) to (v+1,0) as a function of vibrational level and temperature.

**Figure 4a. Time evolution of the VEDF: lines=Boltzmann; symbols=DSMC-LB.**
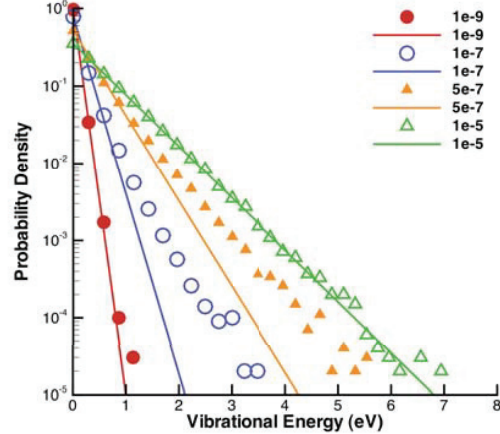
Figure 4b. Time evolution of the VEDF: lines=Boltzmann; symbols=DSMC-FHO.

American Institute of Aeronautics and Astronautics

Having established that the DSMC-FHO model produces transition rates consistent with the quantum classical model, the DSMC model is now applied to the same kind of configurations studied earlier. Figure 4a is a repeat of Fig. 1c included here to facilitate comparison to Fig. 4b that shows the time evolutions obtained with the DSMC-FHO model of the vibrational energy distributions for the same vibrational heating conditions studied in Figs. 1. While the DSMC-FHO model still displays some nonequilibrium, it is significantly less bi-modal in nature than the distributions predicted by the DSMC-LB model.

Figures 5a and 5b show the temperature profiles and vibrational energy distribution evolution for a vibrational cooling case for initial conditions: p=101,325 Pa, Ttr=3,000 K, Tv=10,000 K. In Fig. 5a, results are provided from all four models, both low- and high-fidelity approaches using CFD and DSMC. The results show that the two low-fidelity models (CFD-LT and DSMC-LB) agree with each other and they predict a significantly slower relaxation rate than the two high-fidelity models (CFD-FHO and DSMC-FHO) that again agree with each other. Figure 5b shows the evolution of the vibrational energy distribution obtained with the DSMC-LB model. Careful inspection of the distribution shows that once again it is composed of two populations of molecules: one defined by the initial temperature and the second defined by the final equilibrium temperature. Figure 5c shows the equivalent profiles obtained with the DSMC-FHO model. To a very good approximation, the FHO model predicts that the relaxation process occurs through a sequence of near-Boltzmann distributions, and so once again this model produces a smaller degree of nonequilibrium in comparison to the low-fidelity DSMC-LB approach.
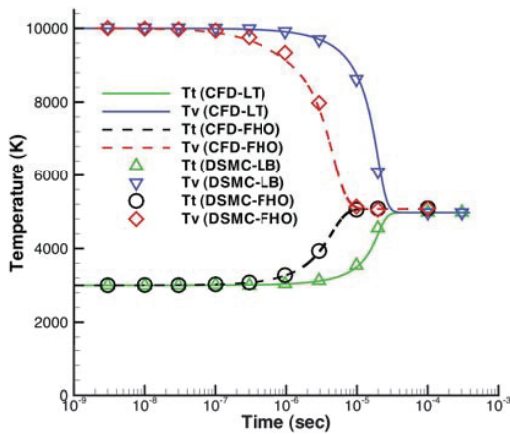
Figure 5a. Relaxation of N_2 in a heat bath for a vibrational cooling environment.
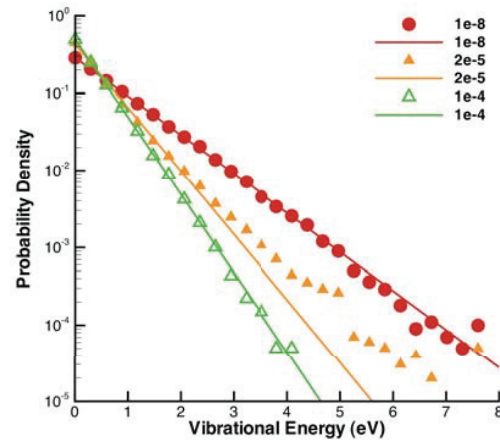
Figure 5b. Time evolution of the VEDF: lines=Boltzmann; symbols=DSMC-LB.
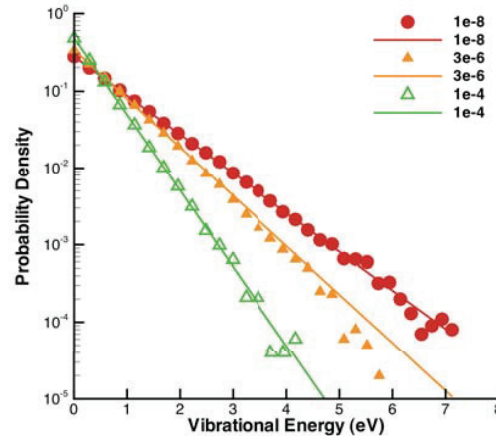
Figure 5c. Time evolution of the VEDF: lines=Boltzmann; symbols=DSMC-FHO.

The DSMC-FHO model is next applied to Alsmeyer's Mach 10 nitrogen shock wave discussed earlier. While the temperature and density profiles are very similar to those obtained with the DSMC-LB model, there are

7
American Institute of Aeronautics and Astronautics

significant differences in the vibrational energy distribution functions, shown in Figs. 6a and 6b. In particular, the distributions obtained with the DSMC-FHO model, in Fig. 6b, again show a significantly reduced level of vibrational nonequilibrium in comparison to the low-fidelity LB approach.
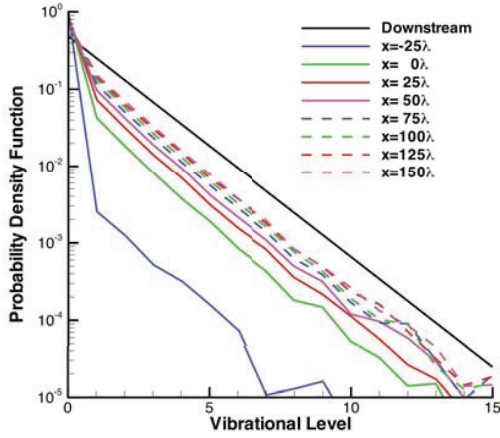
Figure 6a. Spatial evolution of the VEDF in the Mach 10 shock: DSMC-LB.
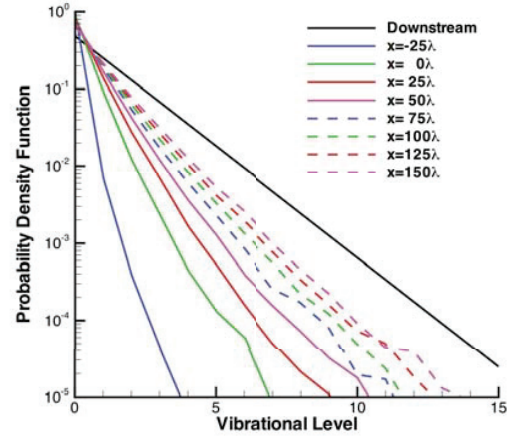
Figure 6b. Spatial evolution of the VEDF in the Mach 10 shock: DSMC-FHO.

C. Carbon Monoxide Studies

Unfortunately, no experimental measurements have been performed in molecular nitrogen to evaluate the differences predicted in vibrational energy distributions by the DSMC-LB and DSMC-FHO models that are shown in Figs. 6. One set of experimental data that does appear to offer the potential to assess the DSMC vibrational relaxation models is the study performed by Meolans and Brun [19] who measured relative vibrational populations in strong shock waves of carbon monoxide. Parameters employed in the DSMC-FHO model for CO are: α=3.6x10^{10} m^{-1}, $S_{VT} = 1/9$ and $S_{VV} = 3/40$. In order to apply the DSMC-FHO model to CO, it is of course necessary to repeat the equilibrium transition rate coefficient studies. Examples of comparisons between the DSMC integrated FHO rates, rates evaluated using the CFD-FHO formulae, and semi-classical calculations of Cacciatore and Billing [20] are shown in Figs. 7a and 7b. Once again, the agreement between the DSMC-FHO and CFD-FHO results is good. Agreement with the semi-classical calculations is less satisfactory.
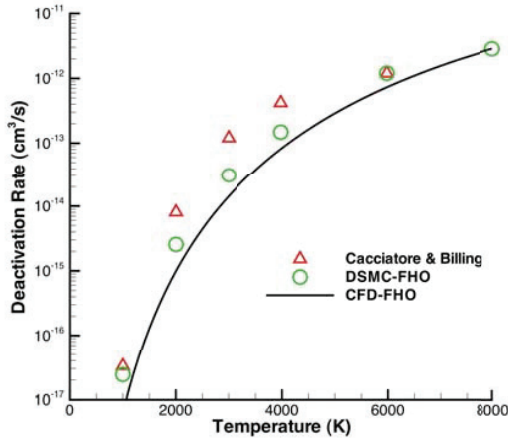
Figure 7a. VT de-excitation rate (1,0) to (0,0) as a function of temperature for CO.
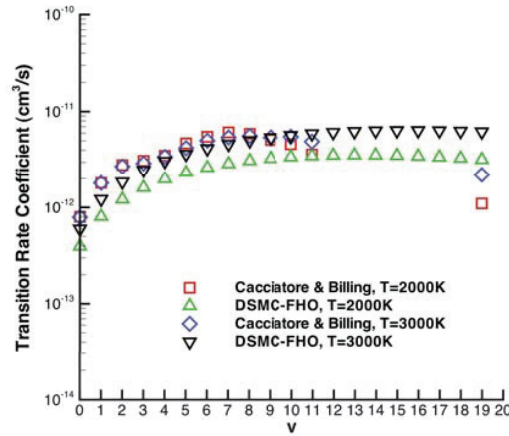
Figure 7b. VV transition rate (v,1) to (v+1,0) as a function of temperature for CO.

Finally, the DSMC-LB and the DSMC-FHO models are applied to the conditions of the Mach 7 carbon monoxide shock wave studied by Meolans and Brun [19]. The transient profiles of the relative population of the v=4 vibrational state obtained with the two DSMC models are compared with the experimental measurements in

8
American Institute of Aeronautics and Astronautics

Figs. 8a and 8b. In Figs. 8, two results from each DSMC simulation are provided. The profile labeled "DSMC" is the actual result from the simulation for the relative population in the v=4 vibrational state. The profile labeled "DSMC-Boltzmann" is the relative population in v=4 determined using the computed vibrational temperature along with an assumption of a Boltzmann energy distribution. Comparison of these two profiles provides an indication of the degree of vibrational nonequilibrium predicted by the two models. In Fig. 8a, the DSMC-LB model predicts a strong degree of vibrational nonequilibrium in the early stages of the vibrational activation process. The actual population predicted by the model is significantly higher than the Boltzmann assumption that is in good agreement with the experimental data in this region of the shock. This behavior is consistent with the nitrogen results reported earlier in this study and is perhaps the most significant finding of the current investigation. Namely, that the DSMC-LB model appears to over-predict the populations of all but the lowest vibrational levels. By comparison, as shown in Fig. 8b, the two DSMC profiles obtained with the DSMC-FHO model are in good agreement with each other and with the experimental measurements. This result indicates, at least for carbon monoxide, that the high-fidelity DSMC-FHO model is able to simulate the state-resolved vibrational relaxation process more accurately than the low-fidelity DSMC-LB approach.
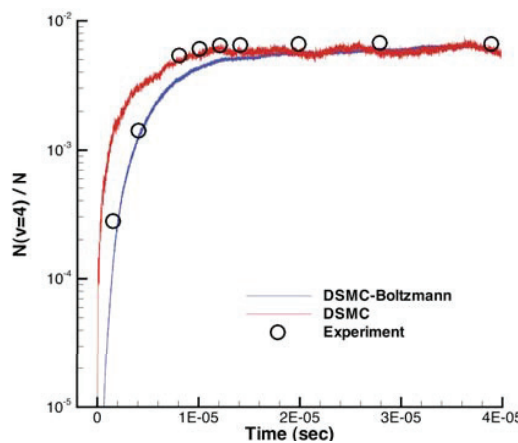
Figure 8a. Profiles of the relative population of v=4 for a Mach 7 shock wave of CO: DSMC-LB.   **Figure 8b. Profiles of the relative population of v=4 for a Mach 7 shock wave of CO: DSMC-FHO.**
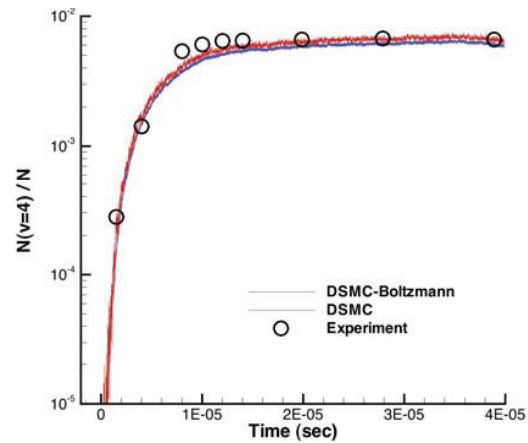
IV. Summary and Conclusion

High fidelity, state-resolved, vibrational relaxation models have been developed in the past for use in CFD computations of hypersonic flows. By comparison, the level of vibrational relaxation modeling using the DSMC technique has not been as sophisticated. In the present study, a high fidelity, state-resolved, vibrational relaxation model for the DSMC technique has been developed, implemented with numerical efficiency, verified to produce expected rate coefficients, and partly validated through its application to a Mach seven shock wave for which experimental measurements of the vibrational levels exist in the literature.

Future work will aim to extend the DSMC-FHO model to include the effects of molecular dissociation. In addition, in the present work, it was not possible to analyze the behavior of the highest vibrational levels due to statistical fluctuations. It is required to employ a numerical weighting scheme in order to track molecules in populations that occur with very small probability. Finally, it is extremely important for the further development of high fidelity physical models for both CFD and DSMC that experiments be performed in air species using advanced, optical diagnostics, under nonequilibrium flow conditions, similar to the shock tube experiment in carbon monoxide that was employed in the current study.

References

[1] Landau, L. and Teller, E., "Theory of Sound Dispersion," Physics Sowjetunion, Vol.10, 1936, pp. 34-43.

[2] Milliken, R.C. and White, D.R., "Systematics of Vibrational Relaxation," *Journal of Chemical Physics*, Vol. 39, 1963, pp. 3209-3213.

[3] Park, C., *"*Review of Chemical Kinetic Problems of Future NASA Missions, I: Earth Entries," *Journal of Thermophysics and Heat Transfer,* Vol. 7, 1993, pp. 385-398.

[4] Haas, B.L. and Boyd, I.D., "Models for Direct Monte Carlo Simulation of Coupled Vibration-Dissociation," *Physics of Fluids A*, Vol. 5, 1993, pp. 478-489.

[5] Adamovich, I.V., Macheret, S.O., Rich, J.W., and Treanor, C.E., "Vibrational Relaxation and Dissociation Behind Shock Waves Part 1: Kinetic Rate Models," *AIAA Journal*, Vol. 33, 1995, pp. 1064-1069.

[6] Adamovich, I.V., Macheret, S.O., Rich, J.W., and Treanor, C.E., "Vibrational Energy Transfer Rates Using a Forced Harmonic Oscillator Model," *Journal of Thermophysics and Heat Transfer*, Vol. 12, 1998, pp. 57-65.

[7] Billing, G.D. and Fisher, E.R., "VV and VT Rate Coefficients in N2 by a Quantum-Classical Model," *Chemical Physics*, Vol. 43, 1979, pp. 395-401.

[8] Adamovich, I.V., Macheret, S.O., Rich, J.W., and Treanor, C.E., "Vibrational Relaxation and Dissociation Behind Shock Waves Part 2: Master Equation Modeling," *AIAA Journal*, Vol. 33, 1995, pp. 1070-1075.

[9] Josyula, E., "Computational Study of Vibrationally Relaxing Gas Past Blunt Body in Hypersonic Flows," *Journal of Thermophysics and Heat Transfer*, Vol. 14, 2000, pp. 18-26.

[10] Boyd, I.D., "Analysis of Vibration-Dissociation-Recombination Processes Behind Strong Shock Waves of Nitrogen," *Physics of Fluids A*, Vol. 4 (1), 1992, pp. 178-185.

[11] Bergemann, F. and Boyd, I.D., "New Discrete Vibrational Energy Method for the Direct Simulation Monte Carlo Method," *Rarefied Gas Dynamics*, Progress in Astronautics and Aeronautics, AIAA, Washington, Vol. 158, 1994, p. 174.

[12] Borgnakke, C. and Larsen, P.S., "Statistical Collision Model for Monte Carlo Simulation of Polyatomic Gas Mixture," *Journal of Computational Physics*, Vol. 18, 1975, pp. 405-420.

[13] Abe, T., "Inelastic Collision Model for Vibrational-Translational and Vibrational-Vibrational Energy Transfer in the Direct Simulation Monte Carlo Method," *Physics of Fluids*, Vol. 6, 1994, pp. 3175-3179.

[14] Wysong, I.J., Wadsworth, D.C., Weaver, D.P., and Campbell, D.H., "Influence of Vibrational Nonequilibrium on Chemically Reacting Rarefied Flows - Toward Experimental Verification of DSMC Models," AIAA Paper 1996-2023, June 1996.

[15] Wadsworth, D.C. and Wysong, I.J., "Vibrational Favoring Effect in DSMC Dissociation Models," *Physics of Fluids*, Vol. 9, 1997, pp. 3873-3884.

[16] Vijayakumar, P., Sun, Q. and Boyd, I.D., "Detailed Models of Vibrational-Translational Energy Exchange for the Direct Simulation Monte Carlo Method," *Physics of Fluids*, Vol. 11, 1999, pp. 2117-2126.

[17] Gimelshein, S.F., Boyd, I.D., Sun, Q., and Ivanov, M., "DSMC Modeling of Vibration-Translation Energy Transfer in Hypersonic Rarefied Flows," AIAA Paper 99-3451, June 1999.

[18] Alsmeyer, H., "Density Profiles in Argon and Nitrogen Shock Waves Measured By Absorption of an Electron Beam," *Journal of Fluid Mechanics*, Vol. 74, 1976, pp. 497-513.

[19] Meolans, J.G. and Brun, R., "Nonequilibrium Vibrational Population Behind Shock Waves: Comparison Theory – Experiments," *Proceedings of the 15th International Symposium on Rarefied Gas Dynamics*, Teubner, Stuttgart, 1986, p. 345.

[20] Cacciatore, M. and Billing, G.D., "Semiclassical Calculation of VV and VT Rate Coefficients in CO," *Chemical Physics*, Vol. 58, 1981, pp. 395-407.

48th AIAA Aerospace Sciences Meeting Including the New Horizons Forum and Aerospace Exposition
4 - 7 January 2010, Orlando, Florida

AIAA 2010-1569

Evaluation of a Hybrid Boltzmann-Continuum Method for High Speed Nonequilibrium Flows

Jonathan M. Burt,[1] Timothy R. Deschenes,[2] and Iain D. Boyd[3]
Department of Aerospace Engineering
University of Michigan, Ann Arbor, MI 48109

Eswar Josyula[4]
U.S. Air Force Research Laboratory
Wright-Patterson Air Force Base, OH 45433

   A series of monatomic gas flows over a cylinder, with a freestream Mach number of 4 and a range of Knudsen numbers, are used to evaluate the unified flow solver (UFS) code. The UFS code combines several compressible gas flow simulation schemes for application to flow problems involving a wide range of Knudsen number (Kn) regimes, and features capabilities for strong coupling between low-Kn and high-Kn schemes along with automatic tree-based grid adaptation. UFS simulation results are compared with results from simulations which employ other codes intended for the same class of problems, and good agreement is generally found. Areas identified for improvement in UFS include calculation of surface quantities and numerical performance of the UFS Boltzmann equation solver.

I.   Introduction

A variety of gas flow problems are characterized by a wide range of local Knudsen number (Kn) regimes, with strong translational nonequilibrium in some portions of the flowfield and near-equilibrium velocity distributions in other flowfield regions. (The Knudsen number, which quantifies the level of translational nonequilibrium in a gas flow, is defined as the ratio of the mean free path to some characteristic length scale based on boundary geometry or gradients.) These problems include hypersonic aerodynamics flows, such as those around atmospheric entry vehicles; rocket exhaust flows at high altitudes; spacecraft gas venting; shock-boundary layer interactions and other flows for which internal shock structure is important; and subsonic flows, such as those within MEMS devices, which involve either very small length scales or low gas density.

   For accurate simulation of high-Kn rarefied regions within these flows, translational nonequilibrium effects must be considered, and either a particle scheme such as the direct simulation Monte Carlo (DSMC) method[1] or a direct simulation method for the governing Boltzmann equation[2] is required. While these methods can be applied to low-Kn regions as well, they tend to be far more computationally expensive than continuum computational fluid dynamics (CFD) methods based on the Navier-Stokes equations while offering the same degree of accuracy in low-Kn regimes. Thus, an optimal combination of accuracy and efficiency for simulation of mixed rarefied-continuum flows generally requires integration of rarefied and continuum schemes within a coupled numerical framework. In this hybrid approach, the simulation domain is divided into rarefied and continuum flow regions through evaluation of a continuum breakdown parameter. DSMC or Boltzmann solver calculations are performed in rarefied regions, a continuum CFD method is applied in continuum regions, and coupling routines are used to exchange conserved quantities or other flow information across continuum breakdown boundaries.

   In recent years, most work on algorithm development for mixed rarefied-continuum flow simulations has focused on hybrid CFD-DSMC techniques.[3-8] This type of technique has been shown to preserve the physical accuracy of DSMC in high-Kn regions, while offering the numerical efficiency of a CFD Navier-Stokes solver in low-Kn regions. However, the inherent statistical scatter in DSMC can make coupling between the two methods difficult, and much of the focus in hybrid DSMC-CFD development has been on scatter reduction to avoid

---

[1] Post-doctoral research fellow, AIAA member.
[2] Graduate student, AIAA student member.
[3] Professor, AIAA associate fellow.
[4] Senior research aerospace engineer, AIAA associate fellow.

Approved for public release; distribution unlimited.

inaccurate or unstable CFD calculations. The scatter problem becomes particularly severe in simulations of highly unsteady flows, subsonic flows, or flow problems (such as those involving gas radiative emission or chemistry) for which accurate characterization is desired for the low-probability tails of the velocity distribution. In these cases, a very large number of DSMC particles may be required for sufficient scatter reduction, and a hybrid CFD-DSMC simulation can be prohibitively expensive.

In one alternative hybrid scheme, a set of direct simulation methods for the Boltzmann equation are coupled to kinetic methods for the compressible Navier-Stokes or Euler equations.[9-13] This hybrid scheme, implemented in the unified flow solver (UFS) code, is not prone to the DSMC statistical scatter problem which may be considered the main drawback in CFD-DSMC techniques. Instead of using a collection of particles to represent the gas velocity distribution within rarefied regions, as in DSMC, nonequilibrium velocity distributions in UFS are modeled using a Cartesian grid in velocity space. Discrete approximations of the advection and collision terms in the Boltzmann equation are employed to update the probability density at grid points in both velocity and physical space, and coupling across continuum breakdown boundaries is performed through two-way information exchange during each simulation time step. The UFS code is based on the open source framework of the Gerris flow solver,[14] and includes capabilities for automatic binary tree-based Cartesian grid adaptation. Solid 2D or 3D objects are easily integrated within the simulated flowfield through the use of cut-cell boundaries, and additional procedures allow optimized load balancing for parallel domain decomposition. Continuum breakdown evaluations are periodically performed during a UFS simulation, for automatic assignment of each grid cell to either continuum or rarefied domains. Performance improvements, relative to DSMC or full Boltzmann solutions, are realized in UFS through the use of continuum CFD methods where appropriate, and through initialization of rarefied domain calculations with (at least partially converged) continuum method solutions. In comparison with DSMC, reduced simulation expense has been demonstrated in UFS simulations of a nozzle/plume expansion flow,[11] and comparable expense to DSMC has been observed in UFS simulations of a hypersonic blunt body flow.[12]

In the current effort, the UFS scheme is applied to a set of high Mach number rarefied/continuum flows over a cylinder, and is evaluated for accuracy and efficiency through comparison with DSMC and CFD Navier-Stokes methods. As previous evaluations of UFS have been carried out for a variety of flow problems, new objectives here include performing a more comprehensive comparison for accuracy and efficiency with both DSMC and CFD, and highlighting limitations, drawbacks or areas to prioritize for future development of the UFS code.

In the following sections, simulation setup and input parameters are described for a number of simulations performed on either UFS or other codes which are used for comparison. The computational expense of various simulations is then discussed, and a general efficiency comparison is made between UFS and the other codes employed in this study. Next, detailed results are presented. The accuracy of UFS simulation results is assessed by comparing surface flux coefficients, contour lines and variation along the stagnation streamline in selected flow properties. Drag coefficients computed from these simulations are then plotted as a function of global Knudsen number, in order to further assess accuracy of UFS simulations, compare with available experimental data, and evaluate the dependence of drag on the cylinder surface temperature. Finally, results are summarized and positive characteristics, potential problems and possible directions for future work involving UFS are discussed.

II. Simulation Setup

As the basis for a series of test problems, we consider a flow of argon over a cylinder with a freestream Mach number of 4. The hard sphere collision model is used, so that collision cross sections are independent of the relative speed between colliding particles and viscosity varies as the square root of temperature.[1] Diffuse reflection with full thermal accommodation to the wall temperature is assumed on the cylinder surface, and the temperature at the wall is set to 1.2 times the freestream temperature. (In simulations for which NS calculations are used over the entire flowfield, a no-slip wall boundary condition is employed.) Simulations are performed for global Knudsen numbers Kn (the ratio of the freestream mean free path to cylinder diameter) of 0.3, 0.03 and 0.003 using various models in UFS. For comparison, additional simulations are performed using the DSMC code MONACO[15] and the Navier-Stokes CFD code LeMANS.[16]

The Kn = 0.3 case is representative of a highly rarefied flow, and is simulated using numerical solutions to the Boltzmann equation and the Bhatnagar–Gross–Krook (BGK) equation.[2] A Navier-Stokes (NS) simulation of this flow is also performed using LeMANS. In the Kn = 0.03 case, large portions of the flowfield are within both rarefied and continuum regimes, and hybrid schemes involving coupled rarefied and continuum flow calculations should give the best combination of accuracy and efficiency. This flow is simulated using UFS with the following options: BGK, NS, hybrid BGK-NS and hybrid BGK-Euler. The accuracy of all UFS results at Kn = 0.3 and 0.03 is assessed through comparison with results from simulations using the DSMC code MONACO. The Kn = 0.003 case,

for which only small portions of the flowfield are in significant thermal nonequilibrium, is used to evaluate the NS solver in UFS by comparing UFS NS results with those from a NS simulation using the LeMANS CFD code. To demonstrate the expected inaccuracy for NS simulations at Kn = 0.3 and 0.03, LeMANS results are also generated for these cases.

MONACO simulations in this study employ unstructured grids which are automatically adapted to the local mean free path using a grid generation utility AFMGEN, and dynamically adaptive DSMC subcells are used to assure sufficiently small mean collision separation values. Spatially uniform time step intervals in MONACO are carefully set to meet DSMC requirements,[1] and numerical weight values are dynamically adapted in each cell to meet standard DSMC guidelines (at least 20 particles per cell) while avoiding any efficiency reduction due to excessive particle populations. LeMANS simulations use a finite volume implicit second-order modified version of the Steger-Warming flux vector splitting scheme,[17] which is less dissipative in boundary layers but switches back to the original form in the vicinity of strong shocks.

In hybrid UFS simulations, a continuum breakdown parameter based on characteristic length scales for velocity and pressure gradients is used to assign flowfield regions to continuum or rarefied domains. Rarefied regions are identified by periodically comparing values of a breakdown parameter S_{NS} to a threshold value of 0.1. Following Ref. 9, the breakdown parameter is defined as

$$S_{NS} = \lambda \sqrt{\left(\frac{\nabla p}{p}\right)^2 + \left[\left(\frac{\partial u}{\partial x}\right)^2 + \left(\frac{\partial v}{\partial y}\right)^2 + \left(\frac{\partial w}{\partial z}\right)^2\right] \Big/ \left(u^2 + v^2 + w^2\right)} \tag{1}$$

where λ is the mean free path, p is the pressure, and (u,v,w) is the bulk velocity. UFS calculations in the rarefied domain utilize either a direct numerical solution to the discretized Boltzmann equation or the BGK approximation to the Boltzmann equation, and the second-order kinetic NS method of Xu[18] is used in the continuum domain.

Spatial and velocity grid independence and solution convergence is verified for all simulations. The full Boltzmann calculation uses a velocity grid of 40×40×20 points, in the x, y and z directions respectively, while BGK calculations are performed on a grid of 40×40×2 points in velocity space. Both Boltzmann and BGK simulations take advantage of velocity distribution symmetry along the z axis, in order to reduce the number of velocity grid points.

III.   Efficiency comparison

Table 1 shows a summary of numerical parameters for 12 different UFS, DSMC, and LeMANS simulations performed as part of this study. Computational expense is comparable for UFS NS and LeMANS simulations at Kn = 0.003, with fewer cells but more iterations in the UFS simulation. Note that the difference in cell count between these two simulations is due in large part to the use of gradient-based mesh adaptation in UFS, which allows for larger cells in low-gradient regions. This difference is partially offset by the use of stretched (i.e. high aspect ratio) cells near the cylinder surface in the LeMANS simulation; UFS requires that square cells be used, so far more cells are needed near the surface for similar grid resolution in the surface-normal direction. At Kn = 0.03 considerable efficiency gains are found in UFS NS calculations relative to LeMANS, presumably due to a larger difference in cell count between UFS and LeMANS at this higher Kn value.

As shown in the table, the DSMC simulation for Kn = 0.03 is almost equally expensive as the corresponding BGK simulation, while DSMC is only 20% as expensive as BGK at Kn = 0.3. As expected, efficiency gains are found in the hybrid BGK-NS and BGK-Euler simulations in comparison to the full BGK simulation at Kn = 0.03, although these gains are smaller than 15% for both hybrid simulations. Given the added complexity of hybrid scheme implementation and the fact that BGK and NS calculations should have comparable accuracy within continuum regions, the similar level of computational expense for BGK and hybrid UFS simulations at Kn = 0.03 seems to indicate that hybrid techniques are not preferable for this case.

The most surprising finding shown in the table is the enormous difference in expense between DSMC and Boltzmann simulations at Kn = 0.3. Here the DSMC simulation requires less than 0.2% of the CPU time needed for the Boltzmann simulation, which corresponds to a difference of over two orders of magnitude in computational expense. As discussed above, a direct numerical solution of the Boltzmann equation should have similar accuracy to DSMC, and holds potential advantages to DSMC in simulating a variety of rarefied or multiscale gas flows (particularly unsteady or subsonic flows, flows for which the tails of the velocity distribution must be characterized with high precision, or cases for which strong coupling with a NS solver is desired). Still, for this particular case it

seems reasonable to conclude that DSMC simulation is preferable to simulation using the UFS Boltzmann solver, assuming that both simulations can provide comparable accuracy.

Simulation method	Knudsen number	Cells	Iterations	Processors	CPU hours
Boltzmann (UFS)	0.3	6515	10000	16	1929.4
BGK (UFS)	0.3	6605	10000	8	18.5
LeMANS NS	0.3	14261	9500	8	4.47
DSMC (MONACO)	0.3	3735	100000 (50000 sampling steps)	8	3.75
BGK (UFS)	0.03	23208	20000	8	66.5
BGK-NS (UFS)	0.03	10490 (582 NS)	20000	8	60.0
BGK-Euler (UFS)	0.03	11271 (874 Euler)	20000	8	56.5
UFS NS	0.03	19719	20000	8	9.88
LeMANS NS	0.03	101959	11700	8	41.3
DSMC (MONACO)	0.03	65189	200000 (100000 sampling steps)	8	64.3
UFS NS	0.003	72446	40000	8	50.9
LeMANS NS	0.003	101959	13500	8	48.0

Table 1. Comparison of simulation parameters and CPU time for UFS, MONACO and LeMANS simulations.

IV. Comparison of simulation results for Kn = 0.3

Figure 1 shows computational grids used in UFS BGK and MONACO DSMC simulations for the Kn = 0.3 case. Note that grids used in UFS calculations are adapted over the course of a simulation, and the BGK grid shown in Fig. 1 is taken from steady state results after a total of 10,000 iterations. As observed in the figure, cell sizes in both the freestream and farfield wake regions are similar in the two simulations, although significant differences are found in cell size within shock layer and nearfield regions. These discrepancies in cell size can be attributed to differences in grid refinement criteria between MONACO and UFS: MONACO cells are refined to the local mean free path, while grid refinement in UFS is based on density and velocity gradients.

In Fig. 2, contours are shown for the maximum gradient length local Knudsen number $Kn_{GLL-max}$, as calculated from DSMC simulation results at Kn = 0.3. The parameter $Kn_{GLL-max}$ is computed as the ratio of the local mean free path to the smallest length scale based on gradients in bulk velocity, density or temperature. The Navier-Stokes equations are usually assumed valid for $Kn_{GLL-max} < 0.05$.[19] As shown in the figure, continuum breakdown occurs over nearly the entire flowfield.

Figure 3 shows contours of bulk velocity magnitude from MONACO, UFS and LeMANS simulations at Kn = 0.3. All values in the legend are normalized by the freestream velocity. Results from Boltzmann, BGK and DSMC simulations are shown in the upper half of the figure, while LeMANS NS and DSMC simulation results are compared in the lower half. As expected, both Boltzmann and BGK solutions show good overall agreement with DSMC, while the BGK results give slightly worse agreement with DSMC than Boltzmann simulation results. Poor agreement is observed between DSMC and NS results through much of the flowfield, which is consistent with the high level of continuum breakdown found in Fig. 2. Most of the discrepancy between DSMC and NS results can be attributed to the failure of assumptions underlying the Navier-Stokes equations; in regions of significant nonequilibrium, as indicated in Fig. 2, gradient-based diffusive transport approximations tend to break down, and the gas velocity distribution function cannot be accurately approximated using small perturbations from equilibrium. Both gradient transport and small perturbation assumptions are used in the NS calculations.

Figures 4 and 5 show contours of normalized density and temperature, respectively, for all simulations at Kn = 0.3. Similar trends are found in both figures as in Fig. 3. In particular, good overall agreement is found between DSMC and Boltzmann simulation results, with only slightly worse agreement between DSMC and BGK. A significantly broader bow shock region, as indicated by temperature contours, is observed in BGK results than in results from either DSMC or Boltzmann simulations. As in Fig. 3, poor agreement is found between DSMC and NS results over nearly the entire flowfield in both Figs. 4 and 5.

Figures 6, 7 and 8 show the variation along the stagnation streamline in the normalized bulk velocity, density and temperature, respectively, from the Kn = 0.3 simulations. In all three figures we find very good agreement

American Institute of Aeronautics and Astronautics

between Boltzmann and DSMC results, with only a small overestimate relative to DSMC in the shock thickness based on either velocity or temperature. Note that, as expected at this high global Kn, the shock is represented in all simulations as a broad region of smooth compression, and (particularly in Fig. 7) the shock, shock layer, and boundary layer cannot be easily distinguished. Noticeable differences are observed, however, between DSMC, BGK and NS results in the level of diffusive transport: A significantly wider shock region is found in the BGK simulation than in the DSMC simulation, while the NS simulation gives a narrower shock and larger near-wall boundary layer gradients.

In Fig. 9, the nondimensional surface pressure coefficient (based on a vacuum reference pressure) is plotted along the cylinder surface for simulations at Kn = 0.3. The angle θ, used for the horizontal axis, is defined such that front and rear stagnation points are located at 0° and 180°, respectively. As expected, excellent agreement is found over the entire surface between Boltzmann and DSMC results, and small but noticeable disagreement between DSMC and BGK occurs for θ > 120°. Note the "stair step" pattern in the UFS simulation results, which is presumably caused by the use of a cut cell boundary condition along the cylinder surface. Implementation of an alternate immersed boundary method, which is currently underway, is anticipated to reduce or eliminate this problem. Results from the NS simulation agree well with DSMC only for θ < 60°, with considerable qualitative disagreement near 180°. Similar trends are observed in Fig. 10, which shows the corresponding variation in the surface friction coefficient. In this figure, very good agreement is found between DSMC, BGK and Boltzmann results over the entire surface, while the friction coefficient is overestimated in the NS simulation by approximately a factor of three at 0° and by over three orders of magnitude at 180°.

Figure 11 shows the surface heat transfer coefficient for the Kn = 0.3 simulations. While surprisingly good agreement (within about 20%) is found between NS and DSMC results at the front stagnation point, the level of disagreement increases rapidly with θ, and the NS surface heat transfer is overestimated by around three orders of magnitude at θ = 180°. Note that somewhat better agreement between NS and DSMC would be expected in Fig. 11, as well as in Figs. 9 and 10, if the NS wall boundary condition included consideration of velocity slip and temperature jump effects.

As in Figs. 9 and 10, good overall agreement is found in Fig. 11 over the entire cylinder surface between DSMC, BGK and Boltzmann simulation results. Slightly larger discrepancies are found between DSMC and BGK than between DSMC and Boltzmann results, with a noticeable underestimate in BGK surface heat transfer along much of the afterbody and a small corresponding overestimate along the forebody. Although recently published UFS results have shown an overestimate in UFS heat transfer by approximately a factor of two,[20] the authors were made aware of a normalization factor of 0.5 in UFS nondimensional heat transfer values which has been applied to values in Fig. 11 and which seems to provide far better agreement with DSMC. With this normalization factor, the overestimate relative to DSMC in stagnation point heat flux is only about 3.8% for the Boltzmann simulation and 9.5% for the BGK simulation.

Much of the error observed in Boltzmann and BGK values, as well as the artificial "stair step" pattern in these values, is likely due to the cut boundary condition, and is expected to be eliminated through the use of the immersed boundary method in place of cut cells. Further error in surface heat transfer from Boltzmaan and BGK simulations may be due to insufficient mesh refinement near the surface, although comparable cell sizes are used in these simulations as in the DSMC simulation and it seems unlikely that mesh resolution accounts for most of the discrepancy.

V. Comparison of simulation results for Kn = 0.03

Figure 12 shows meshes used in UFS BGK and DSMC simulations for the Kn = 0.03 case. As in Fig. 1, differences in local refinement levels are attributed to the fact that DSMC cell size is adapted to the mean free path, while UFS mesh adaptation is based on density and velocity gradients. For both simulations, the shock position is clearly indicated by a sudden increase in mesh refinement levels upstream of the cylinder.

Figure 13 is a contour plot of the maximum gradient length local Knudsen number $Kn_{GLL-max}$ from the DSMC simulation at Kn = 0.03. In comparing this figure with Fig. 2, we find that continuum breakdown (defined by $Kn_{GLL-max} > 0.05$) occurs over a far smaller portion of the flowfield than for the Kn = 0.3 case. For the present case, continuum breakdown is limited to a region surrounding the bow shock, the forebody boundary layer, and a large portion of the wake. Figure 14 shows the boundaries between NS and BGK domains, at steady state, in a hybrid BGK-NS simulation of the Kn = 0.03 case. These boundaries, along which the right side of Eq. (1) is equal to a cutoff value of 0.1, correspond reasonably well to continuum breakdown boundaries shown in Fig. 13. Significant differences between domain boundaries in Fig. 14 and the 0.05 contour line in Fig. 13 are found only in the wake region.

5
American Institute of Aeronautics and Astronautics

In Fig. 15, contours of normalized bulk velocity magnitude are shown for several different simulations at Kn = 0.03. Results are displayed for BGK, hybrid BGK-NS, hybrid BGK-Euler, DSMC, UFS NS and LeMANS NS simulations. Contour lines from both UFS NS and LeMANS NS simulations agree well with those from DSMC through much of the forebody shock layer, but considerable disagreement is found in the wake. The BGK-Euler simulation gives particularly inaccurate results throughout the flowfield, and reduced accuracy is also found for the BGK simulation in wake regions far from the axis. Discrepancies observed between BGK and BGK-NS results in the wake seem to indicate that, in the hybrid BGK-NS simulation, the NS domain may include areas of strong nonequilibrium within the wake where BGK calculations would be more appropriate. This assumption is reinforced by differences, discussed above, between Figs. 13 and 14. As expected, very good agreement is found between BGK, BGK-NS and DSMC simulations within the shock layer upstream of the cylinder.

Figures 16 and 17 show contours of normalized density and temperature, respectively, from simulations of the Kn = 0.03 case. Similar trends are found in both figures as in Fig. 15. As mentioned above in the discussion of Fig. 15, relatively good agreement is found in Figs. 16 and 17 between most simulation results around the shock layer and forebody boundary layer, while particularly large differences from DSMC are observed in results from the hybrid BGK-Euler simulation. The large error in BGK-Euler results is not particularly surprising, because – unlike BGK, DSMC, Boltzmann and NS calculations – the Euler calculations performed in continuum regions completely neglect effects of physical viscosity and diffusive transport, and any differences from a truly inviscid flow are due only to artificial viscosity.

In Fig. 18, the variation in normalized velocity along the stagnation streamline is plotted for all simulations of the Kn = 0.03 case. Very good agreement is found between DSMC and LeMANS NS results, whereas the UFS NS result shows a significantly thinner shock with a corresponding reduction of roughly 10% in the shock standoff distance. Differences between the two NS curves in Fig. 18 can be attributed primarily to the use of very different schemes. As mentioned above, the UFS NS solver uses a kinetic scheme of Xu,[18] while LeMANS uses a modified form of Steger-Warming flux vector splitting.[17] Although the scheme of Xu is expected to provide improved accuracy relative to the Steger-Warming method through a reduction in diffusive and dissipative effects, the better agreement with DSMC found in the LeMANS results seems to indicate that, for this case, the Xu scheme implementation in UFS may not allow sufficient diffusive transport. Further investigation is required to assess whether discrepancies between UFS NS and DSMC results in Fig. 18 are due to numerical problems or physical approximations in the UFS NS solver.

Nearly identical curves are shown in Fig. 18 from the BGK and hybrid BGK-NS simulations, although both give relatively poor agreement with DSMC toward the upstream portion of the shock. A comparison of BGK and DSMC results in this region indicates that the BGK approximation of the Boltzmann equation may produce excessive diffusive transport within the shock. As stated above in the discussion of Figs. 6 and 8, this same trend (excess diffusion in the shock) is also found in a comparison of BGK, Boltzmann and DSMC results for the Kn = 0.3 case. In Fig. 18, as in Figs. 15 through 17, the greatest differences from DSMC are observed in results from the hybrid BGK-Euler simulation. In relation to DSMC, the BGK-Euler simulation overestimates the shock standoff distance by approximately 12%. Despite significant discrepancies in the location and thickness of the shock, all six curves shown in Fig. 18 give relatively good agreement within the post-shock and boundary layer regions.

Figures 19 and 20 show contours of normalized density and temperature, respectively, for the Kn = 0.03 case. Similar trends are found in both figures as in Fig. 18, with comparable differences in shock thickness and shock standoff distance based on either density or temperature. The only prominent trends in Figs. 19 and 20 which are not apparent in Fig. 18 relate to boundary layer thickness. The BGK, BGK-NS and BGK-Euler simulations all noticeably overestimate the boundary layer thickness, as measured by density or temperature, relative to DSMC. Corresponding gradients within the boundary layer are lower in these UFS simulations than in DSMC. In contrast, only very small differences in boundary layer thickness are found in Figs. 19 and 20 between results from UFS NS, LeMANS NS and DSMC simulations. Differences in boundary layer thickness are likely due to excess diffusive transport in BGK calculations, which is also thought to cause the overly thick shocks observed in Figs. 6, 8 and 18.

The surface pressure coefficient for Kn = 0.03 simulations is plotted in Fig. 21. Note that values from the UFS NS simulation are not provided, because the version of UFS used in this study did not allow output of surface quantities at wall boundary cells within the NS domain. Good agreement is observed along the forebody between all pressure coefficient curves, while quantitative (but not qualitative) differences are shown for θ > 90°. The greatest disagreement with DSMC pressure coefficient values at θ > 90° is found in results from the BGK-Euler and NS simulations. As discussed above, error in NS results is likely due to effects of continuum breakdown, while BGK-Euler inaccuracies can be mainly attributed to a lack of diffusive transport in calculations for the Euler equations. Although BGK-NS and NS results are in good agreement for θ > 150°, neither compares well over this portion of the surface with either BGK or DSMC. This trend seems to indicate that, as mentioned in the discussion of Fig. 15,

6

American Institute of Aeronautics and Astronautics

the NS domain in the BGK-NS simulation may include rarefied wake regions which should be assigned to the BGK domain.

Figure 22 shows the variation in the surface friction coefficient for simulations of the Kn = 0.03 case. The most noticeable errors are found in the NS curve, which agrees reasonably well with DSMC over the forebody surface (θ < 90°) but is up to a factor of five greater than DSMC along the afterbody. Most of this discrepancy can be attributed to the lack of a velocity slip/temperature jump boundary condition in NS calculations; due to the high degree of continuum breakdown along the cylinder surface shown in Fig. 13, significant velocity slip is expected. Both DSMC and BGK calculations allow for velocity slip along the surface, and as expected, the lack of wall slip in NS calculations is associated with higher friction coefficient values in the NS results. All UFS simulations tend to slightly over predict surface shear stress along the forebody, with an overestimate relative to DSMC of up to around 50% in the BGK results. Note the slope discontinuity in all curves around θ = 165°, which corresponds to boundary layer separation at the edge of a recirculation zone. In comparing the location of this discontinuity between results from different simulations, we find good overall agreement in the size of the recirculating region. Relative to DSMC, the maximum difference in the θ range for the recirculating region is found in results from the BGK-NS simulation, which overestimates this range by about 30%.

In Fig. 23, the surface heat transfer coefficient is plotted for simulations at Kn = 0.03. As with the friction coefficient values shown in Fig. 22, the NS simulation slightly over predicts the heat transfer over much of the forebody surface, and greatly over predicts this quantity along the afterbody. A maximum relative error (with respect to the DSMC value) of approximately 32% is found at θ = 148°. Significant discrepancies are observed between DSMC and the various UFS results, with a roughly 20% underestimate in heat transfer over much of the surface from the BGK-NS simulation and a somewhat smaller overestimate from the BGK simulation. As mentioned in the discussion of Fig. 11, all UFS simulations exhibit an unphysical "stair step" pattern in the θ range between 90° and 150°. These errors, as well as a lack of smoothness in surface heat transfer curves at smaller θ values, are likely caused by problems with gradient evaluations involving Cartesian cut cells. Note that UFS BGK and NS calculations are entirely deterministic, and fluctuations observed in the UFS results are not due to the type of statistical scatter found in DSMC.

VI. Comparison of simulation results for Kn = 0.003

Figure 24 shows the computational meshes used in UFS NS and LeMANS NS simulations at Kn = 0.003. While the UFS mesh is able to capture high gradient regions within areas of increased refinement, no automatic grid adaption is possible using LeMANS. The LeMANS mesh, which was manually generated using the commercial GAMBIT code, includes a structured region surrounding the cylinder, and an unstructured region of uniform-sized triangular cells which covers much of the wake. In creating the LeMANS mesh, particular effort was made to ensure shock alignment and grid independence. As described in section III, stretched (i.e. high aspect ratio) cells are used in the boundary layer to avoid unnecessarily small cell dimensions in the surface-tangent direction.

In Fig. 25, contours are shown for the maximum gradient length local Knudsen number, as computed from the LeMANS simulation at Kn = 0.003. As expected for such a small Kn value, continuum breakdown (where $Kn_{GLL-max}$ > 0.05) is found to occur only in narrow regions around the bow shock and forebody boundary layer, as well as in portions of the nearfield wake region. This indicates that the NS equations are valid over nearly the entire flowfield, and relatively small errors should result from the near-equilibrium assumptions underlying these equations.

In Fig. 26, contours of normalized bulk velocity magnitude are compared from the two NS simulations at Kn = 0.003. Very good overall agreement is found between the two sets of contour lines, with the largest discrepancies observed in the farfield wake region. Differences in the shape of the $V/V_\infty = 0.8$ contour line far from the axis may be attributed to the presence of a UFS symmetry boundary condition at y = 1 m. Particularly good agreement is found in the shock layer, with a shock standoff distance based on velocity contours which is approximately 5% larger in the LeMANS simulation than in the UFS simulation. Figures 27 and 28 show contours of normalized density and temperature, respectively, from the Kn = 0.003 simulations. In both figures, similar levels of disagreement are found as in Fig. 20, with particularly large differences in the post-shock region far from the axis and in the wake.

The variation in bulk velocity, density and temperature along the stagnation streamline is plotted in Figs. 29, 30 and 31 from the NS simulations at Kn = 0.003. All three figures show very similar trends, with excellent agreement in post-shock values and boundary layer profiles, along with a thicker shock and slightly larger shock standoff distance in the LeMANS simulation. Based on the location of maximum gradients, the UFS simulation is found to underestimate the shock standoff distance by between 4% and 5% relative to the LeMANS simulation.

7
American Institute of Aeronautics and Astronautics

VII. Drag coefficient comparison

In Fig. 32, drag coefficients C_d calculated from UFS, DSMC and NS simulations are plotted as a function of Kn. Data from experiments[21] and additional simulations are also included in the figure for comparison. Symbols labeled "Tratio = 1.2" indicate that the ratio of cylinder wall temperature to freestream temperature is 1.2, as is the case for all simulations described above and included in Fig. 1. Likewise, symbols labeled "Tratio = 4" indicate simulations for which the cylinder wall temperature is four times that of the freestream gas. Several additional simulations using this higher wall temperature have been performed over a wide range of Kn values. Among these added simulations, five are run using the LeMANS NS solver, seven use MONACO, and seven employ the BGK module in UFS. Additional data points, labeled "Boltzmann*, Tratio = 4" are taken from published results of UFS Boltzmann simulations by Kolobov et al.[9]

In Fig. 32, the cylinder surface temperature is shown to have little if any noticeable impact on C_d over the full Kn range considered. Generally good agreement is found between UFS Boltzmann, DSMC and measured values even around the maximum Kn of 10. Good agreement is also found between all UFS, DSMC, NS and experimental data for Kn < 0.1. At higher Kn, however, large overestimates relative to the experimental values are observed in NS C_d predictions, with an overestimate of roughly 70% at Kn = 1. Smaller but still significant errors in C_d are shown in BGK results for Kn > 0.3, with an underestimate relative to DSMC of about 7% at Kn = 10. A noticeable increase with Kn is found in the level of disagreement between DSMC and BGK results. As no such Kn-dependent discrepancies are found between DSMC and Boltzmann results, this disagreement may be attributed to inaccuracies in the BGK collision integral approximation which become increasingly influential at higher Kn.

VIII. Conclusions

Results have been presented from a series of simulations for hard sphere monatomic gas flows over a cylinder at a freestream Mach number of 4. A wide range of global Knudsen numbers have been considered, including one case (Kn = 0.3) involving strong nonequilibrium over nearly the entire flowfield, a second case (Kn = 0.03) involving significant regions of both continuum and rarefied flow, and a third case (Kn = 0.003) for which the NS equations are valid over nearly the full simulation domain. These flow problems have been used to evaluate various models and combinations of models in the UFS code. This code holds great promise in simulating a range of hypersonic gas flow problems, particularly those involving strong two-way coupling between rarefied and continuum regions, as well as unsteady multiscale flows and other flows with translational nonequilibrium for which the inherent statistical scatter in DSMC is unacceptable or problematic.

In comparing efficiency and accuracy of UFS calculations relative to MONACO DSMC and LeMANS NS simulations, a variety of attributes and areas of potential improvement in UFS have been identified. First, the ease with which multiple methods, intended for different Kn regimes, can be strongly coupled within a single simulation is an important positive characteristic for UFS, and capabilities for automatic tree-based Cartesian mesh adaptation greatly reduce the simulation setup time and simplify setup procedures for the user. Unlike DSMC or hybrid DSMC-CFD techniques, UFS has no problems or complications associated with statistical scatter, and there is no loss in precision if UFS calculations are immediately stopped once steady state conditions have been reached. Future code development for UFS may include inclusion of internal excitation or chemistry models which rely heavily on the velocity distribution function, and which may be more accurate when used in direct numerical solutions to the Boltzmann equation than in DSMC.

The major drawback in UFS, as demonstrated in this study, is the enormous computational expense of the Boltzmann solver in relation to DSMC. The Boltzmann simulation of the Kn = 0.3 case was over two orders of magnitude more expensive than the corresponding DSMC simulation. While computational expense may not be a driving concern for this relatively simple type of problem given the desired levels of simulation accuracy and precision, the large discrepancy in simulation efficiency implies that for a given set of computational resources, a DSMC code should be capable of simulating certain more complex rarefied gas flows which would be prohibitively expensive to simulate using the Boltzmann solver in UFS. However, it should be emphasized that – as discussed above – direct numerical simulation of the Boltzmann equation has several advantages over DSMC which may outweigh any disadvantages in efficiency.

Large efficiency gains were realized when BGK calculations were used in place of Boltzmann calculations, although BGK simulations were found to give reduced accuracy relative to Boltzmann and DSMC simulations. Much of the error in BGK results is presumably due to underlying approximations in the BGK equation. Additional errors were found in surface quantities computed using either BGK or Boltzmann solvers; these errors are most likely associated with gradient approximations involving cut cell boundaries, and should be reduced or eliminated through the use of an immersed boundary method.

8
American Institute of Aeronautics and Astronautics

To improve efficiency in the UFS Boltzmann solver without sacrificing simulation accuracy, several possible approaches are suggested: First, a reduced number of nodes in velocity space could potentially be used. This may be accomplished by means of velocity grid adaptation, where calculations for each cell in physical space would involve only those points in velocity space with a relatively high probability density. A related approach would allow for optimized non-uniform grids in velocity space, where the velocity space nodes would be selected in a manner similar to that used in Gaussian quadrature. As described in Ref. 9, the NtCN method currently employed in UFS to evaluate the Boltzmann collision integral should allow for either option.

Acceptable accuracy may be found using fewer velocity space nodes, even without velocity grid adaptation, if only the lower moments of the velocity distribution are needed to calculate macroscopic output quantities of interest.[22] However, a more refined velocity grid is likely required in simulations involving higher Mach numbers or stronger translational nonequilibrium, or in simulations for which higher velocity distribution moments are used to model physical phenomena such as internal energy excitation or chemistry.

Comparable accuracy could also be achieved with a coarser velocity grid if the Boltzmann solver is modified for higher order accuracy in velocity space, although the required modifications may be prohibitively complicated and involve considerable method and algorithm development. Another possible approach to increase efficiency would involve minimizing, for a desired level of accuracy, the number of summation terms used to approximate the collision integral. Related efficiency gains could potentially be found by testing alternate low discrepancy sequences to select velocity space grid points used in this summation.

Acknowledgments

References

[1]Bird, G. A., *Molecular Gas Dynamics and the Direct Simulation of Gas Flows*, Clarendon Press, Oxford, 1994.

[2]Vincenti, W. G., and Kruger, C. H., *Introduction to Physical Gas Dynamics*, Krieger Publishing, Malabar, Florida, 1986.

[3]Schwartzentruber, T. E., and Boyd, I. D., "A Modular Particle-Continuum Numerical Method for Hypersonic Non-equilibrium Gas Flows," *Journal of Computational Physics*, Vol. 225, 2007, pp. 1159-1174.

[4] Wu, J.-S., Lian, Y.-Y., Cheng, G., Koomullil, R. P., and Tseng, K.-C., "Development and Verification of a Coupled DSMC-NS Scheme Using Unstructured Mesh," *Journal of Computational Physics*, Vol. 219, 2006, pp. 579-607.

[5]Kaplan, C. R., Liu, J., and Oran, E. S., "Parallel Hybrid Method for Subsonic Flows: Coupling and Load-Balancing Challenges," AIAA Paper 2006-992, 2006.

[6]Garcia, A. L., Bell, J. B., Crutchfield, W. Y., and Alder, B. J., "Adaptive Mesh and Algorithm Refinement Using Direct Simulation Monte Carlo," *Journal of Computational Physics*, Vol. 154, 1999, pp. 134-155.

[7]Wadsworth, D. C., and Erwin, D. A., "Two-Dimensional Hybrid Continuum/Particle Approach for Rarefied Flows," AIAA Paper 92-2975, 1992.

[8]Hash, D. B., and Hassan, H. A., "Assessment of Schemes for Coupling Monte Carlo and Navier-Stokes Solution Methods," *Journal of Thermophysics and Heat Transfer*, Vol. 10, No. 2, 1996, pp. 242-249.

[9]Kolobov, V. I., Arslanbekov, R. R., Aristov, V. V., Frolova, A. A., and Zabelok, S. A., "Unified Solver for Rarefied and Continuum Flows with Adaptive Mesh and Algorithm Refinement," *Journal of Computational Physics*, Vol. 223, 2007, pp. 589-608.

[10]Kolobov, V. I., Bayyuk, S. A., Arslanbekov, R. R., Aristov, V. V., Frolova, A. A., and Zabelok, S. A., "Construction of a Unified Continuum/Kinetic Solver for Aerodynamic Problems," *Journal of Spacecraft and Rockets*, Vol. 42, No. 4, 2005, pp. 598-606.

[11]Josyula, E., Arslanbekov, R. R., Kolobov, V. I., and Gimelshein, S. F., "Evaluation of Kinetic/Continuum Solver for Hypersonic Nozzle-Plume Flow," *Journal of Spacecraft and Rockets*, Vol. 45, No. 4, 2008, pp. 665-676.

[12]Arslanbekov, R. R., Kolobov, V. I., Frolova, A., Zabelok, S., and Josyula, E., "Evaluation of a Unified Kinetic/Continuum Solver for Computing Heat Flux in Hypersonic Blunt Body Flows," AIAA Paper 2007-4544, 2007.

[13]Dinavahi, S., and Josyula, E., "Simulation of Mach 3 Cylinder Flow using Kinetic and Continuum Solvers," *Department of Defense HPCMP User Group Conference*, San Diego, CA, 2009.

[14]Popinet, S., "Gerris: A Tree-Based Adaptive Solver for the Incompressible Euler Equations in Complex Geometries," *Journal of Computational Physics*, Vol. 190, 2003, pp. 572-600.

[15]Dietrich, S., and Boyd, I. D., "Scalar and Parallel Optimized Implementation of the Direct Simulation Monte Carlo Method," *Journal of Computational Physics*, Vol. 126, 1996, pp. 328-342.

[16]Scalabrin, L. C., and Boyd, I. D., "Development of an Unstructured Navier-Stokes Solver for Hypersonic Nonequilibrium Aerothermodynamics," AIAA Paper 2005-5203, 2005.

[17]Laney, C. B., *Computational Gasdynamics*, Cambridge University Press, 1998.

[18]Xu, K., "A Gas-Kinetic BGK Scheme for the Navier-Stokes Equations and its Connection with Artificial Dissipation and Godunov Method," *Journal of Computational Physics*, Vol. 171, 2001, pp. 289-335.

[19]Wang, W., and Boyd, I. D., "Predicting Continuum Breakdown in Hypersonic Viscous Flows," *Physics of Fluids*, Vol. 15, No. 1, 2003, pp. 91-100.

[20]Lofthouse, A. J., "Hypersonic Blunt Body Thermophysics Using a Unified Kinetic/Continuum Solver," AIAA Paper 2009-3838, 2009.

[21]Maslach, G. J., and Schaaf, S. A., "Cylinder Drag in the Transition from Continuum to Free-Molecule Flow," *Physics of Fluids*, Vol. 6, No. 3, 1963, pp. 315-321.

[22]Josyula, E., Xu, K., Suchyta, C. J., and Bailey, W. F., "Kinetic Methods for Solving the Internal Structure of Shock Waves," AIAA Paper 2009-3841, 2009.
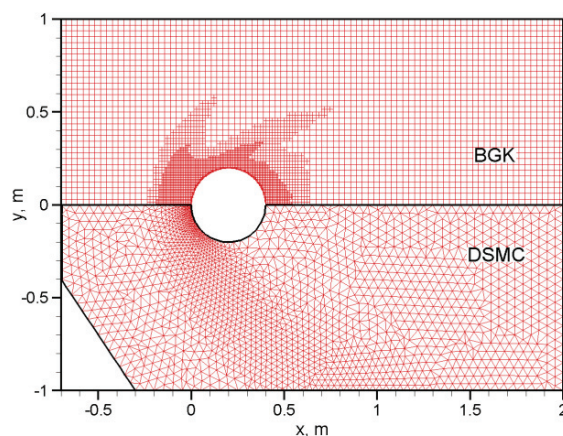
Figure 1. Meshes for UFS BGK and DSMC simulations at Kn = 0.3.
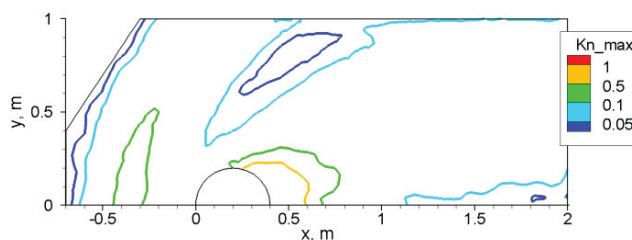
Figure 2. Contours of the maximum gradient length local Knudsen number from the DSMC simulation at Kn = 0.3.
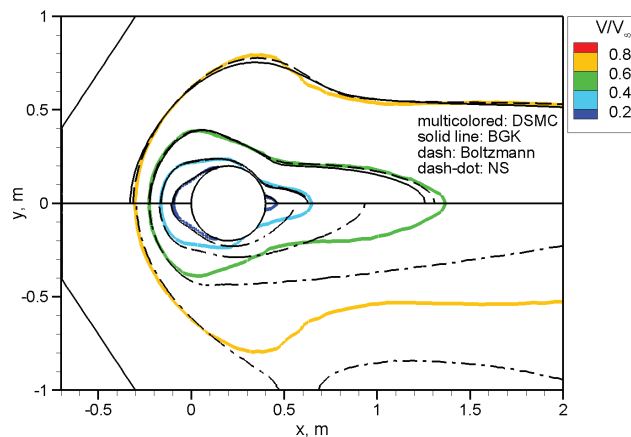
Figure 3. Contours of bulk velocity magnitude for Kn = 0.3. BGK and Boltzmann simulations are both run on UFS, the NS simulation is performed using LeMANS, and the DSMC simulation is run on MONACO.
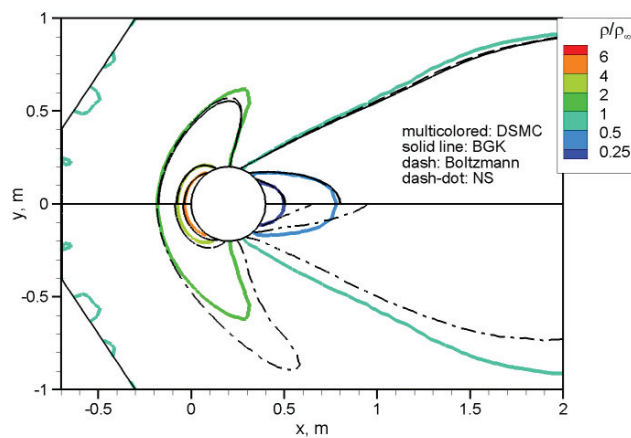
Figure 4. Contours of density for Kn = 0.3. UFS is used for BGK and Boltzmann simulations.
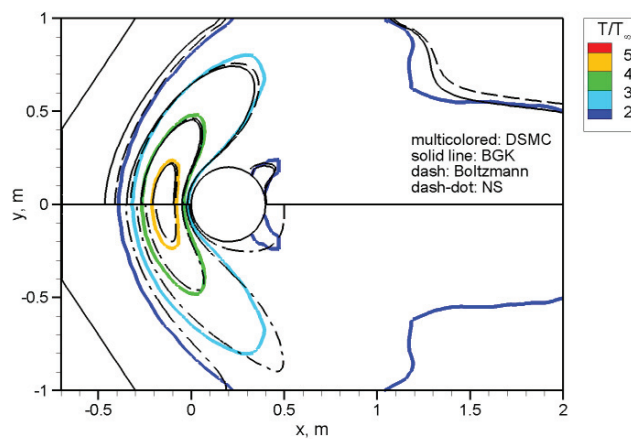
Figure 5. Contours of temperature for Kn = 0.3. UFS is used for BGK and Boltzmann simulations.

Approved for public release; distribution unlimited.
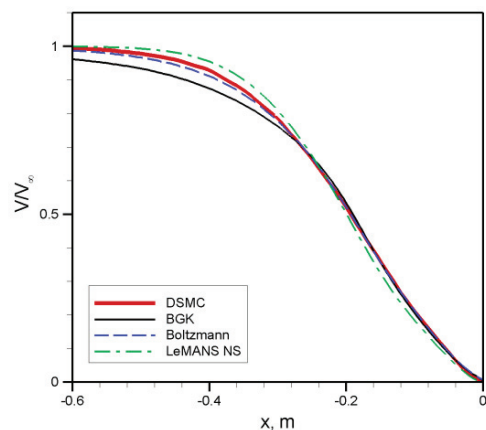
Figure 6. Bulk velocity along the stagnation streamline for Kn = 0.3. UFS is used for BGK and Boltzmann simulations.
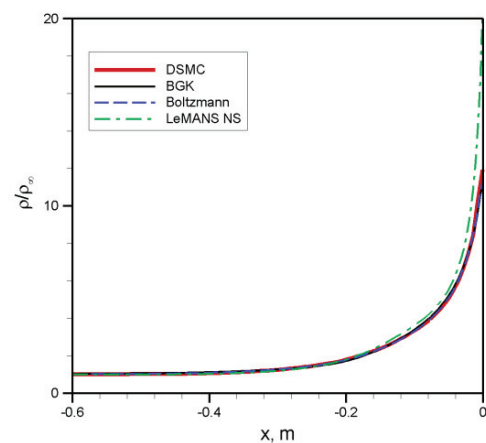
Figure 7. Density along the stagnation streamline for Kn = 0.3. UFS is used for BGK and Boltzmann simulations.
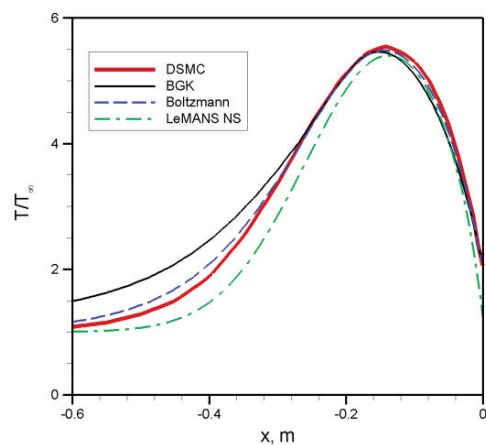
Figure 8. Temperature along the stagnation streamline for Kn = 0.3. UFS is used for BGK and Boltzmann simulations.

American Institute of Aeronautics and Astronautics

Approved for public release; distribution unlimited.
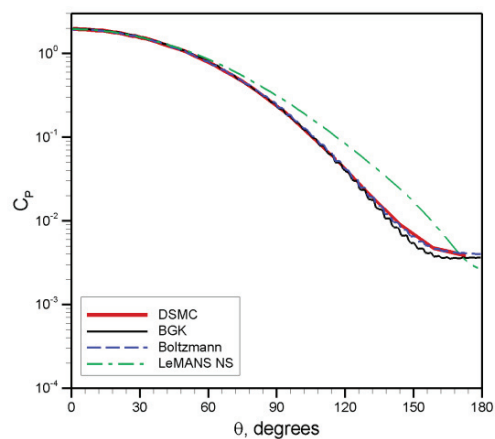
Figure 9. Surface pressure coefficient for Kn = 0.3. UFS is used for BGK and Boltzmann simulations.
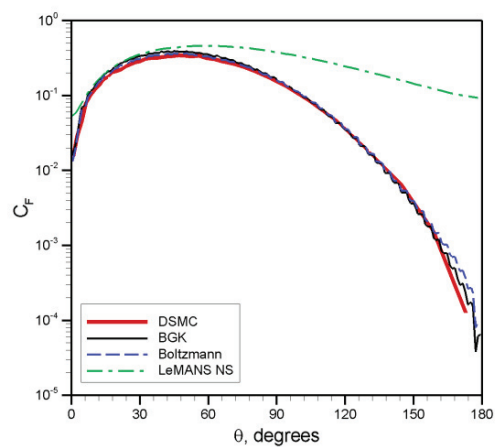
Figure 10. Surface friction coefficient for Kn = 0.3. UFS is used for BGK and Boltzmann simulations.
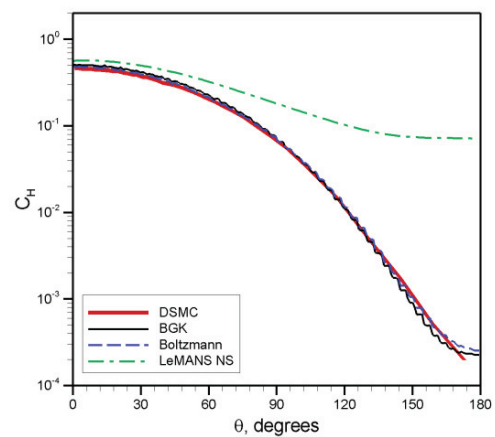
Figure 11. Surface heat transfer coefficient for Kn = 0.3. UFS is used for BGK and Boltzmann simulations.

Approved for public release; distribution unlimited.
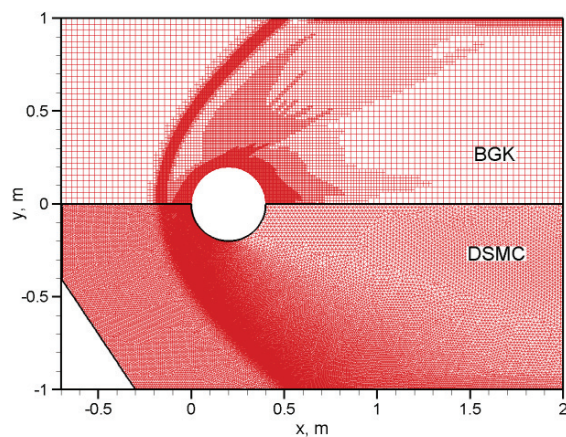
Figure 12. Meshes for UFS BGK and MONACO DSMC simulations at Kn = 0.03.
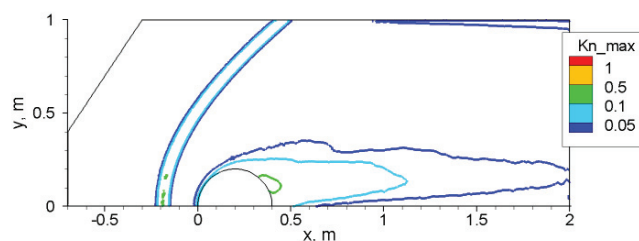
**Figure 13. Contours of the maximum gradient length local Knudsen number from the DSMC simulation at Kn = 0.03.**
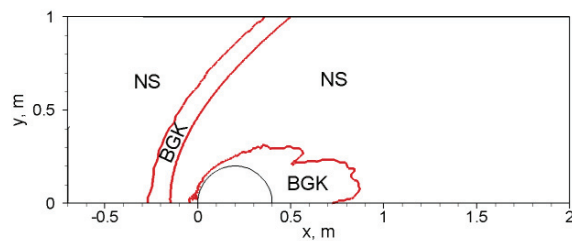
Figure 14. Continuum and rarefied domains for the UFS BGK-NS simulation at Kn = 0.03.

14
American Institute of Aeronautics and Astronautics

Approved for public release; distribution unlimited.
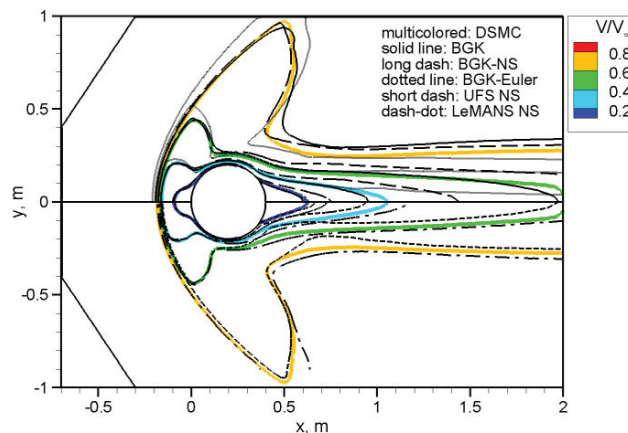
Figure 15. Contours of bulk velocity magnitude for Kn = 0.03. UFS is used for all simulations except the LeMANS NS simulation and the MONACO DSMC simulation.
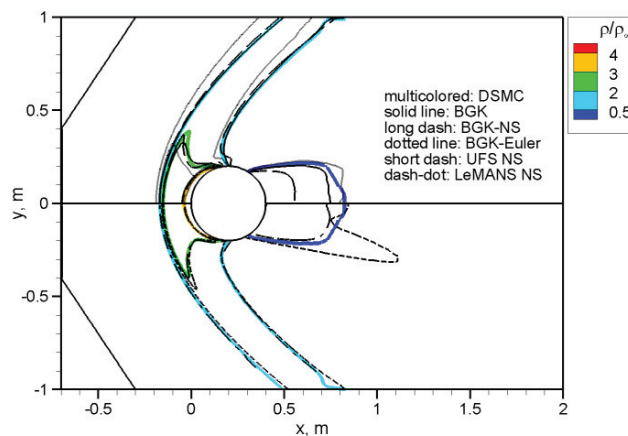
Figure 16. Contours of density for Kn = 0.03. UFS is used for BGK, BGK-NS, and BGK-Euler simulations.
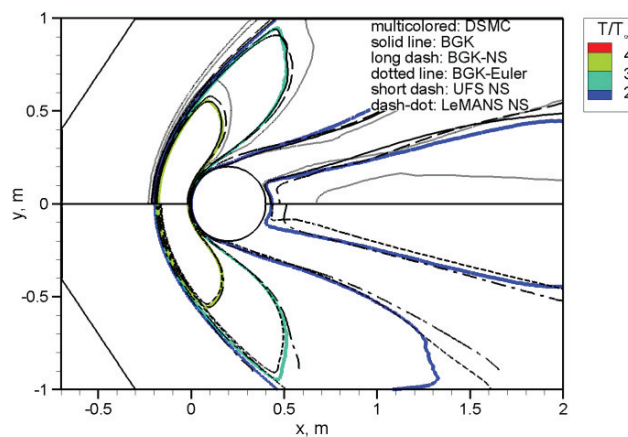
Figure 17. Contours of density for Kn = 0.03. UFS is used for BGK, BGK-NS, and BGK-Euler simulations.
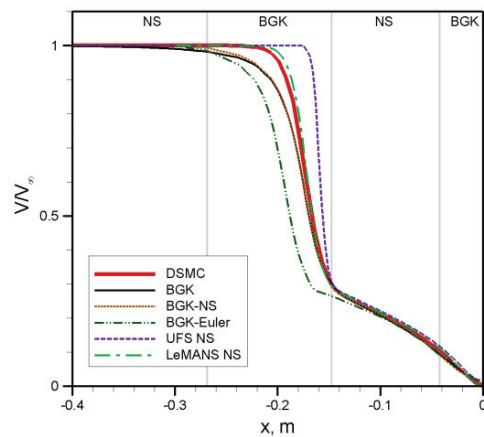
Figure 18. Bulk velocity along the stagnation streamline for Kn = 0.03. UFS is used for BGK, BGK-NS, and BGK-Euler simulations.
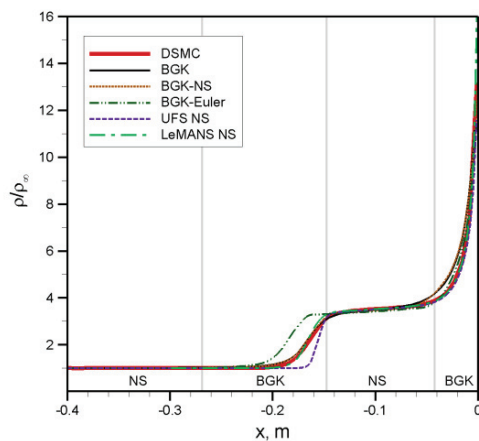
Figure 19. Density along the stagnation streamline for Kn = 0.03. UFS is used for BGK, BGK-NS, and BGK-Euler simulations.
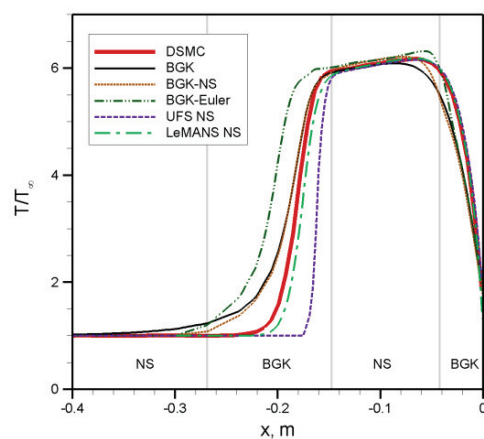
Figure 20. Temperature along the stagnation streamline for Kn = 0.03. UFS is used for BGK, BGK-NS, and BGK-Euler simulations.

16
American Institute of Aeronautics and Astronautics

Approved for public release; distribution unlimited.
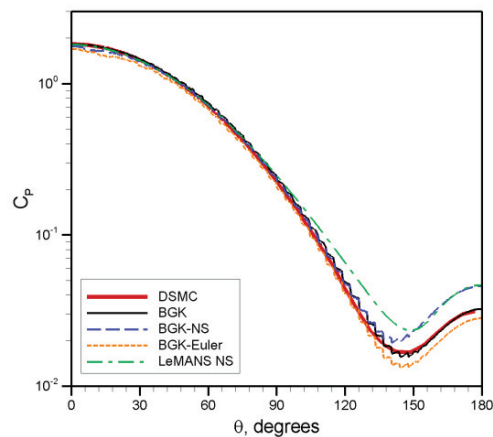
Figure 21. Surface pressure coefficient for Kn = 0.03. UFS is used for BGK, BGK-NS, and BGK-Euler simulations.
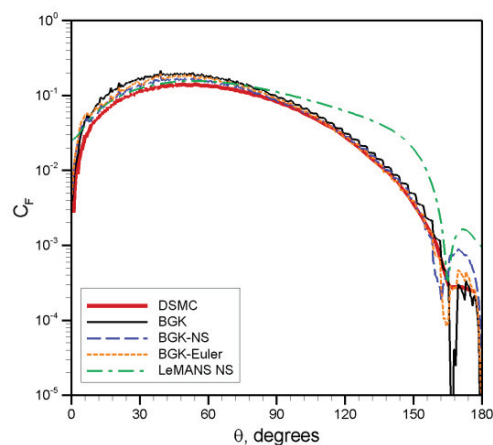
Figure 22. Surface friction coefficient for Kn = 0.03. UFS is used for BGK, BGK-NS, and BGK-Euler simulations.
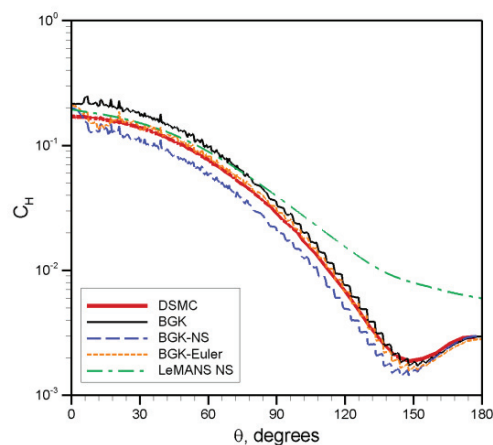
Figure 23. Surface heat transfer coefficient for Kn = 0.03. UFS is used for BGK, BGK-NS, and BGK-Euler simulations.

17
American Institute of Aeronautics and Astronautics

Approved for public release; distribution unlimited.
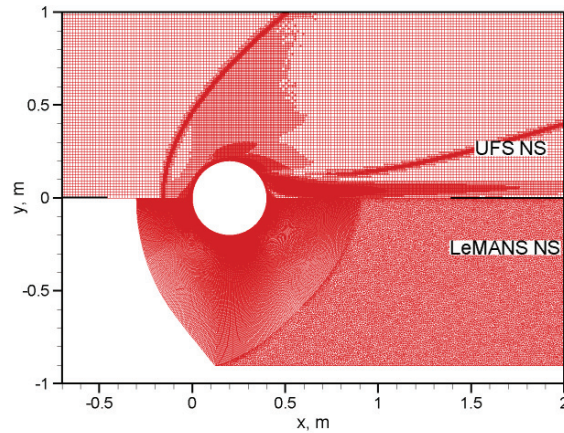
Figure 24. Meshes for UFS NS and LeMANS NS simulations at Kn = 0.003.
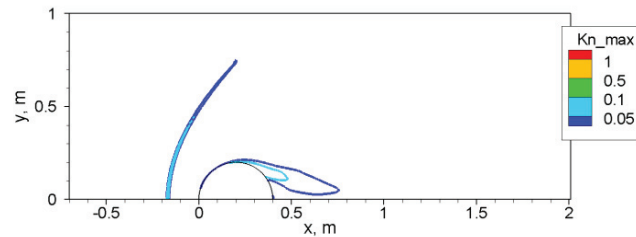
Figure 25. Contours of the maximum gradient length local Knudsen number from the LeMANS simulation at Kn = 0.003.
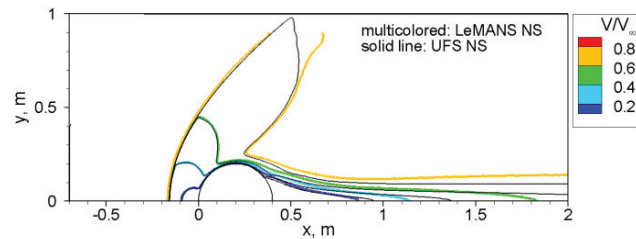
Figure 26. Contours of bulk velocity magnitude for Kn = 0.003.
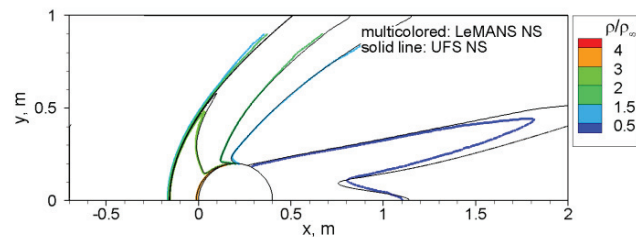
Figure 27. Contours of density for Kn = 0.003.

18
American Institute of Aeronautics and Astronautics

Approved for public release; distribution unlimited.
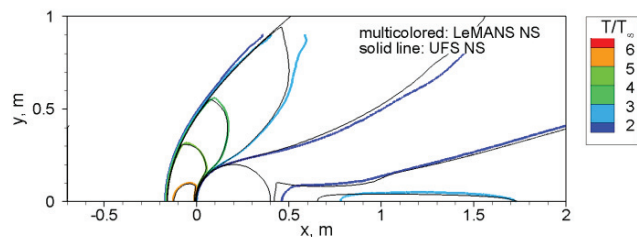
Figure 28. Contours of temperature for Kn = 0.003.

Figure 29. Bulk velocity along the stagnation streamline for Kn = 0.003.

Figure 30. Density along the stagnation streamline for Kn = 0.003.

19
American Institute of Aeronautics and Astronautics

Approved for public release; distribution unlimited.

Figure 31. Temperature along the stagnation streamline for Kn = 0.003.

Figure 32. Variation in drag coefficient with Knudsen number.

A Novel Cartesian Implementation of the Direct Simulation Monte Carlo Method

Jonathan M. Burt[1] and Eswar Josyula[2]
U S ir Force Research a oratory
ri ht Patterson ir Force ase   H

Iain D. Boyd[3]
Department of erospace n ineerin
Uni ersity of Michi an nn r or MI

    A new Cartesian implementation of the direct simulation Monte Carlo (DSMC) method, named the hypersonic aerothermodynamics particle (HAP) code, is presented. This code is intended for rapid setup and simulation of rarefied flow problems, and as a framework for evaluating new physical models and numerical techniques. Unique features include the use of nonuniform Cartesian adaptive subcells, a collision probability modification to reduce errors associated with spatial averaging in collision probabilities, and automatic planar element approximation of analytically defined two or three-dimensional surface geometries. In this work, simulations are performed using both HAP and an established DSMC code for a rarefied hypersonic flow over a flat plate, and excellent overall agreement is found. Additional simulations are employed to demonstrate reduced dependence on cell size through a proposed collision probability modification. Results are also presented for a three-dimensional HAP simulation of hypersonic flow over a blunted cone, and reasonably good agreement with experimental data is observed.

I. Introduction

The direct simulation Monte Carlo (DSMC) method, introduced by Bird nearly 50 years ago,[1,2] has over the past several decades become the dominant technique for numerical simulation of rarefied gas flows. This method involves Lagrangian tracking and binary collision operations among a collection of simulated particles, each representing a large number of atoms or molecules, in a manner which reproduces the underlying physics of the governing Boltzmann equation.

    DSMC is often used in a wide variety of applications related to rarefied gas flow simulation, including aerothermodynamic design and analysis of atmospheric entry vehicles and hypersonic cruise vehicles, simulation of nanoscale and microscale subsonic flows, simulation of exhaust plumes from spacecraft or high altitude rockets, chemical vapor deposition, spacecraft drag calculations, and analysis of basic fluid flow phenomena and instability problems. The popularity of DSMC in this broad range of applications can be attributed to a combination of accuracy, simplicity, computational efficiency, and relatively easy application to complex geometries. In rarefied gas dynamics problems such as those mentioned above, the equilibrating effects of intermolecular collisions may be insufficient to retain a near-equilibrium gas velocity distribution, and the resulting nonequilibrium velocity distributions tend to invalidate underlying assumptions in the Navier-Stokes equations.[2] As a result, standard computational fluid dynamics (CFD) techniques generally provide results of poor or questionable accuracy, and alternate methods[3-5] which reproduce the nonequilibrium characteristics of the Boltzmann equation are required. Among such alternate methods, DSMC is often the most efficient technique which maintains the accuracy of the full Boltzmann equation.

    In this paper, we present a new simplified implementation of DSMC named the hypersonic aerothermodynamics particle (HAP) code. This code is intended to combine the simplicity of problem-specific DSMC implementations with many capabilities of larger generalized DSMC codes,[6-11] and development of the HAP code is motivated in part

---

[1] Research scientist, Universal Technology Corporation, AIAA member.
[2] Senior research aerospace engineer, AIAA associate fellow.
[3] Professor, AIAA associate fellow.

American Institute of Aeronautics and Astronautics

Approved for public release; distribution unlimited.

by a desire to ease implementation and testing of new DSMC models and algorithms. The code is made considerably simpler through the use of a uniform Cartesian grid, and newly developed collision procedure modifications are utilized to reduce spatial discretization errors. As an additional motivation for development of the HAP code, a very simple, intuitive and configurable user interface is desired for rapid simulation setup by inexperienced DSMC users.

The HAP code is described in the following sections, and various features of the code are outlined. Next, errors associated with a lack of grid adaptation to the local mean free path are discussed, and set of new techniques are proposed to reduce these errors. A rarefied hypersonic flow over a flat plate with a sharp leading edge is used as a test case to evaluate the new code, and HAP simulation output quantities are compared with results from established DSMC codes and with available experimental data. A grid refinement study is employed to quantify spatial discretization errors for the flat plate flow, and to demonstrate error reduction through a proposed collision probability modification. HAP simulation results are also compared with experimental data for a three-dimensional test case involving a hypersonic flow over a blunted cone. Finally, conclusions are presented, and planned areas of future work are discussed.

II. Description of DSMC Implementation

A uniform Cartesian grid is employed in HAP for one, two or three-dimensional simulations, and zero-dimensional relaxation calculations may be performed as an additional option. The code can be run in either steady state mode, with time-averaged sampling between a user-designated transient startup time and simulation termination, or in unsteady mode, with multiple short sampling periods. For either mode, results are automatically output during the simulation in a commonly used visualization software format, and multiple zones are employed in unsteady mode for use in generating animations. Output quantities include various macroscopic flowfield variables, surface properties, and surface-integrated forces, moments and heat transfer. In zero-dimensional simulations of homogeneous relaxation problems, nonequilibrium initial conditions may be specified as the superposition of multiple Maxwellian velocity distributions, and the resulting velocity distribution at various elapsed times can be viewed in one, two or three dimensions. Multiple inflow and wall boundary conditions can be used, and immersed bodies may be included within the rectangular (in two dimensions) or cuboidal (in three dimensions) simulation domain. One-dimensional simulations can be performed using Bird's approximate stagnation streamline modeling technique.[2] Full restart capabilities allow calculations to be stopped, started and modified during a simulation with no undesired impact on simulation results.

A. Physical Models and Algorithms

Cartesian ray tracing routines are used to move particles through the grid during each time step. These routines involve tracing a particle's trajectory to the nearest cell face, then moving the particle to the trajectory-face intersection point if the associated distance is less than the product of the time step interval and the particle speed. This type of procedure may be somewhat less efficient than simply moving each particle to some final position at the end of the time step before re-indexing the particle to a new cell.[10] However, the ray tracing technique greatly simplifies calculations involving immersed bodies, and should ease future implementation of parallel domain decomposition and time step adaptation. As in other DSMC codes,[6] ray tracing is performed for a given particle only if that particle is found to exit the assigned cell or impact a solid boundary during the current time step; otherwise more efficient procedures are utilized. If cell residence times are much larger than the time step interval, as is generally the case, then any efficiency reduction due to ray tracing should be small.

Physics models implemented in HAP include the no time counter (NTC) scheme of Bird for collision pair selection, the variable hard sphere (VHS) model for collision dynamics, the Maxwell model for gas-surface interaction, and the harmonic oscillator model for discretized vibrational energy distributions in a vibrationally excited diatomic gas.[2] Simulations can be run for a gas mixture involving an arbitrary number of species. The Larsen-Borgnakke[13] scheme has been implemented for continuous rotational-translational and quantized vibrational-translational energy exchange. As optional alternatives to the NTC collision model, the majorant frequency scheme (MFS) of Ivanov et al.[9] and the scheme of Baganoff and McDonald[14] have also been implemented.

In order to efficiently organize particle information while avoiding excessive memory requirements, HAP employs both cell-based and global dynamic arrays of pointers to particle data. When a new particle either enters the simulation domain or enters a new cell, the memory address for this particle is added to the next unused element in the associated pointer array. Likewise, when a particle exits the cell or the simulation domain, the last used element in the associated pointer array is moved to the position previously occupied by a pointer to this particle, and a variable indicating the number of used elements in the array is decremented by one. The size of both cell-based and global particle pointer arrays is incremented, as necessary, in large blocks; the default block size is 100 for cell-

based arrays and 100,000 for the global array. This use of memory blocks balances a desire to avoid unnecessary memory use with a competing desire to minimize the frequency of computationally expensive memory reallocation for large dynamic arrays. To further improve computational efficiency by reducing memory allocation, the memory location for any particle which exits the simulation domain is added to a linked list of unused particles. The same memory is then assigned, when needed, to a newly generated particle at an inflow boundary.

B. Collision Selection

Although HAP is currently limited to a uniform user-defined cell size, transient adaptive subcell and nearest neighbor procedures are used to select collision pairs, if possible, with sufficiently small separation distances to meet standard DSMC guidelines[2] or some criterion based on the ratio of the mean collision separation (MCS) to the mean free path.[2] If possible, efficient O( ) procedures are utilized to find collision partners from within the same subcell; otherwise a more expensive nearest neighbor search is performed.

As a first step in collision operations during a given time step, NTC or an alternative scheme is used to determine the number of potential collision pairs in a cell. Subcell dimensions within this cell are then computed from the local hard sphere mean free path and a user-designated ratio of subcell size to mean free path. Subcell dimensions may vary among different areas of a cell due to intra-cell variation in the hard sphere mean free path, as described below in Section III.B. Next, all particles are sorted into subcells, using a rapid sorting routine also described below. A prescribed number of particles – equal to the number of potential collision pairs – are then randomly selected, and are paired if possible with previously unpaired particles located within the same subcell. If no unpaired particles are available, or if the only remaining unpaired particle in the same subcell was the last collision partner for the first particle in the pair, then a nearest neighbor from outside this subcell is selected as the second particle in the pair. Finally, once the required number of potential collision pairs has been selected, probabilistic procedures (as outlined below for the NTC scheme) are used to select which of these pairs will collide. Post-collision resampling routines are then performed for all selected pairs, in a manner which is consistent with the VHS model and which enforces momentum and energy conservation.

For nearest neighbor selection as for subcell-based pairing, no two particles are paired together if each of these particles most recently collided with the other. As described by Bird,[8] prevention of repeated collisions between the same two particles is expected to improve overall simulation accuracy, and is particularly important for error reduction when either subcells or nearest neighbor collisions are employed.

As proposed by Macrossan[15] for improved efficiency, the nearest neighbor selection procedure is performed using a randomly ordered array of unselected particles within the cell, and the first particle in this array for which the separation distance is smaller than some tolerance is chosen as the collision partner. For consistency with subcell procedures, the tolerance distance is set in HAP to equal the subcell size. If no particles in this array meet the separation distance criterion, then the nearest neighbor is selected.

In a further modification to nearest neighbor collision selection, a maximum of 30 randomly selected particles are considered as possible collision partners for each particle which requires nearest neighbor identification. This modification was proposed by Bird and by Macrossan[15] to avoid costly O([2]) selection operations in cells which contain a large number of particles, and has been employed in a recent study by Gallis and Torczynski.[16] As an additional option available in HAP, such limited-search nearest neighbor procedures may be performed, in place of subcell based selection routines, to select every collision partner. Note that the number 30 is a rough transition point, identified by Bird et al.,[17] above which nearest neighbor procedures become more expensive than subcell-based collision pairing. Also note that limited searches for collision partner selection, due to either some acceptance distance tolerance or random exclusion of particles within the cell, have previously been called "near neighbor" selection, but this term is not used here in order to avoid confusion.

C. Cut Cell Implementation

Two different options, analytical shapes and externally defined triangulated surfaces, are available in HAP for inclusion of immersed solid bodies within the rectangular or cuboidal simulation domain. For either option, cut cells are employed, with each cut cell containing one or more planar surface elements.

Analytically defined shapes can be used for either two or three-dimensional simulations, and – in contrast to similar capabilities in other DSMC codes[2,9] – these shapes are approximated by a series of planar faces, with one such face per cut cell. This allows relatively simple treatment of complex shapes, and greatly simplifies the process of modifying the code for use with shapes that are not currently available. Monte Carlo procedures for determining cut face properties are performed at simulation startup. For a two-dimensional simulation, these procedures are as follows: First, a large number of random points are generated in each cell. If some, but not all, of these points are within the body, then the cell is designated as a cut cell. Dimensions are determined for the smallest possible

rectangle which includes all random points which are outside the body, and corresponding dimensions are determined for a rectangle including all points inside the body. The and y coordinates of the surface normal vector in this cell are then proportional to the y and coordinate dimensions, respectively, of a third rectangle defined by the intersection region of the first two rectangles. The sign of each normal vector coordinate is determined by checking whether points along axis-aligned lines through the center of the intersection rectangle are inside or outside the body.

For a three-dimensional simulation, a somewhat more complicated procedure is required. In this case, two cuboids containing all random points inside and outside the body are found, and similar procedures as used for a two-dimensional simulation are employed in the central plane of the resulting intersection cuboid. In a three-dimensional simulation involving an analytically defined curved surface, small gaps may exist between planar cut faces in neighboring cells; for simplicity these gaps are treated as grid-aligned surface boundary faces.

While routines used to evaluate planar cut face properties are relatively complex and computationally expensive, these routines are performed only once at simulation startup, and require only that any point in the simulation domain can be established as either inside or outside the solid body. This requirement contrasts with analytical shape capabilities in other DSMC codes, for which expressions defining the surface (as opposed to the volume) of a solid body are required, and for which implementation of new shapes may be complicated and time consuming.[2] As implemented in HAP, the user may choose from a variety of two and three-dimensional shapes including cylinders, spheres, ellipsoids, cuboids, spherically blunted cones, and generic lifting body geometries.

For simulation of three-dimensional flows over arbitrary triangulated surfaces, an optional input file in the ASCII stereo-lithography (STL) format may be used in HAP. STL is a standard format compatible with most commercial CAD packages, and allows curved surfaces to be approximated by a set of contiguous triangular facets. At startup of a HAP simulation, each STL facet is linked to one or more cut cells by generating a large number of random points along the facet and identifying the cell in which each point is located. During particle movement routines, any particle located in a cut cell is considered for collisions with all facets linked to that cell.

D. User Interface

One main attribute of HAP, in contrast to some other DSMC codes intended for general rarefied flow simulation, is an extremely simple, user-configurable and user-friendly interface. The code employs only a single input file, which includes input parameters for global simulation quantities, flow properties, gas species properties and flowfield geometry. These parameters can be rearranged within the input file as desired, and most parameters may be excluded from the file for use with default parameter values.

Uniform numerical weight and time step interval values are utilized, but do not need to be specified directly in the input file. (Implementation and testing of time step adaptation capabilities is currently in progress.) The time step interval is calculated from a user-provided ratio of the time step to the mean collision time at inflow or ambient conditions, with automatic adjustments based on the mean particle transit time across each cell. In contrast to the time step interval, the range of appropriate values for the nondimensional time step input parameter should be relatively problem independent. If the value of this input parameter results in an overly large time step anywhere in the simulated flowfield, then the user is alerted by means of the number of "bad collisions" which is periodically output to the command window and appended to a log file. Here bad collsions are defined as those with a collision probability greater than 1, after adjusting for a maximum of one collision per particle per time step. For additional confirmation that temporal discretization errors are acceptably small, the ratio of the time step interval to the local mean collision time is also included in a field quantity output file. Similarly, the numerical weight (i.e. the number of atoms represented by each simulated particle) is calculated automatically from a user-designated number of particles per subcell based on inflow conditions. This number should generally range between around 2 to 20, and an overly small number can be detected via the ratio of mean collision separation (MCS) to mean free path, as found in the field quantity output file.

An additional numerical parameter – the number of time steps to reach steady state – must still be specified directly by the user for steady state flow simulation. However, the user can monitor transient characteristics in the flow by observing changes in the total numbers of particles, face crossings and collisions per time step; all three quantities are included in a log file. If the flow has not yet reached steady state at initiation of sampling routines, then the user can alter the number of startup time steps and restart the simulation with no loss in accuracy or efficiency.

In addition to a simple user interface and other features described above, one further attribute of HAP is a compact source file. The source code is contained within a single file, which consists of approximately 6500 lines including extensive comments. Several different functions are used within this file for various DSMC operations (e.g. flowfield initialization, particle movement, collisions, sampling) and output file generation, with about 20% of

the source code devoted to the second category. An additional 20% is devoted to automatic generation and initialization of cut cell cells for analytically defined two and three-dimensional surfaces, and to pre-processing for triangulated surface geometries defined in an optional STL input file.

III. Uniform Cartesian Grid Methodology

As mentioned above, HAP employs a uniform Cartesian grid without capabilities for grid adaptation. While this approach has significant advantages associated with reduced code complexity, grid adaptation is required in traditional DSMC algorithms for accurate and efficient simulation of flows involving a wide density range.[2] The most important historical reason for the use of grid adaptation is to limit the separation distance between colliding particles. Accurate simulation of the Boltzmann equation requires that the mean collision separation (MCS) be considerably smaller than the local mean free path,[8] and this condition is violated if collision partners are frequently selected from opposite sides of a cell which is large in comparison to the mean free path. However, the MCS argument for requiring grid adaptation no longer applies when either transient adaptive subcells[8] or nearest neighbor collisions[18] (with a sufficient particle population and appropriate means of avoiding repeated collisions) are employed, as these techniques allow MCS values which are nearly independent of cell size.

There are additional reasons for use of grid adaptation which deserve some discussion: First, higher resolution of simulation results may be desired in regions of relatively high density, and output of field quantities with comparatively low scatter in low density regions can require spatial averaging over larger cell volumes. Although no apparent alternatives to grid adaptation exist for adjustment of output resolution in field quantities, it should be noted that if surface fluxes are the main quantities of interest, then cell size independence can be accomplished by decoupling surface geometry from the cell data structure. In this approach, as used in HAP for three-dimensional triangulated surfaces defined in an optional STL format input file, several surface facets can be located within a single cell, or one facet can extend over several cells.

As an additional argument for grid adaptation in DSMC, the calculation of DSMC collision probability is based on assumptions of uniform density in each cell, and large density variation within a cell can have a significant impact on the calculated collision frequency. Errors associated with uniform density assumptions in DSMC collision probability are discussed in detail below.

As a final reason for grid adaptation, the local mean free path can vary across comparatively large cells in an unadapted grid, and the required size of DSMC subcells to meet a MCS based criterion[8] for simulation accuracy may therefore vary within each cell. Although nearest neighbor pairing can be utilized as an alternative to adaptive subcells, the use of nearest neighbor collision selection may be prohibitively expensive in cells which are significantly larger than the local mean free path and which contain a large number of particles. Limited search "near neighbor" algorithms, as recently employed by Gallis and Torczynski[16] and by Macrossan[15] to improve efficiency relative to standard nearest neighbor procedures, can potentially provide a similar balance of efficiency and accuracy as subcell procedures in such large cells. However, as demonstrated by LeBeau et al,[18] the MCS value depends on the number of particles considered in each search. If a large number of particles per search are required to meet some MCS criterion, then subcell based collision pairing may be more appropriate.

While Cartesian transient adaptive subcell procedures are an efficient means of achieving sufficiently small MCS in large cells which contain a large number of particles,[8] the desired subcell size may differ considerably across a cell due to variation in flowfield quantities over the cell volume. Some error or efficiency reduction is therefore associated with the use of a uniform subcell size within each cell, as is employed in existing Cartesian implementations of the transient adaptive subcell technique.

Although some of the above arguments for using grid adaptation can be resolved for the simpler uniform grid approach in HAP by means of preferential pairing of nearby particles, and by decoupling cell and surface data structures, the last two arguments – errors in collision probability, and variation in appropriate subcell size across a cell – require new modifications to DSMC procedures. These modifications are presented as follows.

A. Gradient-Based Modification to Collision Probability

In order to demonstrate the error in DSMC binary collision probabilities due to internal density variation within a cell, we consider the collision frequency in a simple gas as calculated using the no time counter (NTC) scheme of Bird.[2] The number of potential collision pairs $_{coll}$ is computed as

$$_{coll} = \left\lfloor \frac{1}{2} \frac{(\ -1)}{}(\sigma\ )_{max}\ \Delta t + R \right\rfloor \tag{1}$$

where the operator $\lfloor \rfloor$ rounds to the nearest smaller integer, R is a random number in $[0,1]$, is the numerical weight (i.e. the number of atoms or molecules represented by each particle), is the cell volume, Δt is the time step interval, is the current number of particles in the cell, and $(\sigma)_{max}$ is the maximum product of collision cross section and incident relative speed for all collision pairs in the cell over a large number of time steps. Each of the $_{coll}$ potential collision pairs is then selected to experience a collision with probability

$$P_k = \frac{\sigma_k \;_k}{(\sigma)_{max}} \tag{2}$$

where and k are the particle indices, and σ_k and $_k$ are the collision cross section and relative speed respectively. As follows a Poisson distribution, the expected mean value of (-1) in Eq. (1) should equal $^{-2}$ where $^{-}$ is the value of averaged over a large number of time steps.[8] The mean collision frequency $F(x)$ at a given location x in this cell is therefore

$$F(x) = \frac{2}{\overline{}\Delta t}\langle \;_{coll}P_k\rangle = \frac{\overline{}}{}\langle \sigma_k \;_k\rangle \tag{3}$$

where the operators $\langle\rangle$ indicate an average over all velocity space, weighted by the velocity distribution f and the probability density p in physical space, for all potential collision partners and k. Thus,

$$\langle \sigma_k \;_k\rangle = \iint\iint \sigma(c, c_k)|c - c_k| f(c, x) f(c_k, x_k) p(x, x) p(x_k, x) dx \; dx_k dc \; dc_k \tag{4}$$

where c and c_k represent particle velocities, x and x_k represent particle positions, and the integrals in Eq. (4) are carried out over all phase space for both and k.

The ratio $^{-}/$ in Eq. (3) is the gas number density averaged over the cell volume. If the cell is large in comparison to the local mean free path, then both the number density and the velocity distribution may be strong functions of position x in the cell. If we further assume that the MCS is much smaller than the mean free path, then $f(c, x)p(x, x) \approx f(c, x)\delta(x - x)$ and $f(c_k, x_k)p(x_k, x) \approx f(c_k, x)\delta(x_k - x)$ in Eq. (4), where δ is the Dirac delta. It follows that

$$\langle \sigma_k c_k\rangle \approx \iint \sigma(c, c_k)|c - c_k| f(c, x) f(c_k, x) dc \; dc_k \tag{5}$$

and $\langle \sigma_k \;_k\rangle$ should vary in a physically appropriate way as a function of x. However, Eq. (3) contains no adjustment to the local number density $n(x)$ if $n(x) \neq \;^{-}/$. Some error in F is therefore expected for cells which are large relative to the mean free path and located in high density gradient regions. In particular, if large portions of a cell are consistently unpopulated with particles, then $n(x) > \;^{-}/$ in populated regions, and $F(x)$ will be unphysically low. More generally, if $\nabla n \neq 0$ then $F(x)$ should decrease with increasing cell size, and unphysical preference in collision selection is given to particles in portions of the cell for which $n(x) < \;^{-}/$. Note that, although the NTC scheme is used in the above discussion, the same error due to density gradients is expected for other DSMC collision schemes including the majorant frequency scheme[9] (MFS) and the scheme of Baganoff and McDonald.[14]

As a means of correcting for this error, we first assume that ∇n is uniform over the cell volume. Thus,

$$n(x) = n_c + \nabla n \cdot (x - x_c) \tag{6}$$

where $n_c = \;^{-}/$ is the cell-averaged number density and x_c is the geometric center of the cell. The time-averaged center of mass $\overline{x}_{cm}$ of all particles in the cell is then

$$\overline{x}_{cm} = x_c + \frac{1}{n_c}\int n(x)(x - x_c) dx \tag{7}$$

By substituting Eq. (6) into Eq. (7), and assuming a Cartesian cell of equal length Δ in each coordinate direction, we can express ∇n as a simple function of the vector difference $(\bar{\boldsymbol{x}}_{cm} - \boldsymbol{x}_c)$.

$$\nabla n = \frac{12 n_c}{(\Delta)^2}(\bar{\boldsymbol{x}}_{cm} - \boldsymbol{x}_c) \tag{8}$$

To correct the binary collision probability for effects of spatial density variation, so that the collision frequency $F(\boldsymbol{x})$ in Eq. (3) scales with $n(\boldsymbol{x})$, we multiply the probability P_k in Eq. (2) by the ratio $n(\boldsymbol{x}_k)/n_c$, where $\boldsymbol{x}_k$ is the center of mass of the collision pair. From Eqs. (2), (6) and (8), we find

$$P_k = \frac{\sigma_k k}{(\sigma)_{max}}\left(1 + \frac{12}{(\Delta)^2}(\boldsymbol{x}_k - \boldsymbol{x}_c)\cdot(\bar{\boldsymbol{x}}_{cm} - \boldsymbol{x}_c)\right) \tag{9}$$

As implemented in HAP, this correction is applied to all binary collision probabilities, in order to reduce the error associated with density variation in cells which are large compared to the local mean free path. For simple application of Eq. (9) to a gas mixture, effects of species-based properties (e.g. collision cross section) are neglected and $\bar{\boldsymbol{x}}_{cm}$ is evaluated without biasing to species mass.

In Eq. (9), the time-averaged center of particle mass in a cell $\bar{\boldsymbol{x}}_{cm}$ is calculated by first evaluating the instantaneous center of mass $\boldsymbol{x}_{cm}$ for all particles currently in the cell, then performing an exponential moving average operation

$$(\bar{\boldsymbol{x}}_{cm})_t = \theta(\boldsymbol{x}_{cm})_t + (1-\theta)(\bar{\boldsymbol{x}}_{cm})_{t-\Delta t} \tag{10}$$

where θ is a constant much less than one ($\theta = 0.01$ is used in this work) and t indicates the elapsed simulation time. More complicated and potentially more accurate time-averaging procedures, such as the subrelaxation technique of Sun and Boyd,[19] may be used in place of Eq. (10). Note that, for accurate simulation of an unsteady flow, θ should be much larger than the ratio of Δt to the minimum characteristic transient time scale.

B. Nonuniform Transient Adaptive Subcells

As discussed above, transient adaptive subcells are an efficient means of physically appropriate collision pairing in cells which are large relative to the mean free path. In such cells, a large number of particles may be required for sufficiently small MCS, and subcell indexing is generally much more efficient in these cells than the $O(^2)$ operations associated with nearest neighbor collision selection. However, in the presence of a strong density gradient, the mean free path may vary considerably over the volume of a cell, and division of the cell into subcells based on the cell-averaged mean free path may lead to some reduction in accuracy. Alternatively, the use of overly small subcells – based on estimates of the minimum mean free path anywhere in a cell – can reduce simulation efficiency by creating more subcells than necessary in regions of relatively large mean free path. An excessive number of subcells tends to increase the frequency of expensive searches for collision partners outside the same subcell, using either complicated subcell-based search logic[8] or (as employed in HAP) nearest neighbor routines. Thus, a somewhat improved balance between efficiency and accuracy may be possible by clustering subcells in portions of a cell where the local mean free path is smaller than the cell-averaged value. One procedure for such nonuniform subcell indexing is described as follows.

First, we desire for the subcell length to be some fraction C of the local hard sphere mean free path, which is inversely proportional to the local number density $n(\boldsymbol{x})$. For simplicity, we assume a simple gas; effects of concentration gradients in a gas mixture are neglected. We next assume, as above, that the density gradient ∇n is uniform over the cell volume. The subcell index i in the coordinate direction can then be based on uniform subcell spacing in some alternate coordinate system for which the location $u()$ is related to the global coordinate by $du\,d = n(\ y_c\ _c)$ and $u(\ _c - \frac{1}{2}\Delta) = 0$. Here $(\ _c y_c\ _c) = \boldsymbol{x}_c$ is the cell center location and Δ is the cell length. Hence $du = n(\ y_c\ _c)d$, and from Eqs. (6) and (8), we find

$$u(\ ) = \int_{c-\frac{1}{2}\Delta} \left(n_c + \frac{12 n_c}{(\Delta\ )^2}(\overline{\ }_{cm} - \ _c)(\ ' - \ _c) \right) d\ '$$ (11)

where $\overline{\ }_{cm}$ is the coordinate of the time-averaged center of mass of particles in the cell $\overline{x}_{cm}$. The corresponding subcell index value is then

$$i(\ ) = \left\lfloor (i_{ma} + 1) \frac{u(\ )}{u\left(\ _c + \frac{1}{2}\Delta\ \right)} \right\rfloor$$ (12)

After integration of Eq. (11) and substitution into Eq. (12), we can express the index $i \in [0, i_{ma}]$ in the direction for a given particle location $x = (\ y\ )$ as

$$i(\ ) = \left\lfloor (i_{ma} + 1)\xi(\ )\left(1 + \frac{6}{\Delta}(\overline{\ }_{cm} - \ _c)(\xi(\ ) - 1) \right) \right\rfloor$$ (13)

where

$$\xi(\ ) \equiv \frac{1}{\Delta}(\ - \ _c) + \frac{1}{2}$$ (14)

The maximum index value i_{ma} in Eq. (13) is given by

$$i_{ma} = \left\lfloor \frac{\Delta}{C\langle \lambda \rangle} \right\rfloor$$ (15)

where $\langle \lambda \rangle$ is the hard sphere mean free path averaged over a line segment through the cell center for which $\ \in [\ _c - \frac{1}{2}\Delta,\ _c + \frac{1}{2}\Delta\ ]$. The value of $\langle \lambda \rangle$ is calculated through the approximate expression

$$\langle \lambda \rangle \approx \frac{1}{\sqrt{2}\sigma n_c}\left(1 + 12\left(\frac{\overline{\ }_{cm} - \ _c}{\Delta} \right)^2 \right)$$ (16)

where σ is a reference collision cross section. A derivation of Eq. (16) is included in the Appendix.

To further improve code efficiency by avoiding insufficient particle populations within each subcell, the maximum subcell index i_{ma} can be limited by

$$i_{ma} \le \max \left\{ \left\lfloor \left(\frac{}{\ _{min\ su}} \right)^{1/D} \right\rfloor - 1, 0 \right\}$$ (17)

where D is the number of simulation dimensions and $\ _{min\ su}$ is the minimum desired average number of particles per subcell. ($\ _{min\ su} = 2$ is used in this work.) If $C \approx 1$ in Eq. (15), then the limiting condition in Eq. (17) is likely imposed only in cells where too few particles exist to satisfy standard DSMC guidelines for the MCS, and where some reduction in numerical weight may be needed for accurate simulation. However, the condition in Eq. (17) can be particularly useful if $C \ll 1$, as this allows MCS $\ll \langle \lambda \rangle$ in cells which contain a sufficiently large number of particles, but avoids excessive use of inefficient inter-subcell selection procedures in cells which contain too few particles for the desired MCS value.

In multidimensional simulations, additional subcell indices are required in other coordinate directions. For example, in a three-dimensional simulation, a unique subcell identification number for the particle location

$\mathbf{x} = (\ y\ )$ can be given as $i(\ ) + (i_{ma}+1)\ (y) + (i_{ma}+1)(\ _{ma}+1)k(\ )$, where $(y) \in [0,\ _{ma}]$ and $k(\ ) \in [0, k_{ma}]$ are the subcell indices in the y and $\ $ directions respectively.

By utilizing the proposed subcell indexing procedure, we allow for smaller subcells in regions of increased density and reduced mean free path. For relatively large cells in the presence of a density gradient, subcell lengths may vary significantly along different coordinate directions. However, if $\nabla n = 0$, then Eq. (13) reduces to

$$i(\ ) = \left\lfloor (i_{ma}+1)\left(\frac{1}{\Delta}(\ -\ _c) + \frac{1}{2} \right) \right\rfloor \tag{18}$$

as is used for particle indexing to Cartesian subcells of uniform length.

Both Eqs. (9) and (13), which are employed in HAP for collision selection and subcell indexing respectively, assume a Cartesian cell with uniform length $\Delta\ $ in each coordinate direction. In a cut cell, for which part of the cell is inside a solid body, approximate corrections for the density gradient are enabled by using as $\mathbf{x}_c$ the geometric center of the portion of the cell which is outside the body. This location may be found for each cut cell at simulation startup through a simple Monte Carlo sampling technique, which involves generating a large number of random points throughout the cell volume and discarding any points within the body.

Note that the proposed nonuniform subcell technique follows from an initial assumption that the subcell size should be based on the local mean free path, not solely on the desired number of particles per subcell as in other implementations of the transient adaptive subcell scheme.[8,16] In adapting subcells to the mean free path, we attempt to reduce the MCS only as much as necessary to meet a desired maximum ratio of the MCS to the mean free path, while minimizing the frequency of expensive searches for neighboring particles outside the same subcell. For example, if subcells are scaled in proportion to the mean free path, and if a cell contains enough particles to satisfy some MCS criterion while populating each subcell with a large number of particles, then nearly every collision pair can be efficiently selected from within the same subcell. Under these conditions, computational expense for collision selection scales approximately linearly with the number of particles per cell, and overall simulation efficiency should vary little if the cell size is further increased. It follows that subcell adaptation to the local mean free path is ideally suited to a uniform grid approach, as relatively large cells can be used without significantly impacting either MCS values or simulation efficiency. Similar arguments are used to motivate the use of subcell sizes based on the mean free path in the MONACO DSMC code.[6]

One additional application of the proposed nonuniform subcell technique deserves some mention: As a first step in collision procedures, Eqs. (13) through (17) can be used to efficiently arrange particles into subcells for a cell which is much larger than permitted by standard DSMC guidelines. NTC, MFS or some other scheme can then be independently applied within each subcell, to select collision pairs from among the particles assigned to the same subcell. Eq. (1) is evaluated separately for each subcell, where $\ $ is replaced by the number of particles per subcell, $\ $ is replaced by the subcell volume, and the quantity $(\sigma c_r)_{max}$ is stored as a single value for the entire cell. (Nearest neighbor routines may also be employed to further reduce the MCS, where only particles within the same subcell are considered as potential nearest neighbors.) This approach should eliminate the need for the collision probability modification given as Eq. (9), and should avoid any accuracy loss associated with the uniform gradient assumption in that equation. There are, however, significant drawbacks of this approach relative to the nonuniform subcell approach described above. In particular, additional complexity is required to evaluate the volume of subcells which intersect surface elements for a solid body, and collision partners cannot be selected from among different subcells.

IV. Initial Code Evaluation

For initial evaluation, HAP is applied to a two-dimensional hypersonic flow of N_2 over a flat plate with a sharp leading edge. The plate is aligned with the freestream direction, the freestream Mach number is 20.2, and the Knudsen number based on the total length of the plate is 0.015. The plate surface is diffusely reflecting at a temperature of 290 K, and the freestream temperature is 13.32 K. Using the VHS collision model with parameters recommended for N_2 by Bird,[2] we calculate a freestream mean free path is 1.688 mm. This case is based on tests by Lengrand et al.[20] and Heffner et al.[21] in the SR3 low density wind tunnel at CNRS in Meudon, France.

A corresponding simulation is performed with the DSMC code MONACO,[6] using the same grid, boundary conditions, physical models and numerical parameters. Results are compared between the two simulations in order to highlight any discrepancies which may indicate potential errors in HAP. Published DSMC results of Heffner et al.,[21] as well as experimental data of Heffner et al. and Lengrand et al.,[20] are also used for comparison.

9
American Institute of Aeronautics and Astronautics

HAP and MONACO simulations employ a uniform grid with 128 by 48 square cells of length 1 mm, and with a uniform inflow boundary located 16 cells upstream of the plate leading edge. The time step interval Δt is set to 3.102×10^{-7} s, which is approximately 0.06 times the minimum mean collision time at steady state. The numerical weight   is set to 2.3225×10^{12} for an average of 160 particles per cell in the freestream. Time averaged sampling is performed over 18000 time steps, following a transient startup period of 2000 steps. For reference, various simulation parameters are shown in Table 1. The HAP simulation requires about 5.3 hours of CPU time on a single 1.9 GHz processor, and includes 1.06×10^{6} particles at steady state.

Figures 1 through 4 show isocontour lines for various field quantities from both HAP and MONACO simulations. Coordinates are normalized by the freestream mean free path, and the coordinate system origin is located at the plate leading edge. HAP simulation results are displayed as multi-colored solid lines, while results from the MONACO simulation are shown as black dashed lines. Figures 1, 2, 3 and 4 show respectively contours of Mach number, number density normalized by the freestream value, translational temperature, and rotational temperature. Relatively complex characteristics are observed in the figures, including a highly diffuse oblique shock which forms within a smooth compression region near the leading edge, a low density expansion region within the post-shock area near the surface, and significant rotational temperature lag behind the shock. In all four figures, virtually no noticeable differences are found between results from the two codes; the one exception is a small discrepancy in rotational temperature near the plate surface around $\lambda_\infty = 45$. Although no clear explanation for this discrepancy is apparent, the local gradient in rotational temperature is small, and the relative difference of well under 1% is within the likely range of statistical scatter.

In Fig. 5, normalized density values n/n_∞ from the HAP and MONACO simulations are extracted along a transverse plane at $\lambda_\infty = 44.55$. Experimental data from electron beam fluorescence measurements of Lengrand et al.[20] are also displayed for comparison. As in Fig. 2, excellent agreement is found between density values from the two simulations, and any noticeable differences are within statistical scatter. In contrast, large discrepancies are observed between experimental and simulation data points, with the experiment showing a roughly 30% increase in distance between the plate and the shock center location. Note however that reasonably good agreement is found in the density along the plate and in the maximum density within the shock. Differences between experimental and DSMC density values can be mainly attributed to uncertainty and modeling approximations in gas-surface interaction, high sensitivity of experimental results to the plate angle of attack, and nonuniform freestream conditions in the SR3 experimental facility.[22]

Figures 6 and 7 show profiles of bulk velocity and temperature, respectively, extracted from HAP and MONACO results along the same transverse plane as in Fig. 5. Transverse and longitudinal velocity components in Fig. 6 are normalized by the inflow bulk velocity, and in Fig. 7 translational and rotational temperatures are normalized by the inflow temperature. As in Figs. 1 through 4, no statistically significant disagreement is found between HAP and MONACO results in Figs. 6 and 7.

In Fig. 8, the pressure coefficient C_p is plotted along the plate surface from HAP and MONACO simulation results, with additional published DSMC results of Heffner et al.[21] and experimental data of Lengrand et al.[20] The pressure coefficient is defined as

$$C_p = \frac{P - P_\infty}{\frac{1}{2}\rho_\infty \quad_\infty^{2}} \tag{19}$$

where P is the surface-normal momentum flux, and P_∞, ρ_∞ and $_\infty$ are respectively the freestream pressure, mass density and bulk velocity magnitude. As in Figs. 1 through 7, excellent agreement is observed in Fig. 8 between MONACO and HAP results. However, relative to other DSMC results in Fig. 8, some small but noticeable underprediction is found in the Heffner et al. results, likely due in part to the use of a different set of parameter values by Heffner et al. for the VHS collision model. [1] Considerable disagreement is displayed in Fig. 12 between the experimental data points and all DSMC results, with consistently lower experimental C_p values for $\lambda_\infty > 15$. The dominant source of the discrepancy is unclear, but likely contributors include the potential error sources mentioned above in the discussion of Fig. 5. Note the sharp drop-off in C_p observed in both HAP and MONACO results near the downstream edge of the simulation domain. This trend is likely unphysical, and results from the suction effect of the DSMC vacuum outflow boundary within a small subsonic boundary layer region.

Figure 9 shows the shear stress coefficient, defined as the ratio of the surface tangential momentum flux to the freestream dynamic pressure ½ ρ_∞ $_\infty^{2}$, from HAP and MONACO simulation results. As expected, no discrepancies are observed outside the range of statistical scatter.

Variation in the heat transfer coefficient C_h along the plate surface is shown in Fig. 10. This coefficient is defined as

$$C_h = \frac{}{\frac{1}{2}\rho_\infty \quad_\infty^3} \tag{20}$$

where   is net surface energy flux. Results are displayed from HAP and MONACO simulations described above, along with the published DSMC results of Heffner et al.[21] and the experimental data of Heffner et al. and Lengrand et al.[20] For comparison, results are also plotted in Fig. 10 from an additional HAP simulation for which the thermal accommodation coefficient (TAC) is reduced from 1 to a potentially more realistic value of 0.8. All three sets of DSMC results for TAC = 1 show very good agreement, with no differences between HAP and MONACO values outside the level of statistical scatter. Significantly lower C_h values are found in the experimental results of both Heffner et al. and Lengrand et al, and considerable disagreement is also observed between the two experimental data sets. No dominant source of the discrepancies is apparent, but. gas-surface interaction is a potential contributing factor, as suggested by Heffner et al. and as indicated by the relatively good agreement between the experimental data of Heffner et al. and results from the HAP simulation with TAC = 0.8. Sensitivity to and uncertainty in the plate angle of attack is another likely contributor, and may partly account for the disagreement between the two sets of experimental data. Nonuniform freestream conditions[22] should also reduce the level of agreement between DSMC and experimental results, and may warrant future DSMC simulations which include much of the upstream expansion region in the SR3 facility.

V. Evaluation of Error Reduction Due to Collision Probability Modification

In both HAP and MONACO simulations described above, the cell size is 0.6 times the freestream mean free path and is uniformly less than the local mean free path throughout the simulated flowfield. It is therefore expected that approximations associated with spatial averaging in density over the cell volume, as used to compute collision probabilities in the standard NTC scheme,[2] account for negligibly small errors in the output quantities of interest. However, from the logic outlined in Section III.A, the spatial discretization error in collision probabilities should increase in regions of high density gradient as the cell size is increased. Likewise, the proposed modification to the collision probability, as implemented in HAP, should have a progressively greater impact on simulation results when larger cells are used. In order to quantify the error due to density averaging in collision probabilities, and to demonstrate the effectiveness of the proposed modification in reducing this error, a series of additional HAP simulations are run for the same hypersonic flat plate flow presented above in Section IV. The ratio Δ /λ_∞ is varied by factors of two between 0.6 and 4.8, and simulations are performed both with and without the collision probability modification. The same values are used in all simulations for the numerical weight and time step interval, and transient adaptive subcell procedures should eliminate or greatly reduce any effects of cell size on the mean collision separation. It follows that the discretization error described in Section III.A should be isolated from other DSMC spatial and temporal discretization errors, and only this first error is varied between the different simulations.

Figures 11, 12 and 13 show respectively the variation in pressure, shear stress and heat transfer coefficients along the plate surface, from eight simulations employing different Δ /λ_∞ ratios and using either standard or modified collision probabilities. As shown in the three figures, only very small differences appear in the surface fluxes between results from all simulations employing the modified probabilities, while the standard DSMC simulations display considerably greater disagreement. Errors among the standard DSMC results are particularly noticeable for simulations with normalized cell sizes Δ /λ_∞ of 2.4 and 4.8, which significantly underestimate flux values over much of the plate surface relative to the $\Delta /\lambda_\infty = 0.6$ simulations. In addition, significant overestimates in both shear stress and heat flux are found at $/\lambda_\infty > 60$ for the $\Delta /\lambda_\infty = 4.8$ simulation utilizing standard DSMC collision probabilities. In comparing results between the $\Delta /\lambda_\infty = 4.8$ simulations with and without the collision probability modification, we find large errors in the standard DSMC simulation, and a considerable reduction in these errors when the proposed modification is used. Note that surface fluxes are typically among the output quantities most sensitive to errors in DSMC calculations, and that only very small errors (less than 3%) were observed in a comparison of field quantities between these simulations.

To further quantify the errors associated with spatial density averaging in collision probabilities, and to quantify the error reduction due to the proposed modification, the L∞-norm of the heat transfer coefficient is plotted as a function of normalized cell size $/\lambda_\infty$ in Fig. 14. This norm is calculated as the maximum difference between local C_h values and those for the $\Delta /\lambda_\infty = 0.6$ standard DSMC simulation, normalized by the local C_h value from the same

11
American Institute of Aeronautics and Astronautics

$\Delta /\lambda_\infty = 0.6$ simulation. By assuming that differences in C_h values between modified and standard $\Delta /\lambda_\infty = 0.6$ simulations are primarily due to statistical scatter, we can designate the L∞-norm value for the modified $\Delta /\lambda_\infty = 0.6$ simulation as the minimum L∞-norm level above which statistically significant errors in C_h are detected. This minimum level is displayed as a dashed horizontal line in Fig. 14. Linear trend lines, based on least-squares fits, are also shown in Fig. 14 to highlight general trends among the two sets of data points.

In comparing results with and without the collision probability modification, we find a considerable increase in error with increasing Δ /λ_∞ for the standard DSMC simulations, and a much weaker dependence on cell size when modified collision probabilities are employed. In particular, the maximum local error in C_h is significantly less for the $\Delta /\lambda_\infty = 4.8$ simulation with modified probabilities than for the $\Delta /\lambda_\infty = 1.2$ standard DSMC simulation.

In Fig. 15, the L2-norm in C_h is plotted as a function of Δ /λ_∞ for simulations with and without modified collision probabilities. This norm is a measure of the root-mean-square error in local heat flux, relative to the standard DSMC simulation with $\Delta /\lambda_\infty = 0.6$. The same general trends are observed in Fig. 15 as in Fig. 14, although a somewhat greater dependence on cell size is found for the L2-norm than for the L∞-norm in results from the modified probability simulations.

In both Figs. 14 and 15, a comparatively small – but still significant – increase in error for larger Δ /λ_∞ is found for the modified probability simulations. This increase can be primarily attributed to breakdown in the assumption of a uniform density gradient within each cell. Curvature of the density profile is clearly shown in Fig. 5, due in part to competing effects of compression within the shock, expanding flow in the post-shock region, and relatively stagnant flow along the wall. In Fig. 5, we find that approximations of a locally uniform density gradient should be particularly inaccurate for cells along the plate surface or near the location of maximum density within the shock. For accurate simulation using the proposed modification, it follows that the cell size may need to be limited by length scales, such as $|\nabla n/\nabla \cdot \nabla n|$, which are associated with the curvature of the density profile. Additional reductions in errors related to density averaging may also be possible by repeating the analysis in Section III.A under assumptions that ∇n is a linear function of position within each cell, or by applying independent collision selection procedures in each subcell as suggested in Section III.B.

VI. Comparison with Experiment for Hypersonic Flow Over a Blunted Cone

As an additional test case, we consider a three-dimensional hypersonic flow of N_2 over a spherically blunted cone at a 10° angle of attack. This case is based on a series of experiments by Allegre et al. in the SR3 facility at CNRS,[22,23] and involves a subscale model of the Mars Pathfinder aeroshell. Geometry parameters include a cone angle of 70°, a base radius of 2.5 cm, and curvature radii of 1.25 cm and 1.25 mm at the nose and shoulder respectively. All of these parameters are specified in the HAP input file, for automatic generation of planar surface elements which comprise the aeroshell shape. The freestream Mach number is 20.2, the global Knudsen number (based on cone diameter) is 0.032, and the Reynolds number is 1420. Additional simulation parameters include a freestream temperature of 13.3 K, a wall temperature of 300 K, a wall thermal accommodation coefficient of 1, and collision numbers of 5 and 50 for rotational and vibrational energy respectively. The simulation is performed on a uniform Cartesian grid with 3×10^5 cells and approximately 2×10^6 particles at steady state. Time-averaged sampling is carried out over 22,000 time steps, following a transient startup period of 2000 steps. A CPU time of about 19 hours is required.

Figure 16 shows contours of surface heat flux and streamlines along the symmetry plane. (For reduced simulation expense, calculations were performed only on one side of the symmetry plane, and Fig. 16 includes a mirror image of the direct simulation results.) Some asymmetry in streamlines is observed along the pitching plane, with a stagnation point slightly below the center of the nose region. As expected, the heat flux is highest around the nose, and higher heat flux values are found on the windward side of the forebody than on the lee side. A local maximum in heat flux occurs around the windward shoulder, and a rapid drop-off in heat flux is observed in the strong expansion region along the downstream portion of the shoulder.

In Fig. 17, isocontour lines for normalized density n/n_∞ are shown from HAP simulation results, and from electron beam fluorescence measurements of Allegre et al.[22] Relatively good overall agreement is found, particularly within the forebody shock layer and in the wake expansion regions. Both simulation and experimental results show considerable asymmetry due to the nonzero angle of attack. However, significant discrepancies are observed between the two sets of results, with particularly noticeable differences within near-wake and off-axis shock layer regions. Other differences in Fig. 17 are due to freestream scatter in HAP contour lines at $n/n_\infty = 1$; this results from the use of contour values at the designated inflow condition, and should not be considered either as an indication of excessive statistical scatter or as an example of disagreement with experimental data.

While several possible error sources contribute to the observed differences between HAP and experimental results in Fig. 17, one main probable contributor is the highly nonuniform freestream condition in the experiment. The freestream density distribution was characterized by Allegre et al. through density measurements in an empty test section, and showed considerable differences in both axial and transverse directions.[22] Unfortunately, a HAP simulation involving similarly nonuniform freestream conditions would require additional measurements for freestream velocity and temperature. Effects of freestream translational nonequilibrium or rotational freezing could also contribute to the differences shown in Fig. 17, and accurate simulation of inflow conditions at the test section may require that the simulation domain extend far upstream into the divergent nozzle region of the SR3 facility. For somewhat greater consistency, experimental density values in Fig. 17 are normalized by the local freestream density as measured in the empty test section. Another likely contributor to discrepancies within near-wake region is the presence of the sting in the experiment; exclusion of the sting in the simulation probably reduced the calculated density in this region and contributed to the disagreement observed in Fig. 17.

Variation in surface heat flux along the symmetry plane is shown from both HAP and experimental results in Fig. 18. In observing HAP results, we find significant asymmetry over the forebody surface; the maximum heat flux is located slightly off center, and a local maximum is displayed along the windward forebody shoulder region. Near-zero heat flux is found over much of the back side, with negative flux values in a small region of cold rapidly expanding flow around the downstream portion of the shoulder. Good qualitative agreement is found between HAP and experimental data points, although local differences of over 10% are shown along the forebody. Discrepancies are partly attributable to uncertainty in freestream conditions and gas-surface interaction modeling, among other factors.

VII. Conclusions

A new Cartesian DSMC code, HAP, has been introduced. HAP is intended for fast setup and simulation of relatively small rarefied flow problems, and as a foundation for development and testing of new DSMC models and algorithms. The code is greatly simplified by avoiding complex routines for dynamic grid adaptation, and a series of alternate procedures are employed to compensate for the expected reduction in simulation accuracy when computational cells are not refined to the local mean free path. These procedures include the use of nonuniform transient adaptive subcells refined approximately to the local mean free path, and a new collision probability modification to correct for errors associated with density averaging over the cell volume. In addition to nonuniform subcells and modified collision probabilities, another unique feature of HAP is the ability to automatically generate two and three-dimensional shapes comprising a series of planar surface elements. This avoids a typical requirement to import externally defined boundary geometries for a wide variety of DSMC simulations, and considerably reduces setup time.

For initial code evaluation, a detailed comparison has been performed between results from HAP, other DSMC codes, and two sets of experiments for a rarefied hypersonic flow over a flat plate. Excellent agreement was found between results from the HAP simulation and those from the established DSMC code MONACO, with no observed differences outside expected levels of statistical scatter. Good qualitative agreement was also found with experimental density and surface flux data, and likely explanations were offered for observed discrepancies. As an additional test case, HAP was used to simulate a three-dimensional hypersonic flow over a spherically blunted cone. Both gas density and surface heat flux were compared to published experimental data, with generally encouraging results.

In another study involving the flat plate flow problem, several HAP simulations were performed using different grid refinement levels, both with and without the proposed collision probability modification. Spatial discretization errors associated with collision probability were quantified, and significant error reduction was demonstrated through the proposed modification. To the authors' knowledge, no previous investigation of these errors exist in the literature, and it is hoped that the present work encourages more detailed analysis of this problem. Previous work on spatial discretization errors in DSMC has focused on the effects of the mean collision separation (MCS), and modern DSMC collision selection procedures (e.g. transient adaptive subcells) tend to reduce or eliminate the correlation between MCS and cell size. Even with arbitrarily small MCS, however, spatial discretization errors may persist through a strong cell size dependence in collision probabilities. It should be emphasized that techniques for reducing the MCS, such as nearest neighbor collisions and adaptive subcells, do not reduce errors due to spatially averaged collision probabilities in the presence of a density gradient. Both the collision probability correction and the nonuniform subcell technique presented here are therefore suggested as ways to reduce the influence of cell size on simulation accuracy.

13
American Institute of Aeronautics and Astronautics

Planned areas of future work include implementation of procedures for dynamic time step adaption, parallelization with dynamic load balancing and utilization of shared memory for improved efficiency, and implementation of chemistry routines for simulation of high enthalpy reacting flows. Expected applications include aerothermal analysis of hypersonic technology demonstration vehicles and lifting reentry vehicles at high altitude.

Appendix

A derivation is provided for Eq. (16), which gives an approximate expression for the hard sphere mean free path $\langle\lambda\rangle$ averaged in the ξ coordinate direction over a line segment through the cell center (ξ_c, y_c, z_c) with $\xi \in [\xi_c - \frac{1}{2}\Delta, \xi_c + \frac{1}{2}\Delta]$. From Eq. (6), the number density along the line segment can be expressed as $n(\xi) = n_c + (\partial n/\partial\xi)(\xi - \xi_c)$ where n_c is the cell-averaged number density and $\partial n/\partial\xi$ is assumed constant. The local hard sphere mean free path is therefore

$$\lambda(\xi) = \frac{1}{\sqrt{2}\sigma\left(n_c + \frac{\partial n}{\partial\xi}(\xi - \xi_c)\right)} \tag{A.1}$$

where σ is the hard sphere collision cross section. Integration of Eq. (A.1) over the interval $[\xi_c - \frac{1}{2}\Delta, \xi_c + \frac{1}{2}\Delta]$ gives

$$\langle\lambda\rangle = \frac{1}{\Delta}\int_{\xi_c - \frac{1}{2}\Delta}^{\xi_c + \frac{1}{2}\Delta}\lambda(\xi)\,d\xi = \frac{1}{\sqrt{2}\sigma n_c\Delta\frac{\partial n}{\partial\xi}}\ln\left(\frac{1 + \frac{\Delta}{2n_c}\frac{\partial n}{\partial\xi}}{1 - \frac{\Delta}{2n_c}\frac{\partial n}{\partial\xi}}\right) \tag{A.2}$$

The right side of Eq. (A.2) is undefined when $\partial n/\partial\xi = 0$, and is potentially subject to large truncation error when the term in the parenthesis is close to 1, so an approximate expression for $\langle\lambda\rangle$ is desired. The Taylor series approximation

$$\ln\left(\frac{1+\varepsilon}{1-\varepsilon}\right) \approx 2\varepsilon + \frac{2}{3}\varepsilon^3$$

for an arbitrary variable $\varepsilon \in (-1,1)$ is used to find

$$\langle\lambda\rangle \approx \frac{1}{\sqrt{2}\sigma n_c}\left(1 + \frac{1}{12}\left(\frac{\Delta}{n_c}\frac{\partial n}{\partial\xi}\right)^2\right) \tag{A.3}$$

Finally, we employ Eq. (8) to express $\partial n/\partial\xi$ as a function of the ξ coordinate of the time-averaged particle center of mass in the cell, $\overline{\xi}_{cm}$, and substitute into Eq. (A.3).

$$\langle\lambda\rangle \approx \frac{1}{\sqrt{2}\sigma n_c}\left(1 + 12\left(\frac{\overline{\xi}_{cm} - \xi_c}{\Delta}\right)^2\right) \tag{A.4}$$

References

[1]Bird, G. A., "Approach to Translational Equilibrium in a Rigid Sphere Gas," *Physics of Fluids*, Vol. 6, 1963, pp. 1518-1519.

[2]Bird, G. A., *Molecular Gas Dynamics and the Direct Simulation of Gas Flows*, Clarendon Press, Oxford, 1994.

[3]Alder, B. J., and Wainwright, T. E., "Studies in Molecular Dynamics," *Journal of Chemical Physics*, Vol. 27, 1957, pp. 1208-1209.

[4]Kolobov, V. I., Arslanbekov, R. R., Aristov, V. V., Frolova, A. A., and Zabelok, S. A., "Unified Solver for Rarefied and Continuum Flows with Adaptive Mesh and Algorithm Refinement," *Journal of Computational Physics*, Vol. 223, 2007, pp. 589-608.

[5]Burt, J. M., and Boyd, I. D., "Evaluation of a Particle Method for the Ellipsoidal Statistical Bhatnagar-Gross-Krook Equation,", AIAA paper 2006-989.

[6]Dietrich, S., and Boyd, I. D., "Scalar and Parallel Optimized Implementation of the Direct Simulation Monte Carlo Method," *Journal of Computational Physics*, Vol. 126, 1996, pp. 328-342.

[7]LeBeau, G. J., "A Parallel Implementation of the Direct Simulation Monte Carlo Method," *Computer Methods in pplied Mechanics and n ineerin* , Vol. 174, 1999, pp. 319-337.

[8]Bird, G. A., "The DS2V/3V Program Suite for DSMC Calculations," *Rarefied Gas Dynamics* th *International Symposium*, Vol. 762, 2005, pp. 541-546.

[9]Ivanov, M. S., Markelov, G. N., and Gimelshein, S. F., "Statistical Simulation of Reactive Rarefied Flows: Numerical Approach and Applications," AIAA Paper 98-2669, 1998.

[10]Gao, D., Zhang, C., and Schwartzentruber, T. E., "A Three-Level Cartesian Geometry Based Implementation of the DSMC Method," AIAA Paper 2010-450, 2010.

[11]Wu, J.-S., Tseng, K.-C., and Wu, F.-Y., "Parallel Three-Dimensional DSMC Method Using Mesh Refinement and Variable Time-step Scheme," *Computer Physics Communications*, Vol. 162, 2004, pp. 166-187.

[12]Oran, E. S., Oh, C. K., and Cybyk, B. Z., "Direct Simulation Monte Carlo: Recent Advances and Applications," *nnual Re iew of Fluid Mechanics*, Vol. 30, 1998, pp. 403-441.

[13]Borgnakke, C., and Larsen, P. S., "Statistical Collision Model for Monte Carlo Simulation of Polyatomic Gas Mixture," *Journal of Computational Physics*, Vol. 18, 1975, pp. 405-420.

[14]Baganoff, D., and McDonald, J. D., "A Collision-Selection Rule for a Particle Simulation Method Suited to Vector Computers," *Physics of Fluids* , Vol. 2, No. 7, 1990, pp. 1248-1259.

[15]Macrossan, M. N., "Searching for a Near Neighbor Particle in DSMC Cells Using Pseudo-Subcells," *Journal of Computational Physics*, Vol. 229, 2010, pp. 5857-5861.

[16]Gallis, M. A., and Torczynski, J. R., "Effect of Collision-Partner Selection Schemes on the Accuracy and Efficiency of the Direct Simulation Monte Carlo Method," *International Journal for umerical Methods in Fluids*, 2010 (published online; DOI: 10.1002/fld.2409).

[17]Bird, G. A., Gallis, M. A., Torczynski, J. R., and Rader, D. J., "Accuracy and Efficiency of the Sophisticated Direct Simulation Monte Carlo Algorithm for Simulating Non-continuum Gas Flows," Physics of Fluids, Vol. 21, 2009, 017103.

[18]LeBeau, G. J., Boyles, K. A., and Lumpkin, F. E., "Virtual Sub-cells for the Direct Simulation Monte Carlo Method," AIAA Paper 2003-1031, 2003.

[19]Sun, Q., and Boyd, I. D., "Evaluation of Macroscopic Properties in the Direct Simulation Monte Carlo Method," *Journal of Thermophysics and Heat Transfer*, Vol. 19, No. 3, 2005, pp. 329-335.

[20]Lengrand, J. C., Allegre, J., Chpoun, A., and Raffin, M., "Rarefied Hypersonic Flow Over a Sharp Flat Plate: Numerical and Experimental Results," *Rarefied Gas Dynamics* th *International Symposium*, 1993, pp. 276-284.

[21]Heffner, K. S., Gottesdiener, L., Chpoun, A., and Lengrand, J. C., "Leading Edge Effect on Rarefied Hypersonic Flow Over a Flat Plate," AIAA Paper 91-1749.

[22]Allegre, J., Bisch, D., and Lengrand, J. C., "Experimental Rarefied Density Flowfields at Hypersonic Conditions Over 70-Degree Blunted Cone," *Journal of Spacecraft and Rockets*, Vol. 34, No. 6, 1997, pp. 714-718.

[23]Allegre, J., Bisch, D., and Lengrand, J. C., "Experimental Rarefied Heat Transfer at Hypersonic Conditions Over 70-Degree Blunted Cone," *Journal of Spacecraft and Rockets*, Vol. 34, No. 6, 1997, pp. 724-728.

Table 1. Parameters for HAP and MONACO simulations of hypersonic N_2 flow over a flat plate.

Freestream Mach number	20.2
Global Knudsen number	0.015
Freestream temperature	13.32 K
Plate surface temperature	290 K
Freestream number density	3.716×10^{20} m^{-3}
Freestream mean free path	1.688 mm
Cell length	1 mm
Number of cells	128×48
Time step interval	3.102×10^{-7} s
Numerical weight	2.3225×10^{12}
Total number of time steps	20,000
Number of time steps before sampling	2000

15
American Institute of Aeronautics and Astronautics

Figure 1. Contours of Mach number. HAP results are shown as colored lines, and MONACO results are shown as black dashed lines.
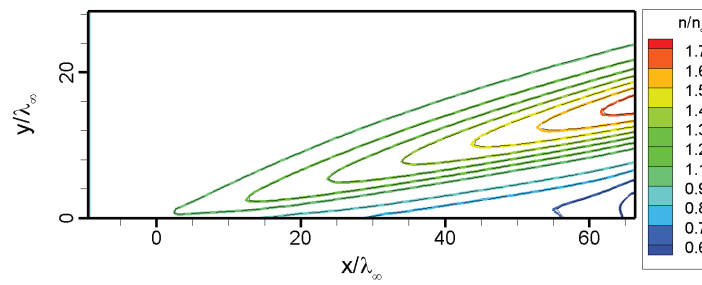
Figure 2. Contours of normalized number density from HAP and MONACO simulations.
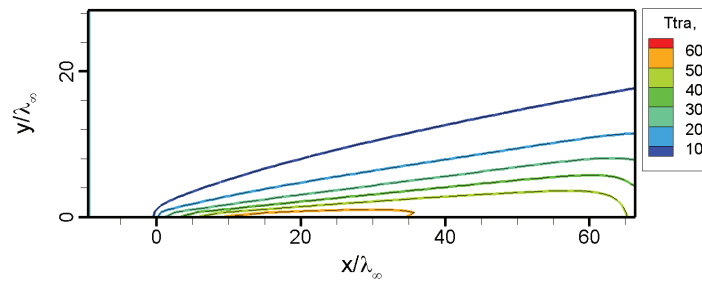
Figure 3. Contours of translational temperature.
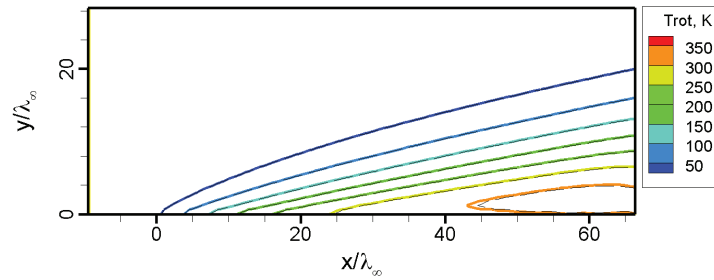
Figure 4. Contours of rotational temperature.
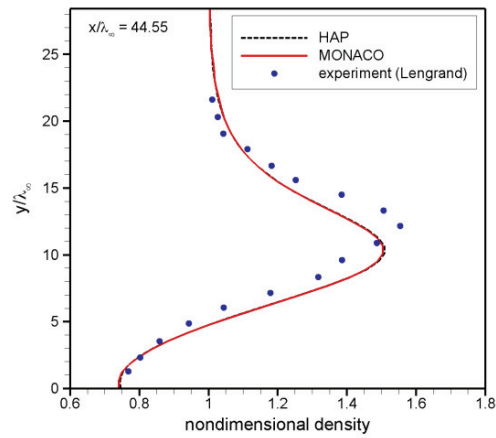
Figure 5. Density profiles along a transverse plane.
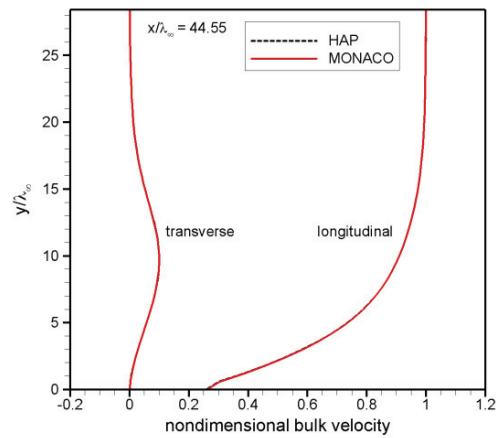
Figure 6. Bulk velocity profiles along a transverse plane.
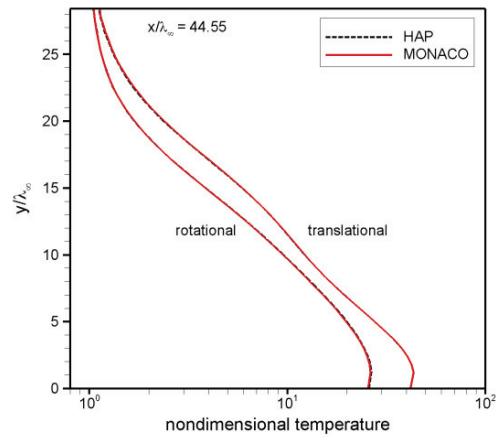
Figure 7. Profiles of translational and rotational temperature along a transverse plane.
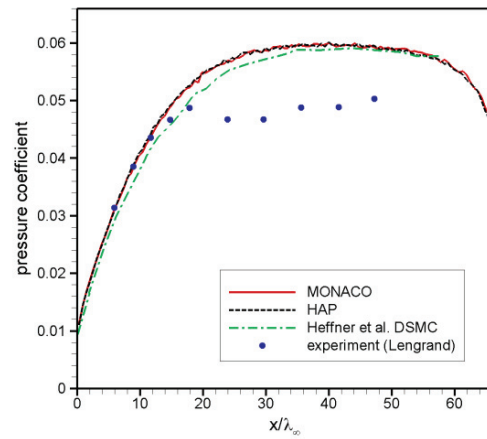
Figure 8. Pressure coefficient along the plate surface.
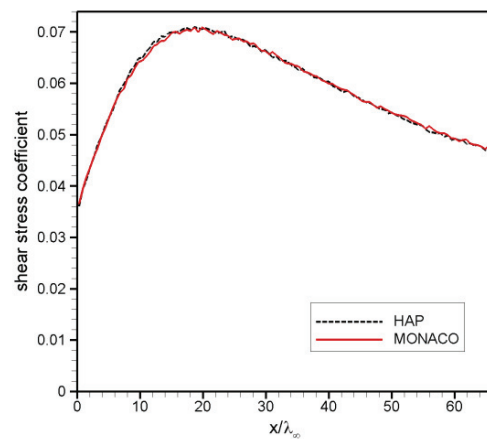
Figure 9. Shear stress coefficient along the plate surface.
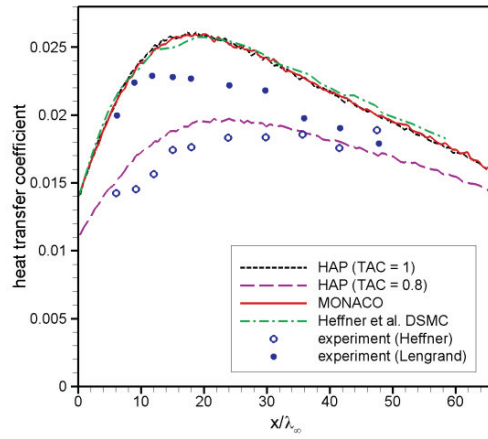
Figure 10. Heat transfer coefficient along the plate surface.
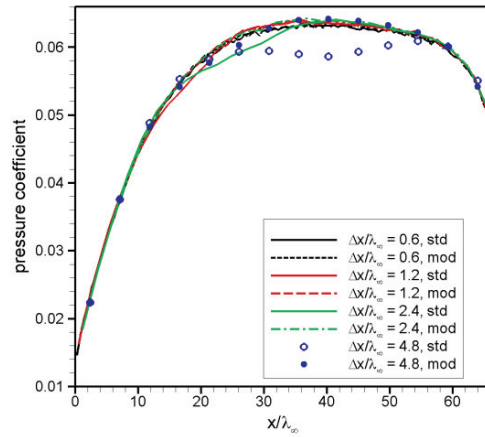
Figure 11. Surface pressure coefficient for various cell sizes, with and without gradient-based collision probability modifications.
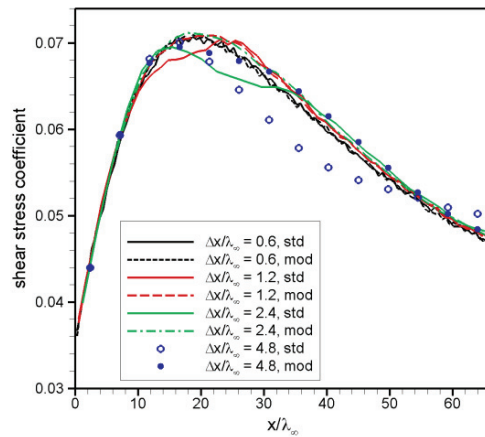
Figure 12. Surface shear stress coefficient for various cell sizes.
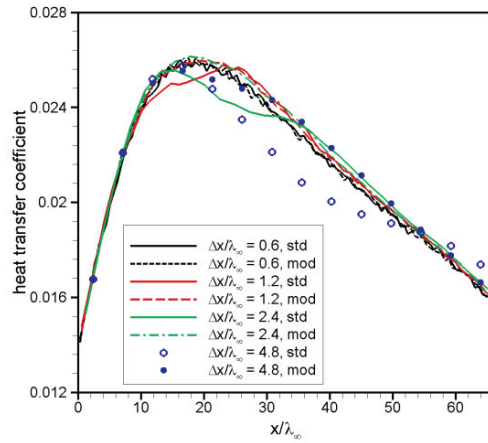
Figure 13. Surface heat transfer coefficient for various cell sizes.
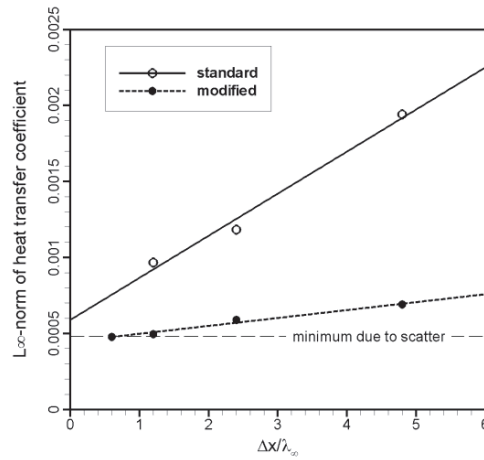
Figure 14. L∞-norm of heat transfer coefficient as a function of cell size, with and without gradient-based collision probability modifications.
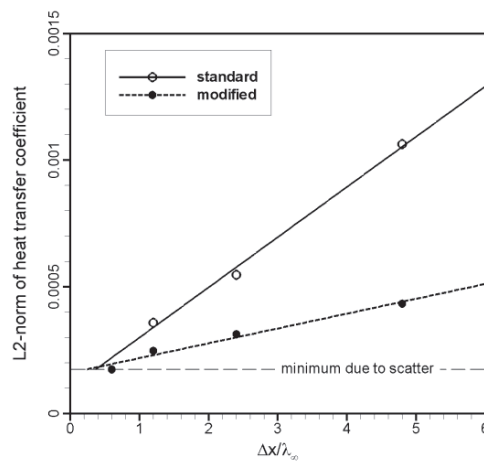
Figure 15. L2-norm of heat transfer coefficient as a function of cell size.
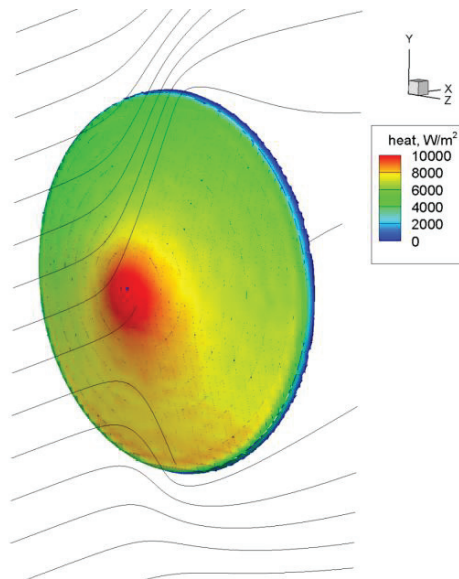
Figure 16. Contours of surface heat flux, and streamlines along symmetry plane, for hypersonic flow over 70° blunted cone at 10° angle of attack.
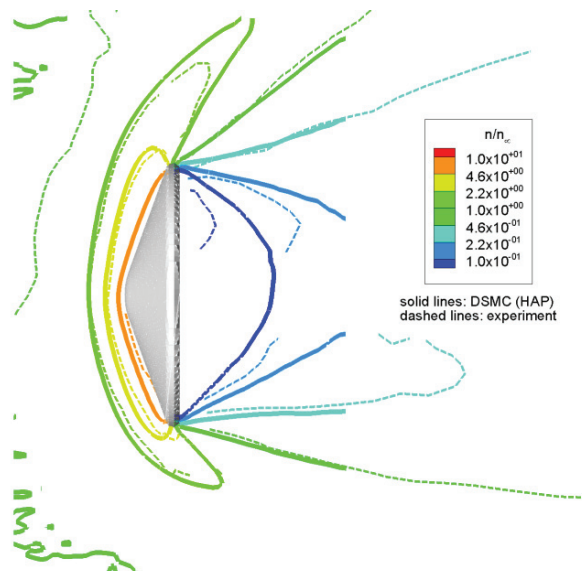
Figure 17. Contours of normalized density along symmetry plane. Dashed lines indicate experimental data.
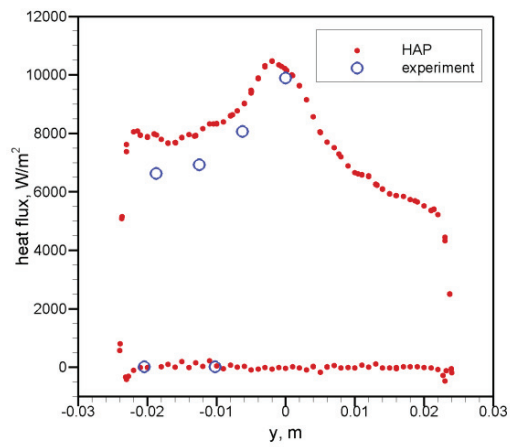
Figure 18. Variation in surface heat flux along symmetry plane.

Novel Cartesian Implementation of the Direct Simulation Monte Carlo Method

Jonathan M. Burt* and Eswar Josyula[†]

U.S. Air Force Research Laboratory, Wright-Patterson Air Force Base, Ohio 45433

and

Iain D. Boyd[‡]

University of Michigan, Ann Arbor, Michigan 48109

A new implementation of the direct simulation Monte Carlo (DSMC) method, named the hypersonic aerothermodynamics particle (HAP) code, is presented. This code is intended for rapid setup and simulation of rarefied gas flow problems and as a framework for evaluating new physical models and numerical techniques. Unique features include the use of nonuniform Cartesian adaptive subcells, a collision probability modification to reduce errors associated with spatial averaging in collision probabilities, and automatic planar element approximation of analytically defined two- or three-dimensional surface geometries. In this work, simulations are performed using both HAP and an established DSMC code for a rarefied hypersonic flow of nitrogen over a flat plate, and excellent overall agreement is found. Comparisons are also performed with available experimental data and published DSMC results for the same flat plate flow problem. Additional simulations are employed to demonstrate reduced dependence on cell size through a proposed collision probability modification. Finally, HAP results are compared with published DSMC data for a hypersonic flow over a cylinder, and a three-dimensional sphere flow problem is used to demonstrate capabilities for automatic generation of planar cut faces over an analytically defined surface.

Nomenclature

C	=	desired ratio of subcell size to local hard sphere mean free path
C_h	=	heat transfer coefficient
C_p	=	pressure coefficient
c	=	particle velocity
D	=	number of simulation dimensions
d_{ref}	=	reference collision diameter
F	=	mean collision frequency
f	=	velocity distribution function
g	=	relative speed between two particles
i_{max}	=	maximum subcell index
N	=	number of particles in a cell
N_{coll}	=	number of potential collision pairs in a cell
n	=	local number density
n_c	=	cell-averaged number density
n_f	=	surface outward normal unit vector
P	=	collision probability
P_∞	=	freestream pressure
p	=	probability density in physical space
q	=	net surface energy flux
R	=	random number in [0,1]
T	=	temperature
V	=	cell volume
V_∞	=	freestream bulk velocity magnitude
W	=	particle numerical weight
x	=	vector coordinate
x_c	=	geometric center of a cell
$\bar{x}_{cm}$	=	time-averaged center of mass of all particles in a cell
Δt	=	time-step interval
Δx	=	cell length
θ	=	time-averaging coefficient
λ	=	mean free path
ρ_∞	=	freestream mass density
σ	=	collision cross section
ψ	=	substitution coordinate for nonuniform subcell assignment
ω	=	viscosity index for variable hard sphere collision model

*Research Engineer, Universal Technology Corporation; jonathan.m.burt@nasa.gov. Member AIAA (Corresponding Author).

[†]Senior Research Aerospace Engineer. Associate Fellow AIAA.

[‡]Professor, Department of Aerospace Engineering. Associate Fellow AIAA.

I. Introduction

THE direct simulation Monte Carlo (DSMC) method, introduced by Bird nearly 50 years ago [1,2], has, over the past several decades, become the dominant technique for numerical simulation of rarefied gas flows. This method involves Lagrangian tracking and binary collision operations among a collection of simulated particles, each representing a large number of atoms or molecules, in a manner that reproduces the underlying physics of the governing Boltzmann equation.

DSMC is often used in a wide variety of applications related to rarefied gas-flow simulation, including aerothermodynamic design and analysis of atmospheric entry vehicles and hypersonic cruise vehicles, simulation of nanoscale and microscale subsonic flows, simulation of exhaust plumes from spacecraft or high-altitude rockets, chemical vapor deposition, spacecraft drag calculations, and analysis of basic fluid flow phenomena and instability problems [3]. The popularity of DSMC in this broad range of applications can be attributed to a combination of accuracy, simplicity, computational efficiency, and relatively easy application to complex geometries. In rarefied gas dynamics problems, such as those mentioned here, the equilibrating effects of intermolecular collisions may be insufficient to retain a near-equilibrium gas velocity distribution, and the resulting nonequilibrium velocity distributions tend to invalidate underlying assumptions in the Navier-Stokes equations [2]. As a result, standard computational fluid dynamics (CFD) techniques generally provide results of poor or questionable accuracy, and

alternate methods [4–6] that reproduce the nonequilibrium characteristics of the Boltzmann equation are required. Among such alternate methods, DSMC is often the most efficient technique that maintains the accuracy of the full Boltzmann equation.

In this paper, we present a new implementation of DSMC named the hypersonic aerothermodynamics particle (HAP) code. This code is intended to combine the simplicity of problem-specific DSMC implementations with many capabilities of larger generalized DSMC codes [7–12]. Development of the HAP code is motivated, in part, by a desire to ease implementation and testing of new DSMC models and algorithms. The code is made considerably simpler through the use of a uniform Cartesian grid for collision operations, and newly developed collision procedure modifications are used to reduce spatial discretization errors. As an additional motivation for development of the HAP code, a very simple, intuitive, and configurable user interface is desired for rapid simulation setup by inexperienced DSMC users.

In the following sections, the HAP code is described, and various features of the code are outlined. Next, errors associated with a lack of grid adaptation to the local mean free path are discussed, and set of new techniques are proposed to reduce these errors. A rarefied hypersonic flow over a flat plate with a sharp leading edge is used as a test case to evaluate the new code, and HAP simulation output quantities are compared with results from established DSMC codes and with available experimental data. A grid refinement study is employed to quantify spatial discretization errors for the flat plate flow and to demonstrate error reduction through a proposed collision probability modification. HAP simulation results are also compared with published DSMC results for a hypersonic cylinder flow problem, and additional results are presented for the three-dimensional simulation of a similar flow over a sphere. Finally, conclusions are presented, and planned areas of future work are discussed.

II. Description of DSMC Implementation

An automatically adapted two-level Cartesian grid is employed in HAP for one, two- or three-dimensional simulations, and zero-dimensional relaxation calculations may be performed as an additional option. The OpenMP interface is used for parallelization on shared memory systems, with a parallel implementation similar to that described by Gao and Schwartzentruber [13]. Dynamic load balancing is used for efficient parallel computation of particle movement, sampling, and collision routines during each simulation time step. The code can be run in either steady-state mode, with time-averaged sampling between a user-designated transient startup time and simulation termination, or in unsteady mode, with multiple short sampling periods. For either mode, results are automatically output during the simulation in a commonly used visualization software format, with no requirement for preprocessing or postprocessing of data files. Output quantities include various macroscopic flowfield variables and surface properties as well as surface-integrated forces, moments, and heat transfer. In zero-dimensional simulations of homogeneous relaxation problems, nonequilibrium initial conditions may be specified as the superposition of multiple Maxwellian velocity distributions, and the resulting velocity distribution at various elapsed times can be viewed in one, two or three dimensions. Multiple inflow and wall boundary conditions can be used, and boundary geometries may be defined either analytically or by means of a triangulated surface mesh file. One-dimensional simulations can be performed using Bird's approximate stagnation streamline modeling technique [2]. Full restart capabilities allow calculations to be stopped, started, and modified during a simulation with no undesired impact on simulation results.

A. DSMC Algorithms and Physical Models

Cartesian ray-tracing routines are used in HAP to move particles through the grid during each time step. These routines involve tracing a particle's trajectory to the nearest cell face, then moving the particle to the trajectory-face intersection point if the associated distance is less than the product of the time-step interval and the particle speed. This type of procedure may be somewhat less efficient than simply moving each particle to some final position at the end of the time step before reindexing the particle to a new cell [11]. However, the ray-tracing technique greatly simplifies calculations involving immersed bodies and should ease future implementation of parallel domain decomposition and time-step adaptation. As in other DSMC codes [7], ray tracing is performed for a given particle only if that particle is found to exit the assigned cell or impact a solid boundary during the current time step; otherwise, more efficient procedures are used. If cell residence times are much larger than the time-step interval, as is generally the case, then any efficiency reduction due to ray tracing should be small.

As in the statistical modeling in low-density environment DSMC code [10], HAP allows for separate cells for collision operations and time-averaged sampling. Collision operations and ray-tracing procedures are performed on a uniform Cartesian grid, whereas sampling procedures can be performed on a two-level Cartesian grid, which is automatically adapted according to the time-averaged local hard sphere mean free path. Time averaging is performed using an exponential moving average, with a default weighting coefficient of 0.01 for the current time step. The ratio of cell size to local mean free path may be specified by the user, following a tradeoff between faster statistical convergence for larger sampling cells and greater output resolution for smaller cells. In a two-level adapted sampling grid, level-one cells are coincident with collision cells, and each level-one cell may be uniformly divided into an arbitrary integer number of level-two cells in each coordinate direction. An efficient indexing routine is employed to determine the level-two cell to which each particle is assigned during sampling operations.

To efficiently organize particle information while avoiding excessive memory requirements, HAP employs both cell-based and global dynamic arrays of pointers to particle data. When a new particle either enters the simulation domain or enters a new cell, the memory address for this particle is added to the next unused element in the associated pointer array. Likewise, when a particle exits the cell or the simulation domain, the last used element in the associated pointer array is moved to the position previously occupied by a pointer to this particle, and a variable indicating the number of used elements in the array is decremented by one. The size of both cell-based and global particle pointer arrays is incremented, as necessary, in large blocks; the default block size is 100 for cell-based arrays and 100,000 for the global array. This use of memory blocks balances a desire to avoid unnecessary memory use with a competing desire to minimize the frequency of computationally expensive memory reallocation for large dynamic arrays.

To further improve computational efficiency by reducing memory allocation, the memory location for any particle that exits the simulation domain is added to a linked list of unused particles. The same memory is then assigned, when needed, to a newly generated particle at an inflow boundary. This use of linked lists for unused particles is similar to that employed in the MONACO DSMC code, although HAP is distinguished from MONACO in the use of dynamic pointer arrays. MONACO employs linked lists to index particles to individual cells, and temporarily copies particle information into cell-based static arrays to better make use of high-speed cache memory during collision operations.

Physics models implemented in HAP include the no-time-counter (NTC) scheme of Bird for collision-pair selection, the variable-hard-sphere (VHS) model for collision dynamics, the Maxwell model for gas-surface interaction, and the harmonic oscillator model for discretized vibrational energy distributions in a vibrationally excited diatomic gas [2]. Simulations can be run for a gas mixture involving an arbitrary number of species. The Larsen-Borgnakke scheme [14] has been implemented for continuous rotational-translational and quantized vibrational-translational energy exchange. As optional alternatives to the NTC collision model, the majorant frequency scheme (MFS) of Ivanov et al. [10] and the scheme of Baganoff and McDonald [15] have also been implemented. Relative to the NTC scheme, the MFS scheme may, in some cases, show reduced sensitivity to time-step size and particle population when the number of collisions per cell per time step is very small, whereas the Baganoff and McDonald scheme is particularly useful in unsteady simulations

for which collisional quantities in each cell can vary significantly and unpredictably over time.

B. Collision Selection

Although HAP is limited to a uniform user-defined cell size for collision operations, transient adaptive subcell and nearest-neighbor procedures are used to select collision pairs, if possible, with sufficiently small separation distances to meet standard DSMC guidelines or some criterion based on the ratio of the mean collision separation (MCS) to the mean free path [2]. If possible, efficient $\mathcal{O}(N)$ procedures are used to find collision partners from within the same subcell; otherwise, a more expensive nearest-neighbor search is performed.

As a first step in collision operations during a given time step, NTC or an alternative scheme is used to determine the number of potential collision pairs in a cell. Subcell dimensions within this cell are then computed from the local hard sphere mean free path and a user-designated ratio of subcell size to mean free path. Subcell dimensions may vary among different areas of a cell due to intracell variation in the hard sphere mean free path, as described in Section III.B. Next, all particles are sorted into subcells, using an efficient indexing routine also described in Section III.B. A prescribed number of particles equal to the number of potential collision pairs are then randomly selected and are paired, if possible, with previously unpaired particles located within the same subcell. If no unpaired particles are available, or if the only remaining unpaired particle in the same subcell was the last collision partner for the first particle in the pair, then a nearest neighbor from outside this subcell is selected as the second particle in the pair. Finally, once the required number of potential collision pairs has been selected, probabilistic procedures (as outlined in Section III.A for the NTC scheme) are used to select which of these pairs will collide. Postcollision resampling routines are then performed for all selected pairs, in a manner that is consistent with the VHS model and that enforces momentum and energy conservation.

For nearest-neighbor selection as for subcell-based pairing, no two particles are paired together if each of these particles most recently collided with the other. As described by Bird [9], prevention of repeated collisions between the same two particles is expected to improve overall simulation accuracy and is particularly important for error reduction when either subcells or nearest-neighbor collisions are employed.

As proposed by Macrossan [16], for improved efficiency, the nearest-neighbor selection procedure is performed using a randomly ordered array of unselected particles within the cell, and the first particle in this array for which the separation distance is smaller than some tolerance is chosen as the collision partner. For consistency with subcell procedures, the tolerance distance is set in HAP to equal the subcell size. If no particles in this array meet the separation distance criterion, then the nearest neighbor is selected.

In a further modification to nearest-neighbor collision selection, a maximum of 30 randomly selected particles are considered as possible collision partners for each particle, which requires nearest-neighbor identification. This modification was proposed by Macrossan [16] to avoid costly $\mathcal{O}(N^2)$ selection operations in cells that contain a large number of particles, and it has also been employed in a recent study by Gallis and Torczynski [17]. As an additional option available in HAP, such limited-search nearest-neighbor procedures may be performed in place of subcell-based selection routines to select every collision partner. Note that the number 30 is a rough transition point, identified by Bird et al. [18], above which nearest-neighbor procedures become more expensive than subcell-based collision pairing. Also note that limited searches for collision-partner selection, due to either some acceptance distance tolerance or random exclusion of particles within the cell, have previously been called "near neighbor" selection, but this term is not used here to avoid confusion.

C. Cut Cell Implementation

Two different options, analytical shapes and externally defined triangulated surfaces, are available in HAP for inclusion of immersed

solid bodies within the rectangular or cuboidal domain of a two or three-dimensional simulation. For either option, cut cells are employed, with each cut cell containing one or more planar surface elements.

Analytically defined shapes can be used for either two or three-dimensional simulations, and, in contrast to similar capabilities in other DSMC codes [2,10], these shapes are approximated by a series of planar faces, with one such face per cut cell. This allows for relatively simple and efficient treatment of complex shapes and greatly simplifies the process of modifying the code for use with shapes that are not currently available. Monte Carlo procedures for determining cut face properties are performed at simulation startup. For a two-dimensional simulation, these procedures are as follows. First, a large number of random points are generated in each cell. If some, but not all, of these points are within the body, then the cell is designated as a cut cell. Vertex coordinates are determined for the smallest possible rectangle that includes all random points that are outside the body, and corresponding coordinates are determined for the smallest rectangle that encloses all points inside the body. The x and y coordinates of the surface-normal vector in this cell are then proportional to the y and x coordinate dimensions, respectively, of a third rectangle defined by the intersection region of the first two rectangles. The sign of each normal-vector coordinate is determined by checking whether points along axis-aligned lines through the center of the intersection rectangle are inside or outside of the body.

For a three-dimensional simulation involving an analytically defined surface geometry, a somewhat more complicated procedure is required. In this case, two cuboids containing all random points inside and outside of the body are found, and similar procedures as used for a two-dimensional simulation are employed in axis-aligned bisection planes for the resulting intersection cuboid. In a three-dimensional simulation involving an analytically defined curved surface, small gaps may exist between planar cut faces in neighboring cells; for simplicity, these gaps are treated as planar surface boundary faces. During a simulation, the number of particles colliding with such gaps in the surface are tracked in a log file, and the user is advised to reduce the cell size when these collisions make up a significant fraction of particle-wall collision events. This fraction depends strongly on the ratio of the surface curvature radius to the cell size, and smaller cell dimensions can be used to reduce the frequency at which particles hit the gaps between cut cell faces for an analytically defined surface. It should be emphasized that the potential presence of gaps between neighboring cut faces as well as the restriction on surface element resolution based on cell size constitute serious deficiencies in the analytical surface definition option as implemented in HAP; these deficiencies should be weighed against benefits associated with greatly reduced setup time relative to the stereo-lithography (STL) surface geometry input capability discussed later in this section.

Although routines used to evaluate planar cut-face properties are relatively complex and computationally expensive, these routines are performed only once at simulation startup and require only that any point in the simulation domain can be established as either inside or outside of the solid body. This requirement contrasts with analytical shape capabilities in other DSMC codes, for which expressions defining the surface (as opposed to the volume) of a solid body are required, and for which implementation of new shapes may be complicated and time-consuming [2]. As implemented in HAP, the user may choose from a variety of two and three-dimensional shapes, including cylinders, spheres, ellipsoids, cuboids, spherically blunted cones, and generic lifting body geometries.

For simulation of three-dimensional flows over arbitrary triangulated surfaces, an optional input file in the ASCII STL format may be used in HAP. STL is a standard format compatible with most commercial computer-aided design packages and allows curved surfaces to be approximated by a set of contiguous triangular facets. At startup of a HAP simulation, each STL facet is linked to one or more cut cells by generating a large number of random points along the facet and identifying the cell in which each point is located. During particle movement routines, any particle located in a cut cell is considered for collisions with all facets linked to that cell. This feature allows for simulation of flows around any fixed three-dimensional

surface and lacks both the potential for gaps between neighboring surface elements and the limitation of one cut face per cell, which are significant drawbacks of the analytically defined surface capability discussed in Section II.C. A simple Monte Carlo procedure for determination of cut-cell volume allows for the presence of split cells, provided that the STL surface is locally convex within each cut cell.

D. User Interface

One main attribute of HAP, in contrast to some other DSMC codes intended for general rarefied flow simulation, is an extremely simple, user-configurable, and user-friendly interface. The code employs a single input file, which includes input parameters for global simulation quantities, flow properties, gas species properties, and flowfield geometry. These parameters can be rearranged within the input file as desired, and most parameters may be excluded from the file for use with default parameter values. No preprocessing is required for an optional STL surface geometry file, and output files for field and surface property visualization are automatically generated without additional postprocessing steps.

Uniform numerical weight and time-step interval values are used but do not need to be specified directly in the input file. (Implementation and testing of time-step adaptation capabilities is currently in progress.) The time-step interval is calculated from a user-provided ratio of the time step to the mean collision time at inflow or ambient conditions, with automatic adjustments based on the mean particle transit time across each cell. In contrast to the time-step interval, the range of appropriate values for the nondimensional time-step input parameter should be relatively problem independent. If the value of this input parameter results in an overly large time step anywhere in the simulated flowfield, then the user is alerted by means of the number of "bad collisions," which is periodically output to the command window and appended to a log file. Here, "bad collisions" are defined as those with a collision probability greater than one, after adjusting for a maximum of one collision per particle per time step. For additional confirmation that temporal discretization errors are acceptably small, the ratio of the time-step interval to the local mean collision time is also included in a field quantity output file. Similarly, the numerical weight (i.e,. the number of atoms represented by each simulated particle) is calculated automatically from a user-designated number of particles per subcell based on inflow conditions. This number should generally range between around 2 to 20, and an overly small number can be detected via the ratio of MCS to mean free path, as found in the field quantity output file. The numerical weight may also be automatically determined and periodically updated during a simulation, based on a desired total number of particles as specified by the user.

An additional numerical parameter, the number of time steps to reach steady state, must still be specified directly by the user for steady-state flow simulation. However, the user can monitor transient characteristics in the flow by observing changes in the total numbers of particles, face crossings, particle-wall collisions, and binary collisions per time step; all four quantities are included in a log file. If the flow has not yet reached steady state at initiation of sampling routines, then the user can alter the number of startup time steps and restart the simulation with no loss in accuracy or efficiency.

In addition to a simple user interface and other features described in Section II, one further attribute of HAP is a compact source code, consisting of approximately 8000 lines. Several different functions correspond to standard DSMC operations (e.g., flowfield initialization, particle movement, collisions, sampling) and output file generation, with about 20% of the source code devoted to the second category. An additional 20% is devoted to automatic generation and initialization of cut cells for analytically defined two and three-dimensional surfaces and to preprocessing for triangulated surface geometries defined in an optional STL input file.

III. Uniform Collision Grid Methodology

As mentioned in Section I, HAP employs a uniform Cartesian grid for binary collision operations, with optional two-level Cartesian grid adaptation for field quantity output. Although a uniform grid approach has significant advantages associated with reduced code

complexity, grid adaptation is required in traditional DSMC algorithms for accurate and efficient simulation of flows involving a wide density range [2]. The most important historical reason for the use of grid adaptation is to limit the separation distance between colliding particles. Accurate simulation of the Boltzmann equation requires that the MCS be considerably smaller than the local mean free path [9], and this condition is violated if collision partners are frequently selected from opposite sides of a cell that is large in comparison with the mean free path. However, the MCS argument for requiring grid adaptation no longer applies when either transient adaptive subcells [9] or nearest-neighbor collisions [19] (with a sufficient particle population and appropriate means of avoiding repeated collisions) are employed, as these techniques allow for MCS values that are nearly independent of cell size.

There are additional reasons for use of grid adaptation that deserve some discussion. First, higher resolution of simulation results may be desired in regions of relatively high density, and output of field quantities with comparatively low scatter in low density regions can require spatial averaging over larger cell volumes. To address these issues, HAP allows for the adjustment of field quantity output resolution by means of an independent adaptive sampling grid. However, it should be noted that, if surface fluxes are the main quantities of interest, then sampling grid adaptation may be unnecessary, and cell size independence can be accomplished by decoupling surface geometry from the cell data structure. In this approach, as used in HAP for three-dimensional triangulated surfaces defined in an optional STL format input file, several surface facets can be located within a single cell, or one facet can extend over several cells.

As an additional argument for grid adaptation in DSMC, the calculation of DSMC collision probability is based on assumptions of uniform density in each cell, and large density variation within a cell can have a significant impact on the calculated collision frequency. Errors associated with uniform density assumptions in DSMC collision probability are discussed in detail in Section III.A.

As a final reason for grid adaptation, the local mean free path can vary across comparatively large cells in an unadapted grid, and the required size of DSMC subcells to meet a MCS-based criterion [9] for simulation accuracy may, therefore, vary within each cell. Although nearest-neighbor pairing can be used as an alternative to adaptive subcells, the use of nearest-neighbor-collision selection may be prohibitively expensive in cells that are significantly larger than the local mean free path and that contain a large number of particles. Limited-search "near neighbor" algorithms, as recently employed by Gallis and Torczynski [17] and by Macrossan [16] to improve efficiency relative to standard nearest-neighbor procedures, can potentially provide a similar balance of efficiency and accuracy as subcell procedures in such large cells. However, as demonstrated by LeBeau et al. [19], the MCS value depends on the number of particles considered in each search. If a large number of particles per search are required to meet some MCS criterion, then subcell-based collision pairing may be more appropriate.

Although Cartesian transient adaptive subcell procedures are an efficient means of achieving sufficiently small MCS in large cells that contain a large number of particles [8], the desired subcell size may differ considerably across a cell due to variation in flowfield quantities over the cell volume. Some error or efficiency reduction is, therefore, associated with the use of a uniform subcell size within each cell, as is employed in existing Cartesian implementations of the transient adaptive subcell technique.

Although some of the arguments presented in this section for using grid adaptation can be resolved for the simpler uniform grid approach in HAP by means of preferential pairing of nearby particles and by decoupling cell and surface data structures, the last two arguments, errors in collision probability and variation in appropriate subcell size across a cell, require new modifications to DSMC procedures. These modifications are presented as follows.

A. Gradient-Based Modification to Collision Probability

To demonstrate the error in DSMC binary collision probabilities due to internal density variation within a cell, we consider the

collision frequency in a simple gas as calculated using the NTC scheme of Bird [2]. The number of potential collision pairs N_{coll} is computed as

$$N_{\text{coll}} = \left\lfloor \frac{1}{2} \frac{WN(N-1)}{V} (\sigma g)_{\text{max}} \Delta t + R \right\rfloor \qquad (1)$$

where the operator $\lfloor \ \rfloor$ rounds to the nearest smaller integer, R is a random number in [0,1], W is the numerical weight (i.e., the number of atoms or molecules represented by each particle), V is the cell volume, Δt is the time-step interval, N is the current number of particles in the cell, and $(\sigma g)_{\text{max}}$ is the maximum product of collision cross section and incident relative speed for all collision pairs in the cell over a large number of time steps. Each of the N_{coll} potential collision pairs is then selected to experience a collision with probability

$$P_{jk} = \frac{\sigma_{jk} g_{jk}}{(\sigma g)_{\text{max}}} \qquad (2)$$

where j and k are the particle indices, and σ_{jk} and g_{jk} are the collision cross section and relative speed, respectively. As N follows a Poisson distribution, the expected mean value of $N(N-1)$ in Eq. (1) should equal $\bar{N}^2$, where $\bar{N}$ is the value of N averaged over a large number of time steps [9]. The mean collision frequency $F(\boldsymbol{x})$ at a given location $\boldsymbol{x}$ in this cell is, therefore,

$$F(\boldsymbol{x}) = \frac{2}{\bar{N}\Delta t} \langle N_{\text{coll}} P_{jk} \rangle = \frac{W\bar{N}}{V} \langle \sigma_{jk} g_{jk} \rangle \qquad (3)$$

where the operators $\langle \ \rangle$ indicate an average over all velocity space, weighted by the velocity distribution f and the probability density p of selected particles in physical space, for all potential collision partners j and k. Thus,

$$\langle \sigma_{jk} g_{jk} \rangle = \iint \iint \sigma(\boldsymbol{c}_j, \boldsymbol{c}_k) |\boldsymbol{c}_j$$
$$- \boldsymbol{c}_k| f(\boldsymbol{c}_j, \boldsymbol{x}_j) f(\boldsymbol{c}_k, \boldsymbol{x}_k) p(\boldsymbol{x}_j, \boldsymbol{x}) p(\boldsymbol{x}_k, \boldsymbol{x}) \, \mathrm{d}\boldsymbol{x}_j \, \mathrm{d}\boldsymbol{x}_k \, \mathrm{d}\boldsymbol{c}_j \, \mathrm{d}\boldsymbol{c}_k \qquad (4)$$

where $\boldsymbol{c}_j$ and $\boldsymbol{c}_k$ represent particle velocities, $\boldsymbol{x}_j$ and $\boldsymbol{x}_k$ represent particle positions, and the integrals in Eq. (4) are carried out over all phase space for both j and k.

The ratio $W\bar{N}/V$ in Eq. (3) is the gas number density averaged over the cell volume. If the cell is large in comparison to the local mean free path, then both the number density and the velocity distribution may be strong functions of position $\boldsymbol{x}$ in the cell. If we further assume that the MCS is much smaller than the mean free path, then $f(\boldsymbol{c}_j, \boldsymbol{x}_j) p(\boldsymbol{x}_j, \boldsymbol{x}) \approx f(\boldsymbol{c}_j, \boldsymbol{x}) \delta(\boldsymbol{x}_j - \boldsymbol{x})$ and $f(\boldsymbol{c}_k, \boldsymbol{x}_k) p(\boldsymbol{x}_k, \boldsymbol{x}) \approx f(\boldsymbol{c}_k, \boldsymbol{x}) \delta(\boldsymbol{x}_k - \boldsymbol{x})$ in Eq. (4), where δ is the Dirac delta. It follows that

$$\langle \sigma_{jk} g_{jk} \rangle \approx \iint \sigma(\boldsymbol{c}_j, \boldsymbol{c}_k) |\boldsymbol{c}_j - \boldsymbol{c}_k| f(\boldsymbol{c}_j, \boldsymbol{x}) f(\boldsymbol{c}_k, \boldsymbol{x}) \, \mathrm{d}\boldsymbol{c}_j \, \mathrm{d}\boldsymbol{c}_k \qquad (5)$$

and $\langle \sigma_{jk} g_{jk} \rangle$ should vary in a physically appropriate way as a function of $\boldsymbol{x}$. However, Eq. (3) contains no adjustment to the local number density $n(\boldsymbol{x})$ if $n(\boldsymbol{x}) \neq W\bar{N}/V$. Some error in F is, therefore, expected for cells that are large relative to the mean free path and located in regions with large density gradients. In particular, if large portions of a cell are consistently unpopulated with particles, then $n(\boldsymbol{x}) > W\bar{N}/V$ in populated regions, and $F(\boldsymbol{x})$ will be unphysically low. More generally, if $\nabla n \neq 0$, then $F(\boldsymbol{x})$ should decrease with increasing cell size, and unphysical preference in collision selection is given to particles in portions of the cell for which $n(\boldsymbol{x}) < W\bar{N}/V$. Note that, although the NTC scheme is used in the preceding discussion, the same error due to density gradients is expected for other DSMC collision schemes, including the MFS [10] and the scheme of Baganoff and McDonald [15].

As a means of correcting for this error, we first assume that ∇n is uniform over the cell volume. Thus,

$$n(\boldsymbol{x}) = n_c + \nabla n \cdot (\boldsymbol{x} - \boldsymbol{x}_c) \qquad (6)$$

where $n_c = W\bar{N}/V$ is the cell-averaged number density, and $\boldsymbol{x}_c$ is the geometric center of the cell. The time-averaged center of mass $\bar{\boldsymbol{x}}_{\text{cm}}$ of all particles in the cell is then

$$\bar{\boldsymbol{x}}_{\text{cm}} = \boldsymbol{x}_c + \frac{1}{n_c V} \int_V n(\boldsymbol{x})(\boldsymbol{x} - \boldsymbol{x}_c) \, \mathrm{d}\boldsymbol{x} \qquad (7)$$

By substituting Eq. (6) into Eq. (7) and assuming a Cartesian cell of equal length Δx in each coordinate direction, we can express ∇n as a simple function of the vector difference $(\bar{\boldsymbol{x}}_{\text{cm}} - \boldsymbol{x}_c)$:

$$\nabla n = \frac{12 n_c}{(\Delta x)^2} (\bar{\boldsymbol{x}}_{\text{cm}} - \boldsymbol{x}_c) \qquad (8)$$

To correct the binary collision probability for effects of spatial density variation, so that the collision frequency $F(\boldsymbol{x})$ in Eq. (3) scales with $n(\boldsymbol{x})$, we multiply the probability P_{jk} in Eq. (2) by the ratio $n(\boldsymbol{x}_{jk})/n_c$, where $\boldsymbol{x}_{jk}$ is the center of mass of the collision pair. From Eqs. (2), (6), and (8), we find

$$P_{jk} = \frac{\sigma_{jk} g_{jk}}{(\sigma g)_{\text{max}}} \left[1 + \frac{12}{(\Delta x)^2} (\boldsymbol{x}_{jk} - \boldsymbol{x}_c) \cdot (\bar{\boldsymbol{x}}_{\text{cm}} - \boldsymbol{x}_c) \right] \qquad (9)$$

As implemented in HAP, this correction is applied to all binary collision probabilities in cells that are large compared with the local mean free path. For simple application of Eq. (9) to a gas mixture, effects of species-based properties (e.g., collision cross section) are neglected, and $\bar{\boldsymbol{x}}_{\text{cm}}$ is evaluated without biasing to species mass.

In a cut cell, for which Eq. (8) is not strictly valid, we employ an approximation to Eq. (9) based on an assumption that the gradient ∇n is generally aligned with the surface-normal direction near a wall boundary. Given a local surface outward normal unit vector $\boldsymbol{n}_f$, which is calculated through an area-based weighted average of surface-normal vectors for all surface facets that are at least partially enclosed by the cut cell, we multiply all collision probabilities in this cut cell by a factor

$$P_{jk} = \frac{\sigma_{jk} g_{jk}}{(\sigma g)_{\text{max}}} \left\{ 1 + \frac{12}{(\Delta x)^2} [(\boldsymbol{x}_{jk} - \boldsymbol{x}_c) \cdot \boldsymbol{n}_f][(\bar{\boldsymbol{x}}_{\text{cm}} - \boldsymbol{x}_c) \cdot \boldsymbol{n}_f] \right\} \qquad (10)$$

where $\boldsymbol{x}_c$ is the geometric center of the portion of the cell within the simulation domain. The location $\boldsymbol{x}_c$ may be found for each cut cell at simulation startup through a simple Monte Carlo sampling technique, which involves generating a large number of random points throughout the cell volume and discarding any points within the body.

In Eqs. (9) and (10), the time-averaged center of particle mass in a cell $\bar{\boldsymbol{x}}_{\text{cm}}$ is calculated by first evaluating the instantaneous center of mass $\boldsymbol{x}_{\text{cm}}$ for all N particles currently in the cell and, then, performing an exponential-moving average operation

$$(\bar{\boldsymbol{x}}_{\text{cm}})_t = \theta(\boldsymbol{x}_{\text{cm}})_t + (1 - \theta)(\bar{\boldsymbol{x}}_{\text{cm}})_{t-\Delta t} \qquad (11)$$

where θ is a constant much less than 1 ($\theta = 0.01$ is used in this work), and t indicates the elapsed simulation time. More complicated and potentially more accurate time-averaging procedures, such as the subrelaxation technique of Sun and Boyd [20], may be used in place of Eq. (11). Note that, for accurate simulation of an unsteady flow, θ should be much larger than the ratio of Δt to the minimum characteristic transient time scale. In the presence of large density gradients, a further adjustment to Eq. (11) may be required to avoid a negative density value, as calculated by Eqs. (6) and (8), at any point in a cell.

One final point deserves mention in introducing the collision probability modification given by Eq. (9): this equation follows from an approximation of a uniform density gradient across each cell. Thus, in the presence of large nonlinear density variation, and particularly in a shock or high Knudsen number boundary layer, the use of Eq. (9) within cells that are much larger than the local mean free path may lead to reduced accuracy relative to traditional DSMC

calculations involving smaller collision cells. To correct for this problem, HAP includes an option to multiply binary collision probabilities by the ratio of the time-averaged density in the smaller sampling cell containing the colliding particles (or, if the colliding particles are located in two different sampling cells, the mean time-averaged density in these two cells) to the time-averaged density in the collision cell. The two-level Cartesian sampling grid is then periodically adapted to the local mean free path during the simulation startup period, and the resulting collision probabilities are not subject to any approximation of linear density variation within each collision cell. This option is employed in the hypersonic cylinders and sphere flow simulations described in Section VI, for which collision cells near the stagnation point are over an order of magnitude larger than the local mean free path.

B. Nonuniform Transient Adaptive Subcells

As discussed in Section II.B, transient adaptive subcells are an efficient means of physically appropriate collision pairing in cells that are large relative to the mean free path. In such cells, a large number of particles may be required for sufficiently small MCS, and subcell indexing is generally much more efficient in these cells than the $\mathcal{O}(N^2)$ operations associated with nearest-neighbor-collision selection. However, in the presence of a strong density gradient, the mean free path may vary considerably over the volume of a cell, and division of the cell into subcells based on the cell-averaged mean free path may lead to some reduction in accuracy. Alternatively, the use of overly small subcells based on estimates of the minimum mean free path anywhere in a cell can reduce simulation efficiency by creating more subcells than necessary in regions of relatively large mean free path. An excessive number of subcells tends to increase the frequency of expensive searches for collision partners outside the same subcell, using either complicated subcell-based search logic [9] or (as employed in HAP) nearest-neighbor routines. Thus, a somewhat improved balance between efficiency and accuracy may be possible by clustering subcells in portions of a cell where the local mean free path is smaller than the cell-averaged value. One procedure for such nonuniform subcell indexing is described as follows.

First, we desire for the subcell length to be some fraction C of the local hard sphere mean free path, which is inversely proportional to the local number density $n(\mathbf{x})$. For simplicity, we assume a simple gas; effects of concentration gradients in a gas mixture are neglected. Next, we assume that the density gradient ∇n is uniform over the cell volume. The subcell index i in the x-coordinate direction can then be based on uniform subcell spacing in some alternate coordinate system for which the location $\psi(x)$ is related to the global coordinate x by $d\psi/dx = n(x, y_c, z_c)$ and $\psi(x_c - 1/2\Delta x) = 0$. Here, $(x_c, y_c, z_c) = \mathbf{x}_c$ is the cell center location, and Δx is the cell length. Hence, $d\psi = n(x, y_c, z_c)dx$, and from Eqs. (6) and (8), we find

$$\psi(x) = \int_{x_c-(1/2)\Delta x}^{x}\left[n_c + \frac{12n_c}{(\Delta x)^2}(\bar{x}_{cm} - x_c)(x' - x_c)\right]dx' \quad (12)$$

where $\bar{x}_{cm}$ is the x coordinate of the time-averaged center of mass of particles in the cell $\bar{x}_{cm}$. The corresponding subcell index value is then

$$i(x) = \left\lfloor (i_{max} + 1)\frac{\psi(x)}{\psi[x_c + (1/2)\Delta x]}\right\rfloor \quad (13)$$

After integration of Eq. (12) and substitution into Eq. (13), we can express the index $i \in [0, i_{max}]$ in the x direction for a given particle location $\mathbf{x} = (x, y, z)$ as

$$i(x) = \left\lfloor (i_{max} + 1)\xi(x)\left[1 + \frac{6}{\Delta x}(\bar{x}_{cm} - x_c)(\xi(x) - 1)\right]\right\rfloor \quad (14)$$

where

$$\xi(x) \equiv \frac{1}{\Delta x}(x - x_c) + \frac{1}{2} \quad (15)$$

The maximum index value i_{max} in Eq. (14) is given by

$$i_{max} = \left\lfloor \frac{\Delta x}{C\langle\lambda\rangle_x}\right\rfloor \quad (16)$$

where C is a constant, and $\langle\lambda\rangle_x$ is the hard sphere mean free path averaged over a line segment through the cell center for which $x \in [x_c - 1/2\Delta x, x_c + 1/2\Delta x]$. The value of $\langle\lambda\rangle_x$ is calculated through the approximate expression

$$\langle\lambda\rangle_x \approx \frac{1}{\sqrt{2}\sigma n_c}\left[1 + 12\left(\frac{\bar{x}_{cm} - x_c}{\Delta x}\right)^2\right] \quad (17)$$

where σ is a reference collision cross section. A derivation of Eq. (17) is included in the Appendix.

To improve simulation accuracy and/or efficiency, the allowable range for the maximum subcell index i_{max} can be limited based on the minimum and maximum desired average number of particles per subcell, which are given as $N_{min,sub}$ and $N_{max,sub}$, respectively. ($N_{min,sub} = 2$ and $N_{max,sub} = 20$ in this work.) The allowable range of i_{max} is

$$i_{max} \in [\lfloor (N/N_{max,sub})^{1/D}\rfloor, \quad \max\{\lfloor (N/N_{min,sub})^{1/D}\rfloor - 1, 0\}] \quad (18)$$

where D is the number of simulation dimensions. In Eq. (18), the maximum allowable value of i_{max} is based on $N_{min,sub}$ and is intended to improve code efficiency by avoiding overly small particle populations within individual subcells. If $C \approx 1$ in Eq. (16), then the maximum limiting condition in Eq. (18) is likely imposed only in cells where too few particles exist to satisfy standard DSMC guidelines for the MCS and where some reduction in numerical weight W may be needed for accurate simulation. However, the maximum condition in Eq. (18) can be particularly useful if $C \ll 1$, as this allows MCS $\ll \langle\lambda\rangle_x$ in cells that contain a sufficiently large number of particles but avoids excessive use of inefficient intersubcell selection procedures in cells that contain too few particles for the desired MCS value. The minimum allowable value of i_{max} is given in Eq. (18) as a function of $N_{max,sub}$. This lower limit on i_{max} is imposed to potentially increase simulation accuracy with a negligible influence on computational expense by effectively dividing up any subcells with an overly large particle population.

In multidimensional simulations, additional subcell indices are required in other coordinate directions. For example, in a three-dimensional simulation, a unique subcell identification number for the particle location $\mathbf{x} = (x, y, z)$ can be given as $i(x) + (i_{max} + 1)j(y) + (i_{max} + 1)(j_{max} + 1)k(z)$, where $j(y) \in [0, j_{max}]$ and $k(z) \in [0, k_{max}]$ are the subcell indices in the y and z directions, respectively.

By using the proposed subcell indexing procedure, we allow for smaller subcells in regions of increased density and reduced mean free path. For relatively large cells in the presence of a density gradient, subcell lengths may vary significantly along different coordinate directions. However, if $\nabla n = 0$, then Eq. (14) reduces to

$$i(x) = \left\lfloor (i_{max} + 1)\left[\frac{1}{\Delta x}(x - x_c) + \frac{1}{2}\right]\right\rfloor \quad (19)$$

as would be used for particle indexing to Cartesian subcells of uniform length.

Similarly to Eq. (9), Eqs. (14) and (17) are derived for a Cartesian cell with uniform length Δx in each coordinate direction. In a cut cell, for which part of the cell is inside a solid body, approximate corrections for the density gradient are enabled by replacing the scalar quantity $\bar{x}_{cm} - x_c$ with the x component of the projection of the vector $\bar{\mathbf{x}}_{cm} - \mathbf{x}_c$ in the local surface-normal direction and by using, as $\mathbf{x}_c$, the geometric center of the portion of the cell that is outside the body.

Note that the proposed nonuniform subcell technique follows from an initial assumption that the subcell size should be based on the local mean free path, not solely on the desired number of particles per

subcell as in other implementations of the transient adaptive subcell scheme [9,17]. In adapting subcells to the mean free path, we attempt to reduce the MCS only as much as necessary to meet a desired maximum ratio of the MCS to the mean free path while minimizing the frequency of expensive searches for neighboring particles outside of the same subcell. For example, if subcells are scaled in proportion to the mean free path and if a cell contains enough particles to satisfy some MCS criterion while populating each subcell with a large number of particles, then nearly every collision pair can be efficiently selected from within the same subcell. Under these conditions, computational expense for collision selection scales approximately linearly with the number of particles per cell, and overall simulation efficiency should vary little if the cell size is further increased. It follows that subcell adaptation to the local mean free path is ideally suited to a uniform grid approach, as relatively large cells can be used without significantly impacting either MCS values or simulation efficiency. Similar arguments are used to motivate the use of subcell sizes based on the mean free path in the MONACO DSMC code [7].

A further comment on subcell sizing by the hard sphere mean free path is appropriate. We use the hard sphere model here only as a simple means of calculating the collision cross section in Eq. (17) and as a way to avoid requiring temperature gradient terms in Eq. (14). If, for example, subcell dimensions were based on the local VHS mean free path, then the substitution coordinate ψ could not be related to x through a simple function of the time-averaged center of mass of particles in the cell. The use of the hard sphere model here may result in the presence of unnecessarily small subcells within high-temperature regions, along with overly large subcells in regions where the temperature is much lower than the VHS reference temperature. Despite such potential problems, we can justify the use of the hard sphere model here due to the simplicity and computational efficiency of the resulting subcell procedures. Any limitations associated with the hard sphere model can be at least partially offset by variation of the coefficient C in Eq. (16).

IV.   Code Evaluation for a Hypersonic Flat Plate Flow

For initial evaluation, HAP is applied to a two-dimensional hypersonic flow of N_2 over a flat plate with a sharp leading edge. The plate is aligned with the freestream direction, the freestream Mach number is 20.2, and the Knudsen number based on the total length of the plate is 0.015. The plate surface is diffusely reflecting at a temperature of 290 K, the freestream temperature is 13.32 K, and the freestream number density is 3.716×10^{20} m^{-3}. Uniform collision numbers of 5 and 50 are employed for rotational and vibrational energy, respectively. We use the VHS collision model with parameters recommended for N_2 by Bird [2], including a collision diameter d_{ref} of 4.17×10^{-10} m at a reference temperature T_{ref} of 273 K and a viscosity index ω of 0.74, and we calculate a freestream mean free path of 1.688 mm based on the equation

$$\lambda = \frac{1}{\sqrt{2}\pi d_{ref}^2 n} \left(\frac{T}{T_{ref}}\right)^{\omega - 1/2} \quad (20)$$

for an equilibrium simple gas. This case is based on tests by Lengrand et al. [21] and Heffner et al. [22] in the SR3 low density wind tunnel at Centre National de la Recherche Scientifique. in Meudon, France.

A corresponding simulation is performed with the DSMC code MONACO [7], using the same grid, boundary conditions, physical models, and numerical parameters. Results are compared between the two simulations to highlight any discrepancies, which may indicate potential errors in HAP. Published DSMC results of Heffner et al. [22] as well as experimental data of Heffner et al. and Lengrand et al. [21] are also used for comparison.

HAP and MONACO simulations employ a uniform grid with 128 by 48 square cells of length 1 mm, with a uniform inflow boundary located 16 cells upstream of the plate leading edge. The time-step interval Δt is set to 3.102×10^{-7} s, which is approximately 0.06 times the minimum mean collision time at steady state. The numerical weight W is set to 2.3225×10^{12} for an average of 160 particles per cell in the freestream. Time-averaged sampling is

Table 1   Parameters for HAP and MONACO simulations of hypersonic N_2 flow over a flat plate

Freestream Mach number	20.2
Global Knudsen number	0.015
Freestream temperature	13.32 K
Plate surface temperature	290 K
Freestream number density	3.716×10^{20} m^{-3}
Freestream mean free path	1.688 mm
Cell length	1 mm
Number of cells	128×48
Time-step interval	3.102×10^{-7} s
Numerical weight	2.3225×10^{12}
Total number of time steps	20,000
Number of time steps before sampling	2,000

performed over 18,000 time steps, following a transient startup period of 2000 steps. For reference, various simulation parameters are shown in Table 1. The HAP simulation requires about 5.3 hours of central processing unit (CPU) time on a single 1.9 GHz processor and includes 1.06×10^6 particles at steady state.

One standard gauge of DSMC simulation efficiency is the CPU time per particle per time step. In the HAP simulation, this ranges from approximately 5.4×10^{-7} s at simulation startup to 1.04×10^{-6} s at steady state, whereas this time is consistently around 5.6×10^{-7} s in the MONACO simulation. Efficiency differences between the two codes can be at least partly attributed to the use of temporary static arrays in MONACO for accessing particle information during collision operations [7], which tends to optimize high-speed cache use through a reduction in the frequency of cache misses. In contrast, HAP does not use static arrays for particle information storage and may be adversely affected by a gradual reduction in contiguous free memory over the course of the simulation. Because of a tradeoff between optimized cache usage and the expense of moving particle information to and from static arrays, the relative efficiency of the two codes seems to be very system-dependent, and comparable CPU times for the two codes have been demonstrated through subsequent tests on other systems.

Figures 1–4 show isocontour lines for various field quantities from both HAP and MONACO simulations. Coordinates are normalized by the freestream mean free path, and the coordinate system origin is located at the plate leading edge. HAP simulation results are displayed as solid gray lines, whereas results from the MONACO simulation are shown as dashed black lines. Figures 1–4 show,
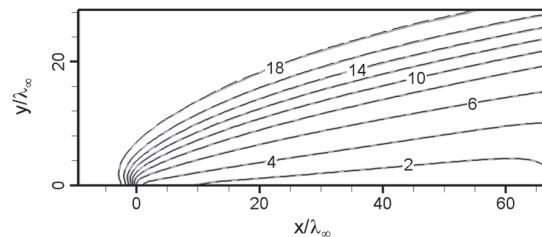
Fig. 1   Contours of Mach number for a hypersonic flat plate flow. HAP results are shown as solid gray lines, and MONACO results are shown as dashed black lines.
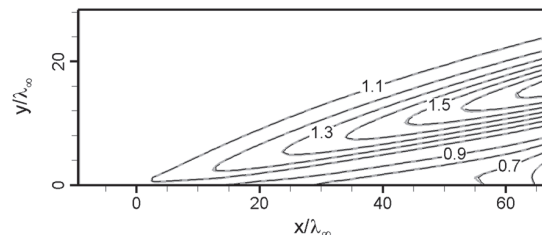
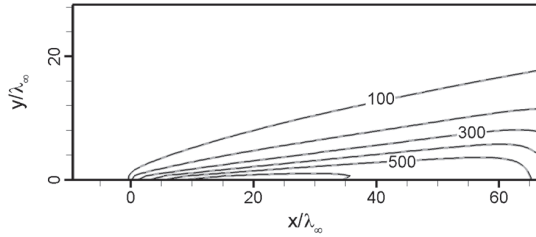**Fig. 2   Contours of normalized number density n/n_∞ from HAP and MONACO simulations.**
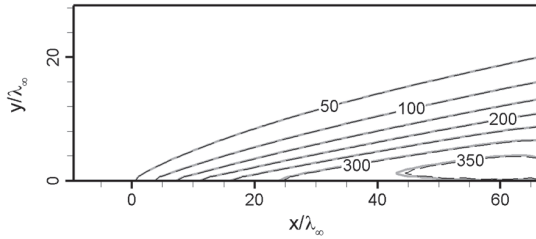
Fig. 3   Contours of translational temperature in K.

Fig. 4   Contours of rotational temperature in K.

Fig. 6   Bulk velocity profiles along a transverse plane.

respectively, contours of Mach number, number density normalized by the freestream value, translational temperature, and rotational temperature. Relatively complex characteristics are observed in the figures, including a highly diffuse oblique shock that forms within a smooth compression region near the leading edge, a low density expansion region within the postshock area near the surface, and significant rotational temperature lag behind the shock. In all four figures, virtually no noticeable differences are found between results from the two codes; the one exception is a small discrepancy in rotational temperature near the plate surface around $x/\lambda_\infty = 45$. Although no clear explanation for this discrepancy is apparent, the local gradient in rotational temperature is small, and the relative difference of well under 1% is within the expected range of statistical scatter.

In Fig. 5, normalized density values n/n_∞ from the HAP and MONACO simulations are extracted along a transverse plane at $x/\lambda_\infty = 44.55$. Experimental data from electron beam fluorescence measurements of Lengrand et al. [21] are also displayed for comparison. As in Fig. 2, excellent agreement is found between density values from the two simulations, and any noticeable differences are within statistical scatter. In contrast, large discrepancies are observed between experimental and simulation data points, with the experiment showing a roughly 30% increase in distance between the plate and the shock center location. Note, however, that reasonably

good agreement is found in the density along the plate and in the maximum density within the shock. Differences between experimental and DSMC density values can be mainly attributed to uncertainty and modeling approximations in gas-surface interaction, high sensitivity of experimental results to the plate angle of attack, and nonuniform freestream conditions in the SR3 experimental facility [23].

Figures 6 and 7 show profiles of bulk velocity and temperature, respectively, extracted from HAP and MONACO results along the same transverse plane as in Fig. 5. Transverse and longitudinal velocity components in Fig. 6 are normalized by the inflow bulk velocity, and, in Fig. 7, translational and rotational temperatures are normalized by the inflow temperature. As in Figs. 1–4, no statistically significant disagreement is found between HAP and MONACO results in Figs. 6 and 7.

In Fig. 8, the pressure coefficient C_p is plotted along the plate surface from HAP and MONACO simulation results, with additional published DSMC results of Heffner et al. [22] and experimental data of Lengrand et al. [21]. The pressure coefficient is defined as

$$C_p = \frac{P - P_\infty}{(1/2)\rho_\infty V_\infty^2} \qquad (21)$$

where P is the surface-normal momentum flux, and P_∞, ρ_∞, and V_∞ are, respectively, the freestream pressure, mass density, and bulk velocity magnitude. As in Figs. 1–7, excellent agreement is observed

Fig. 5   Density profiles along a transverse plane.
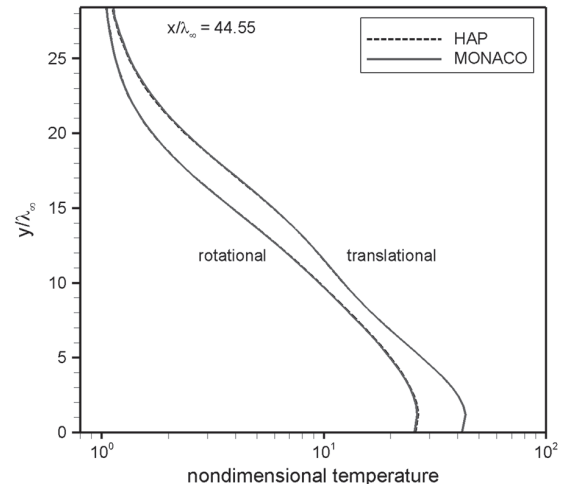
Fig. 7   Profiles of translational and rotational temperature along a transverse plane.

Fig. 8   Pressure coefficient along the plate surface.
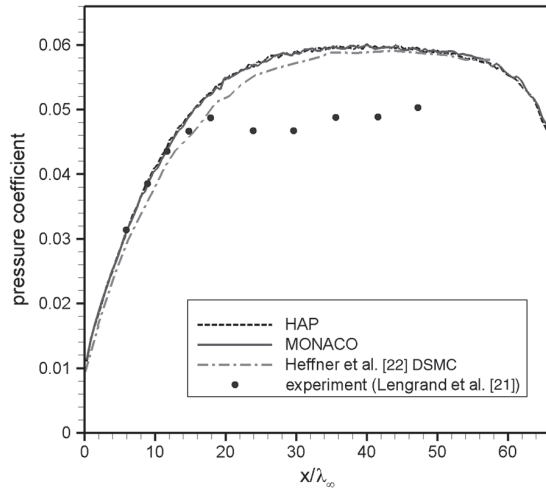
Fig. 10   Heat transfer coefficient along the plate surface.

in Fig. 8 between MONACO and HAP results. However, relative to other DSMC results in Fig. 8, some small but noticeable underprediction is found in the Heffner et al. [22] results, likely due in part to the use of a different set of parameter values by Heffner et al. for the VHS collision model. Considerable disagreement is displayed in Fig. 8 between the experimental data points and all DSMC results, with consistently lower experimental C_p values for $x/\lambda_\infty > 15$. The dominant source of the discrepancy is unclear, but likely contributors include the potential error sources mentioned in the discussion of Fig. 5. Note the sharp drop-off in C_p observed in both HAP and MONACO results near the downstream edge of the simulation domain. This trend is likely unphysical, and results from the suction effect of the DSMC vacuum outflow boundary within a small subsonic boundary layer region.

Figure 9 shows the shear stress coefficient, defined as the ratio of the surface tangential momentum flux to the freestream dynamic pressure $1/2\rho_\infty V_\infty^2$ from HAP and MONACO simulation results. As expected, no discrepancies are observed outside the range of statistical scatter.

Variation in the heat transfer coefficient C_h along the plate surface is shown in Fig. 10. This coefficient is defined as

$$C_h = \frac{q}{(1/2)\rho_\infty V_\infty^3} \qquad (22)$$

where q is net surface energy flux. Results are displayed from HAP and MONACO simulations, along with the published DSMC results
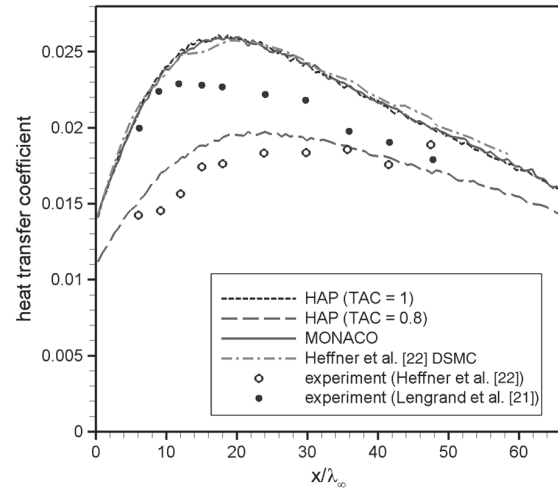
of Heffner et al. [22] and the experimental data of Heffner et al. and Lengrand et al. [21] For comparison, results are also plotted in Fig. 10 from an additional HAP simulation for which the thermal accommodation coefficient (TAC) is reduced from 1 to a potentially more realistic value of 0.8. All three sets of DSMC results for TAC = 1 show very good agreement, with no differences between HAP and MONACO values outside the level of statistical scatter. Significantly lower C_h values are found in the experimental results of both Heffner et al. [22] and Lengrand et al, [21] and considerable disagreement is also observed between the two experimental data sets. No dominant source of the discrepancies is apparent, but gas-surface interaction is a potential contributing factor, as suggested by Heffner et al. and as indicated by the relatively good agreement between the experimental data of Heffner et al. and results from the HAP simulation with TAC = 0.8. Sensitivity to and uncertainty in the plate angle of attack is another likely contributor and may partly account for the disagreement between the two sets of experimental data. Nonuniform freestream conditions [23] should also reduce the level of agreement between DSMC and experimental results, and may warrant future DSMC simulations, which include much of the upstream expansion region in the SR3 facility.

V.   Evaluation of Error Reduction Resulting from Collision Probability Modification

In both HAP and MONACO simulations, the uniform cell length is 0.6 times the freestream mean free path, and this cell length is smaller than the local mean free path throughout the simulated flowfield. It is, therefore, expected that approximations associated with spatial averaging in density over the cell volume, as used to compute collision probabilities in the standard NTC scheme [2], account for negligibly small errors in the output quantities of interest. However, from the logic outlined in Section III.A, the spatial discretization error in collision probabilities should increase in regions of high-density gradient as the cell size is increased. Likewise, the proposed modification to the collision probability, as implemented in HAP, should have a progressively greater impact on simulation results when larger cells are used. To quantify the error due to density averaging in collision probabilities and to demonstrate the effectiveness of the proposed modification in reducing this error, a series of additional HAP simulations are run for the same hypersonic flat plate flow presented in Section IV. The ratio $\Delta x/\lambda_\infty$ is varied by factors of two between 0.6 and 4.8, and simulations are performed both with and without the collision probability modification. The same values are used in all simulations for the numerical weight and time-step interval, and transient adaptive subcell procedures should eliminate or greatly reduce any effects of cell size on the mean collision separation. It follows that the discretization error described in Section III.A should be isolated from other DSMC spatial and

Fig. 9   Shear stress coefficient along the plate surface.

Fig. 11 Surface pressure coefficient for various cell sizes, with and without gradient-based collision probability modifications.

Fig. 13 Surface heat transfer coefficient for various cell sizes.

temporal discretization errors, and only this first error is varied between the different simulations.

Figures 11–13 show, respectively, the variation in pressure, shear stress, and heat transfer coefficients along the plate surface, from eight simulations employing different $\Delta x/\lambda_\infty$ ratios and using either standard or modified collision probabilities. As shown in the three figures, only very small differences appear in the surface fluxes between results from all simulations employing the modified probabilities, whereas the standard DSMC simulations display considerably greater disagreement. Errors among the standard DSMC results are particularly noticeable for simulations with normalized cell sizes $\Delta x/\lambda_\infty$ of 2.4 and 4.8, which significantly underestimate flux values over much of the plate surface relative to the $\Delta x/\lambda_\infty = 0.6$ simulations. In addition, significant overestimates in both shear stress and heat flux are found at $x/\lambda_\infty > 60$ for the $\Delta x/\lambda_\infty = 4.8$ simulation using standard DSMC collision probabilities. In comparing results between the $\Delta x/\lambda_\infty = 4.8$ simulations with and without the collision probability modification, we find large errors in the standard DSMC simulation and a considerable reduction in these errors when the proposed modification is used. Note that surface fluxes are typically among the output quantities most sensitive to errors in DSMC calculations and that only very small errors (less than 3%) were observed in a comparison of field quantities between these simulations.

To further quantify the errors associated with spatial density averaging in collision probabilities and to quantify the error

reduction due to the proposed modification, the $L\infty$ norm of the heat transfer coefficient is plotted as a function of normalized cell size x/λ_∞ in Fig. 14. This norm is calculated as the maximum local difference between C_h values for a given simulation and those for the $\Delta x/\lambda_\infty = 0.6$ standard DSMC simulation, normalized by the local C_h value from the same $\Delta x/\lambda_\infty = 0.6$ simulation. By assuming that differences in C_h values between modified and standard $\Delta x/\lambda_\infty = 0.6$ simulations are primarily due to statistical scatter, we can designate the $L\infty$ norm value for the modified $\Delta x/\lambda_\infty = 0.6$ simulation as the minimum $L\infty$ norm level above which statistically significant errors in C_h are detected. This minimum level is displayed as a dashed horizontal line in Fig. 14. Linear trend lines, based on least-squares fits, are also shown in Fig. 14 to highlight general trends among the two sets of data points.

In comparing results with and without the collision probability modification, we find a considerable increase in error with increasing $\Delta x/\lambda_\infty$ for the standard DSMC simulations and a much weaker dependence on cell size when modified collision probabilities are employed. In particular, the maximum local error in C_h is significantly less for the $\Delta x/\lambda_\infty = 4.8$ simulation with modified probabilities than for the $\Delta x/\lambda_\infty = 1.2$ standard DSMC simulation.

In Fig. 15, the $L2$ norm in C_h is plotted as a function of $\Delta x/\lambda_\infty$ for simulations with and without modified collision probabilities. This norm is a measure of the root-mean-square error in local heat flux relative to the standard DSMC simulation with $\Delta x/\lambda_\infty = 0.6$.

Fig. 12 Surface shear stress coefficient for various cell sizes.
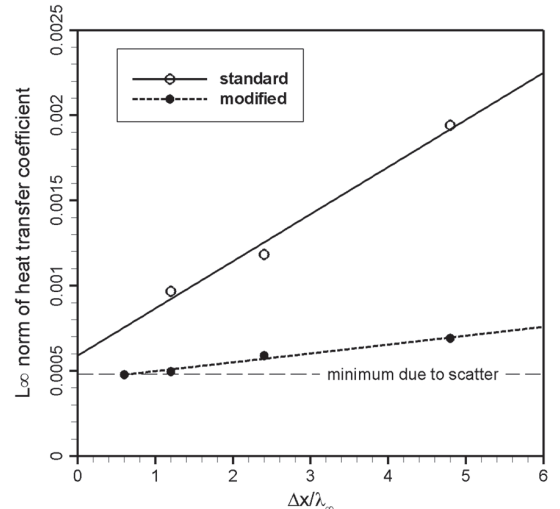
Fig. 14 $L\infty$ norm of heat transfer coefficient as a function of cell size, with and without gradient-based collision probability modifications.

Fig. 15   *L2* norm of heat transfer coefficient as a function of cell size.

Fig. 16   Temperature contours and adapted sampling grid for a hypersonic cylinder flow.
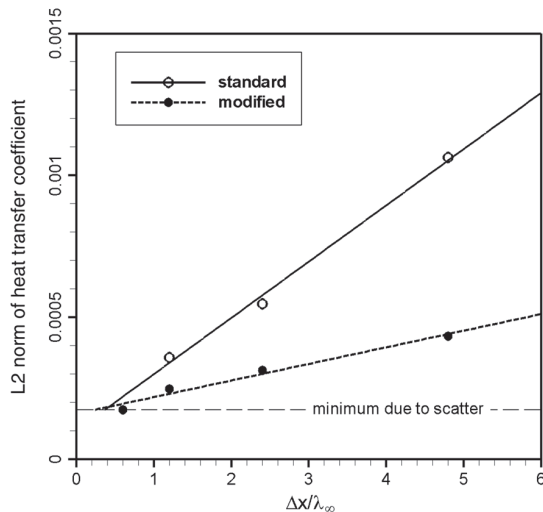
The same general trends are observed in Fig. 15 as in Fig. 14, although a somewhat greater dependence on cell size is found for the $L2$ norm than for the $L\infty$ norm in results from the modified probability simulations.

In both Figs. 14 and 15, a comparatively small but still significant increase in error for larger $\Delta x/\lambda_\infty$ is found for the modified probability simulations. This increase can be primarily attributed to breakdown in the assumption of a uniform density gradient within each cell. Curvature of the density profile is clearly shown in Fig. 5, due in part to competing effects of compression within the shock, expanding flow in the postshock region, and relatively stagnant flow along the wall. In Fig. 5, we find that approximations of a locally uniform density gradient should be particularly inaccurate for cells along the plate surface or near the location of maximum density within the shock. For accurate simulation using the proposed modification, it follows that the cell size may need to be limited by length scales, such as $|\nabla n/\nabla \cdot \nabla n|$, which are associated with the curvature of the density profile. Additional reductions in errors related to density averaging may also be possible by repeating the analysis in Section III.A under assumptions that ∇n is a linear function of position within each cell or by applying the adaptive grid-based nonlinear collision probability adjustment outlined at the end of that section.

VI. Hypersonic Cylinder and Sphere Flow Simulations

As an additional test case to evaluate cut cell capabilities in HAP for an analytically defined surface, we consider a two-dimensional Mach 10 flow of argon over a diffusely reflecting cylinder with a global Knudsen number (based on cylinder diameter) of 0.05. This case is based on that of Lofthouse et al. [24] and Lofthouse [25] and employs the same boundary conditions and VHS parameters given by these authors. The cylinder diameter is 12 in, the inflow and wall temperatures are 200 K and 500 K, respectively, and the inflow velocity is 2624 m/s. The uniform time-step interval of 5×10^{-7} s is approximately 0.45 times the minimum mean collision time, and a numerical weight of 1.9×10^{14} allows a maximum ratio of mean collision separation to local mean free path around 0.2. The collision cell size is set to 0.5 in, and the simulation domain comprises 72 collision cells in the axial direction and 36 cells in the transverse direction.

Nonuniform transient adaptive subcells are used with a ratio of subcell size to hard sphere mean free path of 0.5. The sampling grid is adapted to approximately 0.5 times the local hard sphere mean free path, and the sampling cell-based nonlinear collision probability modification described in the last paragraph of Section III.A is employed. This collision probability modification makes use of a sampling grid that is dynamically adapted periodically during the simulation to determine the local number density at binary collision
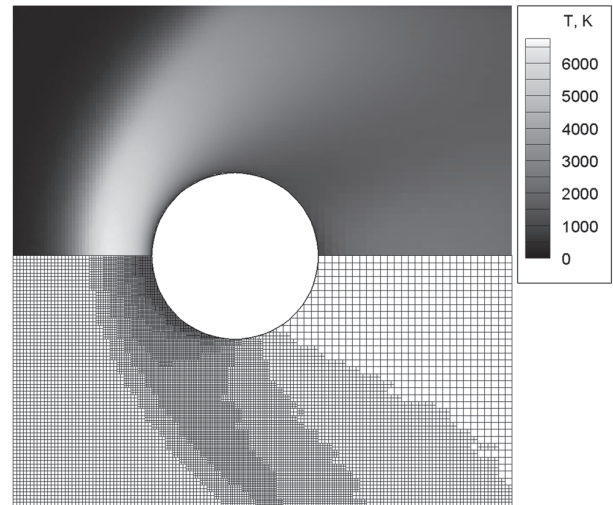
locations without any assumption of linear density variation across each collision cell. As found in Section V, the assumption of linear density variation may be invalid in collision cells that are far larger than the mean free path, and the alternate sampling cell-based modification is required here because the collision cell size is around 16 times larger than the stagnation point VHS mean free path.

Time-averaged output quantity sampling is performed over 12,000 time steps, following an 8000-step startup period. The adapted sampling grid comprises around 16,000 cells, and about 245,000 particles are present at steady state. The simulation is run in parallel on four threads, using a 2.66 GHz Intel Core 2 Quad processor, and requires 21.7 min of wall time.

Figure 16 shows contours of temperature along with the adapted sampling grid. As expected, a diffuse bow shock is found upstream of the cylinder, and a reduced temperature boundary layer forms over the cylinder surface. The highest grid refinement levels are found in the forebody boundary layer, whereas the lowest refinement level (for which sampling cells and collision cells are identical) is observed in the low-density wake region.

In Fig. 17, the surface pressure coefficient and heat transfer coefficient, given by Eqs. (21) and (22), respectively, are plotted as a function of the angle relative to the line from the cylinder center to the stagnation point. Corresponding curves from MONACO DSMC simulation results in Lofthouse et al. [24] are shown for comparison. Excellent agreement is found in Fig. 17 between pressure coefficient
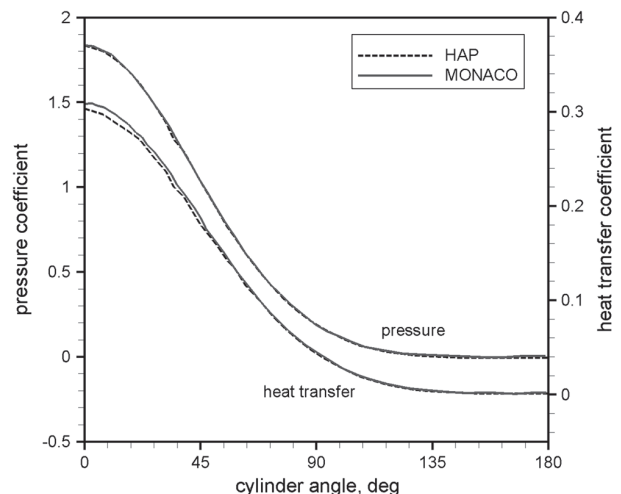
Fig. 17   Comparison of HAP and MONACO results for pressure and heat transfer coefficients along cylinder surface.

values from the two different codes, as expected due to the relatively low sensitivity of this parameter to numerical and physical approximations. In contrast, the surface heat transfer coefficient is typically one of the most sensitive output parameters in hypersonic blunt body flow simulations, and some discrepancies are found in surface heat transfer between the HAP and MONACO results. In particular, the stagnation point heat transfer coefficient is about 2% lower for the HAP simulation. Although this discrepancy could potentially point to an error in HAP results, it should be emphasized that DSMC simulation accuracy tends to correlate with an increase in stagnation point heat flux for this type of flow. A slight overestimate in MONACO results near the stagnation point is, in fact, consistent with subsequent comparisons by Bird [26] involving another case examined in Lofthouse et al. [24], for which peak heat flux values were found to be about 2% higher in the MONACO simulation than in simulations performed using four other DSMC codes. In any case, given the sensitive nature of surface heat flux, we can conclude that the overall level of agreement shown in Fig. 17 is very good.

To demonstrate three-dimensional simulation capabilities in HAP, a three-dimensional simulation has been performed for Mach 10 argon flow over an analytically defined sphere. Symmetry planes along both transverse coordinate axes are used to reduce the computational domain size by a factor of four. The numerical weight for simulated particles is set to 4.4×10^{12}, and all other models and input parameters are identical to those used for the cylinder case described in Section VI. The simulation employs about 865,000 sampling cells and 4×10^6 particles at steady state. Approximately 7.5 h of wall time are required using four parallel threads.

Figure 18 shows results from the sphere flow simulation, including contours of temperature along a symmetry plane, surface heat flux contours, the adapted grid used for field quantity sampling, and the planar cut faces used to approximate the curved surface of the sphere. Note that, for ease of visualization, cut faces that intersect collision cell edges at more than four points are divided into multiple quadrilateral and/or triangular surface elements. In examining the faceted approximation of the spherical surface, we find a very smooth surface that is nearly coincident with the desired analytical shape. Gaps between neighboring surface elements are negligibly small, as expected for such a large ratio of surface curvature radius to collision cell size. The high accuracy of the surface approximation is further suggested by the smoothness of heat flux contours shown in Fig. 18. A comparison of temperature contours between Figs. 16 and 18 shows that, as expected due to three-dimensional expansion effects,

the shock standoff distance is significantly smaller for a hypersonic flow over a sphere than for an equivalent flow over a cylinder. Although it should be emphasized that this is an axisymmetric flow problem and that established DSMC codes with axisymmetric capabilities can simulate this flow at considerably reduced computational expense, the results shown in Fig. 18 may be used to demonstrate the effectiveness of HAP capabilities for automatically generating planar surface elements that approximate a simple three-dimensional shape.

VII. Conclusions

The HAP code, a new Cartesian DSMC code for shared memory parallel systems, has been introduced. HAP is intended for fast setup and simulation of high-Knudsen number gas flow problems and as a foundation for development and testing of new DSMC models and algorithms. A two-level dynamically adaptive grid is employed for time-averaged sampling of field output quantities, whereas binary collisions and particle-ray trace procedures are performed over a separate uniform grid. The code is greatly simplified by avoiding complex routines for collision-grid adaptation, and a series of alternate procedures are employed to correct for errors typically associated with the use of a uniform grid in collision operations. These procedures include collision-pair selection by means of a novel nonuniform transient adaptive subcell scheme as well as a density-based modification to binary collision probabilities. Another unique feature of HAP is the ability to automatically generate two- and three-dimensional analytically defined shapes comprising a series of planar surface elements. This avoids a typical requirement to import externally defined boundary geometries for a wide variety of DSMC simulations and considerably reduces setup time. Externally defined triangulated surface meshes may instead be used for improved surface resolution or for inclusion of complex non-analytical shapes.

For initial code evaluation, a detailed comparison was performed between results from HAP, other DSMC codes, and two sets of experiments for a rarefied hypersonic flow over a flat plate. Excellent agreement was found between results from the HAP simulation and those from the established DSMC code MONACO, with no observed differences outside expected levels of statistical scatter. Good qualitative agreement was also found with experimental density and surface flux data, and likely explanations were offered for observed discrepancies. As additional test cases to demonstrate grid adaptation and cut cell capabilities, simulations were also performed for hypersonic flows over a cylinder and sphere, and surface fluxes were found to agree very well with published DSMC results for the cylinder flow.

In a further part of this work involving the flat plate flow problem, several HAP simulations were performed using different grid-refinement levels, both with and without the proposed collision probability modification. Spatial discretization errors associated with collision probability were quantified, and significant error reduction was demonstrated through the proposed modification. To the authors' knowledge, no thorough investigation of these errors exists in the literature, and it is hoped that the present work encourages more detailed analysis of this problem. Previous work on spatial discretization errors in DSMC has focused on the effects of MCS, and modern DSMC collision-selection procedures (e.g., transient adaptive subcells) tend to reduce or eliminate the correlation between MCS and cell size. Even with arbitrarily small MCS, however, spatial discretization errors may persist through a strong cell-size dependence in collision probabilities. It should be emphasized that techniques for reducing the MCS, such as nearest-neighbor collisions and adaptive subcells, do not reduce errors due to spatially averaged collision probabilities in the presence of a density gradient. The collision probability correction presented here is, therefore, suggested as one simple and effective way to further reduce the influence of cell size on simulation accuracy.

Both the proposed collision probability correction and the nonuniform subcell technique are employed in this work to correct problems associated with the use of a uniform grid for collision operations. Although these techniques are shown to be effective for
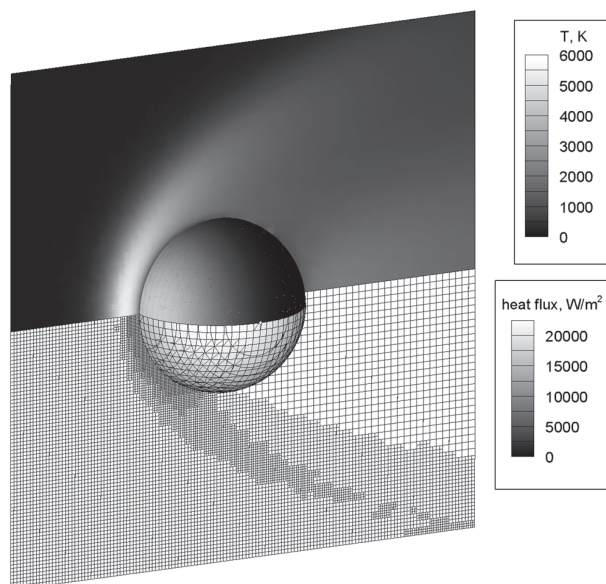

Fig. 18 Temperature contours along a symmetry plane, surface heat flux contours, planar cut faces, and adapted sampling grid for a three-dimensional hypersonic sphere flow simulation.

the uniform collision grid approach, both may be applied to the more general adaptive Cartesian collision grid approach of commonly used DSMC codes. When used either together or independently, the two techniques should help reduce DSMC spatial discretization errors without requiring an increase in either grid refinement or particle population.

Appendix

A derivation is provided for Eq. (17), which gives an approximate expression for the hard sphere mean free path $\langle\lambda\rangle_x$ averaged in the x-coordinate direction over a line segment through the cell center (x_c, y_c, z_c) with $x \in [x_c - 1/2\Delta x, x_c + 1/2\Delta x]$. From Eq. (6), the number density along the line segment can be expressed as $n(x) = n_c + (\partial n/\partial x)(x - x_c)$, where n_c is the cell-averaged number density, and $\partial n/\partial x$ is assumed to be constant. The local hard sphere mean free path is, therefore,

$$\lambda(x) = \frac{1}{\sqrt{2}\sigma[n_c + (\partial n/\partial x)(x - x_c)]} \tag{A1}$$

where σ is the hard sphere collision cross section. Integration of Eq. (A1) over the interval $[x_c - 1/2\Delta x, x_c + 1/2\Delta x]$ gives

$$\langle\lambda\rangle_x = \frac{1}{\Delta x} \int_{x_c-(1/2)\Delta x}^{x_c+(1/2)\Delta x} \lambda(x)\, dx$$
$$= \frac{1}{\sqrt{2}\sigma n_c \Delta x (\partial n/\partial x)} \ell n \left[\frac{1 + (\Delta x/2n_c)(\partial n/\partial x)}{1 - (\Delta x/2n_c)(\partial n/\partial x)}\right] \tag{A2}$$

The right side of Eq. (A2) is undefined when $\partial n/\partial x = 0$ and is potentially subject to a large truncation error when the term in the bracket is close to 1, so an approximate expression for $\langle\lambda\rangle_x$ is desired. The Taylor series approximation

$$\ell n \left(\frac{1 + w}{1 - w}\right) \approx 2w + \frac{2}{3} w^3$$

for an arbitrary variable $w \in (-1, 1)$ is used to find

$$\langle\lambda\rangle_x \approx \frac{1}{\sqrt{2}\sigma n_c} \left[1 + \frac{1}{12}\left(\frac{\Delta x}{n_c}\frac{\partial n}{\partial x}\right)^2\right] \tag{A3}$$

Finally, we employ Eq. (8) to express $\partial n/\partial x$ as a function of the x coordinate of the time-averaged particle center of mass in the cell, $\bar{x}_{cm}$ and substitute into Eq. (A3).

$$\langle\lambda\rangle_x \approx \frac{1}{\sqrt{2}\sigma n_c} \left[1 + 12\left(\frac{\bar{x}_{cm} - x_c}{\Delta x}\right)^2\right] \tag{A4}$$

References

[1] Bird, G. A., "Approach to Translational Equilibrium in a Rigid Sphere Gas," *Physics of Fluids*, Vol. 6, 1963, pp. 1518–1519.
doi:10.1063/1.1710976

[2] Bird, G. A., *Molecular Gas Dynamics and the Direct Simulation of Gas Flows*, Clarendon, Oxford, England, U.K., 1994.

[3] Oran, E. S., Oh, C. K., and Cybyk, B. Z., "Direct Simulation Monte Carlo: Recent Advances and Applications," *Annual Review of Fluid Mechanics*, Vol. 30, 1998, pp. 403–441.
doi:10.1146/annurev.fluid.30.1.403

[4] Alder, B. J., and Wainwright, T. E., "Studies in Molecular Dynamics," *Journal of Chemical Physics*, Vol. 27, 1957, pp. 1208–1209.
doi:10.1063/1.1743957

[5] Kolobov, V. I., Arslanbekov, R. R., Aristov, V. V., Frolova, A. A., and Zabelok, S. A., "Unified Solver for Rarefied and Continuum Flows with Adaptive Mesh and Algorithm Refinement," *Journal of Computational Physics*, Vol. 223, 2007, pp. 589–608.
doi:10.1016/j.jcp.2006.09.021

[6] Burt, J. M., and Boyd, I. D., "Evaluation of a Particle Method for the Ellipsoidal Statistical Bhatnagar-Gross-Krook Equation," *44th AIAA Aerospace Sciences Meeting and Exhibit*, AIAA Paper 2006-989, Reno, NV, 9–12 Jan. 2006.

[7] Dietrich, S., and Boyd, I. D., "Scalar and Parallel Optimized Implementation of the Direct Simulation Monte Carlo Method," *Journal of Computational Physics*, Vol. 126, 1996, pp. 328–342.

doi:10.1006/jcph.1996.0141

[8] LeBeau, G. J., "A Parallel Implementation of the Direct Simulation Monte Carlo Method," *Computer Methods in Applied Mechanics and Engineering*, Vol. 174, 1999, pp. 319–337.
doi:10.1016/S0045-7825(98)00302-8

[9] Bird, G. A., "The DS2V/3V Program Suite for DSMC Calculations," *Proceedings of the 24th International Symposium on Rarefied Gas Dynamics*, Vol. 762, American Instit. of Physics, Melville, NY, 2005, pp. 541–546.

[10] Ivanov, M. S., Markelov, G. N., and Gimelshein, S. F., "Statistical Simulation of Reactive Rarefied Flows: Numerical Approach and Applications," *7th AIAA/ASME Joint Thermophysics and Heat Transfer Conference*, AIAA Paper 1998-2669, Albuquerque, NM, 15–18 June 1998.

[11] Gao, D., Zhang, C., and Schwartzentruber, T. E., "Particle Simulations of Planetary Probe Flows Employing Automated Mesh Refinement," *Journal of Spacecraft and Rockets*, Vol. 48, No. 3, 2011, pp. 397–405.
doi:10.2514/1.52129

[12] Wu, J.-S., Tseng, K.-C., and Wu, F.-Y., "Parallel Three-Dimensional DSMC Method Using Mesh Refinement and Variable Time-step Scheme," *Computer Physics Communications*, Vol. 162, 2004, pp. 166–187.
doi:10.1016/j.cpc.2004.07.004

[13] Gao, D., and Schwartzentruber, T., "Parallel Implementation of the Direct Simulation Monte Carlo Method for Shared Memory Architectures," *48th AIAA Aerospace Sciences Meeting*, AIAA Paper 2010-451, Orlando, FL, 4–7 Jan. 2010.

[14] Borgnakke, C., and Larsen, P. S., "Statistical Collision Model for Monte Carlo Simulation of Polyatomic Gas Mixture," *Journal of Computational Physics*, Vol. 18, 1975, pp. 405–420.
doi:10.1016/0021-9991(75)90094-7

[15] Baganoff, D., and McDonald, J. D., "A Collision-Selection Rule for a Particle Simulation Method Suited to Vector Computers," *Physics of Fluids A*, Vol. 2, No. 7, 1990, pp. 1248–1259.
doi:10.1063/1.857625

[16] Macrossan, M. N., "Searching for a Near Neighbor Particle in DSMC Cells Using Pseudo-Subcells," *Journal of Computational Physics*, Vol. 229, 2010, pp. 5857–5861.
doi:10.1016/j.jcp.2010.04.042

[17] Gallis, M. A., and Torczynski, J. R., "Effect of Collision-Partner Selection Schemes on the Accuracy and Efficiency of the Direct Simulation Monte Carlo Method," *International Journal for Numerical Methods in Fluids*, Vol. 67, No. 8, 2010, pp. 1057–1072.

[18] Bird, G. A., Gallis, M. A., Torczynski, J. R., and Rader, D. J., "Accuracy and Efficiency of the Sophisticated Direct Simulation Monte Carlo Algorithm for Simulating Non-continuum Gas Flows," *Physics of Fluids*, Vol. 21, 2009, p. 017103.
doi:10.1063/1.3067865

[19] LeBeau, G. J., Boyles, K. A., and Lumpkin, F. E., "Virtual Sub-cells for the Direct Simulation Monte Carlo Method," *41st Aerospace Sciences Meeting and Exhibit*, AIAA Paper 2003-1031, Reno, NV, 6–9 Jan. 2003.

[20] Sun, Q., and Boyd, I. D., "Evaluation of Macroscopic Properties in the Direct Simulation Monte Carlo Method," *Journal of Thermophysics and Heat Transfer*, Vol. 19, No. 3, 2005, pp. 329–335.
doi:10.2514/1.12542

[21] Lengrand, J. C., Allegre, J., Chpoun, A., and Raffin, M., "Rarefied Hypersonic Flow Over a Sharp Flat Plate: Numerical and Experimental Results," *Proceedings of the 18th International Symposium on Rarefied Gas Dynamics*, AIAA, Reston, VA, 1993, pp. 276–284.

[22] Heffner, K. S., Gottesdiener, L., Chpoun, A., and Lengrand, J. C., "Leading Edge Effect on Rarefied Hypersonic Flow Over a Flat Plate," *22nd Fluid Dynamics, Plasma Dynamics, and Lasers Conference*, AIAA Paper 1991-1749, Honolulu, HI, 24–26 June 1991.

[23] Allegre, J., Bisch, D., and Lengrand, J. C., "Experimental Rarefied Density Flowfields at Hypersonic Conditions Over 70-Degree Blunted Cone," *Journal of Spacecraft and Rockets*, Vol. 34, No. 6, 1997, pp. 714–718.
doi:10.2514/2.3300

[24] Lofthouse, A. J., Scalabrin, L. C., and Boyd, I. D., "Velocity Slip and Temperature Jump in Hypersonic Aerothermodynamics," *45th AIAA Aerospace Sciences Meeting and Exhibit*, AIAA Paper 2007-208, Reno, NV, 8–11 Jan. 2007.

[25] Lofthouse, A. J., "Nonequilibrium Hypersonic Aerothermodynamics Using the Direct Simulation Monte Carlo and Navier-Stokes Models," Ph.D. Dissertation, Univ. of Michigan, Ann Arbor, MI, 2008.

[26] Bird, G. A., "Sophisticated Versus Simple DSMC," *Proceedings of the 25th International Symposium on Rarefied Gas Dynamics*, Russian Academy of Sciences, Novosibirsk, Russia, 2007, pp. 349–354.

Evaluation of a Hybrid Boltzmann-Continuum Method for High-Speed Nonequilibrium Flows

Jonathan M. Burt[*] and Eswar Josyula[†]

U.S. Air Force Research Laboratory, Wright-Patterson Air Force Base, Ohio 45433

and

Timothy R. Deschenes[‡] and Iain D. Boyd[§]

University of Michigan, Ann Arbor, Michigan 48109

A novel hybrid code for simulation of continuum and/or rarefied compressible gas flows is evaluated for a set of hypersonic blunt-body flow problems. This code, named the unified flow solver, combines several compressible gas-flow simulation schemes for application to a wide range of Knudsen number regimes and features capabilities for strong coupling between low Knudsen number and high Knudsen number schemes along with automatic binary tree-based grid adaptation. Unified flow solver simulations are performed for Mach 4 monatomic flows over a cylinder at various global Knudsen numbers, and simulation results are compared with results from simulations that employ direct simulation Monte Carlo and continuum Navier–Stokes solvers. Although good agreement is generally found, significant differences are identified and are used to highlight limitations or advantages of various simulation schemes in a unified flow solver. Results from this comparison are used to explain discrepancies in an earlier study involving application of similar techniques to a rarefied expansion flow.

I. Introduction

THE effectiveness of intermolecular collisions in driving the distribution of gas molecule velocities toward equilibrium is typically quantified by the Knudsen number Kn, which in turn is defined as the ratio of the mean free path to some characteristic length scale based on boundary geometry or gradients. A variety of gas-flow problems are characterized by a wide range of local Knudsen number regimes, with strong translational nonequilibrium in some portions of the flowfield and near-equilibrium velocity distributions in other flowfield regions. These problems include atmospheric flows around reentry vehicles, launch vehicles and hypersonic cruise vehicles; rocket exhaust flows at high altitudes; spacecraft gas venting; other hypersonic flows for which the internal shock structure is important; and subsonic flows, such as those within MEMS devices, which involve either very small length scales or low gas density.

For accurate simulation of high Knudsen number rarefied regions within these flows, translational nonequilibrium effects must be considered, and either a particle scheme such as the direct simulation Monte Carlo (DSMC) method [1] or a direct simulation method for the governing Boltzmann equation [2] is required. Although these methods can be applied to low Knudsen number regions as well, they tend to be far more computationally expensive than continuum computational fluid dynamics (CFD) methods based on the Navier–Stokes or Euler equations, while offering the same degree of accuracy in low Knudsen number regimes. Thus, an optimal combination of accuracy and efficiency for simulation of mixed rarefied-continuum flows generally requires integration of rarefied and continuum schemes within a coupled numerical framework. In this type of hybrid approach, the simulation domain is divided into rarefied and continuum flow regions through evaluation of a continuum breakdown parameter. DSMC or Boltzmann solver calculations are performed in rarefied regions, a continuum CFD method is applied in continuum regions, and coupling routines are used to exchange conserved quantities or other flow information across continuum breakdown boundaries.

In recent years, most work on algorithm development for mixed rarefied-continuum flow simulations has focused on hybrid CFD-DSMC techniques [3–8]. Such techniques have been shown to preserve the physical accuracy of DSMC in high Knudsen number regions, while offering the numerical efficiency of a CFD Navier–Stokes solver in low Knudsen number regions. However, the inherent statistical scatter in DSMC can make coupling between CFD and DSMC calculations difficult, and much of the focus in hybrid DSMC-CFD development has been on scatter reduction to avoid inaccurate or unstable CFD solutions. The scatter problem becomes particularly severe in simulations of highly unsteady flows, subsonic flows, or flow problems (such as those involving gas radiative emission or chemistry) for which accurate characterization is desired for the low-probability tails of the velocity distribution. In these cases, a very large number of DSMC particles may be required for sufficient scatter reduction, and a hybrid CFD-DSMC simulation can be prohibitively expensive.

In a recently proposed alternate scheme by Xu and Huang [9] for multiscale simulation of mixed rarefied-continuum flows, the Bhatnagar–Gross–Krook (BGK) approximation of the Boltzmann equation [2] is solved in discretized velocity space without operator-splitting between collision and advection processes. The standard BGK operator-splitting approach limits the allowable time-step size to the order of the mean collision time, which can make BGK simulation of low Knudsen number flows prohibitively expensive. In the scheme of Xu and Huang [9], however, collisional modifications are imposed on fluxes across cell interfaces, without any approximations of decoupled collision and advection processes over the time-step interval. As a result, practical calculations for multi-scale flows can be performed by means of a single technique in both rarefied and continuum regions. Despite significant potential, this scheme suffers from reduced efficiency in continuum regions relative to traditional Navier–Stokes schemes, for which only a small number

*Currently Research Scientist, Universal Technology Corporation. Member AIAA.

†Senior Research Aerospace Engineer. Associate Fellow AIAA.

‡Graduate Student, Department of Aerospace Engineering. Student Member AIAA.

§Professor, Department of Aerospace Engineering. Associate Fellow AIAA.

of conserved quantities, not the probability density at a large number of velocity space nodes, are calculated.

Another approach for simulation of mixed rarefied-continuum flows involves coupling DSMC to a particle method intended for continuum flow simulation. One promising scheme of this type is that of Burt and Boyd [10,11], which incorporates a low diffusion particle method to minimize numerical diffusion and dissipation effects typically associated with low Knudsen number particle simulations. The particle–particle hybrid approach benefits from simplified information exchange along continuum breakdown boundaries, but as with the scheme of Xu and Huang [9], this type of approach tends to suffer from relatively low efficiency in continuum flow calculations.

In another alternative hybrid scheme, a set of direct simulation methods for the Boltzmann equation are coupled to kinetic methods for the compressible Navier–Stokes or Euler equations [12–16]. This hybrid scheme, implemented in the unified flow solver (UFS) code, is not prone to the DSMC statistical scatter problem that may be considered the main drawback in CFD-DSMC techniques. Instead of using a collection of particles to represent the gas velocity distribution within rarefied regions, as in DSMC, nonequilibrium velocity distributions in UFS are modeled using a uniform Cartesian grid in velocity space. Discrete approximations of the advection and collision terms in the Boltzmann equation are employed to update the probability density at grid points in both velocity and physical space, and coupling across continuum breakdown boundaries is performed through two-way information exchange during each simulation time step.

The UFS code is based on the open source framework of the Gerris flow solver [17] and includes capabilities for binary tree-based Cartesian grid adaptation. Solid two-dimensional or three-dimensional objects are easily integrated within the simulated flowfield through the use of cut-cell boundaries, and additional procedures allow optimized load balancing for parallel domain decomposition. Continuum breakdown evaluations are periodically performed during a UFS simulation, for automatic assignment of each grid cell to either continuum or rarefied domains. Performance improvements, relative to DSMC or full Boltzmann solutions, are realized in UFS through the use of continuum CFD methods where appropriate and through initialization of rarefied domain calculations with (at least partially converged) continuum method solutions. In comparison with DSMC, reduced simulation expense has been demonstrated in UFS simulations of a nozzle/plume expansion flow [14], and comparable expense to DSMC has been observed in UFS simulations of a hypersonic blunt-body flow [15].

In the current effort, UFS is applied to a set of high-Mach-number rarefied/continuum flows over a cylinder and is evaluated for accuracy and efficiency through comparison with DSMC and CFD Navier–Stokes methods. Although previous evaluations of UFS have recently been carried out for a variety of flow problems, new objectives here include performing a more comprehensive comparison for accuracy and efficiency with both DSMC and CFD for a representative set of hypersonic blunt-body flows, and highlighting limitations and relative advantages of the various schemes employed in UFS. As an additional motivation for this study, results are used to provide some insight regarding the source of discrepancies between DSMC and UFS hybrid simulation results that were observed in previous work [14].

In the following sections, numerical approaches used in this study are outlined, and simulation setup and input parameters are described. Detailed simulation results are then presented. The accuracy of UFS simulation results is assessed by comparing surface flux coefficients, contour plots and the variation along the stagnation streamline in selected flow properties. Next, drag coefficients computed from these simulations are plotted as a function of global Knudsen number, in order to further assess accuracy of UFS simulations, compare with available experimental data, and evaluate the dependence of drag on the cylinder surface temperature. Results are used to help explain discrepancies in a previously published study involving UFS. Considerations of computational expense are then discussed, and general efficiency comparisons are made between

different simulations and techniques employed in this study. Finally, results are summarized and various characteristics, error sources and limitations of simulation techniques in UFS are discussed.

II. Numerical Approaches

A brief overview is provided for several numerical schemes used in this study. Detailed descriptions of these schemes are included in the references, and the reader is referred to these references for further details.

For simulation of rarefied flows or nonequilibrium regions in a mixed continuum-rarefied flowfield, UFS employs numerical solutions to the governing Boltzmann equation on a uniform Cartesian grid in velocity space [2,12]. An explicit solution method for the full Boltzmann equation, with finite time-step intervals, discrete nodes in velocity space and finite volume cells in physical space, is available in UFS with either first- or second-order spatial accuracy. This method makes use of temporal decoupling between advection and collision terms in the Boltzmann equation,

$$\frac{\partial f}{\partial t} + \nabla_r \cdot (\boldsymbol{\xi} f) = I(f) \tag{1}$$

where $\boldsymbol{\xi}$ is a point in velocity space, $\boldsymbol{r}$ is a point in physical space, and $f(\boldsymbol{\xi}, \boldsymbol{r})$ is the local number density in six-dimensional phase space. Linear hyperbolic advection terms on the left side of this equation are considered using standard upwind transport procedures for each velocity space node, and the nonlinear integral term represented by the collision operator $I(f)$ is solved by means of a large number of simulated binary collisions. Velocity space nodes are selected to participate in collisions using low-discrepancy Korobov sequences [12], in order to speed statistical convergence relative to standard Monte Carlo integration techniques.

To avoid expensive evaluations of the collision term in Eq. (1) and to reduce the required number of velocity space nodes, UFS allows the option of solving the BGK approximation of the Boltzmann equation in either two or three-dimensional discretized velocity space [2]. The BGK equation uses a linear relaxation term in place of the nonlinear collision operator $I(f)$ and may be solved deterministically at much lower expense.

The kinetic Navier–Stokes (NS) solver of Xu [18] can be used in UFS for calculations within continuum flowfield regions, where f approaches the low Knudsen number Maxwellian limit and where explicit consideration of the velocity distribution function is unnecessary for accurate simulation. This scheme uses analytical solutions to the BGK equation in calculating fluxes between neighboring finite volume cells and allows consistent kinetic representation of the entire flowfield when coupled to Boltzmann or BGK schemes in a hybrid UFS simulation.

In hybrid UFS simulations performed for this study, a continuum breakdown parameter based on characteristic length scales for velocity and pressure gradients is periodically evaluated throughout the computational grid, in order to assign flowfield regions to either continuum or rarefied domains. Rarefied regions are identified by comparing values of a breakdown parameter S_{NS} to a threshold value of 0.1. Following [12], the breakdown parameter is defined as

$$S_{NS} = \lambda \sqrt{\left(\frac{\nabla p}{p}\right)^2 + \left[\left(\frac{\partial u}{\partial x}\right)^2 + \left(\frac{\partial v}{\partial y}\right)^2 + \left(\frac{\partial w}{\partial z}\right)^2\right]} \Big/ (u^2 + v^2 + w^2) \tag{2}$$

where λ is the mean free path, p is the pressure, and (u, v, w) is the bulk velocity. UFS calculations in the rarefied domain use either Boltzmann or BGK schemes, and Navier–Stokes calculations are performed within continuum regions. Strong coupling between continuum and rarefied flow calculations is employed through two-way exchange of conserved quantities across continuum breakdown boundaries. In particular, the mass, momentum and energy density in

Navier–Stokes cells that border continuum breakdown boundaries are employed to compute the flux into each velocity space node within neighboring Boltzmann/BGK cells, using a near-equilibrium flux approximation. Likewise, fluxes from Boltzmann/BGK cells into neighboring Navier–Stokes cells are calculated through a discrete velocity approximation for unidirectional moments of the local velocity distribution. More discussion of coupling procedures is provided in [12,13].

For comparison with UFS simulation results, additional simulations are run using the DSMC method [1]. As mentioned above, DSMC is a probabilistic method that uses a large collection of particles (each representing a large number of atoms or molecules in the simulated flow) to reproduce the underlying physics of the Boltzmann equation. DSMC calculations avoid the complexity and difficulty of conservatively solving the nonlinear Boltzmann collision term on a discrete velocity grid. Binary collisions are represented in DSMC by conservative velocity resampling among probabilistically selected particle pairs, and advection terms in the Boltzmann equation are replicated by particle movement operations. During each time step in a DSMC simulation, separate procedures are employed for binary collisions, particle movement, the creation of new particles along inflow boundaries, and time-averaged sampling for field and surface flux quantities of interest.

III.   Simulation Setup

As the basis for a series of test problems, we consider a flow of argon over a cylinder with a freestream Mach number of 4. We employ the hard-sphere collision model, for which collision cross sections are independent of the relative speed between colliding particles and for which viscosity varies as the square root of temperature [1]. Note that the hard-sphere model is used to determine collision cross sections only in Boltzmann and DSMC calculations; intermolecular collisions are not directly modeled in BGK and NS simulations, and hard-sphere approximations are instead used to determine the BGK collisional relaxation rate and the NS transport coefficients. Diffuse reflection with full thermal accommodation to the wall temperature is assumed on the cylinder surface, and the temperature at the wall is set to 1.2 times the freestream temperature. The diffuse reflection boundary condition is modeled in UFS Boltzmann and BGK calculations by setting the reflected mass flux from the wall to equal the incident mass flux for each velocity grid node in all wall boundary cells and by setting the corresponding reflected momentum and energy fluxes equal to those expected for a quiescent equilibrium reservoir at the wall temperature. The same boundary condition is modeled in DSMC by means of probabilistic postcollision velocity assignment following any particle-wall collisions. In simulations for which NS calculations are used over the entire flowfield, a no-slip wall boundary condition is employed. Simulations are performed for global Knudsen numbers, based on cylinder diameter, of 0.3, 0.03 and 0.003 using various models in UFS. For comparison, additional simulations are performed using the DSMC code MONACO [19] and the NS CFD code LeMANS [20]. Note that LeMANS simulations use the same hard-sphere transport coefficient approximations employed in the UFS NS calculations.

The $Kn = 0.3$ case is representative of a highly rarefied flow and is simulated using numerical solutions to the Boltzmann equation and the BGK equation [2]. A NS simulation of this flow is also performed using LeMANS. In the $Kn = 0.03$ case, large portions of the flowfield are within both rarefied and continuum regimes, and hybrid schemes involving coupled rarefied and continuum flow calculations should give the best combination of accuracy and efficiency. UFS simulations for this second case employ the following different options: BGK, NS, hybrid BGK–NS, and hybrid BGK–Euler. The accuracy of all UFS results at $Kn = 0.3$ and 0.03 is assessed through comparison with results from simulations using the DSMC code MONACO. The $Kn = 0.003$ case, for which only very small portions of the flowfield experience significant thermal nonequilibrium, is used to independently evaluate the NS solver in UFS by comparing UFS NS results with those from a NS simulation using the

LeMANS CFD code. To demonstrate the expected inaccuracy for NS simulations at $Kn = 0.3$ and 0.03, LeMANS results are also generated for these cases.

MONACO simulations in this study employ unstructured grids that are automatically adapted to the local mean free path using an independent grid-generation utility, and dynamically adaptive DSMC subcells are used to ensure sufficiently small mean collision separation values. Spatially uniform time-step intervals in MONACO are carefully set to meet DSMC requirements based on the minimum mean collision time [1]. Numerical weight values are dynamically adapted in each cell to follow standard DSMC guidelines of at least 20 particles per cell, while avoiding any efficiency reduction due to excessive particle populations. LeMANS simulations use a finite volume implicit second-order modified version of the Steger–Warming flux vector splitting scheme [21], which is less dissipative in boundary layers but switches back to the original form in the vicinity of strong shocks.

Spatial and velocity grid independence and solution convergence is verified for all simulations. The full Boltzmann calculation uses a velocity grid of $40 \times 40 \times 20$ points, in the x, y, and z directions, respectively, and BGK calculations are performed on a grid of $40 \times 40 \times 2$ points in velocity space. Both Boltzmann and BGK simulations take advantage of velocity distribution symmetry along the z axis, in order to reduce the number of nodes in the velocity space grid. Boltzmann collision operations involve 10 simulated collisions per velocity grid node per iteration, as set by default in UFS in order to achieve a reasonable balance between accuracy and efficiency. Locally adaptive time-step intervals are employed in all UFS simulations, based on collisional relaxation times and a Courant–Friedrichs–Lewy criterion [12]. The UFS Boltzmann simulation is performed on 16 processors in the nyx cluster at the University of Michigan, and all other UFS, MONACO, and LeMANS simulations are run using eight processors in the same cluster. The nyx cluster is composed of dual-core AMD Opteron CPUs, with a minimum of 2 Gbytes of memory and two processors per node. High parallel efficiency has previously been demonstrated for UFS, MONACO, and LeMANS on large numbers of processors, so code-specific differences in parallel scalability are assumed to have a relatively small effect on computational expense for all simulations presented here.

IV.   Comparison of Simulation Results for $Kn = 0.3$

Figure 1 shows computational grids used in UFS BGK and MONACO DSMC simulations for the $Kn = 0.3$ case. Note that grids used in UFS calculations are adapted over the course of a simulation, and the BGK grid shown in Fig. 1 is taken from steady-state results after a total of 10,000 iterations. As observed in the figure, cell sizes in both the freestream and far-field wake regions are similar in the two simulations, although significant differences are found in cell
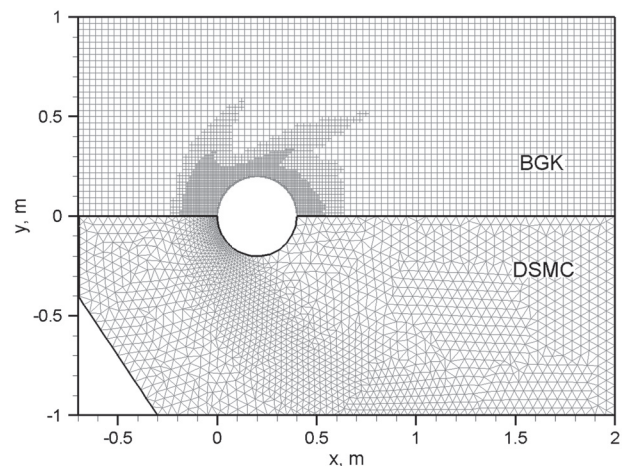

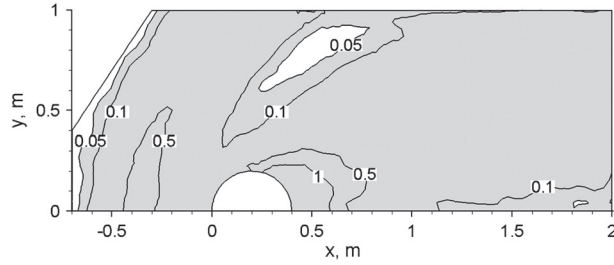**Fig. 1   Meshes for UFS BGK and DSMC simulations at $Kn = 0.3$.**

Fig. 2 Contours of the maximum-gradient-length local Knudsen number from the DSMC simulation at $Kn = 0.3$. Shaded area indicates regions of continuum breakdown.

size within shock layer and near-field regions. These discrepancies in cell size can be attributed to differences in grid refinement criteria between MONACO and UFS: MONACO cells are refined to the local mean free path, and grid refinement in UFS is based on density and velocity gradients.

In Fig. 2, contour lines are shown for the maximum-gradient-length local Knudsen number $Kn_{\text{GLL-max}}$, as calculated from DSMC simulation results at $Kn = 0.3$. The parameter $Kn_{\text{GLL-max}}$ is computed as the maximum ratio of the local mean free path λ to length scales based on gradients in bulk velocity magnitude V, density ρ, or temperature T:

$$Kn_{\text{GLL-max}} = \max\left\{\frac{\lambda}{a}|\nabla V|, \frac{\lambda}{\rho}|\nabla\rho|, \frac{\lambda}{T}|\nabla T|\right\} \quad (3)$$
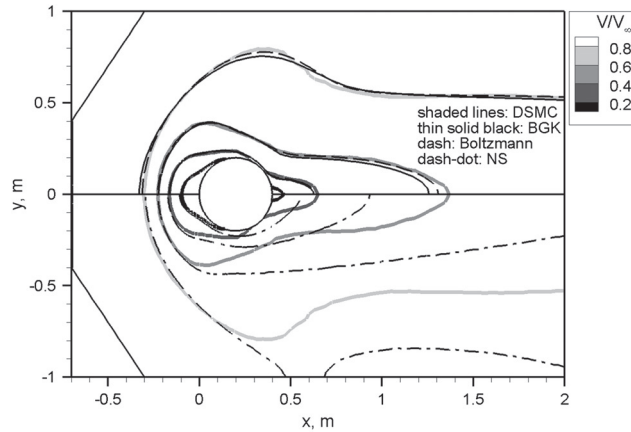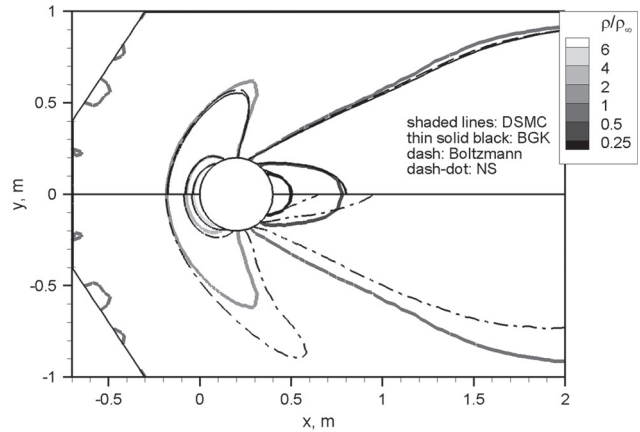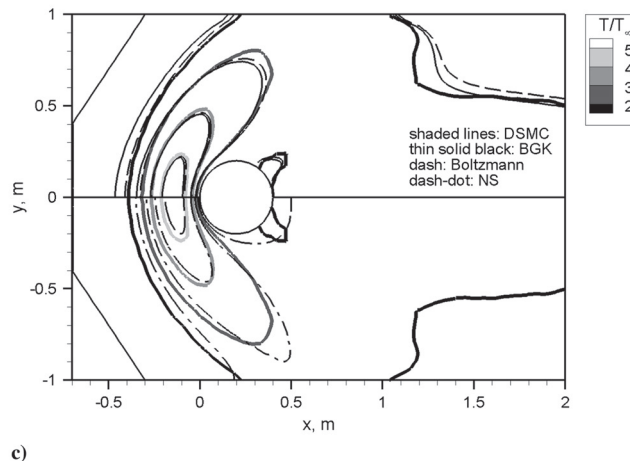
where a is the local speed of sound. The NS equations are usually assumed valid for $Kn_{\text{GLL-max}} < 0.05$ [22], and areas for which this condition is satisfied are shaded in Fig. 2. As shown in the figure, continuum breakdown occurs over nearly the entire flowfield.

Figure 3a shows contours of bulk velocity magnitude from MONACO, UFS and LeMANS simulations at $Kn = 0.3$. All values in the legend are normalized by the freestream velocity. Results from Boltzmann, BGK and DSMC simulations are shown in the upper half of the figure, and LeMANS NS and DSMC simulation results are compared in the lower half. As expected, both Boltzmann and BGK solutions show good overall agreement with DSMC, whereas the BGK results give slightly worse agreement with DSMC than Boltzmann simulation results. Poor agreement is observed between DSMC and NS results through much of the flowfield, which is consistent with the high level of continuum breakdown found in Fig. 2. Much of the discrepancy between DSMC and NS results can be attributed to the failure of assumptions underlying the Navier–Stokes equations; in regions of significant nonequilibrium, as indicated in Fig. 2, gradient-based diffusive transport approximations tend to break down, and the gas velocity distribution function cannot be accurately approximated using small perturbations from equilibrium. Both gradient transport and small perturbation assumptions are used in the NS calculations. The lack of velocity slip and temperature jump boundary conditions in the NS calculations also likely contribute to the disagreement between DSMC and NS results in Fig. 3a, although a nonslip boundary condition cannot by itself explain inaccuracy in a NS solution when strong rarefaction effects are present.

Figures 3b and 3c show contours of normalized density and temperature, respectively, for all simulations at $Kn = 0.3$. Trends in

a)

b)

c)

Fig. 3 Field property contours for $Kn = 0.3$: a) bulk velocity magnitude, b) density, and c) temperature. BGK and Boltzmann simulations are both run on UFS, the NS simulation is performed using LeMANS, and the DSMC simulation is run on MONACO.

both figures are similar to those in Fig. 3a. In particular, good overall agreement is found between DSMC and Boltzmann simulation results, with only slightly worse agreement between DSMC and BGK. A significantly broader bow shock region, as indicated by temperature contours, is observed in BGK results than in results from either DSMC or Boltzmann simulations. As in Fig. 3a, poor agreement is found between DSMC and NS results over nearly the entire flowfield in both Figs. 3b and 3c.

Figures 4 show the variation along the stagnation streamline in the normalized bulk velocity, density and temperature from the $Kn = 0.3$ simulations. In all three figures we find very good agreement between Boltzmann and DSMC results, with only a small overestimate relative to DSMC in the shock thickness based on either velocity or temperature. Note that, as expected at this high global Knudsen number, the shock is represented in all simulations as a broad region of smooth compression, and the shock, shock layer, and boundary layer cannot be easily distinguished. Noticeable differences are observed, however, between DSMC, BGK and NS results in the level of diffusive transport: a significantly wider shock region is

found in the BGK simulation than in the DSMC simulation, and the NS simulation gives a narrower shock and larger near-wall boundary-layer gradients.

In Fig. 5a, the nondimensional surface pressure coefficient (based on a vacuum reference pressure) is plotted along the cylinder surface for simulations at $Kn = 0.3$. The angle θ, used for the horizontal axis, is defined such that front and rear stagnation points are located at $0°$ and $180°$, respectively. As expected, excellent agreement is found over the entire surface between Boltzmann and DSMC results, and small but noticeable disagreement between DSMC and BGK occurs for $\theta > 120°$. Note the stair-step pattern in the UFS simulation results, which is presumably caused by gradient approximations associated with a cut-cell boundary condition along the cylinder surface. Implementation of an alternate immersed boundary method in UFS, which is currently underway, is anticipated to reduce or eliminate this problem. Results from the NS simulation agree well with DSMC only for $\theta < 60°$, with considerable qualitative disagreement near $180°$. Similar trends are observed in Fig. 5b, which shows the corresponding variation in the surface friction coefficient. In this

a)

b)

c)
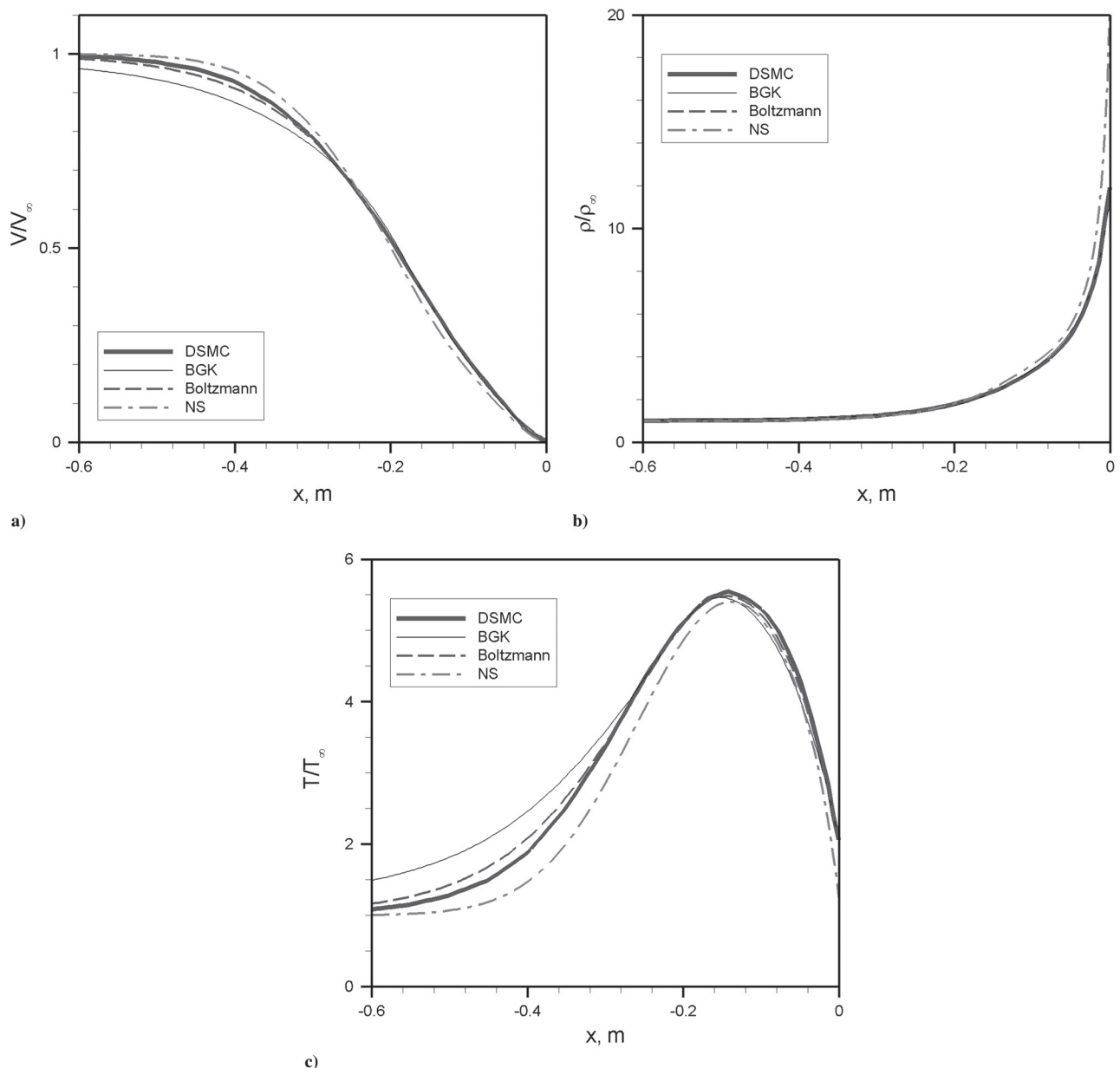
Fig. 4 **Property variation along the stagnation streamline for $Kn = 0.3$: a) bulk velocity magnitude, b) density, and c) temperature. UFS is used for BGK and Boltzmann simulations.**
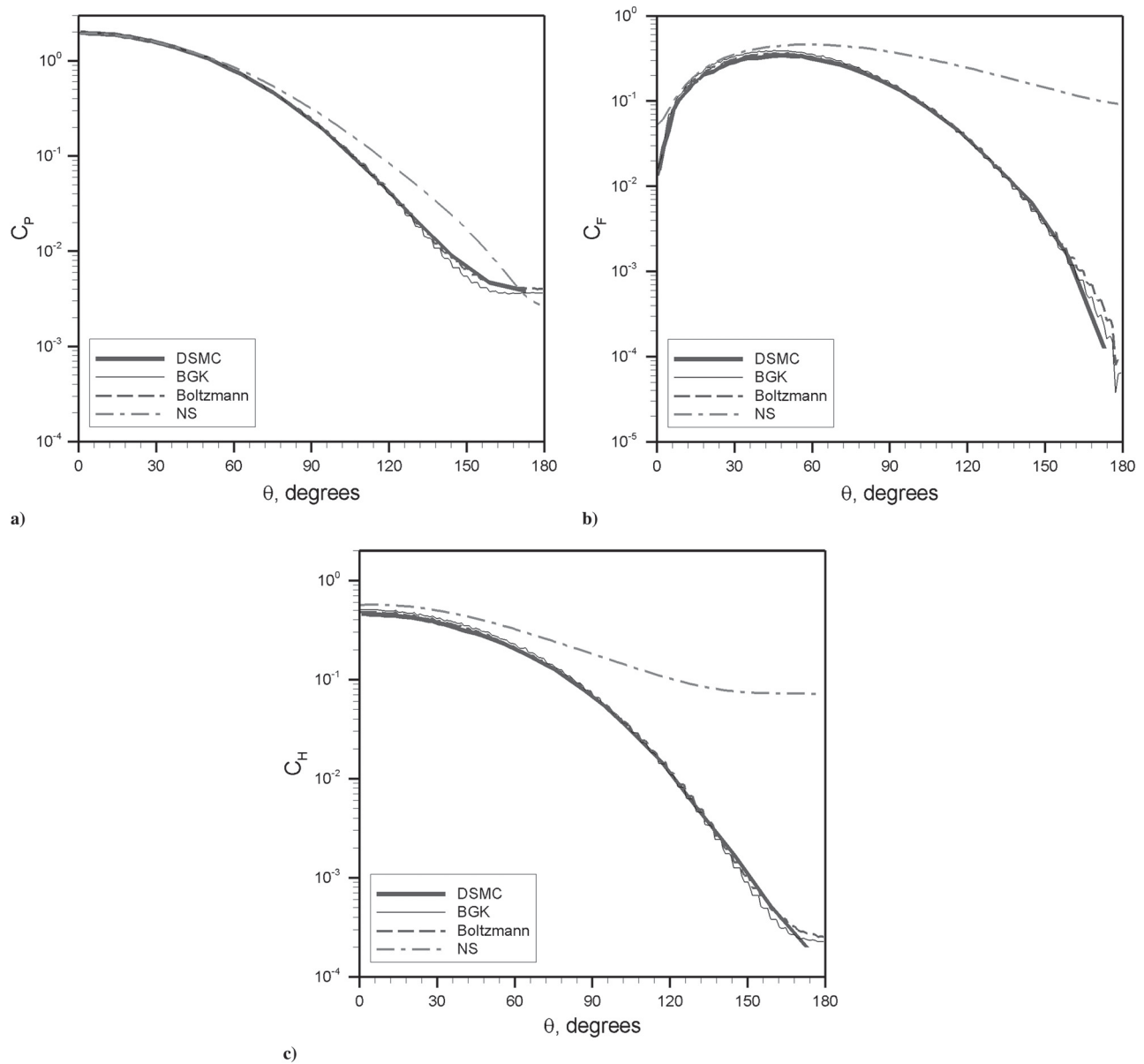
Fig. 5 Surface flux coefficients for $Kn = 0.3$: a) pressure, b) friction, and c) heat transfer. UFS is used for BGK and Boltzmann simulations.

figure, very good agreement is found between DSMC, BGK and Boltzmann results over the entire surface, whereas the friction coefficient is overestimated in the NS simulation by approximately a factor of 3 at 0° and by over three orders of magnitude at 180°.

Figure 5c shows the surface heat transfer coefficient for the $Kn = 0.3$ simulations. Although surprisingly good agreement (within about 20%) is found between NS and DSMC results at the front stagnation point, the level of disagreement increases rapidly with θ, and the NS surface heat transfer is overestimated by around three orders of magnitude at $\theta = 180°$. Note that somewhat better agreement between NS and DSMC would be expected in Fig. 5c, as well as in Figs. 5a and 5b, if the NS wall boundary condition included consideration of velocity slip and temperature jump effects.

As in Figs. 5a and 5b, good overall agreement is found in Fig. 5c over the entire cylinder surface between DSMC, BGK and Boltzmann simulation results. Slightly larger discrepancies are found between DSMC and BGK than between DSMC and Boltzmann results, with a noticeable underestimate in BGK surface heat transfer along much of the afterbody and a small corresponding overestimate along the forebody. Although recently published UFS results have shown an overestimate in UFS heat transfer by approximately a

factor of 2 [23], the authors were made aware of a normalization factor of 0.5 in UFS nondimensional heat transfer values that has been applied to values in Fig. 5c and that seems to provide far better agreement with DSMC. With this normalization factor, the overestimate relative to DSMC in stagnation point heat flux is only about 3.8% for the Boltzmann simulation and 9.5% for the BGK simulation.

Some of the error observed in Boltzmann and BGK values, as well as the artificial stair-step pattern in these values, is likely due to the cut-cell boundary condition and is expected to be eliminated through the use of the immersed boundary method in place of cut cells. Further error in surface heat transfer from Boltzmann and BGK simulations may be due to insufficient mesh refinement near the surface, although comparable cell sizes are used in these simulations as in the DSMC simulation and it seems unlikely that mesh resolution accounts for most of the discrepancy.

Another important contributor to the error in BGK results shown in Fig. 5c is the lack of a Prandtl number correction in BGK calculations. The BGK approximation of the Boltzmann equation gives transport coefficients that are functions of the collision frequency, but that lack the complex dependence on collision dynamics
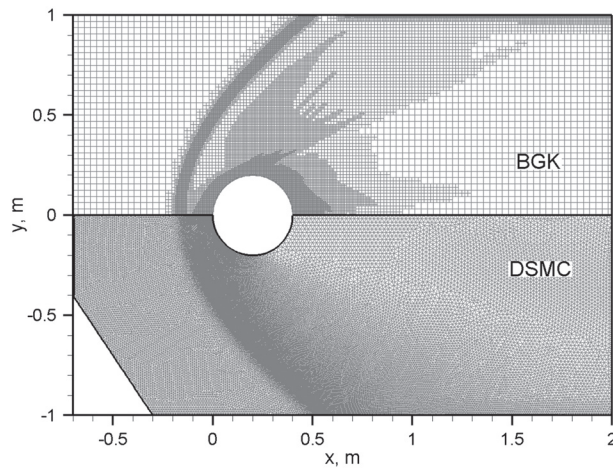
Fig. 6 Meshes for UFS BGK and MONACO DSMC simulations at $Kn = 0.03$.

parameters for transport coefficients derived from the full Boltzmann equation. In particular, in the BGK equation the thermal conductivity cannot be specified independently from the viscosity, which results in a fixed Prandtl number of one. Various modifications of the BGK equation, such as the ellipsoidal statistical BGK equation, have been developed in order to overcome this limitation, and a Prandtl number correction has been implemented in a more recent version of UFS, which was not available for the present study. However, the BGK simulation results presented here should be understood to include errors associated with an underestimate in the gas thermal conductivity. More generally, an unphysical linearization of the collision term in the BGK approximation of the Boltzmann equation should correspond to some accuracy reduction in BGK calculation results.

V. Comparison of Simulation Results for $Kn = 0.03$

Figure 6 shows meshes used in UFS BGK and DSMC simulations for the $Kn = 0.03$ case. As in Fig. 1, differences in local refinement levels are attributed to the fact that DSMC cell size is adapted to the mean free path, whereas UFS mesh adaptation is based on density and velocity gradients. For both simulations, the shock position is clearly indicated by a sudden increase in mesh refinement levels upstream of the cylinder.

Figure 7 is a contour plot of the maximum-gradient-length local Knudsen number $Kn_{\text{GLL-max}}$ from the DSMC simulation at $Kn = 0.03$. In comparing this figure with Fig. 2, we find that continuum breakdown (defined by $Kn_{\text{GLL-max}} > 0.05$) occurs over a far smaller portion of the flowfield than for the $Kn = 0.3$ case. For the present case, continuum breakdown is limited to a region surrounding the bow shock, the forebody boundary layer, and a large portion of the wake. Figure 8 shows the boundaries between NS and BGK domains, at steady state, in a hybrid BGK–NS simulation of the $Kn = 0.03$ case. These boundaries, along which the right side of
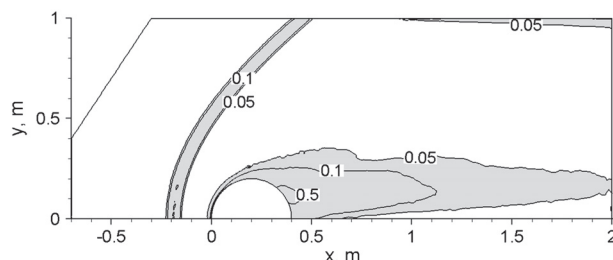
Eq. (2) is equal to the cutoff value of 0.1, correspond reasonably well to continuum breakdown boundaries shown in Fig. 7. Significant differences between domain boundaries in Fig. 8 and the 0.05 contour line in Fig. 7 are found only in the wake region.

In Fig. 9a, contours of normalized bulk velocity magnitude are shown for several different simulations at $Kn = 0.03$. Results are displayed for BGK, hybrid BGK–NS, hybrid BGK–Euler, DSMC, UFS NS and LeMANS NS simulations. Contour lines from both UFS NS and LeMANS NS simulations agree well with those from DSMC through much of the forebody shock layer, but noticeable disagreement is found in the wake. The BGK–Euler simulation gives particularly inaccurate results throughout the flowfield, and reduced accuracy is also found for the BGK simulation in wake regions far from the axis. Discrepancies observed between BGK and BGK–NS results in the wake seem to indicate that, in the hybrid BGK–NS simulation, the NS domain may include areas of strong non-equilibrium within the wake where BGK calculations would be more appropriate. This assumption is reinforced by differences, discussed above, between Figs. 7 and 8. As expected, very good agreement is found between BGK, BGK–NS and DSMC simulations within the shock layer upstream of the cylinder.

Figures 9b and 9c show contours of normalized density and temperature, respectively, from simulations of the $Kn = 0.03$ case. Trends in both figures are similar to those in Fig. 9a. As in Fig. 9a, relatively good agreement is shown in Figs. 9b and 9c between most simulation results around the shock layer and forebody boundary layer, whereas particularly large discrepancies with DSMC are observed in results from the hybrid BGK–Euler simulation. The large error in BGK–Euler results is not particularly surprising, because (unlike BGK, DSMC, Boltzmann and NS calculations) Euler calculations completely neglect effects of diffusive transport and viscous dissipation, and any differences from a truly inviscid flow are due only to artificial viscosity.

In Fig. 10a, the variation in normalized velocity along the stagnation streamline is plotted for simulations of the $Kn = 0.03$ case. Very good agreement is found here between results from DSMC and LeMANS NS simulations. Excellent agreement is also shown in Fig. 10a between BGK and hybrid BGK–NS simulation results, although both give relatively poor agreement with DSMC toward the upstream portion of the shock. A comparison of BGK and DSMC results in this region indicates that the BGK approximation of the Boltzmann equation may produce excessive diffusive transport within the shock. As mentioned above in the discussion of Figs. 4, the same trend of excess diffusion in the shock is also found in a comparison of BGK, Boltzmann and DSMC results for the $Kn = 0.3$ case. In Fig. 10a, as in Figs. 9, the greatest differences from DSMC are observed in results from the hybrid BGK–Euler simulation. In relation to DSMC, the BGK–Euler simulation overestimates the shock standoff distance by approximately 12%. Despite significant discrepancies in the location and thickness of the shock, all curves shown in Fig. 10a give relatively good agreement within the postshock and boundary-layer regions.

Figures 10b and 10c show contours of normalized density and temperature, respectively, for the $Kn = 0.03$ case. Trends in both figures are similar to those in Fig. 10a, with comparable differences in shock thickness and shock standoff distance based on either density or temperature. The only prominent trends in Figs. 10b and
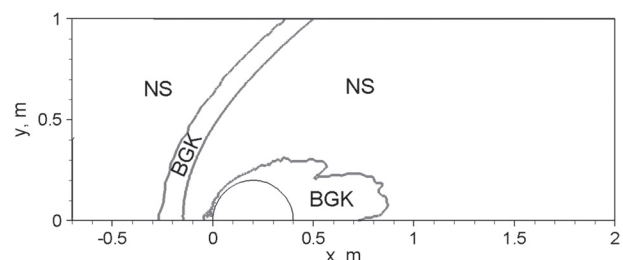

Fig. 7 Contours of the maximum-gradient-length local Knudsen number from the DSMC simulation at $Kn = 0.03$. Shaded area indicates regions of continuum breakdown.

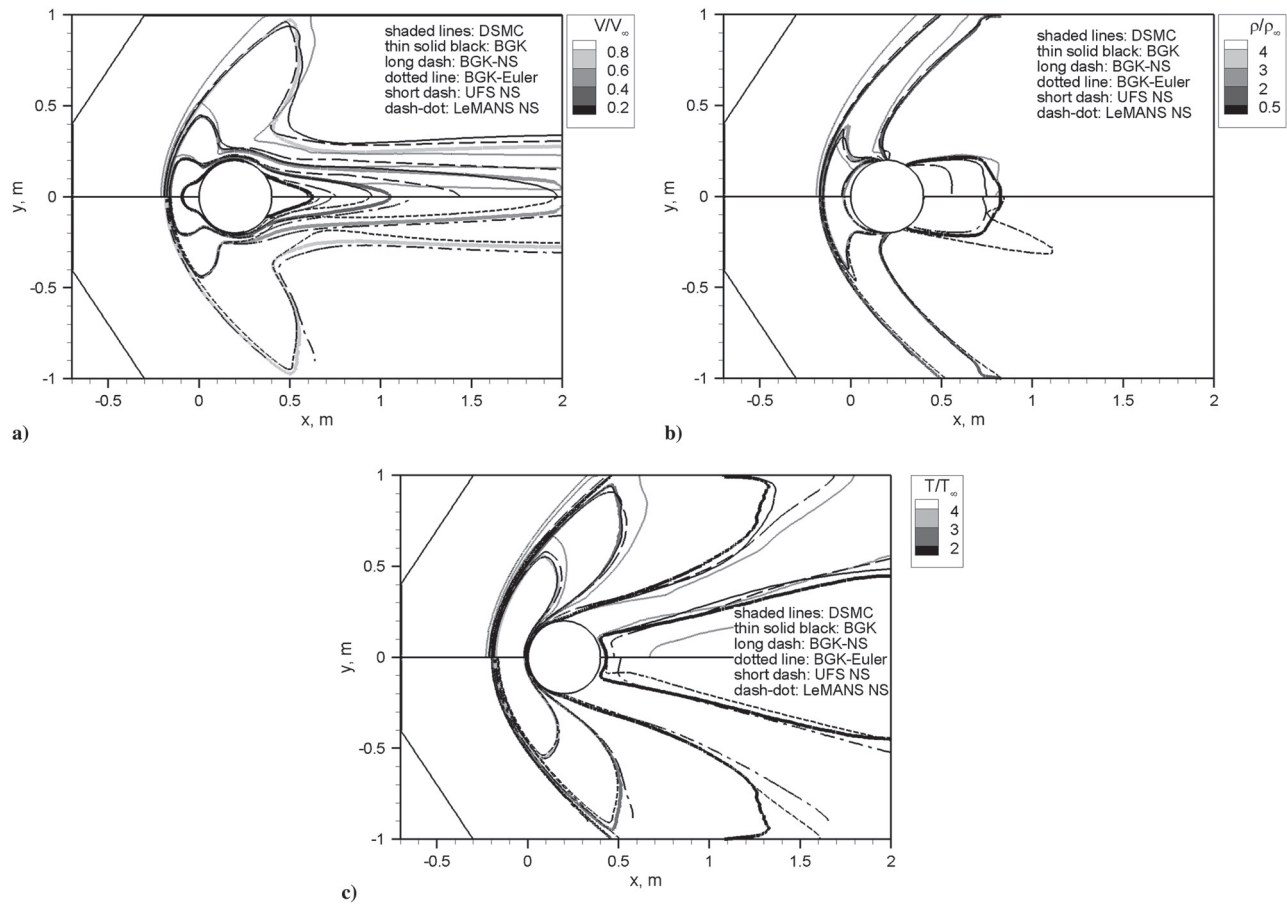**Fig. 8 Continuum and rarefied domains for the UFS BGK–NS simulation at $Kn = 0.03$.**

216

Fig. 9   Field property contours for *Kn* = 0.03: a) bulk velocity magnitude, b) density, and c) temperature. UFS is used for all simulations except the LeMANS NS simulation and the MONACO DSMC simulation.

10c that are not apparent in Fig. 10a relate to boundary-layer thickness. The BGK, BGK–NS and BGK–Euler simulations all noticeably overestimate the boundary-layer thickness, as measured by density or temperature, relative to DSMC. Corresponding gradients within the boundary layer are lower in these simulations than in DSMC. In contrast, only very small differences in boundary-layer thickness are found in Figs. 10b and 10c between results from LeMANS NS and DSMC simulations. Differences in boundary-layer thickness are likely due to excess diffusive transport in BGK calculations; this may be attributed to inaccuracy in the BGK approximation of the collision term in the Boltzmann equation and is also thought to cause the overly thick shocks observed in Figs. 4 and 10a.

Surface pressure coefficients for simulations at *Kn* = 0.03 is plotted in Fig. 11a. Good agreement is observed along the forebody between all pressure coefficient curves, whereas significant quantitative (but not qualitative) differences are found for $\theta > 90°$. The greatest disagreement with DSMC pressure coefficient values at $\theta > 90°$ is shown in results from the BGK–Euler and NS simulations. As discussed above, error in NS results is likely due to effects of continuum breakdown, whereas BGK–Euler inaccuracies can be mainly attributed to a lack of diffusive transport in calculations for the Euler equations. Although BGK–NS and NS results are in good agreement for $\theta > 150°$, neither compares well with BGK or DSMC results over this portion of the surface. This trend seems to indicate that, as mentioned in the discussion of Fig. 9a, the NS domain in the BGK–NS simulation may include rarefied wake regions that should be assigned to the BGK domain.

Figure 11b shows the variation in the surface friction coefficient for simulations of the *Kn* = 0.03 case. The most noticeable errors are found in the NS curve, which agrees reasonably well with DSMC over the forebody surface ($\theta < 90°$) but is up to a factor of 5 greater

than DSMC along the afterbody. Most of this discrepancy can be attributed to the lack of a velocity slip/temperature jump boundary condition in NS calculations; due to the high degree of continuum breakdown along the cylinder surface shown in Fig. 7, significant velocity slip is expected. Both DSMC and BGK calculations allow for velocity slip along the surface, and as expected, the lack of wall slip in NS calculations is associated with higher friction coefficient values in the NS results. All UFS simulations tend to slightly overpredict surface shear stress along the forebody, with an over-estimate relative to DSMC of up to around 50% in the BGK results. Note the slope discontinuity in all curves around $\theta = 165°$, which corresponds to boundary-layer separation at the edge of a recirculation zone. In comparing the location of this discontinuity between results from different simulations, we find good overall agreement in the size of the recirculating region. Relative to DSMC, the maximum difference in the θ range for the recirculating region is found in results from the BGK–NS simulation, which overestimates this range by about 30%.

In Fig. 11c, the surface heat transfer coefficient is plotted for simulations at *Kn* = 0.03. As with the friction coefficient values shown in Fig. 11b, the NS simulation slightly overpredicts the heat transfer over much of the forebody surface and greatly overpredicts this quantity along the afterbody. A maximum relative error (with respect to the DSMC value) of approximately 32% is found at $\theta = 148°$. Significant discrepancies are observed between DSMC and the various UFS results, with a roughly 20% underestimate in heat transfer over much of the surface from the BGK–NS simulation and a somewhat smaller overestimate from the BGK simulation.

The underestimate in BGK–NS heat flux values in Fig. 11c is likely due primarily to some combination of the following factors: First, an overly small temperature gradient (relative to DSMC) is
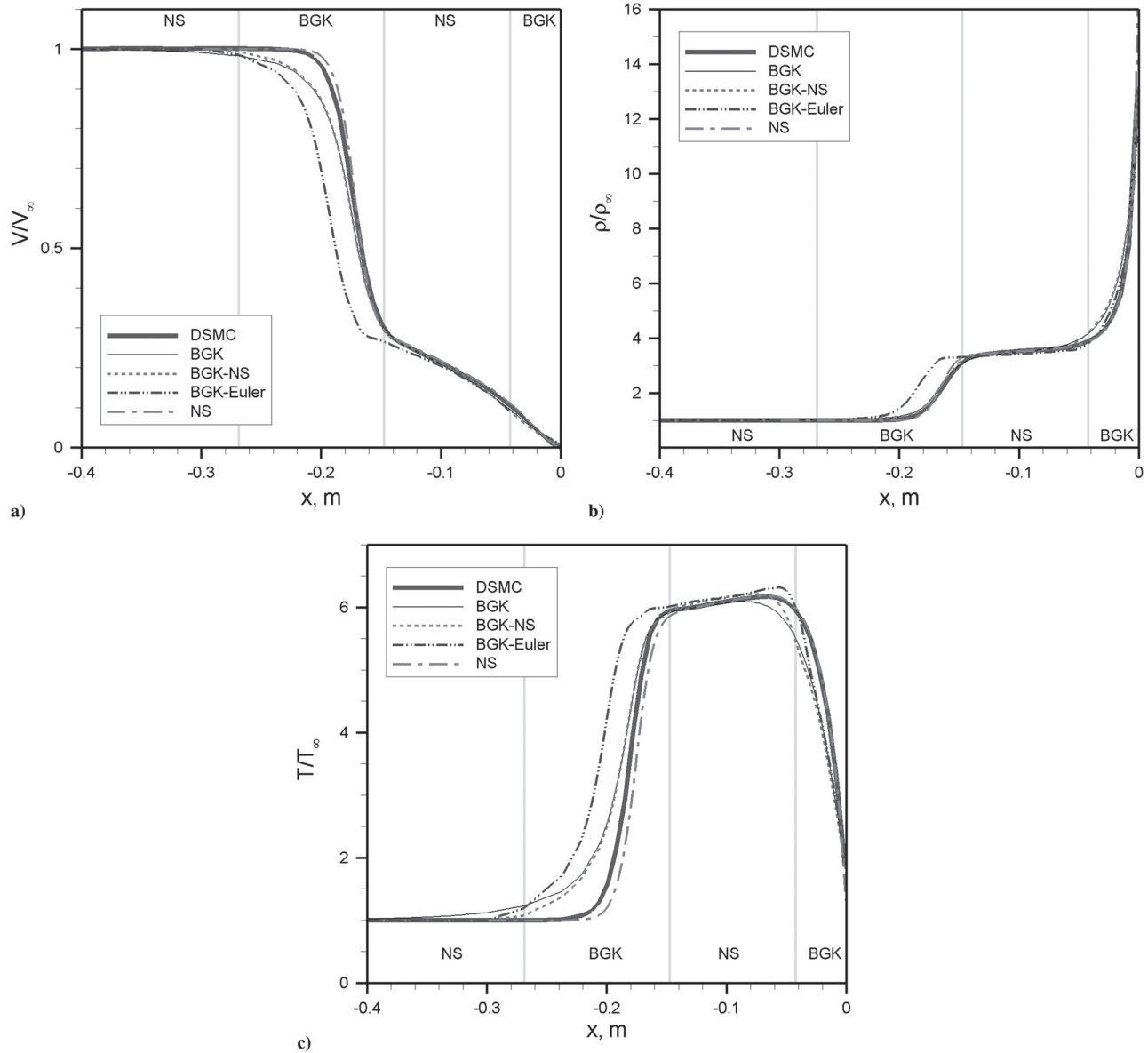
Fig. 10   Property variation along the stagnation streamline for $Kn = 0.03$: : a) bulk velocity magnitude, b) density, and c) temperature. UFS is used for BGK, BGK–NS, and BGK–Euler simulations.

present through much of the forebody boundary layer, as shown in Fig. 10c. Second, the lack of a Prandtl number correction in BGK calculations, as mentioned above in the discussion of Fig. 5c, results in an unphysically low thermal conductivity, which should further reduce surface heat flux. Finally, linearization of collision term in the BGK equation should reduce accuracy in surface heat flux and may contribute to errors in NS-BGK simulation results shown in Fig. 11c. Note that, in contrast to the NS-BGK results in this figure, an overestimate in heat flux is observed over much of the forebody surface for the BGK simulation. Although no clear explanation for this trend is apparent, possible contributors include unphysically high numerical diffusion due to approximations in the BGK collision operator.

As mentioned in the discussion of Figs. 5, UFS simulation results in Figs. 11 exhibit an unphysical stair-step pattern in the θ range between 90 and 150°. These errors, as well as a lack of smoothness in surface heat transfer curves at smaller θ values, are likely caused by problems with gradient evaluations involving Cartesian cut cells. Note that UFS BGK and NS calculations are entirely deterministic, and fluctuations observed in the UFS results are not due to statistical scatter as found in results from DSMC simulations.

VI.   Comparison of Simulation Results for $Kn = 0.003$

Figure 12 shows the computational meshes used in UFS NS and LeMANS NS simulations at $Kn = 0.003$. Although the UFS mesh is able to capture high gradient regions within areas of increased refinement, no automatic grid adaption is possible using LeMANS. The LeMANS mesh, which was manually generated using a commercial code, includes a structured region surrounding the cylinder and an unstructured region of uniform-sized triangular cells that covers much of the wake. In creating the LeMANS mesh, particular effort was made to ensure shock alignment and grid independence. As described in section III, stretched (i.e., high aspect ratio) cells are used in the boundary layer to avoid unnecessarily small cell dimensions in the surface-tangent direction.

In Fig. 13, contours are shown for the maximum-gradient-length local Knudsen number, as computed from the LeMANS simulation at $Kn = 0.003$. As expected for such a small Knudsen number value, continuum breakdown (where $Kn_{GLL\text{-}max} > 0.05$) is found to occur only in narrow regions around the bow shock and forebody boundary layer, as well as in portions of the near-field wake region. This indicates that the NS equations are valid over nearly the entire
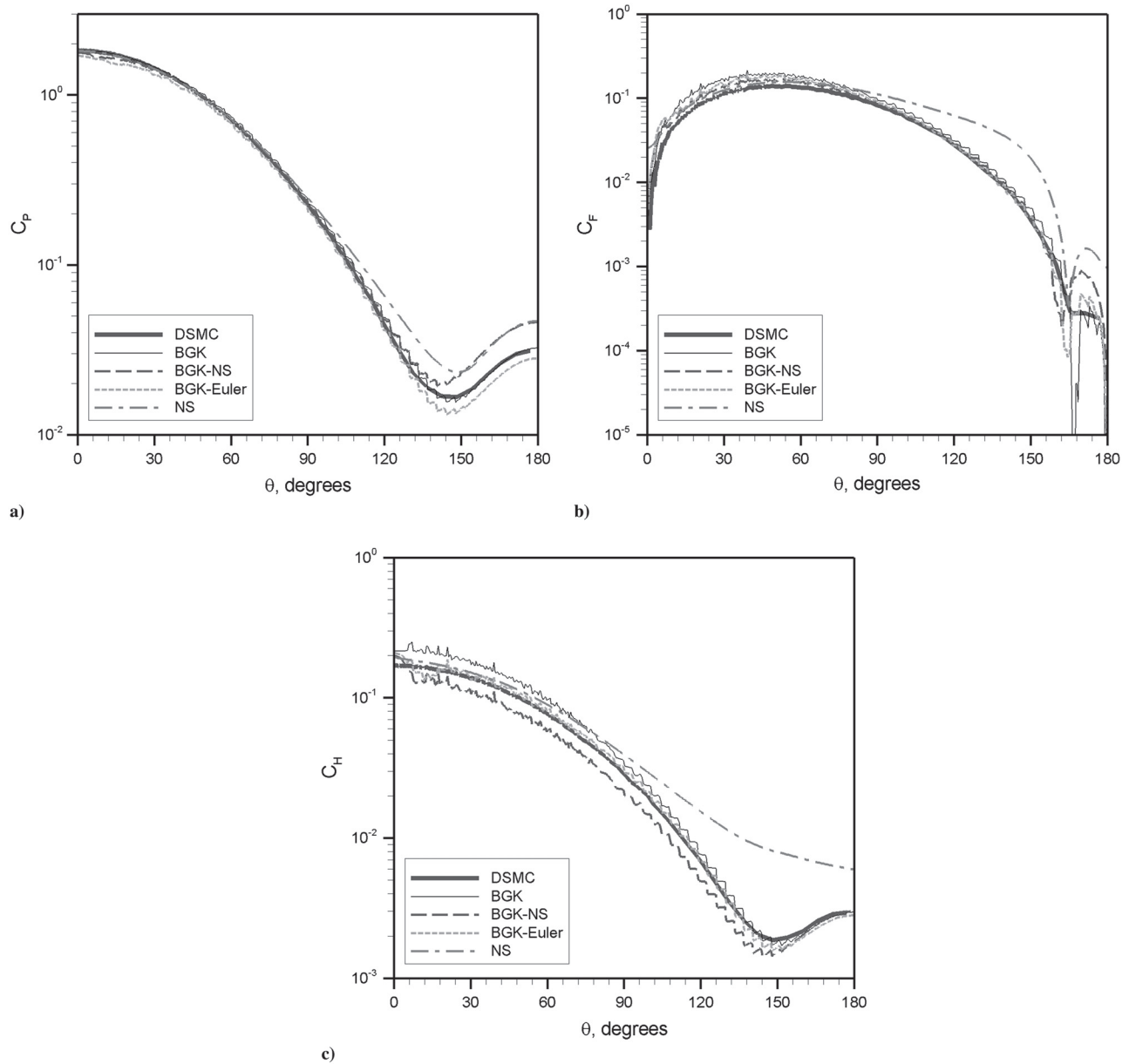
Fig. 11 Surface flux coefficients for $Kn = 0.03$: a) pressure, b) friction, and c) heat transfer. UFS is used for BGK, BGK–NS, and BGK–Euler simulations.

flowfield, and relatively small errors should result from the near-equilibrium assumptions underlying these equations.

In Fig. 14a, contours of normalized bulk velocity magnitude are compared from the two NS simulations at $Kn = 0.003$. Very good overall agreement is found between the two sets of contour lines, with the largest discrepancies observed in the far-field wake region. Differences in the shape of the $V/V_\infty = 0.8$ contour line far from the axis may be attributed to the presence of a UFS symmetry boundary condition at $y = 1$ m. Particularly good agreement is found in the shock layer, with a shock standoff distance based on velocity contours that is approximately 5% larger in the LeMANS simulation than in the UFS simulation. Figures 14b and 14c show contours of normalized density and temperature, respectively, from the $Kn = 0.003$ simulations. In both figures, levels of disagreement are similar to those in Fig. 9c, with the largest discrepancies in the postshock region far from the axis and in the wake.

The variation in bulk velocity, density and temperature along the stagnation streamline is plotted in Figs. 15 for the NS simulations at $Kn = 0.003$. All three figures show very similar trends, with

excellent agreement in postshock values and boundary-layer profiles. However, the LeMANS simulation gives a noticeably thicker shock and a slightly larger shock standoff distance. Based on the location of maximum gradients, the UFS simulation is found to underestimate the shock standoff distance by between 4% and 5% relative to the LeMANS simulation.

The reasonably good overall agreement shown in Figs. 14 and 15 can be seen to indicate that the Xu scheme [18] implementation in UFS and the Steger–Warming scheme [21] implementation in LeMANS both accurately represent the underlying physics of the NS equations, and both provide accurate results over the Knudsen number regimes for which the NS equations are valid. Much of the disagreement observed between LeMANS and UFS NS results in Figs. 14 and 15 can be attributed to the use of different assumptions and approximations between Xu [18] and Steger–Warming [21] schemes. In particular, disagreement in shock thickness may be due to differences in shock-capturing resolution, which are in turn caused by greater numerical diffusion within high pressure gradient regions in the Steger–Warming NS calculations.
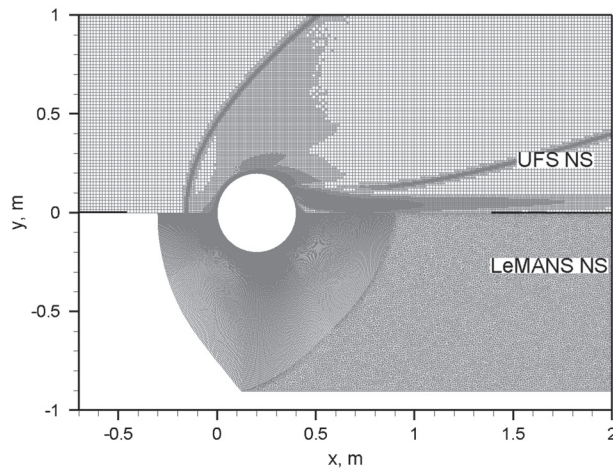
Fig. 12 Meshes for UFS NS and LeMANS NS simulations at $Kn = 0.003$.
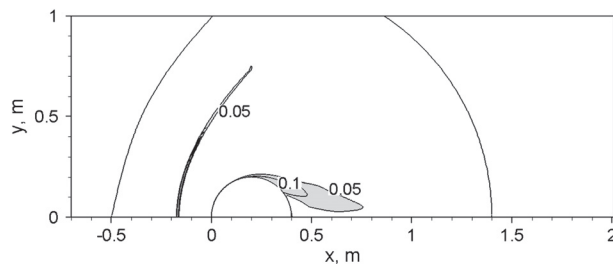
Fig. 13 Contours of the maximum-gradient-length local Knudsen number from the LeMANS simulation at $Kn = 0.003$. Shaded area indicates regions of continuum breakdown.

Fig. 14 Field property contours for $Kn = 0.003$: a) bulk velocity magnitude, b) density, and c) temperature.

VII. Drag Coefficient Comparison

In Fig. 16, drag coefficients C_d calculated from Boltzmann, BGK, DSMC, and NS simulations are plotted as a function of Knudsen number. Data from experiments of Maslach and Schaaf [24] are also included in the figure for comparison. Figure 17 includes data points from a number of additional simulations and is otherwise identical to Fig. 16. Symbols in Fig. 17 labeled "Tratio = 1.2" indicate that the ratio of cylinder wall temperature to freestream temperature is 1.2, as is the case for all simulations described above and included in Fig. 1. Likewise, symbols labeled "Tratio = 4" indicate simulations for which the cylinder wall temperature is four times that of the freestream gas. Several additional simulations using this higher wall temperature have been performed over a wide range of Knudsen number values. Among these added simulations, five are run using the LeMANS NS solver, seven use MONACO, and seven employ the BGK module in UFS. Additional data points, labeled "Boltzmann* Tratio = 4" are taken from published results of UFS Boltzmann simulations by Kolobov et al. [12].

In Fig. 17, the cylinder surface temperature is shown to have little if any noticeable impact on C_d over the full Knudsen number range considered. Generally good agreement is found between UFS Boltzmann, DSMC and measured values even around the maximum Knudsen number of 10. Good agreement is also found between all UFS, DSMC, NS and experimental data for $Kn < 0.1$. At higher Knudsen numbers, however, large overestimates relative to the experimental values are observed in NS C_d predictions, with an overestimate of roughly 70% at $Kn = 1$. Smaller but still significant errors in C_d are shown in BGK results for $Kn > 0.3$, with an underestimate relative to DSMC of about 7% at $Kn = 10$. A noticeable increase with Knudsen-number is found in the level of disagreement between DSMC and BGK results. As no such Knudsen-number-dependent discrepancies are found between DSMC and Boltzmann results, this disagreement may be attributed
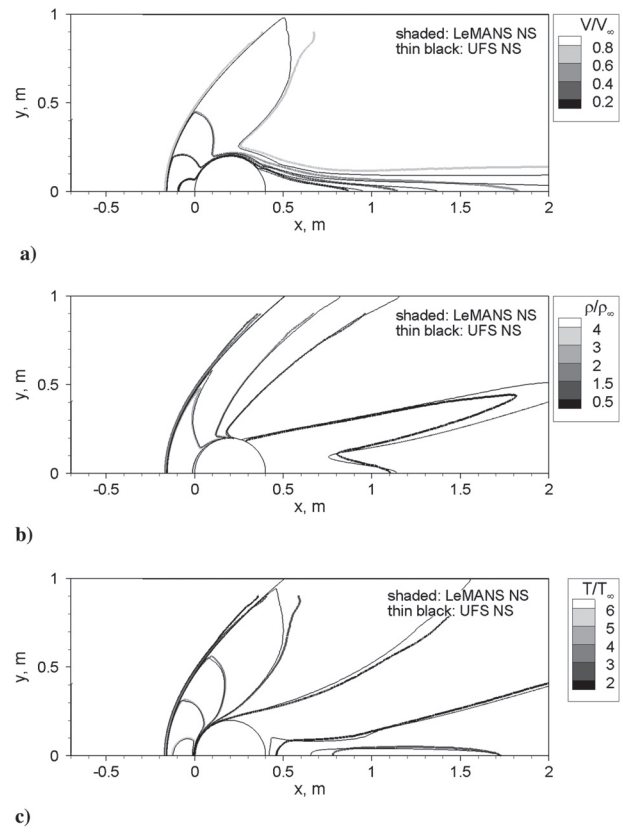
to inaccuracies in the BGK collision integral approximation that become increasingly influential at higher Knudsen numbers.

VIII. Relation of Observed Trends to Discrepancies in Expansion Flow Results

In a recent study of Josyula et al. [14], a rarefied nozzle/plume expansion flow is simulated using both DSMC and the hybrid BGK–Euler option in UFS, and significant differences are observed between the two sets of results. In particular, the centerline density in the plume is overestimated by up to 28% in the UFS simulation. Significant differences are also found in the thickness, position and maximum temperature of the mixing layer, which separates ambient and plume flow regions. Relative to DSMC, the hybrid BGK–Euler simulation is shown to overestimate the mixing-layer thickness based on either density, translational temperature or Mach number contours.

Figure 18, reproduced with permission from [14], shows Mach number contours within the plume from UFS and DSMC simulations. Here, vibrationally excited nitrogen is ejected from a diverging nozzle, with a throat diameter of 0.16 cm and an area ratio of 8, into a low-density ambient background. Among the differences found in a comparison of the upper (UFS) and lower (DSMC) portions of the figure, the UFS simulation gives a significantly thicker mixing layer, higher Mach numbers along both symmetry axes, and reduced Mach numbers along the inner edge of the mixing layer.

Figure 19 shows profiles of translational temperature along a radial plane located 1.15 cm downstream of the nozzle exit. Vertical lines in Fig. 19 denote boundaries between BGK and Euler domains in the UFS simulation. As shown in the figure, the centerline temperature is around 10% higher in the UFS BGK–Euler simulation, the location of maximum translational temperature is slightly further from the centerline in the UFS simulation results, and a wide mixing-layer "tail" projecting radially outward in the DSMC translational
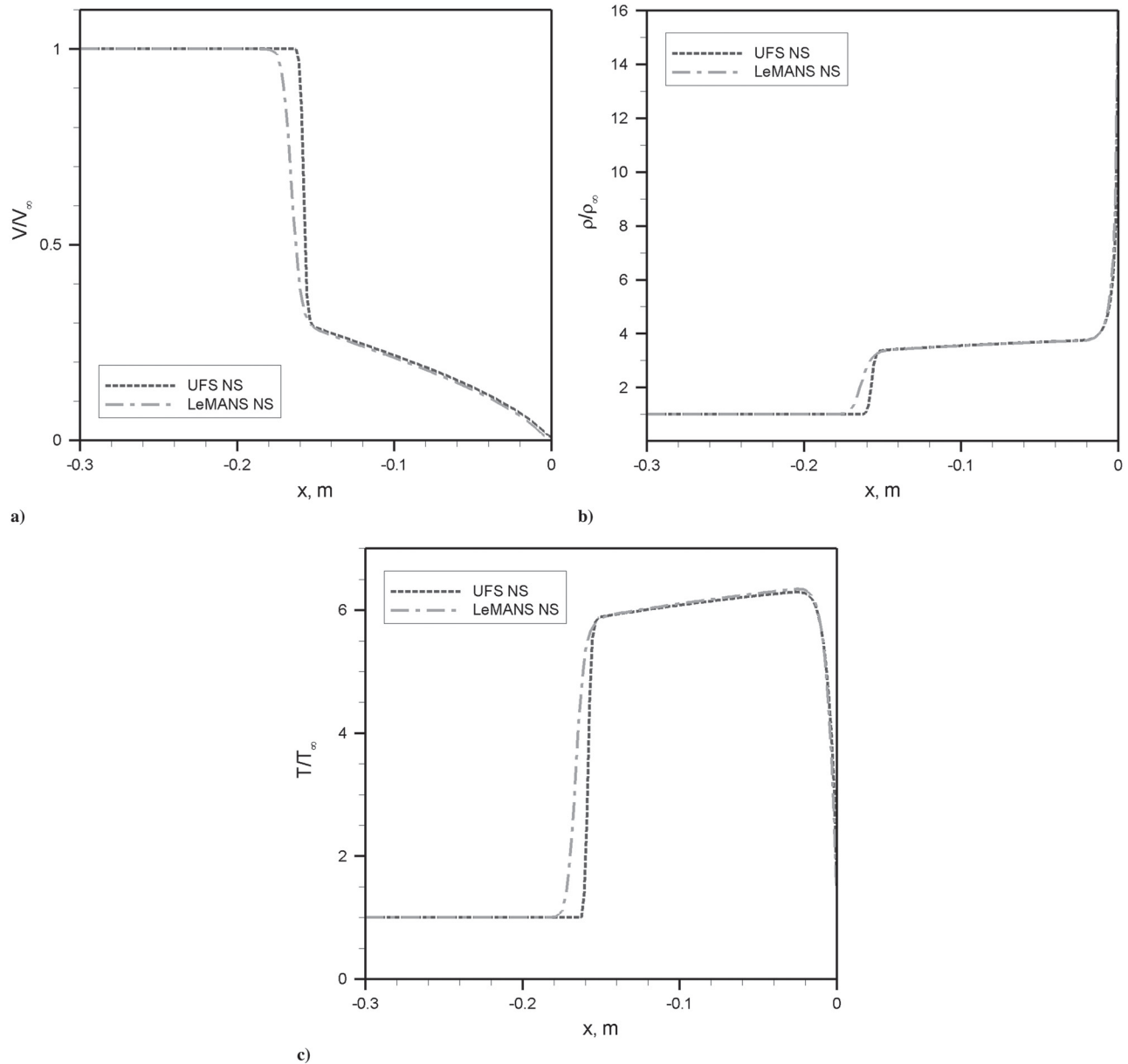
Fig. 15   Property variation along the stagnation streamline for $Kn = 0.003$: a) bulk velocity magnitude, b) density, and c) temperature.

temperature profile is absent in the corresponding profile from the UFS simulation. Although several of these differences are not clearly explained in [14], trends observed in the present study can provide some insight on the causes of the discrepancies.

First, the overestimate of mixing-layer thickness in UFS results of Josyula et al. [14] can be partly explained by numerical diffusion effects in the UFS BGK solver, which are shown to cause an unphysically large shock thickness in Figs. 4 and 10. As found in both the present study and [14], increased numerical diffusion in BGK calculations, relative to full Boltzmann or DSMC calculations, seems to be independent of velocity or spatial grid resolution. Based on comparisons between BGK and Boltzmann results in Figs. 4 and 10, the problem may therefore be attributed to inherent inaccuracy of the BGK equation within high Knudsen number regimes.

The same hybrid BGK–Euler approach used in [14] is also employed here for the $Kn = 0.03$ case, although unlike [14], the current study focuses on a monatomic gas for which no consideration of internal energy relaxation is required. Figures 10a–10c show increased shock standoff distance for the BGK–Euler simulation relative to all other simulations performed for the same flow.

Although the cause of this error is not entirely clear, it may be due to a lack of consideration for physical diffusive transport within the continuum domain, as discussed above. The overestimate in the mixing-layer radial position in BGK–Euler results from [14] may be seen as a qualitatively similar error and is therefore likely attributable to the same cause.

A wide region of elevated temperature is located radially outward from the mixing layer in DSMC results of Josyula et al. [14], but is not present in corresponding BGK–Euler results. [See Figs. 21(b) and 23(b) in [14].] This discrepancy is explained in [14] as an error in DSMC calculations associated with the presence of a nearby freestream inflow boundary. Although the explanation in [14] cannot be discounted, another likely contributor to this discrepancy is the fact that the elevated temperatures are found in a region of very low collision frequency within the Euler domain in the BGK–Euler simulation. As the Euler equations assume an infinitely high collision frequency, any radially outward diffusion of thermal energy from the mixing layer is suppressed in BGK–Euler calculations, and the long mixing-layer tail shown in the DSMC temperature profile should be terminated along the boundary between BGK and Euler domains.
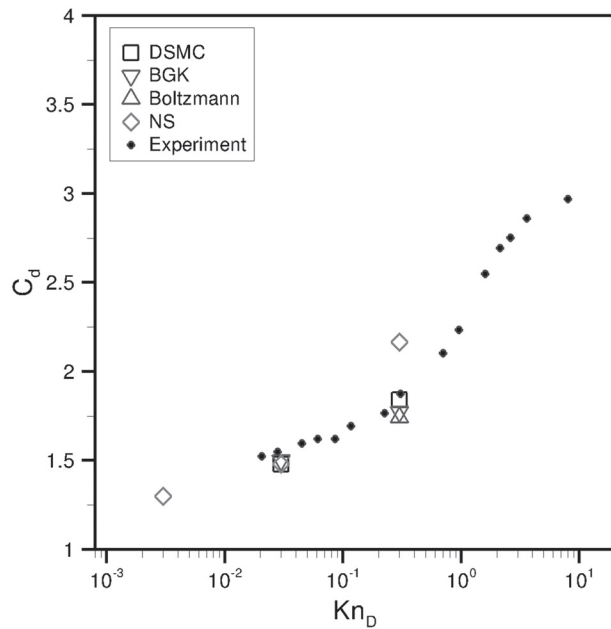
Fig. 16 Variation in drag coefficient with Knudsen number.

A qualitatively similar effect is shown in Fig. 10c, where a sharp cutoff in the temperature boundary layer is observed along the continuum breakdown boundary in BGK–Euler simulation results for the $Kn = 0.03$ case.

IX. Efficiency Comparison

Table 1 shows a summary of numerical parameters for the 12 different UFS, DSMC, and LeMANS simulations that are used to generate the results shown in Figs. 2–15. One important feature in the table is the enormous difference in expense between DSMC and Boltzmann simulations at $Kn = 0.3$. The DSMC simulation for this case requires less than 0.2% of the CPU time needed for the Boltzmann simulation, which corresponds to a difference of over two orders of magnitude in computational expense. Although poor Boltzmann solver efficiency relative to DSMC is expected for a
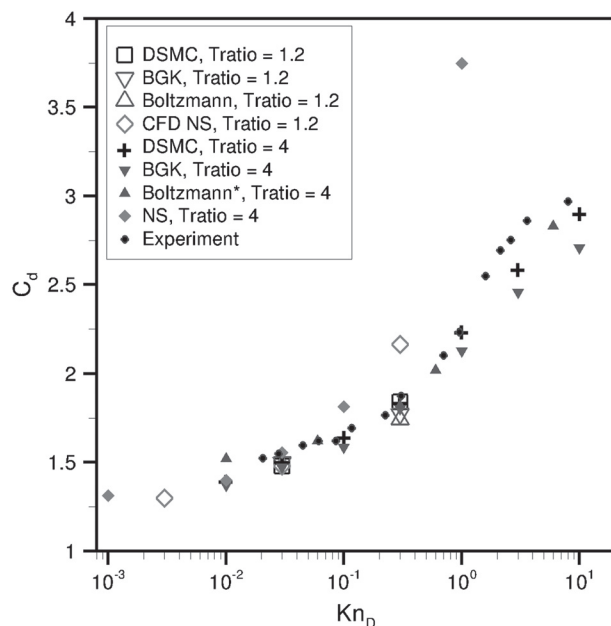
Fig. 17 Variation in drag coefficient with Knudsen number, with results from additional simulations.

a)

b)
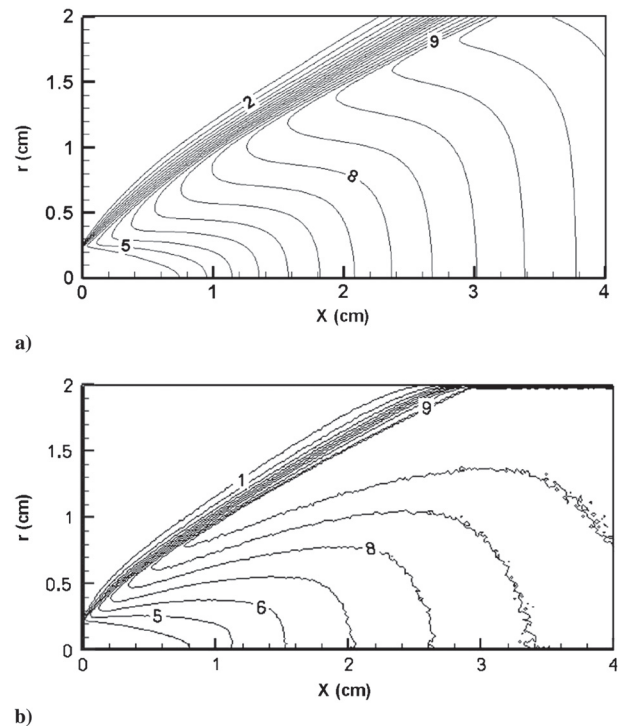
Fig. 18 Plume Mach number contours for UFS BGK–Euler (top) and DSMC (bottom) simulations from [14]. Reproduced with permission.

supersonic flow problem, the magnitude of the difference between DSMC and Boltzmann CPU times is surprising. However, we expect that careful adjustment of the Boltzmann velocity grid domain and refinement level could considerably reduce CPU time for the Boltzmann simulation. Such adjustments would involve balancing various tradeoffs between accuracy and efficiency, which is an active research area [25] but is outside the scope of the present work. As there is currently no systematic technique for velocity grid sizing in a Boltzmann calculation, we have used a velocity grid spacing and domain size conservatively based on standard guidelines as given in UFS documentation.

The very large relative expense of the Boltzmann simulation can be primarily attributed to a few main factors, in addition to the use of potentially nonoptimal velocity grid parameters: First, Boltzmann calculations are performed on a uniform velocity space grid that is not adapted for local efficiency optimization. A relatively large number of nodes are therefore required to adequately approximate
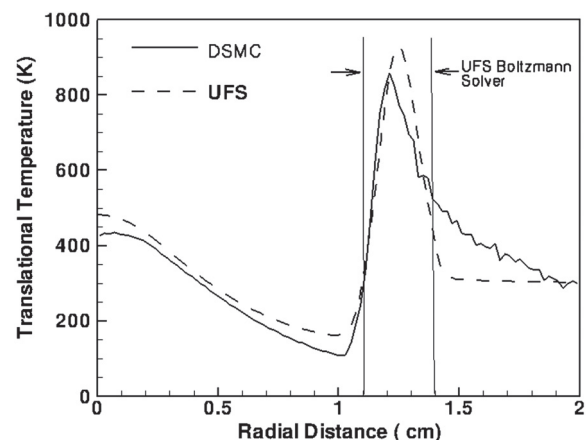
Fig. 19 Translational temperature profiles in the plume for UFS BGK–Euler and DSMC simulations from [11]. Profiles are taken 1.15 cm downstream of the nozzle exit plane. Reproduced with permission.

222

Table 1 Comparison of simulation parameters and CPU time for UFS, MONACO, and LeMANS simulations

Simulation method	Kn	Cells	Velocity space nodes	Particles	CPU h
Boltzmann (UFS)	0.3	6,515	32,000	——	1929.4
BGK (UFS)	0.3	6,605	3,200	——	18.5
NS (LeMANS)	0.3	1,4261	——	——	4.47
DSMC (MONACO)	0.3	3,735	——	107000	3.75
BGK (UFS)	0.03	23,208	3,200	——	66.5
BGK–NS (UFS)	0.03	10,490 (582 NS)	3,200	——	60.0
BGK–Euler (UFS)	0.03	11,271 (874 Euler)	3,200	——	56.5
NS (UFS)	0.03	19,719	——	——	9.88
NS (LeMANS)	0.03	101,959	——	——	41.3
DSMC (MONACO)	0.03	65,189	——	1,860,000	64.3
NS (UFS)	0.003	72,446	——	——	50.9
NS (LeMANS)	0.003	101,959	——	——	48.0

the shape of the velocity distribution within both high- and low-Mach-number regions. In addition, and in contrast to BGK simulations, a three-dimensional velocity grid is required for simulations of a two-dimensional flow. This accounts for the fact that, as shown in the table, 10 times more velocity grid nodes are used in the Boltzmann simulation than in simulations employing the BGK module in UFS.

Another contributing factor for the high computational cost of the Boltzmann solver is increased sensitivity, relative to DSMC, of a discrete velocity Boltzmann simulation to the number of collision operations per time step. A large number of simulated collisions are typically required in Boltzmann calculations for sufficiently small statistical scatter in approximating the velocity distribution function [12]. Factors contributing to the large required number of collisions include a lack of time-averaging for simulation results, optional coupling with NS or Euler calculations in a hybrid simulation and, in particular, the relatively small contributions to the collisional relaxation process for any simulated collision that involves incident velocities in the low-probability tails of the velocity distribution.

As discussed above, numerical solutions to the Boltzmann equation on discrete velocity grids should have comparable accuracy with DSMC and hold potential advantages to DSMC in simulating a variety of rarefied or multiscale gas flows. Discrete velocity Boltzmann methods should be particularly promising for unsteady or subsonic flows, flows for which the tails of the velocity distribution must be characterized with high precision, or cases for which strong coupling with a NS solver is desired. Still, for this particular case it seems reasonable to conclude that DSMC simulation is preferable to simulation using the UFS Boltzmann solver, based on considerations of computational expense.

As shown in Table 1, the DSMC simulation for $Kn = 0.03$ is almost equally expensive as the corresponding BGK simulation, and BGK is roughly five times more expensive than DSMC at $Kn = 0.3$. The apparent increase in relative computational cost for BGK calculations at higher Kn can be attributed almost entirely to Knudsen number dependence in the ratio of cells between BGK and DSMC simulations. Cell size is adapted in BGK and DSMC calculations based, respectively, on flow property gradients and the local mean free path. This leads to somewhat different Knudsen number scaling in the number of cells for BGK and DSMC simulations.

As expected, efficiency gains are found in the hybrid BGK–NS and BGK–Euler simulations in comparison to the full BGK simulation at $Kn = 0.03$, although these gains are smaller than 15% for both hybrid simulations. Given the added complexity of hybrid scheme implementation and the fact that BGK and NS calculations should have comparable accuracy within continuum regions, the similar level of computational expense for BGK and hybrid UFS simulations at $Kn = 0.03$ seems to indicate that hybrid techniques are not preferable for this case.

Computational expense is comparable for UFS NS and LeMANS simulations at $Kn = 0.003$, with fewer cells but more iterations in the UFS simulation. Note that the difference in cell count between these two simulations is due in large part to the use of gradient-based mesh

adaptation in UFS, which allows for larger cells in low-gradient regions. This difference is partially offset by the use of stretched (i.e., high aspect ratio) cells near the cylinder surface in the LeMANS simulation; UFS requires that square cells be used, so far more cells are needed near the surface for similar grid resolution in the surface-normal direction. At $Kn = 0.03$ considerable efficiency gains are found in UFS NS calculations relative to LeMANS, presumably due to a larger difference in cell count between UFS and LeMANS at this higher Knudsen number value.

X. Conclusions

Results have been presented from a series of simulations for hard-sphere monatomic gas flows over a cylinder at a freestream Mach number of 4. A wide range of global Knudsen numbers have been considered, including one case ($Kn = 0.3$) involving strong non-equilibrium over nearly the entire flowfield, a second case ($Kn = 0.03$) involving significant regions of both continuum and rarefied flow, and a third case ($Kn = 0.003$) for which the NS equations are valid over nearly the full simulation domain. These flow problems have been used to evaluate various models and combinations of models in the UFS code and to provide insight on the source of discrepancies found in previous work. Techniques employed in UFS code hold considerable promise for simulating a range of hypersonic gas-flow problems, particularly flows involving strong two-way coupling between rarefied and continuum regions, unsteady multiscale flows with a wide range of local Knudsen number regimes, and other high Knudsen number flows for which the inherent statistical scatter in DSMC is unacceptable or problematic.

As expected, Boltzmann simulation results for the highest Knudsen number case showed excellent overall agreement with DSMC. Large efficiency gains were realized when BGK calculations were used in place of Boltzmann calculations, although BGK simulations were found to give reduced accuracy relative to Boltzmann or DSMC simulations. Much of the error in BGK results is presumably due to underlying approximations in the BGK equation. Additional errors were found in surface quantities computed using either BGK or Boltzmann solvers; these errors are most likely associated with gradient approximations involving cut-cell boundaries and should be reduced or eliminated through implementation of an immersed boundary method in UFS.

A hybrid BGK–NS simulation performed for the $Kn = 0.03$ case showed good overall accuracy, but only small efficiency improvements were demonstrated for this simulation relative to corresponding BGK and DSMC simulations. The added complexity of a hybrid BGK–NS technique may therefore not be warranted for this case. Significantly reduced accuracy was found in a hybrid BGK–Euler simulation for the $Kn = 0.03$ case, demonstrating the importance of diffusive transport effects within continuum regions of this flow. Improved agreement between BGK–Euler and DSMC results is expected if a more conservative continuum breakdown criterion is employed, but results seem to indicate the importance of accounting for viscous effects throughout the simulated flowfield.

An important characteristic demonstrated in this study is the enormous computational expense of the discrete velocity Boltzmann solver in relation to DSMC. The UFS Boltzmann simulation for the $Kn = 0.3$ case was over two orders of magnitude more expensive than the corresponding DSMC simulation. Although computational expense may not be a driving concern for this relatively simple type of problem, the large discrepancy in simulation efficiency implies that, for a given set of computational resources, a DSMC code should be capable of simulating certain more complex rarefied gas flows that would be prohibitively expensive to simulate using the Boltzmann solver in UFS.

The poor relative efficiency of Boltzmann calculations can be primarily attributed to the large number of simulated binary interactions during each iteration, as required for sufficiently low scatter in simulation results. Although DSMC calculations also involve binary collision operations, several important differences exist between DSMC and discrete velocity Boltzmann solvers in both the procedures and characteristics of collision modeling: Most importantly, DSMC particles typically participate in no more than one collision per time step, whereas each velocity grid node in a Boltzmann simulation may be influenced by a large number of binary interactions during each step. This allows for potentially very low scatter in a Boltzmann calculation involving a relatively small number of velocity grid nodes, in contrast to the large expected scatter for a DSMC calculation involving a small number of particles per cell. Although DSMC calculations can achieve arbitrarily low scatter by means of very large particle populations, the additional memory requirements, and the additional computational expense associated with particle movement and cell indexing, generally make the use of large DSMC particle populations impractical as a way to match typical scatter levels in a Boltzmann simulation.

In a second difference between DSMC and Boltzmann collision operations, each binary collision in a Boltzmann calculation influences at least four velocity grid nodes (i.e., two incident velocities and at least two reflected velocities), whereas DSMC binary collisions involve no more than two particles. Additional operations are often required as part of Boltzmann collision procedures in order to enforce conservation of mass, momentum and energy. Third, for faster statistical convergence, Boltzmann collision calculations (including those in UFS) may employ low-discrepancy sequences in place of calls to a random number generator. Fourth, at a given point in velocity space, the frequency of participation in simulated collisions is typically independent of probability density in a Boltzmann simulation but not in DSMC; this tends to result in disproportionately high relative scatter in the tails of a DSMC distribution function. Other differences between DSMC and Boltzmann calculations include the lack of velocity discretization errors in DSMC and the need to define a finite velocity space domain for a Boltzmann simulation.

In comparing attributes and deficiencies between DSMC and the UFS Boltzmann solver, it should be noted that direct numerical simulation of the Boltzmann equation has several advantages over DSMC that in some cases may outweigh any disadvantages in efficiency. In particular, unlike DSMC or hybrid DSMC-CFD techniques, the UFS Boltzmann solver avoids complications associated with large DSMC statistical scatter, with no need for time-averaged sampling and no loss in precision if calculations are immediately stopped once steady-state conditions have been reached. As discussed in the introduction, low scatter is cited as the main reason for employing a Boltzmann solver in UFS, for strongly coupled hybrid calculations of mixed rarefied/continuum gas flows.

Acknowledgments

References

[1] Bird, G. A., *Molecular Gas Dynamics and the Direct Simulation of Gas Flows*, Clarendon Press, Oxford, 1994.

[2] Vincenti, W. G., and Kruger, C. H., *Introduction to Physical Gas Dynamics*, Krieger, Malabar, FL, 1986.

[3] Schwartzentruber, T. E., and Boyd, I. D., "A Modular Particle-Continuum Numerical Method for Hypersonic Non-Equilibrium Gas Flows," *Journal of Computational Physics*, Vol. 225, 2007, pp. 1159–1174.
doi:10.1016/j.jcp.2007.01.022

[4] Wu, J.-S., Lian, Y.-Y., Cheng, G., Koomullil, R. P., and Tseng, K.-C., "Development and Verification of a Coupled DSMC-NS Scheme Using Unstructured Mesh," *Journal of Computational Physics*, Vol. 219, 2006, pp. 579–607.
doi:10.1016/j.jcp.2006.04.013

[5] Kaplan, C. R., Liu, J., and Oran, E. S., "Parallel Hybrid Method for Subsonic Flows: Coupling and Load-Balancing Challenges," AIAA Paper 2006-992, 2006.

[6] Garcia, A. L., Bell, J. B., Crutchfield, W. Y., and Alder, B. J., "Adaptive Mesh and Algorithm Refinement Using Direct Simulation Monte Carlo," *Journal of Computational Physics*, Vol. 154, 1999, pp. 134–155.
doi:10.1006/jcph.1999.6305

[7] Wadsworth, D. C., and Erwin, D. A., "Two-Dimensional Hybrid Continuum/Particle Approach for Rarefied Flows," AIAA Paper 92-2975, 1992.

[8] Hash, D. B., and Hassan, H. A., "Assessment of Schemes for Coupling Monte Carlo and Navier–Stokes Solution Methods," *Journal of Thermophysics and Heat Transfer*, Vol. 10, No. 2, 1996, pp. 242–249.
doi:10.2514/3.781

[9] Xu, K., and Huang, J.-C., "A Unified Gas-kinetic Scheme for Continuum and Rarefied Flows," *Journal of Computational Physics*, Vol. 229, 2010, pp. 7747–7764.
doi:10.1016/j.jcp.2010.06.032

[10] Burt, J. M., and Boyd, I. D., "Extension of a Multiscale Particle Scheme to Near-Equilibrium Viscous Flows," *AIAA Journal*, Vol. 47, No. 6, 2009, pp. 1507–1517.
doi:10.2514/1.40262

[11] Burt, J. M., and Boyd, I. D., "A Hybrid Particle Scheme for Simulating Multiscale Gas Flows with Internal Energy Nonequilibrium," AIAA Paper 2010-820, 2010.

[12] Kolobov, V. I., Arslanbekov, R. R., Aristov, V. V., Frolova, A. A., and Zabelok, S. A., "Unified Solver for Rarefied and Continuum Flows with Adaptive Mesh and Algorithm Refinement," *Journal of Computational Physics*, Vol. 223, 2007, pp. 589–608.
doi:10.1016/j.jcp.2006.09.021

[13] Kolobov, V. I., Bayyuk, S. A., Arslanbekov, R. R., Aristov, V. V., Frolova, A. A., and Zabelok, S. A., "Construction of a Unified Continuum/Kinetic Solver for Aerodynamic Problems," *Journal of Spacecraft and Rockets*, Vol. 42, No. 4, 2005, pp. 598–606.
doi:10.2514/1.10468

[14] Josyula, E., Arslanbekov, R. R., Kolobov, V. I., and Gimelshein, S. F., "Evaluation of Kinetic/Continuum Solver for Hypersonic Nozzle-Plume Flow," *Journal of Spacecraft and Rockets*, Vol. 45, No. 4, 2008, pp. 665–676.
doi:10.2514/1.35431

[15] Arslanbekov, R. R., Kolobov, V. I., Frolova, A., Zabelok, S., and Josyula, E., "Evaluation of a Unified Kinetic/Continuum Solver for Computing Heat Flux in Hypersonic Blunt Body Flows," AIAA Paper 2007-4544, 2007.

[16] Dinavahi, S., and Josyula, E., "Simulation of Mach 3 Cylinder Flow Using Kinetic and Continuum Solvers," *Department of Defense HPCMP User Group Conference*, San Diego, CA, 2009.

[17] Popinet, S., "Gerris: A Tree-Based Adaptive Solver for the Incompressible Euler Equations in Complex Geometries," *Journal of Computational Physics*, Vol. 190, 2003, pp. 572–600.
doi:10.1016/S0021-9991(03)00298-5

[18] Xu, K., "A Gas-Kinetic BGK Scheme for the Navier–Stokes Equations and its Connection with Artificial Dissipation and Godunov Method," *Journal of Computational Physics*, Vol. 171, 2001, pp. 289–335.
doi:10.1006/jcph.2001.6790

[19] Dietrich, S., and Boyd, I. D., "Scalar and Parallel Optimized Implementation of the Direct Simulation Monte Carlo Method," *Journal of Computational Physics*, Vol. 126, 1996, pp. 328–342.
doi:10.1006/jcph.1996.0141

[20] Scalabrin, L. C., and Boyd, I. D., "Development of an Unstructured Navier–Stokes Solver for Hypersonic Nonequilibrium

Aerothermodynamics," AIAA Paper 2005-5203, 2005.

[21] Laney, C. B., *Computational Gasdynamics*, Cambridge Univ. Press, Cambridge, England, U.K., 1998.

[22] Wang, W., and Boyd, I. D., "Predicting Continuum Breakdown in Hypersonic Viscous Flows," *Physics of Fluids*, Vol. 15, No. 1, 2003, pp. 91–100.
doi:10.1063/1.1524183

[23] Lofthouse, A. J., "Hypersonic Blunt Body Thermophysics Using a Unified Kinetic/Continuum Solver," AIAA Paper 2009-3838, 2009.

[24] Maslach, G. J., and Schaaf, S. A., "Cylinder Drag in the Transition from Continuum to Free-Molecule Flow," *Physics of Fluids*, Vol. 6, No. 3, 1963, pp. 315–321.
doi:10.1063/1.1706736

[25] Josyula, E., Xu, K., Suchyta, C. J., and Bailey, W. F., "Kinetic Methods for Solving the Internal Structure of Shock Waves," AIAA Paper 2009-3841, 2009.

Approved for public release; distribution unlimited.

**51st AIAA/ASME/ASCE/AHS/ASC Structures, Structural Dynamics, and Materials Conference
**
12 - 15 April 2010, Orlando, Florida

AIAA 2010-2715

X-HALE: A Very Flexible UAV for Nonlinear Aeroelastic Tests

Carlos E. S. Cesnik[1], Patrick J. Senatore[2], Weihua Su[3], Ella M. Atkins[4]
The University of Michigan, Ann Arbor, MI, 48109-2140

Christopher M. Shearer[5]
U.S. Air Force Institute of Technology, Wright-Patterson AFB, OH, 45433-7765

and

Nathan A. Pitcher[6]
U.S. Air Force Research Laboratory, Wright-Patterson AFB, OH, 45433-5543

The University of Michigan has designed and is currently building an unmanned aerial vehicle, denoted X-HALE, which is aeroelastically representative of very flexible aircraft. The objective of this test bed is to collect unique data of the geometrically nonlinear aeroelastic response coupled with the flight dynamics to be used for future code validation. The aircraft will present specific aeroelastic features (e.g., coupled rigid/elastic body instability, large wing deflection during gust, etc.) that can be measured in flight. Moreover, the airframe construction choice is such that the elastic, inertial and geometric properties can be well characterized. These are requirements driven by the need of the collected data to be used to support validation of coupled nonlinear aeroelastic/flight dynamics codes.

I. Introduction

RECENT advances in airborne sensors and communication packages have given us the opportunity to place them at high-altitudes and for long periods of time. The missions include airborne intelligence, surveillance, and reconnaissance (ISR) for the military;[1] network communication nodes for the military and civilian usage; and general atmospheric research.[2] Because of the mission requirements, the aircraft platforms are characterized by high-aspect-ratio wings and, if existent, slender fuselages, resulting in very flexible vehicles. Improved mission capabilities such as longer loiter times, heavier payload, greater range, etc. drive the demand for greater aerodynamic performance on those systems. Enhanced airframe performance is generally achieved through lightweight, flexible solutions. Modern high-altitude long-endurance (HALE) aircraft designs have become so lightweight and flexible that traditional (linear) design methods are no longer adequate and nonlinear aeroelastic design methods are required to characterize structural and aeroelastic designs (Ref. 20). The wings may undergo large deformations during normal operating loads, exhibiting geometrically nonlinear behavior (Fig. 1).

In the last several years, the US Air Force has been working on a new generation Intelligence, Surveillance, and Reconnaissance (ISR) platform called "Sensorcraft." These are large HALE aircraft, with wing span of approximately 60 m. Three basic platform shapes have been considered: wing-body-tail, single-wing and joined-wing configurations[1] (see Fig. 2). For high structural performance as required for long loiter times, these configurations will lead to generally very flexible aircraft. These flexibility effects may make the response of the vehicle very different from its rigid or linearized models.[10] Engineering analysis on very flexible vehicles will need to include geometrically-nonlinear structural models for the primary structures in order to capture any large deformations that may appear under operational loads. In addition to large deformations, a second characteristic of very flexible aircraft will be very low frequencies of their natural structural vibration modes. Due to this, it should

---

[1] Professor (cesnik@umich.edu), Department of Aerospace Engineering, Associate Fellow, AIAA.

[2] Research Assistant (senatorp@umich.edu), Department of Aerospace Engineering, Member, AIAA.

[3] Post-doctoral Research Fellow (suw@umich.edu), Department of Aerospace Engineering, Senior Member, AIAA.

[4] Associate Professor (ematkins@umich.edu), Department of Aerospace Engineering, Associate Fellow, AIAA.

[5] Lt. Colonel, USAF (christopher.shearer@afit.edu), Dept. of Aeronautics and Astronautics, Member, AIAA.

[6] Captain, USAF (nathan.pitcher@wpafb.af mil), Vehicles Directorate, RBAA.

1
American Institute of Aeronautics and Astronautics

Approved for public release; distribution unlimited.

be expected a strong coupling between the structural dynamics and the rigid-body (flight dynamics) characteristics of the vehicle.
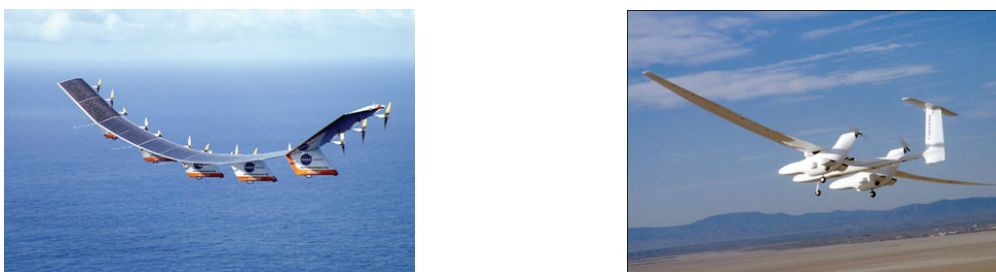
Figure 1. Aerovironment's Helios (left) and Aurora Flight Sciences' Theseus (right) showing large wing deflections (Courtesy NASA Dryden)

Figure 2. Three different "Sensorcraft" configurations[1]

More recently, Aurora Flight Sciences, Boeing Co., and Lockheed-Martin Co. have developed extreme-long duration HALE concepts[4] The combination of high aerodynamic efficiency and low structural weight fraction yields inherently flexible wings and nonlinear structural and flight dynamics. HALE aircraft are expected to be susceptible to large dynamic wing deformations at low frequencies, presenting a direct impact into the flight dynamic characteristics of the vehicle, as was seen in the Helios flight tests[3]. On 26 June 2003, NASA's Helios aircraft[3]:

HP03-2 took off at 10:06 a.m. local time from the Navy Pacific Missile Range Facility (PMRF) located on the island of Kauai, Hawaii. . . . At 10:22 a.m. and 10:24 a.m., the aircraft encountered turbulence and the wing dihedral became much larger than normal and mild pitch oscillations began but quickly damped out. At about 30 min into the flight, the aircraft encountered turbulence and morphed into an unexpected, persistent, high dihedral configuration. As a result of the persistent high dihedral, the aircraft became unstable in a very divergent pitch mode in which the airspeed excursions from the nominal flight speed about doubled every cycle of the oscillation. The aircraft design airspeed was subsequently exceeded and the resulting high dynamic pressures caused the wing leading-edge secondary structure on the outer wing panels to fail and the solar cells and skin on the upper surface of the wing to rip off. The aircraft impacted the ocean within the confines of the PMRF test range and was destroyed. . . . The root causes of the mishap include: [A] lack of adequate analysis methods led to an inaccurate risk assessment of the effects of configuration changes leading to an inappropriate decision to fly an aircraft configuration highly sensitive to disturbances . . . [and] configuration changes to the aircraft, driven by programmatic and technological constraints, altered the aircraft from a spanloader to a highly point-loaded mass distribution on the same structure significantly reducing design robustness and margins of safety.

2
American Institute of Aeronautics and Astronautics

The Helios accident highlighted our limited understanding and limited analytical tools necessary for designing very flexible aircraft and to potentially exploit aircraft flexibility. The number one root cause/recommendation from NASA[3] was

> "[that] more advanced, multidisciplinary (structures, aeroelastic, aerodynamics, atmospheric, materials, propulsion, controls, etc.) time-domain analysis methods appropriate to highly flexible, morphing vehicles [be developed]."

Nonlinear aeroelastic solvers have been under development to improve predictions of aircraft response, stability and overall performance[5-14]. The body of work in the literature associated with the problem of nonlinear aeroelasticity coupled with nonlinear flight dynamics started developing at earnest in the 1990's. Without attempting to be comprehensive, what follows highlights some of the key contributions in the field, and more detailed review can be found in Refs. 10 and 11.

Early nonlinear aeroelastic work in very flexible aircraft was conducted by van Schoor and von Flotow[25]. Their work demonstrated the critical importance of including aircraft structural dynamics when analyzing aircraft flight dynamics of very flexible aircraft. They showed, using linearized analysis about nonlinear equilibrium points, a significant change in the classic rigid-body modes when flexible structural modeling is included. This leads to the conclusion that the coupled effects between these large deflection and vehicle flexibility and flight dynamics (e.g., roll controllability) as well as other aeroelastic effects (e.g., gust response, flutter instability) must be properly accounted for in a nonlinear aeroelastic formulation. Patil, Hodges, and Cesnik[12] studied the aeroelasticity and flight dynamics of HALE aircraft. The results indicate their behavior can be significantly changed due to the large deflection of the flexible wings. Moreover, a linear aeroelastic analysis based on the undeformed geometry may lead to errors when the wings are highly flexible. That study also shows a significant difference between the short period and phugoid modes of a very flexible aircraft when comparing rigid-body, linear aeroelastic, and nonlinear aeroelastic dynamics. The short period and phugoid modes were obtained by linearizing the nonlinear dynamics about a nonlinear equilibrium. In a parallel effort, Drela[6] modeled a complete flexible aircraft as an assemblage of joined nonlinear beams. In his work, the aerodynamic model was a compressible vortex/source-lattice with wind-aligned trailing vorticity. The nonlinear equation was solved by using a full Newton method. Through simplifications of the model, the computational size was reduced for iterative preliminary design. Jones and his co-workers[26, 27] have also worked on the design of HALE. In their work, they described some design challenges associated with these vehicles. From their conclusion, it is shown that standard aircraft design techniques are no longer applicable for these high-aspect-ratio wings.

Besides the work described above, Cesnik and his co-workers have developed a novel and practical solution to the coupled nonlinear aeroelasticity and flight dynamics of very flexible aircraft. Focusing on a reduced number of states to represent the complex nonlinear problem, the framework, named the University of Michigan's Nonlinear Aeroelastic Simulation Toolbox (UM/NAST), provides a suitable plant representation for control design. Several aeroelastic issues in high-altitude long-endurance aircraft have been addressed: nonlinear aeroelastic modeling,[8, 10] integral wing actuation for generating maneuver loads,[22, 23] flutter boundary enhancement[24] gust load alleviation,[21] and overall nonlinear vehicle optimization of unconventional configurations.[22]

All these numerical efforts must eventually be validated against experimental data so they can be applied to new HALE aircraft concepts. The various components of most of the existing codes have been partially validated with limited experimental data coming from bench (*e.g.*, Refs.15-17) and/or small-scale wind tunnel tests (*e.g.*, Refs. 18 and 19). Some of the discipline components have also been compared against well-established numerical solutions (*e.g.*, nonlinear composite beam analyses, rigid flight dynamics, and computational fluid dynamics). However, there has been no validation of the integrated solution that brings the coupling effects between nonlinear aeroelasticity and flight dynamics, since no data is available for such exercise.

This paper describes the on-going effort to design and build a nonlinear aeroelastic test bed, named X-HALE, for test flights. The design and manufacturing of this vehicle is being conducted at the University of Michigan in collaboration with the Air Force Institute of Technology and the Air Force Research Laboratory. This will have multiple test beds from which experimental coupled nonlinear aeroelastic and flight dynamic data will be generated and made available to the community in support of the validation of nonlinear aeroelastic solvers. The following sections discuss in details the design and its expected main aeroelastic characteristics.

II.   Systems Design, Integration, and Fabrication

The primary purpose of X-HALE is to validate nonlinear aeroelastic and flight simulation software. To satisfy this, the systems design and layout must produce an airframe that is consistent and measurable in both real and simulated flight. This is the most unique and challenging aspect of the X-HALE concept as it complicates three of X-HALE's primary subsystems: the wing structure, electronics, and software. Structurally, the wing must be idealized and fabricated as a consistent composite beam to create a representative simulated model. To gather the required strain, control input, and flight condition data a complex array of sensors and supporting data acquisition hardware and software must be integrated without impacting the wing's structural properties. This section will describe the composition of the X-HALE airframe and the integration methods used to guarantee similar flight and simulated platforms.

A. Airframe Layout

The X-HALE is a flexible, high aspect ratio wing-boom-tail type aircraft. It has an 8-m span (constructed with eight identical 1-m sections), 0.2-m chord, four 0.83-m booms with horizontal tails attached, and five motor pods with propellers, batteries, and processor boards (Fig. 3). X-HALE has a mass of 11 kg with an anticipated flight speed ranging from 10 to 19 m/s. Main vehicle sizing characteristics are given in

Table 1. Pitch and roll will be controlled by the horizontal elevons and yaw will be controlled using differential thrust from the motors. Disturbances will be applied with schedule all-movable horizontal tail deflections supplemented by ailerons on the dihedral outer wing sections. Those disturbances will excite wing deformation during flight, and its response will be recorded from a series of on-board sensors. Those sensors are a collection of IMU, strain gages, and accelerometers.
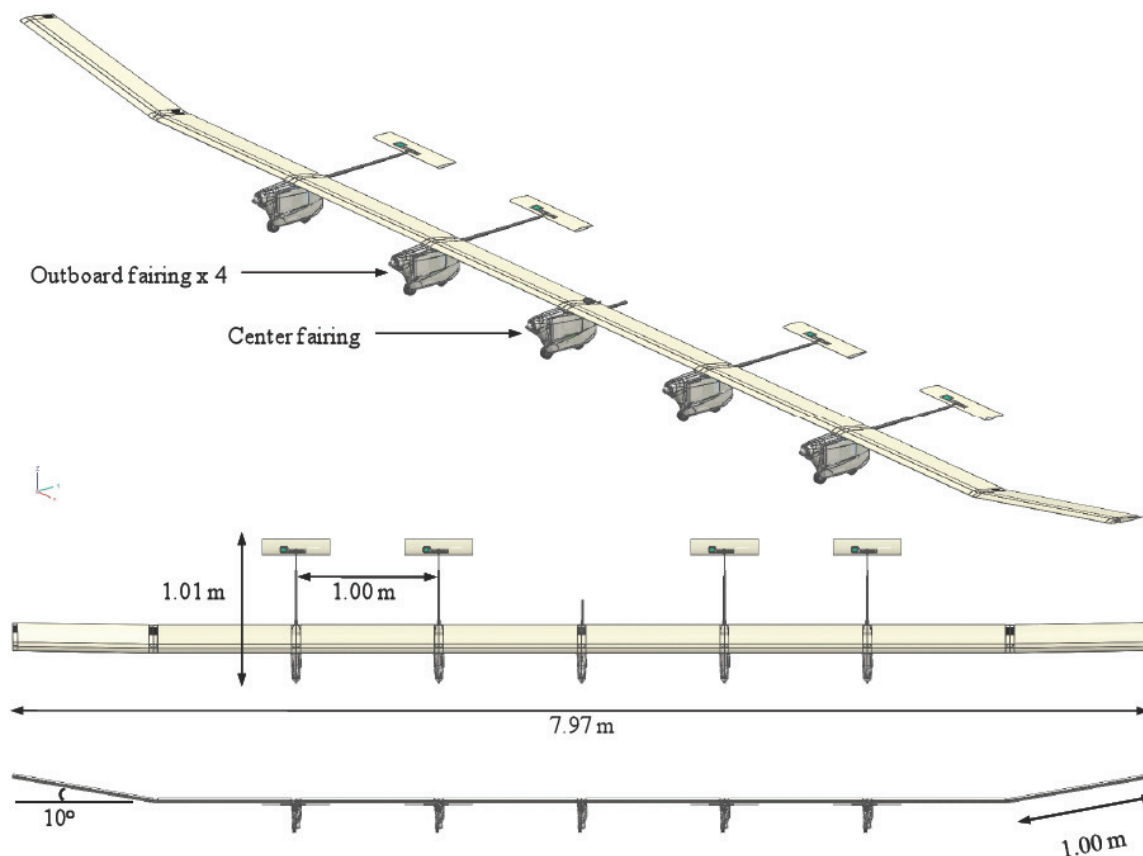
Figure 3. Complete X-HALE CAD assembly: isometric, top, and front views

4
American Institute of Aeronautics and Astronautics

Table 1. X-HALE SUAS main characteristics.

Wing Span	8	m
Chord	0.2	m
Platform Area	1.6	m^2
Aspect Ratio	40	--
Length	0.96	m
Propeller Diameter	0.30	m
Max Payload	7.2	kg
Max Gross Takeoff Weight	11.1	kg
Power/Weight	25.5	W/kg
Airspeed	10 – 19	m/s
Endurance	45	min

Five fairings are suspended at the joint of the six inboard sections. The four outboard fairings are modular, *i.e.*, outfitted with identical hardware and electronics. Each contains a Diamond Systems PC104 stack of an Athena II and DMM I/O expansion card for analog to digital conversion and data acquisition. The four outboard fairings also independently control elevons for pitch authority. The central fairing houses the ground station communication system and a Microbotics MIDG GPS/INS reference system. Additionally, the central fairing controls all RC command conditioning, onboard mixing, and autopilot mode control using a Microbotics Servo Switch/Controller (SSC). Each fairing is powered with two lithium polymer batteries: an 11.1 V/1320 mAh electronics battery, and an 11.1 V/6000 mAh motor battery to power each of the 18W electric outrunner motors. The outboard motors are capable of differential control to enable vehicle yaw. This overall layout and the primary components within each fairing type are displayed in Figs. 4 and 5.
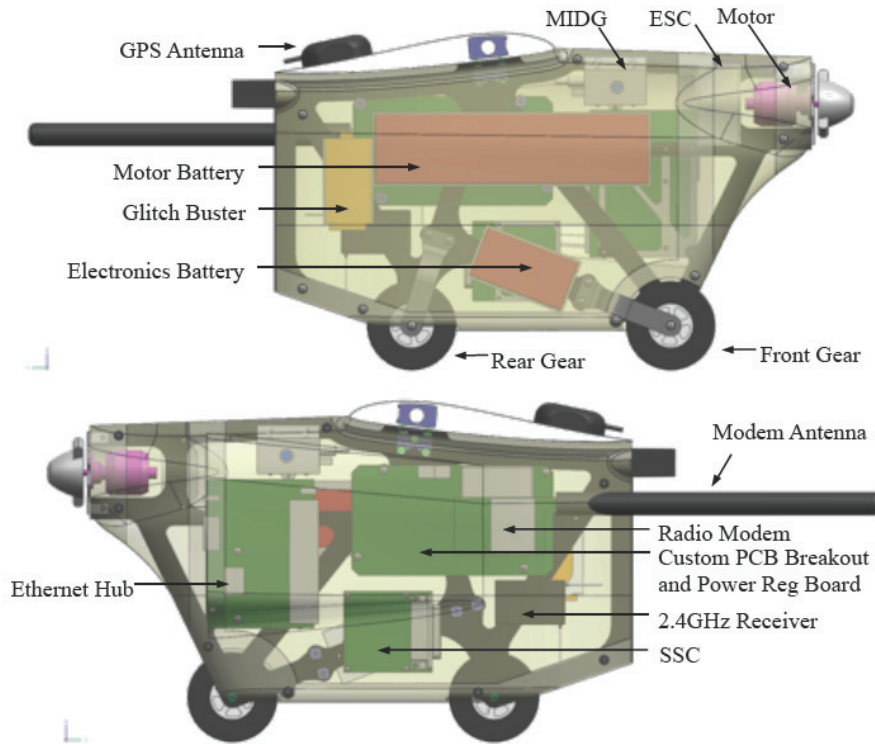
Figure 4. Central fairing assembly

5
American Institute of Aeronautics and Astronautics
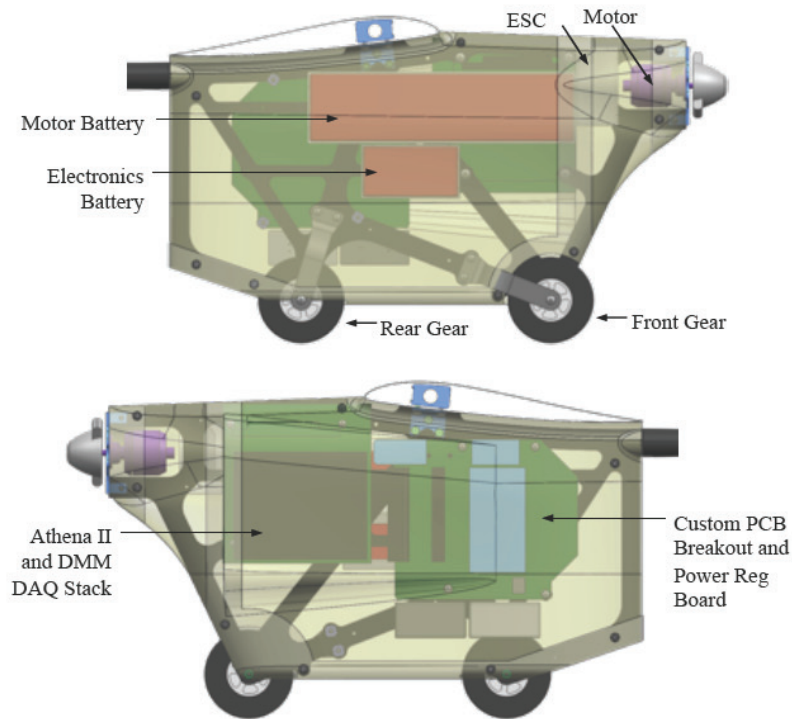
Figure 5. Outboard fairing assembly

Components within each fairing are mounted to a central graphite/epoxy spine. The spine itself is connected to the wing box through custom aluminum L-brackets and joiner located within the wing box of each wing section. This transfers all loads from the fairing through the connection to the wing box only. Finally, the internal components are protected by glass/epoxy skins that are also mounted to the main spine through standoffs and recessed screws. Ram-air intakes designed into the skins profile cool both the motor and primary electronics, such as the Athena II computer and power regulation circuitry, during flight. The rear-flared portion of the skin is also left open to provide an exit vent for the heated air. The skin is identical for each fairing, while the central spine is unique to common outboard fairings. The assembly of the internal fairing structure, skin, and wing joiner is displayed in Fig. 6.
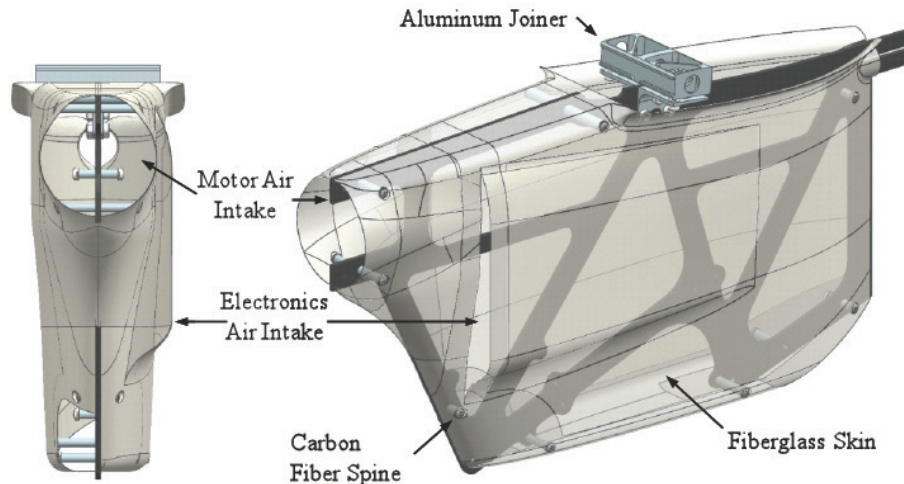
Figure 6. Fairing structure

6
American Institute of Aeronautics and Astronautics

B. Airfoil Selection and Characteristics

Originally, the X-HALE design was inspired by previous HALE aircraft such as Aerovironment's Helios. As a result, the original airframe was a flying wing, which led to reflex type airfoils. Trading C_{m0}, stall angle, and L/D, the final choice was to use the EMX07 reflexed airfoil, displayed with its pressure profile in Fig. 7. Once the design progressed, horizontal tails became an alternative to placing control surfaces within the uniform wing structure. NACA 0012 airfoils were chosen because of the standard behavior of the symmetric airfoil.

EMX 07   Reflexed Profile   NACA 0012
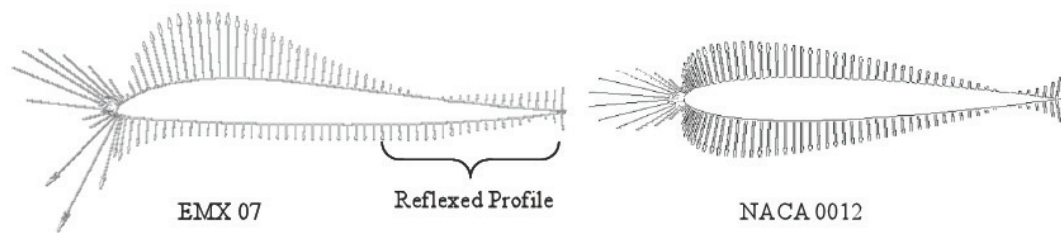
Figure 7. Wing and tail airfoil profiles

With a chord of 0.2 m and 0.12 m, respectively, the wing and tail Reynolds numbers are low, ranging from 150,000 to 93,000 at a 14 m/s reference cruise velocity. This has an effect on the aerodynamic derivatives of each airfoil, but is much more significant for the NACA 0012. Figures 8 and 9 display the basic aerodynamic coefficients for each airfoil at the operating Reynolds number (150,000). Along with those, results for a high Reynolds number of 1,500,000 are included just for comparison. The results displayed in Figs. 8 and 9 show how important it is to provide custom aerodynamic data to a design and/or analysis codes to produce realistic simulation results. Standard aerodynamic derivatives such as 2π for $c_{l\alpha}$ are no longer valid especially for the NACA 0012, which ranges from 4.4 to 12 depending on the angle of attack. This dependence on angle of attack is translated into our UM/NAST simulations through look-up tables and calibration functions in order to produce the most realistic simulation results. Table 2 and Table 3 display the resulting aerodynamic derivatives for both airfoils. All these data were calculated using XFOIL. Two-dimensional wind tunnel tests are under way to verify the validity of these properties for the as-manufactured wing and tail sections.
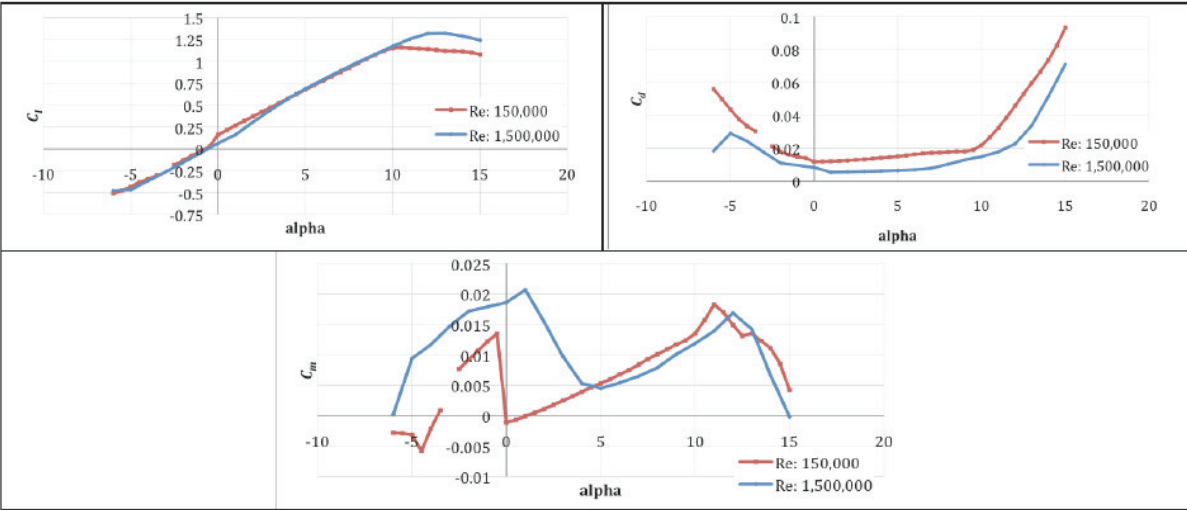
Figure 8. EMX07 airfoil to be used in the main wing (results obtained using XFOIL)
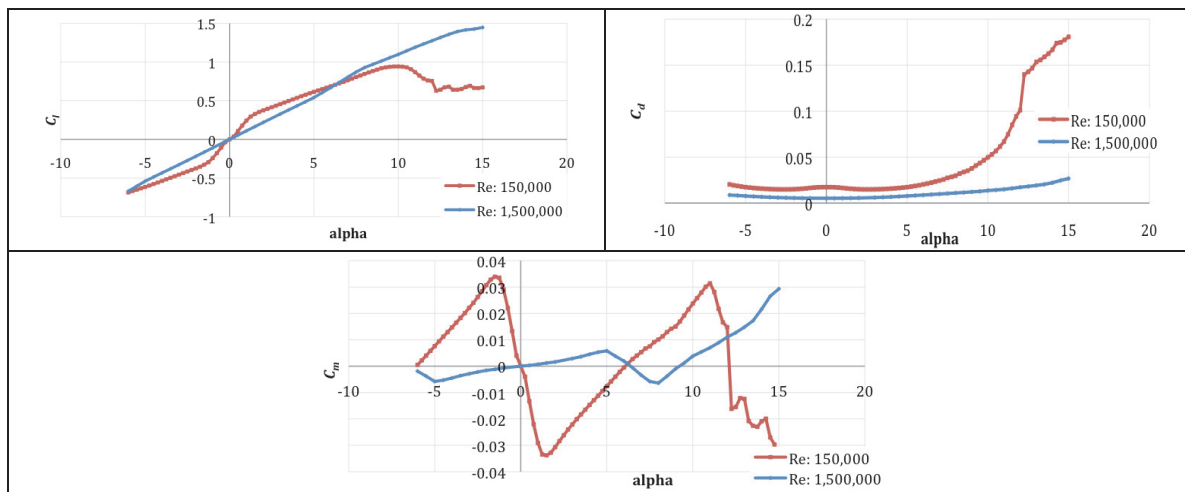
Figure 9. NACA 0012 airfoil to be used in the horizontal tail (results obtained using XFOIL)

Table 2. EMX07 Aerodynamic Derivatives @ Re = 150,000

EMX07	c_l	c_d	c_m
Range (AOA)		*< -0.5*	
$dc_x/d\alpha$	5.8034	-0.4260	0.1641
c_{x0}	0.0717	0.0065	0.0150
Range (AOA)		*(-0.5 to 10)*	
$dc_x/d\alpha$	5.8034	0.0402	0.0815
c_{x0}	0.1630	0.0119	-0.0011
Range (AOA)		*> 10*	
$dc_x/d\alpha$	-0.2521	0.7739	-0.2020
c_{x0}	1.1944	-0.1162	0.0572

Table 3. NACA 0012 Aerodynamic Derivatives @ Re = 150,000

NACA 0012	c_l	c_d	c_m
Range (AOA)	*0 to 1.5*		*0 to 1.5*
$dc_x/d\alpha$	12.0145		-1.2930
c_{x0}	0.0000		0.0000
Range (AOA)	*1.5 to 10*	*0 to 10*	*1.5 to 10*
$dc_x/d\alpha$	4.4746		0.4119
c_{x0}	0.2240	0.0160	-0.0435
A		32.400	
B		-1.306	
C		-0.024	
Range (AOA)		*> 10*	
$dc_x/d\alpha$	0.0000	1.6085	-0.8318
c_{x0}	0.6000	-0.2359	0.1850

8
American Institute of Aeronautics and Astronautics

C. Wing Design and Fabrication[†]

The purpose and challenge for X-HALE is to prototype and study the behavior of high wing flexibility inherent in HALE aircraft through experiment and theory. These inspire multiple design requirements for the wing structure, which include:

- A predictable and controlled cross-sectional properties
- The use of lightweight, flexible, but strong materials
- The ability to be disassembled the vehicle due to transportation and manufacturing constraints
- The structural behavior of a uniform beam despite a modular design

As a result both materials and manufacturing processes are selected and prototyped to satisfy these criteria.

Prepreg composites are used as the primary structural material because of their lightweight, controlled, and documented material properties. The main wing structure is composed of a wing box made from Hexcel E-glass 120/F155 prepreg fabric wrapped around a Rohacell 31-IG high temperature foam core. The wing box includes five continuous layers of E-glass in a 0/90 orientation to provide a robust thickness to the structure. To finish the airfoil profile, additional foam is added to leading and trailing edge and wrapped with a final layer of 0/90 e-glass. This layup composes the majority of the wing and can be visualized in Section B-B and Detail D of Fig. 10. However, 3.18cm (3.18%) from either end of the wing section contains a different layup. This layup includes layers of IM7/977-3 graphite/epoxy unidirectional tape to reinforce and complete the internal geometry of the wing joint, which is shown in Section A-A and Detail C and will be described later. Further details on the layup can be found in Table 4.
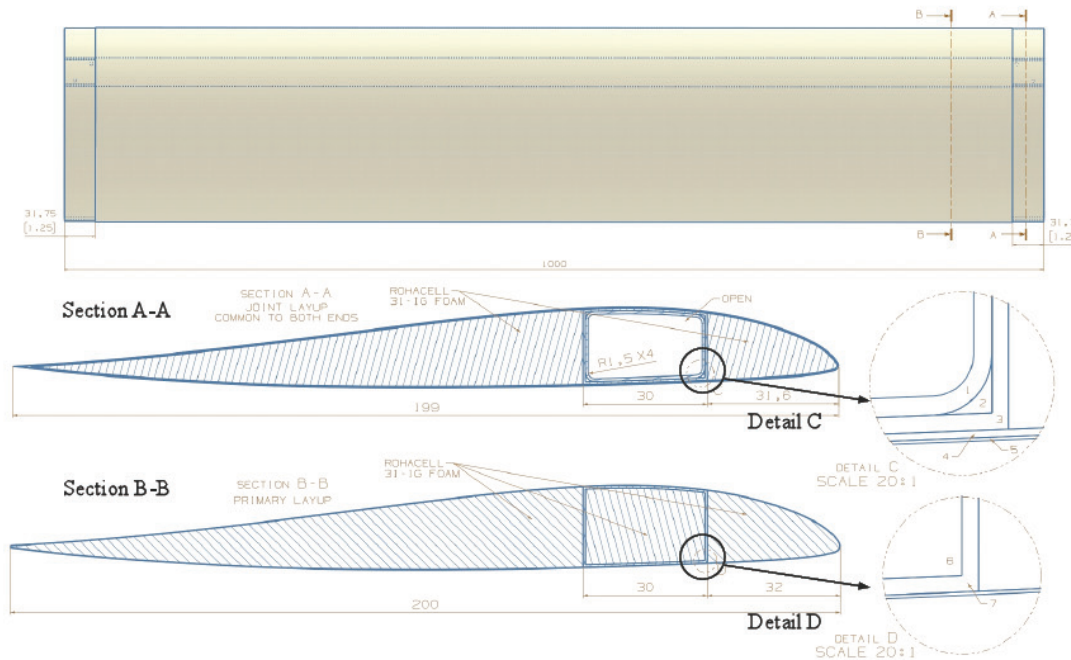
Figure 10. Primary wing layup cross section

Because the layup in section A-A only takes up about 3% of the total mass wing section span, it is not accounted for in the simulation input that will be detailed later in Section III. The purpose of it in our physical model is to create a robust wing joint layup that can easily withstand inertial and landing loads from the fairings.

Meticulous attention has also been given to the fabrication and flight hardware used at each joint. The joint is designed to transfer bending loads through the wing box and torsional loads through the shear skin. Therefore, it must be made with tight tolerances to ensure a uniform load transfer. With this is mind, the inspiration for the current wing box joint hardware is simplicity as it is composed of a single machined aluminum component (Fig. 11). Within this single piece of hardware we have the ability to join both wing sections, fasten the fairing structure, and

---

[†] Although on what follows only the wing is described, similar manufacturing procedure is used for the horizontal tails.

9
American Institute of Aeronautics and Astronautics

234

Approved for public release; distribution unlimited.

route any internal wing wiring without hindering the ability to remove or replace any single primary component. Furthermore, the joiner is machined to match the profile of the aluminum mold insert used to layup and align the internal wing box geometry.

Table 4. Composite Layup Legend for Detail C and D

Label	Plies	Material	Thickness (mm)	Orientation*
1	5	E-Glass 120/F155	0.12	90,90,90,90,90
2	n/a	IM7/977-3 Dowel	1. (diameter)	0
3	5	E-Glass 120/F155	0.12	0,0,0,0,0
4	2	IM7/977-3 Tape	0.137	0,0
5	1	E-Glass 120/F155	0.12	0
6	5	E-Glass 120/F155	0.12	0,0,0,0,0
7	1	E-Glass 120/F155	0.12	0

*0 is along wing span
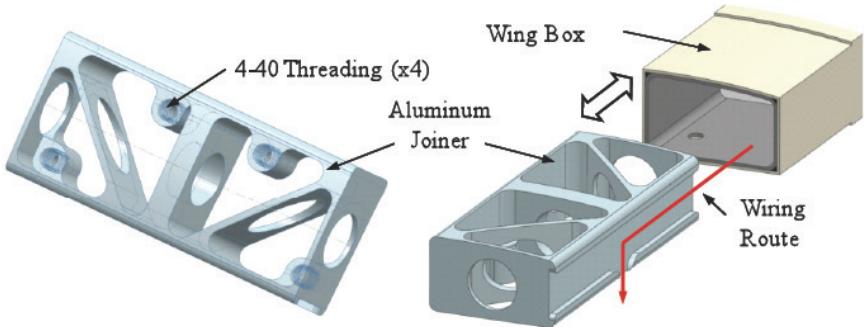
Figure 11. Aluminum joiner and wing box assembly

To help with the transfer of the torsional loads, a fiberglass sleeve is used that slides around the wing joint (Fig. 12). The airfoil profile at the end of each wing section is slightly offset allowing the sleeve to provide a smooth transition for the airfoil surface across the joint. The use of machined components and molds within each joint component is critical in guaranteeing a rigid and straight connection across the wing span satisfying the fourth wing design criterion discussed before.
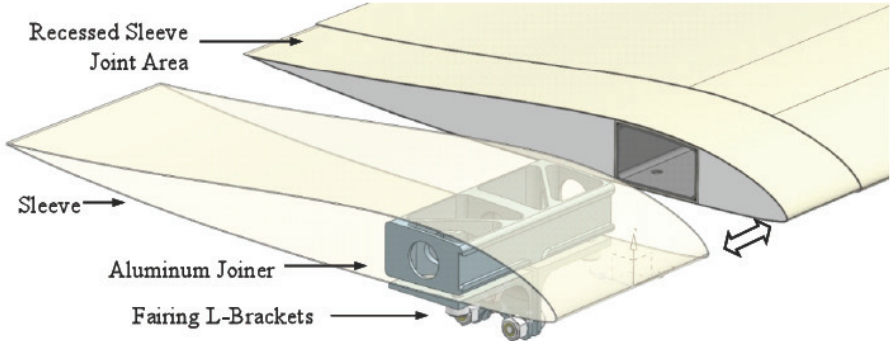
Figure 12. Wing joint composition

Exceptional care has been taken into creating the tools necessary to manufacture identical wing sections. Robust aluminum female molds have been machined in-house on a CNC bed mill and sanded to a mirror finish to both produce the most accurate airfoil profile and smoothest surface finish possible. The use of female molds has another benefit: it allows the foam core to be oversized and compressed by the mold surface when closed, which helps bond strain gages to the internal fiberglass surface and aides in a smooth surface finish.

Two curing cycles are required to create one full wing section. First, the wing box is fabricated. As previously described, layers of E-glass are wrapped around foam sections shaped to the wing box profile and the carbon fiber

American Institute of Aeronautics and Astronautics

that makes up each wing joint, which has already been wrapped around plugs that attached to alignment jigs. The alignment jigs then slide onto pins embedded in the wing mold. At this point the mold will only apply pressure to the top and bottom surface since the airfoil profile is not complete, so solid epoxy leading and trailing edge forms, referred as hardbacks, are placed in the mold to apply pressure to the front and back of the wing box. Once the wing box has completed a curing cycle, foam leading and trail edge section replace the hardbacks, and the entire assembly is wrapped with a single layer of E-glass and additional layer of graphite/epoxy at the wing joints. The wing is again cured in an autoclave producing one complete wing.

D. Sensor Layout and Design

To monitor X-HALE's complex aeroelastic behavior during flight, a sizeable data acquisition network must be used. X-HALE is equipped with four Athena II single board computers. Each has a 500MHz processor, 256MB of RAM, and a 1GB flash card to process and store collected analog data. Each Athena II has a 16 single-ended analog to digital conversion (ADC) circuit that is supplemented with 16 additional differential channels from a stacked PC104 DMM32 I/O expansion card. The airframe is equipped to carry four of those pairs (Fig. 13): one in each outboard fairing.
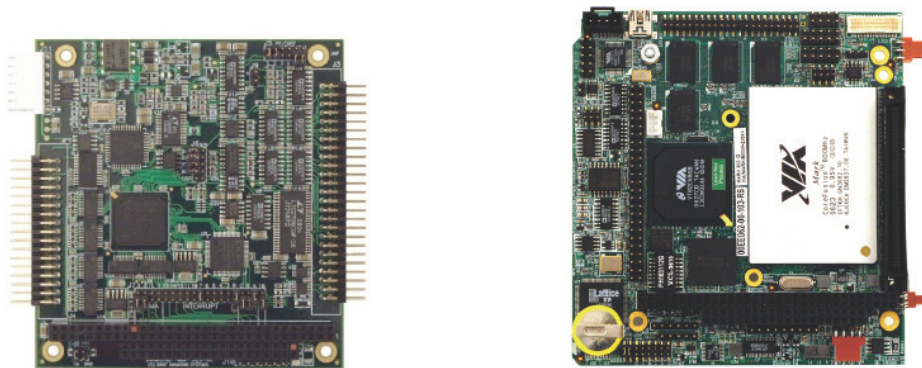
Figure 13. Diamond systems DMM32 I/O PC104 card and Athena II single board computer

Each board is designated to collect data from specific types of sensors at different rates. The sensors onboard X-HALE are categorized into two groups: science and housekeeping sensors. Science data includes all strain gages and accelerometers used in sole support to the aeroelastic tests. On the other hand, housekeeping data includes sensors that also monitor the health of the aircraft, such as temperature and battery voltage; flight conditions, such as airspeed, angle of attack, side-slip angle, Euler angles, and GPS location; and control inputs, such as motor RPM and control surface deflections. The DMM card is tasked with sampling only the strain gage data at 1 kHz. The Athena DAQ circuit samples the accelerometers and housekeeping sensors at lower rates adjustable by the user. Figure 14 and Table 5 describe the positioning of each sensor and their relative DAQ system.
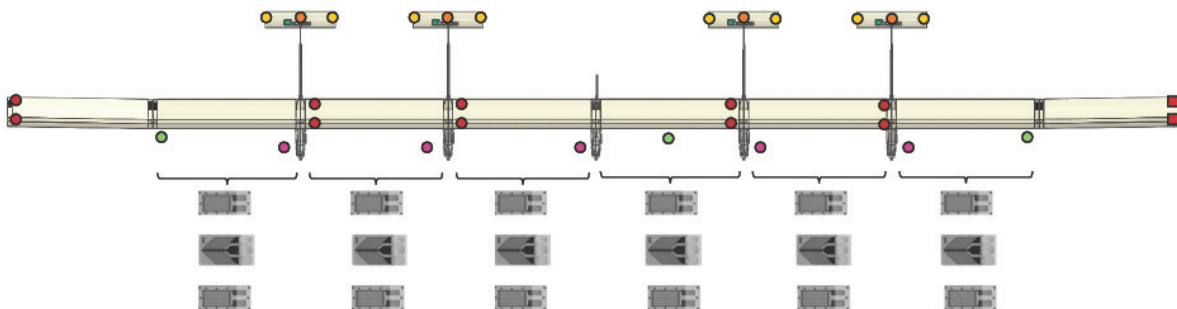
Figure 14. General sensor layout on X-HALE plan-form view

11
American Institute of Aeronautics and Astronautics

Table 5. List of Sensor and Their Positioning on the Plan-form

Board/Sensor	Color	Number	Channels	Type
DMM32 I/O PC104 card		**4**	**64 (Avail)**	
Bending Strain Gage Bridge		26	26	
Shear Strain Gage Bridge		22	22	Differential
In Plane Strain Gage Bridge		16	16	
Athena II board		**4**	**64 (Avail)**	
2 Axis Accelerometer		12	24	
1 Axis Accelerometer		8	8	
5 Hole Probe		3	9	
Tail Potentiometer		4	4	Single Ended
Fairing Housekeeping				
Voltage Divider Circuit		10	10	
Motor RPM		5	5	
Thermocouple*		4	4	

*Not included in central fairing

With 128 possible sensors, it is important that the data be time synchronized. To do this and compile the data from all fairings, the stack in fairing 1 is programmed as a master while the others are programmed as slaves. The master triggers data collection trough a digital pulse. Once this occurs each stack independently samples all science and housekeeping sensors. High-speed science data is stored locally on each Athena II while the housekeeping data is sent to the master via an onboard Ethernet network. The master then stores the data and sends it to a radio modem located in the central fairing to a ground station monitored during flight. To ensure a reliable 1kHz data acquisition rate is possible, the QNX real-time operating system is used and analog data is stored in a high-speed RAM queue capable of supporting over 1/2 hour of continuously acquired data. The ground station operator can specify when to start and stop data acquisition cycles; when active acquisition is inactive data previously stored is then written to permanent storage halting either when writing is complete or when the operator restarts data acquisition.

E. Flight Control System

During the majority of the flight, X-HALE is completely under RC command, with manual servo commands monitored and stored onboard. It is only during cruise flight testing phases that predetermined motor and control surface commands are issued by the onboard master flight computer. In early testing, open loop (scripted) command sequences designed to appropriately excite aeroelastic behaviors will be the only autopilot control capability. Based on analyses from this testing, we will then migrate to a feedback control strategy appropriate for the very-flexible body.

The X-HALE has nine RC components composed of five motors and four tails. Ailerons are also included on each of the dihedral wing sections. However, they will only be used during testing phases of the flight to force deformations into the wing structure. Mixing both on the ground through the RC transmitter and onboard through the SSC allows the pilot to control each RC component through the standard 4 channel thrust, yaw, pitch, and roll joysticks on the transmitter, or trigger the autopilot phase through an additional channel such as a gear or flap switch. All commands are stored onboard and are also sent to the ground station using the Athena II. To supplement the PWM commands, sensors monitor the physical motion of each control component to alleviate any errors in the conversion to mechanical energy. Figure 15 displays a functional graphical diagram of the mixing phases of the RC signals.

Although specific mixing percentages will be determined on the benchtop and refined between early flight tests, the strategy for control mixing will be as follows. Thrust (throttle joystick) will ramp from 0 to 100% equally over all motors to balance battery use given zero yaw (rudder joystick) command. With the need to apply a yawing moment, the two outboard motors will be issued a differential thrust that, within saturation limits, applies the appropriate moment while maintaining the desired total thrust. Similarly, the horizontal tail surfaces will be uniformly deflected in response to elevator commands, with the two outboard tails adjusted in opposite directions to obtain any desired roll moment (commanded with the aileron "stick" on the transmitter).

Each outboard fairing has an all movable tail. The Hitec 5125 digital slim wing servo used for actuation and circuitry used to record the position of the tail are embedded within the NACA 0012 airfoil profile along the tail axel. With this arrangement, the axel is fixed to the boom while the tail rotates around it. The physical angular

12
American Institute of Aeronautics and Astronautics

position of the tail is measured by the change in resistance from a rotary potentiometer to provide a direct measurement of the PWM signal that is sent to the servo. Figure 16 displays the tail and its internal hardware.
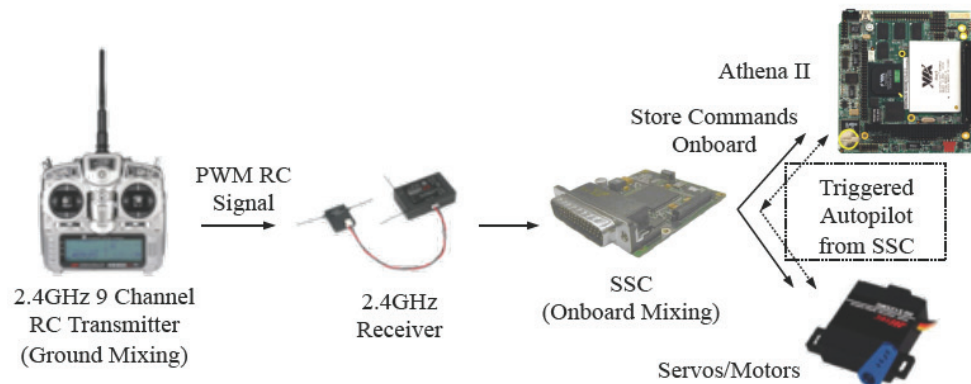
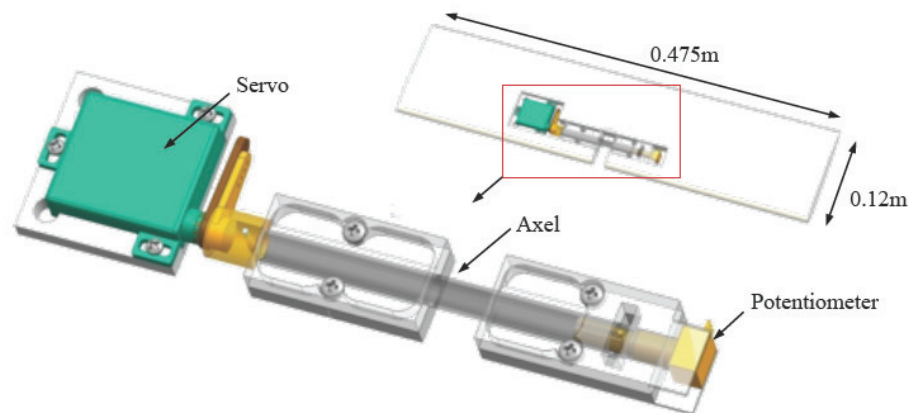**Figure 15. Functional diagram of RC command mixing sequence**

Figure 16. Tail and internal hardware

The X-HALE is propelled by five PJS 1200 outrunner motors, each paired with a 12x6 Graupner CAM folding propeller. Each motor has a maximum static thrust of approximately 10 N with a maximum power draw of 18 W. Wind tunnel tests using a sting balance were completed to track the 6-DOF dynamic force and moment performance of the power train between 10 m/s and 20 m/s. The test setup and thrust results are displayed in Figs. 17 and 18.
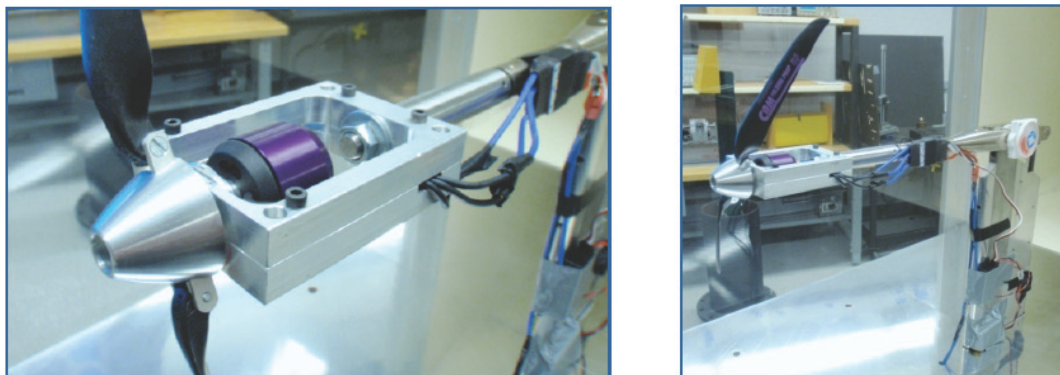
Figure 17. 2'x2' wind tunnel test setup for calibration of the propulsion assembly

13
American Institute of Aeronautics and Astronautics
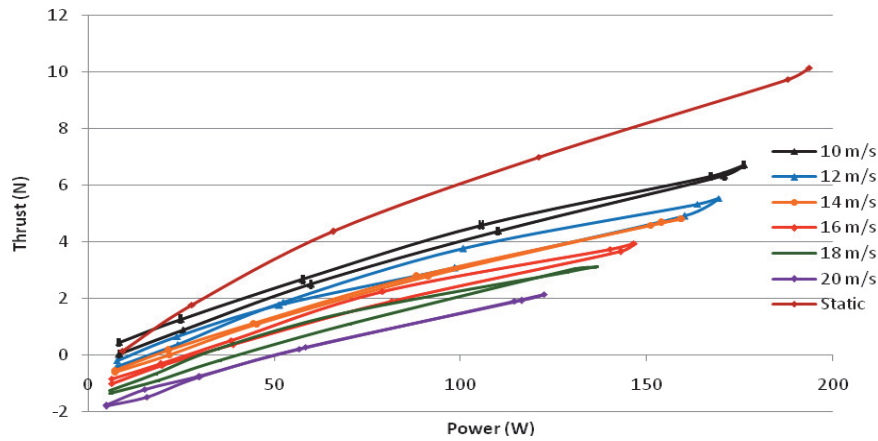
Figure 18. Input power vs. thrust from wind tunnel testing for flight regime velocities

Due to inconsistencies within motor performance characteristics, each motor is tested and calibrated independently. From these tests we can achieve and calibrate an accurate thrust profile across the span of the aircraft.

III. X-HALE Aeroelastic Simulations

A model of the X-HALE was created in UM/NAST to support its nonlinear aeroelastic analysis and design. In what follows, numerical aeroelastic and flight dynamic simulations are performed based on the model and some fundamental aeroelastic characteristics of the model are identified. Extreme flight conditions are presented to indicate the limits in which the design can be taken.

A. Platform Data

Figure 19 illustrates the X-HALE model created in UM/NAST, which features an 8-m span. The outer 1-m long members are built with a dihedral angle of 10°. Five pods are modeled as vertical lifting surfaces with applied follower concentrated forces to simulate the motor thrust. Four tails are modeled as all-movable horizontal surfaces. Member properties are listed in Tables 6 and 7. Note that the booms, tails, and pods are models as rigid members, and no rigidity properties are provided for them. Ailerons are modeled on the outer dihedral members, which occupy 25% of the chord. The inertias of the spine and covers of the pods are neglected, while concentrated inertias are attached inside the pods, which come from mainly the electronic equipments.
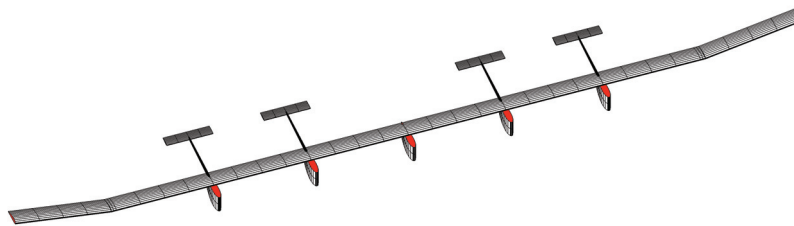
Figure 19. UM/NAST model of the X-HALE aircraft.

B. Trim Results

The vehicle is trimmed for equal lift and weight, and zero pitching moment about its center of gravity at level flight at 30-m altitude. The flight velocity ranges from 12 to 20 m/s. The trim results are plotted in Fig. 20. Figure 21 compares the deformed shape at the trimmed condition (14 m/s) and the reference shape, where the large static deformation can be found. The vehicle is highly flexible and the tip deflection at this trimmed state is about 37% of the half span.

14
American Institute of Aeronautics and Astronautics

Table 6. Member properties of the X-HALE model

	Wing	Booms	Tails	Pods	Units
Ref. axis location (from L.E.)	28.78	50	32.35	60.93	% chord
Center of gravity (from L.E.)	25	50	25	25	% chord
Incidence angle	5	N/A	0	0	deg
Chord length (c) / Diameter (d)	0.20	0.024 (f) 0.013 (r)	0.11	0.37	m
Mass per unit span (m)	0.319	0.01	0.129	--	kg/m
Rotational inertia (I_{xx})	8.09×10^{-4}	2.91×10^{-9}	1.60×10^{-4}	--	kg·m
Rot./flat bend inertia (I_{xy})	0	0	0	--	kg·m
Rot./ in-plane bend inertia (I_{xz})	0	0	0	--	kg·m
Flat bend inertia (I_{yy})	1.22×10^{-5}	1.46×10^{-9}	2.91×10^{-6}	--	kg·m
Flat/in-plane bend inertia (I_{yz})	-6.49×10^{-6}	0	0	--	kg·m
In-plane bend inertia (I_{zz})	7.97×10^{-4}	1.46×10^{-9}	1.57×10^{-4}	--	kg·m
Ext. stiffness (k_{11})	2.14×10^{6}	--	--	--	N
Ext./torsion stiffness (k_{12})	0	--	--	--	N
Ext./ flat bend stiffness (k_{13})	1.54×10^{3}	--	--	--	N
Ext./in-plane bend stiffness (k_{14})	-4.91×10^{4}	--	--	--	N
Torsion stiffness (k_{22})	72.25	--	--	--	N·m²
Tor./flat bend stiffness (k_{23})	0	--	--	--	N·m²
Tor./in-plane bend stiffness (k_{24})	0	--	--	--	N·m²
Flat bend stiffness (k_{33})	119.57	--	--	--	N·m²
Flat/in-plane bend stiffness (k_{34})	-46.34	--	--	--	N·m²
In-plane bend stiffness (k_{44})	6.35×10^{3}	--	--	--	N·m²

Table 7. List of the concentrated inertias of the X-HALE model

	Outboard pods			Center pod			Inner half tail	Outer half tail	Units
	Battery forward cg	Battery aft cg	Remaining assembly	Battery forward cg	Battery aft cg	Remaining assembly			
mass	0.396	0.396	1.057	0.396	0.396	1.025	0.049	0.020	kg
x_{cg}[*]	0.013	0.013	-0.006	0.013	0.013	-0.003	0.073	0.029	m
y_{cg}	0.059	-0.001	0.066	0.059	-0.001	0.043	-0.008	0	m
z_{cg}	-0.069	-0.069	-0.085	-0.069	-0.069	-0.080	-0.001	0	m
I_{xx}	1.160×10^{-3}		1.134×10^{-2}	1.160×10^{-3}		1.476×10^{-2}	4.631×10^{-6}	1.866×10^{-7}	kg·m²
I_{yy}	9.485×10^{-5}		3.209×10^{-3}	9.485×10^{-5}		2.816×10^{-3}	2.282×10^{-5}	1.341×10^{-6}	kg·m²
I_{zz}	1.098×10^{-3}		8.484×10^{-3}	1.098×10^{-3}		2.503×10^{-4}	2.651×10^{-5}	1.311×10^{-6}	kg·m²
I_{xy}	0		-1.212×10^{-3}	0		2.322×10^{-4}	-3.190×10^{-6}	1.000×10^{-10}	kg·m²
I_{xz}	0		1.055×10^{-5}	0		2.267×10^{-5}	-3.057×10^{-7}	0	kg·m²
I_{yz}	0		4.595×10^{-5}	0		4.500×10^{-4}	2.644×10^{-8}	0	kg·m²

C. Flight under Gust Perturbations

Gust response of the vehicle is studied in this section. Figure 22 shows the 1-cosine gust profile for the simulation. The gust is symmetrically applied to the vehicle on its flight path. The maximum gust speed is 4 m/s, while the nominal flight speed is 14 m/s at 30 m altitude.

The aeroelastic and flight dynamic responses of the model with gust perturbation are plotted in Figs. 23 to 27, compared to a flight condition without gust. Overall, the plunging (Fig. 23) and pitching (Fig. 24) oscillations are excited by the gust perturbation. However, the longitudinal motions are stable, as the amplitudes of the oscillations are reduced in the subsequent cycles. Figure 25 shows the velocity of the body reference frame resolved in the inertia frame. Comparing Figs. 23 and 25, one can identify the phugoid motion, which features the exchange between kinematic (longitudinal velocity) and potential energies.

---

[*] The c.g. locations are measured from the root of each member, *i.e.*, the top surfaces for the pod members and the connection point with the boom for the tail members.
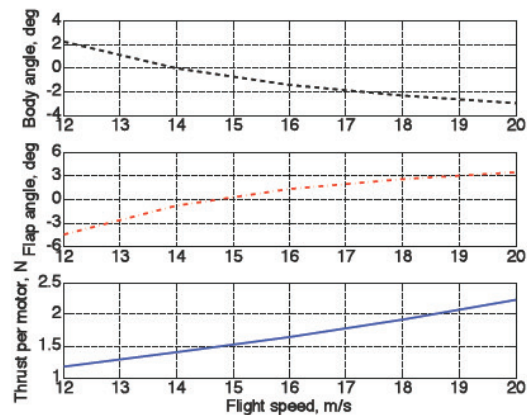
Figure 20. Trim results of the X-HALE model.
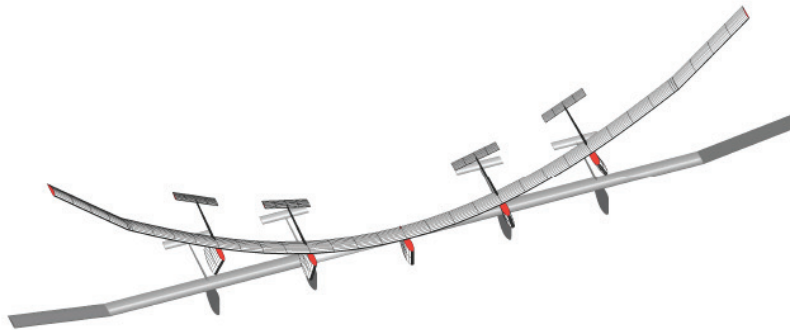
Figure 21. Deformed shape at trim condition (speed: 14 m/s, with vehicle in grey as the undeformed reference shape).
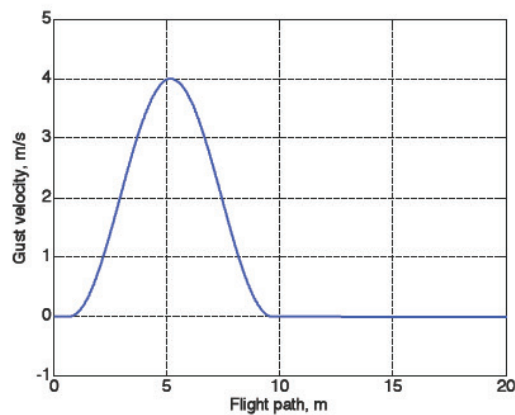
Figure 22. Spatial-distributed gust profile.

Of particular interest is the flexibility of the vehicle. Figure 27 shows the wing tip deflection with the gust perturbation, normalized by the half span of the vehicle. Large wing deformations can be found to be over 43% of the half span during the vehicle's passing the gust region, after which the oscillation in wing bending is reduced. With such large transient deformation, one needs to check the composite layup strains to verify the structural integrity. The maximum and minimum strain components in each composite fiber direction are given in Table 8. The normal strain in the longitudinal direction (ε_{11}) is over 3000 $\mu\varepsilon$. Figure 28 plots the normal strains in the fiber's longitudinal direction, with the minima plotted as positive values. As the local strain components have already gone

16
American Institute of Aeronautics and Astronautics

Approved for public release; distribution unlimited.

beyond 3000 $\mu\varepsilon$ (for a working limit of 4000 $\mu\varepsilon$), this gust profile can be considered as a critical gust input of what the vehicle can sustain.
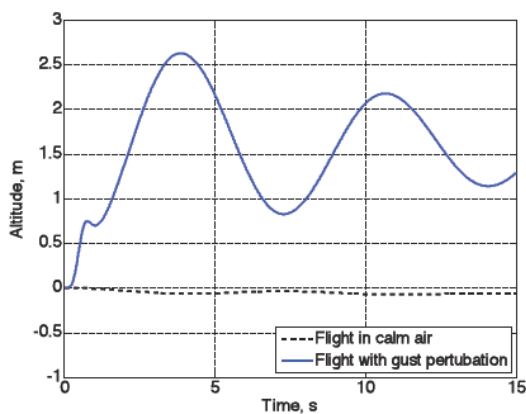
Figure 23. Change of altitude with the gust perturbation.
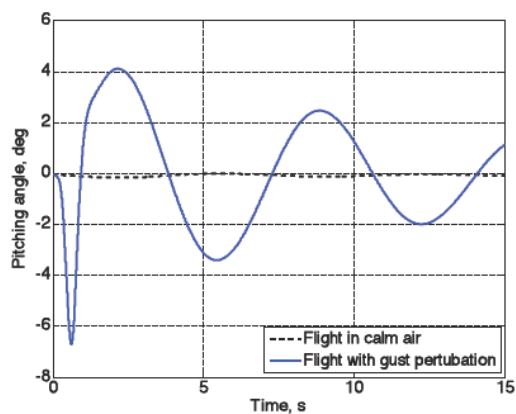
Figure 24. Change of pitching angle with the gust perturbation.
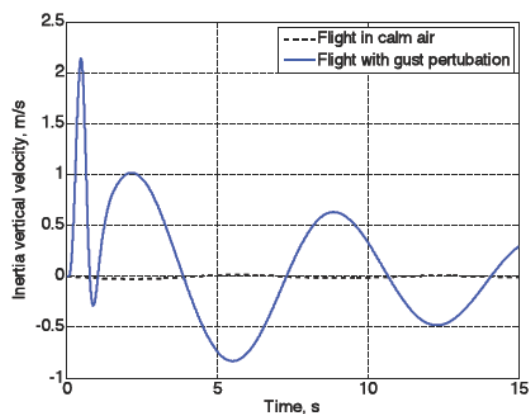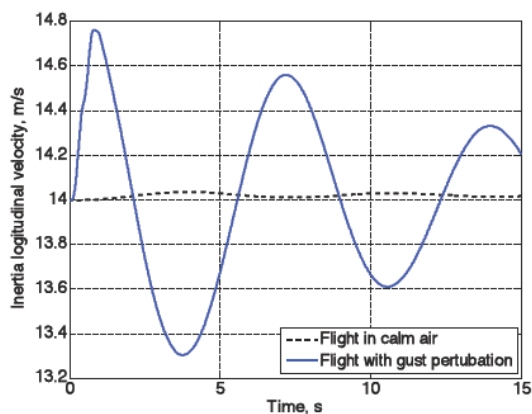
Figure 25. Velocity components in the inertia frame.
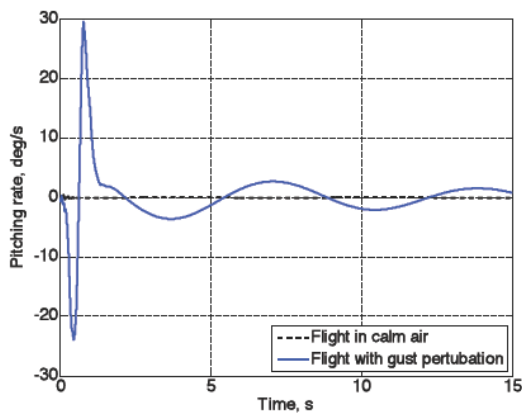
Figure 26. Pitching rate.
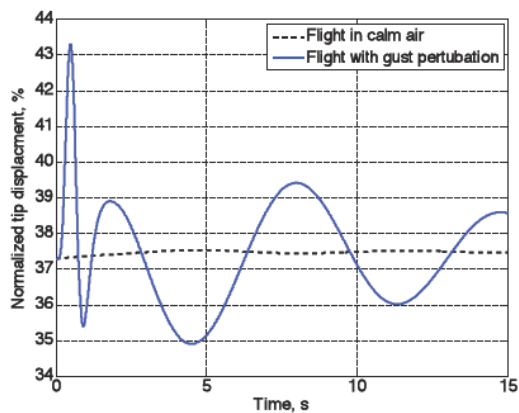
Figure 27. Normalized tip displacement.

American Institute of Aeronautics and Astronautics

Table 8. List of maximum and minimum strains with the gust perturbation

	Maximum ($\mu\varepsilon$)	Minimum ($\mu\varepsilon$)
ε_{11}	3093.4	-3656.0
ε_{12}	895.8	-886.8
ε_{13}	1079.8	-1068.9
ε_{22}	1241.3	-1099.8
ε_{23}	773.0	-778.1
ε_{33}	769.2	-569.9
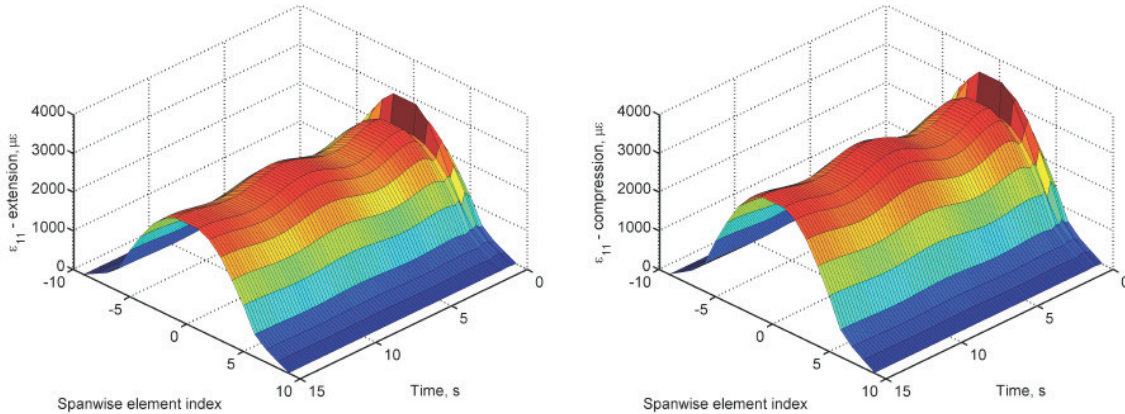
Figure 28. Normal strains in fiber longitudinal direction (ε_{11}, left: extension; right, compression).

D. Roll Simulations

As indicated in the previous section, the vehicle is very flexible. Therefore, its maneuverability needs to be assed to better understand the control surface effectiveness. In this study, the anti-symmetric inputs for the flaps on the dihedral wing members are used to for roll simulations. Figure 29 exemplifies the aileron deflection angle on the left wing. The ailerons start to deflect after 5 seconds (into the simulation) and complete one sinusoidal cycle within 2 seconds. As indicated in Fig. 29, two simulations are performed to study the roll characteristic of the X-HALE model. One has the maximum aileron deflection of 2°, while the other one has the maximum aileron deflection of 5°.
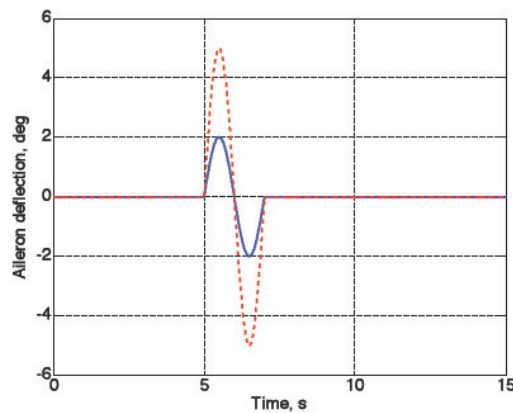
Figure 29. Aileron deflection on the left wing.

First, roll angles and roll rates are compared for the two simulations in Figs. 30 and 31. According to the aileron input, the vehicle is commanded to roll in its positive direction (*i.e.*, right wing down). From the numerical simulation, one my find the vehicle slightly rolls negatively right after the aileron input, which is easier to see in the

18
American Institute of Aeronautics and Astronautics

plot of roll rate (Fig. 31). Right after that, the vehicle rolls back to its positive direction. This positive roll does not hold for a long time before the vehicle starts to develop another negative roll due to the evolution of the commanded aileron deflections. After the one-cycle actuation, the oscillation in roll is developed. From Fig. 30, it can also be seen that the roll motion with 5° actuation is not stable, since the magnitude of roll angle is increased, while the roll after 2° actuation is still stable.

To verify if the instability in roll after the 5° actuation is purely rigid-body instability or it is due to the coupling between the flexible and rigid-body degrees of freedom, one more simulation is carried out where the wing flexibility is neglected. The vehicle is first brought to its nonlinear trimmed state and the wing deformation is locked. Only rigid-body degrees of freedom are considered in this simulation. Figures 32 and 33 compare the results from this simulation with the ones from fully nonlinear simulation above. The rigid-body simulation predicts a stable roll motion. Therefore, the instability observed from the fully nonlinear simulation is due to the coupled wing bending and the roll motion of the vehicle.

The actuations of the aileron deflections cause redistribution of the aerodynamic loads on the wings, from which the roll moment is generated. As a consequence, significant yaw moment to the vehicle is also introduced by the aileron deflections and oscillations in yaw can be observed from Fig. 34. Moreover, some pitching vibration is slighting excited (Fig. 35), which could be unstable when the maximum aileron deflection angle is 5°. At the same time, the redistribution of the aerodynamic loads also results in oscillations of the vehicle's body reference frame in the lateral and vertical directions, as shown in Figs. 36 and 37.
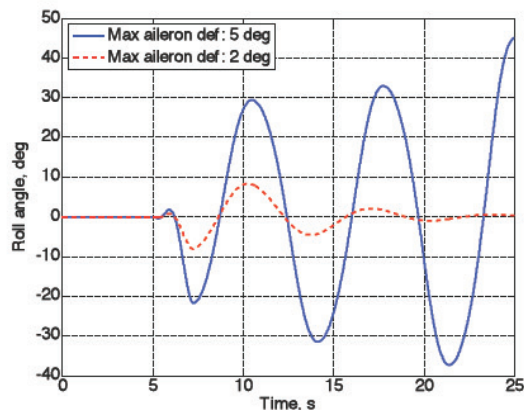
Figure 30. Change in the roll angle of the vehicle with different aileron inputs.
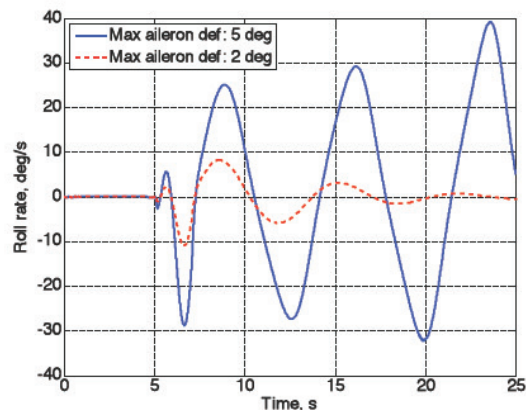
Figure 31. Change in the roll rate of the vehicle with different aileron inputs.
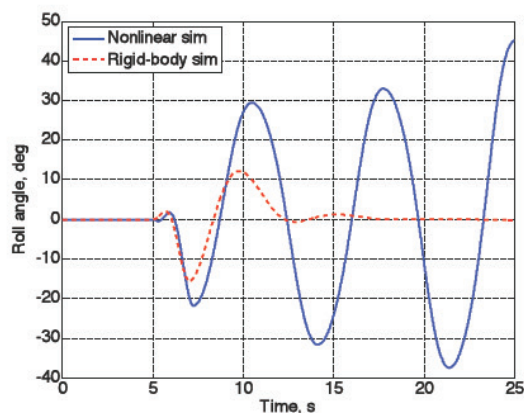
Figure 32. Roll angle from different simulations.
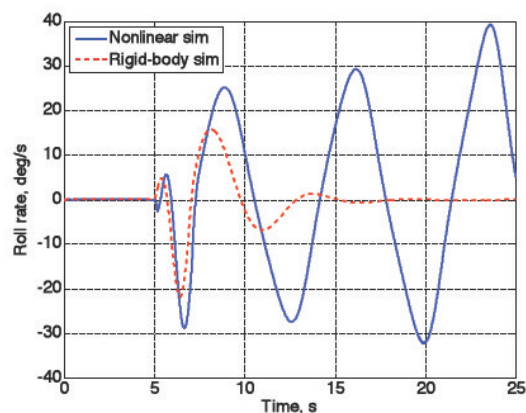
Figure 33. Roll rate from different simulations.

19
American Institute of Aeronautics and Astronautics
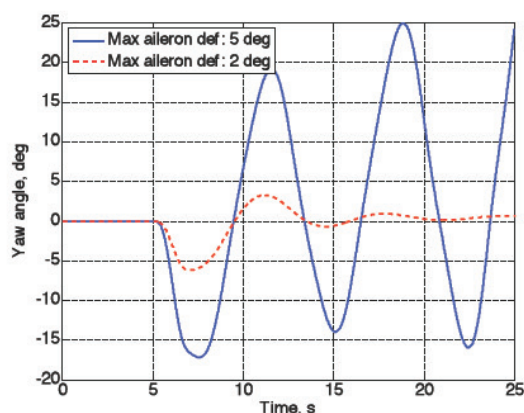
Figure 34. Change in the yaw angle of the vehicle with different aileron inputs.
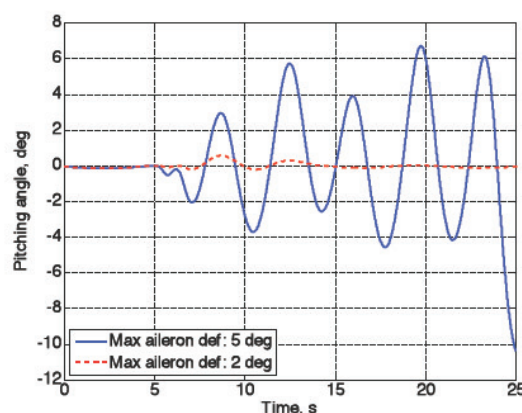
Figure 35. Change in the pitching angle of the vehicle with different aileron inputs.
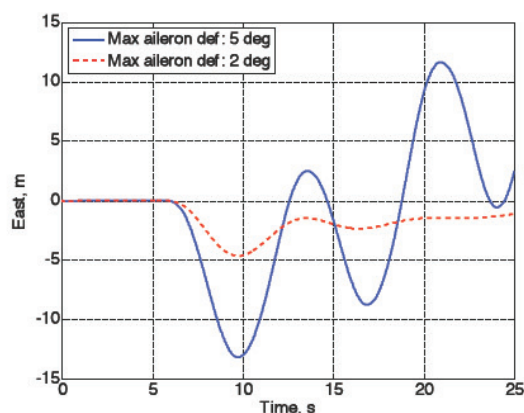
Figure 36. Change in the lateral position of the vehicle with different aileron inputs.
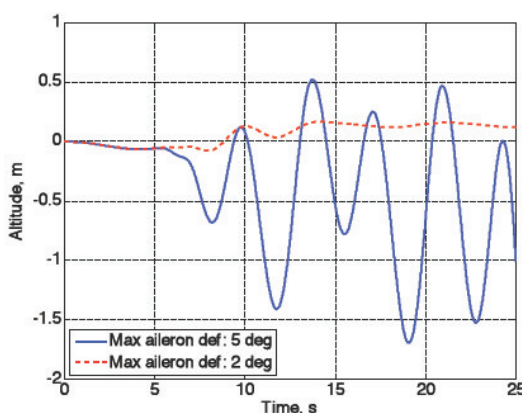
Figure 37. Change in the altitude of the vehicle with different aileron inputs.

Figure 38 shows the wing tip deflections due to the aileron input. It can be seen the additional wing tip deflection due to 2° aileron input is relatively small, compared to the state at initial level flight. The magnitude of the bending oscillation is reduced with time, and the wing deformation is recovering to the steady state. However, for the simulation with 5° aileron input, the wing deformation introduced by the aileron deflection is significantly larger, where the right wing tip deflection can exceed 42% of the half span. It is also clear that the bending oscillation of the wing is increased after the aileron actuation. Therefore, the 5° aileron input case (under this frequency of 0.5 Hz) can be seen as an upper limit for excitation during flight. While in this model the aileron was taken as a full section span (1-m long), in the actual X-HALE it will be no more than 25-cm span. This will allow for an equivalent 20° aileron input for similar vehicle response. Limits on the aileron deflections will be provided by software.

Table 9 lists the strain components in the material direction. Again, one can see the normal stain in the longitudinal direction exceeds 3000 $\mu\varepsilon$. Figure 39 plots the spanwise and spatial distributions of the strain in this direction. The large strain happens after the aileron actuation.
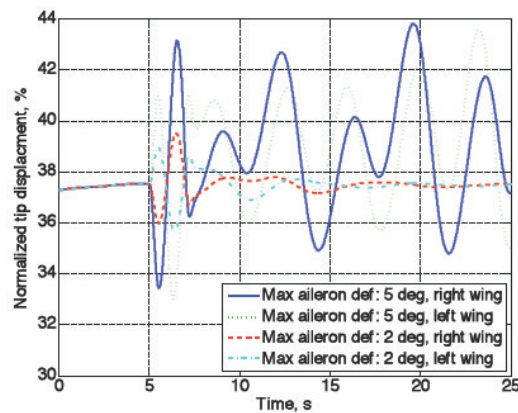
Figure 38. Normalized wing tip deflections.

Table 9. List of maximum and minimum strains with the 5° aileron inputs

	Maximum ($\mu\varepsilon$)	Minimum ($\mu\varepsilon$)
ε_{11}	2881.0	-3499.2
ε_{12}	587.9	-478.4
ε_{13}	708.7	-576.7
ε_{22}	1182.0	-1024.5
ε_{23}	758.8	-756.8
ε_{33}	752.7	-516.5
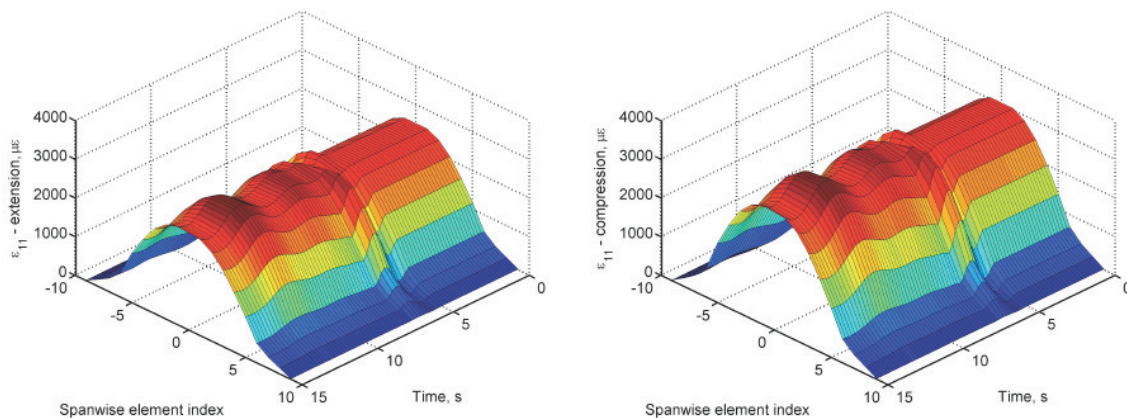
Figure 39. Normal strains in fiber longitudinal direction (ε_{11}, left: extension; right, compression).

IV. Concluding Remarks

This paper introduced the X-HALE UAV as a test bed for nonlinear aeroelastic flight tests. The 8-m span very flexible aircraft is expected to excite coupled nonlinear aeroelastic/flight dynamic coupled responses due to controlled excitation that will provide valuable data in support to code validation. The design and manufacturing processes chosen for the airframe were such that the elastic, inertial and geometric properties can be well characterized. The integrated airframe, on-board computers, controls, and software were presented. A network of strain gages and accelerometers provides measurements for the instantaneous deflection shape. Three 5-hole probes along the wingspan provide basic aerodynamic data. Engine thrust (through rpm measurement), control surface rotations, and center pod inertial measurements are also obtained during flight. Batteries provide power to the five

electric motors for at least 45-minute flights, which will be enough to conduct several test matrix points. Manufacturing of the first flight test vehicle is underway, along with a series of bench tests to fully characterize various structures, aerodynamics, propulsion, electronics and software unique aspects of the X-HALE.

The expected X-HALE aeroelastic behavior was obtained using UM/NAST, a comprehensive preliminary aeroelastic design tool for very flexible aircraft. The design presents significant wing deflections under trimmed condition as desired. It also has the control authority to excite large dynamic responses and to even develop (controlled) aeroelastic instabilities. Due to the large deformation under trimmed condition, the safety margins left for the vehicle to sustain gust perturbations and maneuver has to be monitored closely, as the local normal strains could transiently exceed 3000 $\mu\varepsilon$. From the simulation with anti-symmetric aileron actuations, the roll motion of the vehicle could go unstable. Moreover, complex 3-D rotational and translational motions were observed with the introduced aileron inputs, which indicate possible test point to be explored during flight tests and for which wind tunnel tests would not be feasible.

The first flight of the X-HALE flight test vehicle is expected to occur in June 2010. The goal for this first phase is to assess its handling qualities, its basic aeroelastic response, and how these correlate with UM/NAST predictions. From those, design changes are expected and a new airframe will then be finalize for the aeroelastic flight tests.

Acknowledgments

References

1. Tilmann, C. P., Flick, P. M., Martin, C. A., and Love, M. H., "High-Altitude Long Endurance Technologies for SensorCraft," RTO AVT Symposium on "Novel Vehicle Concepts and Emerging Vehicle Technologies," Brussels, Belgium, April 7–10 2003, MP-104-P-26-1.
2. Whitson, S., "The Proteus, Giving Shape to Forms Unknown," *Private Pilot*, Vol. 33, No. 12, December 1998, pp. 44–50.
3. Noll, T. E., Brown, J. M., Perez-Davis, M. E., Ishmael, S. D., Tiffany, G. C., and Gaier, M., "Investigation of the Helios Prototype Aircraft Mishap," Tech. Rep., NASA, January 2004.
4. Wilson, J. R., "Fly Like a Vulture," *Aerospace America*, Vol. 46, No. 11, November 2008, pp. 28–33.
5. RCAS User's Manual, Version 2.0, US Army Aviation and Missile Command, Moffett Field, CA
6. Drela, M., "Integrated Simulation Model for Preliminary Aerodynamic, Structural, and Control-Law Design of Aircraft," Proceedings of the 40th AIAA/ASME/ASCE/AHS/ASC Structures, Structural Dynamics, and Materials Conference and Exhibit, St. Louis, Missouri, April 12–15 1999, pp. 1644–1656, AIAA Paper No. 99-1394.
7. Cesnik, C. E. S. and Brown, E. L., "Modeling of High Aspect Ratio Active Flexible Wings for Roll Control," Proceedings of the 43rd AIAA/ASME/ASCE/AHS Structures, Structural Dynamics, and Materials Conferences, Denver, Colorado, April 22–25 2002, AIAA Paper No. 2002-1719.
8. Cesnik, C. E. S. and Su, W., "Nonlinear Aeroelastic Modeling and Analysis of Fully Flexible Aircraft," Proceedings of the 46th AIAA/ASME/ASCE/AHS/ASC Structures, Structural Dynamics and Materials Conference, Austin, TX, April 18-21, 2005, AIAA Paper No. 2005-2169.
9. Shearer, C. M., Coupled Nonlinear Flight Dynamics, Aeroelasticity, and Control of Very Flexible Aircraft, Ph.D. thesis, The University of Michigan, Ann Arbor, MI, 2006, PhD Dissertation.
10. Shearer, C. M. and Cesnik, C. E. S., "Nonlinear Flight Dynamics of Very Flexible Aircraft," *Journal of Aircraft*, Vol. 44, No. 5, September - October 2007, pp. 1528–1545.
11. Shearer, C. M. and Cesnik, C. E. S., "Trajectory Control for Very Flexible Aircraft," *Journal of Guidance, Control, and Dynamics*, Vol. 31, No. 2, March-April 2008, pp. 340–357.
12. Patil, M. J., Hodges, D. H., and Cesnik, C. E. S., "Nonlinear Aeroelasticity and Flight Dynamics of High-Altitude Long-Endurance Aircraft," *Journal of Aircraft*, Vol. 38, No. 1, pp. 88-94, 2000.

13. Patil, M. J. and Hodges, D. H., "Flight Dynamics of Highly Flexible Flying Wings," *Journal of Aircraft*, Vol. 43, No. 6, November-December 2006, pp. 1790–1798.

14. Chang, C. S., Hodges, D. H., and Patil, M. J., "Flight Dynamics of Highly Flexible Aircraft," *Journal of Aircraft*, Vol. 45, No. 2, March-April 2008, pp. 538–545.

15. Chandra, R. and Chopra, I., "Structural Response of Composite Beams and Blades with Elastic Couplings," *Composite Engineering*, Vol. 2, Nos. 5-7, 1992, pp. 347-374.

16. Minguet, P. and Dugundji, J., "Experiments and Analysis for Structurally Coupled Composite Blades Under Large Deflections. Part 1 – Static Behavior," Proceedings of the 30th AIAA/ASME/ASCE/AHS/ASC Structures, Structural Dynamics, and Materials Conference, AIAA Paper No. 89-1365, 1989, pp. 1807-1816.

17. Minguet, P. and Dugundji, J., "Experiments and Analysis for Structurally Coupled Composite Blades Under Large Deflections. Part 2 – Dynamic Behavior," *AIAA Journal*, Vol. 28, No. 9, pp. 1580-1588, 1990.

18. Tang, D.M. and Dowell, E.H., "Experimental and Theoretical Study on Aeroelastic Response of High-aspect-ratio Wings," *AIAA Journal*, Vol. 39, No. 8, pp. 1430-1441, 2001.

19. Tang, D.M. and Dowell, E.H., "Experimental and Theoretical Study of Gust Response for High-aspect-ratio Wing," *AIAA Journal*, Vol. 40, No. 3, pp. 419-429, 2002.

20. Palacios, R., Cesnik, C. E. S., and Reichenbach, E., "A Re-examination of the Structural Design Procedures for Very Flexible Aircraft," Proceedings of the International Forum on Aeroelasticity and Structural Dynamics, Stockholm, Sweden, June 18-21, 2007.

21. Su, W. and Cesnik, C.E.S., "Dynamic Response of Highly Flexible Flying Wings," Proceedings of the 47th AIAA/ASME/ASCE/AHS/ASC Structural, Structural Dynamics and Materials Conference, Newport, Rhode Island, 2006.

22. Cesnik, C.E.S. and Brown, E.L., "Active Warping Control of a Joined Wing Airplane Configuration," Proceedings of the 44th AIAA/ASME/ASCE/AHS/ASC Structures, Structural Dynamics, and Material Conference, Hampton, Virginia, 2003.

23. Brown, E.L., "Integrated Strain Actuation in Aircraft with Highly Flexible Composite Wings," Ph.D. Thesis, Mechanical Engineering, Massachusetts Institute of Technology, Cambridge, Massachusetts, 2003.

24. Cesnik, C.E.S. and Ortega-Morales, M., "Active Aeroelastic Tailoring of Slender Flexible Wings," Proceedings of the International Forum on Aeroelasticity and Structural Dynamics, Madrid, Spain, 2001.

25. Van Schoor, M.C. and von Flotow, A.H., "Aeroelastic Characteristics of a Highly Flexible Aircraft," *Journal of Aircraft*, Vol. 27, No. 10, pp. 901–908, 1990.

26. Jones, R.I., "The Design Challenge of High Altitude Long Endurance (Hale) Unmanned Aircraft," *The Aeronautical Journal*, pp. 273-280, 1999.

27. Jones, R.I., "Selection and Comparison of Unmanned Aircraft Configurations," In 12th RPVs International Conference, Bristol, United Kingdom, Sept. 9-11, 1996, Conference Papers (A97-21501 04-01), Bristol, United Kingdom, University of Bristol, 1996.

Approved for public release; distribution unlimited.

Flapping-Wing Structural Dynamics Formulation Based on a Corotational Shell Finite Element

Satish K. Chimakurthi[*] and Carlos E. S. Cesnik[†]
University of Michigan, Ann Arbor, Michigan 48109
and
Bret K. Stanford[‡]
U. S. Air Force Research Laboratory, Wright-Patterson Air Force Base, Dayton, Ohio 45440

Flexible flapping wings have garnered a large amount of attention within the micro aerial vehicle community: a critical component of computational micro aerial vehicle simulations is the representation of the structural dynamics behavior of the flapping-wing structure. This paper discusses the development of a new nonlinear finite element solver that is based on a corotational approach and suitable for simulating flapping plate/shell-like wing structures undergoing small strains and large displacements/rotations. Partial verification and validation studies are presented on rectangular/elliptic wing structures to test the rigid body kinematics, nonlinear statics, and dynamics capabilities of the solver. Results obtained showed good agreement with available analytical/experimental/commercial solutions. The new structural dynamics formulation along with the numerical test cases contribute to the very limited set of tools and examples existing in the flapping-wing micro aerial vehicle literature.

Nomenclature

A	=	stretching stiffness matrix
a	=	global acceleration vector
A_e	=	area of a triangular finite element
B	=	membrane-bending coupling stiffness matrix
B_b	=	strain-displacement matrix corresponding to flexural strains and bending degrees of freedom
B_m	=	strain-displacement matrix corresponding to membrane strains and membrane degrees of freedom
C	=	assembled damping matrix in the global frame
c	=	mean chord length of the wing
C_{el}	=	element local damping matrix
$C_{el\text{-}g}$	=	element global damping matrix
D	=	bending stiffness matrix
D_s	=	plate stiffness
d_e	=	vector of displacements of a material point with respect to the undeformed element frame
d_{pure}	=	18×1 vector of pure deformations of an element
d_{pure}^m	=	6×1 vector of pure deformations at a node
E	=	element frame in the current configuration, Young's modulus
E_o	=	element frame in the undeformed configuration
F	=	assembled external force vector in the global frame
f	=	plunging/flapping frequency
f_{ij}, q_{ij}	=	metrics of conversion from Cartesian coordinates to curvilinear coordinates
F_{el}^p	=	local force vector corresponding to inertial forces due to prescribed rigid body motion
$F_{el\text{-}g}^p$	=	global force vector corresponding to inertial forces due to prescribed rigid body motion
G	=	matrix containing derivatives of shape functions, shear modulus
g	=	global frame
H	=	distribution function used in the thin-plate spline interpolation
h	=	discretized grid spacing
h_a	=	stroke amplitude due to either prescribed plunge motion or flap rotation at the wing root
h_{root}	=	chord-normalized plunge amplitude at the root (ratio of plunge amplitude at the root and chord)
h_s	=	plate thickness
I	=	inertial frame
I_m	=	identity matrix of size 3×3
J	=	Jacobian matrix associated with the transformation from Cartesian to curvilinear coordinates
J	=	torsional constant
j	=	iteration number within the Newton–Raphson iteration loop
J_t	=	diagonal matrix containing inverse of finite element Jacobian matrix as its components
K_b	=	stiffness matrix corresponding to plate bending degrees of freedom
K_{eff}	=	effective stiffness matrix
K_m	=	stiffness matrix corresponding to membrane degrees of freedom
K_t	=	assembled tangent stiffness matrix in the global frame
K_{el}^{dyn}	=	element local dynamic stiffness matrix
K_{el}^{shell}	=	element shell stiffness matrix
$K_{el}^{shell\text{-}p}$	=	element shell stiffness matrix filtered through the projector matrix
K_{el}^{ss}	=	element stress stiffening matrix
M	=	assembled mass matrix in the global frame, typical point in the bilinear interpolation method
M_{el}	=	element local mass matrix
$M_{el\text{-}g}$	=	element global mass matrix
N	=	matrix of shape functions of size 3×18
n	=	time level
N_e	=	number of finite elements

*Research Fellow, Department of Aerospace Engineering. Member AIAA.
†Professor and Graduate Chair, Department of Aerospace Engineering. Associate Fellow AIAA.
‡National Research Council Postdoctoral Fellow. Member AIAA.

N_{mf}	=	2×2 matrix of membrane forces
N_n	=	number of finite element nodes
P	=	typical material point
p	=	distributed transverse load on the plate
$\hat{p}$	=	direction of rotation
P_r	=	projector matrix
p_{int}	=	interpolated solution at an arbitrary point in the bilinear interpolation
$\hat{p}_x, \hat{p}_y, \hat{p}_z$	=	components of the unit rotational pseudovector
q	=	vector of assembled nodal degrees of freedom
q_e	=	finite element nodal degree of freedom vector of size 18×1
q_{dg}^m	=	vector of displacements at node m with respect to the undeformed local element frame
r_{el}^{int}	=	nonlinear local internal force vector
r_{el}^{int-p}	=	nonlinear internal force vector filtered through projector matrix P_r
r_{el-g}^{int}	=	nonlinear global internal force vector
R	=	assembled nonlinear internal force vector in the global frame
R	=	wing length
Re	=	Reynolds number
Rf	=	residual force vector
R_h	=	effective load vector
S	=	current nodal coordinate system, planform area of the wing
S_o	=	initial nodal coordinate system
S_r	=	spectral radius parameter
T	=	transformation matrix used in the computation of pure nodal rotations in the current element frame
$\bar{T}$	=	rotation matrix used to update a nodal coordinate system
t	=	time
T_{EG}	=	transformation matrix from global frame to the current element frame
T_{GE_o}	=	transformation matrix from undeformed element frame to global frame
T_{IG}	=	transformation matrix from global frame to inertial frame
$T_{S_{new}}$	=	rotation matrix corresponding to a nodal triad in the current Newton–Raphson iteration
$T_{S_{old}}$	=	rotation matrix corresponding to a nodal triad in the previous Newton–Raphson iteration
T_{GE}^f	=	expanded form of the transformation matrix T_{GE}
u_E^m	=	pure nodal displacements at a node m
v	=	global velocity vector
v_{el}	=	volume of a finite element
X	=	position vector of a material point with respect to the inertial frame
X_R	=	position vector of the flapping-wing structure's actuation point with respect to the inertial frame
x_e	=	position vector of a material point with respect to the undeformed element frame
x_g	=	position vector of a material point with respect to the global frame
x_o	=	position vector of the origin of an element frame in the undeformed configuration with respect to the global frame
z	=	coordinate along the wingspan
$\alpha_f, \alpha_m, \gamma_{nm}, \beta$	=	parameters related to the generalized-α method
Δq	=	incremental displacements in the Newton–Raphson iteration loop
Δt_s	=	time step in the structural solution
$\theta_{E_1}, \theta_{E_2}, \theta_{E_3}$	=	pure nodal rotations at a node
$\bar{\theta}_x, \bar{\theta}_y, \bar{\theta}_z$	=	incremental rotations of a nodal triad
ν	=	Poisson's ratio
Φ	=	wingbeat amplitude in radians
Ψ	=	rotational pseudovector
ψ	=	magnitude of rotational pseudovector
Ω	=	skew-symmetric matrix of the angular velocity vector $\bar{\omega}$
Ω_{pn}	=	skew-symmetric spin tensor corresponding to pure nodal rotations
$\bar{\omega}$	=	angular velocity vector prescribed at the root
ω_n	=	column vector of incremental rotations of a nodal triad

I. Introduction

FLAPPING-WING micro aerial vehicles (MAVs) are envisioned as being small (maximum dimension of 15 cm), flying at low speeds (10–15 m/s), and equipped with the capabilities of stable hover and vertical takeoff. These vehicles are basically inspired by biological flyers, including large insects and/or small birds. The mechanical properties of a typical insect wing are anisotropic because of its typical membrane-vein type configuration. It was shown that, in a majority of insect species, the spanwise bending stiffness is about one to two orders of magnitude larger than the chordwise bending stiffness [1] and, in general, the spanwise flexural stiffness scales with the third power of the wing chord while the chordwise stiffness scales with the second power of the wing chord [1]. High-speed cine and still photography and stroboscopy indicate that most biological flyers undergo orderly deformation in flight and that a controlled change of wing shape during the beat cycle may prove to be essential for the development of adequate net lift and thrust. The experimentally observed patterns of insect wing deformation indicate that they involve significant camber motions [2]. Finite element (FE) models of thin flapping wings should therefore account for such deformations, and so plate/shell elements will be appropriate to analyze them.

This work describes the development of a new shell element using the corotational (CR) approach [3–5] to analyze flapping-wing structures undergoing large (global) displacements and rotations but small strains. The key motivating factors behind the development of the CR methods are simplicity of formulation and the ability to reuse existing, very efficient, small strain, linear elements. They can also be adapted to have large strains, as shown in [6]. A key motivating factor behind the development of a new shell element is that commercial codes like MSC.Marc are not amenable to implicit coupling with an external computational fluid dynamics solver for fluid–structure interaction computations. Moreover, the proposed formulation is a fundamental step toward other developments in flapping-wing analyses. For example, if one wants to do gradient-based design, model reduction, time-periodic schemes, etc., this formulation can provide convenient Jacobians to support such analyses, while a code like MSC.Marc may not do so in an effective way.

The CR approach was previously applied by several researchers to static modeling of structures undergoing large displacements/rotations and small deformations [4,7]. In many of the cases where the approach was applied in a dynamic context, the structures were limited to beam elements [8–13]. Applications to the dynamics of shell structures are very scarce in literature [14–17]; furthermore, their application to shell elements for flexible multibody system applications, including those of flapping wings, are even more scarce [16,18,19].

As part of the current effort, the static CR formulation for shell elements developed previously by Khosravi et al. [4,5] is adapted to include the dynamics associated with flapping. The static element formulation of [4,5] is new, in that the stiffness matrix for the shell element was developed by combining the discrete Kirchoff triangle (DKT) plate bending element [20] and the optimal triangle (OPT) membrane element [21]. The DKT element was found to be most effective among several nine-degree-of-freedom (DOF) triangular plate elements studied in [20], based on criteria-combining accuracy, computational cost, and simplicity in use. The formulation of the OPT element is based on the assumed natural deviatoric strain template [21], which is a general formulation that can produce a group of elements by assigning different values to some free parameters [4]: a special set of which gives the OPT element, which is

insensitive to aspect ratio of the FE. Furthermore, a projector matrix [22] was applied to the shell stiffness matrix in order to correctly account for its rigid body properties. The tangent stiffness matrix was then obtained by including the effect of stress stiffening in the CR frame using the Green–Lagrange strain-displacement relations. This enables the element to account for larger rigid body structural displacements and rotations than the conventional geometrically nonlinear plate/shell elements, which use von Karman strains with respect to a fixed frame. It may be noted that, although the current work is based on many efforts that already appear in literature, the paper incorporates many disparate techniques that have not been incorporated before. Some of those include the use of the CR-total-Lagrangian (CR-TL) representation of a triangular shell with multi-body dynamics effects, numerical integration with the generalized-α method [23,24], and (more important) the application to flapping-wing structures.

The rest of the paper is organized as follows. Section II describes the entire computational structural dynamics (CSD) formulation in great detail, starting from the definitions of various coordinate systems used in the analysis, the computation of virtual work due to inertial forces, the formulation of the element tangent stiffness and mass matrices, and the time integration of the governing equations of motion using the generalized-α method [23,24]. Section III presents some verification and validation studies for the CSD solver, including examples to illustrate the rigid body kinematics, static, and dynamic response capabilities of the code. Finally, the concluding remarks are made in Sec. IV.

II. Computational Structural Dynamics Formulation (University of Michigan Nonlinear Membrane Shell Solver)

This section presents the theoretical formulation for the structural dynamics solution [University of Michigan Nonlinear Membrane Shell Solver (UM/NLAMS)] that was developed in this work. The geometrically nonlinear shell FE formulation developed here is based on a CR approach and has the capability to handle time-dependent boundary conditions suitable for a flapping-wing problem. The nonlinear structural dynamics solution is based on a flexible multibody-type FE analysis [3,16] of a flapping wing. It relies on the use of a body-fixed floating frame of reference to describe the prescribed rigid body motion and on a CR form of the TL approach [25] to account for geometric nonlinearities. The solution is implemented in the UM/NLAMS, written in Fortran 90. The CR formulation has generated a great amount of interest in the last couple of decades. A comprehensive list of references that discuss this formulation is available in [3]. The idea of this approach is to decompose the motion into rigid body and pure deformational parts through the use of a local frame at each FE, which translates and rotates with the element [26]. The components of the element's internal force vector are first calculated relative to the CR frame and are then transformed to a global frame using a CR transformation matrix. The CR frame transformation eliminates the element rigid body motion so that a linear deformation theory can be used [3] as long as the flexible deformations are small with respect to the element dimensions. Hence, its main advantage is its effectiveness for problems with small strains but large rotations [6].

The CR formulation can be applied in two different forms, as listed next:

1) In the corotational-total-Lagrangian approach (CR-TL), the reference configuration is taken as the initial configuration but translated and rotated in accordance with the motion of the corotating local system.

2) In the corotational-updated-Lagrangian approach (CR-UL), the translated and rotated configuration at the previous time step is taken as the reference configuration during the current time step [27].

The CR-TL approach is used in this work. The key motivation behind the use of it is that the stiffness matrix for the triangular shell element was originally formulated by Khosravi et al. [4] using a CR-TL approach and extensively verified/validated. The current work is an extension of their effort to include flapping-wing dynamics. Application of this method to problems concerning flapping-wing aeroelasticity are not available; however, recent studies by Relvas and Suleman [17,28] reported the development of a method involving the application of CR theory to nonlinear aeroelasticity problems. Relvas and Suleman [17] discussed the coupling of a vortex-ring method with a CR structural solution of a four-noded shell FE and studied the stability of a nonlinear clamped plate subjected to low-speed airflow to illustrate the fluid–structure interaction procedure. In a subsequent effort, the same authors [28] presented the coupling of an Euler flow solver with a nonlinear CR beam FE solver and demonstrated it by studying the dynamic response of two-dimensional NACA 0012 airfoil section resting on a Winkler foundation. Two types of analyses were performed: the first assumed that the airfoil was rigid and the second assumed it to be flexible and discretized the airfoil surface
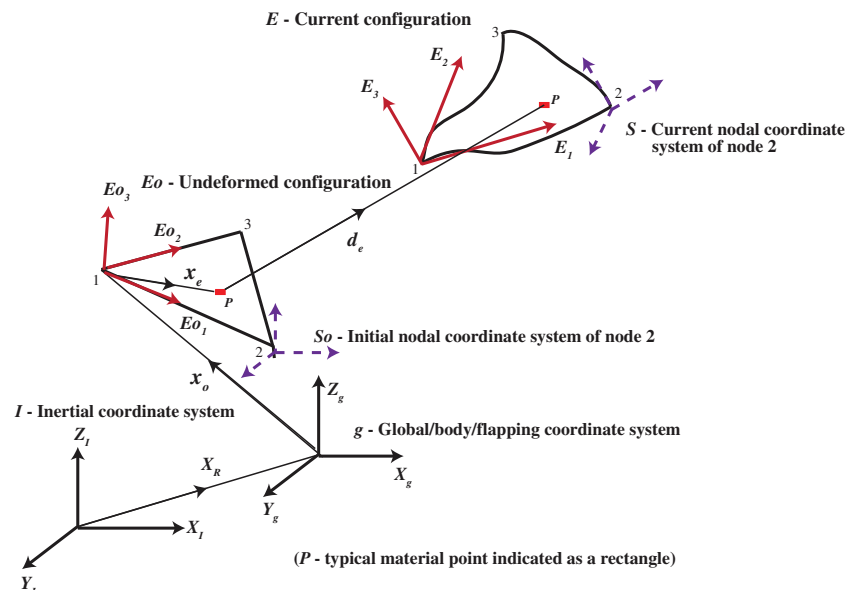

Fig. 1   A schematic showing the undeformed (initial) and deformed configurations of a typical shell element and the various coordinate systems involved in the analysis.

with CR beam elements. The CR approach was successfully applied to analyze flutter and limit-cycle oscillations by Attar and Gordnier [29].

The three key issues identified during a literature survey in the present work concerning the use of a CR formulation are 1) the choice of a suitable local element frame, 2) the choice of a suitable element (this is especially important for triangular shells, since they are obtained as a superposition of membrane and plate models and several combinations are possible), and 3) parameterization of local and global rotations.

The first issue is discussed in [26,30,31]. While several alternatives have been proposed for the choice of the local element frame, for most problems where only small strains are involved, this issue is not important. However, in such a case, it is critical that the local element deformational displacements are small relative to the element dimensions. In the current work, triangular elements will be used for the FE discretization. The specific issues involved in choosing local element frames concerning the use of triangular shell elements are discussed in [7], and the choice of a suitable linear element is discussed in [32]. The development of flapping-wing dynamic FE equations of motion for thin shell structures is discussed next. The formulation is a proposed extension for flapping-wing dynamics of the static CR analysis of shell structures presented previously [4,5,33].

The derivation of flapping-wing equations of motion using nonlinear shell FEs via a CR approach to accommodate prescribed time-dependent boundary conditions involves several key steps discussed next (note that a matrix notation is followed in the formulation).

A. Definition of Coordinate Systems in Analysis

Several coordinate systems are required to fully describe the geometry and deformation of the shell structure. Figure 1 shows a schematic of a typical triangular shell FE in its initial (undeformed) and the deformed (current) configurations. A total of $2 + N_e + N_n$ (where N_e is the number of FEs, and N_n is the number of nodes in the discretized structure) coordinate systems are used in the analysis:

1) The first coordinate system used is an inertial frame that is always fixed in time (I in Fig. 1).

2) The second coordinate system used is a floating (global) frame for which the motion is known in the inertial frame by virtue of the prescribed rigid body motion of the structure (g in Fig. 1).

3) The third coordinate system used is N_e CR frames (one for each element) that translate and rotate with the element as it deforms (E_o and E in Fig. 1).

4) The fourth coordinate system used is N_n nodal coordinate frames (one for each node) that are rigidly tied to their respective nodes and rotate with them (S_o and S in Fig. 1).

The final equations of motion are written with respect to the global frame g.

B. Computation of Inertial Velocities and Accelerations of a Material Point

The position (in the inertial frame) of a material point P (see Fig. 1) in the structure is given by

$$X = X_R + T_{IG}x_g \qquad (1)$$

where X is the position vector in the inertial frame, X_R is the position vector of the structure's actuation point (or the origin of the flapping/global frame) in the inertial frame, x_g is the position vector of P in the global frame, and T_{IG} is a transformation matrix from the global frame to the inertial frame. This matrix is a nonlinear function of the components of the rotational pseudovector Ψ (a unit vector that defines a finite rotation in space) [34], which defines the orientation of the global frame with respect to the inertial frame. The pseudovector is defined as

$$\Psi = \psi\hat{p} \qquad (2)$$

where ψ is the magnitude of rotation, and $\hat{p}$ is the direction of rotation, defined as

$$\hat{p} = \frac{\Psi}{\psi} = \begin{Bmatrix} \hat{p}_x \\ \hat{p}_y \\ \hat{p}_z \end{Bmatrix} \qquad (3)$$

In general, both the magnitude ψ and the direction of rotation $\hat{p}$ could be time dependent. In the case where the direction of rotation is constant, the resultant motion of the tip of the pseudovector will be in a plane. If the direction of rotation changes with time, the motion of the tip will be in three dimensions. The former case is two-dimensional and the latter is three-dimensional rotation [19,34]. The transformation matrix T_{IG} is defined, as in [35]:

$$T_{IG} = I_m + \tilde{\hat{p}}\sin\psi + 2(\tilde{\hat{p}})^2\sin^2\frac{\psi}{2} \qquad (4)$$

where I_m is a 3×3 identity matrix, and the tilde indicates a skew-symmetric matrix. The position vector of the material point with respect to the global coordinate system x_g given in Eq. (1) can be written as

$$x_g = x_o + T_{GE_o}(x_e + d_e) \qquad (5)$$

where x_o is the position vector of the origin of an element frame in the undeformed configuration with respect to the global frame expressed as components in the global frame, T_{GE_o} is the transformation matrix from undeformed element frame to the global frame, x_e is the position vector of the point with respect to the undeformed element frame, and d_e is the vector of displacements of the point with respect to the same. The position vector of the material point in the inertial frame given in Eq. (1) then becomes

$$X = X_R + T_{IG}x_o + T_{IG}T_{GE_o}x_e + T_{IG}T_{GE_o}d_e \qquad (6)$$

The time derivative of the transformation matrix in Eq. (4) is [36]:

$$\dot{T}_{IG} = \Omega T_{IG} \qquad (7)$$

where Ω is a skew-symmetric matrix of the angular velocity vector $\bar{\omega}$ prescribed at the wing root. The velocity and acceleration of the material point can then be computed by successive differentiation of the position vector in Eq. (6) and are given as

$$\dot{X} = \dot{X}_R + \Omega T_{IG}x_o + \Omega T_{IG}T_{GE_o}x_e + \Omega T_{IG}T_{GE_o}d_e \\ + T_{IG}T_{GE_o}\dot{d}_e \qquad (8)$$

$$\ddot{X} = \ddot{X}_R + (\dot{\Omega} + \Omega\,\Omega)T_{IG}(x_o + T_{GE_o}x_e + T_{GE_o}d_e) \\ + 2\,\Omega T_{IG}T_{GE_o}\dot{d}_e + T_{IG}T_{GE_o}\ddot{d}_e \qquad (9)$$

C. Computation of Virtual Work due to Inertial Forces

The virtual work due to inertial forces for an element is given by

$$\delta W = \rho_s \int_{v_{el}} \delta X^T \ddot{X}\,dv_{el} \qquad (10)$$

where δX is the variation of the position vector; that is,

$$\delta X = T_{IG}T_{GE_o}\delta d_e \qquad (11)$$

and v_{el} is the volume of the element. The vector of displacements d_e can be approximated as

$$d_e = Nq_e \qquad (12)$$

where N is a matrix of shape functions of size 3×18, and q_e is the FE nodal DOF vector of size 18×1 with respect to the undeformed element frame. Equation (11) is derived from Eq. (6) by following the regular variational approach. In the variational process, the first, second, and third terms in Eq. (6) vanish, since they are either prescribed or constant. For example, X_R is the position vector of the structure's actuation point with respect to the inertial frame. This is a

prescribed quantity in this work; hence, the variation of this term is simply zero. The variation of the position vector now becomes

$$\delta X = T_{IG} T_{GE_o} N \delta q_e \tag{13}$$

The acceleration vector can be written as

$$\ddot{X} = \ddot{X}_R + (\dot{\Omega} + \Omega\,\Omega) T_{IG}(x_o + T_{GE_o} x_e + T_{GE_o} N q_e)$$
$$+ 2\,\Omega\, T_{IG} T_{GE_o} N \dot{q}_e + T_{IG} T_{GE_o} N \ddot{q}_e \tag{14}$$

Using the previous terms, the virtual work expression in Eq. (10) now becomes

$$\delta W = \rho_s \int_{v_{el}} \{\delta q_e^T N^T T_{GE_o}^T T_{IG}^T \ddot{X}_R + \delta q_e^T N^T T_{GE_o}^T T_{IG}^T (\dot{\Omega}$$
$$+ \Omega\,\Omega) T_{IG} x_o + \delta q_e^T N^T T_{GE_o}^T T_{IG}^T (\dot{\Omega} + \Omega\,\Omega) T_{IG} T_{GE_o} x_e$$
$$+ \delta q_e^T N^T T_{GE_o}^T T_{IG}^T (\dot{\Omega} + \Omega\,\Omega) T_{IG} T_{GE_o} N q_e$$
$$+ 2\delta q_e^T N^T T_{GE_o}^T T_{IG}^T \Omega\, T_{IG} T_{GE_o} N \dot{q}_e$$
$$+ \delta q_e^T N^T T_{GE_o}^T T_{IG}^T T_{IG} T_{GE_o} N \ddot{q}_e\} \, dv_{el} \tag{15}$$

From this expression, the element local mass matrix, gyroscopic damping matrix, dynamic stiffness matrix, and the inertial contribution to the force vector are given by

$$M_{el} = \rho_s \int_{v_{el}} \{N^T T_{GE_o}^T T_{IG}^T T_{IG} T_{GE_o} N\} \, dv_{el} \tag{16}$$

$$C_{el} = 2\rho_s \int_{v_{el}} \{N^T T_{GE_o}^T T_{IG}^T \Omega\, T_{IG} T_{GE_o} N\} \, dv_{el} \tag{17}$$

$$K_{el}^{dyn} = \rho_s \int_{v_{el}} \{N^T T_{GE_o}^T T_{IG}^T (\dot{\Omega} + \Omega\,\Omega) T_{IG} T_{GE_o} N\} \, dv_{el} \tag{18}$$

$$F_{el}^p = -\rho_s \int_{v_{el}} \{N^T T_{GE_o}^T T_{IG}^T \ddot{X}_R + N^T T_{GE_o}^T T_{IG}^T (\dot{\Omega} + \Omega\,\Omega) T_{IG} x_o$$
$$+ N^T T_{GE_o}^T T_{IG}^T (\dot{\Omega} + \Omega\,\Omega) T_{IG} T_{GE_o} x_e\} \, dv_{el} \tag{19}$$

These equations are numerically integrated using a seven-point Gauss quadrature [37]. The element mass matrix in Eq. (16) is consistent. The damping matrix in Eq. (17) is a skew-symmetric matrix arising from Coriolis forces. The stiffness matrix in Eq. (18) is a dynamic term representing the coupling effect between the large rigid body motions and the elastic motions. The elastic portion of the stiffness matrix will be discussed subsequently. The force vector in Eq. (19) is due to the prescribed rigid body motion (inertial contribution that initially appears with a +ve sign on the left-hand side of the equations of motion but is brought to the right with a −ve sign). The first term arises from rigid body translational motion. The second and the third terms arise from rigid body angular and centrifugal accelerations. A fourth term in the forcing vector will arise due to aerodynamic loading.

D. Element Local Deformations (Corotational Approach)

As mentioned previously, the static CR formulation of a shell element, as described in [4,5,33], is used in this work. While full details of the approach are provided in those references, a brief overview of it is presented here while extensively quoting from [4]. Referring to Fig. 1, the origin of the undeformed element frame E_o is chosen at node 1 of the element, and the axis E_{o_1} (i.e., the local x axis) is chosen as the line joining nodes 1 and 2. The axis E_{o_3} (the local z axis) is the normal to the element midplane containing the nodes 1, 2, and 3. The axis E_{o_2} (the local y axis) then defines a Cartesian right-handed coordinate system. The coordinate system denoted by E is the element CR system defined in a similar fashion but in the current

or deformed configuration. The nodal coordinate systems are denoted by S_o and S in the undeformed and deformed configurations, respectively (shown only for node 2 in Fig. 1 for clarity). The orientation of S_o is arbitrary and is chosen to be parallel to the inertial frame in this work. The coordinate system S in the current configuration is obtained by updating its transformation matrix, which defines the current orientation of the node in the global system. This is done after every Newton–Raphson iteration using the following expression:

$$T_{S_{new}} = \bar{T} T_{S_{old}} \tag{20}$$

where

$$\bar{T} = I_m + \frac{\tilde{\omega}_n + 0.5\tilde{\omega}_n^2}{1 + 0.25|\omega_n|^2} \tag{21}$$

$$\omega_n = [\bar{\theta}_x \quad \bar{\theta}_y \quad \bar{\theta}_z]^T \tag{22}$$

$$\tilde{\omega}_n = \begin{bmatrix} 0 & -\bar{\theta}_z & \bar{\theta}_y \\ \bar{\theta}_z & 0 & -\bar{\theta}_x \\ -\bar{\theta}_y & \bar{\theta}_x & 0 \end{bmatrix} \tag{23}$$

The $\bar{\theta}$ quantities are the incremental rotations of triad S computed in the global coordinate system during the previous iteration. Once the nodal coordinate systems in the current configuration are obtained, the next step is the computation of the pure deformations (both displacements and rotations) in the local coordinate system E. Pure nodal displacements at a node m in E may be expressed by the relation,

$$u_E^m = \begin{Bmatrix} u_{E_1}^m \\ u_{E_2}^m \\ u_{E_3}^m \end{Bmatrix} = T_{EG}\Big(q_{dg}^m + x_o^m - q_{dg}^1 - x_o^1\Big) - x_e^m \tag{24}$$

where $m = 1$, 2, and 3. T_{EG} is a transformation matrix from the global frame to the current element frame, q_{dg}^m is the displacement vector of a node m in the global frame, and x_o^m is the position vector of node m in the undeformed element configuration expressed in the global frame. The variable x_o^1 is equal to x_o, introduced in Eq. (5). Pure nodal rotations expressed in E are equal to the components of a skew-symmetric matrix spin tensor defined as

$$\Omega_{pn} = \begin{bmatrix} 0 & -\theta_{E_3} & \theta_{E_2} \\ \theta_{E_3} & 0 & -\theta_{E_1} \\ -\theta_{E_2} & \theta_{E_1} & 0 \end{bmatrix} \tag{25}$$

This tensor is found by using the following expressions:

$$\Omega_{pn} = 2(T - I_m)(T + I_m)^{-1} \tag{26}$$

$$T = T_{EG} T_{S_{new}} T_{GE_o} \tag{27}$$

where the matrices T_{EG} and $T_{GE_o}^T$ transform the components of a vector in the global frame into those in deformed CR and undeformed CR frames, respectively. The vector of pure deformations at a node is given by

$$d_{pure}^m = [u_{E_1}^m \quad u_{E_2}^m \quad u_{E_3}^m \quad \theta_{E_1}^m \quad \theta_{E_2}^m \quad \theta_{E_3}^m]^T \tag{28}$$

The vector of pure element deformations is obtained by combining such vectors at all three nodes of the element and is given by

$$d_{pure} = \begin{pmatrix} d_{pure}^1 \\ d_{pure}^2 \\ d_{pure}^3 \end{pmatrix} \tag{29}$$

E. Element Stiffness Matrix/Nonlinear Internal Force Vector

A three-node triangular shell element involving an optimal membrane element (OPT) [21] and a DKT plate bending element [20] presented in [4,5] is used in this work. Both of these elements are described briefly below:

1) The DKT element formulation is based on discrete Kirchoff theory of thin plates. It begins with independent fields for lateral displacement and for rotation of a midsurface normal line, like in Mindlin elements [38]. In this approach, the strain energy contribution due to shear stresses is neglected, and the normality to the midsurface is enforced at discrete points at the element edges. With these constraints imposed, a 9-DOF element is obtained with two rotations and a displacement at each of the element nodes. Full details of the DKT formulation are given in [38]. As a consequence of the process by which the element is derived, the transverse displacement is not explicitly defined in the interior of the element. Hence, the shape functions required to form the mass, damping, dynamic stiffness, and the stress stiffening matrix (discussed later) along with the force vector are not available. This problem may be overcome by borrowing shape functions from other similar elements. Following [4], for the displacement interpolation, the shape functions corresponding to a Bazeley, Cheung, Irons, and Zienkiewicz plate element [37] are used. The stiffness matrix (of size 9×9) corresponding to the plate bending DOF can be written as [4]

$$K_b = \int B_b^T D B_b \, dA_e \qquad (30)$$

where B_b is the strain-nodal displacement matrix corresponding to bending deformation, D is the bending stiffness matrix, and A_e is the area of the triangular FE.

2) The OPT element is termed optimal because, for any arbitrary aspect ratio, its response for in-plane pure bending is exact. Like the DKT element, the OPT element is based on an assumption on strains, and so the shape functions are borrowed from another triangular membrane element (linear strain triangle-retrofitted) with the same DOFs as that of the OPT element. The stiffness matrix (of size 9×9) corresponding to the membrane DOF is [4]

$$K_m = \int B_m^T A B_m \, dA_e \qquad (31)$$

where B_m is the strain-nodal displacement matrix corresponding to membrane deformation, and A is the stretching stiffness matrix.

The DKT and the OPT element stiffness matrices are combined to form the final shell stiffness matrix of the element and are further modified to include the membrane-bending coupling effect for laminated composite plates:

$$K_{el}^{shell} = \begin{bmatrix} K_m & \int B_m^T B B_b \, dA_e \\ \int B_b^T B B_m \, dA_e & K_b \end{bmatrix} \qquad (32)$$

where B is the membrane-bending coupling stiffness matrix. More details of the stiffness matrices, including the definition of the individual terms, are presented in [4].

The effect of nonlinear stress stiffening is added to the CR formulation by including a geometric stiffness matrix [38]. The expression for stress stiffening is obtained by considering the work done by the membrane forces (computed from the solution of the previous iteration) as they act through displacements associated with small lateral and in-plane deflections. The final expression for the stress stiffening matrix is given by

$$K_{el}^{ss} = \int G^T \begin{bmatrix} N_{mf} & 0_{2\times2} & 0_{2\times2} \\ 0_{2\times2} & N_{mf} & 0_{2\times2} \\ 0_{2\times2} & 0_{2\times2} & N_{mf} \end{bmatrix} G \, dA \qquad (33)$$

The submatrix N_{mf} of size 2×2, for which the components are the membrane forces, is the same as $\tilde{N}$, defined in [4]. More details on the derivation of this expression along with a definition of the individual terms are given in [4,38].

Using the pure element deformations in Eq. (29), the nonlinear internal force vector is computed using the local element shell and dynamic stiffness matrices [after rearranging them according to desired order of DOFs, as in Eq. (29)], as

$$r_{el}^{int} = (K_{el}^{shell} + K_{el}^{dyn}) d_{pure} \qquad (34)$$

Since the pure deformations obtained in Eq. (29) may not really be pure (i.e., without any rigid body components), a projector matrix P_r can be introduced to bring the nonequilibrated internal force vector into equilibrium. The details of the projection are beyond the scope of this paper. The readers are referred to [22] for more details. The local element stiffness matrix computed in Eq. (32) and the internal force vector computed in Eq. (34) are filtered through the projector matrix as follows:

$$K_{el}^{shell-p} = P_r^T K_{el}^{shell} P_r \qquad (35)$$

$$r_{el}^{int-p} = P_r^T K_{el}^{shell} d_{pure} \qquad (36)$$

In computing the projection of the internal force vector, as shown in Eq. (36), the contribution due to the dynamic stiffness matrix is excluded. At this point, if the membrane forces are expected to be significant, the stress stiffness matrix obtained in Eq. (33) should be added to the projected local element stiffness matrix in Eq. (35).

Having obtained the stiffness and mass matrices along with the internal force vector in the element frame, they are all transformed into the global frame before the FE assembly process. The transformation of the element local stiffness matrix, which includes both the elastic and the dynamic stiffness terms, is given as

$$K_{el-g}^{shelldyn-p} = (T_{GE}^f)(K_{el}^{shell-p} + K_{el}^{dyn})(T_{GE}^f)^T \qquad (37)$$

where the transformation matrix T_{GE}^f (previously mentioned) is an expanded form of T_{GE} (which is a transpose of T_{EG}, defined earlier) used to accommodate the transformation of all 18 DOFs of the element. The subscript $-g$ indicates that the corresponding element matrix operates on the global DOFs. The superscript f indicates full/expanded. Similarly, the element mass and the gyroscopic matrices given in Eqs. (16) and (17), respectively, are transformed into the global frame as follows:

$$M_{el-g} = T_{GE_o} M_{el} T_{GE_o}^T \qquad (38)$$

$$C_{el-g} = T_{GE_o} C_{el} T_{GE_o}^T \qquad (39)$$

Furthermore, the element internal force and the prescribed-motion force vectors given in Eqs. (19) and (36), respectively, are transformed to the global frame as

$$r_{el-g}^{int} = T_{GE}^f r_{el}^{int-p} \qquad (40)$$

$$F_{el-g}^p = T_{GE_o}^f F_{el}^p \qquad (41)$$

The global element mass, stiffness, and gyroscopic damping matrices given in Eqs. (37–39), respectively, and the element global internal force and prescribed-motion force vectors given in Eqs. (40) and (41), respectively, are assembled for the entire structure to form global matrices/vectors. The global mass, tangent stiffness, and damping matrices are denoted as M, K_t (assembled form of $K_{el-g}^{shelldyn-p}$ matrix for the entire structure), and C, respectively, while the global internal and the total force vectors are denoted as R and F, respectively.

F. Direct Time Integration of University of Michigan Nonlinear Membrane Shell Solver Governing Equations

The nonlinear structural dynamics FE governing equations of motion can be written as

$$Ma + Cv + R(q) = F \qquad (42)$$

where q is the nodal DOF vector in the global frame, and v and a are the global velocity and acceleration vectors, respectively. In this work, the numerical integration of the governing equations was performed using either the Newmark or the generalized-α methods [23,24]. Reference [23] discussed the application of the generalized-α scheme for linear problems. In this work, it is extended to solve the nonlinear equations of motion in a predictor–corrector-type of framework similar to the one described for the Newmark method in [39]. The generalized-α method discussed in [23] solves second-order differential equations for a discrete time step n, using the standard Newmark relations to update the displacements and velocities, as shown next:

$$q_{n+1} = q_n + \Delta t_s v_n + \Delta t_s^2 [(\tfrac{1}{2} - \beta) a_n + \beta a_{n+1}] \qquad (43)$$

$$v_{n+1} = v_n + \Delta t_s [(1 - \gamma_{nm}) a_n + \gamma_{nm} a_{n+1}] \qquad (44)$$

The balance equation is given by

$$M a_{n+1-\alpha_m} + C v_{n+1-\alpha_f} + R_{n+1-\alpha_f} = F(t_{n+1-\alpha_f}) \qquad (45)$$

where

$$
\begin{aligned}
a_{n+1-\alpha_m} &= (1 - \alpha_m) a_{n+1} + \alpha_m a_n \\
v_{n+1-\alpha_f} &= (1 - \alpha_f) v_{n+1} + \alpha_f v_n \\
R_{n+1-\alpha_f} &= (1 - \alpha_f) R_{n+1} + \alpha_f R_n \\
F(t_{n+1-\alpha_f}) &= (1 - \alpha_f) F_{n+1} + \alpha_f F_n
\end{aligned}
\qquad (46)
$$

Substituting the relations in Eq. (46) into the balance equation in Eq. (45) gives

$$
M[(1 - \alpha_m) a_{n+1} + \alpha_m a_n] + C[(1 - \alpha_f) v_{n+1} + \alpha_f v_n] \\
+ (1 - \alpha_f) R_{n+1} + \alpha_f R_n = (1 - \alpha_f) F_{n+1} + \alpha_f F_n \qquad (47)
$$

Using the Newmark update relation of displacements in Eq. (43), the accelerations become

$$a_{n+1} = \frac{1}{\beta \Delta t_s^2} \left[q_{n+1} - q_n - \Delta t_s v_n - \Delta t_s^2 \left(\frac{1}{2} - \beta \right) a_n \right] \qquad (48)$$

$$a_{n+1} = \frac{1}{\beta \Delta t_s^2} \left[\delta q - \Delta t_s v_n - \Delta t_s^2 \left(\frac{1}{2} - \beta \right) a_n \right] \qquad (49)$$

Substituting this into the velocity update relation equation (44) gives

$$
v_{n+1} = v_n + \Delta t_s (1 - \gamma_{nm}) a_n + \frac{\gamma_{nm}}{\beta \Delta t_s} \delta q - \frac{\gamma_{nm}}{\beta} v_n \\
- \frac{\gamma_{nm} \Delta t_s}{\beta} \left(\frac{1}{2} - \beta \right) a_n \qquad (50)
$$

Substituting the previous two relations equations (49) and (50) in the velocity and acceleration relations of Eq. (46) gives

$$
a_{n+1-\alpha_m} = (1 - \alpha_m) \frac{1}{\beta \Delta t_s^2} \left[\delta q - \Delta t_s v_n - \Delta t_s^2 \left(\frac{1}{2} - \beta \right) a_n \right] \\
+ \alpha_m a_n \qquad (51)
$$

$$
v_{n+1-\alpha_f} = (1 - \alpha_f) \left[v_n + \Delta t_s (1 - \gamma_{nm}) a_n + \frac{\gamma_{nm}}{\beta \Delta t_s} \delta q - \frac{\gamma_{nm}}{\beta} v_n \right. \\
\left. - \frac{\gamma_{nm} \Delta t_s}{\beta} \left(\frac{1}{2} - \beta \right) a_n \right] + \alpha_f v_n \qquad (52)
$$

Using the tangent stiffness method [39], the internal forces at time step $n+1$ (i.e., R_{n+1}) can be written as

$$R_{n+1} = R_n + K_t \delta q \qquad (53)$$

$$R_{n+1-\alpha_f} = (1 - \alpha_f)(R_n + K_t \delta q) + \alpha_f R_n \qquad (54)$$

Substituting the previous set of equations in the balance equation, Eq. (45) becomes

$$K_{\text{eff}} \delta q = R_h \qquad (55)$$

where K_{eff} and R_h are the effective stiffness matrix and the effective load vector, and they are given as

$$K_{\text{eff}} = \frac{1 - \alpha_m}{\beta \Delta t_s^2} M + \frac{1 - \alpha_f}{\beta \Delta t_s} C + (1 - \alpha_f) K_t \qquad (56)$$

$$
\begin{aligned}
R_h ={}& \frac{1 - \alpha_m}{\beta \Delta t_s} M v_n + \frac{1 - \alpha_m}{\beta} \left(\frac{1}{2} - \beta \right) M a_n - \alpha_m M a_n \\
&- C(1 - \alpha_f) V_n - \cdots - C(1 - \alpha_f) \Delta t_s (1 - \gamma_{nm}) a_n \\
&+ C(1 - \alpha_f) \frac{\gamma_{nm}}{\beta} v_n + C(1 - \alpha_f) \frac{\gamma_{nm} \Delta t_s}{\beta} \left(\frac{1}{2} - \beta \right) a_n \\
&- C \alpha_f v_n - (1 - \alpha_f) R_n - \alpha_f R_n + (1 - \alpha_f) F_{n+1} + \alpha_f F_n \quad (57)
\end{aligned}
$$

A step-by-step solution procedure to solve the system of equations using the quantities computed in Eqs. (56) and (57) is given as follows:

1) Initialize q_o and its time derivatives.

2) Select a time-step size Δt_s and a spectral radius parameter S_r ($0 \le S_r \le 1$): this parameter is inversely proportional to the high-frequency dissipation. The time-integration method used in this paper is implicit, and so the choice of time step should be based on the desired solution accuracy and on the stability of the Newton–Raphson algorithm. In the case of flapping-wing simulations, as presented in this work, the time step was also chosen based on the frequency and amplitude of prescribed motion, so the incremental displacements and rotations within a time step (effectively a load step) are small. For example, smaller time steps were needed for larger (i.e., more nonlinear) amplitudes in order to force the Newton–Raphson loop to converge.

3) Compute parameters $\alpha_f = -S_r/(1 + S_r)$ and $\alpha_m = (1 - 2S_r)/(1 + S_r)$.

4) Compute parameters $\gamma_{nm} = 0.5 + \alpha_m - \alpha_f$ and $\beta = 0.25(1 + \alpha_m - \alpha_f)^2$.

5) Form the effective stiffness matrix from the individual mass, damping, and tangent stiffness matrices using Eq. (56).

6) Form the effective load vector equation (57).

7) Solve for the displacement increments using Eq. (55). To improve the solution accuracy and to avoid the development of numerical instabilities, it is generally necessary to employ iterations within each time step in order to maintain equilibrium [39]. The following are the steps to be followed in a typical iteration j within the iterative loop.

1) Evaluate the $(j-1)$th approximation to the acceleration, velocities, and displacements using

$$
a_{co} = \frac{1 - \alpha_m}{\beta \Delta t_s^2}, \qquad a_{c1} = \frac{\gamma_{nm}}{\beta \Delta t_s}, \quad a_{c2} = \frac{1}{\beta \Delta t_s}, \qquad a_{c3} = \frac{1}{2\beta} - 1
$$
$$
a_{c4} = \frac{\gamma_{nm}}{\beta} - 1, \qquad a_{c5} = \frac{\Delta t_s}{2} \left(\frac{\gamma_{nm}}{\beta} - 2 \right)
$$
$$(58)$$

$$
a_{n+1}^{j-1} = a_{co} \delta q^{j-1} - a_{c2} \dot{q}_n - a_{c3} \ddot{q}_n
$$
$$
v_{n+1}^{j-1} = a_{c1} \delta q^{j-1} - a_{c4} \dot{q}_n - a_{c5} \ddot{q}_n, \qquad q_{n+1}^{j-1} = q_n + \delta q^{j-1}
$$
$$(59)$$

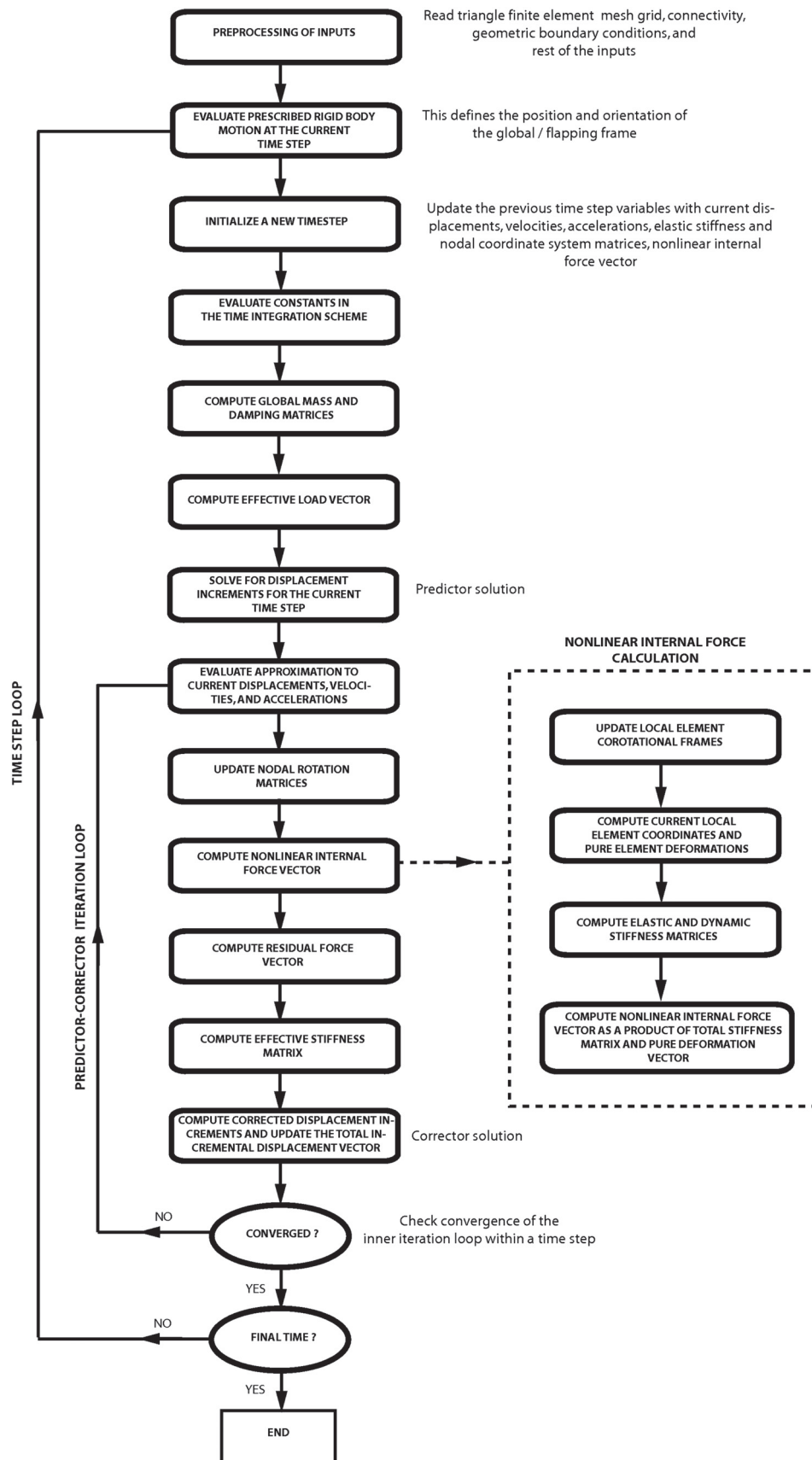2) Update nodal rotation matrices using the new approximation to the solution q [last of Eqs. (20) and (59)].

| PREPROCESSING OF INPUTS | Read triangle finite element mesh grid, connectivity, geometric boundary conditions, and rest of the inputs |

EVALUATE PRESCRIBED RIGID BODY MOTION AT THE CURRENT TIME STEP — This defines the position and orientation of the global / flapping frame

INITIALIZE A NEW TIMESTEP — Update the previous time step variables with current displacements, velocities, accelerations, elastic stiffness and nodal coordinate system matrices, nonlinear internal force vector

EVALUATE CONSTANTS IN THE TIME INTEGRATION SCHEME

COMPUTE GLOBAL MASS AND DAMPING MATRICES

COMPUTE EFFECTIVE LOAD VECTOR

SOLVE FOR DISPLACEMENT INCREMENTS FOR THE CURRENT TIME STEP — Predictor solution

EVALUATE APPROXIMATION TO CURRENT DISPLACEMENTS, VELOCITIES, AND ACCELERATIONS

UPDATE NODAL ROTATION MATRICES

COMPUTE NONLINEAR INTERNAL FORCE VECTOR

COMPUTE RESIDUAL FORCE VECTOR

COMPUTE EFFECTIVE STIFFNESS MATRIX

COMPUTE CORRECTED DISPLACEMENT INCREMENTS AND UPDATE THE TOTAL INCREMENTAL DISPLACEMENT VECTOR — Corrector solution

CONVERGED ? — Check convergence of the inner iteration loop within a time step

FINAL TIME ?

END

TIME STEP LOOP

PREDICTOR-CORRECTOR ITERATION LOOP

NONLINEAR INTERNAL FORCE CALCULATION

UPDATE LOCAL ELEMENT COROTATIONAL FRAMES

COMPUTE CURRENT LOCAL ELEMENT COORDINATES AND PURE ELEMENT DEFORMATIONS

COMPUTE ELASTIC AND DYNAMIC STIFFNESS MATRICES

COMPUTE NONLINEAR INTERNAL FORCE VECTOR AS A PRODUCT OF TOTAL STIFFNESS MATRIX AND PURE DEFORMATION VECTOR

Fig. 2   Nonlinear FE solution process for flapping-wing shell structures implemented in UM/NLAMS.
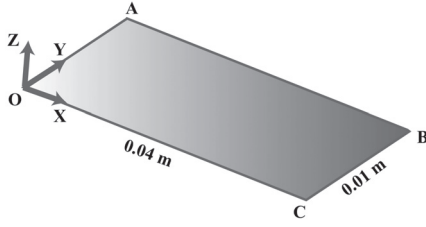
Fig. 3 Rectangular plate configuration used to check rigid body kinematics implementation in UM/NLAMS and MSC.Marc.
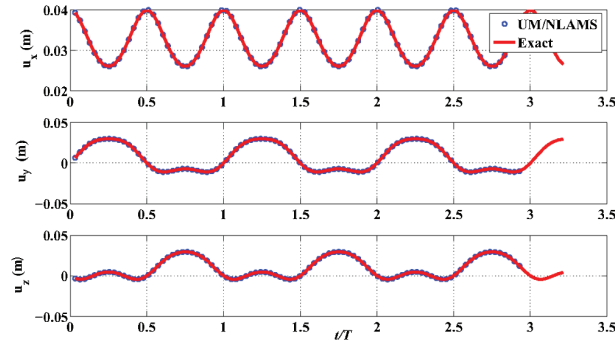
Fig. 4 Displacements extracted at point B in Fig. 3 based on rigid body kinematics prescribed at point A in the same figure.
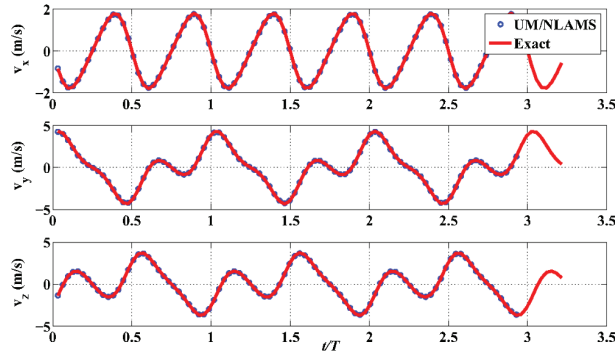
Fig. 5 Translational velocities extracted at point B in Fig. 3 based on rigid body kinematics prescribed at point A in the same figure.

3) Evaluate the $(j-1)$th residual force with

$$
\begin{aligned}
Rf_{n+1}^{j-1} = {}& (1-\alpha_f)F(t_{n+1}) + \alpha_f F(t_n) - M(1-\alpha_m)a_{n+1}^{j-1} \\
& - M\alpha_m a_n - \cdots C(1-\alpha_f)v_{n+1}^{j-1} - C\alpha_f v_n - (1-\alpha_f)R_{n+1}^{j-1} \\
& - \alpha_f R_n
\end{aligned}
\tag{60}
$$

Table 1   Parameters associated with case 1

Parameter	Value
Plate length	0.6 m
Plate width	0.3 m
Plate thickness	0.001 m
Young's modulus	196.2 GPa
Poisson's ratio	0.3
Number of FEs	512
Number of load steps	25
Error limit	10^{-3}

4) Solve for the jth corrected displacements using

$$
K_{\text{eff}} \Delta q^j = Rf_{n+1}^{j-1}
\tag{61}
$$

5) Evaluate the corrected displacement increments with

$$
\delta q^j = \delta q^{j-1} + \Delta q^j
\tag{62}
$$

6) Check for convergence of the iteration,

$$
\frac{|\Delta q^j|}{|q_t + \delta q^j|} \leq \text{tol}
\tag{63}
$$

where tol is convergence tolerance for the iteration.

7) If the solution is not converged, return to the first step; if it does, proceed to the next time step.

For a specific choice of the parameters involved in the generalized-α method, other integration schemes could be obtained. For example, if $\alpha_f = 0$ and $\alpha_m = 0$, the method reduces to the standard Newmark scheme. The primary goal of the generalized-α method is to provide the user with control over high-frequency dissipation while limiting the impact on the low-frequency dynamics. In flapping-wing aeroelastic simulations, this method could prove to be very beneficial in dissipating nonphysical high-frequency oscillations that result due to poor spatial resolution.

The generalized-α method was extended to systems of first-order differential equations by Jansen et al. [40] and later applied by Shearer and Cesnik [24] in the flight dynamic analysis of a highly flexible aircraft.

Figure 2 highlights the key steps involved in the solution process of UM/NLAMS.

III.   Verification and Validation Studies of University of Michigan Nonlinear Membrane Shell Solver

A.   Rigid Body Kinematics

As a check for the rigid body kinematics implementation in the solver UM/NLAMS, a simple test was conducted on a rigid rectangular plate, shown in Fig. 3, actuated at point A with prescribed large amplitude sinusoidal rotation functions in three dimensions (all in phase). The amplitudes of rotation are 30, 45, and 80 deg about X (along span), Y (along chord), and Z (vertical) directions, respectively. Three-dimensional displacements and velocities were extracted at an arbitrary point B (also shown in Fig. 3) and are plotted in Figs. 4 and 5. The results from UM/NLAMS have an excellent correlation with the exact solution computed analytically using the rotation tensor corresponding to the rotation vector [34].

B.   Nonlinear Static Structural Response

Three cantilever plate configurations subjected to different static loads (previously studied in [4,41]) are considered in this subsection. Results presented include tip displacement as a function of the applied load in all the cases discussed.
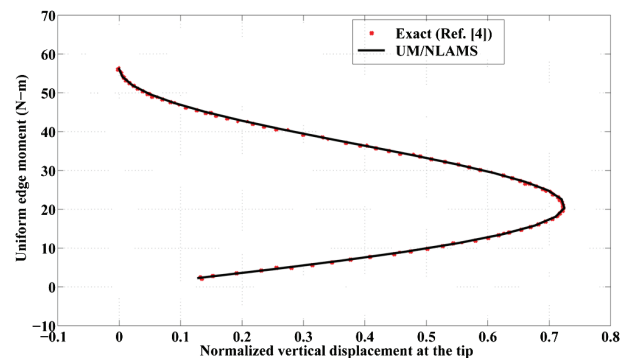

Fig. 6   Normalized tip displacement as a function of the applied moment for the plate in case 1 (displacement is normalized with respect to plate length).
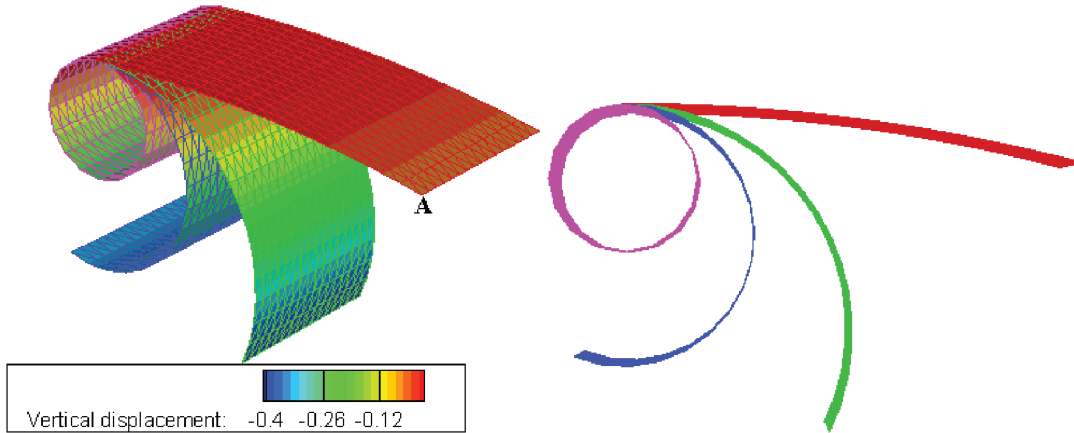
Fig. 7 Snapshots of static wing deformation for the plate in case 1 (legend in meters).
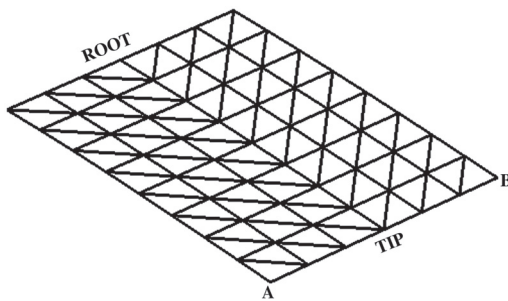

Fig. 8 FE mesh configuration for the plate in case 2.

1. Case 1: Cantilever Plate Subjected to Uniform End Moments

This case is used as one of the reference test cases to evaluate the geometrically nonlinear static capability of UM/NLAMS. It corresponds to a cantilevered isotropic plate of aspect ratio two subjected to uniform applied moments along the tip edge. The key parameters related to this case are included in Table 1. The analytical solution for the case is given in [4] and is used for comparison with results obtained from UM/NLAMS. Figure 6 shows the normalized vertical displacement at a point on the tip (point A in Fig. 7) versus the applied moment. The displacement is normalized with respect to the length of the plate (also for all the cases discussed next unless specified otherwise). The plot compares the solution computed in UM/NLAMS with those provided in [4] (which also discusses validation with analytical solutions). As seen in Fig. 6, there is an excellent match between the two results. The maximum tip deflection obtained in this case is 0.4 m, which corresponds to 73% of the plate length. Because of the applied moment, the cantilever plate forms a circular arc, as shown in Fig. 7. To compute the solution as a function of the applied load, a load control approach was followed in this work: the maximum load in the analysis was broken into several load steps and applied in increments. For each load increment, nonlinear static equilibrium was sought to compute the corresponding static response. The convergence criterion within each load step loop was

chosen as the absolute difference in the Euclidean norm of the entire solution vector computed in any two consecutive Newton–Raphson iterations. For the current case, the tolerance for it was set to 10^{-3}.

2. Case 2: Cantilever Plate Subjected to an End Lateral Load

This case corresponds to an isotropic cantilever plate subjected to a lateral load at one of its free corners (node A of Fig. 8). The key parameters related to this case are included in Table 2. The results obtained from UM/NLAMS are compared with those published in [41]. Figure 9 shows the normalized vertical displacement at the tip (node B of Fig. 8) versus the applied load. As before, the displacement is normalized with respect to the length of the plate. The maximum displacement found in this case was 45% of the plate length. Figure 10 shows snapshots of the static wing deformation for three different load steps. The maximum difference in the static displacement computed in UM/NLAMS and that found in [41] is up to 1% of the plate length. A reason for this is the difference in the solution formulation of UM/NLAMS and that of [41]. While the former is based on the CR form of the TL method, the latter is that of the UL method.

3. Case 3: Cantilever Plate Subjected to an End Lateral Load

This case corresponds to an isotropic cantilever plate subjected to shear forces at the three nodes of the tip (nodes A, B, and C in Fig. 11). The load at nodes A and C is 10 N, whereas at node B, it is 20 N. Similar to the previous two cases, the load is applied incrementally in several load steps. The key parameters related to this case are included in Table 3. The solution obtained from UM/NLAMS in this case is compared with the analytical solution published in [4]. Figure 12 shows the normalized vertical displacement at the tip (node A in Fig. 11) versus the total applied load (sum of the loads on points A, B, and C). The maximum
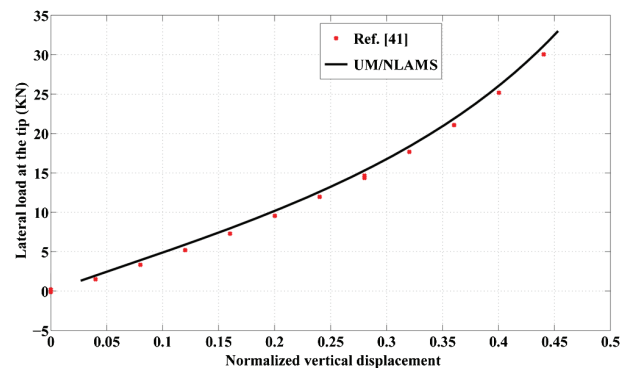
Table 2 Parameters associated with case 2

Parameter	Value
Plate length	40 m
Plate width	30 m
Plate thickness	0.4 m
Young's modulus	0.12 GPa
Poisson's ratio	0.3
Number of FEs	96
Number of load steps	25
Error limit	10^{-4}

Fig. 9 Normalized tip displacement as a function of applied load for the plate in case 2 (displacement is normalized with respect to plate length).
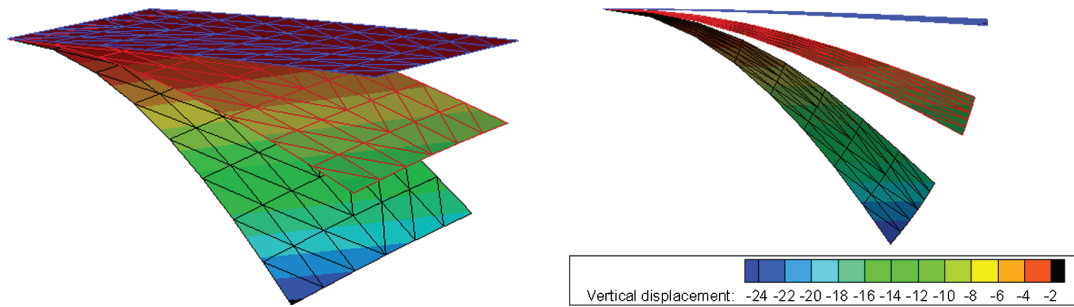
258

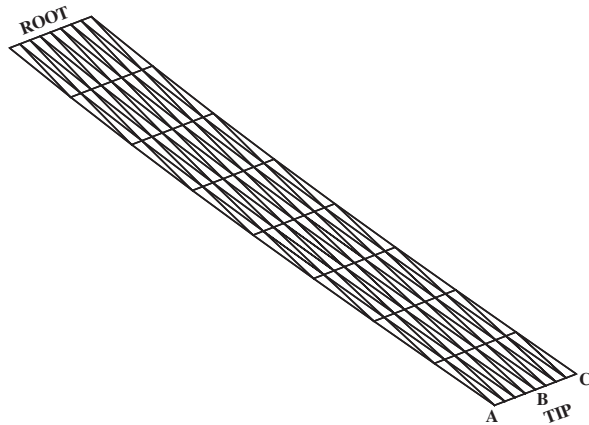**Fig. 10   Snapshots of wing deformation for the plate in case 2 (legend in meters).**

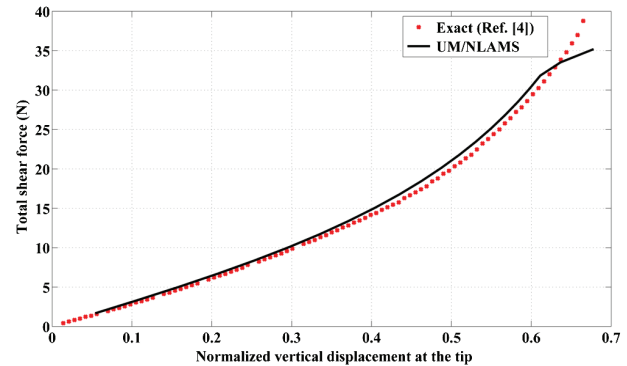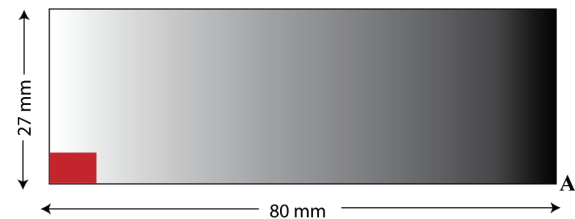**Fig. 11   FE mesh configuration for the plate in case 3.**

Fig. 12   Normalized tip displacement as a function of the magnitude of the total applied load for the plate in case 3 (displacement is normalized with respect to plate length).

displacement found in this case was approximately 68% of the plate length. The agreement is very good up to 60% deformation, after which UM/NLAMS struggles to converge within the maximum number of subiterations (200) within a load step. This presents itself as a softer behavior than that of [4]. The cause for this behavior is unknown and requires further investigation.

C.   Dynamic Structural Response

In this subsection, both rectangular and elliptic plate configurations are actuated with different types of prescribed dynamic motions. In all the cases considered, responses computed using UM/NLAMS are compared with either those from MSC.Marc or with available experimental data. Results presented include tip displacement as a function of time and snapshots of three-dimensional wing deformation.

1.   Case 4: Rectangular Plate Prescribed with Single-Degree-of-Freedom Flap Rotation

A rectangular aluminum plate shown in Fig. 13 was prescribed with a single-DOF large amplitude flap rotation about an axis running through the chord. In the figure, the square block at the wing

Red color indicates the region (5 mm x 5 mm) on the wing that is in contact with the flapping mechanism

Fig. 13   Rectangular flat plate flapping-wing configuration for case 4.

root is constrained in all DOFs with respect to the global frame, and the rotation was prescribed as a sinusoidal variation. This enabled the simulation to start from zero initial displacement and velocity, obviating the need for a special starting procedure, as would have been the case if a sine variation was prescribed. The key parameters

Table 3   Parameters associated with case 3

Parameter	Value
Plate length	0.1 m
Plate width	0.01 m
Plate thickness	0.001 m
Young's modulus	117.72 GPa
Poisson's ratio	0.
Number of FEs	128
Number of load steps	25
Error limit	10^{-4}

Table 4   Parameters associated with case 4

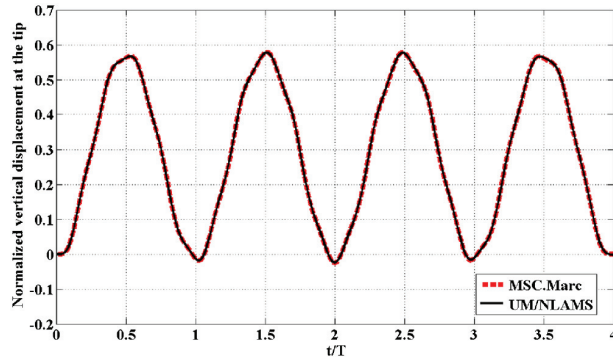| Parameter	Value
Plate length	80 mm
Plate width	27 mm
Plate thickness	0.2 mm
Young's modulus	70 GPa
Poisson's ratio	0.3
Material density	2700 kg/m^3
Prescribed flap rotation profile	1-cosine
Flapping frequency	5, 10, and 30 Hz
Flapping amplitude	17 deg
Time-step sizes	1.5×10^{-4} and 10^{-5} s
Number of FEs	512
Error limit	10^{-4}

259

Fig. 14 Rectangular flat plate response due to flapping excitation (5 Hz) in case 4 (displacement is normalized with respect to plate length).
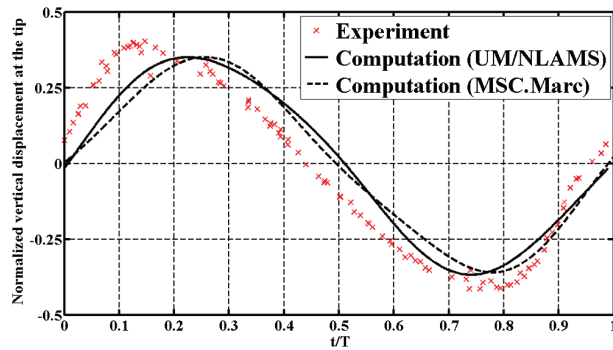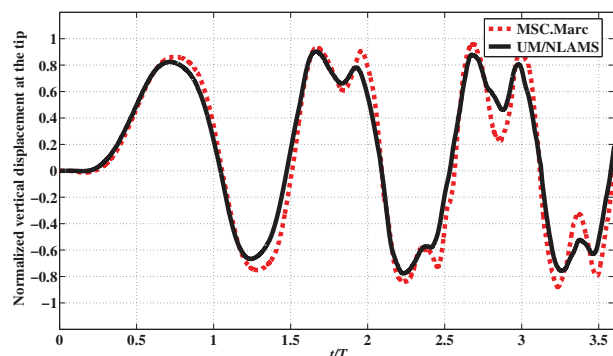
Table 5 Parameters associated with case 5

Parameter	Value
Plate length	0.3 m
Plate width	0.1 m
Plate thickness	0.001 m
Young's modulus	210 GPa
Poisson's ratio	0.3
Material density	7800 kg/m^3
Prescribed plunge profile	1-cosine
Plunge frequency	1.78 Hz
Plunge amplitude	0.0175 m
Time-step size	10^{-3} s
Number of FEs	1150
Error limit	10^{-4}

a check on the absolute difference in the Euclidean norm of the entire solution vector computed in any two consecutive iterations: set to 10^{-4} in the three cases considered here. As seen from the results in Fig. 14, the agreement between UM/NLAMS and MSC.Marc for the 5 Hz frequency is very good. With an increase in frequency (30 Hz), differences start to become apparent (Fig. 16), which is presumably due to the stronger geometric nonlinearities as well as the increased effect of the transient terms in Eq. (42). While the exact cause for the discrepancies will require further investigation, part of the reason could be the fact that MSC.Marc does not use the CR approach. In any case, future studies should be conducted to address which solution is more accurate under higher frequency regimes. Also, as seen in Fig. 15, while the agreement between UM/NLAMS, MSC.Marc, and the experiment is reasonable in amplitude, there is some disagreement in phase. Each computational time step (particularly including assembling of matrices and solving the system of equations) for this case needed 20 s (approximately) of CPU time on a single-node Intel Pentium 4 CPU 3.4 GHz processor.

Fig. 15 Rectangular flat plate response due to flapping excitation (10 Hz) in case 4 (displacement is normalized with respect to plate length).

related to this case are included in Table 4. Figures 14–16 show the normalized vertical displacement at the tip (point A in Fig. 13) as a function of nondimensional time (time normalized with respect to the period of the flap rotation) for three different flapping frequencies: 5, 10, and 30 Hz, respectively. The results are compared with either those obtained from the commercial FE solver MSC.Marc or with available experimental data [42]. The bilinear thin-triangular shell element number 138 is used to discretize the wing in MSC.Marc (also for all the MSC.Marc cases discussed here). The time-integration schemes used are the nondissipative form of the Newmark and the generalized-α methods. The former was used in the 5 and 10 Hz cases, whereas the latter was used in the 30 Hz case with a spectral radius value set to 0.4. The time-step size used in the 5 and 10 Hz cases was 1.5×10^{-4} s and, in the 30 Hz case, it was 10^{-5} s. The convergence criterion for the Newton–Raphson convergence loop is
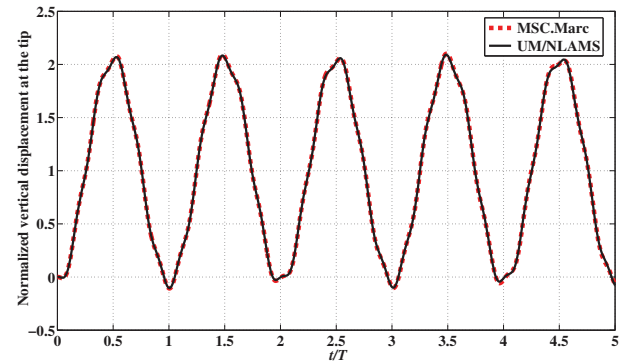

Fig. 17 Rectangular plate response due to plunge excitation in case 5 (displacement is normalized with respect to the amplitude of plunge).
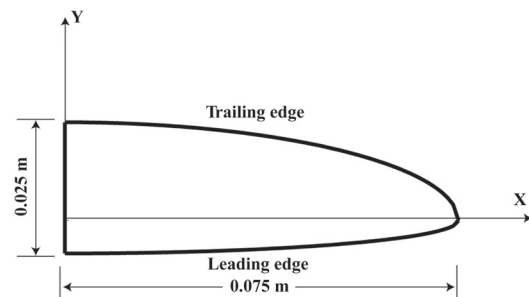

Fig. 16 Rectangular flat plate response due to flapping excitation (30 Hz) in case 4 (displacement is normalized with respect to plate length).

Fig. 18 Zimmerman elliptic plate flapping-wing configuration.

260

Table 6   Parameters associated with case 6

Parameter	Value
Plate length at quarter chord	0.075 m
Plate width at the root	0.025 m
Plate thickness	0.2×10^{-3} m
Young's modulus	7.34 GPa
Poisson's ratio	0.3
Material density	1740 kg/m^3
Prescribed rotation profile	1-cosine
Flap frequency	10 Hz
Flap amplitudes	5, 15, and 5 deg about x, y, and z axes, respectively
Time-step size	1.5×10^{-4} s
Number of FEs	244
Error limit	10^{-4}

2. Case 5: Rectangular Cantilever Plate Prescribed with Pure Plunge Motion

A rectangular cantilever steel plate was prescribed with a pure plunge motion at the root. The key parameters related to this case are included in Table 5. Figure 17 shows the normalized vertical displacement at the tip versus the normalized time, with a comparison between UM/NLAMS and the commercial FE solver MSC.Marc. The displacements and time are normalized with respect to the plunge amplitude and the period of plunge, respectively. The time-integration method used is the Newmark scheme. As seen in Fig. 17, there is an excellent match between the results computed in both the codes. Each computational time step (particularly including assembling of matrices and solving the system of equations) for this case needed 10 s (approximately) of CPU time on a single-node Intel Pentium 4 CPU 3.4 GHz processor.
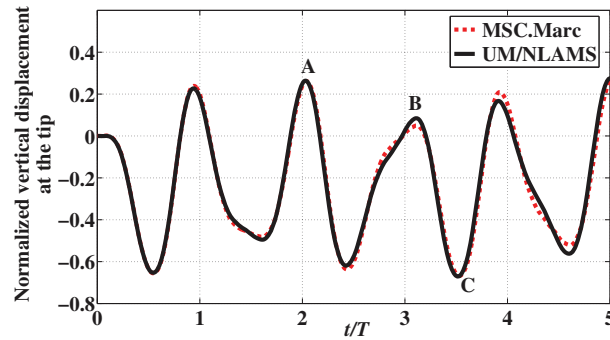
Fig. 19   Elliptic flat plate response to prescribed flap rotations in case 6 (displacement is normalized with respect to plate length).
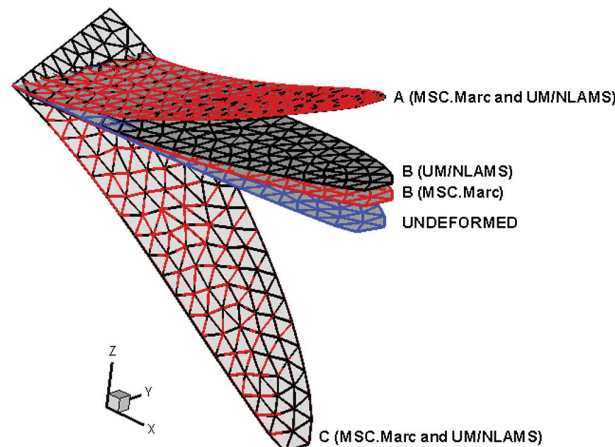
Fig. 20   Snapshot of dynamic wing deformation in case 6 (perspective).
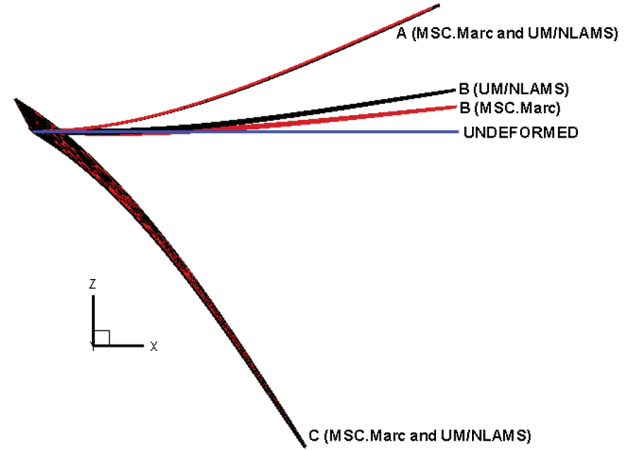
Fig. 21   Snapshot of dynamic wing deformation in case 6 (side view).

3. Case 6: Elliptic Cantilever Plate Prescribed with Rotations About all Axes

An elliptic isotropic plate of the Zimmerman planform (shown in Fig. 18) is cantilevered along the root with respect to the global frame and is actuated at its leading-edge point on the root, with prescribed rotation functions about all three coordinate axes. The Zimmerman planform is simply formed by two ellipses intersecting at the quarter-chord point. Mathematically, it is defined by

$$\left(\frac{x}{R}\right)^2 + \left(\frac{y}{c_1}\right)^2 = 1 \begin{cases} 0 \le x \le R \\ 0 \le y \le c_1 \end{cases}$$
$$\left(\frac{x}{R}\right)^2 + \left(\frac{y}{c_2}\right)^2 = 1 \begin{cases} 0 \le x \le R \\ -c_2 \le y \le 0 \end{cases} \quad (64)$$

where

$$c_1 = 0.75c, \qquad c_2 = 0.75c, \qquad S = \frac{c_1 R\pi}{2} + \frac{c_2 R\pi}{2} = \frac{cR\pi}{2}$$
$$A_r = \frac{4R^2}{S} = \frac{8R}{c\pi} \quad (65)$$

In Eq. (65), c is the chord length at the root, R is the length of the wing defined as the length of the quarter-chord line along the wingspan, and A_r is the aspect ratio of the full wing, which is 7.65 in this case. The key parameters related to this case are included in Table 6. Figure 19 shows the normalized vertical displacement at the tip (quarter-chord point) versus the normalized time, with a comparison between UM/NLAMS and MSC.Marc. As seen from the figure, overall, there is a very good correlation between them, barring some discrepancies at specific time instants. Figures 20 and 21 show snapshots of wing deformation computed in both UM/NLAMS and MSC.Marc for three different time instants (A, B, and C of Fig. 19). As seen from the snapshots, there is an excellent agreement between the three-dimensional wing deformation computed in UM/NLAMS and MSC.Marc at points A and C, but there is a slight discrepancy (approximately 3% of plate length) at point B, which is also seen from Fig. 19.

IV.   Conclusions

The development of a nonlinear structural dynamics solver suitable for analyzing plate/shell-like flapping-wing structures that is based on the CR form of the TL approach was presented. The formulation of the present element is based on the combination of a DKT plate bending element and an OPT membrane element and included a consistent mass and dynamic stiffness/damping matrices to analyze the structural dynamics of a flapping wing. Numerical investigations related to partial verification and validation of the solver are presented. Results showed good agreement between the

solutions obtained using this element with available analytical/ experimental/commercial solutions. While there are several commercial nonlinear FE solvers available, the use of the CR approach that uses existing linear FEs in a nonlinear context resulting in a simplified FE formulation is rare. Furthermore, typical numerical examples presented in this work to illustrate the structural dynamics response of flapping wings will be useful to the flapping-wing community at large.

Acknowledgments

References

[1] S. Combes, S., and Daniel, T., "Flexural Stiffness in Insect Wings I.Scaling and the Influence of Wing Venation," *Journal of Experimental Biology*, Vol. 206, No. 17, 2003, pp. 2979–2987.
doi:10.1242/jeb.00523

[2] Wootton, J., "Support and Deformability in Insect Wings," *Journal of Zoology*, Vol. 193, No. 4, 1981, pp. 447–468.
doi:10.1111/j.1469-7998.1981.tb01497.x

[3] Wasfy, T., "Computational Strategies for Flexible Multibody Systems," *Applied Mechanics Reviews*, Vol. 56, No. 6, 2003, pp. 553–613.
doi:10.1115/1.1590354

[4] Khosravi, P., R. Ganesan, R., and Sedaghati, R., "Co-Rotational Nonlinear Analysis of Thin Plates and Shells," *International Journal of Numerical Methods in Engineering*, Vol. 69, No. 4, 2007, pp. 859–885.
doi:10.1002/nme.1791

[5] Khosravi, P., R. Ganesan, R., and Sedaghati, R., "An Efficient Facet Shell Element for Co-Rotational Nonlinear Analysis of Thin and Moderately Thick Laminated Composite Structures," *Computers and Structures*, Vol. 86, No. 9, 2008, pp. 850–858.
doi:10.1016/j.compstruc.2007.04.010

[6] Tsang, T., "Dynamic Analysis of Highly Deformable Bodies Undergoing Large Rotations," Ph.D. Thesis, Univ. of Arizona, Tucson, AZ, 1993.

[7] Battini, J., "A Modified Corotational Framework for Triangular Shell Elements," *Computer Methods in Applied Mechanics and Engineering*, Vol. 196, Nos. 13–16, 2007, pp. 1905–1914.
doi:10.1016/j.cma.2006.10.006

[8] Behdinan, K., Stylianou, M., and Tabarrok, B., "Co-Rotational Dynamic Analysis of Flexible Beams," *Computer Methods in Applied Mechanics and Engineering*, Vol. 154, Nos. 3–4, 1998, pp. 151–161.
doi:10.1016/S0045-7825(97)00124-2

[9] Elkaranshawy, H., and Dokainish, M., "Co-Rotational Finite Element Analysis of Planar Flexible Multibody Systems," *Computers and Structures*, Vol. 54, No. 5, 1995, pp. 881–890.
doi:10.1016/0045-7949(94)00346-5

[10] Criseld, M., Galvanetto, U., and Jelenic, G., "Dynamics of 3-D Co-Rotational Beams," *Computational Mechanics*, Vol. 20, No. 6, 1997, pp. 507–519.
doi:10.1007/s004660050271

[11] Hsiao, K., and Yang, R., "A Co-Rotational Formulation for Nonlinear Dynamic Analysis of Curved Euler Beam," *Computers and Structures*, Vol. 54, No. 6, 1995, pp. 1091–1097.
doi:10.1016/0045-7949(94)00399-N

[12] Devloo, P., Geradin, M., and Fleury, R., "A Co-Rotational Formulation For the Simulation of Flexible Mechanisms," *Multibody System Dynamics*, Vol. 4, Nos. 2–3, 2000, pp. 267–295.
doi:10.1023/A:1009884131140

[13] Hsiao, K., Lin, J., and Lin, W., "A Consistent Co-Rotational Finite Element Formulation for Geometrically Nonlinear Dynamic Analysis of 3-D Beams," *Computer Methods in Applied Mechanics and Engineering*, Vol. 169, Nos. 1–2, 1999, pp. 1–18.
doi:10.1016/S0045-7825(98)00152-2

[14] Pacoste, C., "Co-Rotational Flat Facet Triangular Elements for Shell Instability Analysis," *Computer Methods in Applied Mechanics and Engineering*, Vol. 156, Nos. 1–4, 1998, pp. 75–110.
doi:10.1016/S0045-7825(98)80004-2

[15] Zhong, H., and Criseld, M., "An Energy-Conserving Co-Rotational Procedure for the Dynamics of Shell Structures," *Engineering Computations*, Vol. 15, No. 5, 1998, pp. 552–576.
doi:10.1108/02644409810225715

[16] Wasfy, T., "Modeling Continuum Multibody Systems Using the Finite Element Method and Element Convected Frames, Machine Elements, and Machine Dynamics," *23rd ASME Mechanisms Conference*, American Soc. of Mechanical Engineers, Fairfield, NJ, 1994, pp. 327–336.

[17] Relvas, A., and Suleman, A., "Fluid Structure Interaction Modelling of Nonlinear Aeroelastic Structures Using the Finite Element Corotational Theory," *Journal of Fluids and Structures*, Vol. 22, No. 1, 2006, pp. 59–75.
doi:10.1016/j.jfluidstructs.2005.09.007

[18] Meek, J., and Wang, Y., "Nonlinear Static and Dynamic Analysis of Shell Structures with Finite Rotations," *Computer Methods in Applied Mechanics and Engineering*, Vol. 162, Nos. 1–4, 1998, pp. 301–315.
doi:10.1016/S0045-7825(97)00349-6

[19] Barut, A., Das, M., and Madenci, E., "Nonlinear Deformations of Flapping Wings on a Micro Air Vehicle," 47th AIAA/ASME/ASCE/ AHS/ASC Structures, Structural Dynamics, and Materials Conference, Newport, RI, AIAA Paper 2006-1662, May 2006.

[20] Batoz, J., Bathe, K., and Ho, L., "A Study of Three-Node Triangular Plate Bending Elements," *International Journal for Numerical Methods in Engineering*, Vol. 15, No. 12, 1980, pp. 1771–1812.
doi:10.1002/nme.1620151205

[21] Felippa, C., "A Study of Optimal Membrane Triangles with Drilling Freedoms," *Computer Methods in Applied Mechanics and Engineering*, Vol. 192, Nos. 16–18, 2003, pp. 2125–2168.
doi:10.1016/S0045-7825(03)00253-6

[22] Nour-Omid, B., and Rankin, C., "Finite Rotation Analysis and Consistent Linearization Using Projectors," *Computer Methods in Applied Mechanics and Engineering*, Vol. 93, No. 3, 1991, pp. 353–384.

[23] J. Chung, J., and Hulbert, G., "A Time Integration Algorithm for Structural Dynamics With Improved Numerical Dissipation," *Journal of Applied Mechanics*, Vol. 60, No. 2, June 1993, pp. 371–375.
doi:10.1115/1.2900803

[24] Shearer, C., and Cesnik, C., "Modified Generalized-α Method for Integrating Governing Equations of Very Flexible Aircraft," 47th AIAA/ASME/ASCE/AHS/ASC Structures, Structural Dynamics, and Materials Conference, Newport, RI, AIAA Paper 2006-1747, May 2006.

[25] Bathe, K., Ramm, E., and Wilson, E., "Finite Element Formulations for Large Deformation Dynamic Analysis," *International Journal of Numerical Methods in Engineering*, Vol. 9, No. 2, 1975, pp. 353–386.
doi:10.1002/nme.1620090207

[26] Battini, J., and Pacoste, C., "On the Choice of Local Element Frame for Co-Rotational Triangular Shell Elements," *Communications in Numerical Methods in Engineering*, Vol. 20, No. 10, 2004, pp. 819–825.
doi:10.1002/cnm.710

[27] Mattiasson, K., and Samuelson, A., "Total and Updated Lagrangian Forms of the Co-Rotational Finite Element Formulation in Geometrically and Materially Nonlinear Analysis," *Numerical Methods for Nonlinear Problems*, Univ. Politecnia de Barcelona, Barcelona, April 1984.

[28] Relvas, A., and Suleman, A., "Application of the Co-Rotational Structural Kinematics and Euler Flow to Two Dimensional Nonlinear Aeroelasticity," *Computers and Structures*, Vol. 85, Nos. 17–18, 2007, pp. 1372–1381.
doi:10.1016/j.compstruc.2006.08.089

[29] Attar, P., and Gordiner, R., "Aeroelastic Prediction of the Limit Cycle Oscillations of a Cropped Delta Wing," *Journal of Fluids and Structures*, Vol. 22, No. 1, 2006, pp. 45–58.
doi:10.1016/j.jfluidstructs.2005.08.010

[30] de Veubeke, B., "The Dynamics of Flexible Bodies," *International Journal of Engineering Science*, Vol. 14, No. 10, 1976, pp. 895–913.
doi:10.1016/0020-7225(76)90102-6

[31] Nygard, M., "The Free Formulation for Nonlinear Finite Elements with Applications to Shells," Dr. Ing., Thesis, Div. of Structural Mechanics, Norwegian Inst. of Technology, Trondheim, Norway, 1986.

[32] Battini, J., and Pacoste, C., "On the Choice of the Linear Element for Corotational Triangular Shells," *Computer Methods in Applied Mechanics and Engineering*, Vol. 195, Nos. 44–47, 2006, pp. 6362–6377.
doi:10.1016/j.cma.2006.01.007

[33] Rankin, C., and Brogan, F., "An Element Independent Co-rotational Procedure for the Treatment of Large Rotations," *Journal of Pressure Vessel Technology*, Vol. 108, No. 2, 1986, pp. 165–174.
doi:10.1115/1.3264765

[34] Argyris, J., "An Excursion into Large Rotations," *Computer Methods in Applied Mechanics and Engineering*, Vol. 32, Nos. 1–3, 1982,

262

pp. 85–155.
doi:10.1016/0045-7825(82)90069-X

[35] Geradin, M., and Cardona, A., *Flexible Multibody Dynamics: A Finite Element Approach*, Wiley, New York, March 2001.

[36] Shabana, A., *Dynamics of Multibody Systems*, Cambridge Univ. Press, New York, 2005.

[37] Zienkiewicz, O., and Taylor, R., *The Finite Element Method*, Butterworth–Heinemann, Maryland Heights, MO, 2005.

[38] Cook, R., Malkus, D., Plesha, M., and Witt, R., *Concepts and Applications of Finite Element Analysis*, Wiley, Hoboken, NJ, 2002.

[39] Subbaraj, K., and Dokainish, M., "Survey of Direct Time-Integration Methods in Computational Structural Dynamics: II. Implicit Methods," *Computers and Structures*, Vol. 32, No. 6, 1989, pp. 1387–1401.
doi:10.1016/0045-7949(89)90315-5

[40] Jansen, K., Whiting, C., and Hulbert, G. M., "A Generalized-α Method for Integrating the Filtered Navier–Stokes Equations With a Stabilized Finite Element Method," *Computer Methods in Applied Mechanics and Engineering*, Vol. 190, Nos. 3–4, 2000, pp. 305–319.
doi:10.1016/S0045-7825(00)00203-6

[41] Hsiao, K., "Nonlinear Analysis of General Shell Structures by Flat Triangular Shell Elements," *Computers and Structures*, Vol. 25, No. 5, 1987, pp. 665–675.
doi:10.1016/0045-7949(87)90159-3

[42] Wu, P., Ifju, P., Stanford, B., Sallstrom, E., Ukeiley, L., Love, R., and Lind, R., "A Multidisciplinary Experimental Study of Flapping Wing Aeroelasticity in Thrust Production," 50th AIAA/ASME/ASCE/AHS/ASC Structures, Structural Dynamics, and Materials Conference, Palm Springs, CA, AIAA Paper 2009-2413, May 2009.

A. Palazotto
Associate Editor

49th AIAA Aerospace Sciences Meeting including the New Horizons Forum and Aerospace Exposition
4 - 7 January 2011, Orlando, Florida

AIAA 2011-857

Experimental Investigation of Corner Flows in Rectangular Supersonic Inlets with 3D Shock-Boundary Layer Effects

W. Ethan Eagle[1] and James F. Driscoll[2]
University of Michigan, Ann Arbor, MI, 48109

John A. Benek[3]
U.S. Air Force Research Laboratory, Wright-Patterson Air Force Base, OH, 45433

Abstract   In a rectangular supersonic inlet the first oblique shock wave will interact with both the sidewall boundary layers and with the corner flows. This can create large, complex 3-D separation zones that reduce the effective flow area and can lead to the unstart of the inlet. Experiments were conducted in the Michigan Glass Wind Tunnel at Mach 2.75 and at Mach 2.0 to quantify these flow separation patterns. Video was recorded of the unsteady formation of separation zones as the inlet starts. Oil streak patterns and Schlieren images indicate that the downward flow caused by the oblique shock forces some of the flow near the corner to move upstream. This flow moving upstream in the corner creates a sidewall separation bubble, which significantly deflects the free stream upstream of the shock wave. Using a six-degree wedge, a "small" corner flow-shock boundary layer interaction (CF-SBLI) separated region was created which was found to be optimum for CFD simulation. Using a ten-degree wedge generated a stronger shock and a "large" CF-SBLI separated region, but the flow area was reduced so much that the inlet was too close to unstart to allow for stable experimental measurements or CFD simulation.

I.   Introduction and Background

INCIDENT oblique shocks[1, 2], compression corners[3, 4], swept fins[4-7], and normal shocks[8-10] generate pressure rises which result in thickening or separation of the boundary layer. Unfortunately, because each flow has different characteristic scales, these flows defy a simple two-dimensional analytic parameterization; further difficulty regarding understanding of shock-foot unsteadiness is still a matter of concern[4, 11-13].

An effort sponsored by the Air Force Collaborative Center for Aeronautical Sciences (AF-CCAS) is underway investigating shock wave boundary layer interaction (SBLI) for applications in the design of next-generation high performance (possibly bleed-less) engine inlets. The effort thus far includes benchmark quality stereo particle image velocimetry (SPIV) data of a single oblique shock interaction. CCAS has developed an experimental database for CFD assessment. Thus measurements from this experiment not only offer a chance for better physical understanding of SBLI, but thanks to careful experimental design and documentation, also enable validation of advanced CFD codes. A CCAS-sponsored workshop on SBLI was held in January 2010 at the Orlando AIAA Aerospace Sciences Meeting, where the first round of CFD validation and comparison to data was completed[14]. The meeting concluded with a discussion of the future of this effort and focused on what work is still needed in the area.

A new set of criteria were developed to enhance the effort that would move towards an '3-D inlet design' investigation rather than a single 2-D shock-boundary layer 'unit physics' problem[15]. One problem arising in realistic inlet geometries, but commonly ignored by the 'unit physics' approach, is the effect of flow field three-dimensionality. Previous results from our experiment have called into question our assumptions of boundary layer behavior in the corner regions. The current experiment adds to our present understanding by visualizing the cause and effect of corner induced three-dimensionality in an oblique shock boundary layer interaction at different shock strengths.

---

[1] Graduate Research Assistant, Aerospace Engineering Department, 1320 Beal Avenue #2004 FXB Ann Arbor, Michigan 48105, AIAA Student Member.
[2] Professor, Aerospace Engineering Department, AIAA Fellow.
[3] Director, Computational Sciences Center, AFRL Air Vehicles Directorate, AIAA Fellow.

1
American Institute of Aeronautics and Astronautics
092407

Approved for public release; distribution unlimited.

The purpose of the present work has been to systematically vary the strength of an oblique shock wave in the Michigan Supersonic Glass Wind Tunnel, and then quantify the sizes and shapes of the various sidewall separation regions. Conditions are varied from "close to unstart" to "far from unstart." Oblique shocks were generated using wedges suspended from the upper wall with angles either six to ten degrees. Separation regions were quantified by recording oil streak patterns on the walls. Shock locations were recorded using a Schlieren system. High-speed video of both the oil streak patterns and the shock wave motions were recorded to understand the time-history of how the separation zones were created during the inlet start-up. Knowledge of this formation sheds light on how the separations later lead to the unsteady unstart of the inlet.

An important aspect of the work is to determine the optimum experimental run conditions. Optimum conditions are defined as those that are best for future CFD modeling as well as for future PIV measurements of the 3-D velocity field. For CFD simulation, it is necessary that a reasonably-sized control volume can be defined that has no reverse flow on either the upstream or downstream boundaries. It was decided that small to moderate separation zones would be best for a first test of CFD models in this demanding 3-D problem. However, the separation zones must be large enough to allow for accurate measurements with PIV, which has a spatial resolution limit. Also, conditions should be "far from unstart" to avoid the possibility that the flow could be unstable. For an inlet that is too close to unstart, small perturbations could lead to undesirable dynamics in either the experiment or the CFD simulation. Additionally, the experimental 3-D flow should be symmetric (separation on the right and left walls should be identical) and as simple as possible. For this reason, the wedge mounted on the top wall was a full-span wedge. Partial-span wedges were previously investigated since they provide less blockage, and provided conditions that were further from unstart. In those cases, the shock became curved before it interacted with the sidewall. This additional complication was avoided by using full span wedges in order to achieve the simplest possible comparison of CFD to the experiment.

The wedge should be suspended from the upper wall because if it is flush mounted, there will be a small recirculation zone in the corner where the upper wall turns at the beginning of the wedge. Thus the shock anchoring can be unsteady, which causes problems when comparing experiment to CFD. With the suspended wedge, the shock is firmly anchored to the sharp leading edge of the wedge. However, it is important that the flow that passes over the top of the suspended wedge be "started." If there is too much blockage of this upper flow, a separation zone can occur between the leading edge of the wedge and the upper wall, which can cause unsteady shock anchoring upstream of the wedge leading edge. To avoid this blockage problem, the upper surface of the wedge is inclined downward.

II.   Experimental Approach

Experiments were conducted in a vacuum-driven supersonic tunnel with nozzles designed to produce Mach 2.0 or 2.75 free-stream flow for a continuous run time of five to ten minutes. The test section is 2.25 inches wide by 2.75 inches tall and the working fluid consists of conditioned air from the laboratory. Flow straightening is employed upstream of the nozzle to enhance uniformity. In the Mach 2.75 and 2.0 configurations the unit Reynolds number was 8.9×10^6 [1/m]. Glass sidewalls along the entire length, as well as in a region along the centerline, ensure adequate optical access for all measurements and flow visualization. In all cases below, the experiment was mounted approximately 22 inches [0.558m] from the throat. Figure 1 is a schematic of the tunnel showing variable wedge mounting options.
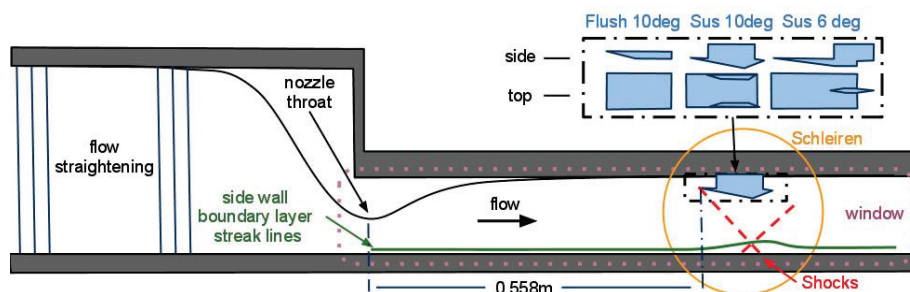

Figure 1. Schematic of the Michigan Glass Wind Tunnel

As seen in Fig. 1, the lower wall of the wind tunnel is flat but it is fed via a bell mouth (not pictured). The tunnel entrance is approximately 200 cm from the region of interest. Previous SPIV measurements showed that this

boundary layer (approximately 1cm in height) has the Log-Law velocity profile associated with turbulent boundary layers at large Reynolds numbers[16]. Several experimental cases are outlined below. The following nomenclature will be used:

- "Full span" indicates the leading edge of the shock generator extends continuously between the two side walls. The shock generator is 2.25 inches wide.
- "Suspended" indicates that the wedge separates the wind tunnel into two flows, a small flow is above and most of the flow is below the wedge. Both flows must remains started. This is accomplished by widening the channel to accommodate both the growth of the boundary layer as well as the side wall supports. Care was taken not to expand this upper flow too aggressively.
- "Flush mounted" indicates the leading edge of the shock generator lies in plane with the top wall.
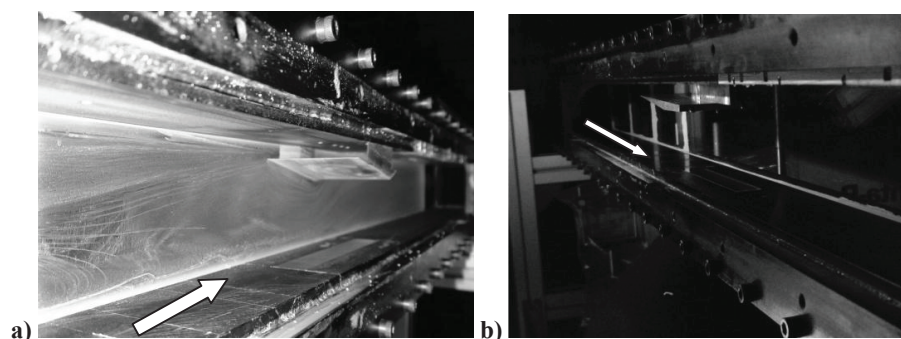
Figure 2. Photographs of the Suspended Shock Generators: (a) Ten Degree (b) Six Degree

Table 1: Test Cases

Case A – Mach 2.75 Full-span suspended 10-degree wedge (Supersonic, but not fully started)
Case B – Mach 2 Full-span suspended 10-degree wedge (Unstarted)
Case C – Mach 2 Full-span flush mounted 10-degree wedge (Upstream shock not anchored)
Case D – Mach 2.75 Full-span flush mounted 10-degree wedge (Anchored but too unsteady)
Case E – Mach 2.75 Full-span suspended 6-degree wedge (Optimum)

With the purpose of exploring corner flows in mind, a full-span wedge geometry was suspended from the top wall of the wind tunnel. As such, an exploratory research program was undertaken as an extension of the CCAS Glass Inlet research program. From the beginning it was understood that large boundary layers would push the experimental geometry to the limits of unstart. One of the four, Case B, did not start and image results for this case have not been included.

A. Visualization methods
1. Oil Flows
Oil flows[17] are an established method for determining flow separation and the flow topology along 'limiting' surface streamlines, including separation zones. In this case the oil mixture is created by mixing kerosene and calcium carbonate powder in ratios five parts to two by volume. Prior to tunnel operation, a three-inch silicone brush is used to apply the combination to the walls of the wind tunnel perpendicular to the expected direction of flow. Once the valve is opened to start the tunnel, viscous forces begin to drag the solution along the wall. Because kerosene is highly volatile, the low-pressure operating condition at Mach 2.75 rapidly evaporates the oil, leaving behind the calcium carbonate in a streak-like pattern. Convergence of these streak lines occur in the side wall as the swept shock moves down the wall. Oil accumulates in regions of flow separation and does not evaporate as readily. Previous references on oil flow visualization technique describe methods for characterizing this swept shock behavior. Variations in streamline convergence indicate the relative strength of this swept shock boundary layer interaction. In each of the cases, the amount of convergence is used to determine the magnitude of flow separation.

3
American Institute of Aeronautics and Astronautics
092407

Photographs were taken of the developing oil flow patterns using a Sony DSC-t70 8.2 Megapixel camera at 720x640 pixel resolution, and video with a Sony HDR-SR12 at 1920x1080 pixel resolution, in both Mach 2 and Mach 2.75 flow arrangements. These videos document the startup transients, the unsteady motion in the recirculation zones, and the relative magnitude of the flow field three dimensionality[18]. Still images, as well as individual frames from the video, were analyzed and data was produced to ensure repeatability and compare the effects of varying the Mach number, wedge angle, and shock generator mounting location. Photographs were taken such that scaling/skewing of images was not a significant factor.

2. Schlieren flow visualization

A Schlieren system was used to identify shock wave locations. An intensified CCD camera was employed to digitize the images at a 1280x 1024 pixel resolution. The light source was an Oriel Labs 100 watt mercury lamp. Image exposures were feasible down to 25 μs resolution, but these images had a dynamic contrast of ~2. Instead images were exposed for 100 μs, and achieved dynamic contrast of ~10. At the leading edge of the shock generator, flow deflection angles were measured from the Schlieren images and checked against estimated values based on the Mach number and the θ-β-M relations.

III.   Results

The cases which follow were an exploratory attempt at finding corner flow-shock boundary layer interactions (CF-SBLI). Images and videos for each of the five test cases in Table 1 are described sequentially. In each case, the shock boundary layer interaction thickens in the corners, reducing the effective core flow area. As the boundary layer in the corner thickens, its influence reaches upstream, in some cases causing shock waves (sometimes called pseudo-shocks) to originate from these corners. Those shocks further disturb the boundary layer. This feedback mechanism may be a precursor to unstart. The size of the corner separation varies with swept shock strength and incoming boundary layer size. Larger flow blockage leads to larger separation, eventually producing unstart. Somewhat surprisingly, large-scale three-dimensionality has little effect on traditional Schlieren imaging, but oil flows for the same region clearly show the dominant three-dimensionality in the boundary layer. Simultaneous oil flows on bottom, right, and left walls confirmed flow symmetry about the channel centerline but the documented images below are from only one side-wall.

A. Case A: M = 2.75 Ten Degree Suspended Wedge

The Case A conditions in Table 1 produced large-scale sidewall separation zones. Figure 3 shows video image and Schlieren results for Case A. The side-wall interaction spans the entire wall, and the primary sidewall separation zone is 2 inches long [5cm, which is 73% of the tunnel height]. Converged CFD results from the University of Cincinnati for a similar ten-degree wedge also show a large corner flow recirculation zone. However, CFD simulations do not tend to converge when sufficiently large sidewall separation zones are created; instead the perturbations caused by the unsteady startup may lead to an inlet unstart in the computations.

The Schlieren image for Case A reveals upstream shock wave which causes the shock off the leading edge to skew to nearly forty degrees. The flow deflection from a ten-degree wedge at Mach 2.75 should be thirty degrees. Clearly in this instance the interaction was too strong and too large for useful assessment of CFD.
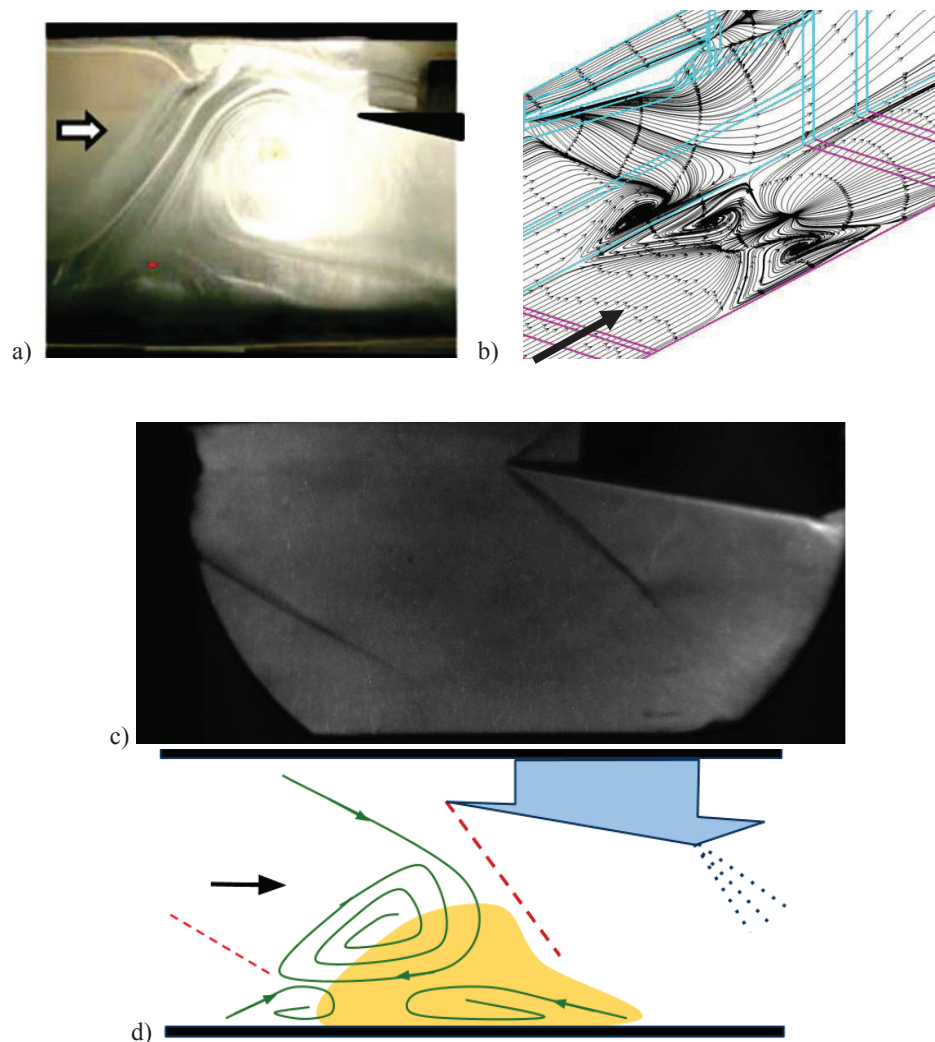
Figure 3. Case A flow patterns caused by a Ten Degree suspended wedge in a Mach 2.75 free stream : a) Oil flow b) CFD 'streak lines' computed at U. of Cincinnati;   c) Schlieren image d) Schematic of Interaction

B. Mach = 2.0 Ten Degree Suspended Wedge
The previous computational study on the Glass Inlet suggested that lowering the Mach number might reduce the size of the separated zone due to the reduction in the shock strength. However, operating at Mach 2 and using the same wedge geometry resulted in unstart. Therefore no further research for the Case B condition was conducted.

C. Mach = 2.0 Ten Degree Flush-Mounted Wedge
Because a Mach 2 interaction is closer to a cruise flight regime Mach number, the next step was to operate the experiment at Case C, which had a reduced amount of blockage compared to Case B. Using a flush-mounted full span wedge, results in a smaller corner interaction than Case A. However, the upstream motion ahead of the shock generator was undesirable. Oil flow investigation of the region indicated that a CF-SBLI occurs at the top wall, causing unsteadiness in the shock foot region.
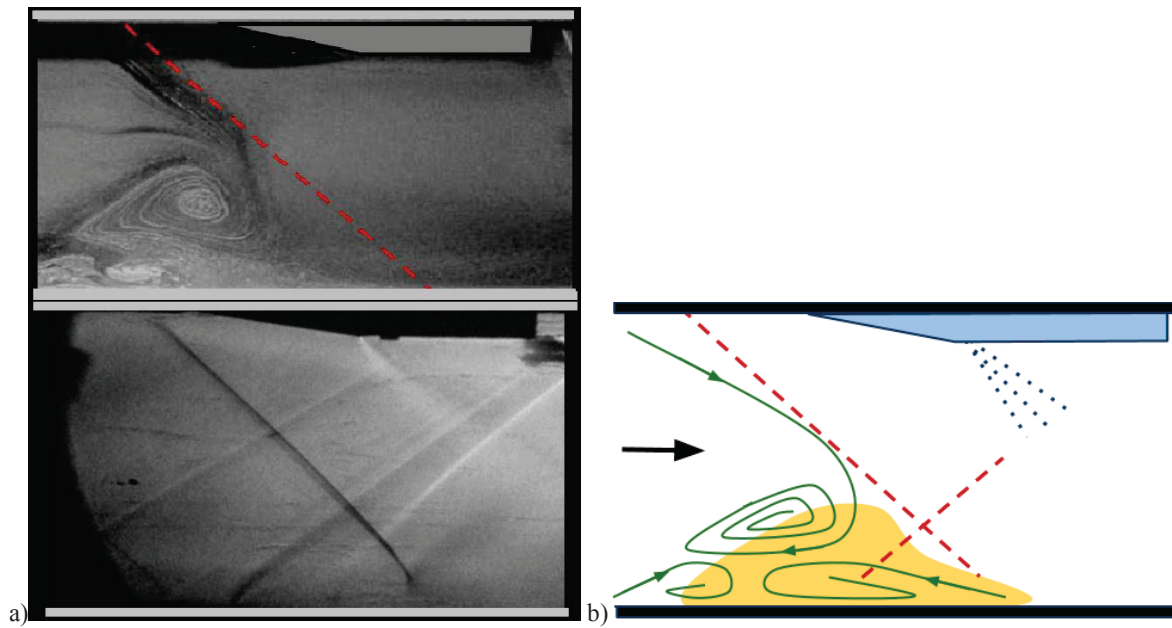
Figure 4. Case C results: Ten Degree Mach 2.0 Flush-mounted wedge a) oil and Schlieren b) schematic of the interaction
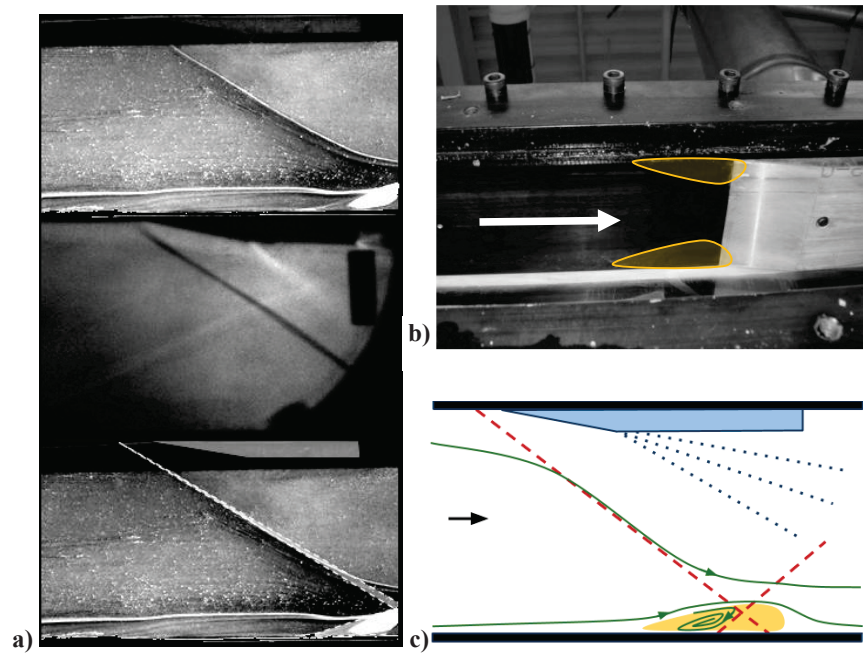

Figure 5. Case D results: Ten Degree Mach 2.75 Flush-Mounted Wedge: a) oil flow and Schlieren visualization b) Top wall CF-SBLI,   c) schematic of interaction

D. Case D: Mach 2.75 Ten Degree Flush-Mounted Wedge
In an attempt to anchor the shock wave to the shock generator and avoid unstart, the ten-degree wedge was installed in the Mach 2.75 wind tunnel. Figure 5 shows the attachment was successful. Surprisingly the sidewall separation was reduced despite an increase in shock strength. This somewhat unexpected result can be explained by examining the oil flow pattern. The increase in sweep of the incident shock actually lowers the normal Mach number of the flow along the sidewall, in this case allowing the flow along the wall to turn upstream underneath the shock before reaching the bottom wall.

E. Case E: Mach 2.75 Six Degree Suspended Wedge
The final test case that provided optimum operating conditions was Case E; it avoided the unstart problems of the previous models by using a free stream Mach number of 2.75, but reduced the shock strength by reducing the flow turning angle. The image in Figure 6 shows that streamlines do not converge under the swept shock for this condition. The corner flow region can still be identified as a separation zone, but is now the optimum size of 2cm x 2 cm.   This is sufficiently large for future PIV studies, which have a limited spatial resolution, and is sufficiently small for future CFD simulations.
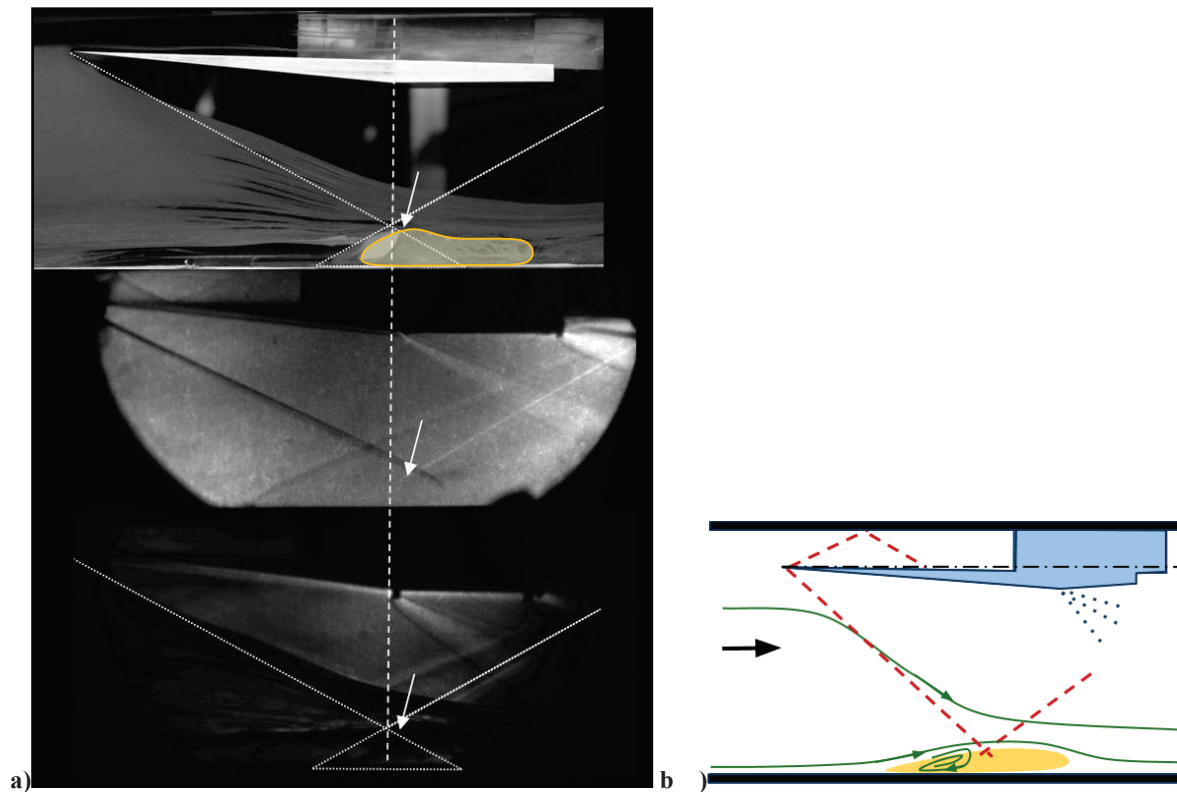

Figure 6.   Six Degree Mach 2.75 Suspended Wedge: a) oil and Schlieren visualization b) schematic of the interaction

F. Centerline Separation Region

In contrast to the partial span wedges previously investigated, oil flow on the bottom wall at the oblique shock reflection generated by a full span wedge did not indicate flow separation on the centerline. However, downstream of the wedge region, converging wall flow streamlines do produce a small centerline recirculation zone.
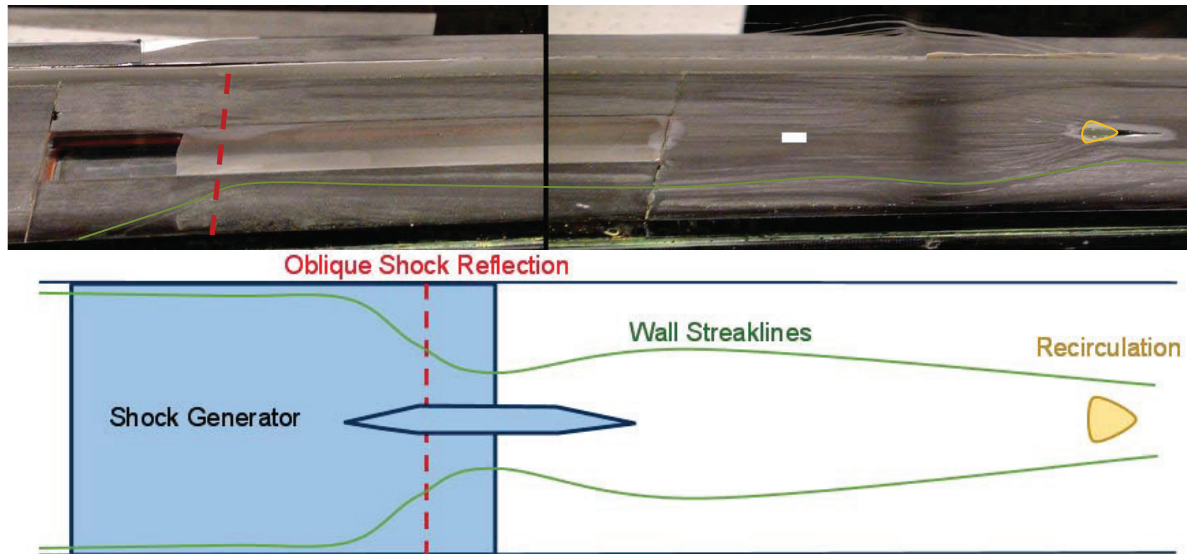

Figure 7. Case E: Bottom wall oil flow

IV. Discussion

A. CF-SBLI mechanism

The mechanism of the corner flow SBLI (CF-SBLI) appears to be similar in each of the five cases (A to E) studied. The primary difference is the size of the streak line pattern and its convergence as the bottom wall is approached. As shown in Figs. 8 and 9, the shock from the leading edge sweeps along the side wall, bending of the streaklines indicates weak CF-SBLI flows while convergence of the streaklines leads to strong CF-SBLI. The bending/convergence creates downflow toward the bottom wall boundary layer. Figure 10 diagrams how the flows might interact in the turbulent corner. Reverse flow caused in the side wall by the adverse pressure gradient moves upstream until it reaches a saddle point. For small-scale features, the saddle point is very close to the wall, making it hard to observe. Flow along the bottom wall appears to bend back toward the free stream in the region of shock reflection. The stronger shock creates a more severe secondary flow and a more severe CF-SBLI.

American Institute of Aeronautics and Astronautics
092407

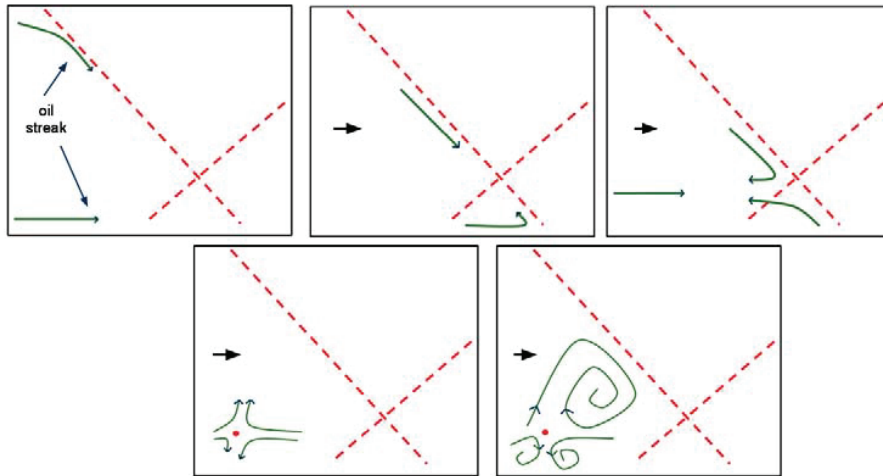Approved for public release; distribution unlimited.

Figure 8. Schematic of the flow deflection near the sidewall, for the Strong CF-SBLI (Case A), based on observed oil patterns.
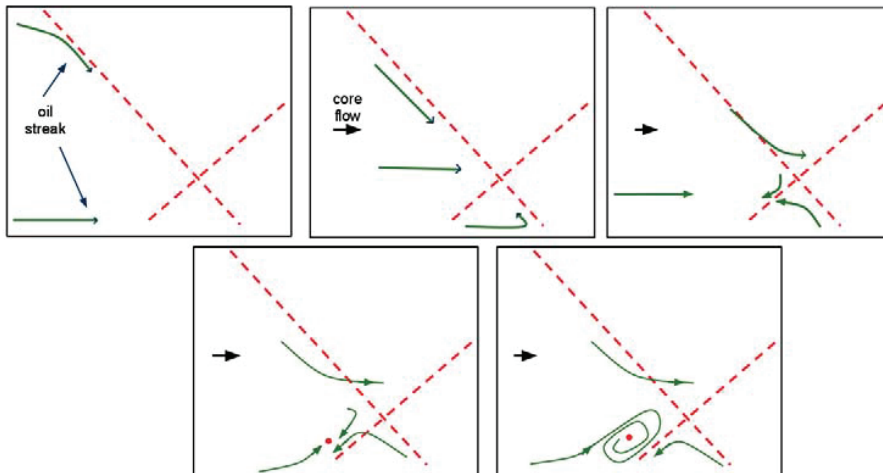

Figure 9. Schematic of the flow deflection near the sidewall, for the Weak CF-SBLI (Case E), based on observed oil patterns.
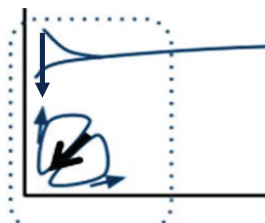

Figure 10. Schematic of Secondary Flows from a Turbulent Corner and Sidewall SBLI

B. Optimum CF-SBLI research conditions

Case E, which is a full span 6-degree suspended wedge at Mach 2.75, exhibits all of the desired characteristics for a more thorough combined experimental / CFD study of the CF-SBLI physics. Moderate corner flow separation occurs downstream of the leading edge. Recirculation from the corner does not reach upstream of the leading edge and boundary layer reattachment occurs quickly downstream, creating a suitable outflow boundary condition for CFD. The 2 cm x 2 cm region is a reasonable control volume for detailed study by the SPIV diagnostics.

The full span wedge is better than the partial span wedge, since the latter produces a curved shock that creates unnecessary complexities. A Mach number of 2.75 is preferred over Mach 2.0 because the latter is too close to inlet unstart. The Mach 2.75 conditions are sufficiently far from unstart that the flow remains steady and impervious to small perturbations. The 10 mm tall initial boundary layer height provided by the experiment is optimum because it can be probed using the spatial resolution achievable with PIV diagnostics and it is a fully equilibrated boundary layer that has a profile that follows the well established Log Law. The Case E conditions created a CF-SBLI control volume region that is approximately 2 cm by 2 cm by 2 cm. This control volume region is optimum for both PIV and CFD future studies.

Acknowledgements

References

1.   Pitt-Ford, C. W., and Babinsky, H. "Micro-Ramp Control for Oblique Shock Wave Boundary Layer Interactions," 2007.
2.   Dupont, P., Piponniau, S., Sidorenko, A., and Debive, J. F. "Investigation by Particle Image Velocimetry Measurements of Oblique Shock Reflection with Separation," *AIAA Journal* Vol. 46, No. 6, 2008, pp. 1365-1370. doi: 10.2514/1.30154
3.   Wu, P. P., and Miles, R. B. "Megahertz Visualzation of Compression-Corner Shock Structures," *AIAA Journal* Vol. 39, No. 8, 2001, pp. 1542-1547.
4.   Panaras, A. "Review of the Physics of Swept-Shock/Boundary Layer Interactions," *Progress in Aerospace Sciences* Vol. 32, 1996, pp. 173-244.
5.   Schmisseur, J. D. "An Experimental Study of Fluctuating wall pressures in a highly swept, sharp fin-induced mach 5 shock wave / turbulent boundary layer interaction." Wright Patterson, 1993, p. 150.
6.   Lu, F. "Upstream influence scaling of Fin-Generated Shock Wave Boundary Layer Interactions," *28th Aerospace Sciences Meeting*. AIAA, Reno, NV, 1990.
7.   Lu, F., and Settles, G. S. "Color surface-flow visualization of fin-generated shock wave boundary layer interactions," *Experiments in Fluids* Vol. 8, 1990, p. 3.
8.   Handa, T., Masuda, M., and Matsuo, K. "ThreeDimensional Structure of Normal Shock WaveTurbulent Boundary Layer Interaction in a Rectangular Duct by a Laser-Induced Fluorescence Method," *Engineering Sciences Reports* Vol. 24, No. 2, 2002, pp. 179-185. doi: 10.1007/s001930050092
9.   Doerffer, P. "An experimental investigation of the Mach number effect upon a normal shock wave — Tubulent boundary layer interaction on a curved wall," *Acta Mechanica* Vol. 76, No. 1, 1989, pp. 35-51. doi: 10.1007/bf01175795
10. Doerffer, P., and Dallmann, U. "Separation Structures Produced by a Normal Shock-Wave Turbulent Boundary-Layer Interaction in a Narrow Wind Tunnel," *19th Fluid Dynamics, Plasma Dynamics and Lasers Conference*. AIAA, Honolulu, Ha, 1987.
11. Clemens, N. T., and Narayanaswamy, V. "Shock Turbulent Boundary Layer Interactions: Review of Recent Work on Sources of Unsteadiness," *38th AIAA Fluid Dynamics Conference*. AIAA, San Antonio, TX, 2009, p. 25.
12. Adamson, T. C., and Messiter, A. F. "Analysis of two-dimensional interaction between shock waves and boundary layers," *Annual Review of Fluid Mechanics* Vol. 12, 1980, p. 35.
13. Green, J. E. "Interactions between shock waves and turbulent boundary layers," *Progress in Aerospace Sciences* Vol. 11, 1970, pp. 235-260, IN9-IN10, 261-340. doi: Doi: 10.1016/0376-0421(70)90018-7
14. Benek, J. A. "Lessons Learned from the 2010 AIAA Shock Boundary Layer Interaction Workshop," *28th AIAA Applied Aerodynamics Conference*. Chicago, IL, 2010, p. 13.

15. Galbraith, D. S., Orkwis, P. D., Turner, M. G., Galbraith, M. C., Eagle, W. E., and Driscoll, J. F. "Design of a Glass Supersonic Wind Tunnel Experiment for Mixed Compression Inlet Investigations," *40th Fluid Dynamics Conference and Exhibit*. Chigago, IL, 2010, p. 17.

16. Lapsa, A. P., and Dahm, W. J. A. "Stereo Particle Image Velocimetry of Nonequilibrium Turbulence Relaxation in a Supersonic Boundary Layer," *Experiments in Fluids*, 2010.

17. Lu, F. K. "Surface oil flow visualization," *The European Physical Journal Special Topics* Vol. 182, No. 1, 2010, pp. 51-63. doi: 10.1140/epjst/e2010-01225-0

18. Pierce, A. J., Lu, F. K., Bryant, D. S., and Shih, Y. "New Developments in Surface Oil Flow Visualization," *27th AIAA Aerodynamic Measurement Technology and Ground Testing Conference*. AIAA, Chicago, Il, 2010.

3-D Inlet Shock-Boundary Layer Interactions - PIV Database for the Second SBLI Workshop

W. Ethan Eagle[*], James F. Driscoll[†],
University of Michigan, Ann Arbor MI 48109,

John A. Benek[‡]

U.S. Air Force Research Laboratory, Wright-Patterson Air Force Base, OH, 45433

Abstract

A unique data base of stereo-PIV velocity measurements has been recorded and analyzed in order to understand the complex flow separation patterns that occur due to a three-dimensional shock-boundary layer interaction (SBLI) within a rectangular inlet. The database will be used for the Second Workshop of CFD predictions of SBLI. This dataset provides the first complete measurements of a three-dimensional SBLI – that is, all three velocity components were measured in all three orthogonal planes (a total of 16 data planes total). An experimental methodology was followed such that the data collected would be of maximum utility for CFD comparisons. These metrics include velocity contours that define the free stream core, the characteristic sonic line and the sizes of corner vortices. The purpose of this paper is to provide methodology and results from the boundary conditions and geometry of the experiment; a later paper will provide the full experimental findings. Access to a website containing the CAD drawings of the experiment, calculations of the metrics of interest, and other information for potential participants in the workshop is available at https://ctools.umich.edu/portal. Access can be granted by contacting the authors at 3d.sbli.workshop@umich.edu.

A. Introduction

The Air Force is interested in high-speed vehicles capable of striking targets with high precision anywhere in the world and in a fleet of reliable, reusable vehicles for space access. The Air Force Research Laboratory (AFRL) is developing air-breathing concept systems to meet these needs. A critical component of this development is the ability to accurately predict the performance of the propulsion flow paths, especially, the inlet system flow stability, which is determined by internal shock systems. Critical physics must be accurately simulated by a high fidelity, physics-based design capability including the interaction between shocks with the inlet wall, boundary layers, and corner flows. The fidelity of the simulation can only be assessed by comparison with validation quality data from experiments that measure all of these key physical phenomena. Such data does not, in general, exist. Therefore, the AFRL in collaboration with the University of Michigan has undertaken to obtain such data [1–3].

This paper provides details for this first set of validation data, which was obtained for an incident oblique shock impinging on a turbulent boundary layer in a three-dimensional rectangular inlet configuration. Contrary to many previous studies that isolated the SBLI 'of interest' from three-dimensional influence, this flow intentionally constitutes a composite of unit problems (a 'unit' problem is one where there is a

---

[*] Graduate Research Assistant, Aerospace Engineering Department, 1320 Beal Avenue #2004 FXB Ann Arbor, Michigan 48105, AIAA Student Member
[†] Professor, Aerospace Engineering Department, AIAA Fellow
[‡] Director, Computational Sciences Center, AFRL Air Vehicles Directorate, AIAA Fellow.

Approved for public release; distribution unlimited.

single, frequently small, region of interest). The test apparatus incorporates many critical features of real non-axisymmetric high speed inlets including shock boundary layer interactions (SBLI) on the side walls (Swept-Shock and/or Fin-Plate), the bottom wall(an Oblique Impinging Shock), and in the corner formed by the interaction of the bottom and side walls, as well as other geometries[4–14]. To the authors' knowledge (see section B.4), this is the first such dataset of it's kind. Furthermore, care has been taken to rigorously document variability and repeatability, making this dataset an excellent candidate not only for phenomenological description, but also computational validation.

To continue the assessment of the state-of-the-art and state-of-the-practice approaches, the second workshop on computational fluid dynamics (CFD) prediction of shock boundary layer interactions (SBLIs) will be held at the 2013 AIAA Fluid Dynamics meeting in San Diego which is planned to run from June 24-27th. The purpose of the workshop is to share prediction methodologies, assess the state of the art in SBLI prediction and determine the most promising methods. One motivation for the second workshop is a lesson that was learned from the first workshop and was reported by Benek [1] to be: "The extent of the coupling between SBLI in the corner flow and tunnel center was not fully appreciated at the time of the measurements. As a result of this lack of understanding, critical corner flow data was not available. Without such information, turbulence models for this type of flow cannot be properly assessed."

That scarce attention has been paid to the effect of the sidewalls in an enclosed inlet on SBLI structure is not surprising. Simulations of traditional SBLI phenomenon often assume two dimensional flow, and often experiments occur in large aspect ratio wind tunnels where the area of interest is confined to the central third (or less) of the span. However, a two dimensional understanding of the challenges of 'unit physics' type problems is not readily translatable to real systems. Interest in validated CFD for such full three-dimensional inlets is ever increasing. The continuing lack of validation-quality experiments using simple geometries (e.g. full span, and without `aerodynamic fences') is our primary concern.

The present study is a logical extension of the first workshop on CFD prediction of SBLI that was held at the 48th AIAA Aerospace Sciences Meeting in January of 2010. Several CFD solutions were submitted which corresponded to four experimentally measured SBLIs. Prior to the meeting four test cases were identified and contributions of solutions were solicited from the aerospace community. A total of 36 solutions from 11 contributors and 9 organizations were submitted. Two summary papers by Benek [1] and DeBonis et al. [2] described the general conclusions. An assessment of the submitted solutions first was performed. This consisted of an assessment of the experimental data, the development of an error metric and the assessment of the CFD data using the error metric. The experimental data for the four test cases came from two different sources: the Institut Universitaire des Systemes Thermiques Industriels (IUSTI) in Marseilles, France and the University of Michigan (UMich)[3]. The data used for comparison consisted of velocities and turbulent stresses measured on a plane parallel with the free stream flow and the tunnel sidewall. An uncertainty analysis of the experimental data had been previously conducted by each of the research groups involved. As part of this work a statistical uncertainty analysis of the UMich. data was performed.

DeBonis et al. [2] concluded that "CFD solutions provided very similar levels of error and in general it was difficult to discern clear trends in the data. For the Reynolds Averaged Navier-Stokes methods the choice of turbulence model appeared to be the largest factor in solution accuracy. Large-eddy simulation methods produced error levels similar to RANS methods but provided superior predictions of normal stresses". In Ref. [1], Benek concluded that the major lessons learned were:

1. High quality, incident SBLI experimental data has been obtained at Michigan and Marseilles that focus on the SBLI interaction region in the center of the tunnel. The extent of the coupling between the corner flow and SBLI near the tunnel center was not fully appreciated at the time of the

2

measurements. As a result of this lack of understanding, critical corner flow data is not available. Without such information, turbulence models for this type of flow cannot be properly assessed.

2. Detailed and comprehensive boundary condition data is as important as measurements in the regions of important physics.
3. Consistency checking of critical measurements is very important. Independent measurement methods are highly recommended.
4. Quantitative measurements such as Schlieren, oil flow, pressure sensitive paint, etc. should not be neglected.
5. RANS and LES models were used that were three-dimensional (with one exception) and completely viscous. The simulations showed that with current resolution, there is a significant variation in the turbulence models predictions in the interaction region.
6. Grid adaptation gave indications of improving agreement with the experiment in the interaction region by concentrating points in regions with larger numerical error. This result suggests that grid effects are at least as important as the turbulence models effects.
7. While the LES and RANS/LES hybrid simulations presented at the workshop cannot be judged to be better that the RANS simulations, the RANS/LES hybrid methods shows promise for complex flows.
8. It is recommended that in the design of the experiments, a computational group should be part of the team.
9. Measurement and experimental error estimates must be provided as part of the data set.

The workshop demonstrated that the requirement for validation quality experiments surpasses those of high quality phenomenological experiments. This difference consists primarily of detailed and comprehensive boundary condition measurements as well as a healthily skeptical attitude towards all experimental observations with regard to precision and uncertainty. In addition, it was determined that qualitative measurements such as schlieren and oil flow should also be included as an integral part of the validation data set. Measurements for the first workshop focused on obtaining data near the tunnel stream-wise symmetry plane. Since the flow was symmetric there, it was assumed that the flow was essentially two dimensional. However, it was found that the flow was significantly influenced by separations caused by the shock boundary layer interaction with the corner flows at the side and bottom wall interactions. This interaction was not characterized by the first measurements in sufficient detail. A partial consequence of this behavior is that the comparisons of simulations and data were not as informative as had been anticipated. For example, the LES or hybrid LES models could not be judged superior to the RANS predictions. It was determined that a second set of experimental data focused on obtaining more complete characterization of the flow, including accurate measurements of the boundary conditions at multiple locations, would be required to make a more refined assessment of CFD simulation capacity for the unit problem.

This paper describes the experimental Stereo-PIV database that recently was recorded at the University of Michigan to specifically consider a 3-D SBLI in a rectangular inlet. Of particular interest is the interaction between the bottom wall separation region, the sidewall separation region and the effects of corner flows. The geometry and experimental test procedures were selected specifically to address the above-stated lessons from the first workshop. The Michigan database consists of two sections. Section One lists the inflow and outflow boundary conditions, as well as the exact geometry of the experiment. It describes the measurement grid used to acquire PIV data and the uncertainty in the measurements. A standard grid of the computational domain in a coarse and fine resolution will also be available on the website. The present paper reports a subset of what is included in Section One, but it does not attempt to report all of the boundary conditions, or details of the computational grid. The reader must access Section One to download all of the information. Section Two of the database contains the stereo-PIV measurements of all three velocity components that were made on 16 different planes. In particular, 7 of these planes represent the first data set, to the authors' knowledge, to record PIV measurements in a field

3

of view inclusive of the centerline and sidewall through an SBLI forming a 'corner interaction' exhibiting strongly three-dimensional character. Section Two also includes wall pressure data, and oil flow images of the skin friction lines on the bottom wall and sidewall. However, data from Section Two will not be made available until a date to be set by the workshop organizers.

B. Experimental Facilities

The first set of stereo-PIV measurement made in the Michigan Glass Wind Tunnel were obtained on the center line of the nominal Mach 2.75 wind tunnel, and they were reported at the first SBLI-workshop [1, 2]. It was understood that away from the centerline the rectangular test section contains a 3-D SBLI because the incident and reflected shocks interacted with the walls and corner flows. Therefore this 3-D SBLI problem was chosen for detailed study.

B1. Michigan Glass Wind Tunnel

The facility is a vacuum-driven supersonic tunnel with a Mach 2.75 nozzle shown in Fig. 1. The run time is up to ten minutes. The stagnation temperature was the measured room temperature of 295.7 K and the stagnation pressure is the measured room pressure of 98.0 kPa. An incident oblique shock is generated by the six degree wedge which is mounted under the upper wall on a strut, as seen in Fig. 1. It is suspended from the top wall of the tunnel by a strut. This offset helps to remove the fluctuating influence of the developing top wall boundary layer. The top face of the wedge is angled at 2 degrees to provide an expansion that helps to prevent the flow from choking in this narrow channel due to blockage.

The nozzle block is a two-dimensional converging diverging nozzle designed using the NOZCX Fortran code using the method of characteristics. The nozzle over-expands slightly to accommodate for boundary layers. The geometry of the converging-diverging nozzle is also potentially critical for computational simulation of the present geometry and an under-sampled array of 163 defining coordinates is available online. The total length of the nozzle is 615mm. From the nozzle exit, the boundary layer continues to develop in the rectangular test section for a length of 172mm before meeting with the suspended wedge at the start of the 'test section.'
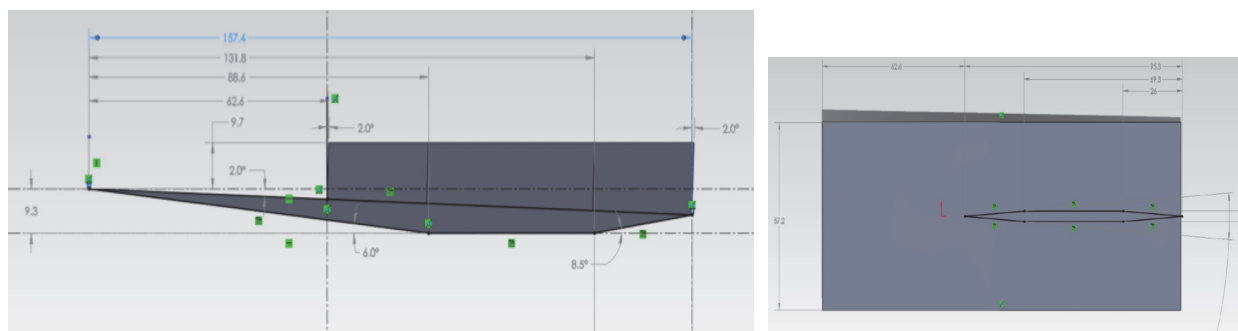

Figure 1. Dimensions of the shock wave generator (wedge and strut) that is mounted on the upper wall.

A slight deviation in the height of the tunnel test section was recently measured 'as installed' compared to as designed. The test section, displayed schematically in Fig 2a, as measured, is 2.25 inches wide by 2.72 inches high (57.15 x 69.08 mm). Three upstream inflow boundary planes are shown in red in Figure 2a. They are located at -144mm -72mm and 0mm and contain information about the core-flow and bottom and sidewall boundary layers. Figure 2b indicates the x-location of the 13 PIV data plane measurements

4

which will be made available in Part II in relation to the six-degree wedge used as a shock generator, and the location of the inviscid shock predicted from simple 2D theory.

The working fluid consists of conditioned air from the laboratory. Flow straightening devices (hexagonal meshes) are used upstream of the nozzle to assure flow uniformity. The unit Reynolds number for the experiment was 8.9 x 10^6/m. Optical access is provided by glass side walls along the entire length of the test section and by an acrylic panel located in the floor of the tunnel along the centerline from x: 45mm to 140mm by z: 12mm to 43mm.
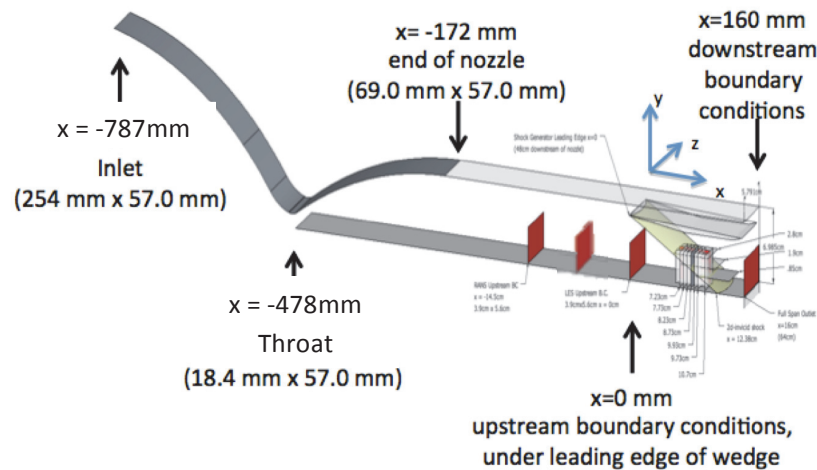
Figure 2a. Schematic of the Michigan Glass Wind Tunnel with flow from left to right. Also shown is the left handed coordinate system was chosen based on the PIV data to keep velocities positive always away from the wall ; [x,y,z] corresponds to the the streamwise coordinate x, vertical coordinate y and tunnel span coordinate z. Note three upstream inflow boundaries at -144, -72 and 0mm from the wedge leading edge. Zoom view of interaction in Fig 1b.
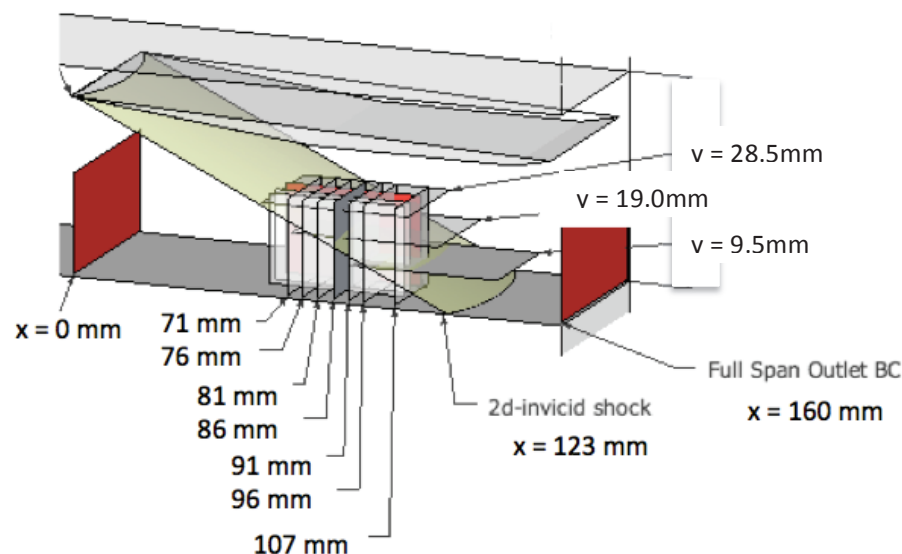

Fig. 2b. Magnified view of the measurement planes seen in Fig. 1a. The plane on the far left is at x=0, which is under the leading edge of the shock generator. This x = 0 plane is denoted TV2 and is the last condition that the inflow boundary conditions of the SBLI are recorded before the interaction. 9 Transverse planes are denoted by their x location in mm in relation to the theoretical 2-D invicid shock reflection point (123mm). The vertical height of each streamwise horizontal planes are shown in mm as well.

5

B2. Stereo PIV Diagnostics

Previously, this "Glass Inlet" wind tunnel has been used to study 2D-SBLI by Lapsa and Dahm [3]. Thus, only a brief outline is presented. Several significant improvements in methodology to align this study with pertinent CFD validation efforts are described. These include pressure, temperature measurements during each run, a correction to the laser triggering and camera timing and a new post-processing method.

Stereoscopic particle image velocimetry (SPIV) produces a single-color cross-correlation PIV measurement. Two interline transfer CCD cameras with 1280x1024 pixel resolution and two Nd:YAG lasers are coordinated by a computer with an onboard programmable timing unit. Each individual particle image is a single-color, double-frame, single-exposure PIV image acquired at an angle 33 degrees to the light-sheet, thus allowing two cameras oriented in a stereo configuration to determine the two in-plane velocity components and the one out-of-plane velocity component over the measurement field-of-view.

To illuminate the seed particles in the field-of-view, a pair of light sheets are created using two frequency-doubled Nd:YAG lasers (one Spectra-Physics Quanta-Ray Pro-250 and one Spectra-Physics GCR-3). The lasers are sequentially triggered to create the double pulse of the 532 nm sheets, each with total energy of approximately 200 mJ. The flashlamps and Q-switches are triggered by TTL signals at 10 Hz with a pulse duration of 10 ns. The interframe time between pulses is controlled by a PC-based programmable timing unit (PTU) and the LaVision DaVis 7.2 PIV acquisition software. Both lasers have a 100 ns intrinsic delay between the rising edge of the trigger pulse and the actual peak in laser energy. This additional delay is significant for the flow conditions used in the present study, and causes the actual interframe time (determined by the peak-to-peak in laser energy) to differ from the target interframe time set by the trigger pulses. Thus the actual delay time between laser pulses is measured before each run with a ThorLabs DET10A/M high-speed photodetector connected to a LeCroy WaveRunner 6030 350 MHz oscilloscope. This actual delay time is input to the DaVis software. To do so, the software is told to use its normal internal delay time plus an additional delay that is just enough to cause the total delay in the software to equal the correct (measured) delay time.

The proper laser sheet thickness was set by the following requirement. The laser sheet thickness must be sufficiently large in comparison to the displacement of the particles in the direction perpendicular to the plane. Otherwise there is excessive loss of data if particles imaged in Frame 1 that do not appear in Frame 2. Thus, a thicker sheet is required for the accuracy of the streamwise velocity in the transverse planes, where the high speed (600 m/s) streamwise flow is normal to the sheet. Camera hardware limits the inter-frame time to a minimum of approximately 500 ns, so the typical out-of-plane particle displacement is approximately 300 μm. Good PIV practice is to have a sheet thickness of four times the typical particle displacement in order to minimize particle dropout. So the thicknesses of the transverse planes were set to 1.25mm. A consistent set of optics was utilized for the streamwise planes, and all sheet thicknesses are listed in Table 1.

Image Plane	$\Delta l[mm]$	dt	$DVR_x = \frac{u_{max}}{\sigma_u}$	$DVR_y = \frac{v_{max}}{\sigma_v}$	$DVR_z = \frac{w_{max}}{\sigma_w}$
Trvs Full Span	1.25±0.25	600 ±10	$\frac{597}{14} = 43$	$\frac{\pm80}{7} = 11$	$\frac{\pm80}{7} = 11$
Transverse	1.25±0.25	600 ±10	$\frac{597}{14} = 43$	$\frac{\pm80}{6} = 13$	$\frac{\pm80}{6} = 13$
Strm Vert	1.0±0.25	600 ±10	$\frac{597}{7} = 85$	$\frac{\pm80}{7} = 11$	$\frac{\pm80}{14} = 6$
Strm Horz	1.25 ±0.25	600 ±10	$\frac{597}{8} = 74$	$\frac{\pm80}{15} = 5$	$\frac{\pm80}{8} = 10$

Table 1: Light sheet thickness, Δl: laser timing, dt: and three components of the dynamic velocity ratio for each measurement plane computed from the maximum particle displacement and the rms pixel uncertainty in each plane.

6

Approved for public release; distribution unlimited.

B3. PIV Particle Seeding

To seed the flow in this study an oil aerosol is generated using a TDA-4B portable Laskin nozzle aerosol generator purchased from ATI Techniques, Inc. The generator consists of an array of six Laskin nozzles that create polydispersed sub-micron particles using a Poly-Alpha Olefin (PAO) oil with density of 819 kg/m^3. This oil also was provided by ATI Techniques. The mean particle diameter is specified to be 0.281 μm. The particle lag time is the time for a particle velocity to decrease to 1/e (37%) of the change in the gas velocity when the gas undergoes a step decrease in velocity, as it does across a shock wave. The particle time constant depends on particle size and particle density, and is computed to be 0.44μs. Samimy showed computationally that particles with Stokes number (St = τ_p/τ_f) of less than 0.25 will adequately track the large scale motions but that for St >0.05 they were not capable of tracking the smallest scales[15]. For a M=2.75 free stream, the characteristic flow time scale at the largest boundary layer condition ($\tau_f = \delta/U$) is 17μs, and thus the measured particle Stokes number is 0.44 μs/17 μs = 0.025 is still within the acceptable range to track the large and small scale motion in the boundary layer and SBLI regions of interest. Of course, there will be larger uncertainty in the velocities measured just downstream of the incident and reflected shock waves. However, these waves are strong only at distances considerably above the sonic line, so we assume that this uncertainty does not significantly affect the data in the SBLI interaction regions. Lapsa [3] measured the particle time lag across a shock wave in the Michigan facility. His results are shown in Fig. 3.
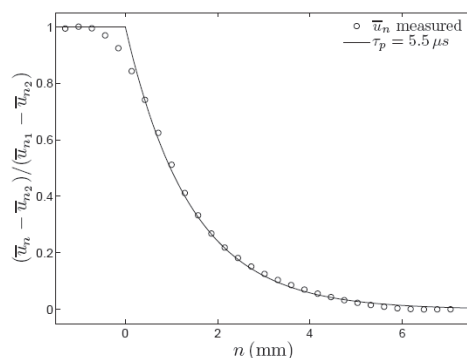

Figure 3. Measured particle response through an oblique shock. The velocity component normal to the shock, u_n, is normalized by the pre-shock (u_{n1}) and post-shock (u_{n2}) velocities and shown as a function of the shock-normal direction, n. An exponential fit to the data reveals the particle relaxation time is 5.5 μs (Lapsa,A. and Dahm W.J.A., [3]).

The particle images are recorded by two SensiCam PCO interline transfer CCD cameras at 3.33Hz (limited by the camera DRAM aquisition). The CCD has a 1024x1280 (*h* x *w*) pixel array and a physical chip size of 6.8x8.6mm^2. The 12-bit signal depth provides sufficient signal dynamic range, and electronic Peltier cooling ensures low noise. Each camera is equipped with a Sigma 70-300 f /4-5.6 APO macro lens to allow up to 1:1 imaging at a minimum focal length of 40.1 cm. For each camera, particle images from the first laser pulse are recorded onto the first frame and then immediately shifted under the submask. The particle images from the second laser pulse are then stored on the second frame.

B4. Prior PIV State of the Art

PIV techniques have been applied to high-speed flows since the late 90's, and significant progress has been made in the understanding of SBLI in the analysis of this data. However, as can be seen from Table 2 and Table 3, although many such studies have been undertaken, all suffer from a lack of measurement away from the centerline [16–22]. Table 4 presents two recent results on 3D-SBLI, one a tomographic

7

PIV data set by Humble and the second, the first PIV measurements made in a sidewall boundary layer by Helmer and Campo.[23–25]

Author	Beresh 1999	Hou 2003	Dupont 2005	Humble 2006
Mach	5 (750 m/s)	2 (497m/s)	2.3 (550 m/s)	2.1 (506 m/s)
$\frac{WidthMeasured}{TunnelWidth}$	$\frac{1mm}{152mm} =< 1\%$	$\frac{1mm}{152mm} =< 1\%$	$\frac{60mm}{170mm} = 35\%$	$\frac{4mm}{280mm} = 1.5\%$
Δt	$1.2\mu s$	$1\mu s$	$1\mu s - 6\mu s$	$2\mu s$
Particle time constant	$54\mu s$	$2.6\ \mu s$	No Report	$2.1\mu s$
Flow time scale δ/U_∞	$25\mu s$	$26\mu s$	$20\mu s$	$38\mu s$
resolution[mm^2]	2x2	0.72 x 0.72	2.2 x 1.1	1.9 x 1.6
vector spacing	64x64 (50%)	32x32	No Report	21x17 (75%)
configuration	boundary layer	90% CR	Full Span OS	40% Span Oblique
orientation	Vertical CL	Vertical CL	6 Horizontal	5 Vertical
number of vector fields	1500	2100	500	1500
validation method	Pitot	None	LDV	None
quantities presented	$\bar{u}, \sqrt{\overline{u'^2}}$	$\bar{u}, \sqrt{\overline{u'^2}}$	$\bar{u}, \sqrt{\overline{u'^2}}$	$\bar{u}, \sqrt{\overline{u'^2}}$ $\sqrt{\overline{v'^2}}, \overline{u'v'}$

Table 2. Previous PIV studies of SBLI 1999-2006

Author	Gana... 2006	Souverein 2008	Lapsa 2009
Mach	2 (510m/s)	1.69 (448 m/s)	2.75 (600m/s)
% Width Measured	$\frac{38mm}{152mm} = 25\%$	$\frac{2mm}{280mm} =< 1\%$	$\frac{8mm}{57mm} = 14\%$
Δt	$2\mu s$	$1.5\mu s$	$0.4\ \mu s$
Particle time constant	$2.6\mu s$	No Report	$5.5\ \mu s$
Flow time scale δ/U_∞	$26\mu s$	$38\mu s$	$17\mu s$
resolution[mm^2]	1.28x1.28	0.43 x 0.43	0.24 x 0.24
vector spacing	32x32(50%)	31x31(75%)	32x32 (50%)
configuration	Ramp	Oblique	60% Span Oblique
orientation	Horizontal	Streamwise	Transverse and centerline
number of vector fields	750	250 - 4000	1500
validation method	None	High-Res PIV	Repeatability
quantities presented	$\bar{u}, \sqrt{\overline{u'^2}}$	$\bar{u}, \sqrt{\overline{u'^2}}$	$\bar{u}, \bar{v},\bar{w}, \bar{\omega}_z, \bar{\omega}_x,$ $\bar{S}_{yy}, \bar{k}, H$

Table 3. Previous PIV and SPIV studies 2006-20010

8

Author	Humble 2009	Helmer 2011
Mach	2.1 (510m/s)	2.05 (524m/s)
% Width Measured	$\frac{14mm}{280mm} = 14\%$	Inside sidewall BL
Δt	2 μs	0.8μs
Particle time constant	2.6 μs	4.4μs
Flow time scale δ/U_∞	40 μs	10.3μs
resolution[mm^2]	Tomo - 2.1x2.1x2.1	0.135 x 0.135
vector spacing (overlap)	42x42x42 (75%)	16x16
configuration	Full Span Ramp	Full Span Ramp / Oblique Shock
orientation	Horizontal	4 Vertical
number of vector fields	750	200+
validation method	None	None
quantities presented	inst. u,v,w, $\|\omega\|$	$\bar{u},\bar{v}, \sqrt{\overline{u'^2}}\sqrt{\overline{v'^2}}, \overline{u'v'}$

Table 4. '3D' PIV and Corner Flow Investigations

Since none but the most recent results include sidewall boundary layers, and none provide simultaneous data from across the width of the interaction, the need for measurements which couple together the centerline and sidewall interaction, that include all three components of the velocity in each plane is clearly apparent.

B5. PIV Data Planes

A total of 16 planes of stereo-PIV data were collected at the locations shown in Fig. 1b. The three streamwise vertical planes are denoted SV1, SV2 and SV3. They are vertical planes that are aligned in the flow direction and thus are parallel to the side wall. The three streamwise horizontal planes are denoted SH1, SH2 and SH3. They are aligned in the flow direction and are parallel to the bottom wall. There are 11 transverse vertical planes. TV0, TV1 and TV2 are where the inflow boundary conditions were measured, and are far upstream of the SBLI. A third transverse vertical plane (TV10) is located far downstream of the SBLI and it is defines the outflow boundary conditions. Stagnation pressure and wall static pressures also were measured at this downstream boundary plane. There are seven transverse vertical planes (TV3 to TV9) that are located in the SBLI region. These data planes are relatively close to each other to better quantify the SBLI region.

The streamwise vertical planes SV1, SV2 and SV3 are sketched in Fig. 2b and they have an upstream boundary at the x-locations listed in Table 5, where x=0 is the leading edge of the shock generator. The dimensions of each plane also are listed. They are located at distances (z) from the sidewall of 17mm, 21 mm and 28 mm respectively.

Image Plane	x	y	z	Δx	Δy	Δz
SV1	70-120	1 - 27	28	0.49mm	0.49mm	1.5mm
SV2	57-100	1- 27	21	0.49mm	0.49mm	1.5mm
SV3	59-106	1- 27	17	0.49mm	0.49mm	1.5mm

Table 5. Dimensions (in mm) of the three streamwise vertical planes. x=0 is the leading edge of the shock generator, Δx is the distance between measurement locations on each plane (interrogation box size).

9

The streamwise horizontal(SH) planes SH1, SH2 and SH3 have an upstream boundary that is listed in Table 6 and their dimensions are indicated. They are located at vertical (y-distances) of 9.5, 19 and 28.5 mm from the bottom wall, respectively.

Image Plane	x	y	z	Δx	Δy	Δz
SH1	90-130	9.5	13-44	0.43	1.5	0.43
SH2	78-125	19	13-42	0.43	1.5	0.43
SH3	59-106	28.5	13-44	0.43	1.5	0.43

Table 6. Dimensions (in mm) of the three streamwise horizontal planes. y is the distance above the bottom wall. Δx is the distance between measurement locations on each plane (interrogation box size).

The coordinates of the eleven transverse vertical (TV) planes TV0 –TV10 are seen in Table 7. TV0, TV1 and TV2 define the inflow boundary conditions while TV10 defines the downstream boundary conditions available in Part I.

Image Plane	x[mm]	y[mm]	z[mm]
TV0(FS)	-144	1-36	1.5-54.5
TV1(FS)	-72	1-36	1.5-54.5
TV2(FS)	0	1-30	1.5-54.5
TV3(IR)	71	1-25	2-35
TV4(IR)	76	1-25	2-35
TV5(IR)	81	1-25	2-35
TV6(IR)	86	1-25	2-35
TV7(IR)	91	1-25	2-35
TV8(IR)	96	1-25	2-35
TV9(IR)	107	1-25	2-35
TV10(FS)	160	1-36	1.5-54.5

Table 7. Dimensions (in mm) of the ten transverse vertical planes. x=0 is the leading edge of the shock generator.

B6. Quality of the Boundary Layer and Repeatability of the Measurements

The bottom wall of the Michigan facility is a flat plate, as seen in Fig. 1a, in order to insure that the boundary layer is fully-developed and has reached equilibrium. Data in Figure 4 indicate that the velocity profile upstream of the SBLI agrees with classical theory for a fully-developed turbulent boundary layer. These PIV measurements were published previously by Lapsa and Dahm [3].

10
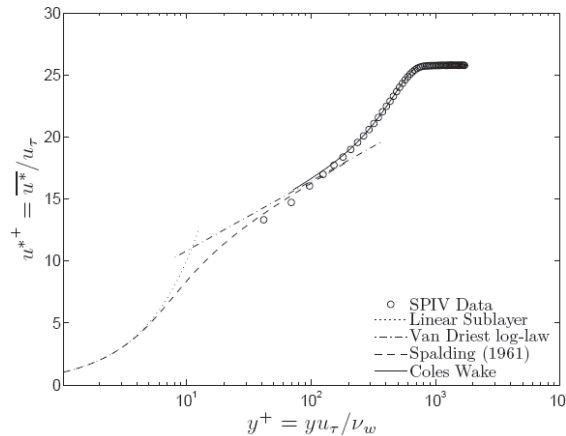
Figure 4. Mean velocity profile measured in the present experiment in the undisturbed boundary layer on the bottom wall, showing that it agrees with the classic theoretical boundary layer structure, using inner variables u+ and y+. The plot shows that the entire outer wake-like region is resolved, with the data point nearest the wall extending into the buffer region (Lapsa and Dahm).

The repeatability associated with the present SPIV diagnostics and facility was carefully recorded and a complete data set is available at the Workshop website. Figure 5 indicates that the horizontal and vertical mean velocity profile measurement were repeatable to within 3% [4].
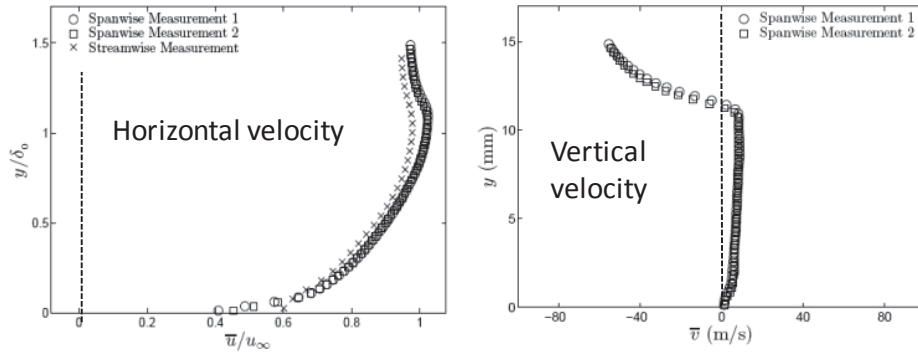
Figure 5. Repeatability of the present Stereo PIV diagnostics and facility, as recorded previously by Lapsa and Dahm [4]. The profiles were recorded on different days.

C. Results

The results presented in this paper will be limited to a list of the metrics that are being considered and a description of the measurements that were made on the inflow boundary. A complete set of results have been recorded and will be made available at the SBLI Workshop website at a later date.

C.1 Metrics

One of the goals of the collaborative experimental-computational effort is to decide on the best metrics to use to compare the results from different research teams. In the previous workshop, several metrics were used, but because the current SBLI problem is three-dimensional, additional metrics are needed. The following is a list of useful metrics.

    a.   Iso-contour curves - of the following quantities, determined in each of the measurement planes (that are defined above):
        1.   Mean velocity U, V, W. Of particular interest is the contour $U = 0.9\ U_{oo}$ that is one definition of the edge of the core flow. Also of interest is the contour U = 220 m/s which corresponds to the free stream sonic velocity, and the contour U = 0.
        2.   R.M.S values of fluctuating quantities u', v', w' and turbulent kinetic energy k.
        3.   Reynolds stress velocity correlations: $\overline{u'v'}, \overline{u'w'}, \overline{v'w'}$
        4.   Normal and shear strain rates $S_{xx}, S_{yy}, S_{zz}, S_{xy}, S_{xz}, S_{yz}$
        5.   Vorticity components $\omega_x, \omega_y, \omega_z$
        6.   Vortex-Stream lines, defined by Adrian (see below), which identify vortex structures that are convected with the flow.
    b. Profiles

11

7. Measured profiles of the above quantities, versus the coordinate that is normal to the wall, have been plotted at selected locations in the interaction region.

   c. Additional metrics of importance

   8. Wall skin friction lines, defined as:

   $dx/\tau_x = dz/\tau_z$ on the bottom wall, and $dx/\tau_x = dy/\tau_y$ on the side wall. These skin friction lines can be computed using CFD and can be compared to the measured oil streak lines recorded in this experimental effort.

   9. The area of the core flow (where $U > 0.9\ U_{oo}$) is a function of the x-coordinate. This area is a global measure of the effective air flow provided by an inlet. It also is useful metric for determining how close the inlet is to an unstart.

   10. Reflected shock locations have been recorded in each of the streamwise vertical planes.

   11. The incident boundary layer thickness has been measured and the velocity profile has been shown previously to agree well with a fully-equilibrated Law of the Wall profile.

Vortex-Stream Lines

Because the flow is three dimensional and highly complex, new visualization methods are needed to properly analyze both the experimental and computational results. PIV developer Ron Adrian, to capture vortex cores convecting in a fast moving freestream, pioneered the vortex-stream line visualization method[26]. These vortex cores are not identifiable when by plotting conventional isolines.   Adrian shows that vortex structures are better identified in the x-z plane, for example, by plotting the following isolines:

$$\frac{dx}{U - U_{AVG}} \quad = \quad \frac{dz}{W - W_{AVG}} \tag{1}$$

U and W are the mean velocity components (ensemble averaged from 1700 images at each (x,z) location in the x-z plane), and U_{AVG} and W_{AVG} are the velocities that are averaged over the entire data plane. Coherent vortices convecting with speed $[U_{AVG}, W_{AVG}]$ become visible using this method, and shock waves are visible as lines where the vortex-streamlines converge, much like the lines of separation that are identified where the skin friction lines converge.

C2. Freestream Mach Number and Axial Velocity

The freestream Mach number and axial mean velocity were determined from the ensemble average PIV measurements of U obtained in the undisturbed free stream from regions of intersection of the streamwise and transverse data planes. The data was processed from a small 3 window by 3 window region, and the mean and fluctuating components are reported in Table 8. The corresponding Mach number was determined from the measured stagnation temperature of 295.7 K. Using the isentropic expansion of the nozzle design(M=2.75) yields an estimate of free stream temperature of 117K and a speed of sound of 217 m/s. While the methodology for evaluating all the data were the same, the processed data shows some variability. In particular, plane TV1 has both the largest u'$_{rms}$ and the largest deviation from the mean velocity than the other PIV data in the set. Independent confirmation of this velocity data will be performed with pitot-static probes and will be made available on the website.

12

Data Set	[x,y,z] mm	U (m/s)	σ_U	M
TV0	[-144,25,17]	598	16.1	2.756
TV0	[-144,25,28]	602.8	16.0	2.774
TV0	[-144,25,39]	608	15.4	2.802
TV1	[-72,25,17]	579	23.3	2.668
TV1	[-72,25,28]	575	24.4	2.650
TV1	[-72,25,39]	576	26.3	2.654
TV2	[0,25,17]	589	17.6	2.714
TV2	[0, 25,28]	591	15.5	2.723
TV2	[0,25,39]	586	13.8	2.701
SV1	[73,15,28]	596	7.3	2.746
TV3	[71,15,28]	603	16.5	2.779
SV3	[71,15,17]	594	8.9	2.737
TV3	[71,15,17]	600	15.8	2.765
			Average M	2.73
			std σ_M	0.049

Table 8. Free stream Mach number and axial mean velocity determined in thirteen locations. σ_u indicates the u component of the rms velocity fluctuation in the measurement.

C3. Inflow Boundary Conditions

Inflow boundary conditions were measured on three transverse vertical planes (TV0, TV1 and TV2) that were shown in Fig. 1b. Only the measurements on TV2 are presented here. Previously Lapsa and Dahm [3] recorded inflow boundary conditions for this Mach 2.75 facility but they were only interested in the centerline region so their measurements did not extend into the corners or near the sidewall region. Data planes TV0, TV1 and TV2 from near sidewall to sidewall (92% of full span) include the near bottom wall to 48% of tunnel height. Preliminary results of a validation criteria underdevelopment are presented in Fig 7. Near wall regions that suffer from spurious laser reflection foul the PIV measurement and a robust criterion will be used to discarded these regions from the data set.
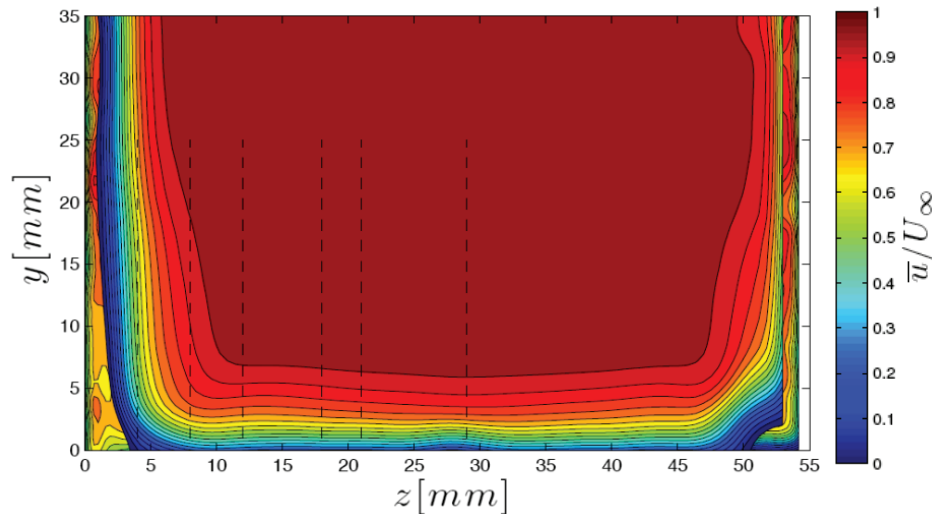
Fig. 6. U-velocity (mean streamwise velocity) on inflow boundary plane TV2. Ensemble average of 1700 images.

13
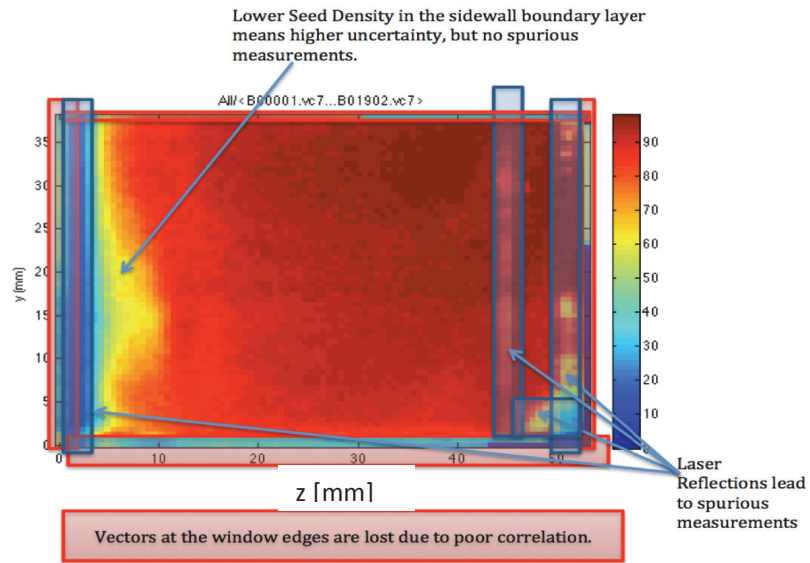
Fig. 7 Spurious data regions indicated using ensemble criterion under development
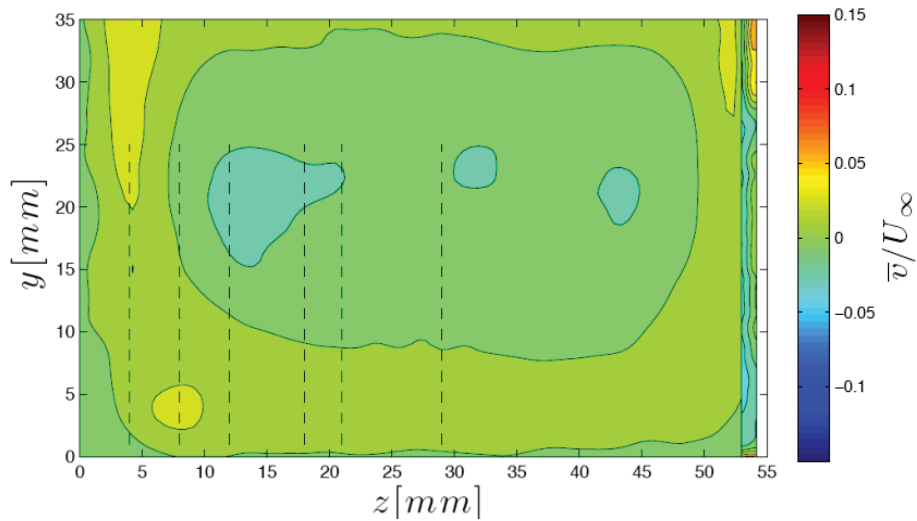
Fig. 8. V-velocity (mean vertical velocity) on inflow boundary plane TV2. Ensemble average of 1700 images. Note that the magnitude of V/U_{oo} is less than 2%.

14

Approved for public release; distribution unlimited.
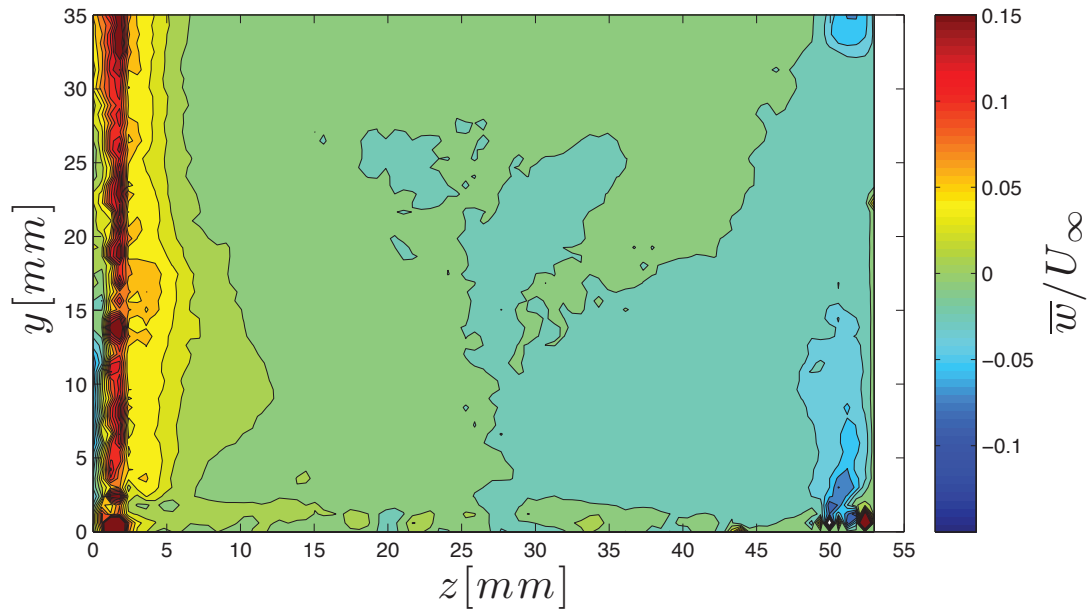
Fig. 9. W-velocity (mean transverse velocity) on inflow boundary plane TV2. Ensemble average of 1700 images. Note that the magnitude of W/U_{oo} is less than 2%. Sidewall data that shows a large deviation is a result of side window reflection. This data will be removed when it is used for comparison.
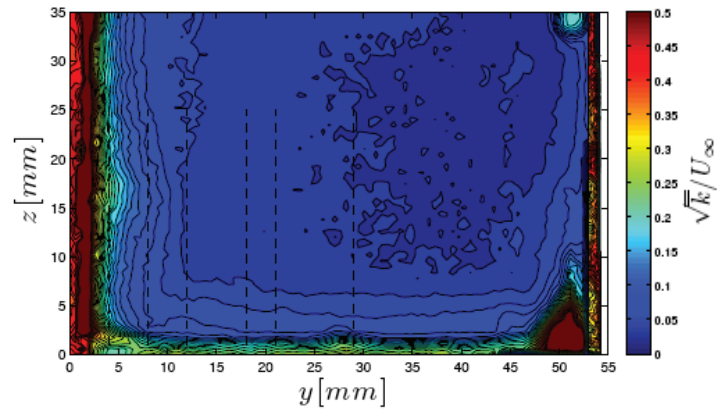
Fig. 10. Turbulence kinetic energy on inflow boundary plane TV2. Ensemble average of 1700 images. Large positive deviations in TKE are due to wall reflections, these spurious data will be removed from the dataset.

15
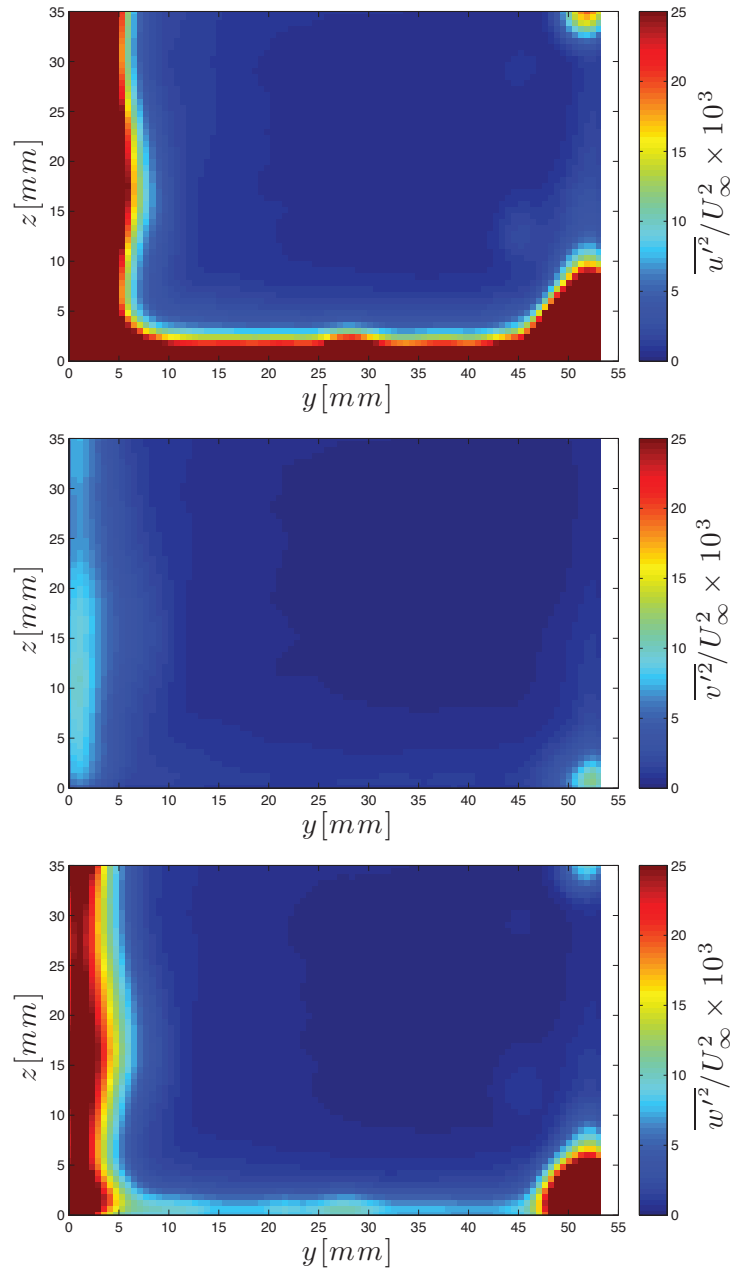
Fig. 11. Mean squared velocity fluctuations on inflow boundary plane TV2. Ensemble average of 1700 images. Large positive deviations in rms are due to reduced signal at the wall. Locations of 'good data' are reported in tables 5-7 above. The lower magnitude of v' in the bottom wall than the sidewall is in good agreement with theory, the very large values of u' and w' in the side wall is due in part to PIV errors in the sidewall data. Figure 14 better compares the magnitudes along the centerline contour.

16
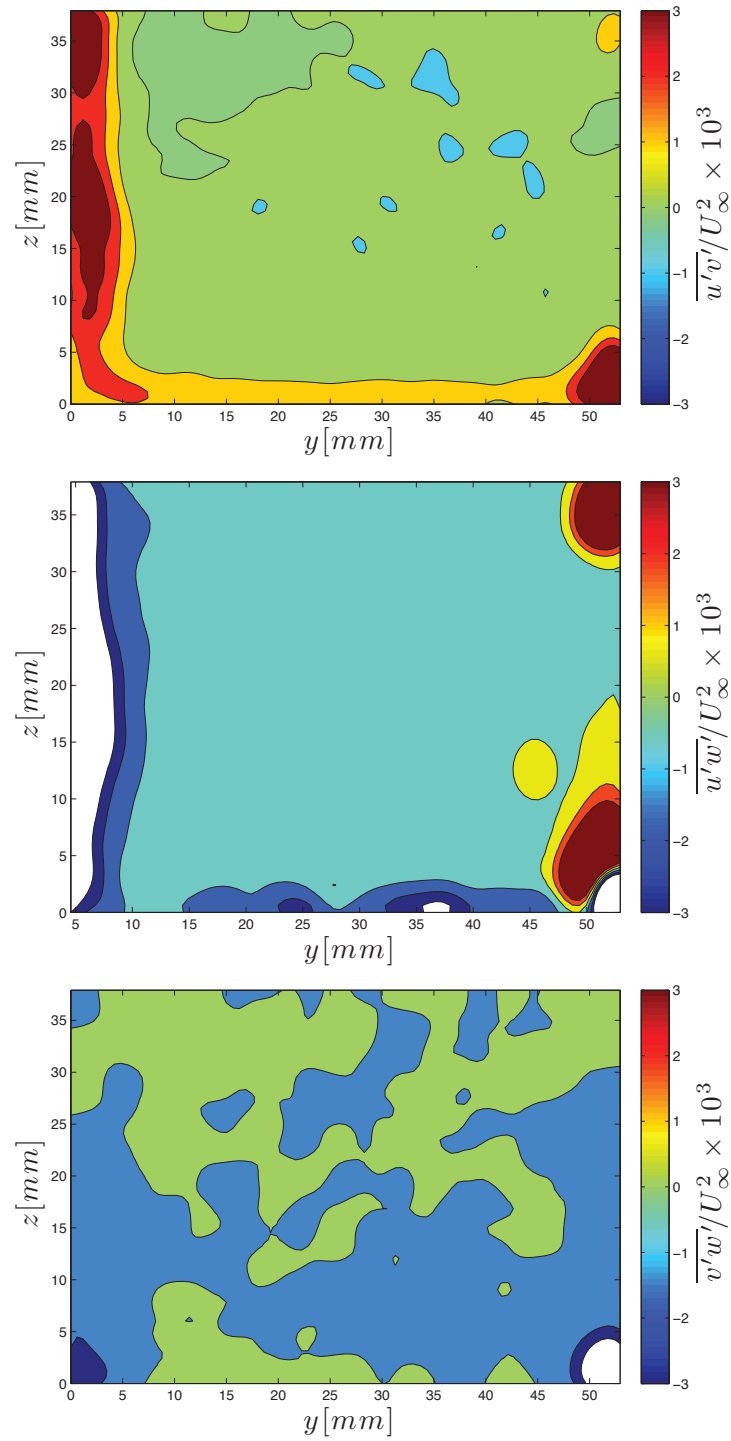
Fig. 12. Reynolds stress velocity correlations on inflow boundary plane TV2. Ensemble average of 1700 images.

17
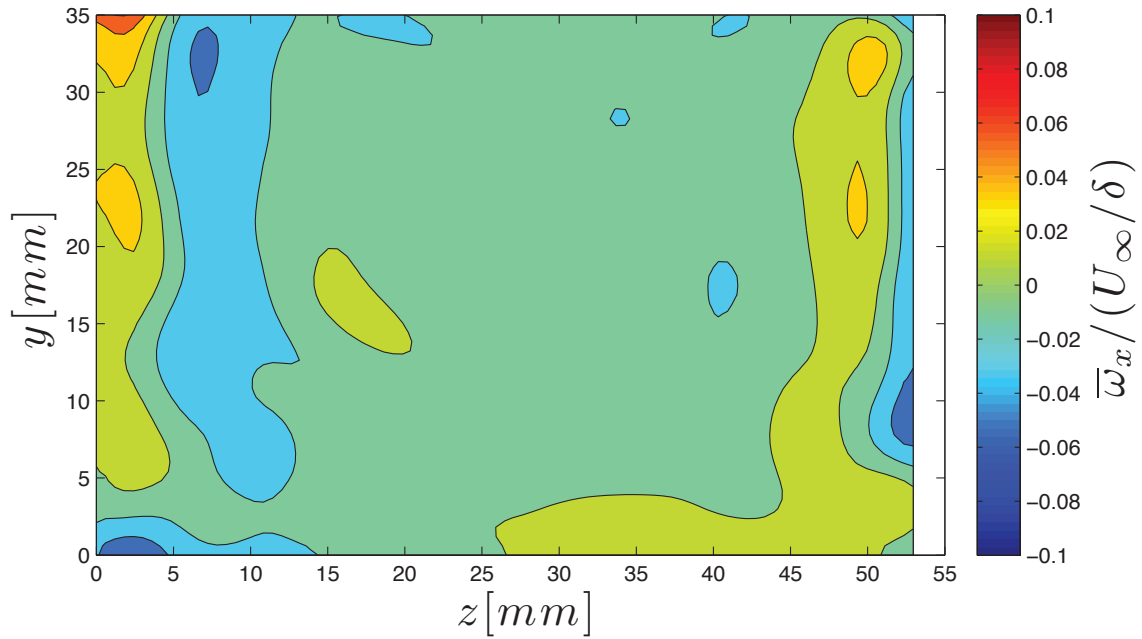
Fig. 13. Mean vorticity ω_x on inflow boundary plane TV2. Ensemble average of 1700 images.

In the profiles in Figure 14, ensemble averages of the measured quantities on the inflow plane TV2 are presented along a contour at the centerline (z = 28.5mm), versus the coordinate that is normal to the wall. We see typical boundary layer behavior in the streamwise direction, and the transverse velocity components are small (< 3%) at the centerline plane of symmetry. As expected, total turbulence kinetic energy increases sharply very near the wall. The dominant component is the streamwise velocity fluctuation, followed by the transverse component. At the distance to the wall measureable with the PIV in the current experiment there is no appreciable rise in vertical velocity fluctuation.

18

Approved for public release; distribution unlimited.
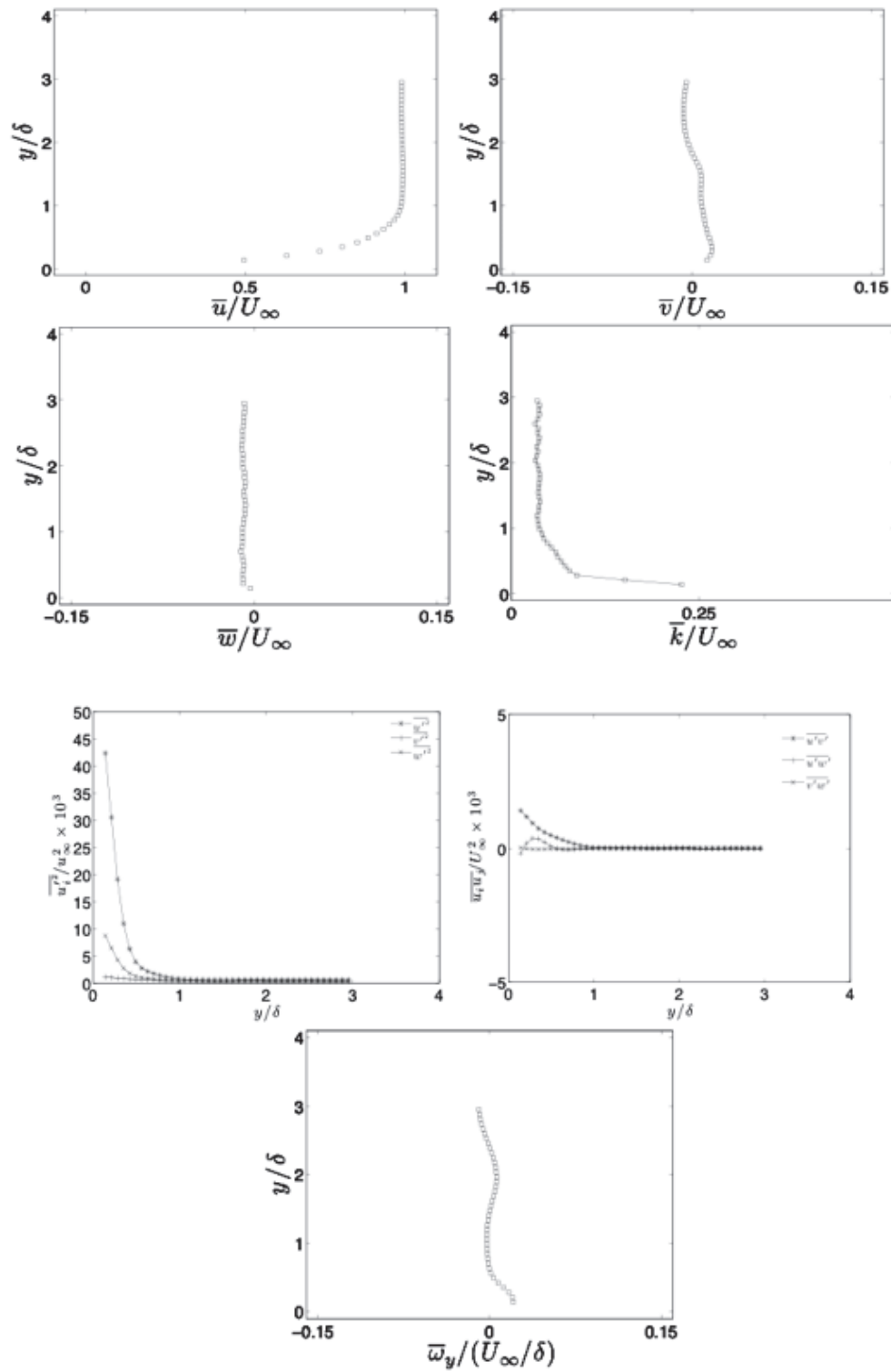
Fig. 14. Some selected profiles of measured quantities on the inflow boundary plane TV2. Ensemble average of 1700 images.

19

In each of the PIV data planes 1700 stereo PIV images were recorded. Two methods to average the data were used. Ensemble averaging provided a standard time-average of each of the instantaneous images. Conditional averaging also was used to identify the separation zone in each instantaneous image. Thus, when the separation zone location oscillates in space, the conditional average is a better description of the separation bubble than the ensemble average.   Figure 14 lists estimates of the PIV statistical uncertainty, when ensemble averages are determined from 1700 images. The theoretical free stream velocity deviates from the measured value by 0.8 %. An uncertainty analysis shows that if 3400 images were recorded rather than 1700 images, the improvement is significantly smaller than other sources of uncertainty. Therefore, efforts to reduce uncertainty should be directed at examining these other sources and not in recording more data. Small uncertainties arise due to day-to-day variation in the room stagnation pressure and temperature (which were recorded and are available one the website), PIV micron sized oil drops lagging behind the flow variations near the shock wave, and possible day-to-day variations in the alignment of the wedge (which was only removed infrequently). Velocity components that were in the PIV laser light sheet plane were measured more accurately than the components that are normal to the plane.

One question that was answered is: 'what is the uncertainty associated with selecting 1732 images over which to ensemble average?' Figure 14 lists the PIV statistical uncertainty. The red boxes indicate the size of the 95% confidence interval. For example, the upper left box indicates that if an ensemble average of 1732 images was recorded, the average value for 1732 images would lie within 0.5 m/s of the true statistical mean if only uncertainty associated with the number of images are considered. That is, if more than 1732 images were recorded, there is a 95% chance that the improvement would be no more than 0.5 m/s (and a typical free stream velocity is 600 m/s). It is concluded that 1732 images are sufficient to make the statistical uncertainty significantly smaller than any systematic error.   Some sources of systematic error include uncertainty in the time between laser pulses (which was measured with a modern digital scope having a very fast and accurate timing chip), uncertainty in the geometric alignment, the room pressure and temperature (which were measured before each run).

	Measured
$u_1\ [m/s]$	$602 \pm$
$v_1\ [m/s]$	$14 \pm$
$u_2\ [m/s]$	$564 \pm$
$v_2\ [m/s]$	$-57 \pm$
$\|u_2\|\ [m/s]$	$566 \pm$

$$\sigma_{\bar{u}} = \frac{\sigma_u}{\sqrt{N}} = \frac{u'_{RMS}}{\sqrt{N}}$$

Free stream: $u'_{RMS} \approx 20$ m/s

$\boxed{\bar{u}_{95\%} = \bar{u} \pm 0.5 \text{ m/s}}$

3DI-SBLI: $u'_{RMS} \approx 100$ m/s

$\boxed{\bar{u}_{95\%} = \bar{u} \pm 2.5 \text{ m/s}}$

$$\sigma_{\bar{v}} = \frac{\sigma_v}{\sqrt{N}} = \frac{v'_{RMS}}{\sqrt{N}}$$

Free stream: $v'_{RMS} \approx 12$ m/s

$\boxed{\bar{v}_{95\%} = \bar{v} \pm 0.25 \text{ m/s}}$

3DI-SBLI: $v'_{RMS} \approx 75$ m/s

$\boxed{\bar{v}_{95\%} = \bar{v} \pm 1.9 \text{ m/s}}$

$$\sigma_{\bar{w}} = \frac{\sigma_w}{\sqrt{N}} = \frac{w'_{RMS}}{\sqrt{N}}$$

Free stream: $w'_{RMS} \approx 12$ m/s

$\boxed{\bar{w}_{95\%} = \bar{w} \pm 0.25 \text{ m/s}}$

3DI-SBLI: $w'_{RMS} \approx 75$ m/s
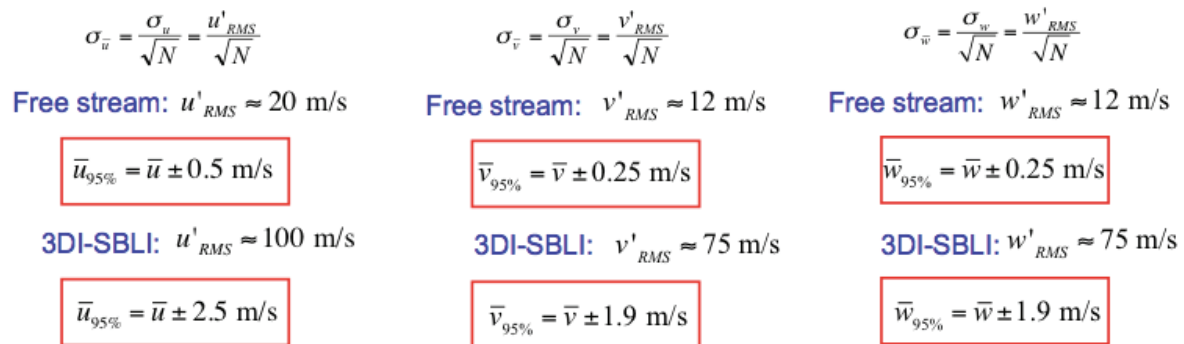
$\boxed{\bar{w}_{95\%} = \bar{w} \pm 1.9 \text{ m/s}}$

Figure 15. PIV statistical uncertainty associated with ensemble averaging N = 1732 images. The red boxes indicate the size of the 95% confidence interval. For example, the upper left box indicates that if an ensemble average of 1700 images was recorded, the value for 1700 images would lie within 0.5 m/s of the true statistical mean if only uncertainty associated with the number of images are considered.

20

D. Discussion of the Physics of 3-D SBLI

The underlying question that we are trying to answer by comparing CFD to experiment should always be 'With what level of confidence can we assert that two flows the same?' Unlike early experimental efforts requiring 'similarity parameters', a validation effort for CFD attempts to match exactly the experimental conditions. The trouble starts when sources of error confound our attempts to compare the two. In an experiment, the 'exact' fluid equations are being solved, but there is always some non-zero uncertainty in the boundary conditions. Conversely in the CFD, the boundary conditions including the geometry are known precisely, but the fluid equations are being approximated. Thus, in all but the simplest flows, there is bound to be disagreement between measured properties of these two flows, and the disagreement is likely amplified by introducing three-dimensionality.

D1. Three-Dimensional Flows

In the face of uncertainty introduced by point to point comparisons, larger systems level quantities have been investigated (see the AIAA Drag Prediction workshop… entering its 6th at this very meeting). The idea is that qualitatively the computed and experimental flow are 'the same' if they show the same trends for these integrated quantities, with one simulation being 'better' the closer it can match the experimental data. However, the lack of relative error estimates for each computation and the experiment leaves room for significant improvement. Additionally, there are other three-dimensional metrics which might improve our confidence that the computed flow and the experimental flow are in-fact 'the same' despite differing slightly in detail.

Several previous authors have set out to explain the coupling between three dimensional flow fields and the primitive quantities (as measured by PIV and others or computed in CFD.) The most notable efforts to uncover new 3-dimensional metrics, in the opinion of the current authors, is the efforts of H. Werle, R. Legendre , Dallman, Tobak and Peake; Perry, Chong, and Cantwell [11], [27–29]. These efforts are all related to topological (critical point) methods of fluid analysis. However, these references are mostly conjecture, based upon flow footprints assessed using oil flow and the flow structures are verified only qualitatively using stream trace visualization. Some selected results, though, are remarkable.

The fundamental principle underlying the topological method is that there is a family of three dimensional flow structures that remains stable over a certain range of conditions. If, or when, flow breakdown occurs, the topological structure of the flow also changes, but eventually (in the absence of very strong transient forcing) adopts a new pattern of critical points. The logical extension to be made from the stability of these topologies is that any two flows which share (either experimental or computationally) the same topological features at a given set of nominal conditions could be considered 'the same' in the topological sense. The two flows are 'analogous' since it is only the relative location (not the number or nature) of their topological features which have varied. The lasting worry of these early authors, however, was the lack of uniqueness of a given shear flow profile. Yet, oddly, similar uneasiness (e.g. what is the global flow behavior, or how did it get to be this way) is not given to isolated velocity profiles, so long as they agree with the log-law!

To settle both of these concerns the current validation effort provides both sets; shear stress lines via oil flow and PIV velocity field information. Using the two, a conclusive link between velocity and shear flow can be established. The conclusion drawn from this effort is the nature and distribution of these critical points, is, in fact, critical to correctly assessing the flow features. Going back to the introduction section, we can explain the drawbacks of the first SBLI workshop in this context as being singularly focused on the velocity field without providing a conclusive three-dimensional link to all the boundary conditions. It

21

was insufficient in this tunnel, despite a log-law centerline velocity profile, to consider the flow 2D near the centerline.

D2. Dominant Physics

Incident oblique shocks, compression corners, swept fins and normal shocks generate pressure rises in the boundary layer that result in thickening or separation of the boundary layer [4-14]. Unfortunately, these flows are sufficiently different in structure that each display characteristic scales impeding global parameterization based on two-dimensional analyses and a developed understanding of shock-foot unsteadiness is still a matter of some concern. To assist the computational modeling of this experiment, critical physical aspects of the interactions are illustrated in Fig.15. The upper figure indicates that vortex structures exist in several places, and they interact. Since RANS computational methods historically have difficulty resolving 'corner flows' accurately, it is imperative that modifications are sought such that each vortex structure that develops is captured in the flow.

The current result also highlights a need for a conceptual shift in our boundary layer flow analysis as we transition from 2D to 3D as well as how to interpret results for boundary layers which encounter separation, which will be discussed in terms of SBLI in the following section. To discuss the topology of critical points, we first need to revisit, as others have, the definition of various key terms in the theory. Much of the following is excerpted from Eagle[30], available from DeepBlue thesis retrieval service, starting August 2013.

Begin by considering skin friction. In the simplest 2D case, the skin friction at the wall is a scalar quantity, and is determined locally, for a Newtonian fluid, by the viscosity, and the wall normal gradient of velocity field, $\tau_w = \mu(du/dy)$. Separation for such 2D flows is defined to occur where a previously positive shear stress at the wall goes to zero, thus indicating that the local wall normal velocity gradient has also gone to zero. From the steady boundary layer equations this condition occurs when a local pressure gradient has caused the streamwise velocity profile to locally go to zero. For some length downstream of this point the wall shear stress is zero or negative. The flow can remain detached or stalled in the region where the local shear is negative, indicating that the local velocity at this point has reversed. Eventually the flow may reattach, that is, the shear stress will slowly return through zero and become positive again. Such a simple picture is well known in undergraduate fluids courses. However, the extension of this principle to non-periodic, non-two dimensional flows requires significant re-thinking. Here enters critical point theory.

In the simplest definition, critical points in the flow are the three dimensional extension of two dimensional separation points. The key difference in three dimensions is that no 'infinite separation line' actually exists (for the three dimensional picture is not a simple extrusion of the 2D case). However, all hope of prediction is not lost. For certain geometries, the locations of many critical points can be predicted a priori given information gleaned from two dimensional experiments. For example, it is possible still to predict when a critical point will occur along a plane of symmetry, due to the somewhat 2 dimensional nature of the flow on this plane. However, when separation occurs in three-dimensional flows there is one key difference from the 2D case. A bifurcation exists in the solution around a single critical point leading to two separate solutions. These solutions depend on the eigenvectors at the critical point, but are more readily described by the secondary flow patterns. There are two types of flow separation, one where the transverse component of velocity converges on the point producing a node and where it diverges from the point producing a saddle. Interestingly these features are indistinguishable when investigating only the plane of symmetry normal to the surface.

This key feature drives us to consider these flows as fundamentally three-dimensional.

22

How the shock reflects off the surfaces contribute considerably to vorticity production of the interaction. Where the shock intersects the bottom wall, a lambda shock occurs and straddles a separation zone. The separation zone can be imagined to be a line vortex that is parallel to the bottom wall as shown. Where the shock reflects from the bottom wall, a centerline separation zone occurs. In the corners, two counter-rotating vortices exist and define a region of separated flow.
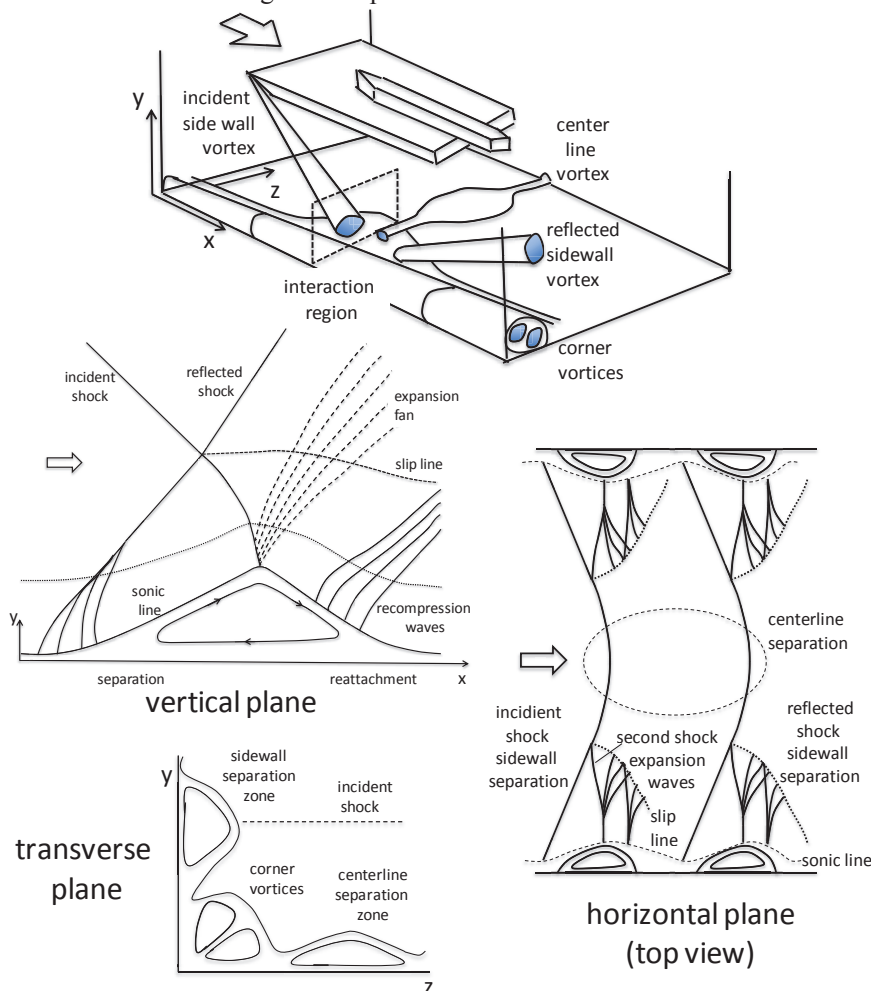

Figure 16. Schematic of the three SBLI unit physics problem that have a strong interaction in a 3-D SBLI in a rectangular inlet.

The mechanism of the corner flow-SBLI appears to be similar to the other SBLI interactions. The primary difference is the strength of the streak line convergence as the bottom wall is approached. The shock from the wedge sweeps along the side wall, converging side wall streak lines and creating down flow toward the bottom wall boundary layer. In the corner, secondary flows created by the adverse pressure gradient due to the original and reflected shocks interact with the turbulent corner flow creating reversed flow and enhancing secondary flow along the bottom wall. The reverse flow moves upstream until it creates a saddle point separation. For small-scale features, the saddle point is very close to the wall, making it difficult to observe. Flow along the bottom wall appears to bend toward the free stream in the region of shock reflection. The stronger the combination of these secondary flows the more severe the corner flow SBLI.

23

E. Conclusions

Improvement in the methodology and careful documentation of experimental data makes this experiment an attractive one for comparison to computation. The computational challenge is to correctly compute all of the underlying physics of a single three-dimensional inlet shockwave boundary layer interaction for the purpose of understanding the prominent interactive features, including aspects of oblique-impinging shocks, crossing shocks, SBLI, and corner flows.

Significant extra care in the experimental design and data gathering phases, including multiple inflow planes, makes this dataset uniquely amenable for CFD validation. In particular, this effort addresses 6 of the 9 areas proposed by Benek[1]. Obviously this includes a full three dimensional interaction, for the assessment of turbulence models in this region(item 1). We also address comprehensive inflow information from 3 data planes(item 2). This data set will provide independent confirmation of the inflow Mach number by pitot, and used flow visualization techniques like oil flow and shadowgraphy combined with wall pressure data in the interaction region (item 3 and 4). Through this process the entire workshop team was invested in the design (item 8) and enough information was gathered during each run to provide reliable estimates of experimental error (item 9).

To have a shot at correctly computing this flow, state of the art in CFD techniques will have to capture the fin-plate SBLI, as well as the sidewall-bottom wall effects that propagate through the corner interaction. Strong gradients at the wall and through the shock provide a significant challenge problem for assessing appropriate stress-limiting techniques in CFD such that shocks are well captured, but turbulence intensity is not artificially dissipated. The three-dimensional nature of the separation requires a careful examination of (and explanations for) various behaviors, such as the large-scale vortical structures near the corners, and the change in separation type along the centerline when compared with previous '2D' intuition.

F. Future Work

The goal of the experimental program has been to keep the total uncertainty in mean quantities below 3%. To quantify this, estimates of the uncertainty in the present experimental data set will be provided on the Workshop website. There are several sources of uncertainty, including a random uncertainty associated with ensemble averaging over a finite number (1700) of data images, and systematic uncertainties in the experimental setup, measurement techniques and atmospheric condition.

To confirm that this goal has been achieved, pitot pressure and static pressures will be measured to independently confirm the PIV velocity measurements. The resulting free stream velocities will be compared to those in Table 1. That the PIV results already agree to within 3% is encouraging since the free stream velocity was measured in planes of different orientations on different days. Further comparisons will be attempted in the SBLI interaction region where there are several locations that data overlap among the ten planes to assess the uncertainty using two methods, similar to how the data in first workshop was analyzed by DeBonis et al. [1].

One approach will be based on estimates provided by the experimental team using techniques from PIV uncertainty quantification. The experimental group is developing metrics that utilize the probability distribution function (PDF) of velocities and velocity derivatives at a point. Comparing the velocity pdfs in place of a simple average with an error bar allows us to perform several validation tasks simultaneously. For example, we can visually assess the relative agreement of measurements taken from multiple planes in terms of the average as well as standard deviation, skewness, and kurtosis, and even assess the affect of changing the number of images required to achieve a statistically stationary average.

24

Comparison of experiment and computations must also contend with effects of the unsteadiness in the shock foot with the bottom wall and the use of conditional averaging will be employed in these regions to determine intermittency. Finally, some new visualization techniques under development that identify three-dimensional critical points as local invariants of the flow field may hold promise for analyzing and comparing this family of separated flows.

A second independent method to estimate experimental uncertainty will be used that was developed by Aeschliman and Oberkampf, and Oberkampf and Roy [31], [32]. The method is based on statistically analyzing the differences in multiple measurements of the various quantities of interest, e.g., u, v, and w, as well as normal and shear stresses. That is, in the PIV database, measurements are made on different planes. Where these planes intersect there are lines in space where the mean statistical quantities are measured on two different days. In the PIV data set, the streamwise and spanwise data planes have different PIV window sizes, times between laser pulses, and other operating parameters. Several CFD analysts in the first workshop noticed a difference in the PIV data where the two measurement planes intersect. Differences between two independent measurements are not unexpected and examining these differences provides some insights into the fundamental uncertainty in the measurement technique.

Acknowledgements

References

[1]   J. A. Benek, "Lessons Learned from the 2010 AIAA Shock Boundary Layer Interaction Prediction Workshop," *AIAA Paper 2010-4825* July 2010.

[2]   J. DeBonis et al., "Assessment of Computational Fluid Dynamics and Experimental Data for Shock Boundary-Layer Interaction," *AIAA Journal*, vol. 50, no. 4, pp. 1-28, 2012.

[3]   A. P. Lapsa and W. J. A. Dahm, "Stereo particle image velocimetry of nonequilibrium turbulence relaxation in a supersonic boundary layer," *Experiments in Fluids*, vol. 50, no. 1, pp. 89-108, Jun. 2010.

[4]   P. J. K. Bruce, D. M. F. Burton, N. a. Titchener, and H. Babinsky, "Corner effect and separation in transonic channel flows," *Journal of Fluid Mechanics*, vol. 679, pp. 247-262, May 2011.

[5]   C. W. P. Ford, H. Babinsky, and P. Ford, "Micro-ramp control for oblique shock wave/boundary layer interactions," in *37th AIAA Fluid Dynamics Conference*, AIAA 2007-4115, June 2007.

25

[6]   P. P. Wu and R. B. Miles, "Megahertz Visualization of Compression-Corner Shock Structures," *AIAA Journal*, vol. 39, no. 8, pp. 1542-1546, Aug. 2001.

[7]   A. G. Panaras, "The effect of the structure of swept-shock-wave/turbulent-boundary-layer interactions on turbulence modelling," *Journal of Fluid Mechanics*, vol. 338, pp. 203-230, May 1997.

[8]   F. K. Lu and G. S. Settlest, "Inception length to a fully developed, fin-generated, shock-wave, boundary-layer interaction," *AIAA Journal*, vol. 29, no. 5, pp. 758-762, May 1991.

[9]   T. Handa and M. Masuda, "Three-Dimensional Normal Shock-Wave/Boundary-Layer Interaction in a Rectangular Duct," *AIAA Journal*, vol. 43, no. 10, 2005.

[10]   P. Doerffer, "An Experimental Investigation of the Math Number Effect upon a Normal Shock Wave -- Turbulent Boundary Layer Interaction on a Curved Wall," *Acta Mechanica*, vol. 51, 1989.

[11]   U. Dallmann, "Topological Structures of Three-Dimensional Vortex Flow Separation," in *AIAA 16th Fluid and Plasma Dynamics Conference*, AIAA Paper 83-1735, July 1983.

[12]   T. Adamson Jr. and A. Messiter, "ANALYSIS OF TWO- DIMENSIONAL INTERACTIONS BETWEEN SHOCK WAVES AND BOUNDARY LAYERS," *Annual Review of Fluid Mechanics*, vol. 12, no. 1, pp. 103–138, 1980.

[13]   J. Green, "Interactions between shock waves and turbulent boundary layers," *Progress in Aerospace Sciences*, vol. 11, pp. 235-340, Jan. 1970.

[14]   J. D. Schmisseur and D. S. Dolling, "Fluctuating Wall Pressures near Separation in Highly Swept Turbulent Interactions," *AIAA Journal*, vol. 32, no. 6, pp. 1151-1157, 1994.

[15]   M. Samimy and S. K. Lele, "Motion of particles with inertia in a compressible free shear layer," *Physics of Fluids A: Fluid Dynamics*, vol. 3, no. 8, p. 1915, Aug. 1991.

[16]   S. J. Beresh, N. T. Clemens, and D. S. Dolling, "Relationship Between Upstream Turbulent Boundary-Layer Velocity Fluctuations and Separation Shock Unsteadiness," *AIAA Journal*, vol. 40, no. 12, pp. 2412-2422, Dec. 2002.

[17]   Y. X. Hou, N. T. Clemens, and D. S. Dolling, "Wide-Field PIV Study of Shock-Induced Turbulent Boundary Layer Separation," in *41st AIAA Aerospace Sciences Meeting* AIAA paper 2003-441, January 2003.

[18]   P. Dupont, C. Haddad, and J. F. Debiève, "Space and time organization in a shock-induced separated boundary layer," *Journal of Fluid Mechanics*, vol. 559, p. 255, Jul. 2006.

[19]   R. a. Humble, F. Scarano, and B. W. V. Oudheusden, "Particle image velocimetry measurements of a shock wave/turbulent boundary layer interaction," *Experiments in Fluids*, vol. 43, no. 2–3, pp. 173-183, Jun. 2007.

26

[20] B. Ganapathisubramani, N. T. Clemens, D. S. Dolling, and P. C. Road, "Effects of upstream boundary layer on the unsteadiness of shock-induced separation," *Journal of Fluid Mechanics*, vol. 585, p. 369, Aug. 2007.

[21] L. J. Souverein, B. W. van Oudheusden, F. Scarano, and P. Dupont, "Application of a dual-plane particle image velocimetry (dual-PIV) technique for the unsteadiness characterization of a shock wave turbulent boundary layer interaction," *Measurement Science and Technology*, vol. 20, no. 7, Jul. 2009.

[22] A. P. Lapsa, "Experimental Study of Passive Ramps for Control of Shock – Boundary Layer Interactions," University of Michigan, PhD Thesis, 2009.

[23] R. A. Humble, G. E. Elsinga, F. Scarano, and B. W. Van Oudheusden, "Three-dimensional instantaneous structure of a shock wave/turbulent boundary layer interaction," *Journal of Fluid Mechanics*, vol. 622, no. 1, p. 33, 2009.

[24] D. B. Helmer, "Measurements of a three-dimensional shock-boundary layer interaction," Stanford University, PhD Thesis, 2011.

[25] L. M. Campo, D. B. Helmer, and J. K. Eaton, "Validation Experiment for Shock Boundary Layer Interactions : Sensitivity to Upstream Geometric Perturbations," in *53rd Structures, Structural Dynamics and Materials Conference*, AIAA paper 2012-1440, April 2012.

[26] R. J. Adrian, K. T. Christensen, and Z. Liu, "Analysis and interpretation of instantaneous turbulent velocity fields," *Experiments in Fluids* vol. 29, no. 95, *pp275-290* March 2000.

[27] R. Legendre, "Separation de courant l'ecoulement laminarire tridimnesionnel," *Rech. Aero*, pp. 3-8, 1956.

[28] M. Tobak and D. J. Peake, "Topology of Three-Dimensional Separated Flows," *Annual Review of Fluid Mechanics*, vol. 14, pp. 61-85, 1982.

[29] M. S. Chong, a. E. Perry, and B. J. Cantwell, "A general classification of three-dimensional flow fields," *Physics of Fluids A: Fluid Dynamics*, vol. 2, no. 5, p. 765, 1990.

[30] W. E. Eagle, "An Experimental Study of Three-Dimensional Inlet Shock-Boundary Layer Interactions by," 2012.

[31]   D. P. Aeschliman, W. L. Oberkampf, and F. G. Blottner, "A Proposed Methodology for Computational Fluid Dynamics Code Verification, Calibration, and Validation," in *16th International Congress on Instrumentation in Aerospace Simulation Facilities*, Jul. 1995

[32] W. Oberkampf and C. J. Roy, *Verification and Validation in Scientific Computing*. Cambridge University Press, 2010.

27

Approved for public release; distribution unlimited.

Design of a Glass Supersonic Wind Tunnel Experiment for Mixed Compression Inlet Investigations

Daniel S. Galbraith[1], Mark G. Turner[2], Paul D. Orkwis[3] and Marshall C. Galbraith[4]
University of Cincinnati, Cincinnati, Ohio, 45221

and

James F. Driscoll[5] and Ethan Eagle[6]
University of Michigan, Ann Arbor, Michigan, 48128

Mixed compression inlets offer a great increase in pressure recovery compared to conventional external compression inlets at Mach numbers above two. These inlets suffer from problems with shock wave boundary layer interactions (SBLI) which cause flow instabilities and severe performance reductions. Previous experiments conducted at the University of Michigan used a wind tunnel with glass side walls with an extensive test section to measure the SBLI associated with a single oblique shock. This work presents a redesign of the single oblique shock experimental setup, using computational fluid dynamics, to also include a downstream normal shock with a diffuser. The new experimental configuration will provide insights into the effects that combined oblique/normal shock boundary layer interactions have on the health of the boundary layer in the diffuser section of a mixed compression inlet. The extensive glass walls of the wind tunnel will allow direct access for optical measurements of the shock boundary layer interactions and the diffuser section.

Nomenclature

AIP	=	Aerodynamic Interface Plane
CFD	=	Computational Fluid Dynamics
NSH	=	Normal Shock Holder
k	=	Turbulent Kinetic Energy
M	=	Mach number
M_∞	=	Inflow Mach number
OSG	=	Oblique Shock Generator
SBLI	=	Shock wave boundary layer interaction
UM	=	University of Michigan
UC	=	University of Cincinnati
ε	=	Eddy dissipation
ω	=	Specific dissipation rate

I. Introduction

Mixed compression inlets provide a greater total pressure recovery than standard external compression inlets for flight Mach numbers above two. These inlets operate by creating a shock train that travels down the diffuser followed by a normal shock, as seen in Figure 1. Inviscid theory shows that static pressure increases with little total pressure loss due to the combination of oblique shocks and a weaker terminal normal shock. However, for

---

[1] MS Graduate Student, Department of Aerospace Engineering & Engineering Mechanics, 745 Baldwin Hall ML 0070, PO Box 210070, Cincinnati, OH 45221-0070, AIAA Student Member.
[2] Associate Professor of Aerospace Engineering & Engineering Mechanics, Department of Aerospace Engineering & Engineering Mechanics, AIAA Associate Fellow.
[3] Professor of Aerospace Engineering & Engineering Mechanics, Department of Aerospace Engineering & Engineering Mechanics, AIAA Associate Fellow.
[4] PhD Graduate Student, Department of Aerospace Engineering & Engineering Mechanics, AIAA Student Member.
[5] Professor, Aerospace Engineering Department, AIAA Fellow.
[6] Doctoral Candidate, Aerospace Engineering Department, AIAA Student Member.

viscous flows these inlets experience SBLIs leading to boundary layer separation and increased total pressure loss that can prevent the inlet from starting. The adverse effects of the SBLIs can be reduced by bleeding out the separated region using aspiration. Sub boundary layer micro ramps have also been used which produce a pair of vortices that effectively cut through the separation bubble, reducing its size. Previous experiments have been conducted to study a single oblique shock reflection by Babinsky[1], Doerffer, et al.[2], and Lapsa[3]. This work is meant as a continuation by following the oblique reflection with a normal shock and a subsonic diffuser, in order to more closely resemble a realistic inlet configuration. This new configuration is being designed via a collaboration between the University of Michigan (UM) and the University of Cincinnati (UC). Wind tunnel experiments are being conducted at UM, while UC is conducting Computational Fluid Dynamics (CFD) simulations on the proposed geometries. The new experiment is being designed with relatively simple geometry to simplify CFD simulations, so that it can be used as a CFD validation test case.
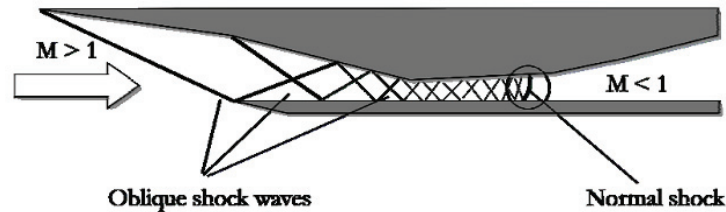
Figure 1. Shock train in a mixed compression inlet.[4]

II.   Previous Experiments

Previous experiments custom built at UM to investigate oblique SBLIs were performed at a Mach number of 2.75 in a vacuum driven tunnel. The test section was 36in long and with a 2.25x2.75in cross section with glass side walls. A SBLI was created by inserting a 7.75° wedge onto the top wall of the wind tunnel to serve as an oblique shock generator (OSG), as shown in Figure 2. The OSG was placed at the far downstream end of the tunnel where the boundary layers would be the thickest in order to increase the resolution of the stereo particle image velocimetry (SPIV) measurements of the boundary layers. However, in this configuration the tunnel did not start. After several design iterations the configuration shown in Figure 3 was found that allowed the tunnel to start. The final configuration consisted of an OSG that was located half the length of the test section downstream of the throat. In addition, the OSG was lowered from the top wall in order for the leading edge to see the supersonic core flow, and not the sub sonic boundary layer. Most importantly, the span of the OSG was reduced from the full span of 2.25in to a span of 1.25in in order to reduce tunnel blockage. Three OSG angles were made: 7.75°, 10° and 12°.
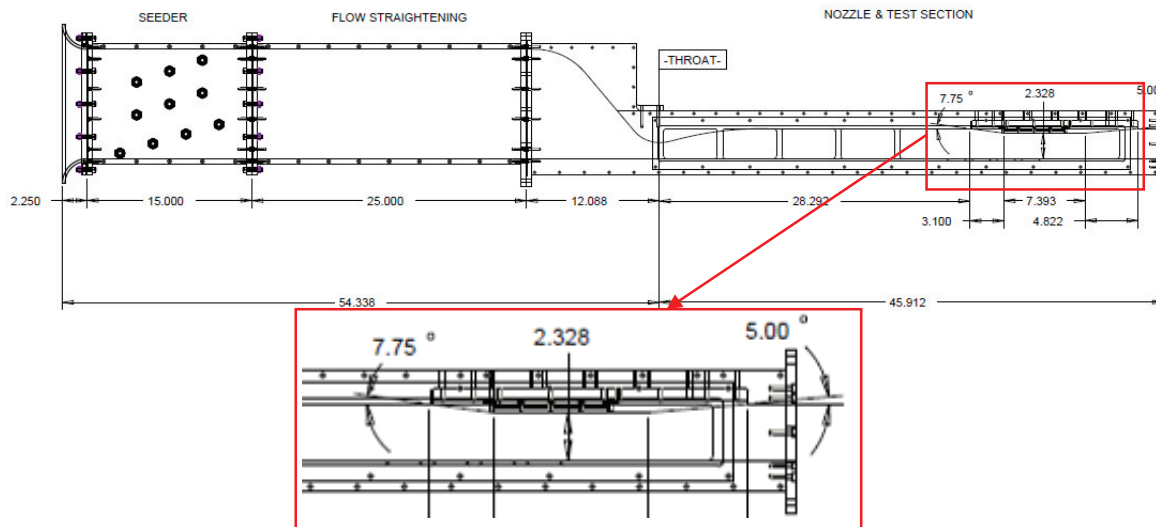
Figure 2. Wind tunnel schematic with the initial OSG installed in the aft segment of the test section.

This configuration was provided as a blind test case to be analyzed using CFD. A workshop was held in Orlando in January 2010 to present the results. An overview of the CFD comparisons is presented by DeBonis et al[5]. One of the current authors analyzed this configuration, but those results could not be submitted since he had access to the experimental results. Some of these results are shown for the M 2.75, 7.75° OSG. Figure 4 shows the computed center plane Mach number for the configuration in Figure 3, and shows a clean SBLI. While this region is ideal, the outside of the side plates produces large vortical separations, as seen in Figure 5. These structures did not prevent the wind tunnel from starting, but required much time and effort to effectively resolve with CFD. Inadequate resolution of these vortical structures can prevent the CFD solution from converging to a steady state, making their existence less desirable in a CFD validation experiment.
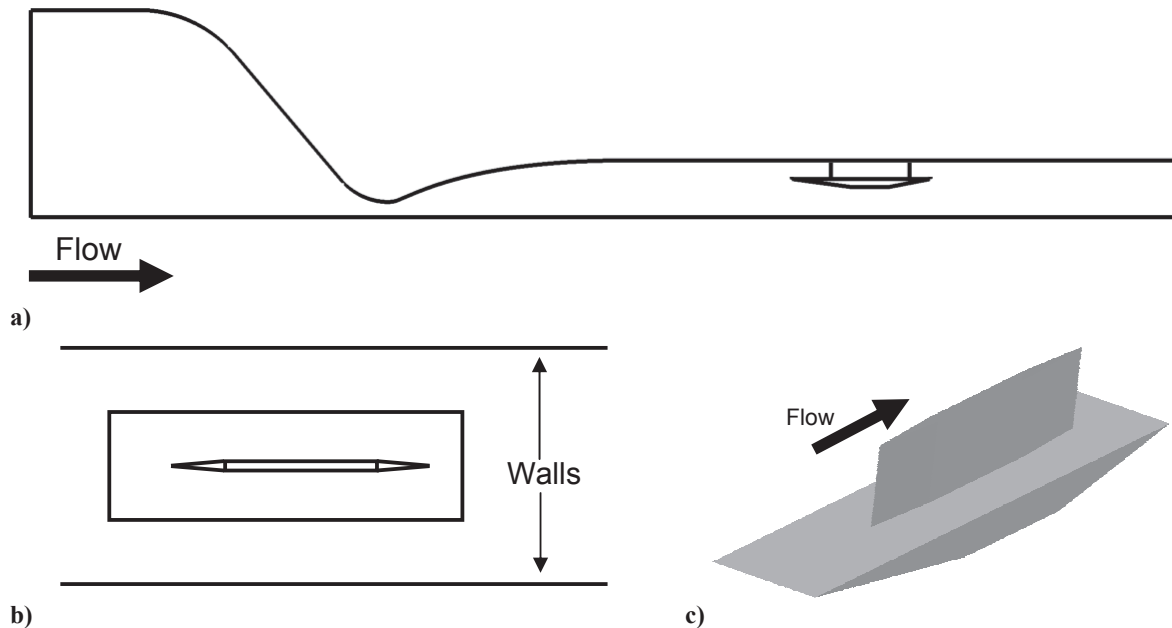
Figure 3. Half span OSG used for previous SBLI experimental study and CFD validation. a) Side view of the tunnel and OSG. b) Top view of OSG relative to the tunnel walls. c) Isometric view of the OSG.
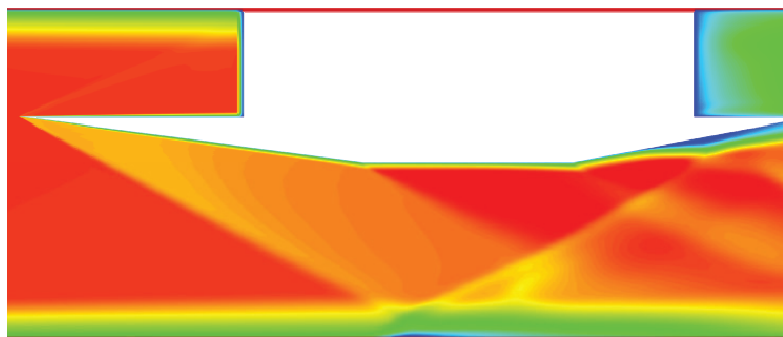
Figure 4. Center plane Mach number (0-2.75) for the 7.75° OSG.

Figure 6 shows iso-surfaces of density gradients in the streamwise direction colored by the derivative of the density gradients in the streamwise direction. This figure shows many shocks, including the desired oblique shock and reflection, but also the shocks emanating from the center strut leading and trailing edge, along with a vortex along the side of the OSG. The leading and trailing edge shocks from the vertical support spill over the sides of the OSG and into the region underneath the OSG.
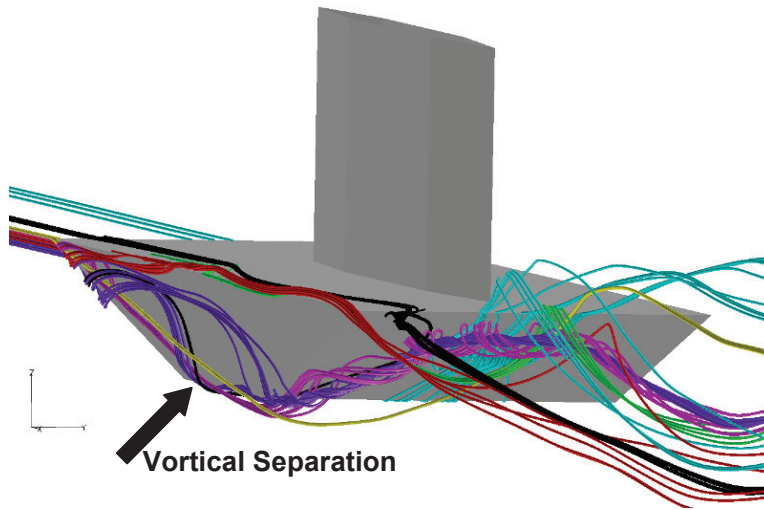
Figure 5. Vortical separation off the side of the OSG.
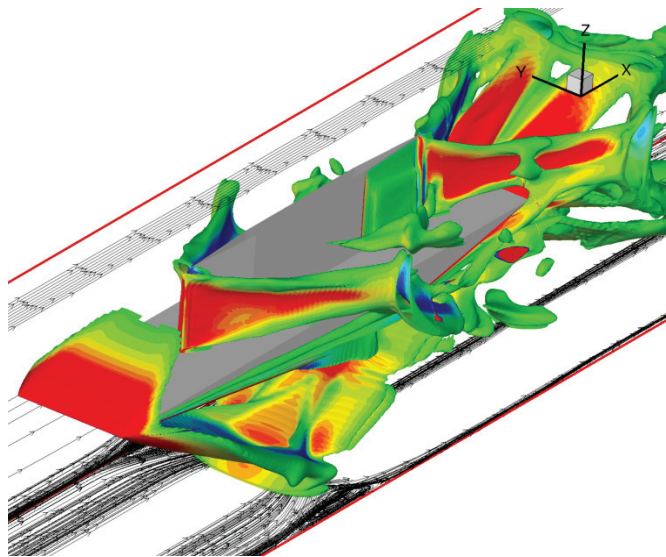
a)
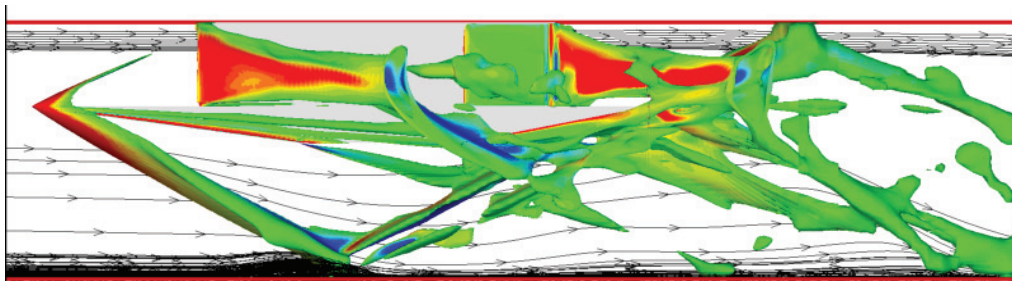
b)

Figure 6. Iso-surfaces of density gradients in the streamwise direction, colored by the derivative of the density gradients in the streamwise direction. a) Isometric view. b) Side view.

4
American Institute of Aeronautics and Astronautics

In this work a full span OSG is proposed to remove the interaction between the regions above and below the OSG and approach more a realistic inlet geometry. This has the added benefit of replacing the single vertical support in the center of the tunnel with two side supports immersed in the side wall boundary layers which reduces the flow field blockage.

III. Design Procedure

The primary purpose of this study is to investigate the effects of an oblique shock reflection followed by a normal shock and a subsonic diffuser on the boundary layer of a mixed compression style inlet. Since the region of interest is the lower wall, the top wall can be configured to generate the required shocks without resembling a realistic inlet geometry. Using these ideas, a full-span OSG is placed in the test section to create the oblique and reflected shocks. A normal shock holder (NSH) is placed downstream of the OSG at a location where the reflected shock will pass between the OSG and NSH. This will transmit the reflected shock to the region above the NSH, and results in the desired main flow field containing one oblique shock reflection followed by a normal shock. The NSH also aids in the positioning of the normal shock; making its location less sensitive to the back pressure since the space between the OSG and NSH acts as an automatic relief valve. The basic design is arrived at by considering two-dimensional inviscid theory coupled with some basic SBLI principles. Three-dimensional viscous effects are not considered in the preliminary design phase; viscous effects are later considered by analyzing the preliminary design using CFD.

The goal of the experiment is to mimic the final oblique and normal shocks in a mixed compression inlet. To achieve this, an experimental design that satisfies the following criteria was sought:

1)   The bottom wall boundary layer should experience an oblique shock reflection followed by a normal shock.
2)   The pressure rise across the oblique shock reflection should be approximately 2.
3)   The distance between the oblique shock reflection and the normal shock should be approximately 15 undisturbed boundary layer thicknesses.
4)   The incident Mach number to the normal shock should be less than 1.3.
5)   The normal shock should occur at the beginning of a subsonic diffuser.
6)   The Mach number downstream of the diffuser should be approximately 0.55.
7)   The boundary layer incoming to the oblique SBLI should be fully turbulent and at least 0.25in high.

Based on measurements from Settles and Lu[6], a pressure rise across the incident and reflected shock of two would result in a SBLI for the oblique shock reflection with at most a minor separation bubble. A minor separation bubble is desirable for the initial configuration to limit the possibility of the following normal shock creating a massive separation bubble. A larger oblique SBLI separation bubble can later be induced by increasing the angle of the OSG. In addition, by separating the oblique shock reflection 15 boundary layer thicknesses from the normal shock, the boundary layer has some time to recover from the shock reflection before being hit by the normal shock. The separation distance is expected to further help in limiting the separation at the normal shock, as well as prevent the two separation bubbles merging into a single separation bubble. An incident Mach number of 1.3 in front of the normal shock is chosen to mimic the final normal shock strength expected in a mixed compression inlet. After the normal shock, the flow will be diffused to Mach 0.55 to represent conditions at the aerodynamic interface plane (AIP) to an engine. A fully turbulent boundary layer approximates the real inlet boundary layer, and the boundary layer height ensures adequate field of view for the SPIV technique[7].

It is important to note that the initial design process relies solely on inviscid theory. A shock train calculator coded in MATLAB[8] determines the shock generator ramp angle based on the inlet Mach number, and the desired Mach number in front of the normal shock using an iterative scheme. This calculator was also used to create Figure 7, which contains three curves describing the Mach number in front of the normal shock based on the OSG angle and the inflow Mach number (M_∞). Based on inviscid theory, an inflow Mach number of 1.80 and OSG ramp angle of 7.17° are required to achieve the desired normal shock incident Mach number and pressure rise across the oblique SBLI of roughly two. The leading edge of the shock generator is placed 1.5 boundary layer thicknesses from the top wall to allow the leading edge to be located in the core flow while maximizing the mass flow under the OSG. Exposing the leading edge to core flow produces the inviscid shock angle as well as prevents the separation bubble that would form if the leading edge of the OSG was mounted to the ceiling of the wind tunnel. In order to allow the normal shock to be placed 15 boundary layer heights from the oblique shock reflection, the tunnel height needs to be doubled from the existing 2.75in test section to a proposed 5.5in. The boundary layer thickness used for preliminary two-dimensional CFD calculations was estimated from a three-dimensional Mach 2.00 calculation of the existing wind tunnel without an OSG or NSH. Based on the initial two-dimensional CFD calculations, the viscous oblique shock reflection was approximated by an inviscid shock reflection that reflects two boundary layer thicknesses

5
American Institute of Aeronautics and Astronautics

above the tunnel floor, due to the presence of the boundary layer. The ramp extends from the leading edge of the OSG to within two boundary layer thicknesses of the oblique shock reflection, as shown in Figure 8.
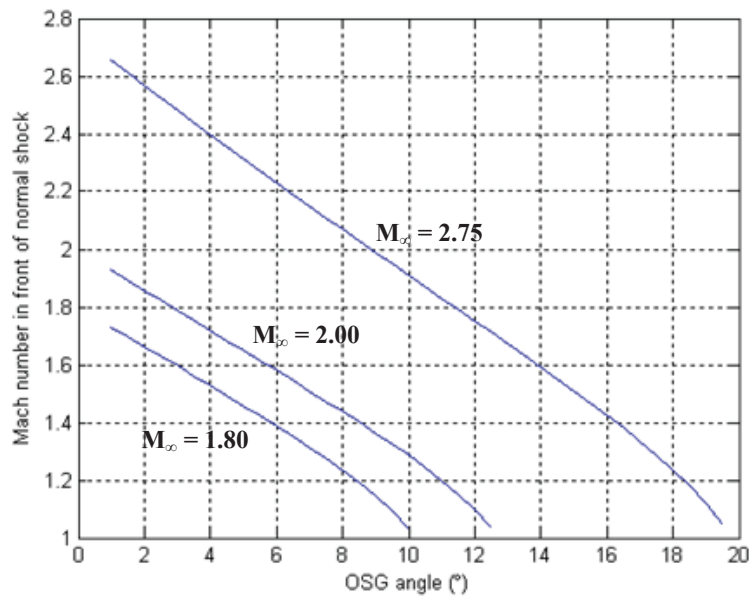

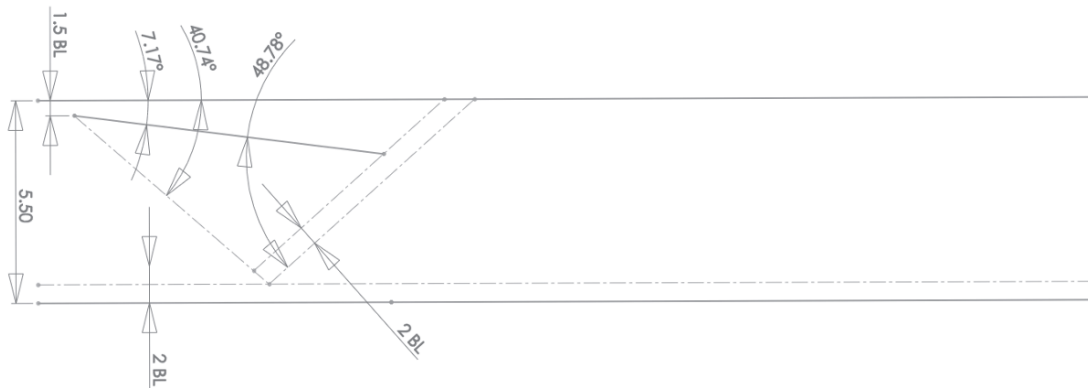**Figure 7. Normal shock Mach number for varying OSG ramp angle based on the inflow Mach number.**

Figure 8. OSG and calculated oblique incident and reflected shocks.

The NSH is located so that the leading edge coincides with a line parallel to the reflected shock, but offset downstream by two boundary layer thicknesses. A wedge angle of 10° on the upper surface of the NHS was set, and the NSH was then designed to taper down in the downstream direction in order to alleviate start up problems that may occur due to a constant area duct, as shown in Figure 9.

Figure 9. Addition of NSH.

6
American Institute of Aeronautics and Astronautics
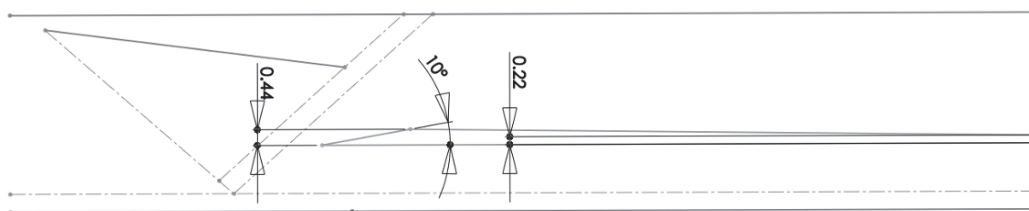
The Mach angle at the lower trailing edge of the OSG determines the maximum vertical location of the shock holder. The Mach cone intersects the NSH 0.1in downstream of its leading edge, as shown in Figure 10 and the close up in Figure 11. This allows for the largest area possible under the NSH while maintaining the two boundary layer thickness safety factor for the reflected shock and ensuring that the resulting expansion wave at the lower corner of the OSG does not interact with the normal shock below the NSH.
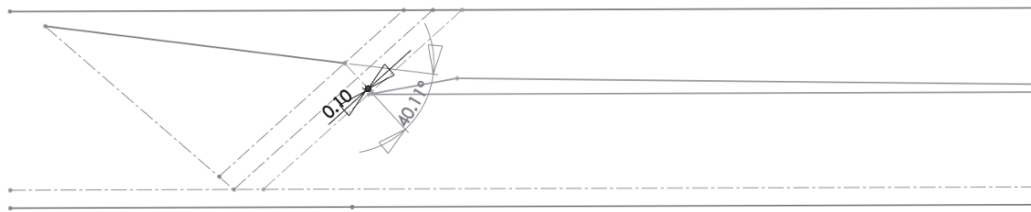
Figure 10. Criteria for the placement of the NSH.
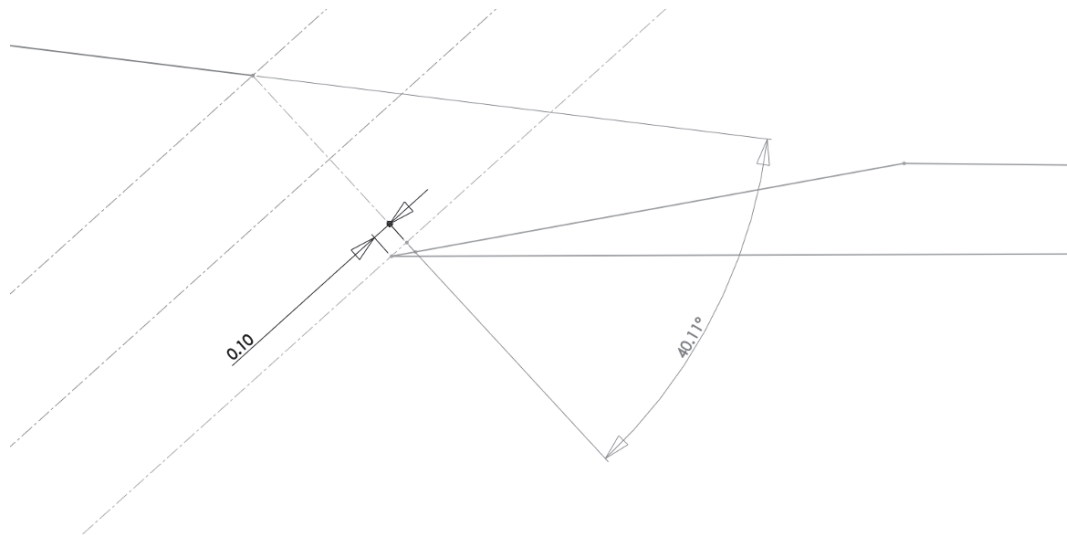
Figure 11. Close up of the leading edge placement of the NSH relative to the Mach cone.

Knowing the geometry of the NSH, the OSG can be completed by making its top wall slope downward at 2° and the back wall expand 5° relative to the NSH, as shown in Figure 12. A slanted upper surface of the OSG accounts for boundary layer growth and reduces the likelihood of choking. However, a large slope results in a strong supersonic expansion which subsequently shocks down at the trailing edge of the OSG to equalize pressure. This in turn creates a separation bubble on the ceiling of the tunnel just downstream of the trailing edge of the OSG. While this separation bubble is not of concern for the experiment, it causes additional difficulties for a CFD calculation since its size must be accurately computed. Hence, the slope on the upper surface of the OSG was set to 2° to limit flow expansion and the subsequent tunnel ceiling separation bubble. The slope on the back wall was also chosen to ensure an expansion in the channel formed between the OSG and NSH, thus preventing the channel from choking.
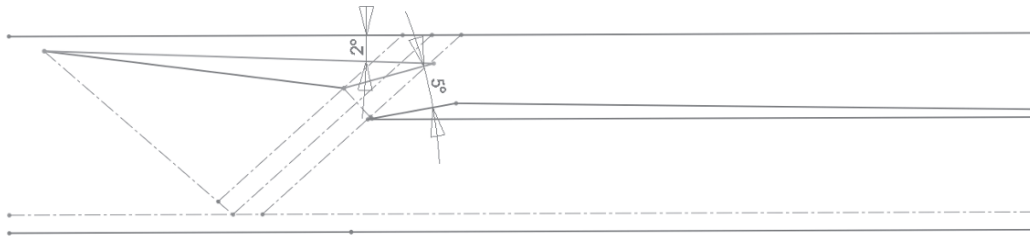
Figure 12. Completed OSG.

The beginning of the diffuser is located 7/8 the distance between the oblique shock reflection and the leading edge of the NSH in order to reduce the effects on the normal shock of the expansion wave at this corner. The diffuser floor slopes downward at 4° to diffuse the flow to Mach 0.55. The required area ratio for the diffuser is based on the Mach number at the leading edge of the NSH and the desired exit Mach number of 0.55. This configuration is shown in Figure 13 and the completed design in Figure 14.
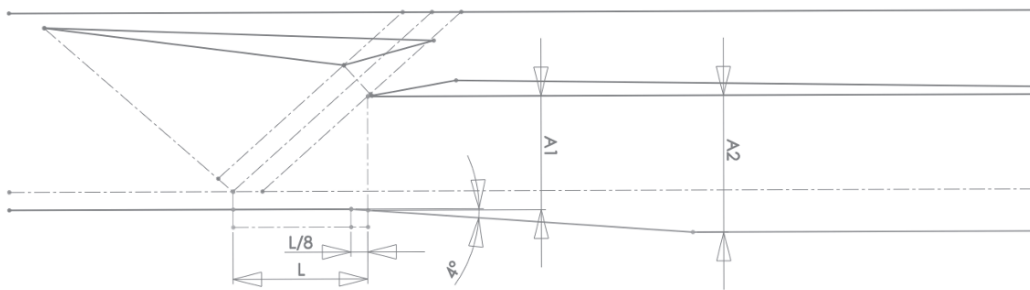
Figure 13. Addition of a diffuser section.
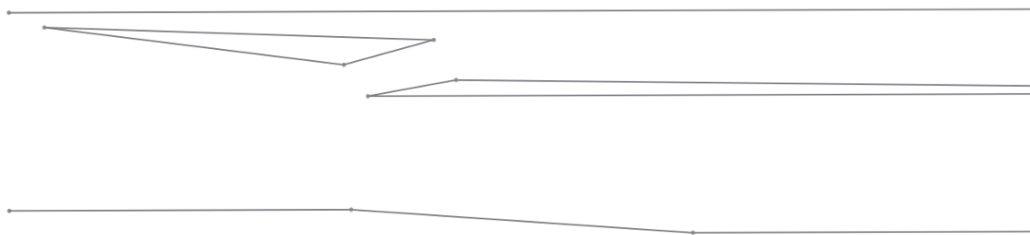
Figure 14. Completed 2D profile of the OSG and NSH with a diffuser in the wind tunnel.

The design is extruded for three-dimensional CFD calculations to create a model with the OSG and NSH spanning the full tunnel width. The design of the test section is a fully parametric model that is dependant on the inlet Mach number and shock generator ramp angle only. The sidewalls are glass, which cannot support the OSG or NSH. They must be supported from above, and this will be done with supports at the sides. The overall area must also account for this additional blockage.

IV.   Flow Solver

All CFD solutions are obtained with the OVERFLOW[9] flow solver which utilizes the Chimera overset mesh technique[10]. The Navier-Stokes equations are solved using a third order accurate upwind finite volume scheme using the HLLC[11] model combined with the Koren[12] limiter. The time integration uses an unfactored SSOR implicit solution algorithm[13] and multi-grid is utilized to accelerate convergence to a steady state. Further convergence gains are achieved by initializing computations of the entire wind tunnel via inviscid 1D nozzle theory. This produces an initial solution with subsonic flow upstream of the throat that accelerates through the throat and then remains at a constant supersonic Mach number through the entire test section.

V. Mesh and Boundary conditions

An overset mesh topology technique was chosen to ease the meshing procedure. While the geometry is relatively simple, the overset mesh technique allows the mesh point density in a certain region to be altered without having to modify the remaining domain. Pointwise[14] and a package of in-house software at the UC Gas Turbine Simulation Laboratory (GTSL) were used for the mesh generation. The 2D mesh in Figure 15 has 382 thousand points in 13 blocks and y+ values less than 2 everywhere, except at the leading edge of the NSH where it is less than 4. The 3D mesh in Figure 16 has 8.5 million points in 14 blocks and y+ values less than 1.
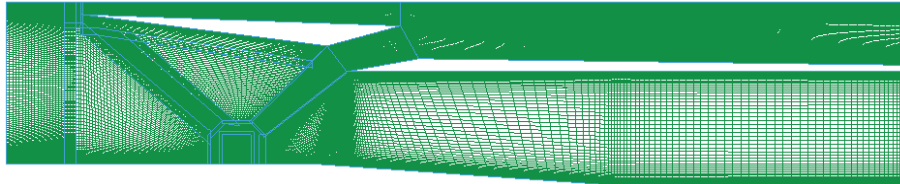
Figure 15. 2D mesh for Mach 1.80 case with OSG and NSH.
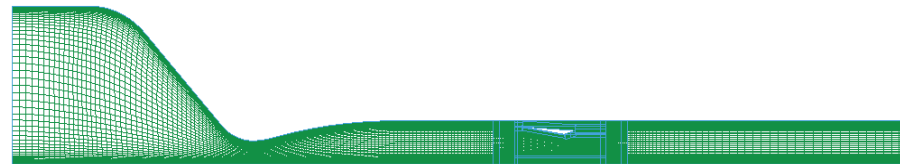
a)
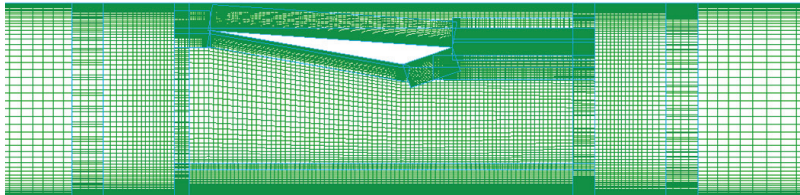
b)
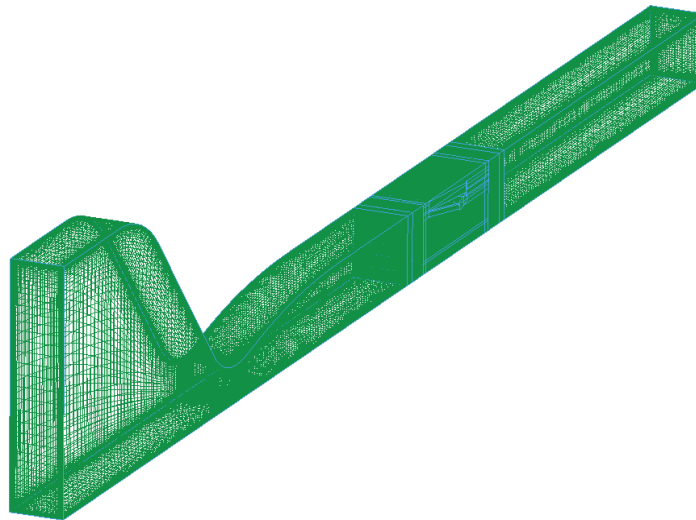
c)

Figure 16. 3D mesh for Mach 2.00 nozzle with 10° OSG configuration. a) Side view. b) Close up of the test section. c) Iso view of the mesh.

Overflow is highly parallel, and the blocks can be decomposed in such a way as to create a parallel simulation that is balanced. Typical runs use 20-90 cores and take 2-8 hours. Care must be taken to fully converge a solution to make sure it is truly steady. A solution can appear to be unchanging, although slowly growing separation regions can cause the oblique shock to move upstream and out the inlet, possibly preventing the tunnel from starting. These corner region separations grow slowly because of the small local time steps associated with constant CFL values for steady state solvers. While the transients are not temporally accurate they do offer clues to tunnel start dynamics.

In all cases a nozzle inlet boundary condition is used which extrapolates mass flow based on the total temperature and total pressure. A pressure outflow boundary condition is used at the tunnel exit, and all solid walls are modeled with viscous, adiabatic walls using pressure extrapolation.

VI. Results

This section presents first a summary of two-dimensional results obtained for the idealized preliminary geometry. Presented next is a study of possible configurations that could utilize existing inlet geometry. These configurations are assessed using steady state simulations to determine if the tunnel will run if started. The results for several possible modifications that run are then presented. Preliminary experience is then reported for time accurate simulations that start with quiescent flow.

A. Two Dimensional Preliminary Design Simulations (Mach 1.80, 5.50in Height, 10° OSG)
The initial two-dimensional CFD results are summarized in Figures 17 and 18, which show computed Mach number and density gradient contours respectively for the 5.5in tall configuration. The inlet boundary condition was generated from a constant area duct, since an actual Mach 1.80 nozzle geometry does not currently exist for the experimental facility. This duct is computed in isolation and then a slice of the solution is taken from the point where the boundary layers correspond to the desired thickness. This slice is then used as the inlet boundary condition.

As shown in the figures, the initial configuration has a diffuser starting half way between the oblique shock reflection and the NSH leading edge. The simulations show a large separation bubble at the beginning of the diffuser that creates a shock wave at the diffuser entrance. To reduce the effect of this shock, the beginning of the diffuser was moved back to 7/8 the distance between the oblique shock and shock holder leading edge. This was the first of several design changes driven by the CFD findings.

Figure 17 also shows the flow acceleration in the channel above the OSG and the shock system that equalizes the pressure aft of the OSG. Although the upper channel is not generally considered important for a SBLI study it does become important if it chokes or unstarts. The CFD results show a shock system that induces a large separation on the ceiling. This system must be considered because it limits the effective expansion of the upper channel flow and could prevent tunnel start.

The two dimensional preliminary design simulations demonstrate that the desired design parameters can be obtained with the proposed configurations. However, they do not include three-dimensional effects, which will be shown to be extremely important.
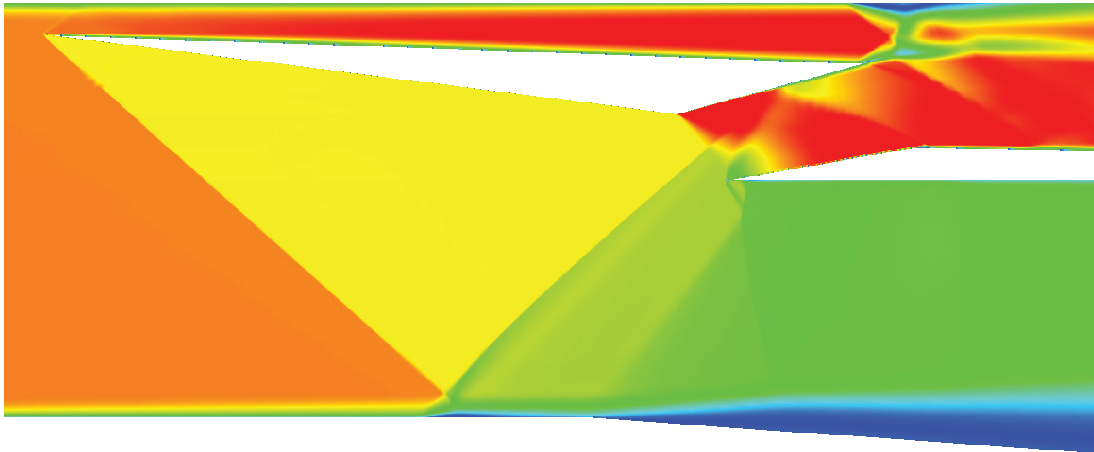
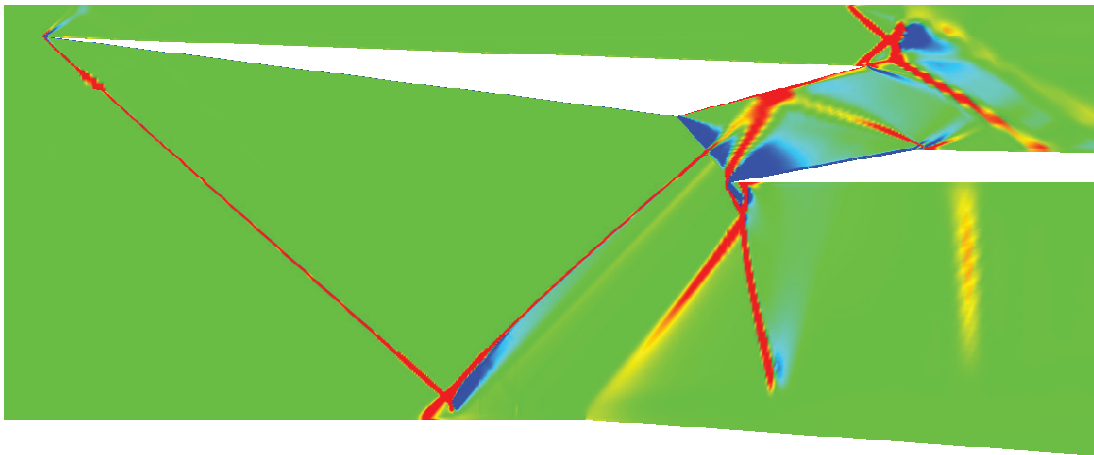**Figure 17. 2D results for the 5.50in tunnel with Mach 1.80 inflow. Contours of Mach number ranging from Mach 0-2.**

Figure 18. 2D results showing contours of density gradients. Red areas represent shocks while blue areas represent expansions.

B. Modified Configuration Studies Aimed at Existing Tunnel Geometry

It should be noted that the two dimensional design discussed above requires the construction of a new wind tunnel inlet, hence, the team decided to explore whether a design could be created that would utilize one of the existing wind tunnel inlets for Mach numbers 2.00 or 2.75. The authors noted that the previous investigations with this tunnel had difficulty starting if the shock generators spanned the entire tunnel, and that this led to a partial span OSG design in the previous work that produced very three dimensional flow. To explore these possibilities and understand better the starting problem, experiments were performed sans a NSH to investigate the flow field generated by a single OSG in the current 2.25x2.75in test section tunnel at Mach numbers of 2.00 and 2.75.

With this in mind, Table 1 illustrates the 3D CFD simulations completed to identify the running limitations of the tunnel, initially with only the OSG installed. This table shows the parameters that were modified in order to explore the sensitivity of the design: tunnel geometry, design Mach number, wedge angle, wedge length, and tunnel width.

Table 1. Configurations simulated to investigate running limitations.

Design Mach Number	Width (in)	Length (% of initial design)	OSG Angle (°)	Tunnel Start?
2.75	4.50	100	10.0	Yes

2.75	2.25	100	10.0	Yes
2.00	4.50	100	10.0	No
2.00 (Inverted nozzle)	2.25	100	10.0	No
2.00	2.25	100	10.0	No
2.00	2.25	75	10.0	No
2.00	2.25	50	10.0	Yes
2.00	2.25	75	8.5	No
2.00	2.25	50	8.5	Yes

C. Turbulence Model

Experiments showed that the Mach 2.75 cases with a 10° wedge angle would start. However, the initial CFD simulations predicted corner separation growth in the tunnel which prevented the passage under the OSG from starting. These simulations were obtained with a 3rd order accurate representation of the SST turbulence model. The turbulence model was reduced to 1st order accuracy while maintaining a 3rd order accurate discretization of the Navier Stokes equations. This resulted in the simulated tunnel starting and matching the experimental experience. It was found that the higher order turbulence model produces overshoots and undershoots of k, ω and ε that caused the separation bubbles to grow and prevent the simulated tunnel from starting. The 1st order SST model has more dissipation and allowed the tunnel to start; hence it was used for all future calculations. It is recognized that the SST model may produce larger separations and blockage than reality, but since the CFD is being used to design the experiment, a conservative approach was taken.

D. Mach 2.00 Cases

The preliminary design was based on a Mach 1.80 flow, hence it was felt that the closest existing nozzle would be the Mach 2.00 configuration. Unfortunately, it was found that this geometry was even harder to start numerically than the Mach 2.75 case, even with the 1st order SST model. The initial Mach 2.00 configuration was computed with a 10° OSG but would not start. Detailed analysis of the solution found that the flow coming out of the supersonic nozzle was top/bottom asymmetric, with thicker boundary layers on the bottom wall. The nozzle was inverted so as to place some of the OSG metal blockage in the fluid blockage, since there were greater losses already on the lower wall, with the thought of possibly reducing the overall blockage. Unfortunately, this effect was not great enough to allow the tunnel to start and the inverted nozzle concept was abandoned.

Wedge length and angle were the next parameters to be investigated. The length of the OSG was reduced in order to reduce the blockage in the tunnel. A more benign 8.5° OSG was also tested, which produced a Mach number of 1.4 in front of the NSH, just above the desired 1.3 Mach number. The OSG length was reduced to 75% and 50% of its original length. Unfortunately, neither 75% case started for the 10° or 8.5° OSG angles, but both cases started with the 50% length wedge, indicating that the reduction in blockage was sufficient. However, the 50% length option is undesirable because it results in significant flow field nonuniformity entering the diffuser. In addition, the NSH would need to be positioned within the flow boundary layer in order for the expansion fan from the lower trailing edge of the OSG to impinge on the upper surface of the NSH. However, the results do suggest further study is warranted directed at finding a combination of length and angle that might be more beneficial.

It should be noted that these simulations are steady state and do not simulate the start up of the tunnel in a physically realistic unsteady manner. However, they do indicate whether a certain configuration runs if started. The authors realize that this is a less restrictive condition and is not sufficient to demonstrate actual starting but is a necessary condition. The design process assumes that once a starting configuration is found with steady state analysis, unsteady simulations can be conducted to explore the unsteady startup transients.

E. Started Tunnel Configuration Results

The next sections present the cases from Table 1 that started.

1. Effect of Higher Mach Number (Mach 2.75, 2.25x2.75in, 10° OSG)

A 10° full span OSG experimental configuration developed to study starting criteria is being used in experimental tests with the Mach 2.75 nozzle at UM, and was also simulated at UC. The CFD results in Figure 19 show the Mach 2.75, 2.25in tall tunnel. The boundary layers seem thicker than in the 5.50in tall tunnel, but this is due to the height difference of the tunnel. Furthermore, this simulation is computed with an actual nozzle, rather than a manufactured inlet condition, hence producing more accurate boundary layers. An oblique shock can be seen generated off the OSG that reflects off the tunnel floor. This creates a small bubble of low velocity flow in the

bottom wall boundary layer. This low velocity region then generates a compression wave upstream of the shock reflection. It can also be seen that the bottom corners of the tunnel generate large separated flow regions. These are the features that can easily grow until the passage below the OSG chokes, and prevents the tunnel from starting. The turbulence intensity is also shown in each of these solutions since the turbulence model has considerable influence on the separated regions, and hence the overall solution. The turbulence intensity calculated is very low (less than 0.2%) in the free stream, but is much larger in the boundary layers as expected.

Also shown in the figure is a three dimensional plot of the flow field containing isosurfaces of a small value of negative streamwise velocity to identify the separated flow regions. These plots should be compared for each configuration as they give a qualitative view of the corner separations that govern this flow field.
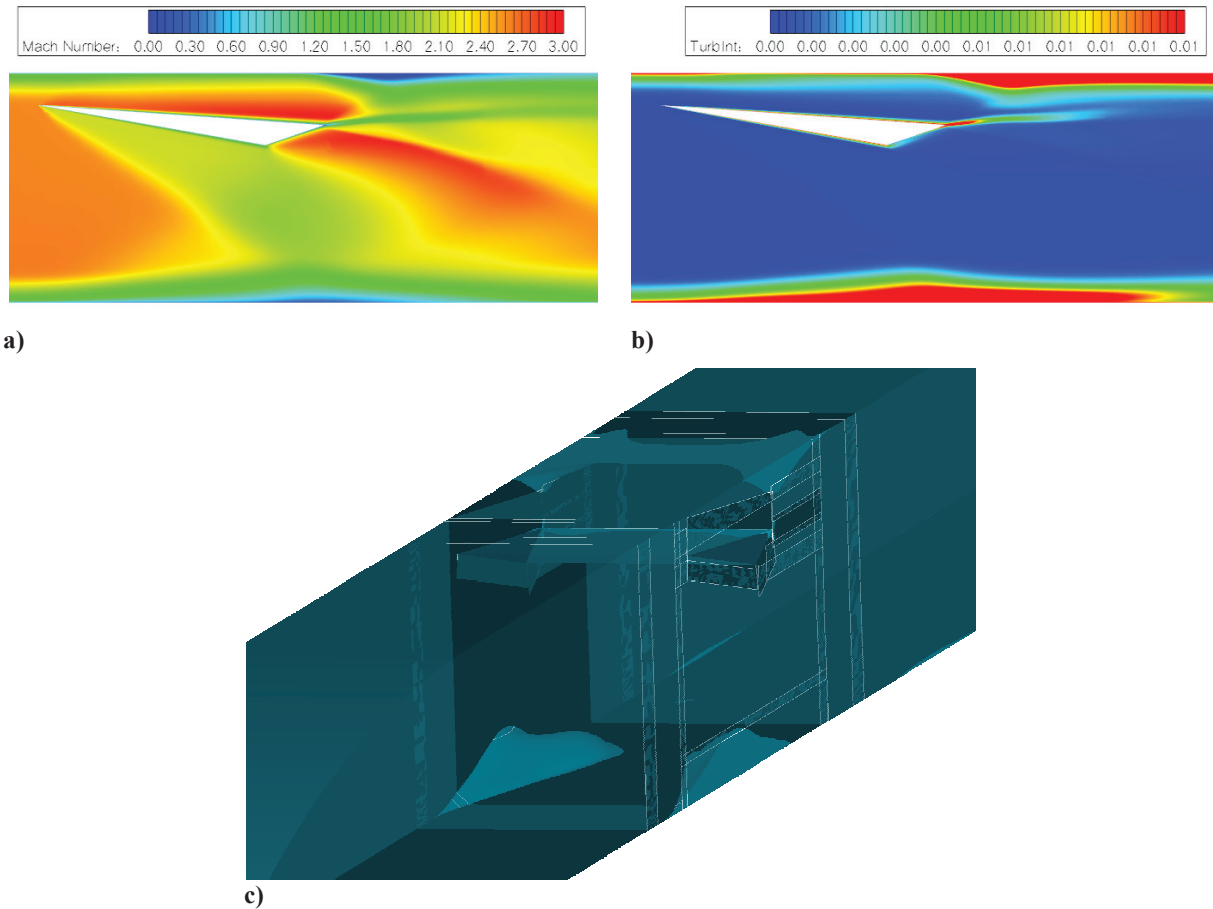

a)

b)

c)

Figure 19. Mach 2.75, 10° OSG case. a) Tunnel centerline colored by Mach contours from 0.0 – 3.0, b) Tunnel centerline colored by turbulent intensity contours from 0 – 1% c) Tunnel with iso surfaces of separated regions.

2. Effect of Tunnel Width (Mach 2.75, 4.50x2.75in, 10° OSG, double wide)

It was felt that the corner separation blockage could be reduced if the tunnel were twice its original width, i.e., broadened from 2.25in to 4.50in. A mesh was generated for this configuration with double the number of spanwise points, hence maintaining the same grid quality as the 2.25in wide case. The solution obtained with the double width tunnel is shown in Figure 20. A very similar flow field was produced, with the exception of a small separation bubble on the floor of the tunnel towards the centerline. The absolute blockage however is very similar to the 2.25in width case, showing that absolute blockage is relatively independent of the tunnel width but its three dimensional distribution might change. It is good to note that the SBLI looks much cleaner; resembling a 2D SBLI with a more defined reflected shock of the leading edge of the separation bubble in this configuration compared to the 2.25in

wide tunnel. However, it is again noted that this configuration produces a higher post reflected shock Mach number than desired.
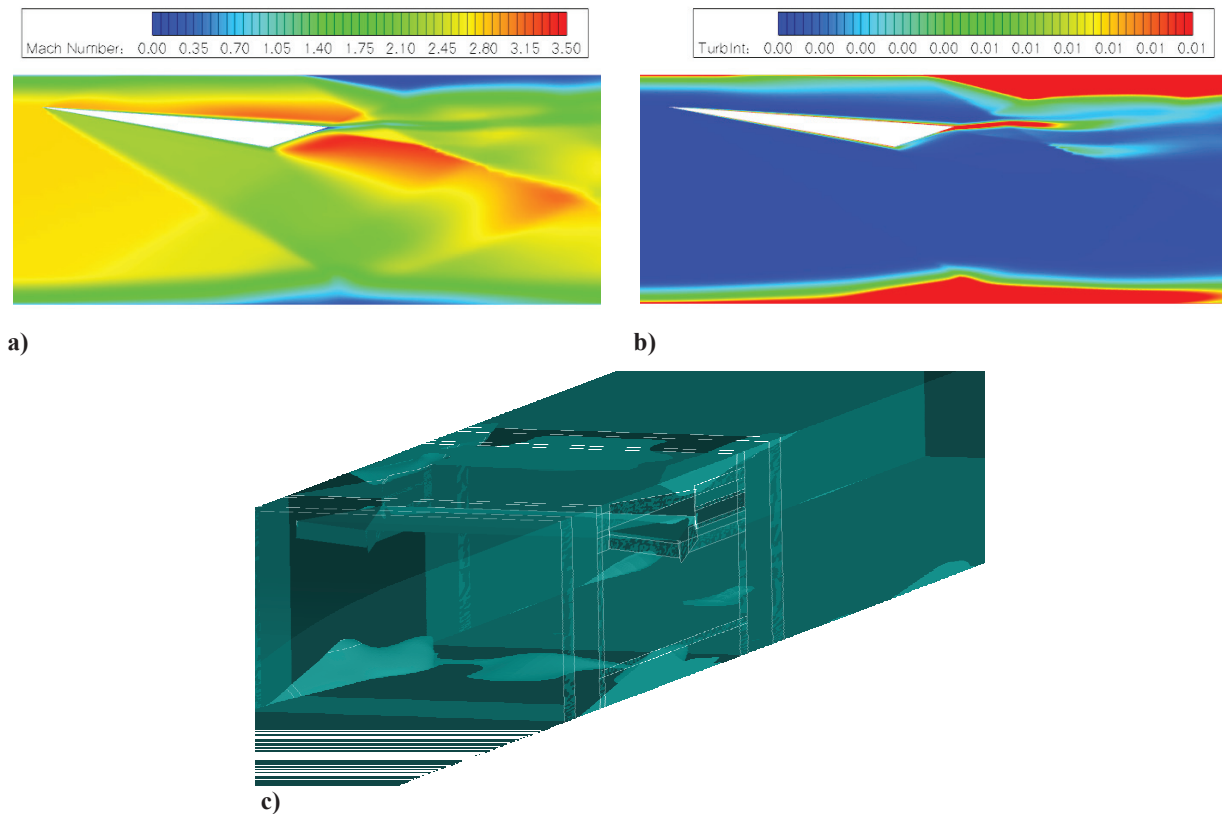

a)

b)

c)

Figure 20. Mach 2.75, 10° OSG case. a) Tunnel centerline colored by Mach contours from 0.0 – 3.0, b) Tunnel centerline colored by turbulent intensity contours from 0 – 1% c) Tunnel with iso surfaces of separated regions.

3. Effect of Mach number and Wedge Length (Mach 2.00, 2.25x2.75in, 10° OSG, 50% wedge design length)

The 10° wedge case was computed with the Mach 2.00 nozzle. The tunnel failed to start in this, due to the large corner separations along the bottom wall growing until the channel below the OSG choked. The OSG was scaled down to 75% of its design length, which reduced its thickness and the blockage in the tunnel. This configuration also failed to start for the same reasons. The OSG was then shortened to 50% of the design length, and this configuration allowed the tunnel to start, as shown in Figure 21. However, an installed NSH in this configuration would have very nonuniform flow before the normal shock and as such does not meet the design requirements. In order to intersect the expansion wave from the OSG, and make the reflected shock pass over the NSH, it would have to be placed very low in the tunnel and would nearly be immersed in the bottom boundary layer.

4. Effect of Wedge Angle (Mach 2.00, 8.5° OSG, 50% wedge design length)

The final configuration presented is shown in Figure 22, which uses the M 2.00 nozzle with an 8.5° angle OSG. This configuration will produce a Mach number of 1.4 in front of the normal shock (had the NSH been included). This case started but again has considerably nonuniform flow in the region before the normal shock because of the interaction of the reflected shock and the OSG expansion wave.
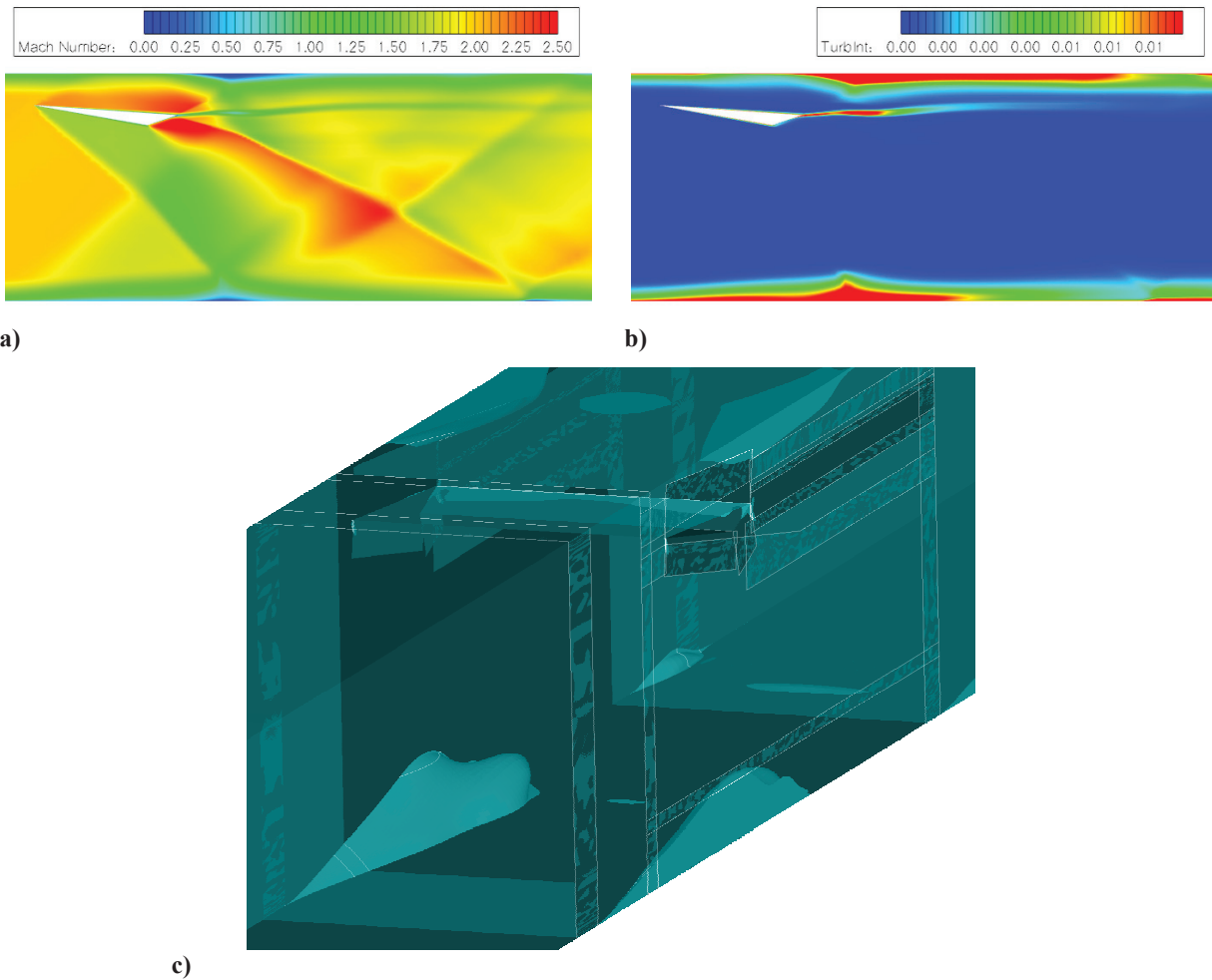
Figure 21. Mach 2.75, 10° OSG, 50% wedge design length. a) Tunnel centerline colored by Mach contours from 0.0 – 2.5, b) Tunnel centerline colored by turbulent intensity contours from 0 – 1% c) Tunnel with iso surfaces of separated regions.

F. Unsteady Start from Quiescent Flow

It was observed that the existing nozzles are asymmetric top/bottom. The flow along the top curved wall accelerates more than along the bottom wall producing thinner boundary layers along the top wall than along the bottom wall. This is beneficial for the current investigation since the bottom boundary layer needs to develop to a certain thickness in a short distance. However, the steady state simulations ignore the start up transients.

For this reason UC computed several simulations from quiescent initial conditions with an instantly applied low backpressure. The results showed that a large separation bubble is produced on the bottom wall and a smaller one on the top wall once the flow is sufficiently accelerated. These bubbles travel downstream and for some cases are purged from the tunnel. The results suggest that these separation bubbles can cause transient startup problems due to the additional blockage they produce. These results should be considered preliminary since they do not time accurately model the exit pressure drop, but they do suggest that if these separation bubble cause too many problems a symmetric nozzle may be needed.
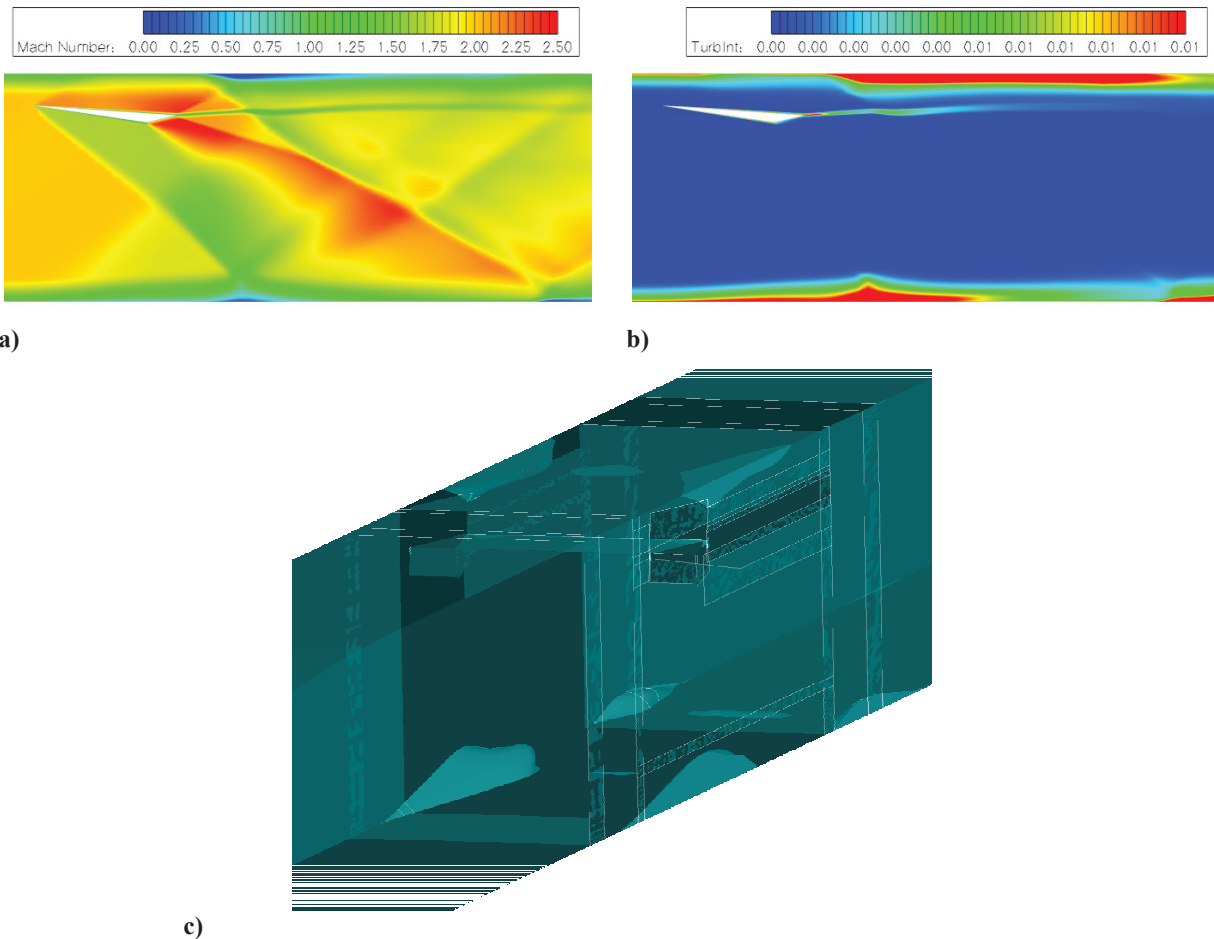
Figure 22. Mach 2.00, 8.5° OSG, 50% wedge design length. a) Tunnel centerline colored by Mach contours from 0.0 – 2.5, b) Tunnel centerline colored by turbulent intensity contours from 0 – 1% c) Tunnel with iso surfaces of separated regions.

VII.   Conclusions and Future Work

The design of a new supersonic inlet test configuration has been explored in CFD while some configurations have simultaneously been run experimentally. This combined CFD and experimental approach will lead to better understanding, and a more robust final design. Design goals have been established, and the design space has been explored considering a new tunnel as well as using an existing tunnel at the University of Michigan. The design has been parameterized, and a meshing procedure has been set up so the mesh can easily be modified for different wedge and tunnel geometries. Preliminary simulations have been completed that verify the design procedure, and give insight into the behavior of the flowfield in the tunnel. However, in order to start the existing Mach 2.00 and Mach 2.75 configurations, the geometry had to be modified until there was little room left in the flowfield to insert the NSH. Some of the design constraints could be relaxed in order to start and run the tunnel, but it would compromise some of the design goals. It is also possible to use the existing tunnels to help further explore some of the design parameters experimentally. However, in order to meet all the design objectives, it is recommended that a new tunnel be designed with an inflow design Mach number of 1.8. This tunnel would resemble the configuration described in the design procedure section, but it would be optimized to produce a more desirable amount of blockage and would also allow for a sufficient runtime to conduct the experiment. This tunnel would most likely be taller to give more room between the oblique shock reflection and the normal shock. It would also be wider to produce a cleaner SBLI as seen in the double wide configuration.

Acknowledgments

References

[1]Pitt Ford, C. W., Babinsky, H., "Micro-Ramp Control for Oblique Shock Wave/Boundary Layer Interactions," AIAA 2007-4115, June 2007.

[2]Doerffer, P., Hirsch, C., Dussauge, J-P., Babinsky, H., Barakos, G.N. (Eds), Unsteady Effects of Shock Wave induced Separation: (Notes on Numerical Fluid Mechanics and Multidisciplinary Design), Springer.

[3]Lapsa, A.P., "Experimental Study of Passive Ramps for Control of Shock–Boundary Layer Interactions," Ph. D. Dissertation, Aerospace Engineering Dept., University of Michigan, Ann Arbor, MI, 2009.

[4]Seddon J., Goldsmith E.L., Intake Aerodynamics, Blackwell 2nd Ed. 1999.

[5] DeBonis, James R., Oberkampf, William L., Wolf, Richard T., Orkwis, Paul D., Turner, Mark G., and Babinsky, Holger, "Assessment of CFD Models for Shock Boundary-Layer Interaction," AIAA-2010-4823, Chicago, IL, June, 2010.

[6]Settles, G. S., Frank K. Lu, F. K., "Conical Similarity of Shock/Boundary-Layer Interactions Generated by Swept and Unswept Fins," AIAA journal, Vol. 23, No. 7, July 1985.

[7]Nagel, Z. and Dahm, W.J.A. "Direct assessment of spatial resolution in particle-image velocimetry measurements," University of Michigan, MI, 2008

[8]MATLAB, R2008a, The MathWorks, Inc., MA 2010.

[9]P.G. Buning, D.C. Jespersen, T.H. Pulliam, W.M. Chan, J.P. Slotnick, S.E. Krist, K.J. Renze, Overflow User's Manual, Version 1.8g, NASA Langley Research Center, Hampton, VA, 1999.

[10]Benek, J. A., Steger, J. L., and Dougherty, F. C. "A Flexible Grid Embedding Technique with Application to the Euler Equations." AIAA Paper 83-1944, 1983.

[11]Toro, E. F., Spruce, M., and Speares, W., "Restoration of the Contact Surface in the HLL Riemann Solver," Shock Waves, Vol. 4, 1994 pp 25-34.

[12]Koren, B., "Upwind Schemes, Multigrid and Defect Correction for the Steady Navier-Stokes Equations," Proceedings of the 11th International Conference in Numerical Methods in Fluid Dynamics, edited by D. L Dwoyer, M. Y. Hussani, and R. G. Voigt, Springer-Verlag, Berlin 1989.

[13]Tramel, R. W. and Nichols, R. H., "A Highly Efficient Numerical Method for Overset-Mesh Moving–Body Problems," AIAA-97-2040, June 1997.

[14]Pointwise, Ver. 16.03, Pointwise, Inc., Fort Worth, TX, 2010.

51st AIAA/ASME/ASCE/AHS/ASC Structures, Structural Dynamics, and Materials Conference
 18th
12 - 15 April 2010, Orlando, Florida

AIAA 2010-2960

Implicit LES Simulations of a Flexible Flapping Wing

Raymond E. Gordnier [*]

Air Force Research Laboratory, Wright-Patterson AFB, OH 45433-7512

Peter J. Attar [†]

University of Oklahoma, Norman, OK

Satish Kumar Chimakurthi [‡] Carlos E. S. Cesnik [§]

University of Michigan, Ann Arbor, MI

A high-order (up to 6th order) Navier-Stokes solver is coupled with a structural solver that decomposes the equations of three-dimensional elasticity into cross-sectional, small-deformation and spanwise, large-deformation analyses for slender wings. The resulting high-fidelity aeroelastic solver is applied to the investigation of both a rigid and moderately flexible rectangular wing undergoing a pure plunging motion. Comparisons of the computed results demonstrate good agreement with available experimental measurements. A description of the complex interaction between the unsteady aerodynamics and the flexible wing structural dynamics is given. Connections between the results of this analysis and the enhanced aerodynamic loads for the flexible wing are made.

I.   Introduction

The flexible flapping wing features a number of attractive characteristics that have driven interest in their application to micro air vehicle (MAV) development. The flapping wing is able to simultaneously provide both lift and thrust for the vehicle. The inherent flexibility of the structure may be used to adapt to unsteady aerodynamic loadings (gusts and crosswinds) and provide for very agile flight maneuvers. Flapping wing MAVs also have the potential to effectively meet the requirements for both hovering and perching.

The highly nonlinear aerodynamics and unsteady aero/structural coupling present a host of technical challenges to be overcome when simulating a flapping wing MAV design. MAVs operate at low Reynolds numbers requiring a unified computational approach for laminar, transitional, and turbulent flows. Coupling of transition with the surface motion and deformation further complicates the problem. Highly unsteady vortex generation and vortex interactions dominate the nonlinear aerodynamic behavior and are strongly linked to the flapping motion and flexibility. Unconventional structural materials and layout as well as large structural deflections give rise to highly nonlinear structural behavior limiting the applicability of conventional linear modal structural modeling.

While a significant body of work has been undertaken to understand the aerodynamics and structural dynamics of MAVs (see References 1–3) there is still much to be understood about the aerodynamics of flapping flight and the aeroelasticity of flapping wings. Recently, Heathcote et al.[4] conducted experimental measurements of a rectangular wing with NACA0012 airfoil section oscillating in pure heave as a canonical problem to investigate the effect of spanwise flexibility on thrust, lift and propulsive efficiency of flapping wings. Tang et al.,[5] Chimakurthi et al.[6] and Aono et al.[7] have developed a computational aeroelasticity framework to analyze flexible flapping wings for MAVs. Their computational framework couples a low order (2nd order) Navier-Stokes solver with a structural solver UM/NLABS which decomposes the equations of 3-D elasticity into cross-sectional and spanwise analyses for slender wings. They then applied this solver to plunging wing problem investigated by Heathecote et al.

---

[*]Senior Research Aerospace Engineer, Computational Sciences Branch, Air Vehicles Directorate, Associate Fellow, AIAA
[†]Assistant Professor, Department of Mechanical and Aerospace Engineering, Member, AIAA
[‡]Graduate Research Assistant, Department of Aerospace Engineering, University of Michigan, Ann Arbor, MI 48109
[§]Professor, Department of Aerospace Engineering, University of Michigan, Ann Arbor, MI 48109, Associate Fellow, AIAA

American Institute of Aeronautics and Astronautics

In the present paper the low order Navier-Stokes solver in this computational framework is replaced by a high-order (up to 6th order) implicit large eddy simulation (ILES) solver for the Navier-Stokes equations. This aerodynamic solver has been shown to successfully simulate the mixed laminar/transitional/turbulent vortical flows that dominate the aerodynamics of these low Reynolds number problems (see for instance References 8 and 9). Computations are performed with the new high-order aeroelastic solver for the flexible flapping wing case investigated experimentally by Heathcote et al.[4] and computationally in References 5–7. A description of the resulting transitional flow over the dynamic, flexible wing as well as its its impact on the coupled fluid-structural response is presented.

II. Aerodynamic Solver

A. Governing Equations

The governing equations solved are the three-dimensional, compressible Navier-Stokes equations. These equations are cast in strong conservative form introducing a general time-dependent curvilinear coordinate transformation $(x, y, z, t) \rightarrow (\xi, \eta, \zeta, \tau)$. In vector notation, and employing non-dimensional variables, the equations are:

$$\frac{\partial}{\partial \tau}\left(\frac{\vec{U}}{J}\right) + \frac{\partial \hat{F}}{\partial \xi} + \frac{\partial \hat{G}}{\partial \eta} + \frac{\partial \hat{H}}{\partial \zeta} = \frac{1}{Re}[\frac{\partial \hat{F}_v}{\partial \xi} + \frac{\partial \hat{G}_v}{\partial \eta} + \frac{\partial \hat{H}_v}{\partial \zeta}] \tag{1}$$

Here $\vec{U} = \{\rho, \rho u, \rho v, \rho w, \rho E\}$ denotes the solution vector and J is the transformation Jacobian. The inviscid and viscous fluxes, $\hat{F}, \hat{G}, \hat{H}, \hat{F}_v, \hat{G}_v, \hat{H}_v$ can be found, for instance, in Ref. 10. In the expressions above, u, v, w are the Cartesian velocity components, ρ the density, p the pressure, and T the temperature. All flow variables have been normalized by their respective freestream values except for pressure which has been nondimensionalized by $\rho_\infty u_\infty^2$. The system of equations is closed using the perfect gas law $p = \rho T / \gamma M_\infty^2$, Sutherland's formula for viscosity, and the assumption of a constant Prandtl number, $Pr = 0.72$.

B. Spatial Discretization

A finite-difference approach is employed to discretize the flow equations. For any scalar quantity, ϕ, such as a metric, flux component or flow variable, the spatial derivative ϕ' along a coordinate line in the transformed plane is obtained by solving the tridiagonal system:

$$\alpha \phi'_{i-1} + \phi'_i + \alpha \phi'_{i+1} = b \frac{\phi_{i+2} - \phi_{i-2}}{4} + a \frac{\phi_{i+1} - \phi_{i-1}}{2} \tag{2}$$

where $\alpha = \frac{1}{3}$, $a = \frac{14}{9}$ and $b = \frac{1}{9}$. This choice of coefficients yields at interior points the compact five-point, sixth-order algorithm of Lele.[11] At boundary points 1, 2, $IL - 1$ and IL, fourth- and fifth-order one-sided formulas are utilized which retain the tridiagonal form of the interior scheme.[12, 13]

Compact-difference discretizations, like other centered schemes, are non-dissipative and are therefore susceptible to numerical instabilities due to the growth of spurious high-frequency modes. These difficulties originate from several sources including mesh non-uniformity, approximate boundary conditions and nonlinear flow features. In order to ensure long-term numerical stability, while retaining the improved accuracy of the spatial compact discretization, a high-order implicit filtering technique[14, 15] is incorporated. If a component of the solution vector is denoted by ϕ, filtered values $\hat{\phi}$ are obtained by solving the tridiagonal system,

$$\alpha_f \hat{\phi}_{i-1} + \hat{\phi}_i + \alpha_f \hat{\phi}_{i+1} = \Sigma_{n=0}^{N} \frac{a_n}{2} (\phi_{i+n} + \phi_{i-n}) \tag{3}$$

Equation 3 is based on templates proposed in Refs. 11 and 16, and with proper choice of coefficients, provides a $2N$th-order formula on a $2N + 1$ point stencil. The coefficients, $a_0, a_1, \ldots a_N$, derived in terms of the single parameter α_f using Taylor- and Fourier-series analysis, are given in Ref. 12, along with detailed spectral filter responses. In the present study, an eighth-order filter operator with $\alpha_f = 0.3$ is applied at interior points. For near-boundary points, the filtering strategies described in Refs. 15 and 17 are employed. Filtering is applied to the conserved variables, and sequentially in each coordinate direction.

American Institute of Aeronautics and Astronautics

Approved for public release; distribution unlimited.

C.   Time Integration

For wall-bounded viscous flows, the stability constraint of explicit time-marching schemes is too restrictive and the use of an implicit approach becomes necessary. For this purpose, the implicit approximately-factored scheme of Beam and Warming[18] is incorporated and augmented through the use of Newton-like subiterations in order to achieve second-order temporal and sixth-order spatial accuracy. In delta form, the scheme may be written as

$$
\begin{aligned}
&\left[J^{-1^{p+1}} + \phi^i \Delta\tau \delta_\xi^{(2)}\left(\frac{\partial \hat{F}^p}{\partial U} - \frac{1}{Re}\frac{\partial \hat{F}_v^p}{\partial U}\right)\right] J^{p+1} \times \left[J^{-1^{p+1}} + \phi^i \Delta\tau \delta_\eta^{(2)}\left(\frac{\partial \hat{G}^p}{\partial U} - \frac{1}{Re}\frac{\partial \hat{G}_v^p}{\partial U}\right)\right] J^{p+1} \times \\
&\left[J^{-1^{p+1}} + \phi^i \Delta\tau \delta_\zeta^{(2)}\left(\frac{\partial \hat{H}^p}{\partial U} - \frac{1}{Re}\frac{\partial \hat{H}_v^p}{\partial U}\right)\right]\Delta U = -\phi^i \Delta\tau \left[J^{-1^{p+1}}\frac{(1+\phi)U^p - (1+2\phi)U^n + \phi U^{n-1}}{\Delta\tau}\right. \\
&\left. + U^p(1/J)_\tau^p + \delta_\xi\left(\hat{F}^p - \frac{1}{Re}\hat{F}_v^p\right) + \delta_\eta\left(\hat{G}^p - \frac{1}{Re}\hat{G}_v^p\right) + \delta_\zeta\left(\hat{H}^p - \frac{1}{Re}\hat{H}_v^p\right)\right]
\end{aligned}
\tag{4}
$$

where

$$
\phi^i = \frac{1}{1+\phi}, \quad \Delta U = U^{p+1} - U^p.
\tag{5}
$$

For the first subiteration, $p = 1$, $U^p = U^n$ and as $p \to \infty$, $U^p \to U^{n+1}$. The spatial derivatives in the implicit (left-hand-side) operators are represented using standard second-order centered approximations whereas high-order discretizations are employed for the explicit terms (right-hand side). Although not shown in Eqn. 4, nonlinear artificial dissipation terms[19, 20] are appended to the implicit operator to enhance stability. In addition, for improved efficiency, the approximately-factored scheme is recast in diagonalized form.[21] Any degradation in solution accuracy caused by the second-order implicit operators, artificial dissipation and the diagonal form are eliminated through the use of subiterations. Typically, three subiterations are applied per time step.

D.   Implicit Large Eddy Simulation Methodology

The implicit large eddy simulation (ILES) method to be used in the present computations was first proposed and investigated by Visbal et al.[22] The underlying idea behind the approach is to capture with high accuracy the resolved part of the turbulent scales while providing for a smooth regularization procedure to dissipate energy at the represented but poorly resolved high wavenumbers of the mesh. In the present computational procedure the 6th-order compact difference scheme provides the high accuracy while the low-pass spatial filters provide the regularization of the unresolved scales. All this is accomplished with no additional sub-grid scale models as in traditional LES approaches. An attractive feature of this filtering ILES approach is that the governing equations and numerical procedure remain the same in all regions of the flow. In addition, the ILES method requires approximately half the computational resources of a standard dynamic Smagorinsky sub-grid scale LES model. This results in a scheme capable of capturing with high-order accuracy the resolved part of the turbulent scales in an extremely efficient and flexible manner. The ILES solver is embedded in a high-order overset-grid scheme which is utilized to provide flexibility for modeling complex geometries. It also serves as a domain decomposition mechanism for application of the high-order approach on massively-parallel, high-performance computing platforms.

E.   Boundary Conditions

The boundary conditions for the flow domain are prescribed as follows. At the solid surface, the no slip condition is applied, requiring that the fluid velocity at the wing surface match the surface velocity. In addition, the adiabatic wall condition, $\frac{\partial T}{\partial n} = 0$, and the normal pressure gradient condition $\frac{\partial p}{\partial n} = 0$ are specified. Along the O-grid cut spatial periodicity is imposed by means of a grid overlap region. The flow is assumed to be symmetric at the symmetry plane.

The treatment of the farfield boundaries is based on the approach proposed and evaluated previously in Ref. 23 for some acoustic benchmark problems. This method exploits the properties of the high-order, low-pass filter in conjunction with a rapidly stretched mesh. As grid spacing increases away from the region of interest, energy not supported by the stretched mesh is reflected in the form of high-frequency modes which are annihilated by the discriminating spatial filter operator. An effective "buffer" zone is therefore created using a few grid points in each coordinate direction to rapidly stretch to the farfield boundary. No further need for the explicit incorporation of complicated boundary conditions or modifications to the governing equations is then required. Freestream conditions are specified along the inflow portion of the

American Institute of Aeronautics and Astronautics

Approved for public release; distribution unlimited.

farfield boundary, while simple extrapolation of all variables is used on the outflow portion of the boundary. Freestream conditions are also specified on the spanwise farfield boundary.

III. Structural Dynamics Solver (UM/NLABS)

The geometrically-nonlinear structural dynamics solution is based on an asymptotic approach to the equations governing the dynamics of a general 3-D anisotropic slender solid.[24, 25] It is implemented in the University of Michigan's Nonlinear Active Beam Solver (UM/NLABS) computer code. Assuming the presence of a small parameter (the inverse of the wing aspect ratio) allows for a multi-scale solution process, in which the problem is decomposed into separate cross-sectional (small-scale) and longitudinal (long-scale) analyses. The longitudinal problem solves for average measures of deformation of the reference line under given external excitations. The cross-sectional problem solves the local deformation for given values of the long-scale variables. Both problems are tightly coupled and together provide an efficient approximation to the displacement field in the original 3-D domain. A flow diagram of the process is shown in Figure 1.
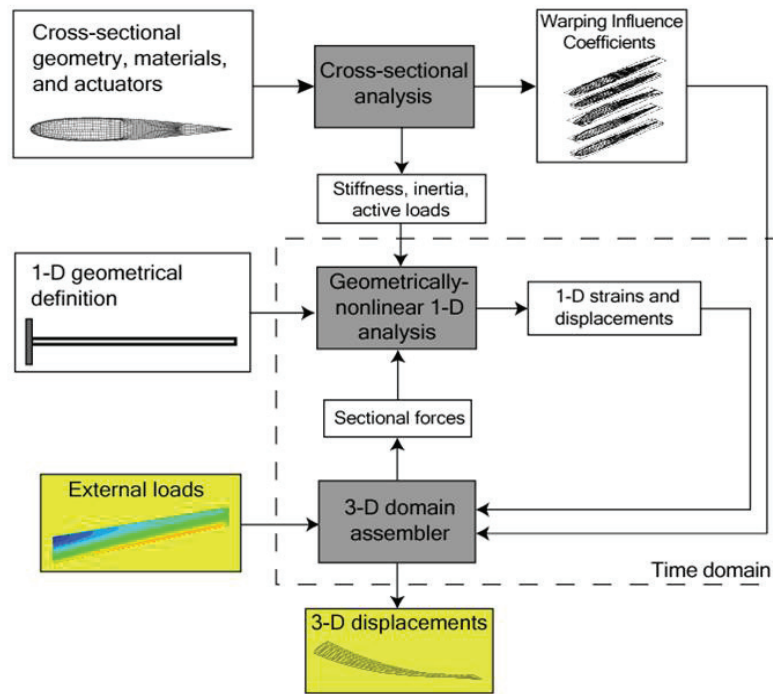
Figure 1. Asymptotic solution process for 3-D slender structures implemented in UM/NLABS

The structural formulation follows the variational-asymptotic method for the analysis of composite beams.[26] The equations of motion for a slender anisotropic elastic 3-D solid are approximated by the recursive solution of a linear 2-D problem at each cross section,[25] and a 1-D geometrically-nonlinear problem along the reference line.[24] This procedure allows the asymptotic approximation of the 3-D warping field in the beam cross sections, which are used with the 1-D beam solution to recover a 3-D displacement field. The warping was approximated for the elastic degrees of freedom of a Timoshenko-beam model (extension and transverse shear, γ, and twist, bending about two directions, κ) and augmented with an arbitrary set of functions approximating the sectional deformation field (amplitude, q, and its derivative along the spanwise direction, q'. These capture "non-classical" deformations, which are referred to as *finite-section modes*. And these new deformation modes are not restricted to be as small as the fundamental warping field. The solution of a variational problem yields the warping field corresponding to 1-D beam strains $\{\gamma, \kappa, q, q'\}$. In its first

order approximation, it can be written as [25]

$$w(x_1, x_2, x_3) = w_\gamma(x_2, x_3)\gamma(x_1) + w_\kappa(x_2, x_3)\kappa(x_1) + w_{q_n}(x_2, x_3)q_n(x_1) + w_{q'_n}(x_2, x_3)q'_n(x_1) + HOT \quad (6)$$

where $\left\{\begin{array}{cccc} w_\gamma & w_\kappa & w_{q_n} & w_{q'_n} \end{array}\right\}$ are the first-order warping influence coefficients. Using this approximation for the warping field, the cross-section problem gives the strain energy per unit length of the beam:

$$v = \frac{1}{2}\left\{\begin{array}{cccc} \gamma^T & \kappa^T & q^T & q'^T \end{array}\right\}[S]\left\{\begin{array}{c} \gamma \\ \kappa \\ q \\ q' \end{array}\right\} + HOT, \quad (7)$$

Here, the constant matrix $[S]$ is the first-order asymptotic approximation to the stiffness matrix. The integration of the kinetic energy can be directly done as function of the 1-D variables, yielding:

$$KE = \frac{1}{2}\left\{\begin{array}{ccc} V_B^T & \Omega_B^T & \dot{q}_n^T \end{array}\right\}[M]\left\{\begin{array}{c} V_B \\ \Omega_B \\ \dot{q}_n \end{array}\right\} \quad (8)$$

where the constant matrix $[M]$ is the inertia matrix for the cross section. From the resulting 1-D problem, the geometrically-nonlinear dynamic equations of equilibrium along the reference line (as presented in Ref. 24) are written as

$$\begin{aligned}
\left(\frac{d}{dt} + \tilde{\Omega}_B\right)P_B &= \left(\frac{d}{dx} + \tilde{K}_B\right)(F_B - f_1) + f_0 \\
\left(\frac{d}{dt} + \tilde{\Omega}_B\right)H_B + \tilde{V}_B P_B &= \left(\frac{d}{dx} + \tilde{K}_B\right)(M_B - m_1) + (\tilde{e}_1 + \tilde{\gamma})F_B + m_0 \\
\frac{d}{dt}Q_t &= \frac{d}{dx}(Q_{s_1} - f_{s_1}) - (Q_{s_0} - f_{s_0}).
\end{aligned} \quad (9)$$

where the generalized forces and momenta are all expressed in their components in a reference frame attached to the deformed beam reference line. The first two equations imply equilibrium of forces and moments. The last equation in Eqns. 9 includes the set of equilibrium equations corresponding to the finite-section modes. With the warping influence coefficients given by Eq. 6, the applied forces per unit length in Eq. 9 are

$$\begin{aligned}
f_0 &= \int_{A(x)} \mu_B \, dA \\
f_{s_0} &= \int_{A(x)} \left(\Psi_q^T + w_q^T\right)\mu_B \, dA \\
m_0 &= \int_{A(x)} \xi_B \mu_B \, dA \\
f_1 &= \int_{A(x)} w_\gamma^T \mu_B \, dA \\
f_{s_1} &= \int_{A(x)} w_{q'}^T \mu_B \, dA \\
m_1 &= \int_{A(x)} w_\kappa^T \mu_B \, dA
\end{aligned} \quad (10)$$

The present implementation of this formulation follows the approach described in Ref. 24, where the solution to Eq. 9 is done by means of a finite-element discretization on a mixed-variational form of the equations. Therefore, although they are analyzed independently, the small and long-scale problems are intimately linked in the detailed approximation to the solution. This is particularly important in the generation of the solid side of an aeroelastic model: the interface of the structural model consists of the actual wetted surfaces of the vehicle, without extrapolations from the motion of a reduced-dimension structural model, nor the assumption of rigid cross sections required by beam theories.

IV.   Aerodynamic/Structural Coupling

Coupling of the aerodynamics with the wing structural response occurs through the imposed aerodynamic loads and the resulting structural deflection of the wing, which is returned to the aerodynamic grid. Communication between the noncoincident aerodynamic and structural surface meshes is accomplished using a local bilinear interpolation procedure[27] for the physical quantities to be passed between the aerodynamic and structural solvers. Implicit coupling of these two sets of equations is achieved by a global subiteration strategy. During each subiteration the aerodynamic forces are updated in the structural solver and the new surface displacements are provided to the aerodynamic solver. Using this approach the temporal lag between the aerodynamic and structural equations may be eliminated and a complete synchronization of the aerodynamic/structural equation set is achieved. Any factorization or linearization errors introduced in the equations may also be eliminated using this global subiteration procedure. The resulting coupled procedure retains second order temporal accuracy.

When solving fluid/structure interactions, the aerodynamic mesh must be allowed to move in accordance with the motion of the structural surface. A simple algebraic method described in Ref. 28 deforms the aerodynamic mesh to accommodate the wing motion. This grid motion strategy has proved adequate for the wing motions considered in the present work.

V.   Results

The problem to be addressed is the simulation of a three-dimensional rectangular wing with a uniform NACA0012 cross section oscillating in water in pure heave. Water tunnel studies have been performed by Heathcote et al.[4] to study the effect of spanwise flexibility on the thrust, lift, and propulsive efficiency for this configuration. A schematic of the experimental setup is shown in Figure 2a. Three wings of 0.3-m span
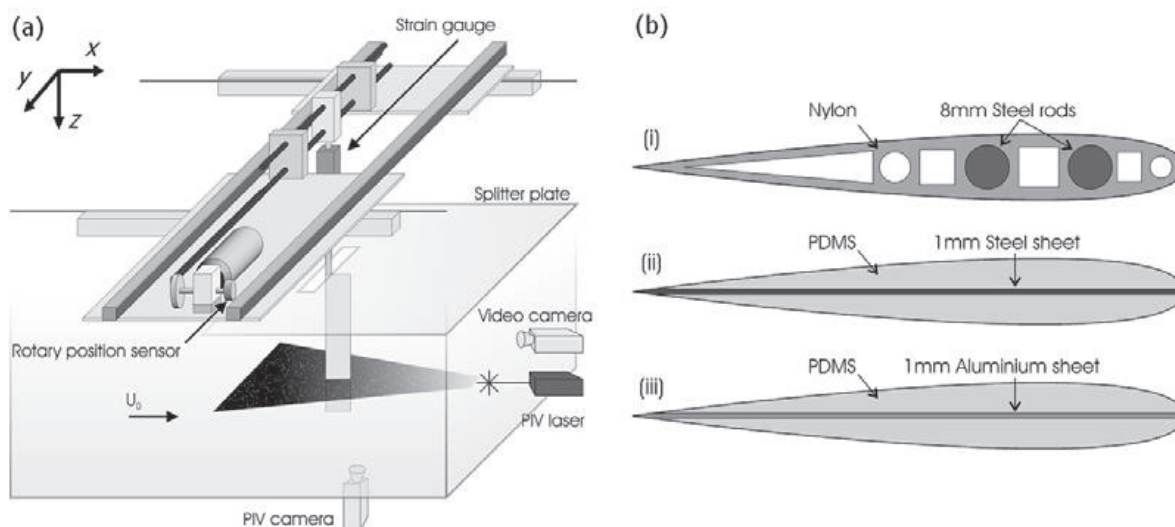

Figure 2. Experimental setup and wing cross-section.[4] (a) Water-tunnel experimental setup (b) Inflexible (i), Flexible (E=210 Gpa) (ii), and Highly flexible (E=70 Gpa) (iii) wing cross-sections

and 0.1-m chord with increasing flexibility were constructed, Fig. 2b. The leading edge at the wing root was actuated by a prescribed oscillatory plunging motion, $z = z_{root} sin(2k\,t)$, Figure 3, where z_{root} is the non-dimensional heave amplitude and $k = \frac{\omega c}{2U_\infty}$ is the reduced frequency. The cases computed in the present work specified the following values for these parameters: $k = 1.82$, period $T = 1.726$, $z_{root} = 0.175$ and Reynolds number, $Re = 3.0 \times 10^4$.

A grid system of 13 overset meshes has been developed around the NACA0012 wing for the fluid dynamic computations. The main grid for the wing is shown in Fig. 4 where every other mesh point has been removed for clarity. The main grid consist of $503 \times 355 \times 229$ mesh points in the circumferential, spanwise and normal directions respectively. The maximum spacing in the chordwise direction is $\Delta x = 0.0075$ and the minimum
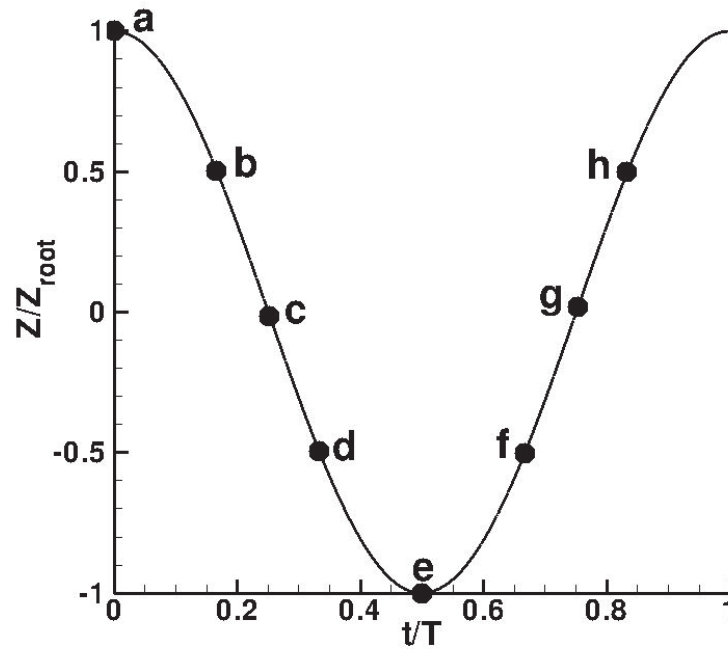
American Institute of Aeronautics and Astronautics
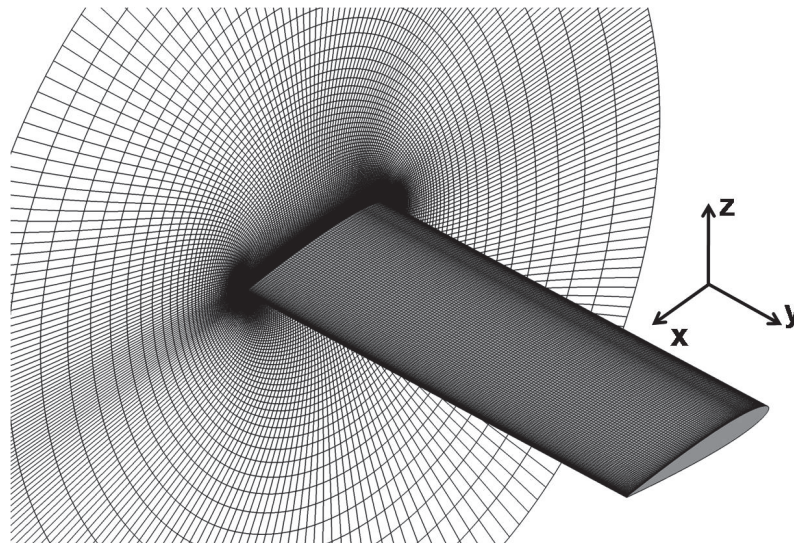
324

Approved for public release; distribution unlimited.

Figure 3. Wing Root Motion

Figure 4. Fluid dynamics grid for NACA0012 wing

American Institute of Aeronautics and Astronautics

Approved for public release; distribution unlimited.

spacing at the wall is $\Delta z = 0.0001$. In the spanwise direction a uniform spacing $\Delta y = 0.01$ is specified over the majority of the wing with the grid spacing being reduced to $\Delta y = 0.001$ at the wing tip. The main wing grid extends a quarter chord past the wing tip and 2.6 chord lengths away from the airfoil. An additional 12 overset meshes have been developed to resolve the blunt wing tip region and to extend the mesh to the farfield boundaries. These meshes are progressively coarsened in the farfield where less mesh resolution is required. The overall mesh system extends 100 chord lengths in the body normal direction and 50 chord lengths in the spanwise direction. This overset mesh system was further decomposed into 497 subdomains which were each assigned to individual processors for parallel processing.

Computations for a rigid and flexible wing structure are performed. In the rigid wing case (corresponding to the "inflexible" wing case in Heathcote et al.'s experiment[4]), the structure is considered to be infinitely stiff. For the flexible wing case a beam finite-element discretization with 39 elements along the semi-span is used. Chordwise deformation was reported as being negligible in the experiment,[4] therefore, a beam model with six elastic degrees of freedom, corresponding to extension, twist, and shear and bending in two directions, was chosen. The beam reference line (cantilevered to a plunging frame of reference) is chosen along the leading edge of the wing and cross-sectional properties are evaluated with respect to the leading edge point. Furthermore, the properties are uniform throughout the semi-span. The contribution of the PDMS rubber material (used in the experimental wing configuration) to the overall mass and stiffness properties was found to be negligible; therefore, only the stainless steel (E= 210 GPa) stiffeners (rectangular thin strip) were considered in the evaluation of cross-sectional properties (Figure 2 (b)). The 3D structural solution is obtained by using 75 recovery nodes on each cross section resulting in a structured grid of 3000 interface points which define the solid side of the aeroelastic interface.

A. Comparison with Experiment - Rigid Wing

Heathcote et al.[4] performed PIV measurements of the vortical structures in the wake of the plunging wing. Figure 5 compares the wake vortex structure for the computation, Fig. 5a, with the experimental PIV
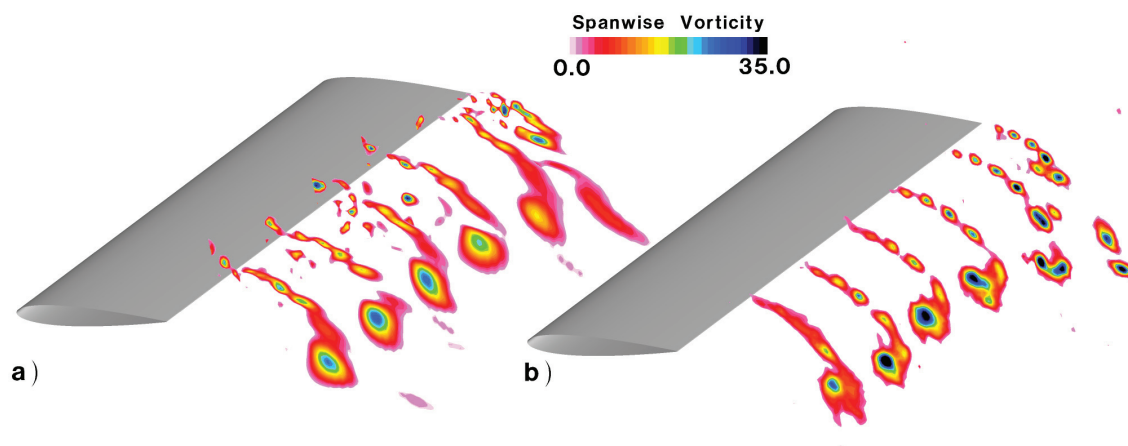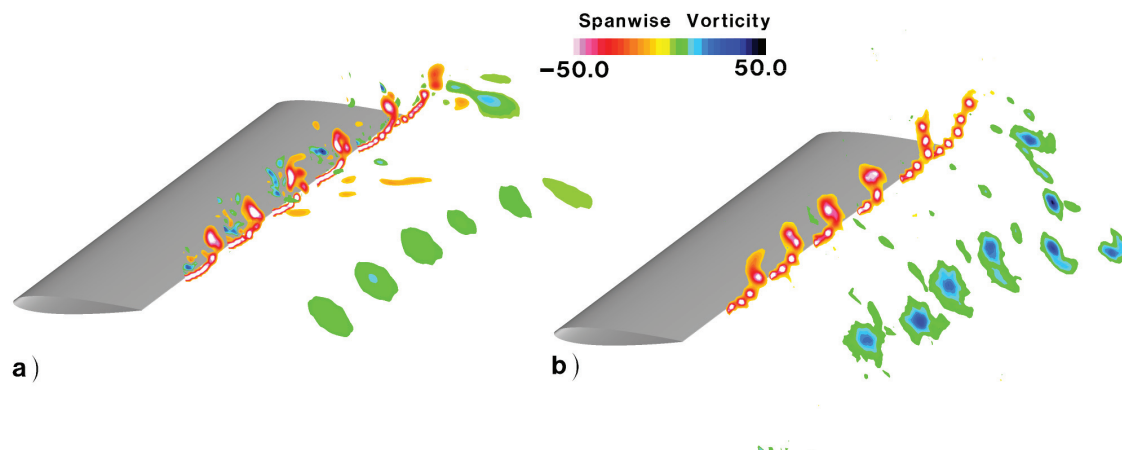

Figure 5. Comparison of wake structure at various spanwise stations at the peak of the upstroke, t/T=0.0 for the rigid wing: a) Computation, b) Experiment

measurements, Fig. 5b. Good overall agreement is seen between the experiments and computations. The computation captures the small scale structures in the wing wake as well as the general character of the shed vortical structure. The strength of the shed vortex is somewhat weaker in the computations as the vortex has already convected into a region where the grid has started to stretch. This mesh was not specifically designed to capture wake features. A second comparison is made at the midpoint of the downstroke in Figure 6. The

Figure 6. Comparison of wake structure at various spanwise stations at the midpoint of the downstroke, t/T=0.25 for the rigid wing: a) Computation, b) Experiment

high-order fluid solver has captured well both in character and strength the fine scale vortical structures being shed from the trailing edge of the wing. The previously shed vortical structure that has convected further downstream is still present in both the computation and experiment. These results demonstrate the ability of the high-order computational solver to capture the fine details of this highly unsteady flowfield.

Figure 7 plots the time histories of the thrust coefficient for both the computation and the experiment. The experimental thrust coefficient shows small differences between the thrust produced by the downstroke and the upstroke of the wing with the thrust on the downstroke exhibiting a slightly higher peak and trough. The present computations as well as previous computations by Chimakurthi et al.[6] did not show this behavior. The computed thrust agrees well with the lower thrust coefficient peaks produced during the upstroke in the experiment.

The computed lift coefficient time history for the rigid wing plunge case is compared with inviscid theory[29] in Figure 8. Good agreement is seen between the inviscid theory and the current computations. This can be explained by the fact that for this high value of reduced frequency ($k = 1.82$) the magnitude of the lift coefficient is dominated by the acceleration of the airfoil (noncirculatory lift, Figure 8) which scales with k^2. The circulatory term primarily gives rise to the lag observed in the lift coefficient time history. Similar results have been shown by Visbal[8] for a plunging airfoil.

B. Comparison with Experiment - Flexible Wing

For the flexible wing case the time history of the computed wing tip deflection agrees well with the experimentally measured deflection, Figure 9. The maximum computational deflection, $z/z_{root} = 1.59$, matches
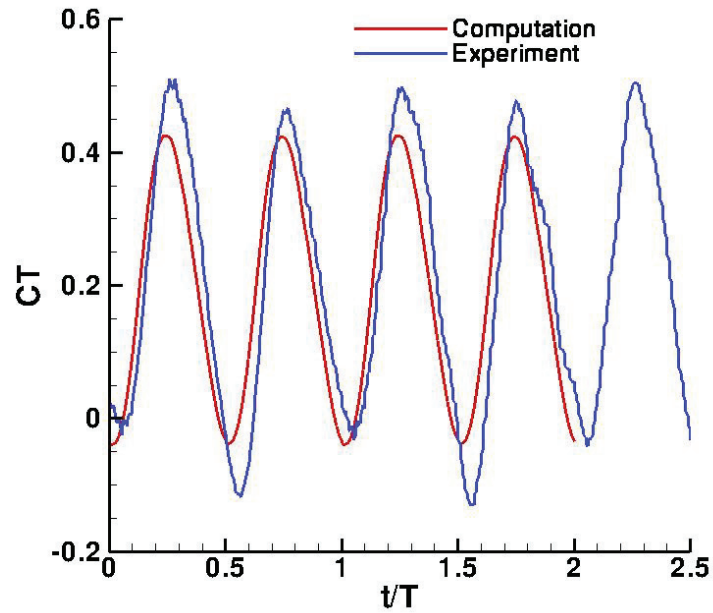
American Institute of Aeronautics and Astronautics

Figure 7. Comparison of the experimental and computational time histories of the thrust coefficient for the rigid wing

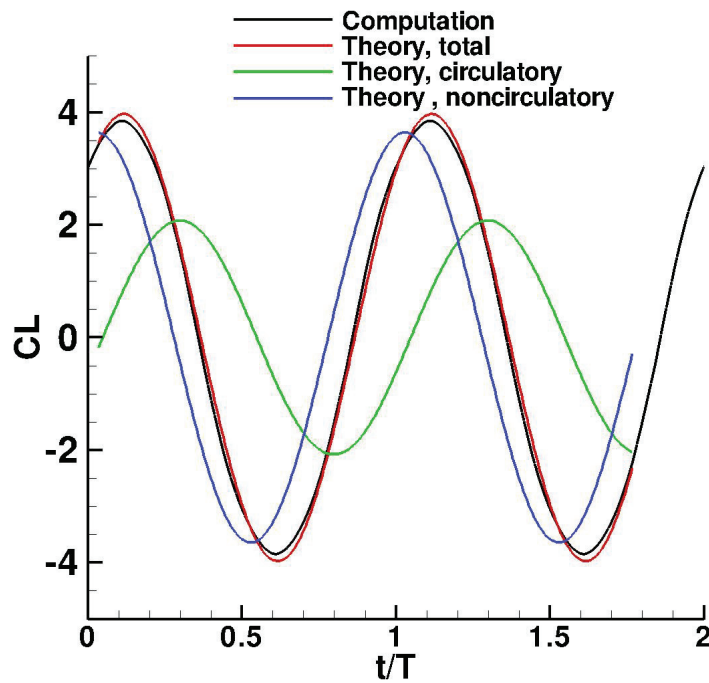**Figure 8. Comparison of the lift coefficient with theory[29] for the rigid wing**

American Institute of Aeronautics and Astronautics
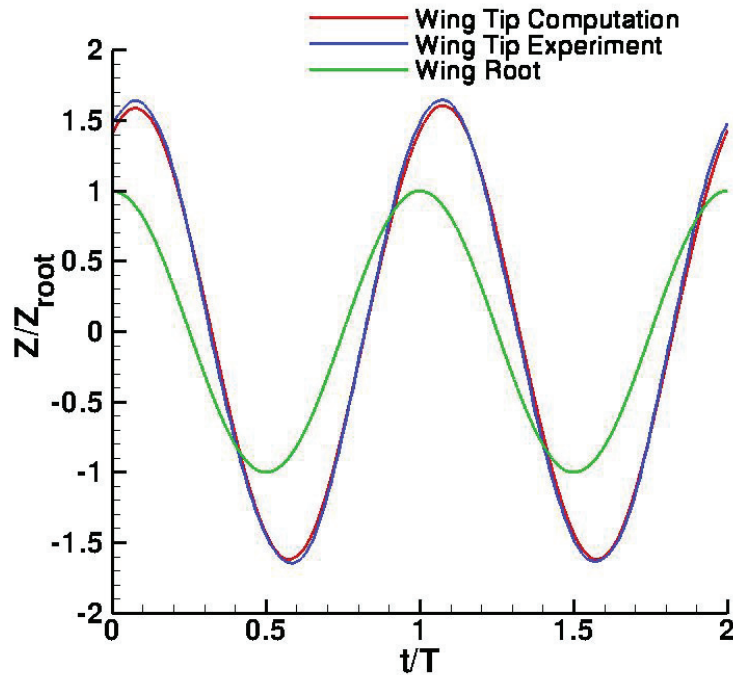
Approved for public release; distribution unlimited.

Figure 9. Comparison of the computed wing tip displacement with experiment for the flexible wing

within 3% the maximum experimental wing tip deflection, $z/z_{root} = 1.64$. A negative phase lag is observed in both the experiment and the computation with the experimental value $\phi = -25.1°$ being close to the computational value $\phi = -27.2°$. This good agreement between the computation and experiment indicates that the structural model adequately represents the structural dynamics of the flexible wing.

Figures 10 and 11 demonstrate the good agreement between the computed and experimentally measured wake vortical structures as in the rigid case. At each time instant the computation has reproduced the general character of the shed vortical structure. In addition the fine scale vortical features in the separated shear layer are also replicated in the computations.

The resulting experimental and computational thrust coefficient time histories are plotted in Figure 12. As in the rigid wing case, the experimental thrust coefficient shows larger peaks during the downstroke and smaller peaks during the upstroke of the plunging wing. This difference between the downstroke and upstroke is not observed in the computation which exhibits a more symmetric response between the downstroke and upstroke. The computations agree more closely with the thrust produced on the upstroke in the experiment though the maximum thrust produced is less.

C. Effect of Flexibility - Wing Flowfield

As was seen in Figure 9, the flexible wing exhibits a significant deflection at the wing tip due to the inherent flexibility of the structure and this deflection lags the imposed plunging motion at the wing root. This results in a spanwise variation in the deflection of the wing, Figure 13, as well as the development of a spanwise variation in the effective angle of attack, Fig. 14, which results from the velocity of the wing surface, $\alpha_{eff} = tan^{-1}(-\frac{dz}{dt}/U_\infty)$. Figure 15 demonstrates the impact of these effects on the global flowfield development on the upper surface of the wing. In this figure isosurfaces of vorticity magnitude are plotted with the isosurfaces being colored by the pressure coefficient. Figures 15 a-h correspond to the points a-h on the plunge cycle in Figure 3. Corresponding surface pressure coefficient contours on the upper surface are displayed in Figures 16 a-h. Due to the relatively symmetric response between the downstroke and the upstroke of the wing in the computation an understanding of the flow on the under surface of the wing can
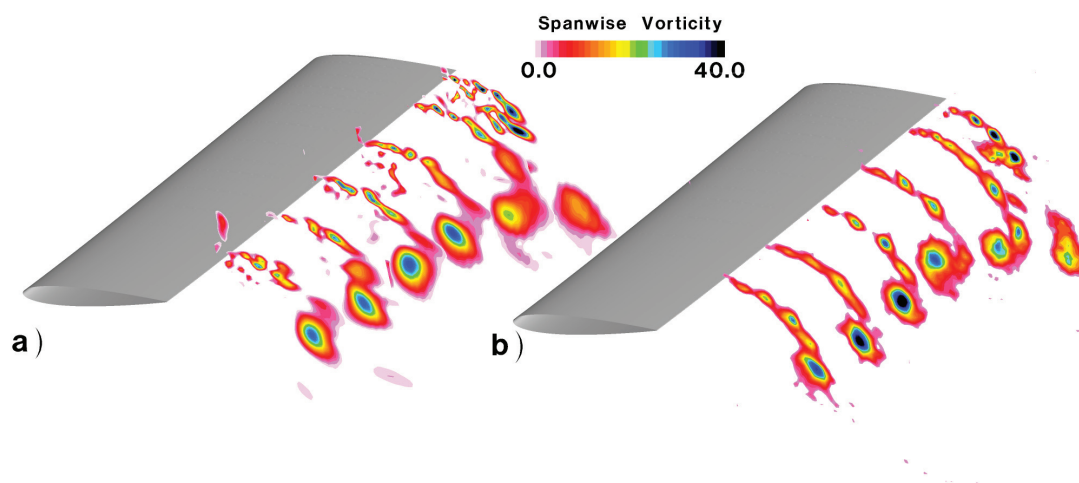
American Institute of Aeronautics and Astronautics

Approved for public release; distribution unlimited.

Figure 10. Comparison of wake structure at various spanwise stations at the peak of the upstroke, t/T=0.0 for the flexible wing: a) Computation, b) Experiment
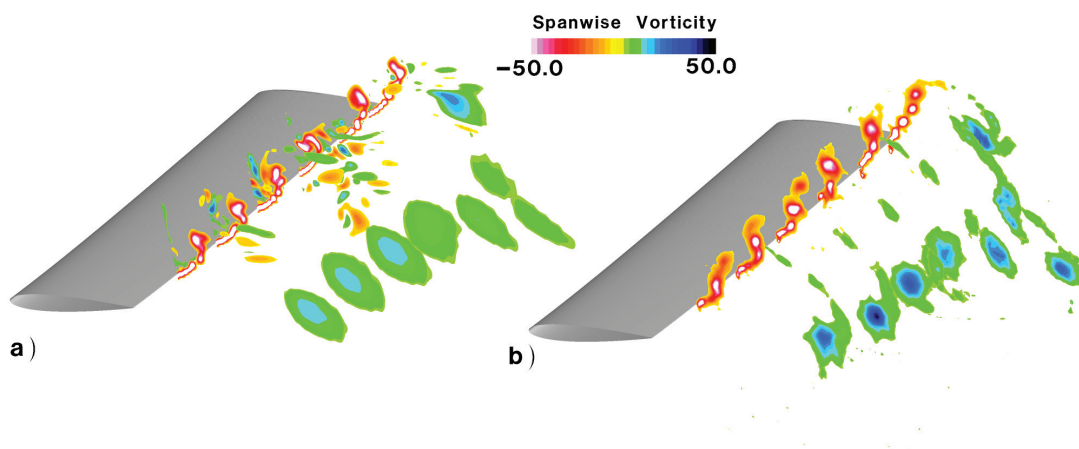

Figure 11. Comparison of wake structure at various spanwise stations at the midpoint of the downstroke, t/T=0.25 for the flexible wing: a) Computation, b) Experiment
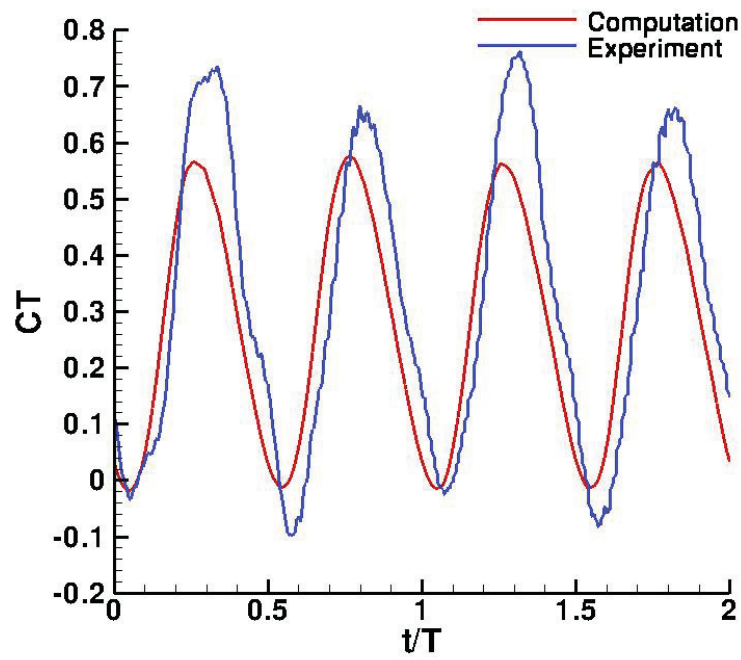
American Institute of Aeronautics and Astronautics

330

Approved for public release; distribution unlimited.

Figure 12. Comparison of the experimental and computational time histories of the thrust coefficient for the flexible wing

American Institute of Aeronautics and Astronautics

331

Approved for public release; distribution unlimited.
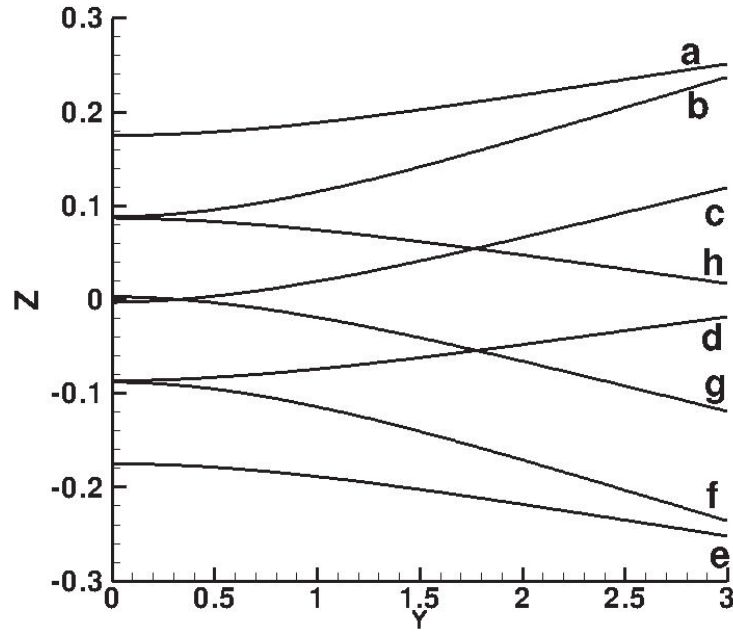
Figure 13. Spanwise deflection of the wing leading edge at points (a)-(h) in the plunge cycle, Fig. 3
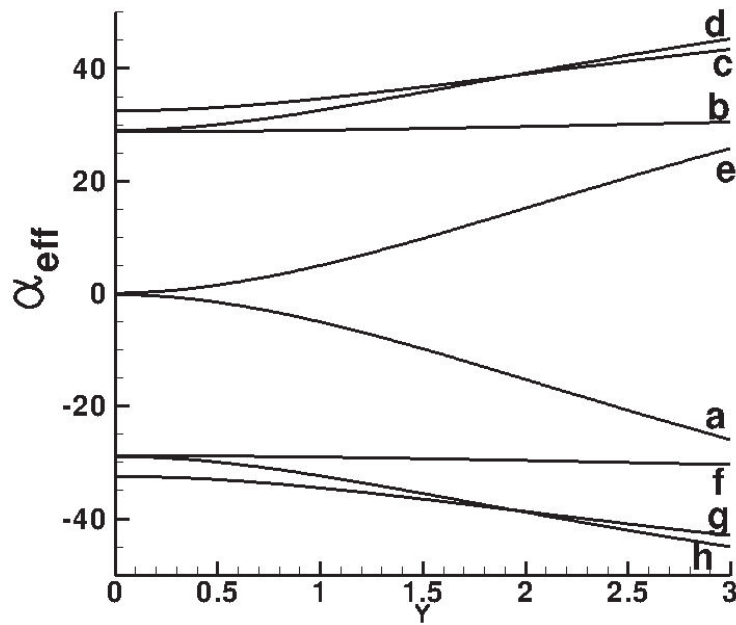
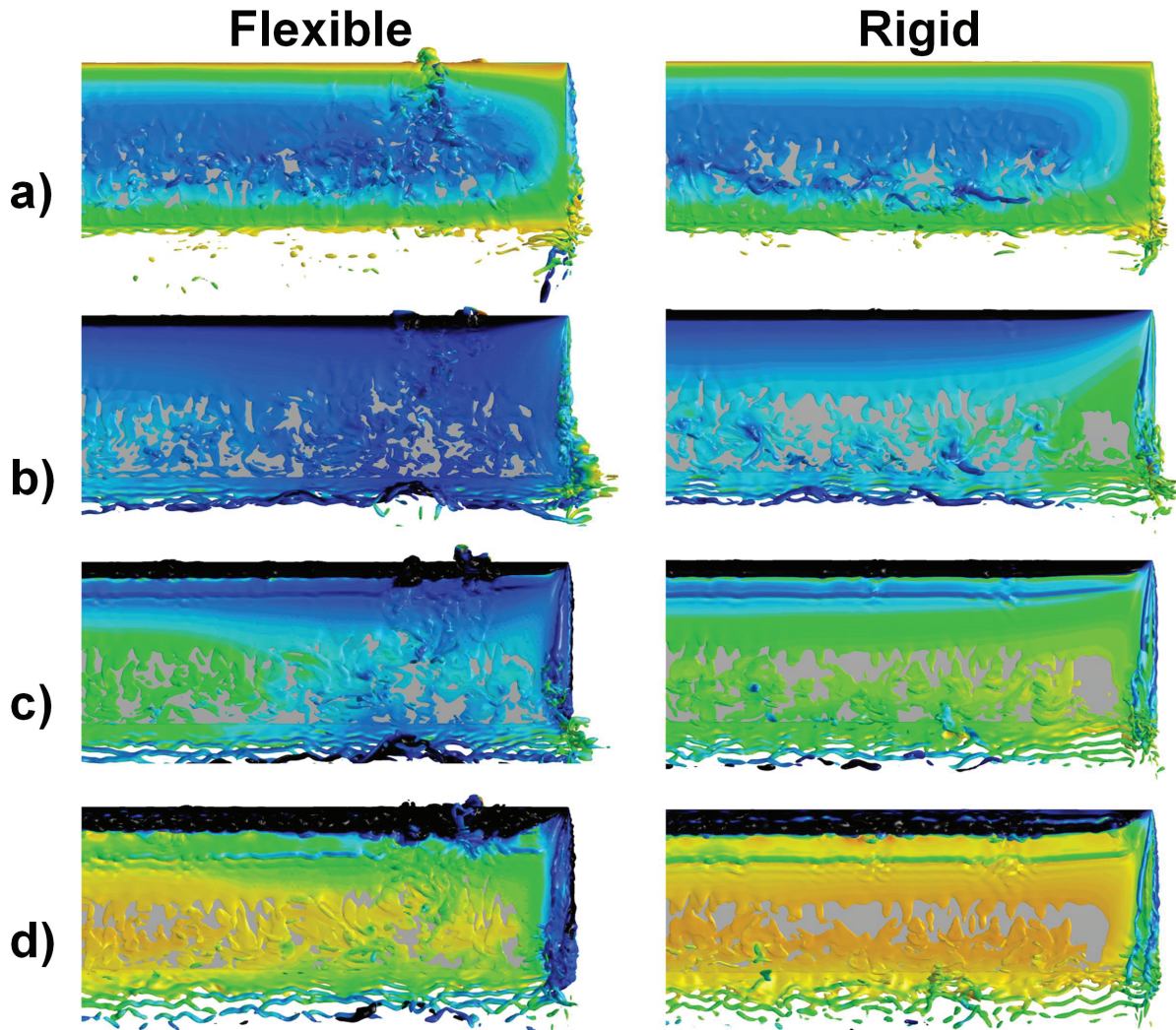**Figure 14. Spanwise variation of the effective angle of attack at points (a)-(h) in the plunge cycle, Fig. 3**

Approved for public release; distribution unlimited.

Figure 15. Comparison of Flow Structure (Isosurfaces of Vorticity Magnitude Colored by Pressure Coefficient) on the Wing Upper Surface for the Rigid and Flexible Cases

American Institute of Aeronautics and Astronautics

333

Approved for public release; distribution unlimited.
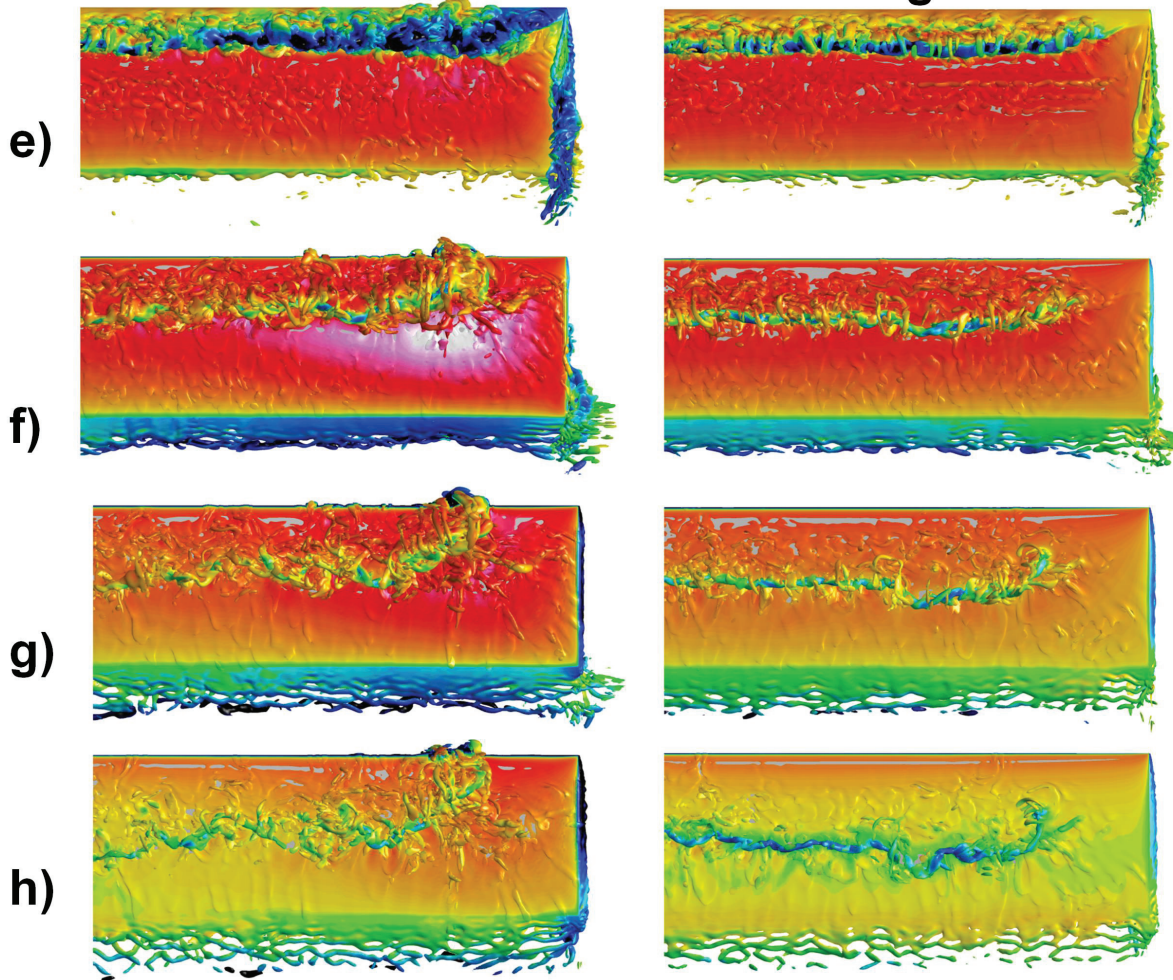
Figure 15. continued

be obtained by matching (a-d) for the topside with (e-h) for the bottomside in Figures 15 and 16 for the downstroke and viceversa for the upstroke.

At the top of the plunge cycle, Figure 15a, only minor differences between the rigid and flexible wing flowfields are observed. For the rigid wing distinct remnants of the previously shed leading edge vortex may still be seen near the trailing edge. For the flexible wing only dispersed small scale structures are seen except outboard on the wing where a concentrated region of small scale structures is observed. The presence of this feature will be discussed subsequently. The flexible wing exhibits higher pressure at the leading edge which results from the increasingly negative effective angle of attack towards the wing tip, Fig. 14.

During the downward plunging motion of the wing, the flowfield on the upper surface is characterized by the development of two features, the leading edge vortex and the tip vortex, Figures 15a-e. The rigid wing flowfield exhibits a fairly two-dimensional development except in the region very near the tip where the leading edge vortex is pinned to the wing tip leading edge. In contrast the flexible wing flowfield shows notable spanwise variation and distinct differences from the rigid wing. The leading edge vortex that develops increases in strength outboard on the wing due to the increase in effective angle of attack, Figure 14. This results in lower values of pressure underneath this vortex than what is obtained on the rigid wing. The wing tip vortices are also stronger for the flexible wing, Figures 15c-e. A corresponding low pressure band develops underneath the tip vortex, Figures 16c-e.
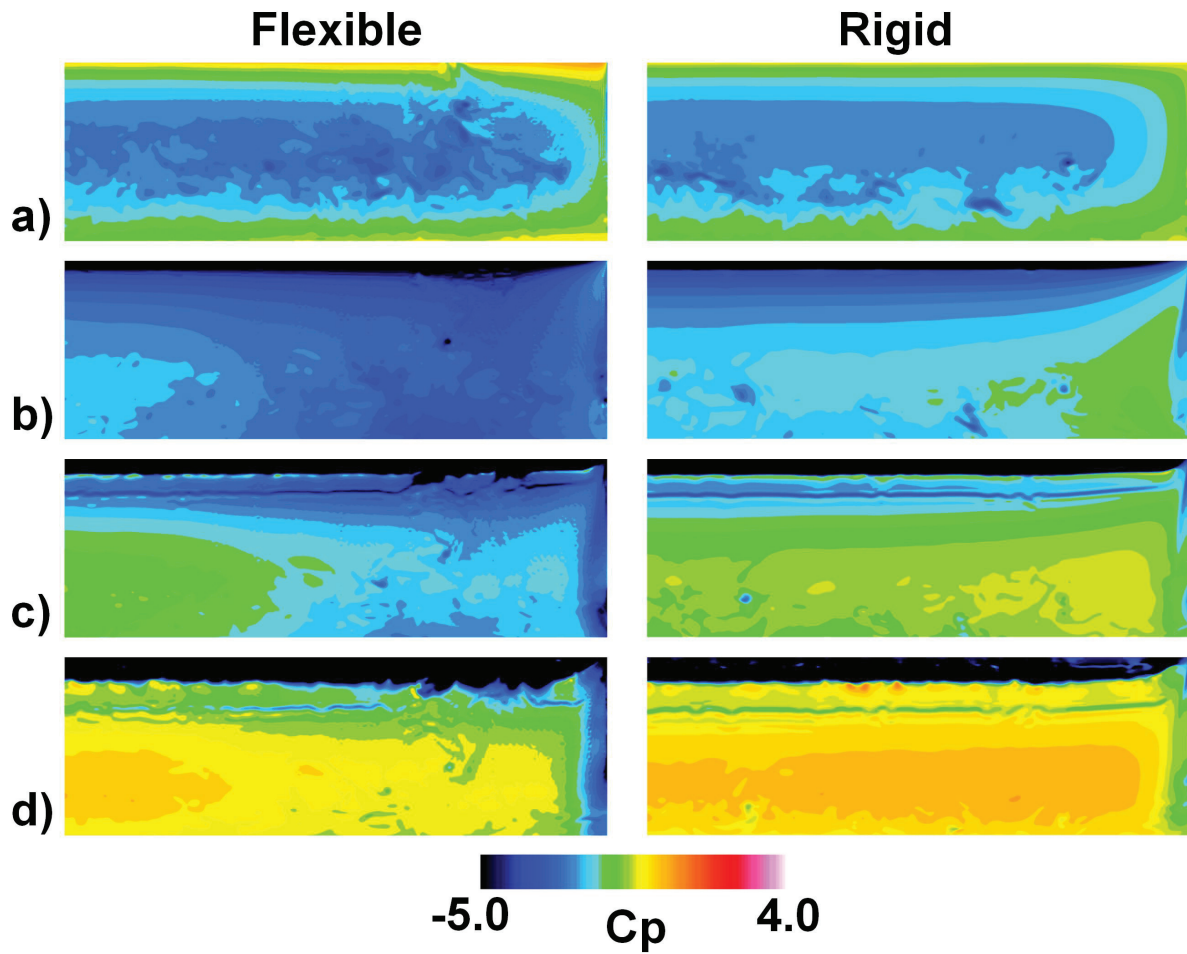
American Institute of Aeronautics and Astronautics

Approved for public release; distribution unlimited.

Flexible   **Rigid**

Figure 16. Comparison of Surface Pressure Coefficient on the Wing Upper Surface for the Rigid and Flexible Cases

Flexible **Rigid**
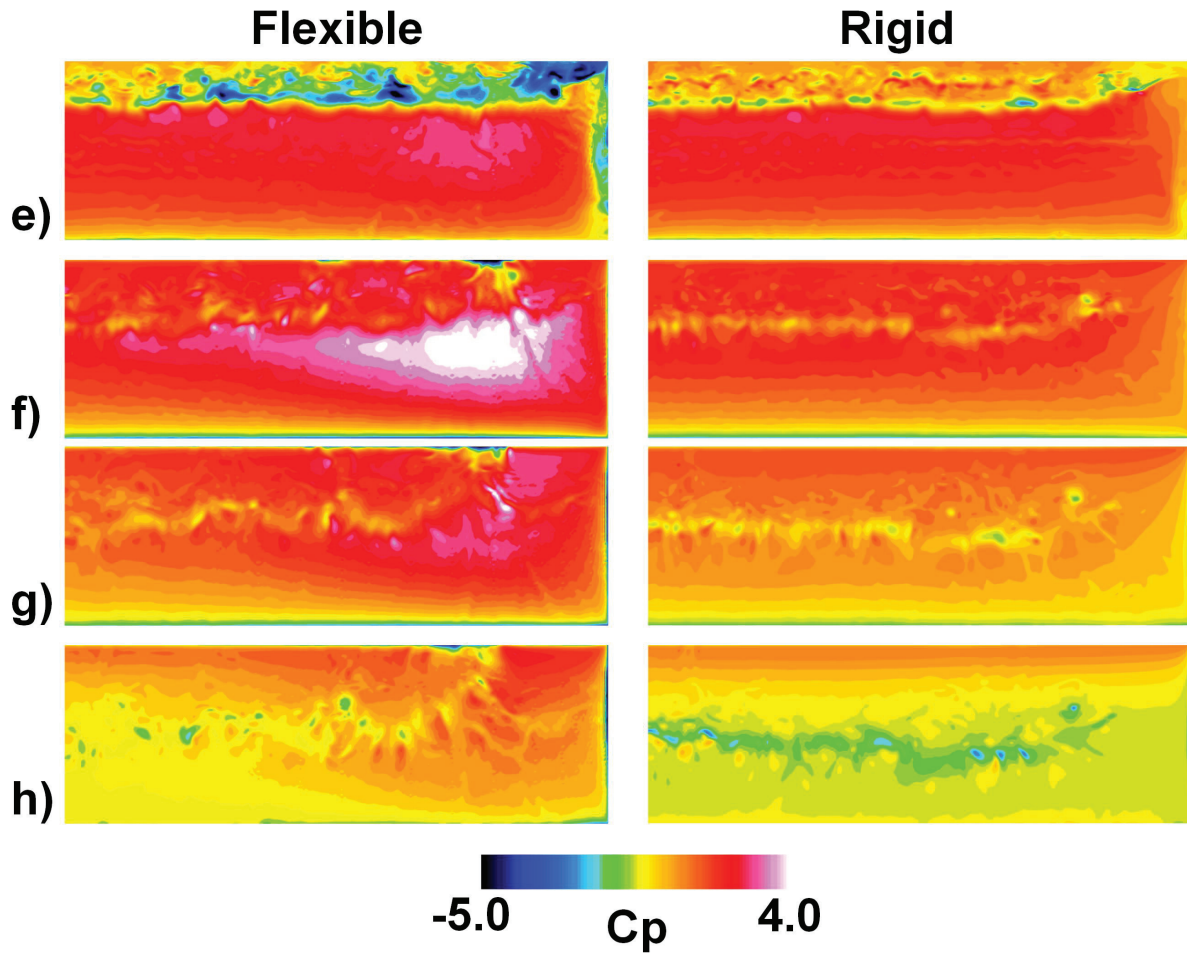
e)

f)

g)

h)

-5.0 Cp 4.0

Figure 16. continued

During the downstroke a laminar leading edge vortex system emerges on the upper surface, Figures 15b,c. As the wing moves from the midstroke to the bottom of the plunge motion, Figures 15c-e, this laminar vortex system undergoes flow transition with a fully transitional flow present at the bottom of the downstroke. A detailed description of this type of transition process for a typical wing section undergoing plunging motion may be found in Visbal.[8] This transition process is enhanced for the flexible wing where the leading edge vortex is strengthened due to the larger effective angle of attack on the outboard portion of the wing, Fig. 14.

As the wing slows and reverses direction, the leading-edge vortex is shed convects downstream, Figs. 15e-h and 16e-h. The vortex on the rigid wing tends to remain fairly intact and two-dimensional until it approaches the trailing edge, Figures 15h,a. In contrast, the leading edge vortex on the flexible wing tends to break apart and be much more three-dimensional in character. Outboard on the flexible wing at $y \approx 2.22$ a large region of turbulent flow exists at the terminus of the leading edge vortex, Figure 15f. This region of turbulent flow persists in leading edge region during the full upstroke of the wing and is only convected downstream after the wing commences the downstroke. This interesting behavior develops due to the large motion-induced negative pitch down that occurs for the flexible wing in this region. Figure 17 compares the time histories of the effective angle of attack for the rigid and flexible wings. During the portion of the wing upstroke from points (e, $t/T = 0.5$) to (h, $t/T = 0.83$) the flexible wing undergoes a more severe pitch down motion than the rigid wing from $\alpha_{eff} = 24.5°$ to $\alpha_{eff} = -45°$. This rapid pitch down restricts the vorticity from propagating downstream. This feature is reminiscent of the flow behavior observed by Visbal[8] for high frequency low amplitude plunge oscillations of a wing section.

A distinct high pressure zone is also noted on the flexible wing during the upstroke, Fig. 16f. This
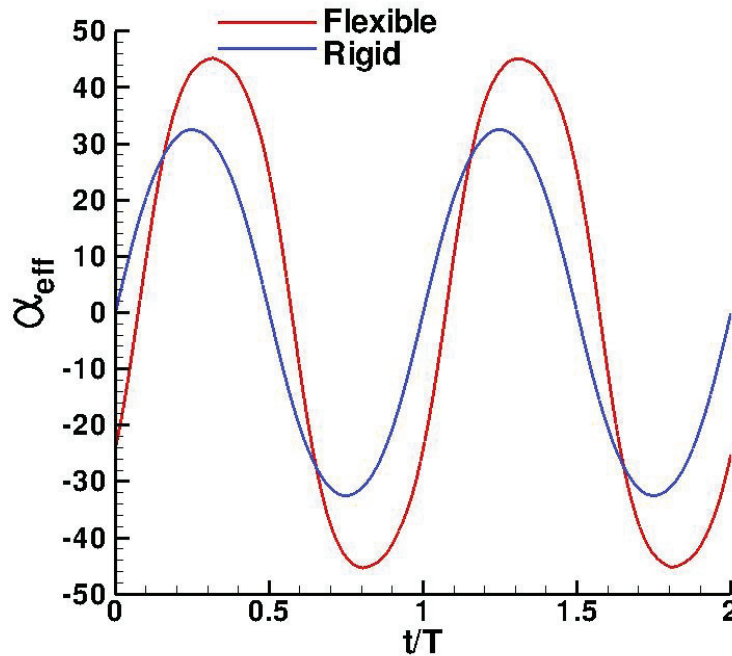
American Institute of Aeronautics and Astronautics

Approved for public release; distribution unlimited.

Figure 17. Temporal variation in the effective angle of attack at the wing tip for the rigid and flexible wings

phenomena arises predominantly from the large deceleration and reversal of direction of the wing. Figure 18 compares the acceleration at the wing tip for the rigid and flexible cases. The peak acceleration, $d^2z/dt^2 = 3.95$, occurs at $t/T = 0.59$ and is 1.7 times the peak acceleration observed for the rigid case, $d^2z/dt^2 = 2.32$. These markedly higher accelerations as a result of the wing flexibility create greater noncirculatory effects (see Figure 8). This increase in the noncirculatory behavior results in the development of these higher pressure regions. Equivalent lower pressures outboard on the undersurface, Figure 16b, are also observed.

VI.   Effect of Flexibility - Forces and Moments

The experimental measurements of Heathcote[4] demonstrated that the limited flexibility in the case computed in the present paper produced an enhanced thrust coefficient. This effect is reproduced in these computations and is shown in Figure 19. The mean thrust generated increases from $CT_{mean} = 0.195$ for the rigid wing to $CT_{mean} = 0.278$ for the flexible wing, an increase of 42%. This is consistent with the experimentally reported increase in thrust of 50%. The peak thrust generation and the corresponding maximum difference between the thrust for the rigid and flexible wing occurs over the midportion of the downstroke and upstroke. This corresponds to the portion of the motion where the formation of the leading edge vortex occurs. As discussed previously, flexibility of the wing leads to the formation of a stronger leading edge vortex which in turn leads to higher suction levels around the leading edge of the airfoil and therefore higher thrust.

Enhanced lift is also obtained due to the flexibility of the wing. Figure 20 displays the time histories of the lift coefficient for the rigid and flexible wings. The peaks in the lift time histories correlate with the locations of maximum peak accelerations, Figure 18. The higher peak lift in the flexible case is consistent with the significantly larger peak accelerations. These greater accelerations give rise to stronger noncirculatory loads that arise from the previously described high and low pressure zones.

The impact of flexibility on the moment coefficients about the quarter chord point is also investigated. The rolling moment (considering only the half-wing computed) and pitching moment are plotted in Figures 21

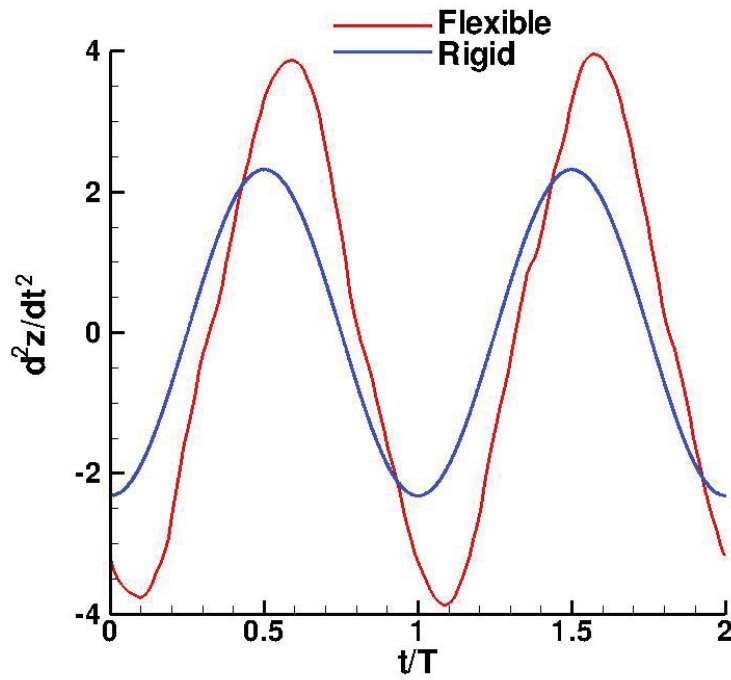Approved for public release; distribution unlimited.

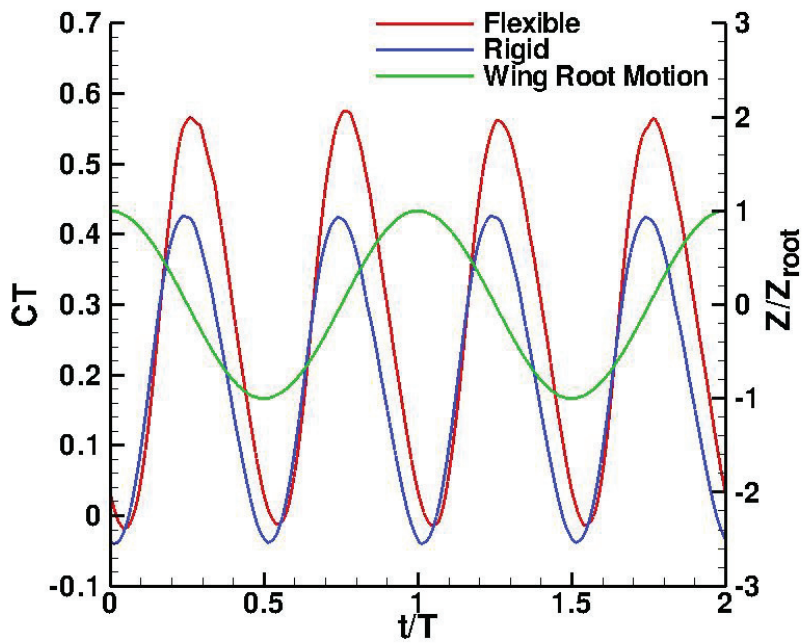Figure 18. Temporal variation of acceleration at the wing tip for the rigid and flexible wings

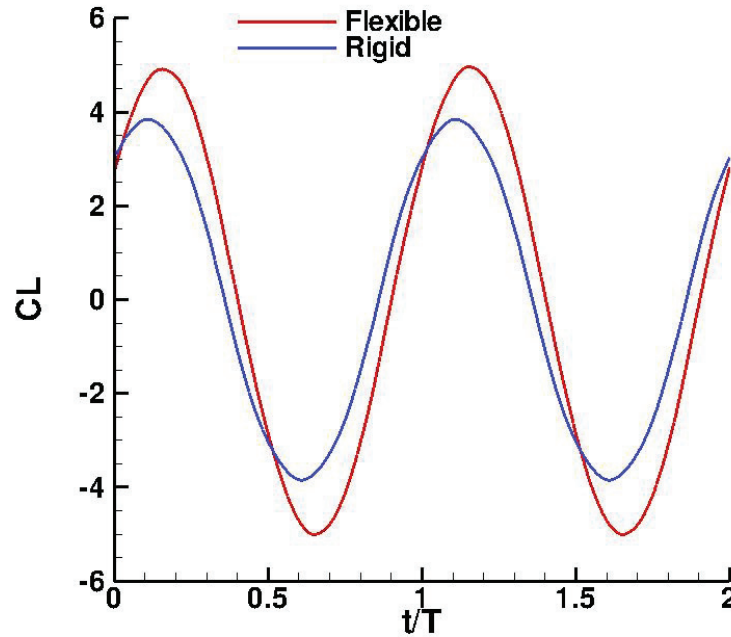Figure 19. Effect of Flexibility on Generated Thrust Coefficient

Figure 20. Effect of Flexibility on Generated Lift Coefficient

and 22 respectively. Both the pitch and roll moment coefficient vary with the same frequency but lag the plunge motion. The flexible wing has higher peak values of both the rolling and pitching moment that occur during the initial portion of the upstroke and downstroke. The enhancement of these moments is associated with the development of the high pressure zone seen in Fig. 16f and a corresponding lower pressure on the opposite surface, Fig. 16b. The yawing moment (again only for the half-wing computed), Figure 23, exhibits a frequency similar to the thrust coefficient. As in the case of the thrust coefficient, the higher values of yawing moment in the flexible case are attributable to the strengthening of the leading edge vortex due to the increased effective angle of attack that results from the flexibility of the wing.

VII.   Conclusions

High fidelity computations for a rigid and plunging flexible wing have been performed. The computational solver used couples a high-order Navier-Stokes solver with a geometrically nonlinear structural solver based on the dynamics of a general three-dimensional anisotropic slender solid. Computed results are compared with available experimental measurements demonstrating good agreement between the computation and experiment.

The longitudinal flexibility of the wing gives rise to significant spanwise variations in the wing deflection, motion-induced effective angle of attack and wing acceleration. These effects produce a complex interaction between the vortex dynamics and the structural motion. The higher effective angles of attack achieved result in the development of a stronger leading edge vortex system outboard on the flexible wing. Outboard towards the tip of the wing the more rapid effective pitch down and pitch up motions in the flexible case inhibit the convection of the leading edge vorticity. The larger wing accelerations associated with the flexible wing produce corresponding regions of higher and lower pressure on the wing upper and lower surfaces due inviscid effects.

The spanwise variation and increased strength of the leading edge vortex system in the flexible case produces enhanced thrust as well as larger yawing moments. Increased noncirculatory loads due to the
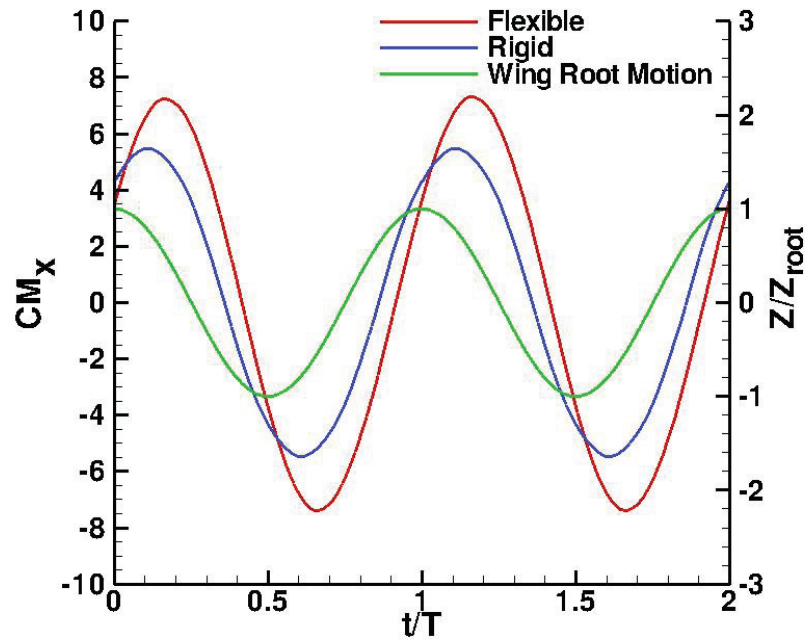
American Institute of Aeronautics and Astronautics

Approved for public release; distribution unlimited.

Figure 21. Effect of Flexibility on Rolling Moment Coefficient
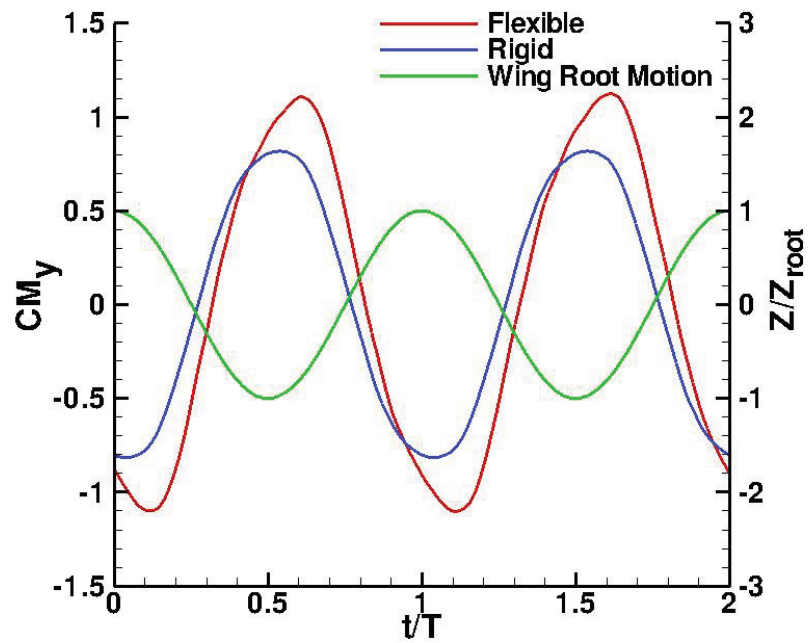
Figure 22. Effect of Flexibility on Pitching Moment Coefficient

American Institute of Aeronautics and Astronautics

340

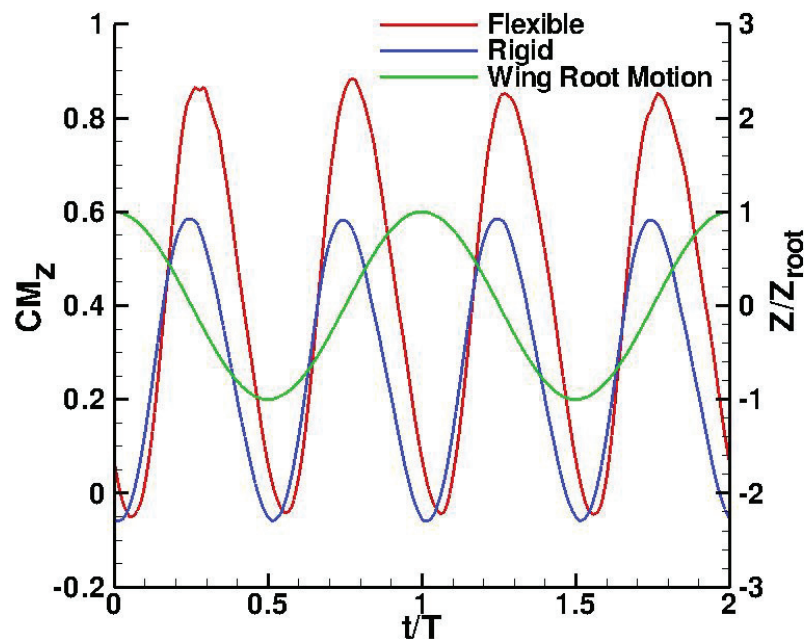Approved for public release; distribution unlimited.

Figure 23. Effect of Flexibility on Yawing Moment Coefficient

larger values of acceleration achieved by the flexible wing result in higher peak lift, rolling moment and pitching moment coefficients.

VIII. Acknowledgments

References

[1]Shyy, W., Lian, Y., Tang, J., Viieru, D., and Liu, H., *Aerodynamics of Low Reynolds Number Flyers*, Cambridge University Press, New York, 2008.

[2]Mueller, T. J., *Fixed and Flapping Wing Aerodynamics for Micro Air Vehicle Applications*, Vol. 195 of *Progress in Aeronautics and Astronautics*, AIAA, New York, 2001.

[3]Shyy, W., Ifju, P., and Viieru, D., "Membrane Wing-Based Micro Air Vehicles," *Applied Mechanics Review*, Vol. 58, No. 1-6, 2005, pp. 283–301.

[4]Heathcote, S., Wang, Z., and Gursul, I., "Effect of Spanwise Flexibility on Flapping Wing Propulsion," *Journal of Fluids and Structures*, Vol. 24, No. 2, 2008, pp. 183–199.

[5]Tang, J., Chimakurthi, S., Palacios, R., Cesnik, C. E. S., and Shyy, W., "Computational Fluid-Structure Interaction of a Deformable Flapping Wing for Micro Air Vehicle Applications," AIAA-2008-0615, January 2008.

[6]Chimakurthi, S., Tang, J., Palacios, R., Cesnik, C. E. S., and Shyy, W., "Computational Aeroelasticity Framework for Analyzing Flapping Wing Micro Air Vehicles," *AIAA Journal*, Vol. 47, No. 8, 2009, pp. 1865–1878.

[7]Aono, H., Chimakurthi, S., , Cesnik, C. E. S., Liu, H., and Shyy, W., "Computational Modeling of Spanwise Flexibility

Effects on Flapping Wing Aerodynamics," AIAA-2009-1270, January 2009.

[8]Visbal, M. R., "High-Fidelity Simulation of Transitional Flows Past a Plunging Airfoil," *AIAA Journal*, Vol. 47, No. 11, November 2009, pp. 2685–2697.

[9]Gordnier, R. E., "Implicit LES Simulations of a Low Reynolds Number Flexible Memrane Wing Airfoil," AIAA-2009-0579, January 2009.

[10]Anderson, D., Tannehill, J., and Pletcher, R., *Computational Fluid Mechanics and Heat Transfer*, McGraw-Hill Book Company, 1984.

[11]Lele, S., "Compact Finite Difference Schemes with Spectral-like Resolution," *Journal of Computational Physics*, Vol. 103, 1992, pp. 16–42.

[12]Gaitonde, D. and Visbal, M., "High-Order Schemes for Navier-Stokes Equations: Algorithm and Implementation into FDL3DI," Tech. Rep. AFRL-VA-WP-TR-1998-3060, Air Force Research Laboratory, Wright-Patterson AFB, 1998.

[13]Visbal, M. and Gaitonde, D., "High-Order Accurate Methods for Unsteady Vortical Flows on Curvilinear Meshes," *AIAA Paper 98-0131*, January 1998.

[14]Gaitonde, D., Shang, J., and Young, J., "Practical Aspects of High-Order Accurate Finite-Volume Schemes for Electromagnetics," *AIAA Paper 97-0363*, Jan. 1997.

[15]Visbal, M. and Gaitonde, D., "High-Order Accurate Methods for Complex Unsteady Subsonic Flows," *AIAA Journal*, Vol. 37, No. 10, 1999, pp. 1231–1239.

[16]Alpert, P., "Implicit Filtering in Conjunction with Explicit Filtering," *J. Comp. Phys.*, Vol. 44, 1981, pp. 212–219.

[17]Gaitonde, D. and Visbal, M., "Further Development of a Navier-Stokes Solution Procedure Based on Higher-Order Formulas," *AIAA Paper 99-0557*, January 1999.

[18]Beam, R. and Warming, R., "An Implicit Factored Scheme for the Compressible Navier-Stokes Equations," *AIAA Journal*, Vol. 16, No. 4, 1978, pp. 393–402.

[19]Jameson, A., Schmidt, W., and Turkel, E., "Numerical Solutions of the Euler Equations by a Finite Volume Method Using Runge-Kutta Time Stepping Schemes," *AIAA Paper 81-1259*, 1981.

[20]Pulliam, T., "Artificial Dissipation models for the Euler Equations," *AIAA*, Vol. 24, No. 12, 1986, pp. 1931–1940.

[21]Pulliam, T. and Chaussee, D., "A Diagonal Form of an Implicit Approximate-Factorization Algorithm," *Journal of Computational Physics*, Vol. 39, No. 2, 1981, pp. 347–363.

[22]Visbal, M. R., Morgan, P. E., and Rizzetta, D. P., "An Implicit LES Approach Based on High-Order Compact Differencing and Filtering Schemes (Invited)," AIAA-2003-4098, June 2003.

[23]Visbal, M. and Gaitonde, D., "Very High-Order Spatially Implicit Schemes for Computational Acoustics on Curvilinear Meshes," *Journal of Computational Acoustics*, 2001.

[24]Palacios, R. and Cesnik, C. E. S., "A Geometrically Nonlinear Theory of Active Composite Beams with Deformable Cross Sections," *AIAA Journal*, Vol. 46, No. 2, 2008, pp. 439–450.

[25]Palacios, R. and Cesnik, C. E. S., "Cross-Sectonal Analysis of Non-homogenous Anistropic Active Slender Structures," *AIAA Journal*, Vol. 43, No. 12, 2005, pp. 2624–2638.

[26]Cesnik, C. E. S. and Hodges, D. H., "VABS: A New Concept for Composite Rotor Blade Cross-Sectional Modeling," *Journal of the American Helicopter Society*, Vol. 42, No. 1, 1997, pp. 27–38.

[27]Smith, M. J., Hodges, D., and Cesnik, C. E. S., "Evaluation of Computational Algorithms Suitable for Fluid-Structure Interactions," *Journal of Aircraft*, Vol. 37, No. 2, 2000, pp. 282–294.

[28]Melville, R. B., Morton, S. A., and Rizzetta, D. P., "Implementation of a Fully-Implicit, Aeroelastic Navier-Stokes Solver," AIAA 97-2039, June 1997.

[29]Fung, Y., *An Introduction to the Theory of Aeroelasticity*, Dover, 1993.

American Institute of Aeronautics and Astronautics

Approved for public release; distribution unlimited.